



**Adama Science and Technology University**  
**Research and Centers of Excellence Directorate**

---

---

## **Proceedings of the Third National Research Symposium**

*“Emerging Technologies for Building Green Economy”*

---

---



**May 24 – 25, 2024**

**Adama, Ethiopia**



## Organizing Committee

**Dr. Alemu Disassa (Chairperson)**

**Dr. Yadeta Chimdessa (Secretary)**

**Dr. Alemayehu Wakjira**

**Dr. Shimeles Lemma**

**Dr. Getinet Asrat**

**Dr. Dinsefa Mensur**

**Dr. Esmael Adem**

**Dr. Belay Brehane**

**Dr. Temesgen Debelo**

**Dr. Getachew Alemayehu**

**Dr. Andinet Kebede**

**Dr. Perumalla Janaki**

**Dr. Alemu Gizaw**

**Dr. P. SelveKumar**

**Dr. Ashenafi Hailu**

**Mr. Bejiga Yadecha**

**Mr. Mengistu Gelaw**

**Mr. Kuma Waktole**

**Miss Soreme Dirba**

**Mr. Simon Mekonen**

## Main Theme of the Symposium

**Emerging Technologies for Building Green Economy**

## Sub-Themes of the Symposium

❖ **Emerging Technology**

❖ **Manufacturing and Infrastructure**

❖ **Energy**

❖ **Natural Resources Management  
and Environment**

**Organized by:**

**Office of Vice President for Research and Technology Transfer  
Research and Centers of Excellence Directorate**

**Hosted by:**

**School of Mechanical, Chemical and Materials Engineering  
Office of Associate Dean for Research and Technology Transfer**



Copyright © 2024, Adama Science and Technology University. All Rights Reserved.

### **Disclaimer**

Adama Science and Technology University is not responsible for the contents reflected in the articles published in the proceedings of this National Research Symposium. The contents of this document are solely the responsibility of the authors.

The proceedings or any part(s) cannot be reproduced in any form without written permission from the University.

Inquires should address to:  
Research and Centres of Excellence Directorate  
Adama Science and Technology University  
P.O.Box 1888, Adama, Ethiopia  
Tel: +251-22-211-1797



## Table of Contents

Subject	Page
Preface	i
Message from the Organizing Committee	ii
Welcoming Address	iii
Opening Speech	v
Keynote Address	vii
Plenary Sessions	vii
<b>Syndicate 1</b>	<b>1</b>
The effect of cycling protocol and electrolyte on fast charging/discharging of anode-free Li-metal batteries <i>Tamene Tadesse Beyenea, Wei-Nien Su, Hongjie Dai, Bing-Joe Hwang</i>	2
Biofuel potential and invasive species control: exploring Prosopis juliflora pod mash for sustainable energy production <i>Mebrahtu Haile, Hadgu Hishe, Desta Gebremedhin</i>	17
Hetero-nanostructures for sustainable energy application via plasmon-enhanced photo/electrocatalysis <i>Lemma Teshome Tufa, Birhanu Bayissa Gicha, Cheru Fekadu Molla, Jaebeom Lee</i>	28
Estimation of abattoir waste for bio-energy as sustainable management in Eastern Ethiopia <i>Sina Temesgen, Fekade Ketema</i>	38
Butanolysis of Jatropha oil using glycerol enriched non-calcined calcium oxide: optimization of the process <i>Yadessa Gonfa Keneni, Jorge Mario Marchetti</i>	49
Implementation of non-axisymmetric moving heat source modeling in disc geometry and material selection <i>Kejela Temesgen Deressa, Demiss Alemu Ambie</i>	64
Synthesis and characterization of pores bioactive glass nanomaterials for bone tissue engineering <i>Fetene Fufa Bakare, Tsion Chuni, Tadele Hunde Wondimu</i>	83
Performance evaluation of low-emission 'injera' baking biomass gasifier stove <i>Assefa Tesfaye Hailu</i>	89
<b>Syndicate 2</b>	<b>101</b>
Steady state experimental study on the advanced stationary engine combustion mode operation (RCCI) <i>Habtamu Deresso Disassa, Venkata Ramayya Ancha, Ramesh Babu Nallamothe</i>	102
Sustainable advanced composites materials from waste: fabrication, properties and de-ployment <i>Belay Tave Wondmagegnehu</i>	113
Fatigue life assessment of electric multi-unit high-speed train wheel tread considering structural flexibility <i>Awel Momhur, Zhao Y. X., Abrham Gebre</i>	125
Single fiber characterization in light of micromechanical analysis and mechanical modeling of 'enset' plant fiber and its composite <i>Abebayehu Abdela, Bart Buffel, Belete Sirahbizu, Frederik Desplentere</i>	140



Evaluation of waste glass powder as partial replacement for mineral filler in asphalt concrete mixes <i>Destaw Kifile, Emer T. Quezon, Abel Tesfaye</i>	150
Jute reinforced poly lactic acid bio-composite for production of ceiling fan blades <i>Neway Seboka</i>	166
Experimental investigation of (Ba <sub>(1.6-3/2X)</sub> Sr <sub>2.4</sub> Na <sub>2</sub> Nb <sub>10</sub> O <sub>30</sub> : xHo <sup>3+</sup> ) ferroelectric nanomaterials by solid state reaction methods for optoelectronic applications <i>Solomon H. D., Menberu M. W., Nebiyu G. D.</i>	183
Assessment of compatibility and work rate of tractors and implements at Wonji Shoa Sugar Estate <i>Cherinet Gosaye, Tsegaye Dinku</i>	200
<b>Syndicate 3</b>	<b>208</b>
Chromium speciation in water using paper-based devices with online oxidation <i>Abdellah Muhammed, Ahmed Hussien, Takashi Kaneta</i>	209
Efficiency of slow sand filtration in removing bacteria and turbidity from drinking water in central Ethiopia <i>Ephrem Guchi, Seyoun Leta, Eline Boelee</i>	217
Analysis of Cyprus papyrus wastewater treatment efficiency in glass fiber constructed wetland under different density <i>Abere Amogn, Ayalew Wondie, Derege Tsegaye</i>	229
Application of Supervisory Control and Data Acquisition (SCADA) and Internet of Things (IoT) for efficient management of urban water supply systems <i>Bahar Adem Beker, Mitthan Lal Kansal</i>	240
Enhancing deforestation detection: remote sensing approach using satellite imagery in Gambella National Park, Ethiopia <i>Gizatie Desalegn Taye</i>	253
Spatiotemporal variations of water quality parameters in selected semi-arid young res-ervoirs in Tigray, Northern Ethiopia <i>Kalayu Mesfin Arefayne, Mekonen Teferi, Tsehaye Asmelash, Tsegazebe Hadush Haileselesie</i>	260
Application of artificial neural network to streamflow and hydrological drought fore-casting for sustainable water resource development in Ethiopia <i>Kassa Abera Tareke</i>	273
Co-precipitation technique synthesis of Co, Ni co-doped WO <sub>3</sub> nanoparticles: structural, optical and electrical properties <i>Wegene Lema Lachore, Fekadu Gashaw Hone, Dinsefa Mensur Andoshe, Muluaalem Abebe Mekonnen</i>	283



## Preface

The transformation of a nation can basically be achieved through the advancement of science and technology. Ethiopia has long recognized the role of science and technology in bringing about sustainable development. The country has envisioned transforming itself into a middle-income country in 2025. To this end, Ethiopia has exerted relentless efforts to materialize science and technology in the country. Thus, it has made science and technology the pillar of its top priorities for transformation of the economy.

As one of the universities mandate to spearhead the transformation process, Adama Science and Technology University (ASTU) is looking forward to excel in science and technology. Its goal is to develop highly qualified, capable, competent, and innovative human resource in the field of science and technology so as to transfer relevant scientific knowledge and skills required for nation building. The university also committed to conduct need based problem solving researches for alleviating the problems of the region and the country at large. To this end, the university is working in collaboration with industries in its vicinity whereby its staff members are contributing a great deal in alleviating problems. Moreover, ASTU has set centers of excellence as a platform where academia can meet stakeholders.

ASTU’s development into a full-fledged science and technology university has helped it to forge strong linkage, cooperation, and partnership with various national and international universities, development sectors, stake-holders, and relevant personalities. To showcase its all-round efforts, ASTU has organized its third national research symposium titled “Emerging Technologies for Building Green Economy”. This is a timely and broad agenda that is seen as a part of the national plan of transformation of the country. Thus, this research symposium aims to further strengthen the contribution of ASTU in development endeavours of the country at large.



## Message from Organizing Committee



**Alemu Disassa (PhD)**

*Vice President, RTT*

*Chair of the Organizing Committee*

Honorable Guests, Dear Participants, on behalf of the organizing committee, I would like to welcome you all to the 3<sup>rd</sup> National Research Symposium of Adama Science and Technology University organized on the theme *“Emerging Technologies for Building Green Economy”*.

Since its establishment as full-fledged Science and Technology University, ASTU has been exerting tremendous effort to foster research culture among its staff. Over the last few years, it has conducted various national and regional researches, community service and consultancy service projects that led to new policy initiatives and generation of new development insights. The establishment of eight centers of excellence and the construction of state-of-the-art Research Park in ASTU also witness the commitment of the university towards nurturing

research culture.

In the effort to disseminate its research outputs and create a platform which allows the academia in ASTU share scientific knowledge and thought with national and international scholars, ASTU had successfully held four international research symposiums and two national research symposiums so far. These symposiums have helped a lot in increasing our national and international collaborations besides nurturing better research culture in our university.

The 3<sup>rd</sup> National Research Symposium is also aimed at consolidating our national and international research collaboration and eventually helping ASTU achieve its vision of becoming a national hub for science and technology researches. The overwhelming response that we have received from several senior and young researchers and scientists to our “Call-for-paper” witnesses the relevance and timely nature of the theme of this symposium. The theme of ASTU’s 3<sup>rd</sup> National Research Symposium was designed to offer comprehensive range of sessions that include: Emerging Technology, Manufacturing and Infrastructure, Energy and Natural Resource Management and Environment. A total of 29 researchers, including five distinguished speakers, are expected to present their works at plenary and syndicate sessions. Nearly 200 participants from higher learning institutions, industries, research institutions, federal and regional sector offices are expected to take part in this symposium. Thus, I am very much confident that the participants can learn a lot from the symposium.

Finally, I would like to convey my appreciation to the School of Mechanical, Chemical and Materials Engineering for hosting the symposium. I would also like to thank all the participants for accepting our invitation to share us your scientific knowledge and expertise. I wish you all a fruitful scientific sessions and very pleasant stay in Adama City.



## Welcoming Speech



**Lemi Guta (PhD)**  
*President, ASTU*

Excellency Mr. Melaku Aebel, Minister, Ministry of Industry and ASTU Supervisory Board Chairman,  
Honorable Board Members of ASTU,  
Dear Vice presidents of ASTU,  
Distinguished Professors from Various National and International Institutions,  
Scientific Paper Presenter,  
Invited Guests from Industries and Various Government Sector Bureaus,  
ASTU Staffs in Attendance,  
Media Personnel,  
Ladies and gentlemen  
All Protocols Observed

On behalf of the management of ASTU and myself, I would like to welcome you all to **the 3<sup>rd</sup> National Research Symposium** of Adama Science and Technology University **organized on the theme "Research on Emerging Technologies for Building Green Economy"**.

Adama Science and Technology University was reestablished in 2014 as one of the two science and technology universities in Ethiopia with especial mandate of producing internationally competent graduates and conducting problem driven researches that could bring meaningful impact on the advancement of science and technology in Ethiopia. To this end, ASTU has established eight centers of excellence and identified eight (8) major research thematic areas in the national economic priority of the country and undertaken over three hundred national and regional researches, community service and consultancy service projects that led to new policy initiatives and generation of new development insights.

The scientific knowledge generated from most of these projects have been published on reputable journals and disseminated to national and international audiences. Besides, ASTU has organized several research symposiums and workshops on which its academia shared their scientific knowledge and research findings.

This 3<sup>rd</sup> National Research Symposium has been organized by School of Mechanical, Chemical and Materials Engineering in collaboration with Research and Centers of Excellence Directorate with the primary aim of consolidating our national and international research collaboration and eventually becoming a national hub for science and technology researches.

In the two days national research symposium (May 24-25, 2024), over 30 distinguished professors and researchers will share us their scientific knowledge and research findings in both plenary and syndicate sessions. The presentations mainly focus on the application of emerging technologies such as **Biotechnology, Nanotechnology, AI, and Drone Technology** in wider areas of our economic activities.

I am quite confident that this symposium will serve all the academia and experts from industries in attendance to share their scientific knowledge and figure out future areas of collaboration for joint research and technology transfer projects.



*Dear Participants, ladies and gentlemen,*

Before, I wind up my speech I would like to warmly thank SoMCME, OVPRTT and all units of our university that have been involved in the facilitation of the successful organization of this symposium.

Once again, I would like to thank you all for accepting our invitation to share us your scientific knowledge and expertise in this symposium.

Finally, wishing you a successful scholarly discussion, I now cordially invite H. E. Mr. Melaku Alebel, Minister, Ministry of Industry and ASTU Supervisory Board Chairman to come to the stage and officially open the symposium.

**Thank You!**

**Horaa Bulaa!**



## Opening Speech



**H.E. Mr. Melaku Alebel**  
*Minister, Ministry of Industry*  
*ASTU Supervisory Board Chairman*

Honorable Board Members of ASTU,  
Respected ASTU Management;  
Distinguished Professors from Various National and  
International Institutions,  
Scientific Paper Presenter,  
Invited Guests from Industries and Various Government  
Sector Bureaus,  
All ASTU Staffs in Attendance,  
Media Personnel,  
Ladies and gentlemen  
All Protocols Observed

It gives me a great pleasure to deliver an opening speech on **the 3<sup>rd</sup> National Research Symposium on Research on Emerging Technologies for Building Green Economy**” organized by Adama Science and Technology University.

We all are quite aware that our world is moving towards the fourth industrial revolution, which is predominantly characterized by digitalization of the overall socio-economic activities of a country. Hence, in this ever dynamic digital world, international competitiveness of a given country largely relies on its effective utilization of a wide range of emerging technologies in its overall development endeavors. Effective utilization of digital technologies, no doubt, will play unprecedented role in boosting the overall economic advancement of a country. This is the secret behind a leap-frogging economic growth and industrialization of those Asian Tigers: Hong Kong, South Korea, Singapore and Taiwan.

Being a developing country, Ethiopia could also harness the benefits of emerging technologies in general and digital technologies in particular as major development tools to accelerate its economic growth within the shortest possible time. Perhaps, to properly function as a country and as an individual in the existing and forthcoming digital world, the use of these technologies is not a choice that we make, but a necessity that we should meet.

Cognizant of these realities, the Government has taken tremendous measures over the last couple of years. “**Digital Ethiopia 2025**” is one of the national initiatives of our government to ensure the digital transformation of the overall economic activities of the country. This initiative, as it has been reiterated by our Prime Minister, is “**a first step and a call for action**” in building prosperous future Ethiopia.

### **Ladies and gentlemen;**

One can confidently witness that, as a result of such unwavering commitment of our government, digitization and digital business transactions have shown a quantum leap in Ethiopia over the last couple of years.



The designation of the two universities: Adama Science and Technology University and Addis Ababa Science and Technology University and as science and technology universities with especial mandate of promoting science, innovation and technology in Ethiopia could also be taken as an evidence of the commitment of the government to build knowledge based and digital economy.

Hence, as a leading science and technology university, Adama Science and Technology University is expected to play a leading role in transferring and generating technologies and innovations that could address the immediate needs of the economic priorities of our country. One way of doing these could be the organization of such type of national research symposiums. I strongly believe that, such types of research symposiums are appropriate platforms where scholarly debates are made to create new scientific knowledge and where ideas are framed for further research collaborations.

I hope, it is with this major objective that ASTU has organized its 3<sup>rd</sup> National Research Symposium with the motto ***“Research on Emerging Technologies for Building Green Economy”***. As I managed to learn from the themes of the symposium, the main objectives of this research symposium is to share scientific knowledge on the application of cutting-edge emerging technologies such as Biotechnology, Nanotechnology, AI, Drone Technology in wide ranges of economic and development sectors in Ethiopia.

As can be seen from the selected themes, these emerging technologies have broader areas of application such as manufacturing, agriculture, energy generation and utilization, environmental protection and natural resource management, health service provision, and construction industry among others.

To make a long story short, the development in the area of digital technology is moving faster from “smart” to “intelligent”. Recently, intelligent digital gadgets are replacing those smart gadgets in various sectors.

Therefore, as a country, we need to move faster to cope up with these ever-changing technological advancements. In this regard, higher learning institutions such as ASTU have got lot of assignments to do. In addition to organizing such types of research symposiums, ASTU must strengthen its ties with renowned international research institutes and strongly engage in producing, selecting and adapting best technologies that could transform the industrial and agricultural productivity and service sectors in Ethiopia.

In this regard, I can assure you that the government of Ethiopia is fully committed to provide you with all the necessary support in your endeavor to promote the application of these emerging technologies in various sectors of our country.

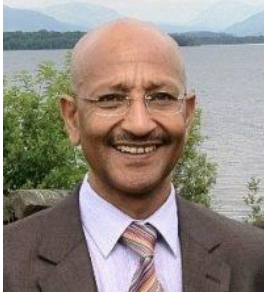
Finally, wishing you a fruitful scholarly deliberations, I now declare that ***the 3<sup>rd</sup> National Research Symposium on Research on Emerging Technologies for Building Green Economy***” organized by Adama Science and Technology University is officially opened.

**Thank You!**

**Horaa Bulaa!**



## Keynote Address



### Prof. Daniel Kitaw

Professor of Industrial Engineering at AAU, an affiliate professor at New Mexico State University, USA and lectures at Polytechnic of Turin, Italy and at Nuremberg University, Germany

**Topic:** Technology Catch-up and Window of Opportunity

## Plenary Sessions



### Prof. Sossina M. Haile

The Walter P. Murphy Professor of Materials Science and Engineering at Northwestern University, Illinois, USA. She is known for developing the first solid acid fuel cells.

**Topic:** Energy of the Future



### Prof. Abi Tadesse Mengesha

Professor of Inorganic and Materials Chemistry, Former Dean of the Science Faculty and Dean of the School of Graduate Studies, Haramaya University

**Topic:** Emerging Technologies



### Eng. Lelissa Daba

Chemical Technologist,  
Ministry of Mines  
Former Director of Ethiopian Cleaner Production Centre (ECPC)

**Topic:** Challenges & Opportunities of Ethiopia's Manufacturing Industry



### Dr. Hundessa Dessalegn Demsash

Ass. Professor at Addis Ababa University (AAU) and CEO of Ethiopian Chemical Industry Corporation

**Topic:** Current Status of University-Industry Linkage, Opportunities & Challenges



## Syndicate 1



## The Effect of Cycling Protocol and Electrolyte on Fast Charging/Discharging of Anode-Free Li-Metal Batteries

Tamene Tadesse Beyene<sup>1,2,\*</sup>, Wei-Nien Su<sup>3</sup>, Hongjie Dai<sup>4</sup>, and Bing-Joe Hwang<sup>1,5</sup>

<sup>1</sup>Department of Chemistry College of Natural Sciences, Jimma University, P.O.Box 378, Jimma Ethiopia

<sup>2</sup>Nano Electrochemistry Laboratory, Graduate Institute of Applied Science and Technology, National Taiwan University of Science and Technology, Taipei 106, Taiwan.

<sup>3</sup>Department of Chemistry, Stanford University, Stanford, CA, California 94305-4401, USA.

<sup>4</sup>National Synchrotron Radiation Research Center, Hsin-Chu 30076, Taiwan

<sup>5</sup>Applied Research Center for Thin-Film Metallic Glass, National Taiwan University of Science and Technology, Taipei, 106, Taiwan

\*Corresponding author, e-mail: [tamene.tadesse@ju.edu.et](mailto:tamene.tadesse@ju.edu.et)

### ABSTRACT

The combined effect of concentrated electrolyte and cycling protocol on the cyclic performance of anode free battery (AFB) is evaluated systematically. In-situ deposition of Li in the AFB configuration in the presence of a concentrated electrolyte containing fluorine donating salt and resting the deposit enables the formation of stable and uniform SEI. The SEI intercepts undesirable side reaction between the deposit and solvent in the electrolyte and reduces electrolyte and Li consumption during cycling. The synergy between the laboratory prepared concentrated 3M LiFSI in the ester-based electrolyte and our resting protocol significantly enhanced cyclic performances of AFBs in comparison to the commercial carbonate-based dilute electrolyte, 1M LiPF<sub>6</sub>. Benefitting from the combined effect, Cu||LiFePO<sub>4</sub> cells delivered excellent cyclic performance at 0.5 mA/cm<sup>2</sup> with average CE of up to 98.78% retaining reasonable discharge capacity after 100 cycles. Furthermore, the AFB can also be cycled at a high rate up to 1.0 mA/cm<sup>2</sup> with a high average CE and retaining encouraging discharge capacity after 100 cycles. The fast cycling and stable performance of these cells are attributed to the formation robust, flexible and tough F-rich conductive SEI on the surface of the in-situ deposited Li by benefiting from the combined effect of the resting protocol and the concentrated electrolyte. A condensing understanding of the mechanism of SEI formation and material choice could facilitate the development of AFBs as a future advanced energy storage devices.

**Keywords:** Anode Free, Ether-Based Electrolyte, Resting Protocol, Solid Electrolyte Interface, Synergy

### 1. INTRODUCTION

The fast evolution of electric vehicles amplifies the increasing needs for the rechargeable batteries with high energy density (Liu et al., 2018; Xiang et al., 2018). From all the possible solid-state negative electrodes in rechargeable secondary batteries, Li metal is regarded as the most encouraging due to its very high specific capacity (3862 mAh g<sup>-1</sup>) (Suo et al., 2018; Zhao et al., 2018), the most negative redox potential (-3.04 V vs normal hydrogen electrode) (Xiang et al., 2018) and low gravimetric density (0.534 g cm<sup>-3</sup>). Moreover, Li metal matches different kinds of cathode materials having very large capacity (Chang et al., 2018; Li et al., 2018) and high voltage (Chang et al., 2018; Zhao et al., 2018). However, the growth Li dendrites (Qian et al., 2015; Liu et al., 2017; Li et al., 2018; Ma et al., 2019) and uncontrolled volume expansion (Li et al., 2018; Wang et al., 2018; Zhao et al., 2018) that induces breaking and repeated formation of new solid electrolyte interface (SEI) hindered its practical application for decades (Lopez et al., 2018). Lately, different strategies for effective operation of lithium metal batteries (LMBs) including electrolyte formulation (Ong et al., 2015; Qian et al., 2015; Haregewoin et al., 2016; Zhao et al., 2018), anode surface engineering and novel changing structures of the anode current collectors (Khurana et al., 2014; Assegie et al., 2018; Gu et al., 2018; Tripathi et al., 2018; Zou et al., 2018), use of solid state and polymer electrolyte (Yang et al., 2015; Lee et al., 2017; Huang et al., 2018; Pang et al., 2018; Wu et al., 2018; Zhang et al., 2018), use of dual-salt electrolytes and electrolyte additives (Liu et al., 2016; Zheng et al., 2017; Li et al., 2018), application of concentrated electrolytes (Basile et al., 2016; Qian et al., 2016; Suo et al., 2018) and modifying separators (Wu et al., 2018; Zhang et al., 2018; Zhao et al., 2018) have been employed. Furthermore, simultaneous deposition and in-situ formation of SEI on the Li deposit in anode free batteries (AFBs) also practiced in recent years to circumvent the obstacles associated to the direct use of Li metal as a



negative electrode (Qian et al., 2016; Wotango et al., 2017; Yan et al., 2018). In the presence of appropriate SEI forming electrolytes, AFBs could mitigate dendritic growth during plating and stripping of Li via in-situ forming good SEI. Such SEI films are conductive enough to allow tunneling of  $\text{Li}^+$  ions and enable to deposit beneath of the layer while it prevents electron and solvent transfer (Lindgren et al., 2016; Tripathi et al., 2018). Once formed, the SEI layer in AFBs acts as a shell for the underneath deposit and prevents parasitic side reaction between freshly deposited Li and solvents in the electrolytes (Li et al., 2018; Li et al., 2018). However, the deposition of Li underneath of the SEI imposes tensile stress on the SEI layer (Li et al., 2018). If the in-situ formed SEI is fragile and brittle, it will respond to the tensile stress by breaking. With the SEI cracking, underneath Li will be necked to the electrolyte. Whenever there is contact between liquid electrolytes and Li, new SEI will form to prevent direct contact between the liquid electrolyte and necked Li (Li et al., 2018). Repeated rupture of SEI and formation of new SEI consumes abundance of active Li (Kozen et al., 2017) and electrolyte during cycling (Li et al., 2018) leading to accumulations of side reaction (Liu et al., 2017), electrolyte dry out (Cheng et al., 2015) and severe corrosion of Li-metal anode. This is one major cause for the capacity fading and low coulombic efficiency (CE) in lithium metal batteries (LMBs) (An et al., 2016) in general and AFBs in particular. In AFBs, the Li source is limited only to the cathode material and any loss of Li from such cognate source leads to early lifespan expiration. In order to increase the cycle life of AFBs, suppression of Li consumption in the process of SEI formation is crucial. To do this, an effort to complete SEI formation process during the early stage and its features/qualities such as flexibility, self-healing and strength are very important.

In principle, the SEI formation process completes during the initial charging since it blocks the flow of electrolyte and electron in and out once it formed (Cheng et al., 2015). However, the challenges mentioned earlier and huge volume expansion induce SEI breaking if the SEI is fragile and brittle. For SEI to withstand the tensile strain obstructed by the volume expansion during Li deposition underneath, it should have some amount of flexibility (Liu et al., 2017; Xie et al., 2018) and self-healing (Li et al., 2018) characters without consuming excess Li and electrolyte. Recently, Li et al. introduced that in-situ formed SEI from fluorine donating species in the electrolyte happens to have a large amount of LiF which provides flexibility character due unique properties of LiF (Li et al., 2018; Ma et al., 2019). The presence of limited amount of  $\text{ROCO}_2\text{Li}$  functionalities along with the excess LiF also improves the flexibility of the SEI and reduce SEI fracture. (Ma et al., 2019) When a battery is discharged at a high rate, the thermal energy of the battery increases and tends to melt some dendrites formed during charging. The dissolution of dendrites and dead Li at high rate stripping smoothens the anode surface which could play role in healing the broken SEI and prepared good environment for the uniform distribution of  $\text{Li}^+$ -ion flux in the follow up cycle. (Zheng et al., 2017) As a result of this, the amount Li and electrolyte consumed for continuous formation of the SEI will be reduced.

Here, we report a smart method of SEI formation protocol in AFBs in the presence of fluorinated ether based concentrated electrolyte. In our new cycling protocol, we have rested the AFB after slow first deposition for 24 hours before moderately high rate stripping to smoothen the SEI formed during deposition. The schematic representation of our cycling protocol using laboratory prepared 3M LiFSI in DOL/DME (1:1) called 3LiFSI hereafter for simplicity and commercial 1MLiPF<sub>6</sub> in EC/DEC (1:1, v/v) (simply called 1LiPF<sub>6</sub>) is given by scheme in Fig. 1 a-c. The pronounced morphological difference was observed from the SEM images of Cu substrate retrieved from Cu||LFP cell at deferent stages. Deposition of Li (in Cu||LFP cell) in the laboratory prepared electrolyte and resting the deposit for 24 hours resulted in very uniform morphology relative to the normal cycling (Fig. 1d-f). The SEI formed by our cycling protocol conveyed excellent flexibility and resisted the tensile stress imposed by Li deposition beneath of the SEI in the follow-up cycles (Fig 1g-i). Thus SEI film remained uniform without any sign of fracture for long charge/discharge cycles.

In contrary, no uniform and SEI cracking was clearly observed in the normal protocol using the same electrolyte, same cell configuration and the same cycling rate (Fig. 1h).

Thus, the synergistic effect between our cycling protocol and the laboratory prepared ether-based electrolyte enabled the formation of very stable and robust SEI and prolonged cycle life and increased CE of both Cu||Li cell and Cu||LFP cell at high current density. Cu||Li cell cycled in the concentrated fluorinated electrolyte using this special protocol manifested extraordinary electrochemical performance at a high current density (2 mA/cm<sup>2</sup>) and



cycled up to 1500 cycles with average CE 99.88%. Interestingly, the new cycling protocol also enabled Cu||LFP cell to be cycled at 0.5 mA/cm<sup>2</sup> with average CE of more than 98.7% retaining 40% of its initial discharge capacity after 90 charge-discharge cycles. The extraordinary cyclic performance of these batteries at such high current density is attributed to the synergistic effect between cycling protocol and the electrolyte which substantially favored formation of very stable SEI and suppressed repeated consumption of Li and electrolyte during electrochemical cycling. Low rate depositing and resting of the deposit reinforces the preferential decomposition of LiFSI salt that forms a LiF-rich solid SEI layer, which is beneficial to stabilize the Li metal anode/electrolyte interface, uniform growth of Li films, and suppress the further corrosion of Li metal. The 1,3-Dioxolane (DOL) also get enough chance to decompose and form ROCO<sub>2</sub>Li which provides flexibility to the SEI and enables it resist tensile strain during Li deposition in the follow up cycles. (Zhao et al., 2018) However, the high concentration of the solute and low LUMO energy of DME prevent its decomposition in the potential window of LFP and this mitigated formation of less stable SEI from solvent decomposition. To the best of our knowledge, the high CE and long cycle life demonstrated in this work are among the best ever reported for LMBs in general and AFBs in particular.

## 2. MATERIALS AND METHODS

### 2.1. Material

Cathode material LiFePO<sub>4</sub> (LFP) with a surface area loading 11.0 mg/cm<sup>2</sup> and having a nominal areal capacity of 1.6 mAh/cm<sup>2</sup> was supplied by Aleees (Advanced Lithium Electrochemistry Co., Ltd, Taiwan). The LFP electrode overlay with proportion 90:5:5 (active material: Carbon Black, Supper P: Polyvinylidene fluoride, PVDF) was punched into discs and further dried at 90 °C under vacuum overnight. The battery grade lithium bis (fluorosulfonyl)imide (LiFSI), 99.0%, was obtained from Fluorochem Ltd. This was vacuum dried at 90 °C for two days in Argon filled glove box (< 0.1 ppm O<sub>2</sub> and < 0.1 ppm H<sub>2</sub>O) before use. Battery grade solvent 1,2-Dimethoxyethane (DME), 99.5%, was purchased from Sigma Aldrich and battery grade solvent 1,3-Dioxolane (DOL), 99.5%, was purchased from ACROS ORGANICS. The solvents were treated with 10 weight % of 3Å molecular sieve for three days to remove trace moisture impurities before use.

### 2.2. Electrochemical Measurements and Physical Characterizations

The anode free (Cu||LFP) and half-cell (Cu||Li) were evaluated using CR2032 coin-type cell. The anode free and half-cells were assembled using bare Cu foil as anode substrate (anode current collector), LiFePO<sub>4</sub> coated on Al foil as a cathode, trilayer Celgard 2325 (PP/PE/PP) porous membrane used as the separator, laboratory prepared of the ether-based electrolytes 3M LiFSI in DME/DOL (1:1, v/v), (referred as 3LiFSI hereafter for simplicity), and commercial 1 M LiPF<sub>6</sub> in EC/DEC (1:1, v/v), (referred simple as 1LiPF<sub>6</sub> for simplicity), were used. The Cu foil substrate was washed by immersing it in 1 M HCl and shaking gently for 10 min, followed by rinsing with distilled water and acetone three times and then rapidly drying under vacuum. All of the cell assembly/disassemblies were carried out in an Ar-filled glove box. The cells were cycled between 3.0 and 3.8 V versus Li/Li<sup>+</sup> at different current densities starting from 0.2 mA/cm<sup>2</sup> using a computer controlled Arbin BT-2000 battery tester at room temperature. For the assembly, 60 µL electrolyte were used for the fabrication of both kinds (Cu||Li and Cu||LFP) of batteries. In both cases, 19 mm diameter Cu disc electrodes were used as anode current collector. Discs of LiFePO<sub>4</sub> coated on Al foil (13 mm in diameter) were punched with an active surface area of 1.326 cm<sup>2</sup> to be used as a positive electrode. Electrochemical impedance spectroscopy (EIS) of the cells was measured after fully discharged for anode free cells at different stages of the cycling at a frequency range from 0.01 to 100,000 Hz with a perturbation amplitude of ±10 mV using a BioLogic Science Instruments coupled with a Frequency Response Analyzer by the help of EC-Lab V10.40 software.

For the morphological characterization of Li on Cu substrates, scanning electron microscopy (SEM) images analysis was done with an FEI Quanta 200 scanning electron microscope, operating at an acceleration voltage of 20 kV. X-ray photoelectron spectroscopy (XPS) was conducted using a wide-range beamline (BL24A) at the National Synchrotron Radiation Research Center (NSRRC) in Taiwan. All reported binding energies were corrected using the signal for the Au peak (Au 4f) at 84 eV.



### 3. RESULTS AND DISCUSSION

#### 3.1 Electrochemical Performance

In order to inquire into the synergistic effect between the electrolyte and cycling protocol on the electrochemical performance of Cu||Li (half-cell) and Cu||LFP (anode free), the charge/discharge behaviors these cells were conducted in detail. The proof of concept of the cycling protocol for the electrochemical performance of Cu||Li cell at 1.0 mA/cm<sup>2</sup> is given in Figure 2. Here time controlled plating was employed to plate and strip (1.6 mAh/cm<sup>2</sup>) of Li which is equal to the nominal areal capacity of the LFP cathode employed in the anode free battery fabrication. The electrochemical performance of this half-cell battery (Cu||Li) was used as a starting point to judge the effectiveness of our new cycling protocol and explain the challenge in AFBs in comparison. The synergistic effect of the cycling protocol and electrolyte was clearly seen from their cycling performance. The cycling performance of Cu||Li cell in 1LiPF<sub>6</sub> was observed relatively very poor; the voltage polarization increased after every cycle which led to decrease CE of the cell even after using our new protocol. The CE decreased drastically and the cell failed after 36 charge-discharge cycles in which the average CE after these cycles become only 83.65% (Fig.1 a, d, Table 1).

**Table 1:** Summary of the electrochemical performance of Cu||Li cell cycled at 1.0 mA/cm<sup>2</sup> with different cyclic strategies and in different electrolytes (<sup>a</sup>The average CE was calculated only for the first 36 due to internal shorting after 36 cycles; <sup>b</sup>The average CE was calculated for the whole 100 cycles including the ICE)

Electrolyte/Cycling strategy	ICE	CE of some selected cycles				<CE>	Voltage Polarizations of selected cycles (mV)			
		25 <sup>th</sup>	50 <sup>th</sup>	75 <sup>th</sup>	100 <sup>th</sup>		10 <sup>th</sup>	25 <sup>th</sup>	35 <sup>th</sup>	50 <sup>th</sup>
Rested-1LiPF <sub>6</sub>	94.56	88.1	5.32	-	-	83.65 <sup>a</sup>	65.4	131	>200	>200
Normal-3LiFSI	92.82	98.71	98.85	99.04	99.07	98.75 <sup>b</sup>	57	57.5	50.1	52.8
Rested-3LiFSI	91.98	99.69	100.90	99.85	99.87	99.65 <sup>b</sup>	54	49	41	44

Replacing the commercial 1LiPF<sub>6</sub> by the laboratory prepared 3LiFSI electrolyte significantly improved the cycling performance of Cu||Li cell even using the normal protocol since it contains good SEI forming components. The average CE of the cell using this electrolyte reached 98.75% during the first 100 charge-discharge cycles (Fig. 2, b & d, Table 1). The cyclic performance of Cu||Li cell in the 3LiFSI electrolyte using the new cycling protocol overwhelmingly improved showing very low voltage polarization and extraordinary high average CE. The average CE of this cell reached 99.65% during the first 100 cycles. The voltage polarization of this cell becomes almost constant and remained 45 mV in average at such high current density (Fig. 2c & d, Table 1). Summary of the entire cyclic performances of this three cell is given in Table 1.

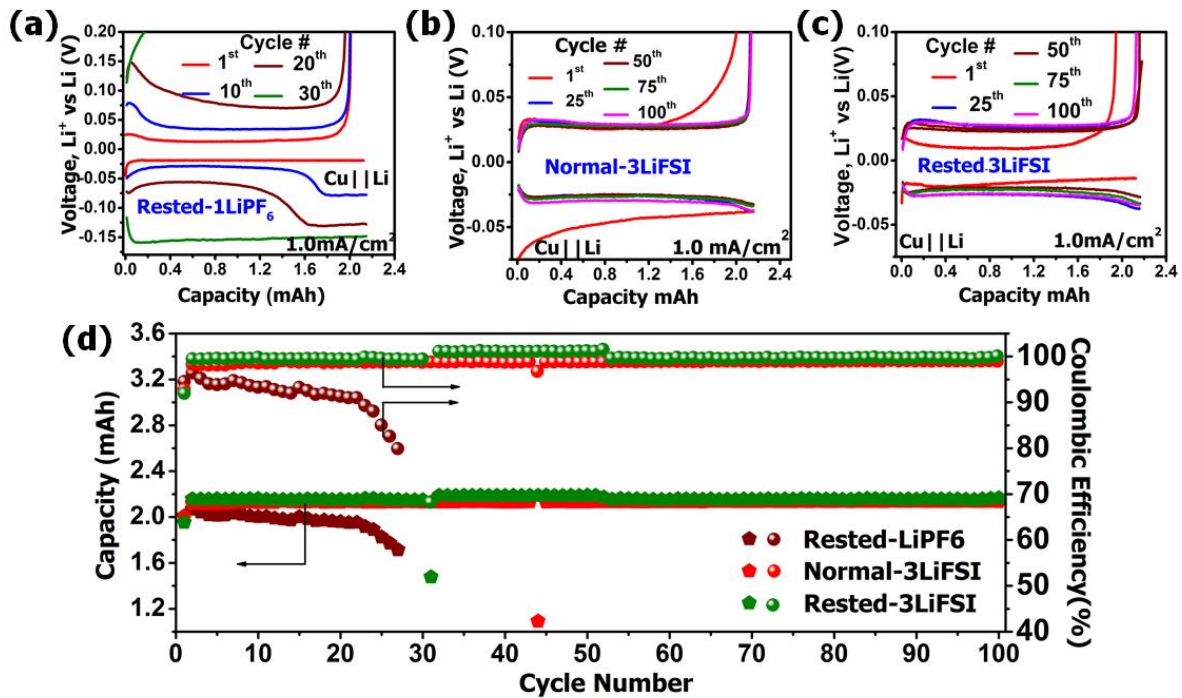


**Figure 1:** Cycling performance of Cu||Li half-cells cycled at  $1.0 \text{ mA/cm}^2$  with different cyclic strategies and in different electrolytes. A capacity of  $1.62 \text{ mAh/cm}^2$  was used to plate the Li metal, in which plating was controlled by time (for 98 minutes) while stripping was voltage controlled. (a-c) Charge/discharge voltage profile of a cell (a) in 1MLiPF<sub>6</sub> in which the cell was rested for 24 hours after the first cycle plating, (b) in 3MLiFSI in which the cell normally cycled without resting after the first cycle plating, (c) in 3MLiFSI in which the cell was rested for 24 hours after the first cycle plating, and (d) comparisons CE and stripping capacity of the cells in different electrolytes with different cycling conditions

The potency of the synergistic effect of the electrolyte and cycling protocol was further checked using Cu||LFP configuration (in which limitedness of the Li source only to cathode is more challenging) and showed the surprising result. Figure 3 shows the electrochemical performance of Cu||LFP cell cycled at  $0.2 \text{ mA/cm}^2$  using either 1LiPF<sub>6</sub> or 3LiFSI varying the cycling protocol. The combined effect of the electrolyte 1LiPF<sub>6</sub> and the cycling protocol was seen relatively poorer compared to the 3LiFSI electrolyte. The Cu||LFP battery cycled in 1LiPF<sub>6</sub> using the optimized protocol manifested very poor performance as it is seen in Fig 3a, d. The average CE of this cell is very low and retained less than 30% at 15<sup>th</sup> cycle. The cyclic performance of the Cu||LFP cell in the laboratory-prepared 3LiFSI was much better than the commercial 1LiPF<sub>6</sub> electrolyte even when cycled using the normal conventional protocol. This battery showed very large average CE of 98.3% while retained 49% of its initial discharge capacity after 50 charge-discharge cycles (Fig. 3b, d). Exceptionally, the cyclic performance of Cu||LFP cell in the 3LiFSI using the optimized protocol further improved and its average CE reach 98.9% retaining 57% its initial discharge capacity after 50 cycles (Fig. 3c, d). This much cyclic performance quite unprecedented as far as this quite young discipline, AFB, is concerned. Such extraordinary cyclic performance of the cell is attributed to the formation of good SEI which consumes a relatively small amount of Li and electrolyte during the formation process which certain amounts of flexibility character to resist the tensile stress imposed on it while Li is deposited underneath in the follow up cycles.

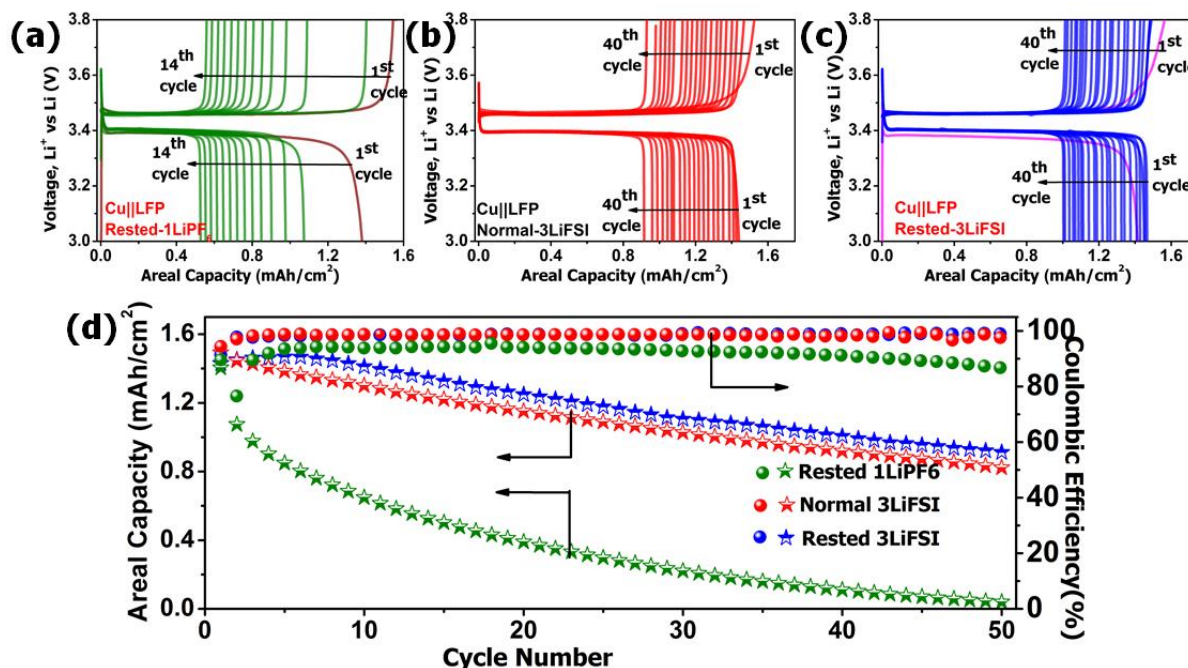


**Figure 2:** Electrochemical performance of anode free, Cu||LFP, cells using different electrolytes cycled at 0.2 mA/cm<sup>2</sup> strategies (a-c) Charge-discharge voltage profile of anode free cell cycled (a) in commercial 1MLiPF<sub>6</sub>-EC/DEC (1:1, v/v) in which the battery was rested for 24 hours after first plating. (b) in laboratory prepared 3MLiFSI-DOL/DME (1:1, v/v) and the cell was cycled normally (c) in laboratory prepared 3MLiFSI-DOL/DME (1:1, v/v) in which the battery was rested for 24 hours after first plating. (d) Comparison of coulombic efficiency and discharge capacity profiles in different electrolytes and using different cycling.

Based on excellent electrochemical performance both Cu||Li and Cu||LFP obtained using the new protocol so far, we have performed long cycle test using the ether-based electrolyte and the optimized protocol. The cyclic performance of half-cell (Cu||Li) and full cell (Cu||LFP) at different current densities are given in Fig. 4. Cu||Li cell cycled using our protocol exhibited exceptional cyclic performance. The coulombic efficiencies of half-cells improved boldly and the batteries cycled without short-circuiting for long cycles (Fig 4a, b, d). Low rate long cycle performance of the Cu||Li half-cell was undertaken when a nominal capacity of 1.60 mAh/cm<sup>2</sup> using time controlled plating protocol. Cu||Li half-cell cycled at 0.2 mA/cm<sup>2</sup> shown excellent cyclic stability having average CE more than 99.9% for more than 220 cycles). Increasing cycling rate to 0.5 mA/cm<sup>2</sup>, while depositing almost equal amounts Li (~1.60 mAh/cm<sup>2</sup>), did not affect the performance the Cu||Li half-cell too much than only slightly increasing voltage polarization of the battery. The average CE of Cu||Li half-cell cycled at 0.2 mA/cm<sup>2</sup> in the 3LiFSI electrolyte using the optimized protocol is found 99.96% after 500 cycles.

When measured at a deposition capacity of 1.62 mAh cm<sup>-2</sup> and a current density of 1 mA cm<sup>-2</sup>, the cell with Cu||Li configuration exhibited a long cycle life over 1000 cycles with an average CE as high as 99.99% in the concentrated ether-based electrolyte and using the optimized resting protocol (Fig. 4b, d). Most importantly, Cu||Li cell cycled using the optimized protocol in the concentrated laboratory prepared electrolyte manifested extraordinary cyclic performance and be able to attain more than 1500 cycles with average CE of 99.88% at 2.0 mA/cm<sup>2</sup> (Fig. 4c, d). The relative low average CE is due to the CE of the cell during the few initial formation cycles and relatively low number of cycles involved in the average CE calculation. It is worth mentioning that such exceptional cyclic performance at a very high rate is attributed to the unprecedented formation and stabilization of SEI by our cycling protocol in the presence of the laboratory-prepared concentrated electrolyte.

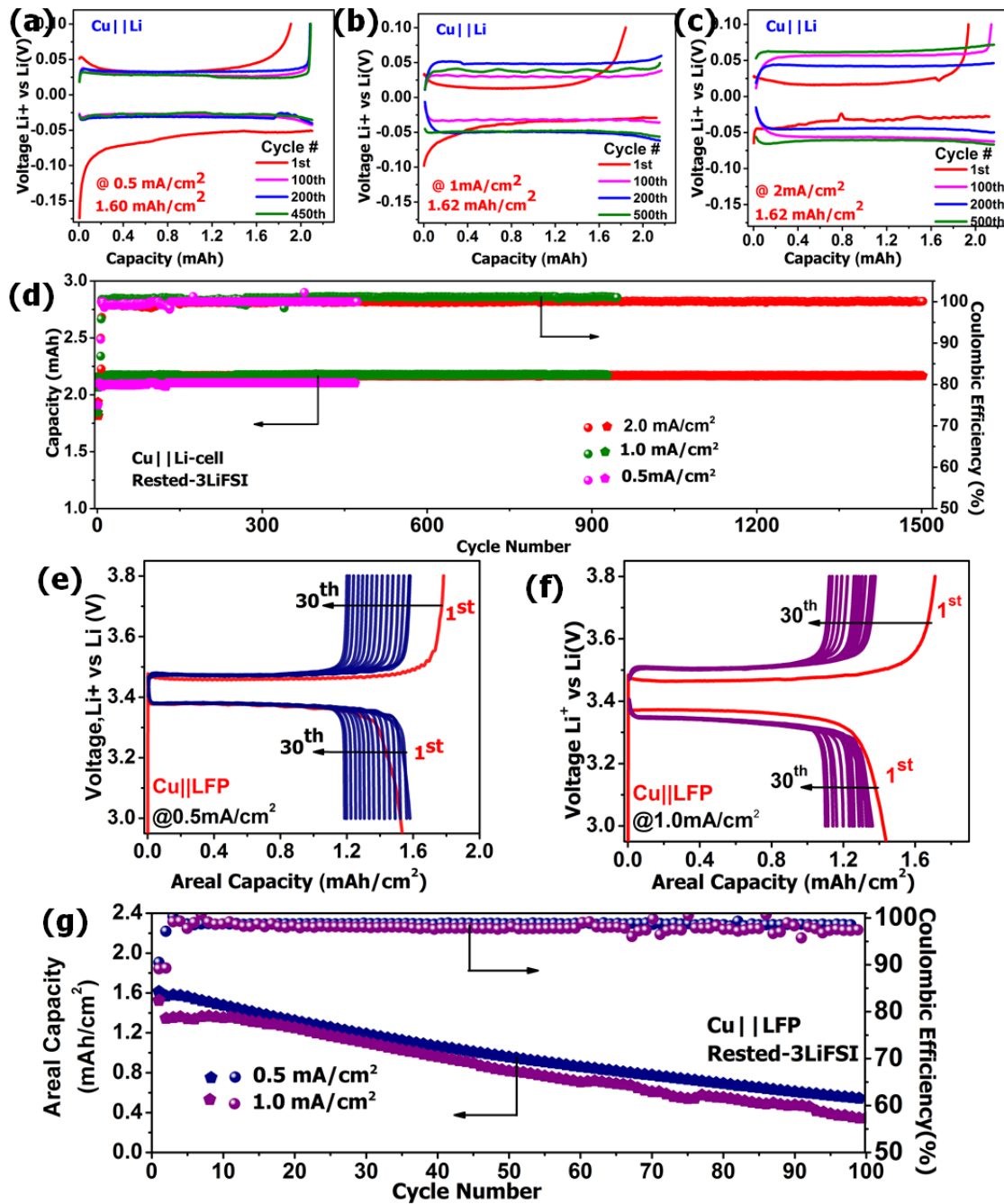


**Figure 3:** Electrochemical performances of different batteries in the 3LiFSI (ether based) electrolyte using the optimized protocol. (a-d) Cu||Li cell cycled @ different rates (a-c) Charge-discharge voltage profile of (a) cell cycled @ 0.5 mA/cm<sup>2</sup> (b) cell cycled @ 1.0 mA/cm<sup>2</sup> (c) cell cycled @ 2.0 mA/cm<sup>2</sup> (d) Combined CE and stripping capacity summary of cells in 'a', 'b', and 'c' (e-g) Cu||LFP cell cycled @ different rates (e & g) Charge-discharge voltage profile in which the less polarized curve (red) at the middle indicates the initial conditioning (e) @ 0.5 mA/cm<sup>2</sup> (f) @ 1.0 mA/cm<sup>2</sup> (f) Combined discharge capacity and CE summary of 'e' and 'f'.

High rate and long cycle electrochemical performance of Cu||LFP cell is given in Figure 4e-g. After conditioning using our optimized protocol, the Cu||LFP cell cycled in the 3LiFSI electrolyte at 0.5 mA/cm<sup>2</sup> for more than 100 cycles retaining reasonable capacity. The charge-discharge voltage profile of this very stable and show very little voltage polarization even after 100 cycles. The average CE of this AFB is quite high and remained 98.78 during these 100 cycles. This battery retained about 37% of its initial discharge capacity after these charge-discharge cycles which is very promising achievement as far as this new and challenging field is concerned (Fig 4e, g). More importantly the cyclic performance of AFB with the same configuration and material was also tested at 1.0 mA/cm<sup>2</sup> check the effect of high rate cycling. Along with increasing rate, the cyclic performance of the



battery only slightly decreased compared with the low rate performance. Accordingly, voltage polarization increased, average CE decreased (98.2%) and comparatively the battery retained less discharge capacity (30%) after 100 cycles (Fig. 4f, g). The relative decreased performance at high rate is attributed to consumption of electrolytes and Li due to repeated SEI formation to repair the SEI cracking that causes by the high rate Li deposition underneath of the SEI.

Moreover, Cu||LFP cell was capable of withstanding rate change from 0.2 to 2.0 mA/cm<sup>2</sup>. From the rate capability test, the discharge capacity of the battery increased by 8% when the cycling rate is decreased from 2.0 to 0.2 mA/cm<sup>2</sup>. Entirely this battery capable of retaining more than 78% its initial discharge capacity (@0.2 mA/cm<sup>2</sup>) after 40 cycles which is an extraordinary achievement as far as anode free battery is concerned. The decrease in capacity observed in the rate capability test is also attributed to the slight consumption of Li and electrolyte in the SEI formation process and dead Li formation.

Some scholars recently claimed that fast rate stripping of Li smoothens the anode surface and inhibit dendritic Li growth to some extent and prolongs cycle life of AFBs. (Jiangfeng Qian, Brian D. Adams et al. 2016, Zheng, Engelhard et al. 2017) We have confirmed this argument by charging our AFB battery at slow rate (0.2 mA/cm<sup>2</sup>) discharging at high rate (1.0 mA/cm<sup>2</sup>) after being conditioned initially using the optimized protocol. The charge/discharge voltage profile of this battery is given in supportive information.

In contrast to the conventional LMBs, even AFBs assigned as Rested-3FSI showed some amount capacity fading during cycling. Such capacity fading is caused by the formation of some dead Li and consumption of Li and electrolyte in the process of SEI formation. These are induced by the volume expansion during cycling which either detaches active Li from the electrode and leads them to lose electron accessibility or cracks the SEI. When SEI ruptures, deposited Li will be necked to the liquid electrolytes and new SEI began to form. In AFBs, Li<sup>+</sup>-ion source only from the cathode material and a single loss from such cognate source reduce the capacity of the battery in the follow-up cycles.

In order to confirm the pronounced effect of limited Li source in AFBs, we have plated less than 100% excess Li onto the Cu foil and used it as current collector in anode free battery. Pre-lithiation of Cu foil with this much amount Li improved the electrochemical performance of the battery to a greater extent. The battery (Cu@Li||LFP) showed no sign of capacity fading even when cycled at 1.0 mA/cm<sup>2</sup> more than 60 cycles. After 60 cycles, the capacity of the battery decreased slightly and retained more than 50% of its initial discharge capacity after 160 cycles at such high current density. The relative better stability of the Cu@Li||LFP cell compared to the Cu||LFP cell is due to replacement of Li consumed by repetitive SEI formation and dead Li from the pre-lithiated. For this reason, the formations of dead Li and SEI fracture and formations of new SEI are the main reason for capacity fading in AFBs in general. Thus further reduction of amount Li and electrolyte consumed in the SEI process could be the future direction of this work.

To check the compatibility of our new protocol to other battery systems, we have fabricated a full cell consisting of Meso Carbon Micro Beads (MCMB) anode with the configuration of MCMB||LFP cell and cycled at 1.0 mA/cm<sup>2</sup> using the 3LiFSI electrolyte and the optimized protocol. In spite, earlier scholars claimed that ether based electrolytes lack compatibility with carbon anode, our cell is cycled with very high CE (99.99%) for more than 200 cycles at this rate retaining more than 84% of its initial discharge capacity.

### 3.2 Electrolyte and SEI Layer Evolution

Our recent work on the effect of concentrated dual-salt electrolyte in stabilizing in-situ deposited Li in anode free battery revealed that LiFSI with low LUMO energy is thermodynamically unstable and tends to decompose at the negative electrode to form a passivation layer (SEI) on the in-situ deposited Li. However, the breaking and reformation of such SEI layer consume Li- metal, and electrolyte which leads to cycle life expiration at early stages. In this work, resting Li deposited at a low rate in 3LiFSI electrolyte enabled to form more uniform, strong and flexible SEI (Figure. 1d-i). The XPS result of Li deposited on Cu substrate revealed that the inorganic components in the SEI comprehensively varied along with the electrolyte and cycling protocol (Fig.5).

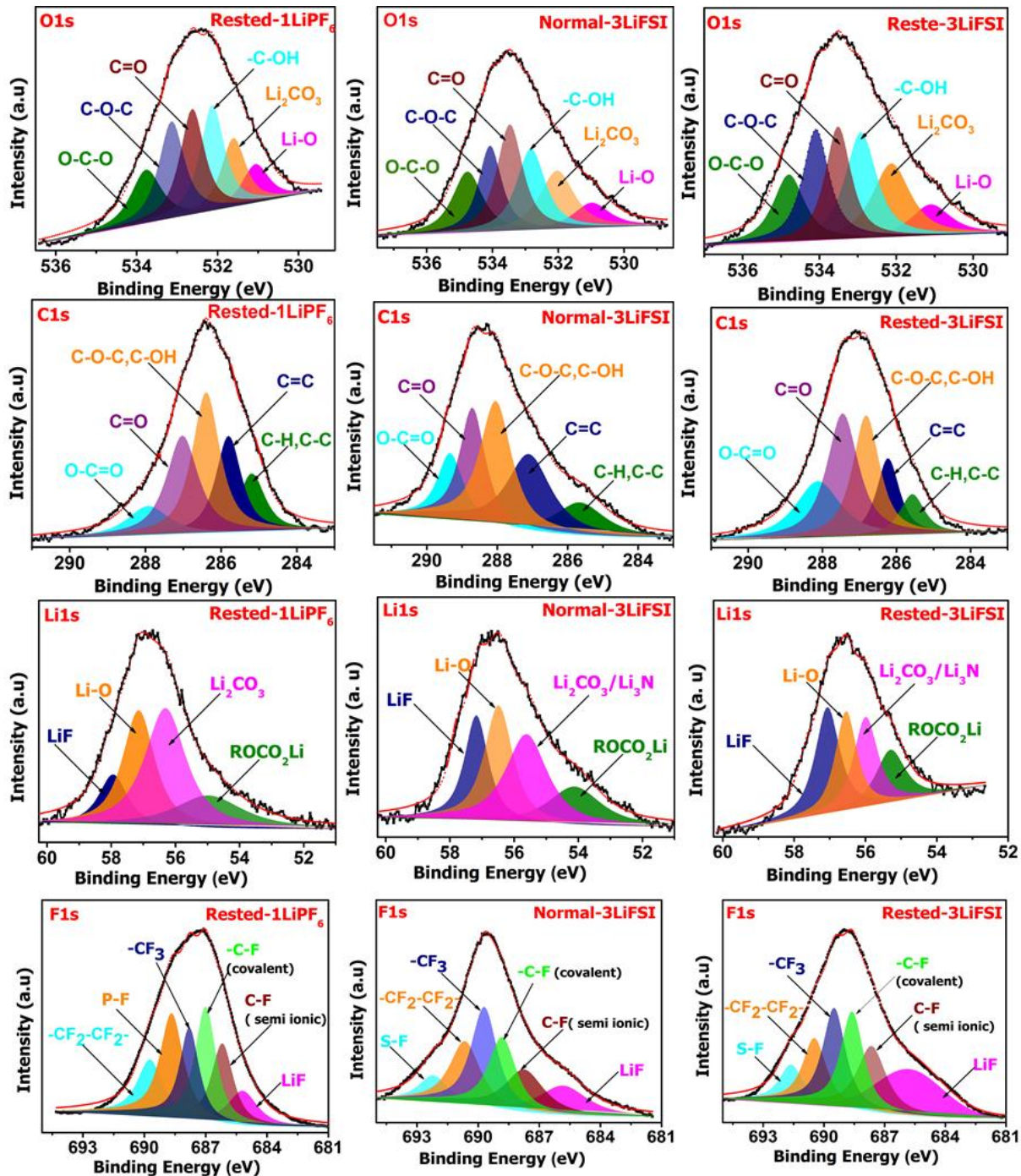


**Figure 4:** X-ray photoelectron spectroscopy (XPS) analysis of in-situ formed Li anodes on Cu substrate after 5<sup>th</sup> cycles in Cu||LFP coin type cell. The black color represents the original data while the dashed red line presents the fit. The other color schemes represent the different functional groups as indicated by an arrow.

The relative intensities of peaks of inorganic components like LiF, Li<sub>2</sub>O, and Li<sub>2</sub>CO<sub>3</sub> for the system represented as Rested-1LiPF<sub>6</sub> are the least. The low XPS peak intensity could be attributed to the low concentration of the electrolytes and tendency its components towards decomposition. (Qian et al., 2015; Bai et al., 2016) Low concentration of the electrolyte guides formation of SEI with excess organic moieties like polyolefin since solvent molecules get high chance to contact with Li metal. In addition, the tendency the salt in donating fluorine in the SEI formation process is very lesser and hence less inorganic species like LiF will form. (Zhang, 2006) Thus resting AFBs involving such electrolyte after deposition favors formation SEI with more organic components which increase the film thickness and increases charge transfer resistance. Hence, Li diffusion Li across such



interface will be impeded and decrease cycle life of the battery. In the concentrated 3LiFSI electrolyte, the solvent molecules will get lesser chance to contact with the Li and thus less organic components will appear in the SEI.

In contrary, the solute particles get enough chance to decompose and for inorganic component rich SEI. In Fig. 5 it can be simply observed that the 3LiFSI electrolyte in both the normal-3LiFSI and Rested-LiFSI favored the formation of inorganic components like LiF in the SEI layer. As a result, the AFBs involving this electrolyte was cycled for long cycles, without rapid capacity fading, compared to those involving the baseline electrolyte (Fig. 3a-d).

Resting the battery involving 3LiFSI after slow rate deposition enables it to form more uniform, robust and flexible SEI as observed in Fig.5. The peak intensities in the XPS measurement for LiF boldly increased and improved the cyclic performance of AFB involving this cycling protocol. The relative increment of the peak intensity of the C-F bond (semi ionic) in F1s, obtained from the reductive decomposition of the DOL solvents, in the Rested-3FSI was also observed in Fig. 5. Such semi ionic backbone together with the LiF enables the SEI more flexible and helps it to resist the tensile strain imposed on the SEI during Li deposition underneath of the SEI.

### 3.3 Electrochemical Impedance Spectroscopy Measurement

Electrochemical impedance spectroscopy (EIS) measurement of the anode free battery involving the laboratory prepared electrolyte (3LiFSI) and the baseline electrolyte (1LiPF<sub>6</sub>) was undertaken in order to estimate conductivity of the electrolytes and the surface film resistance developed as the result of the formation of the SEI (Fig. 6a-c). Correspondingly, the charge transfer resistance for the anode free cell containing 1LiPF<sub>6</sub> became larger while the bulk resistance of this cell was found relatively lower (Fig. 6a). This could be due to the formation of resistive SEI from the decomposition of carbonate electrolytes which impedes charge transfer across the interface. The relative low bulk resistance of this cell (Table 2) has also resulted from lower concentration of the electrolyte. On the other hand, the charge transfer resistance a cell assigned as Normal-3LiFSI showed almost miniature similarity with Rested-3FSI in both the charge transfer and bulk resistance due to the tendency of the electrolyte to decompose and form SEI (Table 1).

**Table 2.** Comparative summary of the real impedance of batteries at different discharge cycles. The data were obtained from Z-fit of Nyquist plot by EC-Lab software

Cycle Number	Electrolyte/Cycling strategy	Re (Z)/Ohm/Z-fit result	
		R <sub>s</sub>	R <sub>ct</sub>
1	Rested-1MLiPF <sub>6</sub>	2.93 ± 0.42	32.34 ± 0.62
	Normal-3MLiTFSI	4.24±0.38	19.28± 0.45
	Rested-3MLiTFSI	6.63 ± 0.38	18.63 ± 0.43
5	Rested-1MLiPF <sub>6</sub>	3.37 ± 0.41	18.32± 0.67
	Normal-3MLiTFSI	3.44± 0.08	13.32 ± 0.54
	Rested-3MLiTFSI	4.072 ± 0.38	16.7 ± 0.42
10	Rested-1MLiPF <sub>6</sub>	3.37 ± 0.41	23.64± 0.62
	Normal-3MLiTFSI	3.81±0.10	13.14±0.63
	Rested-3MLiTFSI	5.51 ± 0.41	17.68 ± 0.75
15	Rested-1MLiPF <sub>6</sub>	3.96 ± 0.40	26.79 ± 0.59
	Normal-3MLiTFSI	3.59± 0.37	15.59± 0.61
	Rested-3MLiTFSI	5.83 ± 0.42	18.47 ± 0.48
20	Rested-1MLiPF <sub>6</sub>	4.60 ± 0.36	27.63 ± 0.67
	Normal-3MLiTFSI	3.71± 0.30	17.84± 0.57
	Rested-3MLiTFSI	5.80 ± 0.41	± 0.70

The slightly larger value for the AFBs cycled in 3LiFSI using the optimized protocol is attributed to the formation of tough SEI involving both the organic and inorganic components as revealed by the XPS measurements and other characterization techniques. Thus in spite, it improves strength and flexibility of the SEI, resting of the film after deposition could thicken the SEI and slightly increases the impedance of the cell at the initial stages. The electrochemical performance of the Normal-3LiFSI is lower than the Rested-3LiFSI indicating that low Rct value alone cannot guarantee the cyclic performance of the battery.

### 3.4 Cyclic Voltammetry

The Cyclic voltammogram of Cu||LFP cell cycled in the potential region of 2.5V-3.9V at a scan rate of 0.2 mV/s using either the commercial 1LiPF<sub>6</sub> (baseline electrolyte) or concentrated dual salt electrolytes was given Fig. 6d, e. In the baseline electrolyte, the formation of SEI was observed from the slightly broader peak formed during the first cycle. In the follow-up cycles, both the anodic and the cathodic peaks decreased indicating the resistive nature of the SEI formed during the first cycle (Fig. 6d).

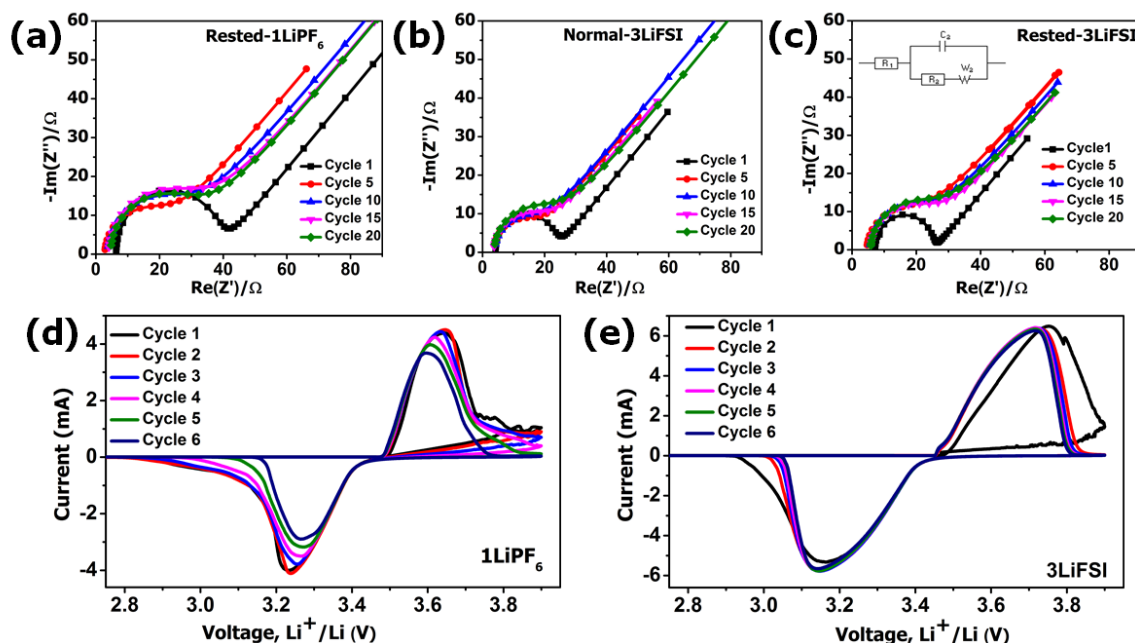


**Figure 5:** (a-c) Nyquist plot of anode-free Cu||LFP cells with (a) Commercial 1MLiPF<sub>6</sub>-EC/DEC (1:1, v/v) in which the cell was rested for 24 hours after the 1<sup>st</sup> plating, (b) Laboratory prepared 3MLiFSI-DOL/DME (1:1, v/v) in which the cell was normally cycled without resting after first deposition and (c) Laboratory prepared 3MLiFSI-DOL/DME (1:1, v/v) in which the cell was kept resting after the first deposition. All EIS data were collected at fully discharged state of the cells (d-e) Cyclic voltammogram of Cu||LFP cell in the potential region of 2.5V-3.9V at a scan rate of 0.2 mV/s using either (c) Commercial 1MLiPF<sub>6</sub>-EC/DEC (1:1, v/v) or (e) Laboratory prepared 3MLiFSI-DOL/DME (1:1, v/v).

It is also observed that there is a large anodic peak shift towards low voltage. Such a peak shift could be attributed to high voltage polarization induced by SEI formation which is resulted from huge electrolyte and Li consumption.

In the 3LiFSI electrolyte, a broad anodic peak was observed indicating the formation of conductive SEI (Figure. 6e). After formation of the SEI, the peak intensities of the SEI further increased indicating high ion conductive nature and uniformity of the SEI which allows diffusion of Li back and forth. Thus this also provides a piece of additional information for the formation of good SEI during the electrochemical process of AFB battery involving Cu||LFP. In addition, the relatively high peak current having constant values (~6 mA) after the first cycle indicates that high stability of the film formed and hence high capacity retention at constant current flow. The slight shift of anodic peak current (decreasing peak width) indicates after every cycle indicates that slight formation of SEI after first formation cycle. Such small shift is also in a good agreement with electrochemical

charge/discharge test and other characterization techniques which slightly reduces CE of the battery after the first cycle.

### 3.5 Anode Morphological Evaluation

To get insight into the morphology of Li plating and stripping, the SEM image of Li deposited on Cu substrate evaluated at different cycles. In the baseline electrolyte, rough and non-uniform Li deposition was observed which induces dendrite formation due to non-uniform Li flux distribution in the follow-up cycles (Fig. 7d). Morphology of Li deposition in the laboratory prepared (3LiFSI) electrolyte is more uniform and much better than the baseline electrolyte (Fig. 7e). The morphology of the Li deposition in the 3LiFSI electrolyte was further improved by lowering the deposition current and resting the deposit for to 24 hours to allow the cell form good SEI via the reductive decomposition of component of the fluorine donating salt (LiFSI).

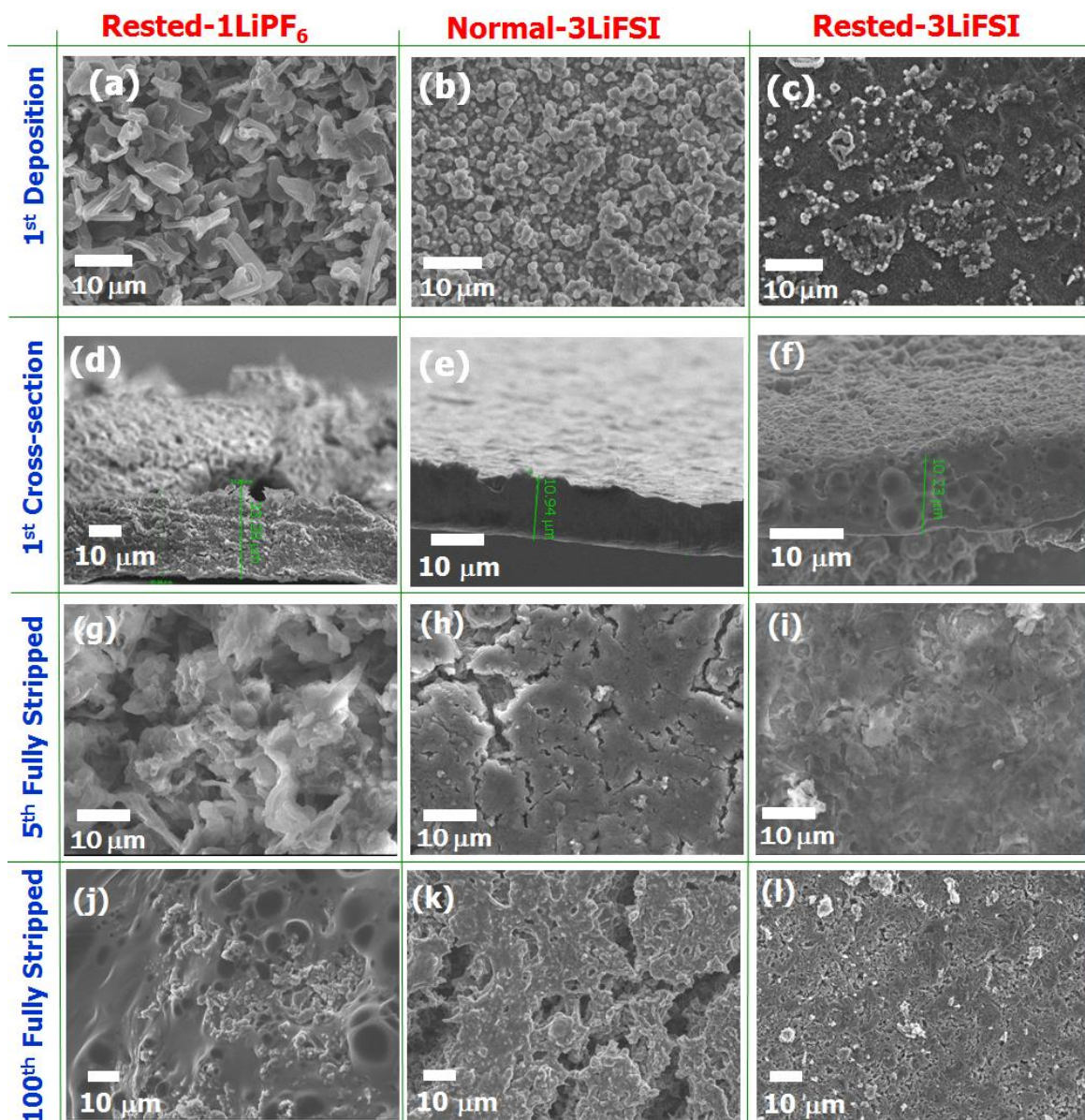


**Figure 6:** SEM morphological evaluation of Li-anode on Cu substrate retrieved from Cu||LFP cell after cycled @ 0.2 mA/cm<sup>2</sup> in different electrolytes and cycling protocol. The rows represent cycle number and its stage while the columns represent the electrolyte and cycling condition as it is written

The formation of the SEI is clearly observed from the surface in comparison to the unrested deposit (Fig. 7f). Morphological evaluations of the Li deposit on Cu substrate is again undertaken after 5 cycles fully discharged



state to see the effect cycling. Accordingly, the morphology of Li film cycled in the baseline electrolyte was found rough indicating the growth of Li dendrite during cycling (Fig. 7g). In contrary, the morphology deposited film in 3LiFSI electrolyte formed SEI that could protect growth of Li dendrite and remained uniform after cycling. In the battery cycled using the normal protocol, the deposition of Li underneath induced SEI cracking due to its fragility (Fig. 7h). Surprisingly, the morphology of Li film retrieved AFB cycled in the laboratory prepared electrolyte using our optimized protocol is pretty uniform with no sign of SEI cracking after 5 cycles (Fig. 7i). Formation of such uniform SEM image is attributed to the synergistic effect between the laboratory prepared ether based electrolyte (3LiFSI) and our optimized protocol which enables formation of good SEI in the process.

#### 4. CONCLUSION

The synergistic effect of cycling protocol and the concentrated electrolyte on the cyclic performance of the Cu||Li half-cell and Cu||LFP anode free cells were carefully studied. Interestingly, a substantial difference in the cyclic performance of both Cu||Li half-cell and Cu||LFP anode-free was observed. Consequently, Cu||Li cells manifested extraordinary cyclic performance and cycled up to 1500 cycles at the high rate of 2.0 mA/cm<sup>2</sup> with average CE of 99.88% benefiting from the combined effects of our resting protocol and the laboratory-prepared concentrated electrolyte (3LiFSI). More importantly, Cu||LFP cell also delivered excellent performance at 0.5 mA/cm<sup>2</sup> with the average CE of up to 98.78% retaining around 40% of the initial discharge capacity after 100 cycles. In addition, the AFB was also cycled at a higher rate up to 1.0 mA/cm<sup>2</sup> with an average CE of 98.2 retaining reasonable discharge capacity after 100 cycles cell. The comparably high electrochemical performance of these cells at a high rate is attributed to the formation of stable, robust and flexible SEI as a result of the combined effect between the optimized cycling protocol and the laboratory-prepared concentrated electrolyte. The concentrated electrolyte with high fluorine donating salt (LiFSI) enabled the formation of good SEI by relatively reducing the solvent interaction with Li surface. In the more dilute, 1LiPF<sub>6</sub> electrolyte, the solvent to salt ratio is quite large and the solvents are found to continuously react with the in-situ deposited Li to form unstable thick SEI. The compositions of the SEI and their relative intensities were analyzed by XPS measurement and revealed that the combined effect between resting and the concentrated electrolyte offered an advantage to form SEI with more inorganic species like LiF. The highly stable and conductive nature of the SEI resulted from the combined effect leads to highly stable voltage profiles during cycling of Cu||LFP cells and improved performance. This study provides a path towards effective investigations of AFBs as a hope for future advanced energy storage devices.

#### ACKNOWLEDGMENTS

This work was financially aided by Ministry of Science and Technology (MOST) (106-2923-E 011-005, 105-3113-E-011-001, 105-ET-E-011-004-ET, 104-2923-M-011-002-MY3, 104-2911-1-011-505-MY2, 103-2221-E-011-156-MY3), the Applied Research Center for Thin-Film Metallic Glass from the Featured Areas Research Center Program within the framework of the Higher Education Sprout Project by the Ministry of Education of Taiwan, Taiwan's Deep Decarbonization Pathways toward a Sustainable Society Project (AS-KPQ-106- DDPP) from Academia Sinica as well as the facilities support from National Taiwan University of Science and Technology (NTUST) and National Synchrotron Radiation Research Centre (NSRRC) are also acknowledged.

#### REFERENCES

- An, S. J., J. Li, C. Daniel, D. Mohanty, S. Nagpure and D. L. Wood (2016). "The state of understanding of the lithium-ion-battery graphite solid electrolyte interphase (SEI) and its relationship to formation cycling." *Carbon* 105: 52-76.
- Assegie, A. A., J.-H. Cheng, L.-M. Kuo, W.-N. Su and B.-J. Hwang (2018). "Polyethylene oxide film coating enhances lithium cycling efficiency of an anode-free lithium-metal battery." *Nanoscale* 10(13): 6125-6138.
- Bai, P., J. Li, F. R. Brushett and M. Z. Bazant (2016). "Transition of lithium growth mechanisms in liquid electrolytes." *Energy & Environmental Science* 9(10): 3221-3229.
- Basile, A., A. I. Bhatt and A. P. O'Mullane (2016). "Stabilizing lithium metal using ionic liquids for long-lived batteries." *Nature Communications* 7: ncomms11794.



- Chang, J., J. Shang, Y. Sun, L. K. Ono, D. Wang, Z. Ma, Q. Huang, D. Chen, G. Liu, Y. Cui, Y. Qi and Z. Zheng (2018). "Flexible and stable high-energy lithium-sulfur full batteries with only 100% oversized lithium." *Nature Communications* 9(1): 4480.
- Chang, W. J., S. H. Kim, J. Hwang, J. Chang, D. w. Yang, S. S. Kwon, J. T. Kim, W. W. Lee, J. H. Lee, H. Park, T. Song, I.-H. Lee, D. Whang and W. Il Park (2018). "Controlling electric potential to inhibit solid-electrolyte interphase formation on nanowire anodes for ultrafast lithium-ion batteries." *Nature Communications* 9(1): 3461.
- Cheng, X.-B., R. Zhang, C.-Z. Zhao, F. Wei, J.-G. Zhang and Q. Zhang (2015). "A Review of Solid Electrolyte Interphases on Lithium Metal Anode." *Advanced science* (Weinheim, Baden-Wurttemberg, Germany) 3(3): 1500213-1500213.
- Gu, Y., W.-W. Wang, Y.-J. Li, Q.-H. Wu, S. Tang, J.-W. Yan, M.-S. Zheng, D.-Y. Wu, C.-H. Fan, W.-Q. Hu, Z.-B. Chen, Y. Fang, Q.-H. Zhang, Q.-F. Dong and B.-W. Mao (2018). "Designable ultra-smooth ultra-thin solid-electrolyte interphases of three alkali metal anodes." *Nature Communications* 9(1): 1339.
- Haregewoin, A. M., A. S. Wotango and B.-J. Hwang (2016). "Electrolyte additives for lithium ion battery electrodes: progress and perspectives." *Energy & Environmental Science* 9(6): 1955-1988.
- Huang, G., J. Han, C. Yang, Z. Wang, T. Fujita, A. Hirata and M. Chen (2018). "Graphene-based quasi-solid-state lithium-oxygen batteries with high energy efficiency and a long cycling lifetime." *NPG Asia Materials*.
- Jiangfeng Qian, Brian D. Adams, Jianming Zheng, W. Xu, Wesley A. Henderson, Jun Wang, Mark E. Bowden, Suochang Xu, Jianzhi Hu and J.-G. Zhang (2016). "Anode Free Rechargeable Lithium Metal batteries." *Advanced Functional Materials* 26: 7094–7102.
- Khurana, R., J. L. Schaefer, L. A. Archer and G. W. Coates (2014). "Suppression of Lithium Dendrite Growth Using Cross-Linked Polyethylene/Poly(ethylene oxide) Electrolytes: A New Approach for Practical Lithium-Metal Polymer Batteries." *Journal of the American Chemical Society* 136(20): 7395-7402.
- Kozen, A. C., C.-F. Lin, O. Zhao, S. B. Lee, G. W. Rubloff and M. Noked (2017). "Stabilization of Lithium Metal Anodes by Hybrid Artificial Solid Electrolyte Interphase." *Chemistry of Materials* 29(15): 6298-6307.
- Lee, Y.-G., S. Ryu, T. Sugimoto, T. Yu, W.-s. Chang, Y. Yang, C. Jung, J. Woo, S. G. Kang, H. N. Han, S.-G. Doo, Y. Hwang, H. Chang, J.-M. Lee and J.-Y. Sun (2017). "Dendrite-Free Lithium Deposition for Lithium Metal Anodes with Interconnected Microsphere Protection." *Chemistry of Materials* 29(14): 5906-5914.
- Li, G., Z. Liu, Q. Huang, Y. Gao, M. Regula, D. Wang, L.-Q. Chen and D. Wang (2018). "Stable metal battery anodes enabled by polyethylenimine sponge hosts by way of electrokinetic effects." *Nature Energy* 3(12): 1076-1083.
- Li, L., S. Basu, Y. Wang, Z. Chen, P. Hundekar, B. Wang, J. Shi, Y. Shi, S. Narayanan and N. Koratkar (2018). "Self-heating-induced healing of lithium dendrites." *Science* 359(6383): 1513-1516.
- Li, N.-W., Y. Shi, Y.-X. Yin, X.-X. Zeng, J.-Y. Li, C.-J. Li, L.-J. Wan, R. Wen and Y.-G. Guo (2018). "A Flexible Solid Electrolyte Interphase Layer for Long-Life Lithium Metal Anodes." *Angewandte Chemie International Edition* 57(6): 1505-1509.
- Li, S., M. Jiang, Y. Xie, H. Xu, J. Jia and J. Li (2018). "Developing High-Performance Lithium Metal Anode in Liquid Electrolytes: Challenges and Progress." *Advanced Materials* 30(17): 1706375.
- Li, X., M. Banis, A. Lushington, X. Yang, Q. Sun, Y. Zhao, C. Liu, Q. Li, B. Wang, W. Xiao, C. Wang, M. Li, J. Liang, R. Li, Y. Hu, L. Goncharova, H. Zhang, T.-K. Sham and X. Sun (2018). "A high-energy sulfur cathode in carbonate electrolyte by eliminating polysulfides via solid-phase lithium-sulfur transformation." *Nature Communications* 9(1): 4509.
- Lindgren, F., C. Xu, L. Niedzicki, M. Marcinek, T. Gustafsson, F. Björefors, K. Edström and R. Younesi (2016). "SEI Formation and Interfacial Stability of a Si Electrode in a LiTDI-Salt Based Electrolyte with FEC and VC Additives for Li-Ion Batteries." *ACS Applied Materials & Interfaces* 8(24): 15758-15766.
- Liu, F.-Q., W.-P. Wang, Y.-X. Yin, S.-F. Zhang, J.-L. Shi, L. Wang, X.-D. Zhang, Y. Zheng, J.-J. Zhou, L. Li and Y.-G. Guo (2018). "Upgrading traditional liquid electrolyte via in situ gelation for future lithium metal batteries." *Science Advances* 4(10): eaat5383.
- Liu, P., Q. Ma, Z. Fang, J. Ma, Y.-S. Hu, Z.-B. Zhou, H. Li, X.-J. Huang and L.-Q. Chen (2016). "Concentrated dual-salt electrolytes for improving the cycling stability of lithium metal anodes." *Chin. Phys. B* 25: 078203.
- Liu, S., X. Xia, S. Deng, D. Xie, Z. Yao, L. Zhang, S. Zhang, X. Wang and J. Tu "In Situ Solid Electrolyte Interphase from Spray Quenching on Molten Li: A New Way to Construct High-Performance Lithium-Metal Anodes." *Advanced Materials* 0(0): 1806470.
- Liu, Y., Q. Liu, L. Xin, Y. Liu, F. Yang, E. A. Stach and J. Xie (2017). "Making Li-metal electrodes rechargeable by controlling the dendrite growth direction." *Nature Energy* 2: 17083.
- Lopez, J., Y. Sun, D. G. Mackanic, M. Lee, A. M. Foudeh, M.-S. Song, Y. Cui and Z. Bao (2018). "A Dual-Crosslinking Design for Resilient Lithium-Ion Conductors." *Advanced Materials* 30(43): 1804142.



- Ma, J.-l., F.-l. Meng, Y. Yu, D.-p. Liu, J.-m. Yan, Y. Zhang, X.-b. Zhang and Q. Jiang (2019). "Prevention of dendrite growth and volume expansion to give high-performance aprotic bimetallic Li-Na alloy–O<sub>2</sub> batteries." *Nature Chemistry* 11(1): 64-70.
- Ong, M. T., O. Verners, E. W. Draeger, A. C. T. van Duin, V. Lordi and J. E. Pask (2015). "Lithium Ion Solvation and Diffusion in Bulk Organic Electrolytes from First-Principles and Classical Reactive Molecular Dynamics." *The Journal of Physical Chemistry B* 119(4): 1535-1545.
- Pang, Q., A. Shyamsunder, B. Narayanan, C. Y. Kwok, L. A. Curtiss and L. F. Nazar (2018). "Tuning the electrolyte network structure to invoke quasi-solid state sulfur conversion and suppress lithium dendrite formation in Li–S batteries." *Nature Energy* 3(9): 783-791.
- Qian, J., W. A. Henderson, W. Xu, P. Bhattacharya, M. Engelhard, O. Borodin and J.-G. Zhang (2015). "High rate and stable cycling of lithium metal anode." *Nature communications* 6: 6362.
- Suo, L., W. Xue, M. Gobet, S. G. Greenbaum, C. Wang, Y. Chen, W. Yang, Y. Li and J. Li (2018). "Fluorine-donating electrolytes enable highly reversible 5-V-class Li metal batteries." *Proceedings of the National Academy of Sciences* 115(6): 1156-1161.
- Tripathi, A. M., W.-N. Su and B. J. Hwang (2018). "In situ analytical techniques for battery interface analysis." *Chemical Society Reviews* 47(3): 736-851.
- Wang, A., S. Kadam, H. Li, S. Shi and Y. Qi (2018). "Review on modeling of the anode solid electrolyte interphase (SEI) for lithium-ion batteries." *npj Computational Materials* 4(1): 15.
- Wotango, A. S., W.-N. Su, E. G. Leggesse, A. M. Haregewoin, M.-H. Lin, T. A. Zegeye, J.-H. Cheng and B.-J. Hwang (2017). "Improved Interfacial Properties of MCMB Electrode by 1-(Trimethylsilyl)imidazole as New Electrolyte Additive To Suppress LiPF<sub>6</sub> Decomposition." *ACS Applied Materials & Interfaces* 9(3): 2410-2420.
- Wu, F., W. Fitzhugh, L. Ye, J. Ning and X. Li (2018). "Advanced sulfide solid electrolyte by core-shell structural design." *Nature Communications* 9(1): 4037.
- Wu, J., H. Zeng, X. Li, X. Xiang, Y. Liao, Z. Xue, Y. Ye and X. Xie (2018). "Ultralight Layer-by-Layer Self-Assembled MoS<sub>2</sub>-Polymer Modified Separator for Simultaneously Trapping Polysulfides and Suppressing Lithium Dendrites." *Advanced Energy Materials* 8(35): 1802430.
- Xiang, J., L. Yuan, Y. Shen, Z. Cheng, K. Yuan, Z. Guo, Y. Zhang, X. Chen and Y. Huang (2018). "Improved Rechargeability of Lithium Metal Anode via Controlling Lithium-Ion Flux." *Advanced Energy Materials*: 1802352.
- Xie, J., J. Ye, F. Pan, X. Sun, K. Ni, H. Yuan, X. Wang, N. Shu, C. Chen and Y. Zhu "Incorporating Flexibility into Stiffness: Self-Grown Carbon Nanotubes in Melamine Sponges Enable A Lithium-Metal-Anode Capacity of 15 mA h cm<sup>-2</sup> Cyclable at 15 mA cm<sup>-2</sup>." *Advanced Materials* 0(0): 1805654.
- Yan, C., X.-B. Cheng, Y. Tian, X. Chen, X.-Q. Zhang, W.-J. Li, J.-Q. Huang and Q. Zhang (2018). "Dual-Layered Film Protected Lithium Metal Anode to Enable Dendrite-Free Lithium Deposition." *Advanced Materials* 30(25): 1707629.
- Yang, C.-P., Y.-X. Yin, S.-F. Zhang, N.-W. Li and Y.-G. Guo (2015). "Accommodating lithium into 3D current collectors with a submicron skeleton towards long-life lithium metal anodes." *Nature Communications* 6: 8058.
- Zhang, H., X. Liao, Y. Guan, Y. Xiang, M. Li, W. Zhang, X. Zhu, H. Ming, L. Lu, J. Qiu, Y. Huang, G. Cao, Y. Yang, L. Mai, Y. Zhao and H. Zhang (2018). "Lithiophilic-lithiophobic gradient interfacial layer for a highly stable lithium metal anode." *Nature Communications* 9(1): 3729.
- Zhang, S. S. (2006). "A review on electrolyte additives for lithium-ion batteries." *Journal of Power Sources* 162(2): 1379-1394.
- Zhao, C.-Z., P.-Y. Chen, R. Zhang, X. Chen, B.-Q. Li, X.-Q. Zhang, X.-B. Cheng and Q. Zhang (2018). "An ion redistributor for dendrite-free lithium metal anodes." *Science Advances* 4(11): eaat3446.
- Zhao, W., J. Zheng, L. Zou, H. Jia, B. Liu, H. Wang, M. H. Engelhard, C. Wang, W. Xu, Y. Yang and J.-G. Zhang (2018). "High Voltage Operation of Ni-Rich NMC Cathodes Enabled by Stable Electrode/Electrolyte Interphases." *Advanced Energy Materials* 8(19): 1800297.
- Zheng, J., M. H. Engelhard, D. Mei, S. Jiao, B. J. Polzin, J.-G. Zhang and W. Xu (2017). "Electrolyte additive enabled fast charging and stable cycling lithium metal batteries." *Nature Energy* 2: 17012.
- Zou, P., Y. Wang, S.-W. Chiang, X. Wang, F. Kang and C. Yang (2018). "Directing lateral growth of lithium dendrites in micro-compartmented anode arrays for safe lithium metal batteries." *Nature Communications* 9(1): 464.



## Biofuel Potential and Invasive Species Control: Exploring *Prosopis juliflora* Pod Mash for Sustainable Energy Production

Mebrahtu Haile<sup>1,\*</sup>, Hadgu Hishe<sup>1</sup>, Desta Gebremedhin<sup>2</sup>

<sup>1</sup>Department of Land Resource Management and Environmental Protection, College of Dryland Agriculture and Natural Resources, Mekelle University, Ethiopia

<sup>2</sup>Department of Chemistry, College of Natural and Computational Sciences, Mekelle University, Ethiopia

\*Corresponding author, e-mail: [mebrahtu.haile@mu.edu.et](mailto:mebrahtu.haile@mu.edu.et)

### ABSTRACT

Fuels obtained from renewable resources have garnered significant enthusiasm in recent decades due to concerns about fossil fuel depletion and climate change. This study aimed to investigate the potential of *Prosopis juliflora* pods mash for bio-ethanol production and its hydrolysis solid waste for solid fuel. Various parameters, such as acid concentration, hydrolysis times, fermentation times, fermentation temperature, and pH, were evaluated for their impact on bio-ethanol production using *Saccharomyces cerevisiae* yeast. The results showed that increasing acid concentration (up to 1 molar H<sub>2</sub>SO<sub>4</sub>) led to an increase in sugar content, reaching a maximum of 96.13%v/v. Optimal conditions for bio-ethanol production were found at 1 molar H<sub>2</sub>SO<sub>4</sub> concentration (4.2%v/v), 48 hours fermentation time (5.1%v/v), 20 minutes hydrolysis time (5.57%v/v), 30°C fermentation temperature (5.57%v/v), and pH 5 (6.01%v/v), resulting in a maximum bio-ethanol yield of 6.01%v/v. The solid waste remaining after bio-ethanol production exhibited potential for use as a solid fuel, with a calorific value of 18.22 MJ/kg. These findings demonstrate the promising potential of *Prosopis juliflora* pods mash for bio-ethanol production and suggest a viable solution for addressing disposal challenges associated with solid waste, contributing to the exploration of renewable fuel sources in the face of fossil fuel depletion and climate change.

**Keywords:** bio-ethanol, fermentation, invasive species, pods mash, *Prosopis juliflora*, *Saccharomyces cerevisiae*, solid fuel

### 1. INTRODUCTION

One of the greatest challenges for the growing society in this century is to meet the energy demand for transportation, heating, lighting and industrial processes, which have a significant impact on the environment. World population and increased urbanization have directly or indirectly influenced the energy demand (Akpan *et al.*, 2008). In developing countries, especially in rural areas, 2.5 billion people rely on biomass, to meet their energy needs for cooking (Zuzarte, 2007). As in many other countries in the region, fuel supply in Ethiopia is mainly biomass-based (94.3 % of total energy supply) (Ministry of Mines and Energy, 2011).

Modern fuels are those that are controlled to provide consistent energy, efficient and clean when combusted, such as biofuels or electricity (Zuzarte, 2007). Bio-ethanol is a biofuel which has long been recognized as a fuel suitable for a variety of applications, including transportation and cooking (Prasad *et al.*, 2009). It is one of the safe and environmentally friendly energy since it is made from plants; it does not release any new carbon dioxide (CO<sub>2</sub>) into the air, unlike fossil fuels which return carbon that was stored beneath the surface for millions of years. It can be made from any sugary or starchy and from cellulosic biomass such as wood, paper pulp or agricultural waste (Pikūnas *et al.*, 2003). Nowadays, research on non- food crops and cellulosic materials has been getting great attention worldwide, because they are cheap, easily available, and profitable as compared to food crops and also reduce inflation of the cost of food crops used for bio-production (Choge *et al.*, 2007).

One of the fastest growing trees which have the potential to substitute food crops for bio-ethanol production could be *Prosopis juliflora*. It is a tree species native to Northern Mexico and Southern U.S. that survives droughts and thrives in sunny arid regions. The plant fixes its own nitrogen, requires no seeding, fertilization or irrigation, and grows on dry, nutrient-poor soils (Shiferaw *et al.*, 2004). It is a truly promising tree for drylands, because of its multiple and important potential and actual uses, as well as its remarkable resistance to drought, heat, and poor soils (citation!!). Most often, the tree grows only to become a thorny shrub, but its complex and deep-ranging root system allow it to tap different water tables, both at the surface and deep underground, which makes it a very hardy crop (citation!!). The roots also act as an energy storage mechanism, because once a tree is cut down, new shoots spring up rapidly from the existing roots (Pasicznik *et al.*, 2001).



The pods produced by *Prosopis* species are legume pods, high in sugars, starches, and protein. The pods are used as a source of food for human being in history, however, it has turned out to be less important as a human food, somewhat essential as animal feed since the past decades. The pods vary significantly in size between species and even among the population and individual trees of some species (Bravo *et al.*, 1994; Pasiecznik *et al.*, 2001). Pods of all *Prosopis* species are composed of an exocarp, sometimes fleshy mesocarp, fibrous endocarps and hard seeds. The form and relative amounts of each vary widely between species, with several *Prosopis* species having a high percentage of mesocarp favored as a source of food and feed (Choge *et al.*, 2007). *Prosopis juliflora* was introduced to Ethiopia in the 1970s and planted in few areas in the Rift Valley (Abebe, 1994). The species, however, has been spreading in the pastoral areas, making vast rangelands unavailable for grazing, where its removal and management has become already beyond the capacity of the local communities (Admasu 2008; Ryan, 2011). The species has large coppicing potential, which makes its removal very difficult and expensive. The invasiveness of the species has been aggravated by animals which feed on it, such as camel, goats, and cattle in Afar (Hailu *et al.*, 2004).

*Prosopis juliflora* is found dominantly on the arid part of Ethiopia like Afar, some parts of Oromia, Dire Dawa, Tigray, Somali, Southern Nations, Nationalities and Peoples (SNNP) and Amahara regions (Steele, 2009). It is a fast-growing tree species and it will be a good source of bio-ethanol production to reduce dependence on the rapidly increasing price of petroleum crude and products, as well as to manage its invasion in the environment. The conversion of the various parts of the species into alternative uses could also create new jobs that benefit farmers and pastoral communities, for instance by improving their access to livestock feeds and income from bio-ethanol production. In addition, the conversion of the pods into bio-ethanol and the seeds into biochar have the advantage of controlling its invasion into a new area. The main objective of this research was to evaluate the potential of *P. juliflora* pods for bio-ethanol production and its solid waste by-product as solid fuel.

## 2. MATERIALS AND METHODS

### 2.1 Collection of samples

The pods of *P. juliflora* were collected at Amibara, one of the severely invaded woredas from Afar region, Ethiopia. Healthy *P. juliflora* trees were selected and dry pods were collected. The composite pods collected were taken in plastic bags and dispatched to Mekelle University laboratory for further work. The experiment was conducted in a laboratory at Mekelle University, Adigrat medical laboratory and Geological survey of Ethiopia central laboratory, following the methods mentioned in Onuki (2005).

### 2.2 Dry and Milling

The *P. juliflora* pods were sun-dried and broken down to a fine powder using a hammer mill process. Grinding increased surface area of the pods and enhance the contact between starch and acid or water. The seed of *P. juliflora* was hard to mill by hammer milling and only the pod was used for this experiment and we recommend the seeds to be used as a biochar feedstock. Compared to the amount of the pod, the amount of seed obtained from a large collection of the pod was very small in amount/content and not economical to use alone for bio-ethanol production.

### 2.3 Determination of Moisture Content

The *P. juliflora* pod was dried using an oven at 105 °C followed by cooling in a desiccator over silica gel (0% relative humidity) and weighing until a constant weight. The moisture content was determined as in equation 1:

$$\text{Moisture content (\%)} = \frac{w_1 - w_2}{w_1} \times 100 \quad (1)$$

Where  $w_1$  and  $w_2$  are the weights of the sample before (g) and after drying (g), respectively

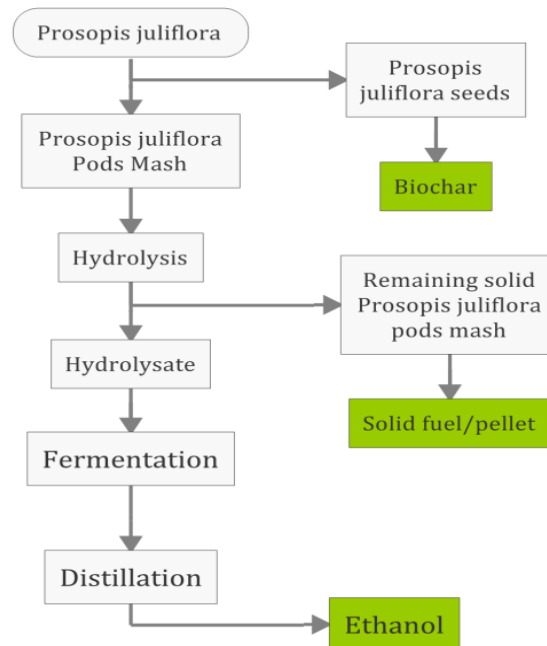


**Fig. 1:** The path for the production of bio-ethanol and its value-added from *P. juliflora* pods mash

## 2.4 Hydrolysis

The *P. juliflora* pod powder (25 g) was hydrolyzed (pretreated) employing different concentrations of sulfuric acid (each of 0.5, 1, 1.5, 2, 2.5 and 3 molar) and with 250 ml of distilled water in 500 ml Erlenmeyer flask and separately heated at 90 °C for 15 minutes. After hydrolysis, the liquid fraction was cooled, filtered and determined for glucose concentration. The distilled water and acid hydrolysates were adjusted to pH 5 by adding concentrated sulfuric acid and 2N sodium hydroxide, and the solutions were filtered and prepared for fermentation (Dawson and Boopaty, 2008).



**Fig. 2** Hydrolysis process

## 2.5 Fermentation

### 2.5.1 Source of microorganism for fermentation

*S. cerevisiae*, purchased from the local market was used in the experiments. The yeast was first dissolved in warm water and left for 10 min before being used. Then the prepared solutions were taken into the flask containing hydrolysate sample. Batch fermentations of hydrolysis were carried out in 500 ml Erlenmeyer flask incubated with 5 g/l *S. cerevisiae* at 30 °C as described in the literature (Thuesombat *et al.*, 2007). The hydrolysates of water (Treatment 1), 0.5 molar (M) sulfuric acid treated hydrolysate (Treatment 2), 1 M sulfuric acid treated hydrolysate (Treatment 3), 1.5 M sulfuric acid treated hydrolysate (Treatment 4), 2 M sulfuric acid treated

hydrolysate (Treatment 5), 2.5 M sulfuric acid treated hydrolysate (Treatment 6) and 3 M sulfuric acid treated (Treatment 7) was taken.



**Fig. 3** Samples prepared for fermentation

### 2.5.2 Ethanol fermentation

After scarification, the substrates were allowed to ferment in yeast (*S. cerevisiae*). The set up was left under anaerobic condition for 24 h with the different H<sub>2</sub>SO<sub>4</sub> concentrations (0, 0.5, 1, 1.5, 2, 2.5 and 3 M) to select the best treatment type for bio-ethanol production. The substrate with the best bio-ethanol yield was subjected for optimization with different periods of fermentation times (6, 12, 24, 36, 48 and 72 h), hydrolysis times (5, 10, 15, 20, 25, 30 min), and fermentation temperatures (25 °C, 30 °C, 35 °C and 40 °C), pH (4, 5, 6, 7 and 8)(Ayele *et al.*, 2012) keeping the optimized parametrs constant.

### 2.6 Ethanol recovery

#### 2.6.1 Distillation method

The bio-ethanol was separated from the fermented sample by fractional distillation. The fermented solution was heated to force the lowest boiling material into the vapor phase. The vapors were passed over the fractional column and the bulb of a thermometer at which point vapor was determined. The vapor was condensed to a liquid in the horizontal condenser that was cooled by a flow of cold water. The distillate was collected in a receiver. The weight of the distillate was measured.

#### 2.6.2 Yield calculations

First, the gram of bio-ethanol was calculated based on the collected amount and concentration of bio-ethanol and expressed on a weight basis. The bio-ethanol yield was then calculated based on the gram of bio-ethanol and the sample taken.

$$Ge = \frac{(Ce \times Ac)}{100} \quad (2)$$

Where Ge, Ce and Ac are the gram of bio-ethanol (g), concentration of bio-ethanol and the amount collected (g)

$$\text{Yield of bioethanol (\%)} = \frac{\text{Gram of bioethanol (g)}}{\text{Sample (g)}} \quad (3)$$

### 2.7 Analytical Methods

#### 2.7.1 Determination of sugar contents

The sugar contents of the samples during saccharification of the substrates were estimated as per the method described in Ayele *et al* (2012). Fehling method was used to determine the reducing sugar concentration. 50 ml of the hydrolyzed sample solution was taken and dissolved in 10 ml of distilled water and mixed with 2 ml of cons. HCl acid and was heated for a period of 10 min. The obtained sample was neutralized by adding NaOH and

prepared in 300 ml conical flask and taken into the burette. The 10 ml of Fehling solution was taken and mixed with 90 ml of distilled water in 250 ml Erlenmeyer flask and Methyl blue indicator was added. The conical flask solution was titrated with burette solution in boiling conditions until disappearance of blue color and the volume at which brick red color observed were recorded. For each sample the sugar content was calculated by using the formula given below:

Sugar content (%)

$$= \frac{300 \text{ mL} \times f}{v} \times 100\% \quad (4)$$

Where the  $f$ -Fehling factor (0.051);  $v$ -volume used in the titration (titrate value) (ml)

### 2.7.2 Determination of Ethanol Concentration

The Fourier Transform Infrared (FTIR) (65, PerkinElmer, UK) response was calibrated using different concentrations of pure ethanol. The measurement was carried out in reflectance mode where ZnSe (Zinc selenide) window was used as a sample holder. After the absorbance of pure ethanol was recorded the calibration curve was constructed first in weight-to-weight and then converted to volume-to-volume concentration units. The concentrations of ethanol were determined using the absorbance obtained for each sample from the calibration curve.

### 2.7.3 Standard Solution of ethanol

The calibration curve was constructed using the absorbance values obtained for the different ethanol concentrated solutions (Fig. 4). The data points were fitted with a second order polynomial fit of the form.

$$y = ax^2 + bx + c \quad (5)$$

Where  $y$  and  $x$  represent the absorbance and the concentration respectively,  $a$  and  $b$  are fit values that represent second and first order slope, respectively, and  $c$  is the absorbance bias where the concentration is 'zero'. From the fit  $c = 0.00159$ ,  $a = -0.00064 \text{ mol}^{-2} \text{ L}^2$  and  $b = 0.05363 \text{ mol}^{-1} \text{ L}$  were at  $p$ -value  $< 0.0001$ .

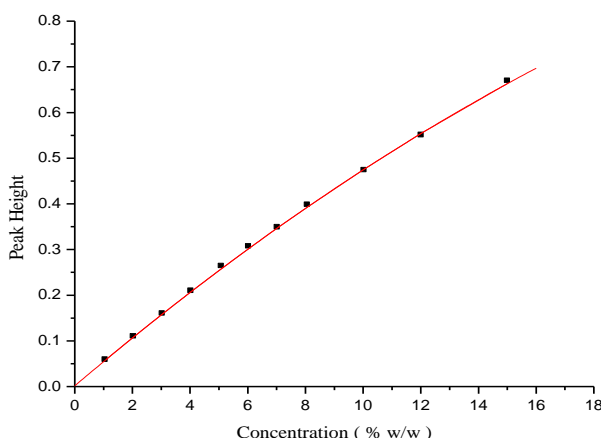


Fig. 4 Calibration curve for ethanol standard solution

The value of  $b$  is more than one order of magnitude greater than  $c$  indicating the absorbance residual bias is very small leading to the high sensitivity of the method with a standard deviation of  $SD = 0.00334$ . The regression value of  $R^2 = 0.99972$  further confirms the reliability of the fit. The calibration curve revealed excellent accuracy and sensitivity, and therefore, was used for determining the concentrations of the samples from the absorbance reading.



### 2.7.4 Determination of *P. juliflora* pod Calorific Value after Hydrolysis

The solid waste after hydrolysis of *P. juliflora* was characterized for solid fuel. The sample waste after hydrolysis was taken for calorific value determination with bomb adiabatic calorimetric instrument and calculated by using the formula given below:

$$Hg = \frac{TW - e_1 - e_2 - e_3}{m} \quad (6)$$

Where Hg = Gross Heat Combustion

T = Temperature difference (°C)

W = energy equivalent of calorimetric in Cal/ °C (2420 Cal/ °C)

e<sub>1</sub> = correction in calories for heat of formation of HNO<sub>3</sub> (24.2 Cal) \* titrate volume (ml)

e<sub>2</sub> = correction in calories for heat formation of H<sub>2</sub>SO<sub>4</sub> (13.7 Cal) \* content of sulfur (negligible)

e<sub>3</sub> = correction in calories for heat formation of fuse wire (2.3) \* length of fuse wire combusted (cm)

m = weight of sample

## 3. RESULTS AND DISCUSSION

### 3.1 Effect of Acid Concentration on Sugar Content

The values of sugar contents obtained from *P. juliflora* in this study were shown in figure 5. This *P. juliflora* reducing sugars were saccharified with different H<sub>2</sub>SO<sub>4</sub> concentrations and distilled water at 90 °C and 15 min hydrolysis time after the determination of moisture content (15.65%).

Figure 5 shows that *P. Juliflora* pods mash has 57.34% sugar content after it was saccharified with distilled water. The sugar content increased with an increase in acid concentration up to 1 M, and at this concentration, the highest value of 96.13% sugar content was obtained. Further increase in acid concentration led to a decrease in sugar content (Fig. 5). The increase of sugar contents in acid treated samples with increasing acid concentration may be due to a complete and fast conversion of cellulose to glucose and hemicelluloses to C<sub>5</sub>-sugars (Nutawan *et al.*, 2010) and as the solution was more concentrated, the monomeric sugars (xylose, glucose) may further be oxidized to undesirable by-products such as furfural, hydroxyl methyl furfural (HMF), etc. by sulfuric acid on glucose (Joshi *et al.*, 2011; Nutawan *et al.*, 2010).

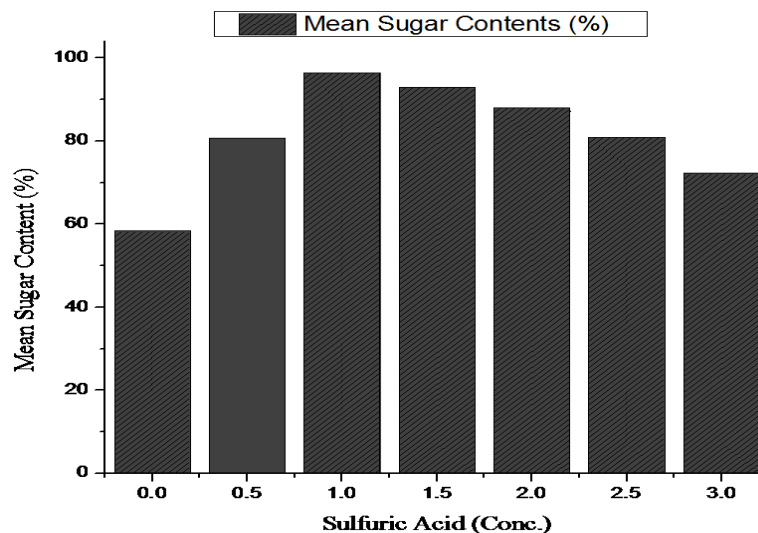


Fig. 5 The effect of acid concentrations on sugar content

### 3.2 Parameters Affecting Bio-Ethanol Production

#### 3.2.1 Acid concentration

The optimum acid concentration determination was carried out with distilled water and different concentrations of H<sub>2</sub>SO<sub>4</sub>, while keeping all the other parameters constant, *i.e.* 90 °C hydrolysis temperatures, 15

min hydrolysis time, pH 5, 24 h fermentation time and 30 °C fermentation temperature were applied for all concentration samples.

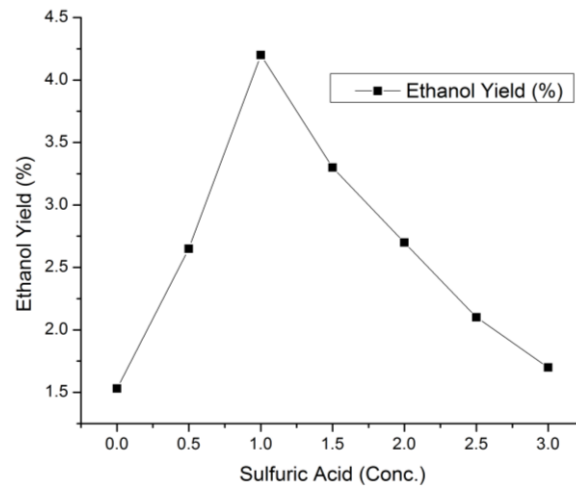


**Fig. 6** The effect of acid concentration on bio-ethanol production

Figure 6 shows that the bio-ethanol yields obtained in distilled water and 0.5 M H<sub>2</sub>SO<sub>4</sub> concentrations were 1.53% and 2.65% v/v, respectively, and the maximum bio-ethanol yield of 4.2% v/v was obtained in 1 M of H<sub>2</sub>SO<sub>4</sub> concentrations. Further increase in acid concentration (1.5, 2, 2.5 and 3 M H<sub>2</sub>SO<sub>4</sub>) resulted in a decrease in bio-ethanol yield of 3.3, 2.7, 2.1 and 1.7% v/v, respectively. Decreasing bio-ethanol yield at a higher acid concentration may be due to degradation of monomeric sugars to undesirable by-products or may be derived from dehydrating or oxidizing effect of sulfuric acid on glucose instead of forming bio-ethanol (Nutawan *et al.*, 2010).

### 3.2.2 Fermentation time

As shown in Figure 7, the optimization of fermentation time for bio-ethanol production were adjusted ranged from 6-72 h keeping the other parameters constant (1 M H<sub>2</sub>SO<sub>4</sub> – optimum acid concentration obtained from the previous experiment, 90 °C hydrolysis temperature, 15 min hydrolysis time, pH 5 and 30 °C fermentation temperatures).

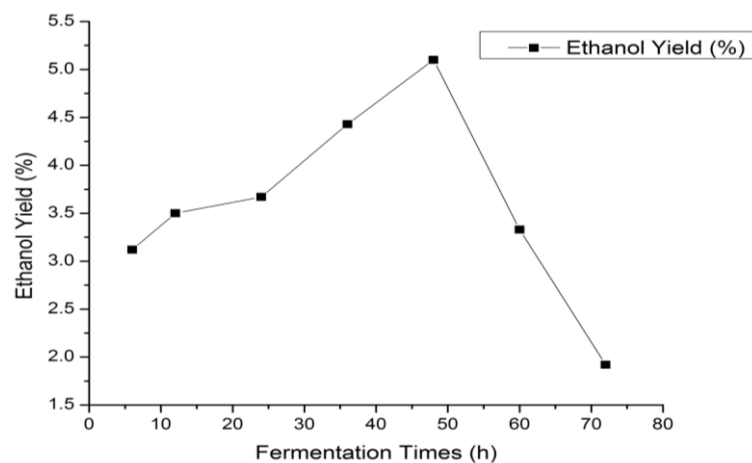


**Fig. 7** The effect of fermentation time on bio-ethanol production

Figure 7 shows that bio-ethanol yield obtained at 6, 12, 24 and 36 h fermentation times were 3.12%, 3.5%, 3.67% and 4.43% v/v, respectively. At 72 h fermentation time, the least bio-ethanol concentration (1.92% v/v) was found, whereas, the maximum bio-ethanol yield (5.1% v/v) was obtained at 48 h fermentation time. The result revealed that the amount of bio-ethanol increased with increase in fermentation time up to a maximum of 48 h fermentation times, and then after it starts to decrease. This may be due to the consumption of sugar by the microorganisms or the hydrolysate does contain significant levels of metabolic inhibitors (e.g., furfural and HMF) that can interfere with fermentation (Weil *et al.*, 2002).

### 3.2.3 Hydrolysis time

Hydrolysis time was taken as another parameter for bio-ethanol production optimization. In the optimization of hydrolysis time, the solutions were kept for 5, 10, 15, 20, 25 and 30 min, pH 5 and 30 °C fermentation temperature, heated at hydrolysis temperature of 90 °C, while keeping the other optimized parameters constant. The result showed that bio-ethanol yield in 5, 10, 15, 20, 25 and 30 minutes of hydrolysis times, which were given 3.78%, 4.72%, 5.16%, 5.57%, 4.4% and 2.83% v/v, respectively. The maximum bio-ethanol yield (5.57% v/v) was obtained at 20 min hydrolysis time (Fig. 8). The result showed that the bio-ethanol yield increases with hydrolysis time and reaches optimum at 20 min. The result obtained is in agreement with what was reported by Ayele *et al.* (2012).

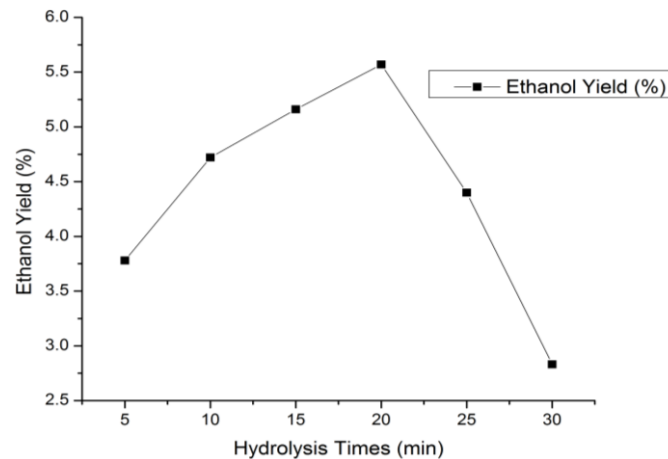


**Fig. 8** The effect of hydrolysis time on bio-ethanol production

The bio-ethanol yield was decreased beyond 20 min as hydrolysis time increases, may be due to the fact that longer residence time makes the sugars further oxidize to form inhibitors (furfural) (Nutawan *et al.*, 2010).

### 3.2.4 Fermentation temperature

As in figure 9, the optimization of fermentation temperature was carried out in 25, 30, 35 and 40 °C, whereas all the optimized, as well as hydrolysis temperature (90 °C) and pH 5 was kept constant.

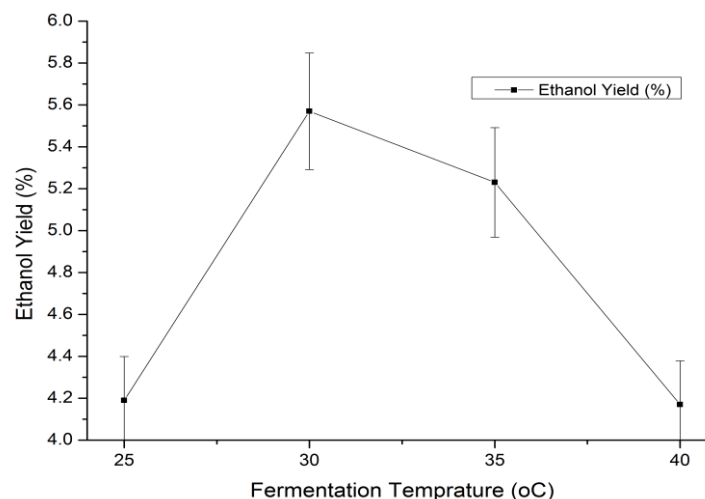


**Fig. 9** The effect of fermentation temperature on bio-ethanol production

The bio-ethanol yields obtained with fermentation temperatures of 25, 30, 35 and 40 °C were 4.19%, 5.57%, and 5.23% and 4.17% v/v respectively (Fig. 9). According to these results, bio-ethanol yield increases from 25 °C - 30 °C fermentation temperature. However, increasing the temperature beyond 30 °C decreased the bio-ethanol yield of *P. juliflora* pods mash. As the result shows, the bio-ethanol yield was found maximum at 30 °C (5.57%

v/v). Fermentation temperature is one of the major constraints that determine the bio-ethanol production. Too high temperature kills yeast, and low temperature slows down yeast activity (Hoi, 2003).

### 3.2.5 pH value

Besides the other parameters, the pH value of the bio-ethanol production was optimized keeping all other parameters constant. The pH from 4-8 was taken and the result revealed that 4.5, 6.01, 5.31, 2.7 and 2.2% v/v respectively (Fig. 10). The maximum bio-ethanol yield was found at pH 5. It is worthwhile to mention that the concentration of bio-ethanol obtained (6.01% v/v) by the hydrolysis of the *Prosopis juliflora* pods mash is satisfactory compared to the maximum amount of bio-ethanol obtained from fermentation of Poultry manure (5 g/L) (Woldesenbet et al., 2013), spent coffee ground after biodiesel production (6.5 g/L) (Haile et al., 2013), wet coffee waste (6.12 g/L) (Woldesenbet et al., 2016). However, the result of this study is very low as compared with bio-ethanol potential of Sugarcane bagasses (10.2 g/L) (Raghavendra and Havannavar, 2007) and Banana peels (9.8 g/L) (Manikandan and Saravanan, 2008).

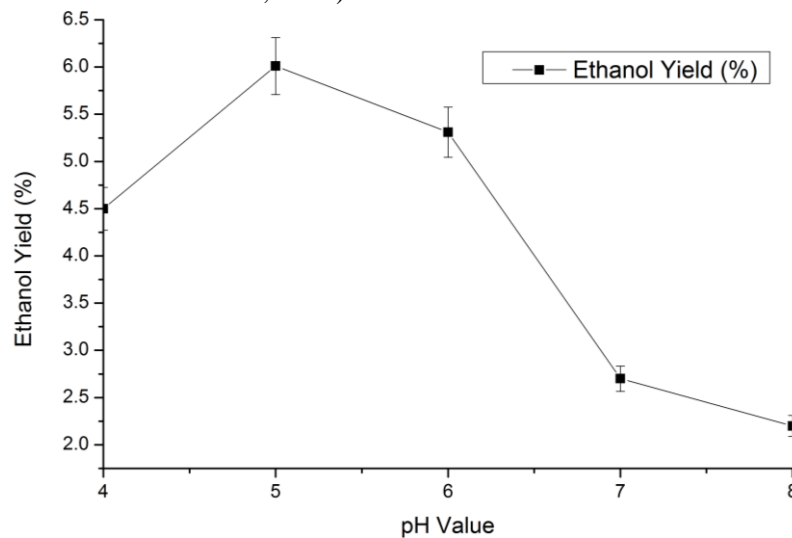


Fig. 10 The effect of pH value on bio-ethanol production

### 3.3 *P. juliflora* as a Solid Fuel Potential after Hydrolysis

The calorific value of *P. juliflora* after bio-ethanol production was recorded as 18.22 MJ/kg. In particular, it has high calorific value compared to the conventional biomass, as in (Hoi, 2003), like bagasse (7.7-8 MJ/Kg), rice husks (14 MJ/Kg), coffee husk (16 MJ/Kg) and wood (8.4- 17) but less than the calorific value of spent coffee ground (20.8 MJ/kg) after hydrolysis and spent coffee ground and glycerin ratio (glycerin content from 20-40%) (19.3-21.6 MJ/Kg) (Haile et al., 2013; Haile, 2014). This result showed the possibility of utilizing *P. juliflora* after hydrolysis as a raw material for solid fuel production. This has a significant contribution to energy supply, while also solving the disposal of wastes after hydrolysis.

## 4. CONCLUSIONS

The aim of this work was to evaluate *P. juliflora* pods as a potential alternative feedstock for bio-ethanol production and its by-product as a solid fuel. The findings of the present result concluded that *P. juliflora* has the potential for bio-ethanol production, as well as solid fuel after hydrolysis. The maximum amount of bio-ethanol yield (6.01% v/v) was obtained after 1 M H<sub>2</sub>SO<sub>4</sub>, 48 h of fermentation time, 20 min of hydrolysis time, pH (5) and 30 °C of fermentation temperature. However, the produced quantity of bio-ethanol is not proportioned to the amount of sugar content in the samples due to *S. Cerevisiae* yeast can ferment only C6 sugars. Additionally, the calorific value of *P. juliflora* after hydrolysis (18.22 MJ/kg) implies the possibility of combining hydrolysis *P. juliflora* for bio-ethanol production with energy production. This contributes to minimizing the use of fuelwood, charcoal, dung cakes, agricultural residues and fossil fuel as the energy source, which has various reported environmental consequences. Additionally, its use contributes to minimizing rising bio-ethanol production from first generation feedstocks such as food crop which has its impact on food security. Based on these premises, we



argue that *P. juliflora* is a promising alternative feedstock for bio-ethanol production and the findings in this study imply alternative means to reduce the global warming arising from combustion of fossil fuel and arresting the invasiveness of the species in various localities in Ethiopia.

## ACKNOWLEDGMENTS

We would like to acknowledge Mekelle University for the recurrent financial support that allowed us to undertake the research work.

## REFERENCES

- Abebe, T. (1994) Growth-performance of some multi-purpose trees and shrubs in the semiarid areas of southern Ethiopia. *Agroforestry Systems*, 26, 237-248.
- Admasu, D. (2008) *Invasive plants and food security: The case of Prosopis juliflora in the Afar region of Ethiopia*. FARM-Africa, IUCN, 1–13.
- Akpan, U.G., Alhakim, A. A. & Ijah, U. J.J. (2008) Production of ethanol Fuel from Organic and Food Wastes. *Leonardo Electronic Journal of Practices and Technologies* ISSN 1583-1078, 1-11.
- Ayele, K., Mesfin, R. & Araya, A. (2012) Potential of Bioethanol Production and Optimization Test from Agricultural Waste; the Case of Wet Coffee Processing Waste (Pulp). *International Journal of renewable energy research*, 2 (3).
- Bravo, L., Grados, N. & Saura-calixto, F. (1994) Composition and potential uses of mesquite pods (*Prosopis pallida* L) - comparison with carob pods (*Ceratonia siliqua* L). *Journal of the Science of Food and Agriculture* 65, 303-306.
- Choge, S.K., Pasiecznik, N.M., Harvey, M., Wright, J., Awan, S.Z., & Harris, P.J. (2007) *Prosopis pods* as human food, with special reference to Kenya. Nairobi, *Kenya Forest Research Institute*, 33 (3), 419-424.
- Dawson, L. & Boopat, R. (2008) Cellulosic ethanol production from sugarcane bagasse without enzymatic saccharification. *Bioresources* 3, 452-460.
- Hailu, S., Demel, T., Sileshi, N. & Fassil, A. (2004) Some biological characteristics that foster the invasion of *P. juliflora* (Sw.) DC. At Middle Awash Rift Valley, North-eastern Ethiopia. *Journal of Arid Environment* 58, 34-153.
- Hoi, W. (2003) *Potential of biomass utilization for energy in Asia Pacific experience of the Philippine situation*, Forest Research Institute. Kepong, Kuala Lumpur Malaysia.
- Joshi, B., Raj Bhatt, M., Sharma, D., Joshi, J., Malla, R. & Sreerama, L. (2011) Lignocellulosic ethanol production: Current practices and recent developments. *Biotechnology and Molecular Biology Review*, 6(8), 172-182.
- Haile, M. (2014) Integrated volarization of spent coffee grounds to biofuels. *Biofuel Research Journal* 2, 65-69.
- Haile, M., Araya, A., & Nigist, A. (2013) Investigation of Waste Coffee Ground as a Potential Raw Material for Biodiesel Production. *International journal of renewable energy research*, 3 (4).
- Manikandan K, Saravanan S. Kinetics studies on bio-ethanol production from banana peel waste using mutant strain of *Saccharomyces cervisiae*. *Indian J Biotechnol.* 2008;7:83–88.
- Ministry of Mines and Energy (2011) *Energy Policy of Ethiopia*, Japan International Cooperation Agency (JICA) Tokyo international center.
- Nutawan, Y., Phattayawadee, P., Patranit, T. & Mohammad, N. (2010) Bioethanol Production from Rice Straw. *Energy Research J.* 1, 26-31.
- Onuki, S. (2005) Bioethanol, Industrial production process, and recent studies; USA organic and food wastes. *Journal of Practices and Technologies*, 13, 1-11.
- Pasiecznik, N.M., Felker, P., Harris, P.J., Harsh, L.W., Cruz, G., Tewari, J.C., Cadoret, K. & Maldonado, L.J. (2001) *The Prosopis juliflora – Prosopis pallida* Complex: a monograph. HDRA, Coventry, UK, pp 162.
- Pikūnas, A., Pukalskas, S. & Grabys, J. (2003) Influence of composition of gasoline-ethanol blends on parameters of internal combustion engines. *Journal of kones internal combustion Engines*, 10, 3-4.
- Prasad, M.P., Rekha, S., Tamilarasan, M. & Subha, K.S. (2009). Production Of Bioethanol Using Various Agricultural Raw Materials By Two Step Enzymatic Process. *Advanced Biotech*, 41 – 43.
- Raghavendra B, Havannavar Geeta SG. Pre-treatment of agroresidues for release of maximum reducing sugar. *Karnataka J Agric Sci.* 2007;20:771–772.
- Ryan, F. (2011) US Forest Service Technical Assistance, Trip to Ethiopia: Invasive species management. Report Submitted to USAID.



- Shiferaw, H., Teketay, D., Nemomissa, S. and Assefa, F. (2004). Some biological characteristics that foster the invasion of *Prosopis juliflora* (Sw.) DC. at Middle Awash Rift Valley Area, northeastern Ethiopia. *Journal of Arid Environments*, 58: 134–153
- Steele, P., Breithaupt, J., & Labrada, R. (2009) *Increased food security: control and management of Prosopis*. Proceedings of an Expert Consultation, 4, Awash (Ethiopia), FAO.
- Thuesombat, P., Thanonkeo, P., Laopaiboon, L., Laopaiboon, P., Yunchalard, S., Kaewkannetra, L. & Thanonkeo, S. (2007) The batch ethanol fermentation of Jerusalem artichoke using *saccharomyces cerevisiae*. *Journal of sciences and Technology* 7:93-96.
- Weil, J., Dien, B., Bothast, R., Hendrickson, R., Mosier, N. & Ladisch, M. (2002) Removal of fermentation inhibitors formed during pretreatment of biomass by polymeric adsorbents. *Ind. Eng. Chem. Res.* 41, 6132–6138.
- Woldesenbet AG, Shiferaw G, Chandravanshi BS. Bio-ethanol production from poultry manure at Bonga Poultry Farm in Ethiopia. *Afr J Environ Sci Technol.* 2013;7:435–440.
- Woldesenbet AG, Woldeyes B, Chandravanshi BS. Bio-bio-ethanol production from wet coffee processing waste in Ethiopia. Springerplus. 2016; 5(1): 1903.
- Zuzarte, F. (2007) *Ethanol for Cooking - Feasibility of Small-scale Ethanol Supply and its Demand as a Cooking Fuel: Tanzania Case Study*. KTH School of Energy and Environmental Technology, Heat and Power Technology, Stockholm, Sweden.



## Hetero-Nanostructures for Sustainable Energy Application via Plasmon-Enhanced Photo/Electrocatalysis

Lemma Teshome Tufa<sup>1,2,\*</sup>, Birnanu Bayissa Gicha<sup>3</sup>, Cheru Fekadu Molla<sup>1</sup>, Jaebeom Lee<sup>2,\*</sup>

<sup>1</sup>Department of Applied Chemistry, School of Natural Sciences, Adama Science and Technology University, Ethiopia

<sup>2</sup>Research Institute of Materials Chemistry, Chungnam National University, South Korea

<sup>3</sup>Environmental Science Program, Haramaya University, Ethiopia

\*Corresponding author, e-mail: LTT, [lemmat2003@yahoo.com](mailto:lemmat2003@yahoo.com); JBL, [nanoleelab@cnu.ac.kr](mailto:nanoleelab@cnu.ac.kr)

### ABSTRACT

Enhancing the efficiency and selectivity of photo/electrocatalytic reactions has become increasingly promising through plasmon-enhanced photo/electrocatalysis using hetero-nanostructures. Plasmonic nanostructures (PNSs), characterized by features such as localized surface plasmon resonance (LSPR), play a crucial role in augmenting photo/electrocatalytic activities. The unique properties of LSPR enable PNSs to concentrate incident light, facilitate charge separation, and trigger surface reactions, thereby improving overall catalytic performance. This work details the preparation of plasmonic core-shell Au@Pd nanoparticles (NPs) and Au@Fe<sub>x</sub>O<sub>y</sub> nanorods (NRs) for plasmon-enhanced photo/electrocatalysis. The focus is on the rational design and synthesis of hetero-nanostructures, emphasizing the optimization of composition, size, shape, and interface properties. Additionally, the exploration extends to various combinations of plasmonic sources with semiconductors of diverse morphologies to achieve heightened photocatalytic activity. The research encompasses applications in water splitting, organic pollutant removal, and energy conversion. Addressing challenges, including material optimization, reproducibility, stability, band alignment, and understanding plasmon-material interactions in hetero-nanostructures, is integral to advancing the field. The synergistic combination of plasmonics and nanotechnology holds great potential for advancing green technologies and addressing critical global issues.

**Keywords:** Au@Pd NPs, Au@Fe<sub>x</sub>O<sub>y</sub> NRs, LSPR, Plasmonics, Photo/electrocatalysis

### 1. INTRODUCTION

The continuous consumption of combustion energy has demonstrated its lack of sustainability, primarily due to the impending depletion of remaining fossil fuel reserves and the adverse environmental impacts it entails. Addressing these pressing concerns requires tackling the paramount scientific challenge of developing technologies capable of generating renewable fuels and chemicals from diverse, sustainable feedstocks. This imperative effort is crucial for steering society towards a sustainable future. Heterogeneous catalysis, positioned at the core of modern industry, has significantly enhanced the efficiency of chemical manufacturing processes. Typically, achieving reasonable rates for target chemical production involves employing harsh reaction conditions, including elevated temperatures and pressures. As an example, consider the traditional Haber–Bosch method used for synthesizing ammonia (NH<sub>3</sub>) at a rate of 150 million tons per year from N<sub>2</sub> and H<sub>2</sub>. This process typically operates within the temperature range of 300–500 °C and under pressures of 200–300 atm. Additionally, nearly half of the global H<sub>2</sub> production stems from the energy-intensive steam reforming of methane (CH<sub>4</sub> + H<sub>2</sub>O → CO + 3H<sub>2</sub>), requiring high temperatures (800–1000 °C) and substantial energy input (Lukajtis et al., 2018; Van der Ham et al., 2014). Therefore, it is necessary to create sustainable catalytic processes that leverage renewable energy sources as the primary input. One potential solution in this striving involves harnessing photocatalysis driven by solar energy (Low et al., 2017).

Plasmon-enhanced photoelectrocatalysis using hetero-nanostructures has emerged as a highly promising research area with significant potential for advancing the field of energy conversion and environmental remediation (Lee et al., 2021; S. Li et al., 2021). Plasmon-enhanced photo/electrocatalysis, which combines the principles of plasmonics, photoelectrochemistry, and catalysis, has attracted considerable attention due to its ability to utilize solar energy for the conversion of light into chemical energy or to drive important chemical reactions. A key component of this technology is the integration of hetero-nanostructures, which combine different materials on a nanoscale. The hetero-nanostructures, often based on metal nanoparticles, aka., plasmonic nanoparticles



(PNPs) and semiconductors or metal oxides, exhibit unique and synergetic properties facilitating efficient charge carriers' generation and transport.

Plasmonic nanoparticles (PNPs), such as gold or silver, possess unique optical properties that arise from the collective oscillation of conduction electrons in response to incident light, known as localized surface plasmon resonance (LSPR) (Gelle & Moores, 2019). The LSPR phenomenon enables efficient light absorption and scattering in the vicinity of PNPs, leading to enhanced photon harvesting and improved charge generation. The conversion of solar energy into chemical fuels represents the most promising route for achieving a sustainable energy economy. A photoelectrochemical (PEC) cell for water splitting (Fujishima & Honda, 1972) uses semiconductors to split water into pure hydrogen ( $H_2$ ) and oxygen ( $O_2$ ).  $H_2$  is an ideal energy vector for transportation, energy storage, and the production of electricity at zero-carbon emission. Hetero-nanostructures, composed of a combination of semiconductor materials and plasmonic NPs, provide a platform to exploit the synergistic effects of both components. The design and engineering of hetero-nanostructures play a crucial role in maximizing their photoelectrocatalytic performance (Wang & Fang, 2020; Zhao et al., 2018). The metal-semiconductor (M-S) heterostructure is a topic of great interest not only for its practical applications but also for its theoretical and experimental significance. Exploring the properties of the M-S junction can provide valuable insights into the characteristics of its constituent components.

Recent research has revealed that even a very simple structure without periodic arrangements in nature has surprising multiple functions, which by far exceed our expectations. J. Huang, *et al.* (Huang et al., 2017) prepared bifunctional  $Au@TiO_2$  core-shell NPs film with good stability for clean water generation by photocatalysis and solar evaporation. Wei *et al.* also synthesized a photoanode composed of highly ordered ZnO/CdS nanotube arrays (ZnO/CdS/NTAs) decorated with Au NPs for photoelectrochemical water splitting (Wei et al., 2017). Several other studies have also reported plasmon-enhanced photocatalytic water splitting with semiconductors. For instance, Dutta *et al.* (2019), demonstrated plasmon-assisted oxidation photocurrent enhancement in ultrathin (10–20 nm) hematite film by utilizing gold nanostructures that support gap-plasmon resonances. However, few attempts were made to thoroughly analyze the influence of the design of the core-shell plasmonic nanostructures on the enhancement of the photoelectrochemical  $H_2$  generation.

This work endeavors to develop a plasmonic photoelectrode for efficient  $H_2$  production through water splitting by precisely manipulating the plasmonic characteristics of the materials involved. Utilizing plasmonic core-shell  $Au@Pd$  nanoparticles (NPs) and Ni-doped Au core with  $FexOy$  shell nanowires (Ni-Au@ $FexOy$  NWs) as electrocatalysts, the electrocatalytic activity of the  $Au@FexOy$  NWs is tailored by adjusting the surface oxidation state of the shell and introducing an additional nickel metallic layer. This enhances the catalytic performance, promoting rapid electron kinetics within the electrode for increased reaction efficiency. Furthermore, the introduction of an angled magnetic field-induced deposition of NWs allows for marginal adjustments in both transverse and longitudinal orientations via an external magnetic field. This control mechanism enables the optimization of the electrochemical and optical properties of the one-dimensional structure, thus enhancing the overall performance of photoelectrochemical water splitting.

## 2. MATERIALS AND METHODS

### 2.1 Synthesis of Nanoparticles (NPs)

Optimization of material nanostructures were carried out for specific energy conversion systems. In particular, we focus on water splitting (hydrogen energy) as representative examples of large- and small-scale energy conversion schemes. The details are as follow:

### 2.2 Synthesis of Au NPs and $Au@Pd$ NPs

Au NPs were prepared using a modified version of the Turkevich-Frens method (Kimling et al., 2006).  $Au@Pd$  core-shell NPs were synthesized by selective reduction of  $H_2PdCl_4$  on AuNP seeds in the presence of *L*-ascorbic acid. The shell size was determined by varying the concentration of  $H_2PdCl_4$ .



### 2.3 Fabrication of Au@FexOy NWs and Ni-Au@FexOy NWs

A solution was prepared by dissolving 4 mmol of iron (III) chloride hexahydrate in a mixture of EG (20 mL) and DEG (20 mL) to obtain a clear solution. To this solution, 35 mmol of sodium acetate and 0.59 mmol of HAuCl<sub>4</sub>·3H<sub>2</sub>O were added and vigorously stirred until fully dissolved. The resulting suspension was then transferred to a 50 mL Teflon-lined stainless-steel autoclave and heated at 210°C for 8 hours. Upon completion of the reaction, the product was washed multiple times with distilled water and ethanol, followed by drying at 60°C for 6 hours. To stabilize the Au@FexOy NWs, 50 mg of the dried product was suspended in a 50 mL solution of citric acid (0.6 mg/mL) and refluxed for 3 hours at 90°C with mechanical stirring in a round-bottom flask. Afterward, the products were washed with water and ethanol before suspension in water for analysis. The synthesis of nickel-doped Au@FexOy NWs involved a hydrothermal technique, where 1.0 mg/mL of Au@FexOy NWs and 6 mmol of nickel (II) nitrate hexahydrate were dissolved in 30 mL of water. The clear solution obtained was then transferred to a 50 mL Teflon-lined stainless autoclave, sealed, and maintained at 220°C for 8 hours in an electric oven. Upon cooling to room temperature, the Ni-doped Au@FexOy MagPlas NWs were retrieved and washed several times with DI water.

### 2.4 Characterization of Nanomaterials

The morphology and core shell structure of plasmonic NPs were characterized by a field emission scanning electron microscope and transmission electron microscope. The UV–visible spectrometer, X-ray diffraction, X-ray photoelectron spectroscopy (XPS), analyses were utilized to optical properties of the nanofilm, identification of the phase of nanomaterials, and analyze the surface chemistry of the material, respectively. Cyclic voltammetry, linear sweep voltammetry, chronoamperometry, and electrochemical impedance spectroscopy (EIS) were carried out by means of the electrochemical potentiostat.

### 2.5 Electrochemical and Photoelectrochemical Measurements

Photoelectrochemical analysis was carried out at room temperature using an Iviumstat workstation from Eindhoven, Netherlands. The experimental setup included a Pt wire counter electrode and an Ag/AgCl reference electrode. All electrochemical tests were conducted in a 1.0 M KOH aqueous solution, with the measured potentials converted to reversible hydrogen electrode (RHE) values using the formula:

$$ERHE = E_{Ag/AgCl} + E_{O_{2}/H_{2}} + 0.059 \text{ pH} \quad (1)$$

Before performing electrochemical measurements, cyclic voltammetry (CV) was repeated at a scan rate of 100 mV/s until reaching a steady state. Once steady state was achieved, CVs were recorded at a scan rate of 100 mV/s within the range of -0.5 to 0.5 V vs Ag/AgCl. Linear sweep voltammetry (LSV) was conducted at a scan rate of 5 mV/s. Electrochemical impedance spectroscopy (EIS) was carried out at a potential of 1.45 V vs RHE across a frequency range from  $2 \times 10^4$  to 0.1 Hz.

## 3. RESULTS AND DISCUSSION

### 3.1 Characterization of Core-shell Au@Pd NPs and Ni-Au@FexOy NWs

Core-shell Au@Pd nanoparticles were synthesized by reducing H<sub>2</sub>PdCl<sub>4</sub> on Au nanoparticle seeds with L-ascorbic acid. Different shell thicknesses of Pd (2, 5, and 8 nm) were produced, labeled as Au@Pd-1, Au@Pd-2, and Au@Pd-3, respectively. X-ray diffraction (XRD) analysis of unsupported Au@Pd core-shell particles was conducted to investigate lattice constants and assess mixing/alloying at the Au@Pd interface (**Fig. 1a**). The observed peaks at  $2\theta = 40^\circ, 46^\circ, 68^\circ,$  and  $82^\circ$  corresponded to the (111), (200), (220), and (311) planes of face-centered cubic (fcc) palladium. Notably, these signals partly overlapped with diffraction peaks from the (111), (200), (220), and (311) planes of fcc gold structures, located at  $2\theta = 38^\circ, 45^\circ, 65^\circ,$  and  $77^\circ$  (Miller et al., 2016). Analysis based on the Au 220 and Au 331 reflections indicated a lattice parameter of 4.058 Å, demonstrating a contraction compared to the literature value of 4.0786 Å for Au. Conversely, the Pd lattice parameter, determined from the Pd 200 and Pd 220 reflexes, measured 3.914 Å compared to a literature value of 3.8902 Å, indicating a



slight expansion in the Pd lattice. The XRD patterns of the Au@Pd-1, Au@Pd-2, and Au@Pd-3 nanoparticles displayed characteristic peaks of both monoatomic Au and Pd, confirming the composite structural formation of Au@Pd nanoparticles, consistent with previous literature (Fu et al., 2014; Harpeness & Gedanken, 2004).

Interestingly, in contrast to previous studies, only Au diffraction patterns were detected in the Au@Pd core-shell structure, potentially attributed to minimal Pd content in the samples (below ~0.5 at%) and/or an extremely thin Pd shell (~0.8 nm) (Jose & Jagirdar, 2008). Previous research by Harpeness and Gedanken indicated diffraction peaks corresponding to both Au and Pd in Au/Pd core/shell NPs, composed of a 9 nm Au core and a 3 nm Pd shell thickness (Harpeness & Gedanken, 2004). To validate the uniform distribution of Au and Pd within the Au@Pd samples, various areas of the samples were examined using the selected area electron diffraction (SAED) technique. Generally, the SAED patterns (**Fig. 1c**) displayed polycrystalline forms across all NPs. Notably, the SAED patterns of Au@Pd NPs aligned with the diffraction patterns obtained from XRD results (**Fig. 1a**), indicating the presence of (111), (200), (220), and (311) planes of both Au and Pd.

To explore the morphologies of the Au@Pd core-shell NPs, transmission electron microscopy (TEM) was employed, revealing findings showcased in **Fig. 1b and c**. Typically, the Au NPs appeared nearly spherical, with average sizes of approximately 16, exhibiting smooth surfaces. These gold seeds were enveloped by a thin palladium layer, a strategy aimed at augmenting their electrocatalytic attributes. According to Henning *et al.*, adjusting the reaction time allows for easy control over the thickness of the palladium layer (Henning et al., 2013). Palladium was deposited onto existing gold seeds over two-hour duration, a practice derived from earlier studies demonstrating this timeframe as optimal for catalytic performance (Cheong et al., 2013; Henning et al., 2013). Thicker palladium layers, however, diminish synergistic effects, consequently reducing catalytic efficiency. In contrast, Pd NPs synthesized without the addition of Au colloids exhibited rougher surfaces, with average diameters of 30 and 52 nm (Srisombat, Nonkumwong, Suwannarat, Kuntalue, & Ananta, 2017), owing to a distinct method utilized for core-shell preparation. Upon coating the Au core with a Pd shell, increased surface roughness was observed in the Au@Pd NPs (**Fig. 1b**). TEM analysis revealed an average particle size of 22.78 nm and a spherical shape for the Au@Pd NPs. Clearly, the sizes of Au@Pd NPs gradually increase with an increasing of Pd content, indicating a rising of Pd coverage thickness. This observation indicates that the thickness of Pd coating layer can be tailored by changing the Au:Pd atomic ratio, consistent with Hu *et al.* (Hu et al., 2005). Remarkably, increasing Pd content resulted in larger Au@Pd NP sizes, likely indicating a thicker Pd shell layer. Additionally, TEM images of Au@Pd NPs, presented in **Fig. 1c** with insets SAED, demonstrated ring-like diffraction patterns with dispersed bright spots. This signifies heightened crystallinity in the Au@Pd core-shell NPs with increased Au sources, although maintaining polycrystalline structures across all samples, as evidenced by the ring patterns.

High-resolution transmission electron microscopy (HRTEM) analysis of a representative Au@Pd image (**Fig. 1d**) validated the successful formation of the well-dispersed Au core and Pd shell, showcasing an average diameter. In TEM imaging, gold appears darker due to its higher electron density. The fast Fourier transform (FFT) (see inset in **Fig. 1d**) of the selected area indicated reflections assignable to (111), (200), (220), and (311). The scanning transmission electron microscopy (STEM) image distinguished a bright core corresponding to Au and a low contrast intensity corresponding to the Pd shell, owing to the distinct atomic numbers (*Z*) of Au (79) and Pd (46) (Gurmessa et al., 2020). Furthermore, STEM analysis (**Fig. 1e**) confirmed the well-developed spherical Au@Pd core-shell NPs via a successive reduction approach, ensuring better control over shape and atomic ratio (Srivastava et al., 2013). Energy-dispersive X-ray spectroscopy (EDS) elemental mapping depicted orderly arranged hierarchical core-shell Au@Pd structures (**Fig. 1f**), highlighting Au atoms in red (**Fig. 1g**) and Pd atoms (**Fig. 1h**). EDS scanning confirmed the core as primarily composed of Au, while Pd predominantly formed the shell in the examined NPs. STEM-EDS analysis (**Fig. 1i**) reaffirmed the consistent composition of the Au and Pd NP samples.

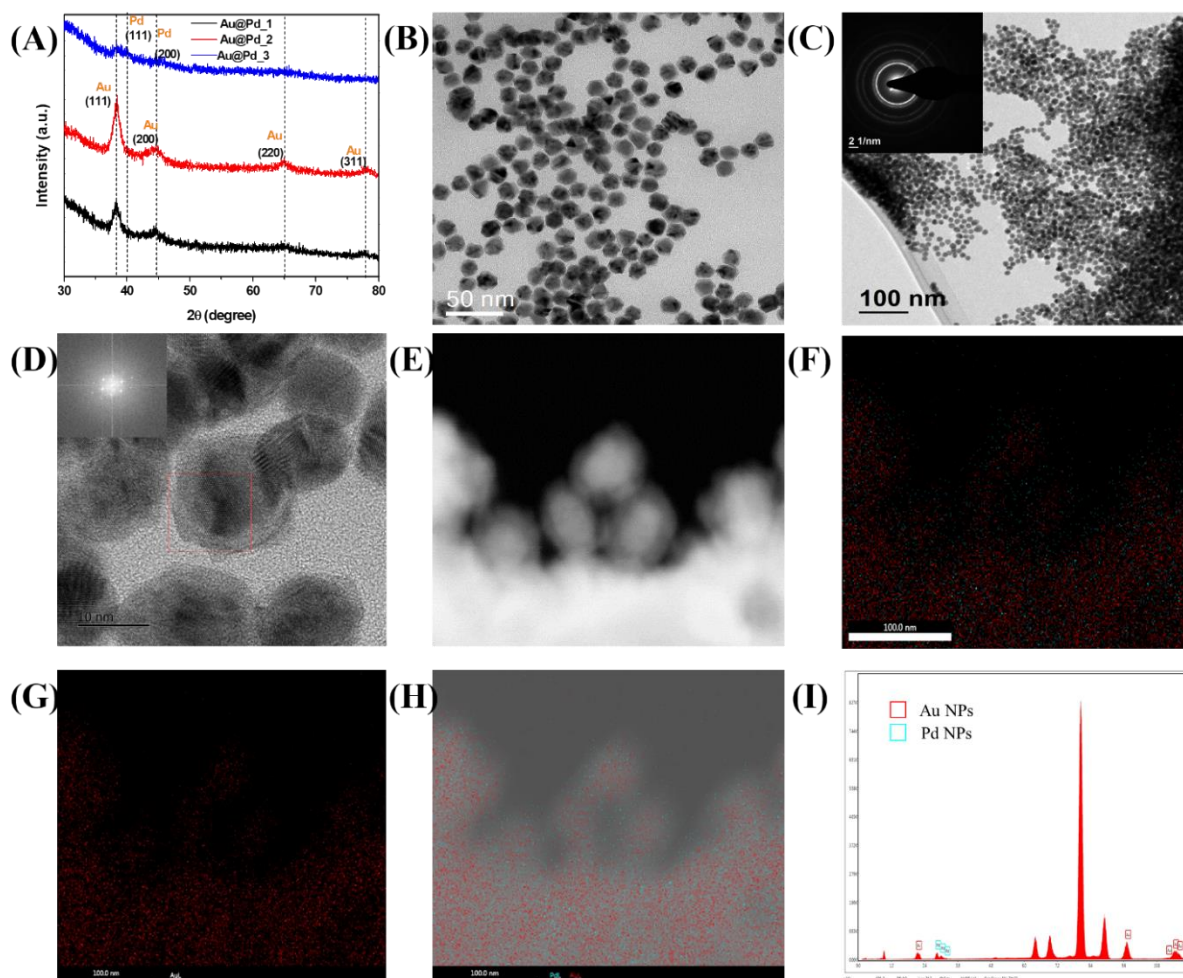


**Fig. 1: Microscopy and spectroscopy characterization of Au@Pd core-shell NPs:** (a) XRD spectra of Au@Pd core-shell NPs. (b), TEM image, (c) TEM image (inset SAED patterns), (d) HRTEM image (inset indicates FFT of the selected area), (e) STEM images, and (f-i) The EDS mapping of Au@Pd core-shell particles.

Surface engineering with nickel was achieved through a hydrothermal method to enhance the electro-catalytic properties of Fe<sub>x</sub>O<sub>y</sub>. **Fig. 2a-d** depicts scanning electron microscopy (SEM) and transmission electron microscopy (TEM) images of Au@Fe<sub>x</sub>O<sub>y</sub> and Ni-Au@Fe<sub>x</sub>O<sub>y</sub> nanowires, respectively. The Au core appears black with sharp edges, while numerous small iron oxide particles make up the shell. It's notable that the shell, initially composed of small Fe<sub>3</sub>O<sub>4</sub> nanoparticles with a diameter of 4.95 nm, transforms into larger nanoparticles (approximately 15 nm) upon Ni doping, while the Au cores remain unaffected. This transformation is attributed to the rearrangement of iron oxide materials near nickel ions, altering the thermodynamic equilibrium during the nickel doping process. Further investigations will elucidate the precise mechanism behind this phenomenon. TEM and STEM images of end-opened Ni-Au@Fe<sub>x</sub>O<sub>y</sub> nanowires are presented in **Fig. 2e, f**, with corresponding high-resolution TEM (HRTEM) images shown in **Fig. 2g-i**, revealing various lattice planes associated with (202), (311), and (511) of the Fe<sub>3</sub>O<sub>4</sub> shell (ICDD no. 1-088-0315). As Ni is doped onto the pristine Au@Fe<sub>x</sub>O<sub>y</sub> nanowire film, the surface becomes rougher, forming a bimetallic layer. The high angular dark-field scanning transmission electron microscopy (HAADF-STEM) image in **Fig. 2j** highlights the presence of both single crystal Au cores and gray Ni-Fe<sub>x</sub>O<sub>y</sub> nanoclusters. Additionally, the STEM-EDS image (**Fig. 2k-o**) clearly shows signals of Fe, O, Au, and Ni elements, indicating successful nickel doping onto the pristine Au@Fe<sub>x</sub>O<sub>y</sub> nanowire film.

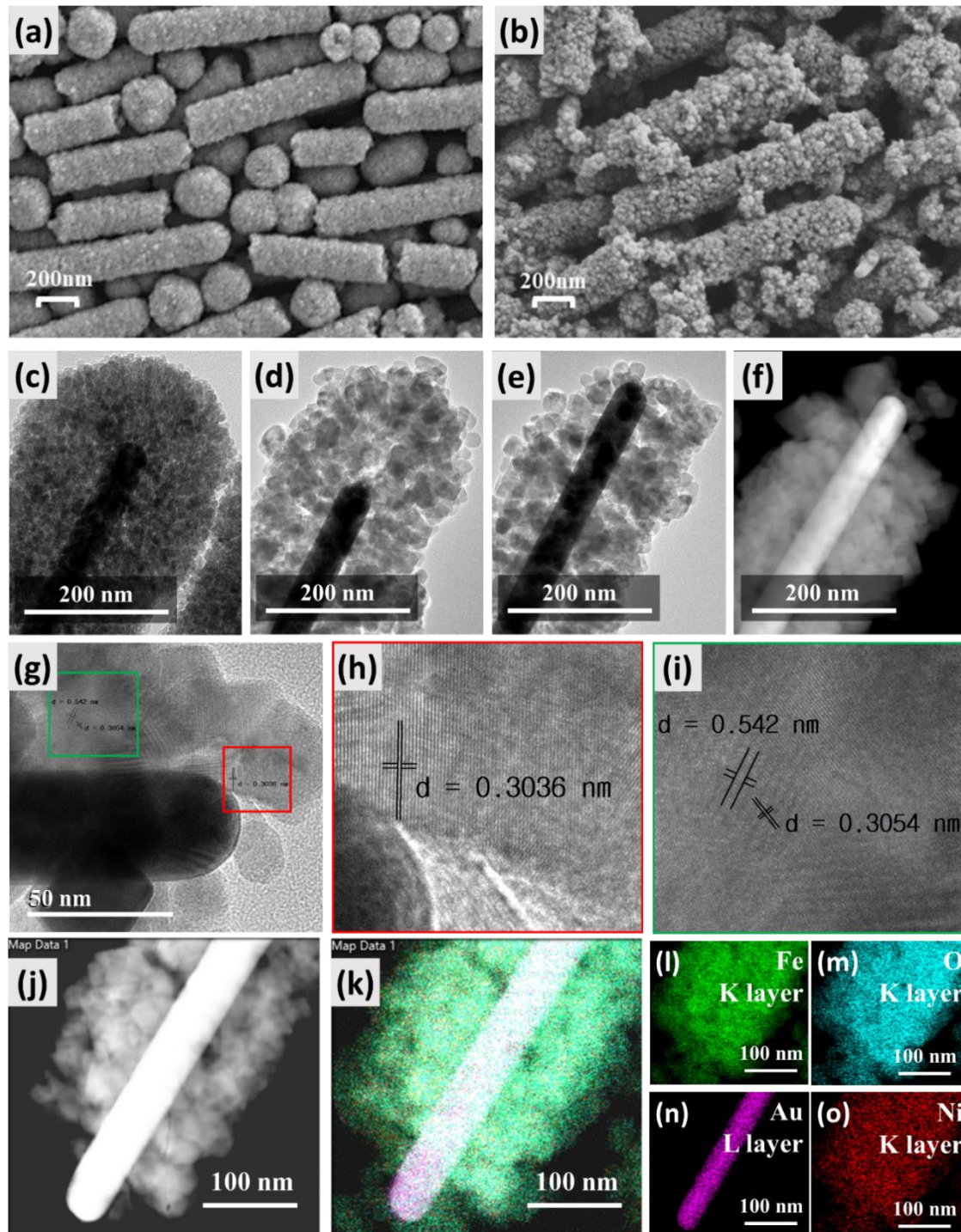


**Fig. 2. Electron microscopic characterization of Au@FexOy NWs and Ni-Au@FexOy NWs.** SEM images of (a) Au@FexOy NWs and (b) Ni-Au@FexOy NWs; TEM images of (c) Au@FexOy NW and (d) end-closed Ni-Au@FexOy NW; (e) TEM and (f) STEM images of end-opened Ni-Au@FexOy NW and (g-i) its HRTEM images of Ni-Au@FexOy NW, (j) HADDF-STEM image of Ni-Au@FexOy NWs electrode and (k-o) the corresponding STEM-EDS elemental mapping images for Au, Fe, Ni, and O, respectively.

### 3.2 Plasmon Enhanced production of H<sub>2</sub> and O<sub>2</sub>

Photoelectrochemical (PEC) assessments were conducted using a three-electrode setup comprising a 3 M Ag/AgCl reference electrode and a platinum wire as the counter electrode. This setup operated in a 0.1 M potassium phosphate buffer containing 0.1 M sodium sulfite (Na<sub>2</sub>SO<sub>3</sub>) at pH 7.2. The investigation focused on

the PEC characteristics of plasmonic-based photoelectrodes in the presence of 0.1 M sodium sulfite ( $\text{Na}_2\text{SO}_3$ ), acting as an effective hole scavenger. To gain insights into this matter, photocurrent responses of Au@Pd were measured at 15 mV vs. RHE (**Fig.3**). The results revealed an immediate increase in current upon illumination, indicating electrocatalytic enhancement likely triggered by plasmon-induced hot electrons (photoelectron-chemical effect)(Yang et al., 2016). Subsequently, the current gradually saturated, potentially due to the photothermal effect. Comparing the currents at these two stages led to the conclusion that the photoelectrochemical effect played a more significant role in enhancing the photocurrent than the photothermal effect. Additional support for this conclusion was derived from the plots of current density versus temperature with and without light irradiation. If the SPR-induced photothermal effect dominated the enhancement, the difference in current densities with/without light irradiation at various temperatures should be minimal, resulting in nearly parallel lines.

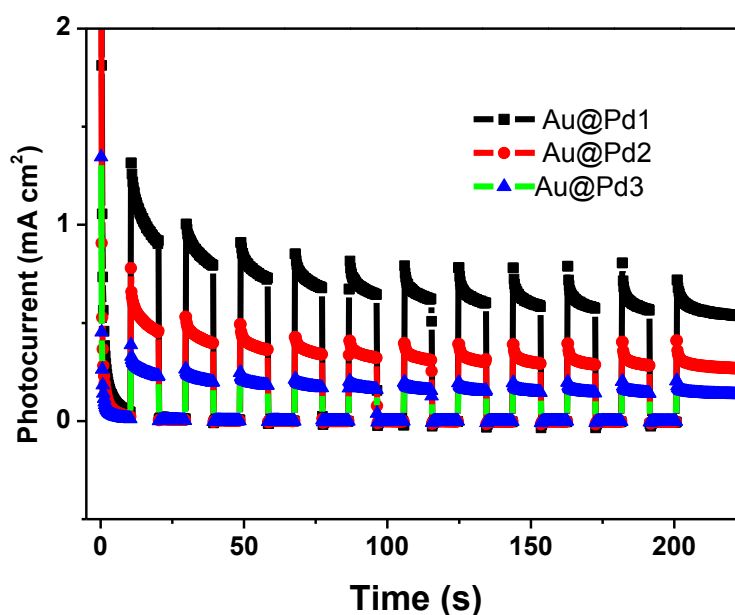


**Fig. 3:** Photocurrent response measured at 1.23 VRHE (Chopping current–time (J–t) curves)

The Ni-doped sample, arranged transversely, underwent annealing at 300 °C to optimize its electrochemical performance in 1.0 M KOH electrolyte. Comparatively, no electrocatalytic activity was observed on FTO glass, while significant enhancement was evident in the current of hematite electrodes with the transverse deposition of Au@FexOy nanowires. Moreover, Ni-Au@FexOy nanowires exhibited a higher current density of 2.01 mA·cm<sup>-2</sup> at 1.23 V vs RHE compared to Au@FexOy nanowires, which had a current density of 1.52 mA·cm<sup>-2</sup> at 1.23 V vs. RHE (**Fig. 4a**), suggesting a strong correlation between surface engineering through nickel introduction and oxidation state with electrocatalytic performance. Photocurrent under chopped light (chopped LSV) of Au@FexOy and Ni-Au@FexOy is recorded, showing significant differences in photo-responses. The photocurrent density of Ni-Au@FexOy nanowires was approximately 2.21 mA·cm<sup>-2</sup> at 1.23 VRHE, while Au@FexOy nanowires showed 1.38 mA·cm<sup>-2</sup> at 1.23 V<sub>RHE</sub>. **Fig. 4b** illustrates the percentage ABPE (% ABPE) as a function of applied potential, with Au@FexOy and Ni-Au@FexOy nanowires exhibiting ABPE of 0.74 and 0.92%, respectively, at 1.15 and 1.14 V vs. RHE. As shown in **Fig. 4c**, incident photo-to-electron conversion efficiency (IPCE) analysis confirmed heightened light-harvesting contributes to enhanced water oxidation capability and durability. Additionally, electrochemical impedance spectroscopy (EIS) revealed a significant reduction in charge transport resistance upon Ni incorporation into Au@FexOy nanowires, demonstrating the synergistic effect of Ni and Fe in reducing defect-mediated electron-hole recombination.

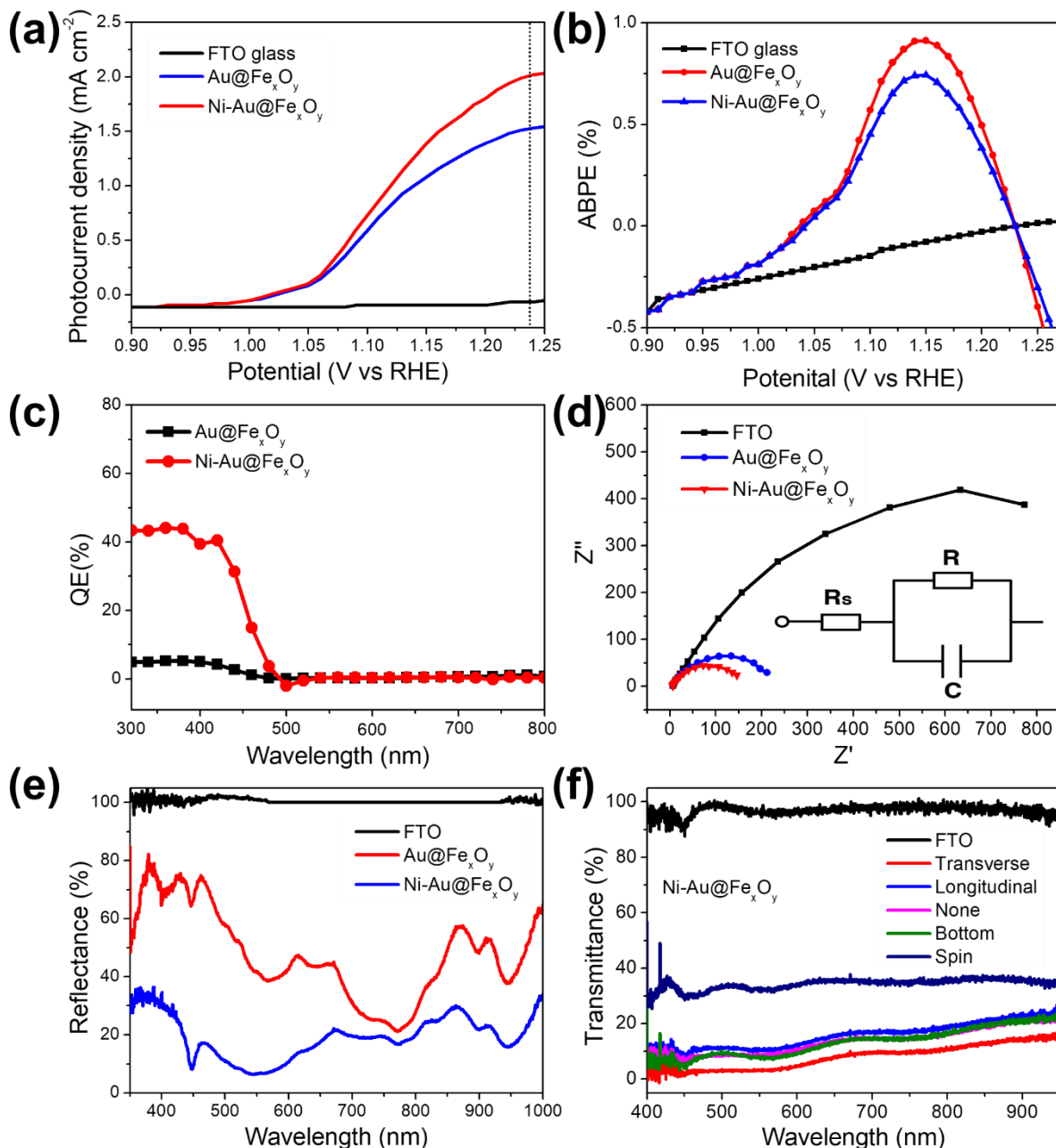


**Fig. 4.** Photoelectrochemical and optical properties of Au@Fe<sub>x</sub>O<sub>y</sub> NWs and Ni-Au@Fe<sub>x</sub>O<sub>y</sub> NWs films. (a) The photocurrent potential curves at 1.23 V vs. RHE, (b) Applied bias photon-to-current efficiency, (c) IPCE, (d) Impedance spectra using 1 M KOH electrolyte under 1.5 G sunlight and the inset shows the equivalent circuit model, (e) reflectance spectra, and (f) Transmittance spectra of Ni-Au@Fe<sub>x</sub>O<sub>y</sub> NWs.

Intrinsic optical properties of synthesized Au@Fe<sub>x</sub>O<sub>y</sub> and Ni-Au@Fe<sub>x</sub>O<sub>y</sub> nanowires were investigated, revealing strong absorption peaks at various wavelengths (**Fig. 4e**). The peak observed at approximately 445 nm corresponds to the characteristic UV-vis extinction pattern of Fe<sub>x</sub>O<sub>y</sub>, while the broad peak between 540-570 nm corresponds to the transverse mode plasmon resonance of the gold segment. Transmittance decreased from 95% of FTO glass to around 10-30% when Ni-Au@Fe<sub>x</sub>O<sub>y</sub> nanowires were deposited onto FTO glass with various arrangements, with the transversely arranged sample, exhibiting the highest current density (2.01 mA·cm<sup>-2</sup> at 1.23 V vs RHE), showing the lowest transmittance (**Fig. 4f**).



#### 4. CONCLUSIONS

The investigation into plasmon-enhanced electrocatalysis utilizing Au@Pd core-shell nanoparticles (NPs) and Ni-Au@FexOy nanowires (NWs) present a promising pathway for advanced catalytic applications, unveiling key insights through meticulous analysis across morphological, structural, optical, and electrochemical domains. The synthesis and characterization techniques employed in this study confirmed the successful formation of Au@Pd core-shell NPs with controlled morphologies and well-defined structures, demonstrating spherical shapes with size variations correlating with changes in Pd content. Structural characterization techniques, including XRD and selected area electron diffraction, validated the composite structural formation of Au@Pd NPs, emphasizing their polycrystalline nature. Optical property analysis revealed intriguing behavior in the absorption peak originating from the Au core. Furthermore, employing a magnetic field-induced transverse arrangement method, rugged forest morphology of Au@FexOy nanowires was utilized to activate electrodes on FTO substrates, studying the effect of surface engineering through nickel introduction onto FexOy and oxidation of FexOy to facilitate an efficient contact interface and decrease charge recombination centers. The resulting Ni-Au@FexOy nanowires exhibited substantially improved efficiency in solar water splitting, including enhanced light absorption and photocurrent density (2.01 mA·cm<sup>-2</sup> at 1.23 V vs RHE), attributed to accelerated OER kinetics and low overpotential of trimetallic Ni-Au@FexOy nanowires.

#### ACKNOWLEDGEMENTS

The authors would like to thank Postgraduate program of Adama Science and Technology University (ASTU/AS-R/013/2021), Ethiopia, for financially supporting this research. This research was also supported by Brain Pool program funded by the Ministry of Science and ICT through the National Research Foundation of Korea (NRF-2021H1D3A2A01099457, 2022H1D3A2A01093556).

#### REFERENCES

- Chen, T., Xu, J., Arsalan, M., Sheng, Q., Zheng, J., Cao, W., & Yue, T. (2019). Controlled synthesis of Au@ Pd core-shell nanocomposites and their application for electrochemical sensing of hydroquinone. *Talanta*, *198*, 78-85.
- Cheong, S., Graham, L., Brett, G. L., Henning, A. M., Watt, J., Miedziak, P. J., . . . Tilley, R. D. (2013). Au-Pd core-shell nanoparticles as alcohol oxidation catalysts: effect of shape and composition. *ChemSusChem*, *6*(10), 1858-1862.
- Dutta, A., Naldoni, A., Malara, F., Govorov, A. O., Shalaev, V. M., & Boltasseva, A. (2019). Gap-plasmon enhanced water splitting with ultrathin hematite films: the role of plasmonic-based light trapping and hot electrons. *Faraday discussions*, *214*, 283-295.
- Dutta, S., Ray, C., Mallick, S., Sarkar, S., Roy, A., & Pal, T. (2015). Au@ Pd core-shell nanoparticles-decorated reduced graphene oxide: a highly sensitive and selective platform for electrochemical detection of hydrazine. *RSC advances*, *5*(64), 51690-51700.
- Fu, G., Liu, Z., Chen, Y., Lin, J., Tang, Y., & Lu, T. (2014). Synthesis and electrocatalytic activity of Au@ Pd core-shell nanohorns for the oxygen reduction reaction. *Nano Research*, *7*, 1205-1214.
- Fujishima, A., & Honda, K. (1972). Electrochemical photolysis of water at a semiconductor electrode. *Nature*, *238*(5358), 37-38.
- Gellé, A., & Moores, A. (2019). Plasmonic nanoparticles: Photocatalysts with a bright future. *Current Opinion in Green and Sustainable Chemistry*, *15*, 60-66.
- Gurmessa, S. K., Tufa, L. T., Kim, J., Lee, K.-I., Kim, Y.-M., Tran, V. T., . . . Park, T. J. (2020). Colorimetric detection of mycobacterium tuberculosis ESX-1 substrate protein in clinical samples using Au@ Pd nanoparticle-based magnetic enzyme-linked immunosorbent assay. *ACS Applied Nano Materials*, *4*(1), 539-549.
- Harpeness, R., & Gedanken, A. (2004). Microwave synthesis of core-shell gold/palladium bimetallic nanoparticles. *Langmuir*, *20*(8), 3431-3434.
- Henning, A. M., Watt, J., Miedziak, P. J., Cheong, S., Santonastaso, M., Song, M., . . . Tilley, R. D. (2013). Gold-palladium core-shell nanocrystals with size and shape control optimized for catalytic performance. *Angewandte Chemie International Edition*, *52*(5), 1477-1480.
- Hu, J.-W., Zhang, Y., Li, J.-F., Liu, Z., Ren, B., Sun, S.-G., . . . Lian, T. (2005). Synthesis of Au@ Pd core-shell nanoparticles with controllable size and their application in surface-enhanced Raman spectroscopy. *Chemical Physics Letters*, *408*(4-6), 354-359.



- Huang, J., He, Y., Wang, L., Huang, Y., & Jiang, B. (2017). Bifunctional Au@TiO<sub>2</sub> core-shell nanoparticle films for clean water generation by photocatalysis and solar evaporation. *Energy conversion and management*, 132, 452-459.
- Jose, D., & Jagirdar, B. R. (2008). Au@Pd core-shell nanoparticles through digestive ripening. *The Journal of Physical Chemistry C*, 112(27), 10089-10094.
- Kimling, J., Maier, M., Okenve, B., Kotaidis, V., Ballot, H., & Plech, A. (2006). Turkevich method for gold nanoparticle synthesis revisited. *The Journal of Physical Chemistry B*, 110(32), 15700-15707.
- Lee, S., Sim, K., Moon, S. Y., Choi, J., Jeon, Y., Nam, J. M., & Park, S. J. (2021). Controlled assembly of plasmonic nanoparticles: from static to dynamic nanostructures. *Advanced Materials*, 33(46), 2007668.
- Li, S., Miao, P., Zhang, Y., Wu, J., Zhang, B., Du, Y., . . . Xu, P. (2021). Recent advances in plasmonic nanostructures for enhanced photocatalysis and electrocatalysis. *Advanced Materials*, 33(6), 2000086.
- Li, X., Li, C., Xiang, D., Zhang, C., Xia, L., Liu, X., . . . Chen, W. (2019). Self-limiting synthesis of Au-Pd core-shell nanocrystals with a near surface alloy and monolayer Pd shell structure and their superior catalytic activity on the conversion of hexavalent chromium. *Applied Catalysis B: Environmental*, 253, 263-270.
- Liu, G., & Lin, Y. (2005). Electrochemical sensor for organophosphate pesticides and nerve agents using zirconia nanoparticles as selective sorbents. *Analytical chemistry*, 77(18), 5894-5901.
- Low, J., Yu, J., Jaroniec, M., Wageh, S., & Al-Ghamdi, A. A. (2017). Heterojunction photocatalysts. *Advanced Materials*, 29(20), 1601694.
- Lukajtis, R., Hołowacz, I., Kucharska, K., Glinka, M., Rybarczyk, P., Przyjazny, A., & Kamiński, M. (2018). Hydrogen production from biomass using dark fermentation. *Renewable and Sustainable Energy Reviews*, 91, 665-694.
- Luo, C., Yang, J., Li, J., He, S., Meng, B., Shao, T., . . . Zhou, X. (2020). Green synthesis of Au@N-CQDs@Pd core-shell nanoparticles for enhanced methanol electrooxidation. *Journal of Electroanalytical Chemistry*, 873, 114423.
- Miller, H., Bellini, M., Vizza, F., Hasenöhrl, C., & Tilley, R. (2016). Carbon supported Au-Pd core-shell nanoparticles for hydrogen production by alcohol electroreforming. *Catalysis Science & Technology*, 6(18), 6870-6878.
- Mohite, S. V., Kim, S., Bae, J., Jeong, H., Kim, T. W., Choi, J., & Kim, Y. (2023). Defects Healing of the ZnO Surface by Filling with Au Atom Catalysts for Efficient Photocatalytic H<sub>2</sub> Production. *Small*, 2304393.
- Srisombat, L., Nonkumwong, J., Suwannarat, K., Kuntalue, B., & Ananta, S. (2017). Simple preparation Au/Pd core/shell nanoparticles for 4-nitrophenol reduction. *Colloids and Surfaces A: Physicochemical and Engineering Aspects*, 512, 17-25.
- Srivastava, S. K., Hasegawa, T., Yamada, R., Ogino, C., Mizuhata, M., & Kondo, A. (2013). Green synthesis of Au, Pd and Au@Pd core-shell nanoparticles via a tryptophan induced supramolecular interface. *RSC advances*, 3(40), 18367-18372.
- Van der Ham, C. J., Koper, M. T., & Hetterscheid, D. G. (2014). Challenges in reduction of dinitrogen by proton and electron transfer. *Chemical Society Reviews*, 43(15), 5183-5191.
- Wang, H., Wang, C., Yan, H., Yi, H., & Lu, J. (2015). Precisely-controlled synthesis of Au@Pd core-shell bimetallic catalyst via atomic layer deposition for selective oxidation of benzyl alcohol. *Journal of Catalysis*, 324, 59-68.
- Wang, W., & Fang, J. (2020). Mesoporous SiO<sub>2</sub>-derived g-C<sub>3</sub>N<sub>4</sub>@CdS core-shell heteronanostructure for efficient and stable photocatalytic H<sub>2</sub> production. *Ceramics International*, 46(2), 2384-2391.
- Wei, R.-B., Kuang, P.-Y., Cheng, H., Chen, Y.-B., Long, J.-Y., Zhang, M.-Y., & Liu, Z.-Q. (2017). Plasmon-enhanced photoelectrochemical water splitting on gold nanoparticle decorated ZnO/CdS nanotube arrays. *ACS Sustainable Chemistry & Engineering*, 5(5), 4249-4257.
- Yang, H., Wang, Z.-H., Zheng, Y.-Y., He, L.-Q., Zhan, C., Lu, X., . . . Tong, Y. (2016). Tunable wavelength enhanced photoelectrochemical cells from surface plasmon resonance. *Journal of the American Chemical Society*, 138(50), 16204-16207.
- Zhao, X., Feng, J., Liu, J., Lu, J., Shi, W., Yang, G., . . . Cheng, P. (2018). Metal-Organic Framework-Derived ZnO/ZnS Heteronanostructures for Efficient Visible-Light-Driven Photocatalytic Hydrogen Production. *Advanced Science*, 5(4), 1700590.



## Estimation of Abattoir Waste for Bio-Energy as Sustainable Management in Eastern Ethiopia

Sina Temesgen, Fekade Ketema

Haramaya University College of Health and Medical Sciences, Harar City, Ethiopia

\*Corresponding author, e-mail:

### ABSTRACT

Now a day, our environment facing by serious problems due to high volumes of waste, inadequate disposal system in worldwide particularly in developing countries. Despite it is not well quantified for sustainable management particularly in Eastern Ethiopia. The aim of this study was to estimate abattoir waste generated for bio-energy as sustainable management. A cross-sectional study was conducted. All number of slaughtered livestock such as cattle, goats and sheep were collected from December, 2018 to January, 2019 from each registry municipalities. For abattoir waste generation Aniebo mathematical model was applied. "One cattle could produce 12.6kg of BL, 8.0 kg of IW, 6.4kg of TW and 11.8kg of BN (total 38.8). Similarly, oneslaughter Goat/sheep/ could generate 0.72kg (blood waste), 1.25 kg (intestinal content waste), 0.8kg (tissue waste) and 2.06kg (bone waste (total 4.83kg). For estimation of green gases emissions from disposal site, global warming potentials are used to convert masses of different greenhouse gases into a single carbon dioxide-equivalent metric. The study reported that about 4.40 ton/day and 1,606t on/year of abattoir waste was estimated and 2,581 kgCo<sub>2</sub>/day and 887,768 kgCo<sub>2</sub>/year of greenhouse gases was estimated from disposal sites of abattoirs. When return into bioenergy, about 233m<sup>3</sup>/day and 85,139m<sup>3</sup>/year of biogas and 324kg/day and 111,249kg/year of bio-fertilizer were estimated. Into cost, about \$160(4578ETB)/day and \$55,645 (1,589,216ETB)/year of price was estimated from disposed abattoir waste sites. The study concluded that huge amount of biogas and dry bio-fertilizer yields could produce from abattoir waste through anaerobic digester. Therefore, install anaerobic digester plant is recommended to ensure environmental safety and public health, while proper disposal is for short term.

**Keywords:** Abattoir, Biogas, Bio-fertilizer, Management, Sustainable, Waste

### 1. INTRODUCTION

Livestock production in abattoirs is considered a potential food for the world's needy people and huge amount of abattoir wastes are generating from them in all parts of the world (FAO, 2010). Especially, low-income countries show rapid urban growth that is putting extraordinary pressure on gigantic amount of abattoir waste in the urban (Ezeoha et al., 2000). The production of meat, from farm to fork, includes not just meat for human consumption and useful by-products like leather and skin, but also waste. Abattoir operations produce a characteristic highly organic waste with relatively high levels of suspended solid, liquid and fat (Aneibo et al., 2009). This becomes a major pollutant and the possibility to increase of greenhouse gases, when the abattoir wastes are not properly managed; in addition, when it discharges into waterways, it can introduce enteric pathogens and excess nutrients into surface water (Alonge, 1991).

As global meat consumption has increased by threefold per capita that leads huge amount of abattoir wastes production, which is major environmental challenge in all parts of the world particularly in developing countries (Fearon et al., 2014). The seriousness of environmental and health problems has been reported by so many scholars who have been reported to contaminate and increase the level of nitrates in ground water and cause methaemoglobinaemia (Abiade et al., 2006). Moreover, these problems are happening due to lack of well design of abattoir, lack of regulations on restriction and prohibition of abattoir wastes discharge, the insufficient skill of human power, poor quality of equipment of abattoir, lack of political awareness (Chukwu, 2008). In most of these countries there is no organized strategy for disposal of solid as well as liquid wastes generated in abattoirs (Akinro et al., 2011).

As FAO (2009) reported, these dumped as solid abattoir wastes washed away, it has a potential to pollute air, water and soil leading to health hazards (FAO, 2009). Abattoir wastes affect air quality, agriculture, potable water supplies, and aquatic life, which are pose risks to human (Adeyemi and Adeyemo, 2007). Yet, Eastern Ethiopia abattoirs have been releasing their huge amount of waste into open environment without any management system.



In addition, there wasn't data available on quantification of abattoir waste and greenhouse gases estimation as well as estimation of bioenergy as sustainable management in Eastern Ethiopia, which the aim of this study.

## 2. MATERIALS AND METHODS

### 2.1 Study Settings

The study was conducted in Eastern Ethiopia. The first three study areas are Harar Abattoir; Haramaya University Abattoir Enterprise and Haramaya abattoirs, which are found in Harar; Haramaya University and Haramaya towns; about 503 km, 508km and 527km, respectively far from the national capital Addis Ababa, respectively. They are characterized by subtropical highland climate, throughout the year, afternoon temperatures are warm to very warm, cool at mornings and rain falls between March and October (<https://en.wikipedia.org/wiki/Harar>, n.d.)

The second study is Dire Dawa abattoir, which is found in Dire Dawa Admiration and far 453km from Addis Ababa. It has 9°36'N 41°52'E latitude and longitude with Coordinates of 9°36'N 41°52'E. The city is characterized by hot semi-arid climate. The region has two rain seasons; that is, a small rain season from March to April ([https://en.wikipedia.org/wiki/Dire\\_Dawa](https://en.wikipedia.org/wiki/Dire_Dawa), n.d.).

### 2.2 Study Design

A cross sectional study was conducted in selected abattoirs of Eastern Ethiopia, from February 1 to February 30, 2019.

### 2.3 Quantitative Variables Determination

#### 2.3.1 Methods of abattoir waste estimation

All number of slaughtered livestock (cattle, goats and sheep) were collected from December, 2018 to January, 2019 from each registry municipalities. For abattoir waste generation (Aniebo, et al., 2009) mathematical model was applied. “One cattle could produce 12.6kg of BL, 8.0 kg of IW, 6.4kg of TW and 11.8kg of BN (total 38.8). Similarly, one slaughter Goat/sheep/ could generate 0.72kg of Blw, 1.25 kg of IW, 0.8kg of Tw and 2.06kg of Bnw (total 4.83kg).

$$\sum(Blw + Bnw + IW + TW)N \dots\dots\dots (1)$$

Where Blw=blood waste, Bnw=bone waste, Iw = intestinal content waste and Tw=tissue waste and “N” is number of slaughtered livestock

#### 2.3.2 Estimation of GHGs emissions from disposal site

Global Warming Potentials (GWPs)” are used to convert masses of different greenhouse gases into a single carbon dioxide-equivalent metric. Accordingly, Greenhouse emission from dumping sites (IPCC, 2000; B-sustain., 2013b; JGCRI, 2018) mathematical computation factor was used.

$$[(Q \times DOC \times DOCF \times F1 \times 1.336) - R] \times (1 - OX) \times 25 \dots\dots\dots (2)$$

Where: Q = Quantity of abattoir waste expressed in tones/kg/ from waste records ; DOC= Degradable Organic Carbon expressed as a proportion of abattoir waste ( default value (DV= 0.12) ); DOCF= Fraction of degradable organic carbon dissimilated for the abattoir waste (DV=0.7); F1= Methane fraction generate from dumping gas (DV=0.50); 1.336= Conversion rate of carbon to methane; R= Recovered methane during the year, measured in tones (here no recovered CH<sub>4</sub>); OX=Oxidation factor (DV=0.1 for well-managed ) and (DV= 0 for unmanaged ); and 25=CH<sub>4</sub> global warming potential used to convert the quantity of methane emitted to CO<sub>2</sub>e from the quantity of abattoir waste produced.

#### 2.3.3 GHG emissions from biogas

This is important to compare the emission of Greenhouse gases from disposal sites and with biogas emission if it implements. Thus, B-Sustain (2013a) and IPCC (2000) mathematical computation were used to estimate the



gases.

$$\text{GHG emissions (tCO}_2\text{e)} = Q_j \times \text{EF}_j \dots\dots\dots(3)$$

Where: **t** is unit for waste either by ton or kg; CO<sub>2</sub>e is CO<sub>2</sub> in equivalence; Q<sub>j</sub> is the quantity of waste by type j (here is only abattoir waste); EF<sub>j</sub> is the emission factor of waste type j for biogas (0.02kgCO<sub>2</sub>e)

**2.3.4 Estimation of biogas production from abattoir waste**

Biogas production potential of abattoir waste was estimated following the coefficient described in (Ngumah, et al., 2013; Rao, et al., 2000).According to these method, 1ton (1000Kg) of abattoir waste can produce 53m<sup>3</sup> biogas that is 1Kg of abattoir waste can produce 0.053m<sup>3</sup> of biogas. Hence, the volume of biogas produced (VBP) may be obtained using equation 4.

$$\text{VBP} = \text{AWG} * 0.053\text{m}^3/\text{kg} \dots\dots\dots (4)$$

**2.3.5 Estimation of energy from biogas**

According to (Ngumah, et al., 2013) the energy potential of biogas generated is based on the calorific value (high heating value) of the methane content and (Rohstoffe, 2009) stated that the average calorific value of biogas is 21-23.5 MJ/m<sup>3</sup> (approximately 22.0 MJ/m<sup>3</sup>). Commonly, energy is expressed as Kilo Watt hour (KWh) and 3.6 MJ is equal to 1KWh. If the 22.0 MJ/ m<sup>3</sup> of biogas is converted to KWh, 1 m<sup>3</sup> of biogas has an energy potential of 6.1 KWh. Energies (electricity and heat) potential of biogas was estimated based on the energy conversion methods formulated by (Banks, et al., 2011) . According this method, the efficiency of biogas to be converted to electricity is 35% and, therefore, the electricity production potential of 1m<sup>3</sup> of biogasis 2.14 KWh (i.e. its energy potential of 6.1 KWh X 0.35). Therefore, the Electricity production potential (EPP), (KWh), may be obtained using the following formula:

$$\text{EPP} = \text{VBP} * 2.14\text{kWh} \dots\dots\dots (5)$$

Similarly, Banks (2009) indicated that the efficiency of biogas to be converted to heat energy is 50% and, thus the heat production potential of 1 m<sup>3</sup> of biogas is 3.1 KWh (that is, energy potential of 6.1 KWh X 0.5). The heat production potential (HPP), (KWh), may be estimated as:

$$\text{HPP} = \text{VBP} * 3.1\text{KWh} \dots\dots\dots(6)$$

**2.3.6 Estimation of cost from biogas energy**

Amount of energy produced was estimated based on the current Ethiopian Electric PowerCorporation (EEPCO, 2018) into cost; i.e.1kWh of electricity or heat equals to 0.57ETB or \$0.02.

$$\text{Cost} = (\text{Equation } 5^* \text{ X } 0.57 \text{ ETB}) + (\text{Equation } 6^* \text{ X } 0.57 \text{ ETB}) \dots\dots\dots (7)$$

**2.3.7 Estimation of fuels equivalence with biogas**

As (B-sustain., 2013b) energy estimation, utilization 1m<sup>3</sup> of biogas equivalent to coefficient factorof 0.45kg Liquefied Petroleum Gas (LPG), 0.6kg kerosene(K), 3.50kg charcoal/fire wood, 0.4kg furnace oil (F), 0.7kg petrol (P) and 0.5kg diesel(D) in the same activities.

$$\sum \text{CFF} * \text{N} \dots\dots\dots (8)$$

Where, CFF: each of above coefficient factor; N: Volume of biogas produced (i.e from equation 4

**2.3.8 Bio-fertilizers yield estimation methods**

According to (Ngumah, et al., 2013) the coefficients used in estimating bio-fertilizer yields were based on the fraction of the dry mass (DM) portion of organic waste that is not converted to biogas. Therefore, in this study, bio-fertilizer was estimated based on the coefficient fraction of the Dry Mass (DM) and Volatile Solid (VS) portion of abattoir waste. According to (Deublien & Steinhauer, 2008), the DM percentage of fresh organic wastes was given as 15% for abattoir waste, while the Volatile Solids (VS) is the potentially dry mass (DM) of abattoir waste



converted into gas (i.e dry mass minus mineral content), which was calculated by multiplying 85% with DM of abattoir waste. In this study, the following formulas were used for calculating DM and VS.

$$DM = AWG \text{ (kg)} * 0.15 \text{ (15\%)} \dots\dots\dots (9)$$

$$VS = DM * 0.85 \text{ (85\%)} \dots\dots\dots (10)$$

Bio-Fertilizer Yield (BFY) of the abattoir waste was calculated considering DM (equations 9) and VS (equation 10). But according to Burke (2000), 60% of VS is the actual fraction taken to be converted to biogas and therefore, the remaining 40% portion of VS was considered in BFY computation. Hence the following formula for computing the potential of BFY was deduced as:

$$BFY = (DM - VS) + (40\% * VS) \dots\dots\dots (11)$$

### 2.3.9 Estimation of cost from bio-fertilizer production

Based Ethiopian Agriculture Ministry Report (2017/18) report, 50kg of UREA and DAP fertilizers are equal to 1230 and 1, 1455 Ethiopian Birr (ETB), respectively. We assumed that the price of Bio-fertilizer yields (BFY) was reduced by half (□50%) from current price of chemical fertilizers (UREA and DAP). This reduction was assumed that, the bio fertilizer and its benefits among our farmers may have low acceptance due to limited awareness about it.

$$\text{Cost of BFY} = 50\text{kg of BFY} * 23.70\text{USD (600ETB)} \dots\dots\dots (12)$$

### 2.4 Inclusion and exclusion criteria

Inclusion Criteria: For estimation of abattoir potential, slaughtered cattle, sheep and goats were inclusive from four selective abattoirs. Exclusion Criteria: Slaughtered camels and pigs from four selective abattoirs were inclusive and in case of survey part, all daily abattoir workers and who haven't willingness to participate from selected abattoirs won't participated.

### 2.5 Data Quality Assurance and Analysis

Data was assured using validated studies, livestock were counted in each year by animal sciences experts. Data was entered on simple excel and then analysis waste generation, bio-energy, cost analysis by charts.

### 2.6 Ethical Consideration

Permission to conduct this “Grant research” was provided by Haramaya University Research Office and approved by Ethics Committee of Haramaya University. Then, Haramaya University Health and Medical Sciences was written the formal letter to Haramaya, Haramaya University Enterprise, Harar and Dire Dawa Municipality Authority abattoir service for realization of legal research. To ensure confidentiality, the participants were briefed about the purpose and written informed consent was secured from each participant.

## 3. RESULTS

### 3.1 Abattoir Waste Composition and Generation

Annually, about 12339, 39281, 10170 and 4380 of livestock such as cattle, goats and sheep were slaughtered in Harar Abattoir, Dire Dawa Abattoir, Haramaya and Haramaya University Enterprise (HU-E) abattoirs, respectively. During production of meat about 224.37ton/year, 1,015.59ton/year, 192.25ton/year and 174. 19 ton/year of abattoir wastes was estimated from Harar abattoir; Dire Dawa city; Haramaya town; and Haramaya University enterprise abattoirs, respectively (Table 1).

**Table 1:** Annual slaughtered livestock and estimated abattoir waste from the selected abattoirs, 2019

Name of abattoirs	Livestock (no)	Principal type of abattoir waste compositions				Total waste (ton)
		Blood waste (ton)	Bone waste (ton)	Intestinal content (ton)	Tissue waste (ton)	
Harar	12,339	72.33	68.61	46.42	37.01	224.37
Dire Dawa	39,281	316.17	318.36	213.49	167.57	1,015.59
Haramaya	10,170	49.41	78.24	36.62	27.97	192.25
HU-E	4,380	56.57	52.97	35.92	28.73	174.19
Grand total	66,170	494.47	518.19	33.24	261.29	1,606.40

From total abattoir waste generated, the percentage of abattoir waste compositions weight is generated from each abattoir is varied separately. For instance, 30, 30, 31 and 41% of bone composition and 32, 32, 31 and 21% of blood waste was estimated from Harar, HU- Enterprise, Dire Dawa and Haramaya abattoirs, respectively (Figure 1).

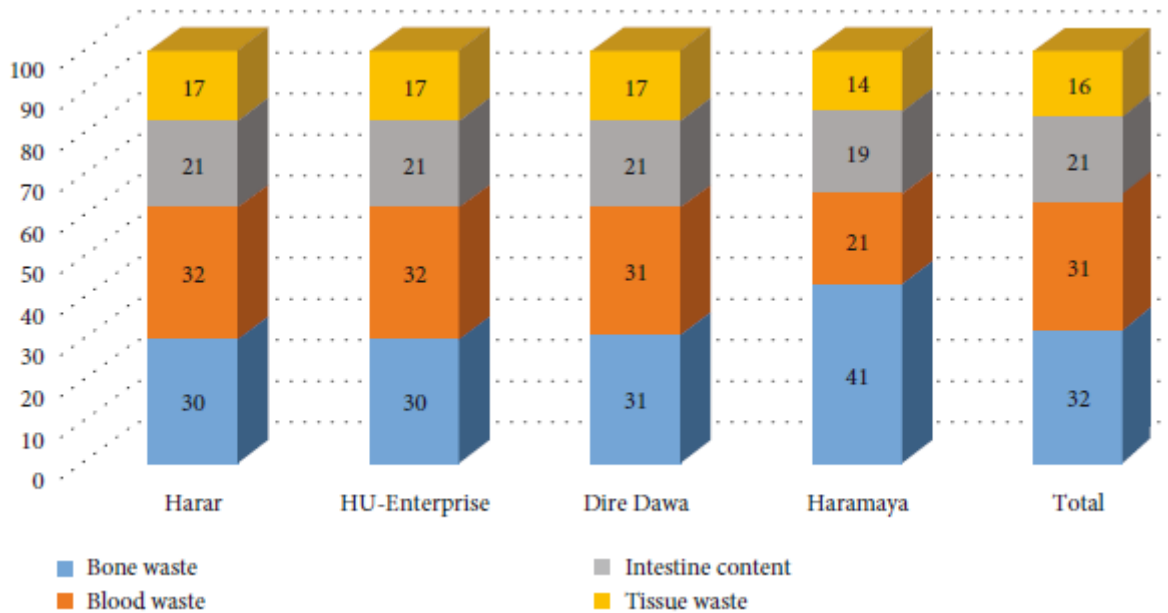


**Figure 1:** Percentage of Waste Compositions rate of each abattoir from Dec. 1, 2018 to Jan, 2019

Field observation showed that huge amount of abattoir wastes was disposed on surrounding environmental. From four abattoirs, improper waste disposal system was observed.

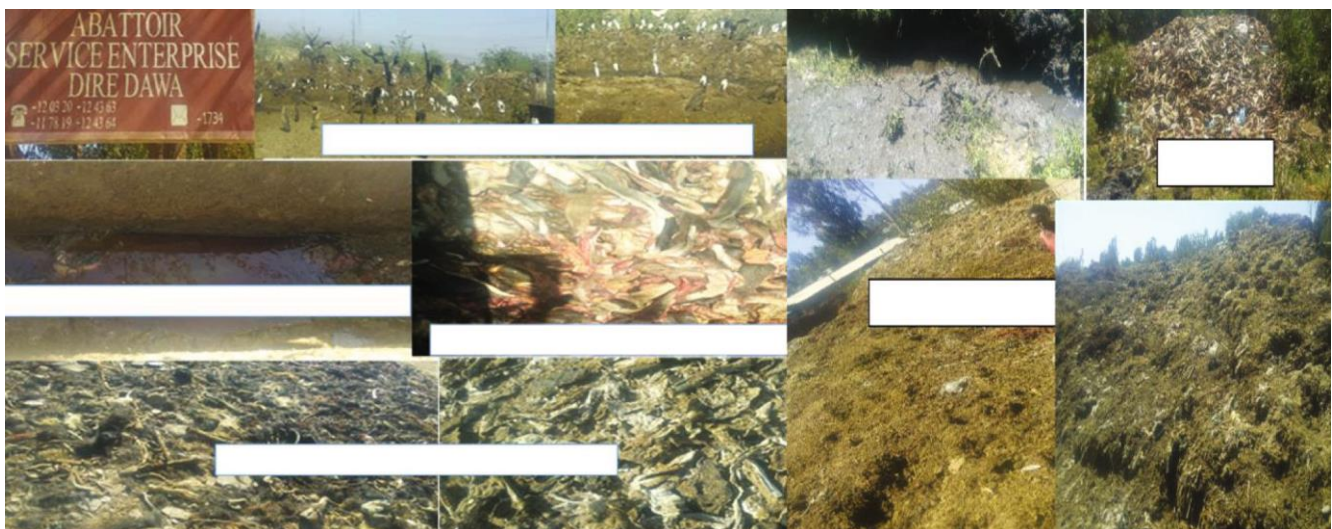


**Figure 2** Waste disposal site of abattoir waste from selected municipality abattoirs, March, 2019



### 3.2 Green House Gases Emission from Dumping Sites

About 181,630.74tonCO<sub>2</sub>eq of greenhouse gases emission were estimated from 1,606.40 ton of abattoir waste estimated (Table 1) from the disposed sites of four abattoirs (Table 2).

Table 2: Annual estimation greenhouse gas emission from disposal sites of abattoirs, 2019

Name of abattoirs	GHG emission from dumping sites (*tonCO <sub>2</sub> e)			
	Daily	Weekly	Monthly	Annually
Harar	0.073	0.516	2.213	26.942
Dire Dawa	0.334	2.337	10.016	118.941
Haramaya	0.062	0.316	1.283	15.353
HU-E	0.057	0.401	1.718	20.393
Grand total	0.528	3.571	15.230	181.631

**NB:** \*tonCO<sub>2</sub>e= A ton of carbon dioxide equivalent, also abbreviated as tonCO<sub>2</sub>eq is a metric measure used to compare the emissions from various greenhouse gases on the basis of their global-warming potential (GWP).

### 3.3 Biogas Production and Its Cost

The table shows about 11892m<sup>3</sup>/year, 53826m<sup>3</sup>/year, 10189m<sup>3</sup>/year and 9263.87 m<sup>3</sup>/year of biogas production was estimated from Harar; Dire Dawa; Haramaya; and HU-E abattoirs, respectively (Table 2). From these biogases about 104336.99 kWh/year, 282049.65kWh/year, 282049.65kWh/year and 48,542.68kWh/year of electricity and heat energy was estimated from Harar town municipality, Dire Dawa municipality city, Haramaya town municipality and Haramayauniversity enterprise abattoirs, respectively (Table 3). When converted biogas into cost, about \$1254.3, \$5624.2, \$1072.2 and \$971.1 cost was estimated annually from Harar Abattoir; Dire DawaAbattoir; Haramaya Abattoir; and HU-E abattoir, respectively (Table 3).

Table 3 Annual Estimation of Energy from estimated biogas of selected abattoirs, 2019

Name of abattoirs	Estimated waste (ton)	Estimated biogas (*m <sup>3</sup> )	Estimated energy from produced biogas and its cost			
			Heat (**kWh)	Electricity (kWh)	Total energy (kWh)	Estimated cost (***)
Harar	224.366	11,891.61	25,448.1	78,888.94	104,336.99	1,254.3
Dire Dawa	1,015.591	53,826.27	115,188.2	166,861.4	282,049.65	5,624.2
Haramaya	192.253	10,189.25	21,805.00	31,586.7	53,391.67	1,072.2
HU-E	174.193	9,263.87	19,824.68	28,718.0	48,542.68	971.1
Grand total	1,606.403	85,139.20	182,197.9	263,931.5	446,129.41	8,901.6

\*m<sup>3</sup>: cubic meter = 1,000 kg. \*\*kWh: kilowatt hour. \*\*\*United States dollar (USD): 1 = 28.5163: Ethiopian currency (ETB), April 2019.

### 3.4 Anaerobic Reduction of Greenhouses gases

From 26.94tonCO<sub>2</sub>eq/year of greenhouses gases/GHG/ estimated from disposal sites, AD could reduce 22.44tonCO<sub>2</sub>eq/year of GHGs emission and only 4.49 tonCO<sub>2</sub>eq/year of GHGs was estimated from anaerobic digester (Table 4).



Table 4 Estimation of potential reduction of GHGs emission using anaerobic digester per a year

Annual reduction of GHGs (tonCO <sub>2</sub> eq) using anaerobic digester				
Name of abattoirs	Estimated waste (ton)	GHG estimated from dumping	Estimated of GHGs from AD	Potential of AD reduction
Harar	224.366	26.942	4.486	22.437
Dire Dawa	1,015.591	118.941	20.312	101.558
Haramaya	192.253	15.354	3.843	19.225
HU-E	174.193	20.393	3.482	17.418
Grand total	1,606.403	181.631	32.127	160.640

### 3.5 Biogas Equivalence with Fuel fossil

The following table shows that from 85,139.20m<sup>3</sup>/year of biogas estimated, could cover 36.10ton of Liquefied Gas or 48.130 ton of Kerosene or 280.758 ton of Charcoal or 32.10 ton of Furnace oil or 56.15 ton of Petrol or 40.12 ton of Diesel per a year in same functions (Table 5).

Table 5 Equivalence of estimated biogas with other fossil fuels from selected abattoirs, 2019

Name of abattoirs	Estimated biogas (m <sup>3</sup> )	Annual substitution of expensive fuels by utilization of biogas					
		Liquefied gas (ton)	Kerosene (ton)	Charcoal (ton)	Furnace oil (ton)	Petrol (ton)	Diesel (ton)
Harar	11,891.61	5.355	7.140	41.648	4.760	8.330	5.950
Dire Dawa	53,826.27	23.640	31.520	18.388	21.013	36.774	26.267
Haramaya	10,189.25	3.050	4.067	23.725	2.711	4.745	3.389
HU-E	9,263.87	4.052	5.403	31.516	3.602	6.303	4.502
Grand total	85,139.20	36.097	48.130	280.758	32.087	56.152	40.108

NB: unit for biogas is cubic meter, while unit for all fossil fuels is ton (1 ton = 1,000 kilograms).

### 3.6 Bio-Fertilizer Production from Abattoir Waste and Its Cost

About 16.502 ton/year, 72.852ton/year, 9.404 ton/year and 12.49 ton/year of bio-fertilizer was estimated from Harar, Dire Dawa, Haramaya and Haramaya University enterprise abattoirs, respectively (Table 6). About 19.0/day and \$6933.7/year; \$85.9/day and \$30609.9/year; \$16.3/day and \$3951.3/year; and \$14.7/day and \$5248.3/year of bio-fertilizer was estimated from Harar, Dire Dawa, Haramaya and Haramaya University enterprise, respectively (Table 6).

Table 6 Annual Estimation of bio-fertilizer production from abattoir waste of abattoirs, 2019

Name of abattoirs	Abattoir waste (ton)	Estimated residual for biofertilizer and its cost benefits			
		Dry mass/DM (ton)	Volatile solid/VS (ton)	Biofertilizer (ton)	Estimated cost (US dollar)
Harar	224.37	33.68	28.63	16.502	6,933.7
Dire Dawa	1,015.59	148.68	126.38	72.852	30,610
Haramaya	192.25	19.19	16.31	9.404	3,951.3
HU-E	174.19	25.49	21.67	12.491	5,248.3
Grand total	1,606.40	227.04	192.98	111.249	46,743.2

NB: United States dollar (USD) 1 = 28.5163 Ethiopian currency (birr), April 2019 exchange.

## 4. DISCUSSION

The study was sought to focus on abattoir waste generation from selected Eastern Ethiopia abattoirs. These abattoir serving as slaughterhouse for slaughtering livestock such as cattle, goats and sheep. Therefore, the researchers were considered these livestock in this study. The study revealed that the average number of livestock slaughtered in these four selected abattoirs were onehundred, sixty-nine per day and sixty thousand, one hundred seventy per year (Table 1). More than twenty-five thousand per a day and more than nine million meat per a year



was produced from December 1<sup>st</sup>, 2018 to January 30<sup>th</sup>, 2019, which was distributed to the surrounding community. However, during meat production, huge amount of abattoir wastes is generation from these selected abattoirs which was estimated using (Aniebo, et al., 2009) mathematical computation approach was used to estimate abattoir waste generation due to its complexity and difficulty. Based on this assumption, about four thousand, four hundred one kilogram per day and one million five hundredthirteen thousand five hundred ninety kilo gram per year of abattoir waste was estimated from the selected abattoirs (Table 2). In fact, the number of slaughtered livestock were varied among months due to the existence of different fasting and meat-eating holidays (Table 2). Such occurrence could result varies abattoir waste generation produced the throughout the year.

The main principal abattoir waste compositions such as blood waste, bone waste, intestinal content waste and tissue were considered in this study. However, the percentage of these abattoir waste compositions obtained was varied generated among selected abattoirs (Table 2). That means the proportion of abattoir waste compositions generated from selected abattoirs were not be same. This is because of slaughtered livestock type (such as cattle, goats and sheep). For instance, when high number of goat and sheep slaughtered in abattoir it was resulted high amount of bone was estimated and followed by blood, intestinal content and tissue waste, respectively. Such type of waste composition estimation was observed in Haramaya and Dire Dawa Abattoirs. But, blood waste composition was highest among abattoir waste compositions in Harar and Haramaya University Enterprise where purely cattle were slaughtered; and then followed by bone, intestinal content and tissues waste composition, respectively (Figure 2). Therefore, overall composition was varied among the selected abattoirs due to type of slaughtered livestock.

When we compare the current abattoir waste estimated (2,782.44 kg/day and 991,178.68 kg/year) generated from Dire Dawa Municipality abattoir is slightly higher than with finding obtained from Hawassa abattoir, Hawassa Town (2,530 kg/day and 923,995 kg/year) (Tolera, et al., 2019); Minna abattoir, Abuja Nigeria (i.e. 2,394 kg/day and 873,810 kg/year) (Ahaneku & Njemanze, 2015); Tamale abattoir, Ghana (i.e. 2,134 kg/day and 778,910 kg/year) (Frederick, et al., 2010). However the finding obtained from Harar Municipality abattoir (615 kg/day and 224,518 kg/year); Haramaya abattoir (527 kg/day and 127,948 kg/year); Haramaya University Enterprise (477 kg/day and 169,944 kg/year) was smaller than the finding reported by (Frederick, et al., 2010; Ahaneku & Njemanze, 2015; Tolera, et al., 2019).

Moreover, the current abattoir waste generate could contrast with other organic municipality waste that are generating from the households of same situation. Accordingly, the current estimated abattoir waste (4,401 kg/day and 1,513,590 kg/year) generated from four selected abattoirs, Eastern Ethiopia is higher than municipality waste (422.7 kg/kg/day and 154,285.5 kg/year) generated from 85 households of Aweday Eastern Ethiopia (Beneberu, 2011). Therefore, this is indicating that huge amount of abattoir waste is generating from few numbers of abattoir operations as compared to other waste generating from many different institutions and households. But, there is no attention either from government and ownership/private or owner enterprise.

The other scope of study was estimating the greenhouse gases emission from disposal sites. To do it, (IPCC, 2000) and GWPs factors were considered to convert masses of different greenhouse gases into a single carbon dioxide-equivalent metric (CO<sub>2</sub>-e), by multiplying a mass of a particular gas by its GWP gives the mass of carbon dioxide emissions that would produce the same warming effect. The emissions are multiplied by 25 to calculate the carbon dioxide equivalent (CO<sub>2</sub>-e) emissions. Despite of fact that methane (CH<sub>4</sub>) vented to the atmosphere is considered an emission as this action would be adding to atmospheric. The study conducted on the issue of abattoir waste disposal site indicated that improper disposal of wastes like abattoir waste is one of the big problems for climate change over all the world due to greenhouse gases/GHG/ emission from their disposal sites (Chukwu, 2008). Thus, based on IPCC factors, it is possible to estimate the amount of GHG emission from disposal sites of the selected abattoirs. Accordingly, more than five hundred twenty kilogram of greenhouse gases per a day and more than one thousand eighty kilogram of carbon dioxide equivalent of greenhouse gases per a year were estimated from four selected abattoir disposal sites (Table 3). Hence, this amount of gases contribute to climate change, could enhance greenhouse effect on surrounding that is expected to have widespread consequences as many scholars indicated (Chukwu, et al., 2011).



In this study estimation of bio energy was considered as sustainable management for abattoir waste. Using Rao et al. (2000), using anaerobic digester, about 233 m<sup>3</sup>/day and 80,220m<sup>3</sup>/year of biogas production was estimated from four selected abattoirs (Table 4) and which have many benefits. Of these benefits, obtain alternative bio-energy such as heat and electricity. Using equations (5 & 6), about 1, 222kWh /day and 420,354 kWh /year of energy was estimated from 233m<sup>3</sup>/day and 80,220m<sup>3</sup>/year of biogas was estimated from selected abattoirs, respectively (Table 5). When in turned into cost, 24.4USD (697ETB)/day and 8901.6 USD (254,230ETB)/year of price was estimated from these selected abattoirs (Table 6).

The second benefits of biogas is to substitute the other expensive fossil fuels such as liquefied petroleum gas /LPG/, kerosene, charcoal, furnace oil, petrol and diesel fuel with the equivalence functions. Because biogas is a "cleaner" than wood fuel, kerosene, petrol, liquefied petroleum gas (LPG), diesel, and furnace oil replacing conventional fuels those using for different purpose( (Charles, 2009). As Table 7 shows estimated biogas from each abattoirs could cover an average per capita consumption of charcoal that can be used for daily activities (such as for cooking, heating and boiling water) of the surrounding communities. This indicated that using such amount of biogas could reduce demand for firewood/charcoal which implies saving some forest resources and protect the environment from threats.

As illustrated above emission of greenhouse gasses from the disposal sites of selected municipal abattoirs are one of the significant sources of air pollution at surrounding cities fully and at national level particular. Meanwhile, the reduction, control and recycling of such gasses is of great importance from hygienic and global perspectives. Hence, install biogas technology has a potential to reduce amount of greenhouse gases emitted from disposal sites of surrounding environment as indicated in Table 8

The third benefit of biogas is that it can give supplementary for economy prosperity, social and for country development. Annually, more than fifty-five-thousand-dollar biogas and bio-fertilizer estimated from four selected abattoirs. As scholar said, biogas improving economic of the country or abattoir itself through the means of creating markets for surrounding community by leading to lesser the cost for finite fossil fuels and charcoal with their drawback (Salman, 2008). So that better social advantages can lead to new sources of employment and potentially lifting communities out of poverty. So that present finding encourages 2nd GTP targeted, that recommended as "Every governments' organization should increase their internal resource mobilization of income benefits not less than five percent of their governmental allocation (i.e. >5% of normal budget allocation from government) ( NPC, 2018)

The second product of anaerobic digester is bio-fertilizer production. Using (Deublien & Steinhauser, 2008) coefficient fraction model (equation 11, 12 and 13), about 323.50kg/day and 111,249kg/year of bio-fertilizer was estimated from four selected abattoir (Table 9). As land coverage, the current estimated bio-fertilizer (111,249kg/year) from four abattoir sites can cover about 2,225 hectares /year with its advantage and efficiency of soil. A study conducted by agronomies described under their website if someone utilize bio-fertilizer, the users could be increased from 15% to 25% of total crop yield under ideal agronomic (<http://agriinfo.in/page.>, n.d.). Now day, such benefits are important considerations both by government or users. Actually, the users and farmers are convinced about substantial savings in cost of production through reduced usage of chemical fertilizers, getting similar yield and also well keeping of soil composition and health (Chima, et al., 2013). Essentially, bio-fertilizer reduces water and soil pollution, loss of micro-organisms and beneficial insects; overall reduction in soil fertility is some of the ill effects of chemical fertilizers. So that this study gives a clue of bio-fertilizers significance which hold promising future in reducing soil quality problems with optimum crop yield for users and farmers as well (Renuka, 2013). Hence, utilization of chemical fertilizers for future agricultural growth would mean further loss in soil quality and increased environmental pollution, as the result bio-fertilizer is important to reduce such problems.

When in turned into price, about 3,882ETB/day and 1334, 986ETB/year of cost was estimated based on current chemical fertilizer price (FEAR, 2019). By considering market feasibility, was considered how bio-fertilizer is perceived in terms of value offered for money spent by customers. In such circumstances, the researchers have decided the price of bio fertilizers along with the risk and responses was weighed. In fact, the



current price of chemical fertilizers or inorganic fertilizer used at national level was less halved (<50%) to estimate the cost of the current bio-fertilizer. That means such amount of price from inorganic fertilizer was reduced by half and the present estimated bio-fertilizer cost, which could be covered two times of hectares as compare to inorganic chemical coverage. In other hands, this income generation is also supplementary of internal revenue for the abattoirs themselves. Therefore, AD is best technology for abattoir treatment due to the potential to reduce pollution, greenhouse gases emissions as compared to other waste treatment. In addition, it has a benefit to mitigate global climate changes (i.e. biogas); and optimize and keep soil health (i.e. bio fertilizer).

## 5. CONCLUSION

The present study shows that large quantity of abattoir waste was generated as compared to other waste generated, which was directly disposed into the surrounding environment without any disposal system. Moreover, the study revealed that the amount of greenhouse gases emitted from the disposal sites of the selected abattoirs could contribute to climate change. Furthermore, the study indicated that huge amount of biogas and bio fertilizer yield obtained through anaerobic digester indicated that abattoir waste have a potential benefit to ensure environmental safety and public health as means of sustainable management. Thus, the study found that the municipality should design abattoir waste treatment technology for sustainable management to safeguard the environment from greenhouse emission and ensure public health for the as long-term plan, while proper abattoir waste disposal will be forwarded as short-term management.

## ACKNOWLEDGEMENTS

Mostly, we acknowledge Haramaya University in general and Research "Theme I: Productivity and Environmental Sustainability for Food Security and Poverty Alleviation and Research Group and Partnership Directorate of Haramaya University in particular for settled financial support which was coded as HUKT-2018-01-03-63. In addition, we thank Harar town Municipality, Haramaya Town Municipality, Haramaya University Enterprise abattoir and all abattoir services for their contributions.

## REFERENCE

- Ahaneku, I. & Njemanze, C., 2015. Flow Analysis of Abattoir Solid Waste Management System in Minna, Nigeria. *Res. J. Dairy Sci.*, 41(2), pp. 165-172.
- Akinro, A. & Ologunagba, I., 2011. Environmental implications of unhygienic operation of a city abattoir in Akure, Western Nigeria. *ARP Journal of Engineering and Applied Sciences*, 4(9), p. 311–315.
- Aniebo, A., SN., W. & (2009)., O. I., 2009. Abattoir Blood Waste Generation in River State and its Environmental Implications in the Niger Delta. *J. Toxicol. Environ. Chem.*, 91(3), pp. 619-625.
- Banks, C., Chesshire, M., Heaven, S. & Arnold, R., 2011. Anaerobic digestion of source segregated domestic food waste: performance assessment by mass and energy balance. *J. Technol. Biores.*, 102(2), pp. 612-620.
- Beneberu, S., 2011. Generation, composition and characteristics of urban solid waste in a major khat producing and marketing area in Eastern Ethiopia. *IJEP*, 1(5), pp. 9-16.
- B-sustain., 2013b. *Biogas equivalence fossil Fuels and its emission comparison.*, AUS: Bioenergy . Charles, B., 2009. *Optimization of anaerobic digestion to provide energy output via conversion*, Australia : EPA.
- Chima, C., Ngumah, J., Ogbulie, J. C. & Orji, E. A., 2013. Biogas potential of organic waste in Nigeria. *Journal of Urban and Environmental Engineering*, 7(1), pp. 110-116.
- Chukwu, O., 2008. Analysis of ground water pollution from abattoir waste in Minna, Nigeria. *Research Journal of Dairy Science*, 2(4), pp. 74-77.
- Chukwu, O., Adeoye, P. & Chidiebere, I., 2011. Abattoir wastes generation, management and the environment: Minna, Nigeria. *African Journal of Engineering*, 1(6), pp. 100-109 .
- Deublien, D. & Steinhauer, A., 2008. *Biogas from Waste and Renewable Resources*, Wiley-VCH Verlag GmbH & Co.; 4 ed. AUS: Press.
- EEPCO, 2018. *Ethiopian Electric Power Corporation: Energy conversion resource*, A.A: Agriculture .
- Evans, J. D., 1996. *Straightforward statistics for the behavioral sciences.* .. 2 ed. USA: Pacific Grove, CA: Brooks/Cole Publishing.
- FEAR, 2019. *Federal Ethiopian Agriculture report: Report on chemical price in Ethiopia*, Addis Ababa



- Frederick, A., Ayum, T., Gifty, A. & Samuel, A., 2010. Microbial Quality of Chevron and Mutton Sold in Tamale Metropolis of Northern Ghana. *J. Appl. Sci. Environ. Manage*, 14(4), pp.53-55.
- <http://agriinfo.in/page..>, n.d. *Promotion of biofertilizer on agriculture production* , s.l.: s.n.
- [https://en.wikipedia.org/wiki/Dire\\_Dawa](https://en.wikipedia.org/wiki/Dire_Dawa), n.d. *History of Dire Dawa Administration City* , s.l.: s.n.
- <https://en.wikipedia.org/wiki/Harar>, n.d. History of Harar town.
- IPCC, 2000. Intergovernmental Panel on Climate Change: National Greenhouse Gas Inventories and uncertainty management in national greenhouse gas inventories. IPCC
- JGCRI, 2018. *Joint Global Change Research Institute; Documentation: Global Change Assessment Model (GCAM): Documentation for GCAM*, Geneva: FAO.
- Ngumah, C., Ogbulie, J., Orji, J. & Amadi, E., 2013. Biogas Potential of Organic Waste Nigeria,. *J.Urban Environ. Engineer.* , 7(1), pp. 110-116.
- NPC, 2018. *National Planning Commission : Federal Democratic Republic of Ethiopia Growth and Transformation Plan II (GTP II) (2015/16-2019/20)*, Addis Ababa: FEDR.
- Rao, M. S., P., S. S., K., S. A. & ., S. M. S., 2000. Bioenergy conversion studies of the organic fraction of MSW: assessment of ultimate bioenergy production potential of municipal garbage. *J. Applied Energy* , 66(1), p. 75–87.
- Renuka, K., 2013. *Biofertilizers\_Opportunities\_and\_Challenges\_pd..india* retrieved from ww, Indian : Indian Agriculture .
- Rohstoffe, F., 2009. *Biogas basisdaten Detschland- Comrehensive overview of the biogas station in Germany.*, Germany : Agriculture .
- Salman, Z., 2008. *Waste-to-energy consultant , waste-to-energy conversion* , SDF: Austrilia . Tolera, S. T., Sota, S. ..., Ermias., D. & .H., M. T., 2019. Waste Generation and Physicochemical Qualities of Abattoir Wastewater in Hawassa City, Ethiopia. *EAJHBS*, 3(1), pp. 23-234.



## Butanolysis of Jatropha Oil Using Glycerol Enriched Non-Calcined Calcium Oxide: Optimization of the Process

Keneni, Yadessa Gonfa Keneni<sup>1,\*</sup>, Jorge Mario Marchetti<sup>2</sup>

<sup>1</sup>Department of Biology, College of Natural and Computational Science, Hawassa University, Hawassa, Ethiopia

<sup>2</sup>Faculty of Sciences and Technology, Norwegian University of Life Sciences, Drøbakveien 31, Ås 1432, Norway

\*Corresponding author, e-mail: [yagvtoliyad07@gmail.com](mailto:yagvtoliyad07@gmail.com)

### ABSTRACT

Interest of using fuels from renewable sources, such as biodiesel from non-edible oils has increased due to fluctuation of fossil fuel market and environmental benefits of fuels from renewable sources. Production of biodiesel using heterogeneous catalysts such as calcium oxide (CaO) is more preferable as such catalysts can be reused, eases separation of products and avoid extensive product washing steps. CaO can be used in various forms of which the glycerol enriched CaO is the least studied. Butanolysis of Jatropha oil using glycerol enriched non-calcined CaO as heterogeneous catalyst was carried out to investigate the influences of reaction temperature and butanol: oil molar ratio on Jatropha oil conversion ( $X_{JOB}$ ) and yield of fatty acid butyl esters ( $Y_{FABEs}$ ). Central composite design involved two factors (reaction temperature and butanol: oil molar ratio) and two levels factorial ( $2^2$ ) was used to determine the impacts of the factors on  $X_{JOB}$  and  $Y_{FABEs}$  and to optimize the reaction process. From the main factors and their interactions, temperature was found to highly affect both the  $X_{JOB}$  and  $Y_{FABEs}$ . As curvatures are statistically significant ( $p \leq 0.05$ ), second order models (quadratic models) were found to be more suitable to optimize the butanolysis process. Based on regression models and response surface methodology, the maximum  $X_{JOB}$  (98.16%) and  $Y_{FABEs}$  (95.79%) were predicted to be obtained at the optimum temperatures of 87.35 and 90.48 °C and butanol: oil molar ratios of 9.13:1 and 13.24:1, respectively. Maximum  $Y_{FABEs}$  of 95.64% was also experimentally obtained at the optimum conditions predicted for the  $Y_{FABEs}$ . From the results obtained for the experimental ranges investigated, the present study suggested that glycerol enriched non-calcined CaO can be used as a good alternative catalyst for biodiesel production using butanol. More studies are also suggested for upscaling the reaction process of the current experiments by using more integrated reaction factors.

**Keywords:** biodiesel, butanolysis, calcium oxide, glycerol, Jatropha curcas L. oil, optimization

### 1. INTRODUCTION

The interest of using fuels from renewable sources, such as biodiesel, has increased in recent years due to political and economic instability of the fossil fuel market, and also because of the positive environmental benefits of the fuels from renewable sources (Colombo et al., 2017; Uzar, 2020; Vakulchuk et al., 2020). Biodiesel contributes less to global warming and contains less contaminant in its emission due to the renewable nature and organic origin of the feedstock (Neupane, 2022; Videsh et al., 2009).

Biodiesel is a liquid fuel that consists of mono alkyl esters of long chain fatty acids derived from lipid such as vegetable oils, animal fats and microalgae oils (Colombo et al., 2017; Pinzi et al., 2014; Shinde and Kaliaguine, 2019). It is usually produced through the transesterification reactions of the oils with short-chain alcohols using homogeneous or heterogeneous catalysts (Colombo et al., 2017; Shinde and Kaliaguine, 2019). The catalysts used can be either acidic, basic or enzymatic in nature and employing each kind of catalyst has its own benefits and limitations (Shinde and Kaliaguine, 2019).

Biodiesel has still difficulties to be competitive with petroleum diesel without fiscal incentives, mostly due to the price of the raw materials and the processing costs (Ferrero et al., 2015; Sosa-Rodríguez and Vazquez-Arenas, 2021). The cost of feedstock alone accounts about 75% of the overall biodiesel production cost (Ahmad et al., 2011; Atabani et al., 2012), and hence using inexpensive feedstock such as non-edible oils, wasted oils and animal fats has been identified as a promising solutions in this regard (Ahmad et al., 2011; Atabani et al., 2012; Sani et al., 2014). The other alternatives to reduce the price of biodiesel is employing cost effective biodiesel manufacturing process, particularly by using low-cost catalysts (Taufiq-Yap et al., 2012; Welela Meka, 2023).

The majority of biodiesel is produced through homogeneous base catalyzed transesterification of edible vegetable oils using methanol, and the most commonly used catalysts are KOH and NaOH (Shinde and



Kaliaguine, 2019). These catalysts result in fast reaction rates under mild reaction conditions (Kouzu et al., 2009), however, the oil and the alcohol must be substantially anhydrous, and the free fatty acid (FFA) content of the oil should be low to avoid the saponification side reaction (Abbaszadeh et al., 2012; Di Serio et al., 2007). Generation of large amount of wastewater to purify the products and incapability of catalyst reuse are also among the limitations of using these catalysts (Boey et al., 2011). Homogenous acid catalysts such as HCl and H<sub>2</sub>SO<sub>4</sub> are efficient in terms of overcoming the saponification side reactions (Shibasaki-Kitakawa et al., 2007), but difficulties of catalyst recycling, requirement of higher temperature and alcohol to oil molar ratio, and serious environmental and corrosion problems are some of the limitations of these catalysts (Brahmkhatri and Patel, 2013; de Rezende et al., 2008; Shibasaki-Kitakawa et al., 2007). Moreover, enzymatic catalysts are less sensitive to FFA and moisture content of the oil (Brahmkhatri and Patel, 2013; Shibasaki-Kitakawa et al., 2007), however, the requirement of more stringent reaction conditions, long reaction time and being expensive are some of the disadvantages of using enzymes (Boey et al., 2011; Brahmkhatri and Patel, 2013). One of the possible solutions to overcome these problems is using heterogeneous catalysts (Kouzu et al., 2009).

Using heterogeneous catalysts might significantly reduce the processing costs associated with homogeneous catalysis (Ferrero et al., 2015; Sosa-Rodríguez and Vazquez-Arenas, 2021) as they can be reused, ease separation of products and avoids the extensive product washing steps (Atadashi et al., 2013; Brahmkhatri and Patel, 2013; Shibasaki-Kitakawa et al., 2007). Heterogeneous basic catalysts are more reactive than heterogeneous acid catalysts as the basic ones require relatively shorter reaction time and lower reaction temperature (Dai et al., 2018). Among the basic heterogeneous catalysts, CaO has been extensively used for transesterification reactions as it processes high basicity, low solubility in alcohols and low cost (Avhad and Marchetti, 2016). It can be reused, has tolerance to moisture and FFA content of the oil and is non-corrosive and environmentally friendly (Boey et al., 2011). CaO can be used in various forms such as single oxide (Cho et al., 2009; Colombo et al., 2017; Verziu et al., 2011), mixed oxides (Taufiq-Yap et al., 2014; Wong et al., 2015) and supported (Lani et al., 2020; Wan and Hameed, 2011; Xie and Zhao, 2013) forms. Moreover, the glycerol-CaO complex form of CaO which is designated as glycerol-enriched CaO or calcium diglyceroxide (CaDg) has been used as a catalyst for biodiesel production (Avhad et al., 2018; Avhad et al., 2016; Ferrero et al., 2015).

Concerning the formation of CaDg in CaO catalyzed transesterification reaction, several studies reported the structural transformation of CaO catalyst during the progress of the reaction (Kouzu et al., 2008; Kouzu et al., 2010; León-Reina et al., 2013). At the beginning of the reaction, CaO is the active phase, however, as the transesterification reaction proceeds, the produced glycerol (C<sub>3</sub>O<sub>8</sub>H<sub>3</sub>) reacts with CaO and produces CaDg (Ca(C<sub>3</sub>O<sub>7</sub>H<sub>3</sub>)<sub>2</sub>) (León-Reina et al., 2013). Kouzu et al. (Kouzu et al., 2008; Kouzu et al., 2010) found that the probability of CaDg formation in the transesterification reaction matrix is higher than that of calcium methoxide as glycerol is more reactive with CaO than methanol. CaDg consists of an isolated tetramer (Ca<sub>4</sub>(C<sub>3</sub>H<sub>7</sub>O<sub>3</sub>)<sub>8</sub>) and is bound by a complex H-bond network (León-Reina et al., 2013) and this structure of CaDg contributed to its outstanding physiochemical properties and good catalysis ability (Sánchez-Cantú et al., 2014). CaDg catalyst has been reported to show superior catalytic activity in biodiesel production compared to CaO because the presence of basic oxygen anions, formed due to the interruption of the surface crystal structure, which can easily abstract protons from the -OH groups of methanol and form methoxide ion on the surface (Gupta et al., 2015).

Transesterification has been generally carried out using methanol or ethanol as these alcohols are considered as good fatty acid acyl acceptors (Sun et al., 2019). Accordingly, investigations of biodiesel production using glycerol-enriched CaO as catalyst have focused on the transesterification of oil with methanol or ethanol (Avhad et al., 2018; Avhad et al., 2016; Ferrero et al., 2015; Hsiao et al., 2019; León-Reina et al., 2013) using calcined CaO (Avhad et al., 2018; Avhad et al., 2016; Ferrero et al., 2015; León-Reina et al., 2013). Although butanol is less corrosive and less soluble in water, and thus, has a greater miscibility with the oil phase, its use in biodiesel production has not been so extensively studied (Navas et al., 2020; Steen et al., 2008). Using butanol for transesterification has several advantages over methanol or ethanol since its longer chain favors the properties biodiesel produced and its blend with conventional diesel. For instance, the butyl ester has a higher energy value than the analogues methyl or ethyl esters since it contains more carbon atoms (Navas et al., 2020). Moreover,



butanol can be produced from different biological resources, including organic wastes, through fermentation and, thus, it is renewable (Amiri and Karimi, 2018; Kolesinska et al., 2019). Hence, regarding these promising properties of butanol in biodiesel production, more research work is needed (Navas et al., 2020).

In several studies, commercial CaO was calcined prior to utilizing it as catalyst for transesterification to activate the active site that might be poisoned by CO<sub>2</sub> and H<sub>2</sub>O from the air (Calero et al., 2014; Reyero et al., 2014; Verziu et al., 2011). However, this might add some costs to the overall biodiesel production procedures. To our knowledge, no study has been carried out on the transesterification of non-edible oils such as *Jatropha* oil, using glycerol-enriched non-calcined commercial CaO using butanol.

The objective of the present work is to investigate the catalytic butanolysis of *Jatropha* (*Jatropha curcas* L.) oil using glycerol-enriched non-calcined commercial CaO and to determine the influences of the variations of reaction temperature and butanol: oil molar ratio on oil conversion and fatty acid butyl ester yield, and to optimize the reaction process.

The current paper presents two new issues that have not been done in other works of biodiesel production from non-edible plant oils such as *Jatropha* oil, using glycerol enriched CaO. Firstly, in the present study, the transesterification reaction was carried out using 1-butanol while either methanol or ethanol was used in the transesterification reactions of the previous works. Secondly, non-calcined commercial CaO was enriched with glycerol and used as a catalyst in the present work. In previous studies, calcined commercial CaO or calcium oxide prepared from natural calcium sources through calcination, have been used.

## 2. MATERIALS AND METHODS

### 2.1. Reagents and Materials

*Jatropha* (*Jatropha curcas* L.) oil that was extracted from the seed collected from Ethiopia was used for the experiment. The oil was extracted from the seeds with Soxhlet extractor using hexane as solvent and thimble with single thickness (37x130 mm). The physico-chemical properties of the oil was determined and the results were published elsewhere (Yadessa Gonfa et al., 2021). The calcium oxide used for the reaction was purchased from Honeywell Company. The 1-butanol, glycerol, tetradecane, pyridine, acetone, methanol and hexane used were purchased from Sigma-Aldrich. A rotary evaporator (Rotary Vapo R-3, Butchi Labortechnik AG, CH-9230, Switzerland) with vacuum pump was used to separate butanol from the reaction mixture after transesterification reaction.

### 2.2. Set up of the experiments

Both the synthesis of the glycerol-enriched CaO and transesterification of *Jatropha* oil with butanol using glycerol enriched CaO as catalyst, were performed in a three-necked glass reactor from Quark Glass, with a capacity of 500ml. A cooling condenser connected to a tap water was inserted into the middle neck of the reactor to cool the evaporated butanol during the reaction and reflux it into the reactor. A thermostat that was attached to the digital heating plate was inserted into the glass reactor via one of the side necks to measure the temperature of the reaction mixture. The third neck of the glass reactor was connected to a syringe through which the samples of the reaction mixture were taken. The lower part of the reactor was also connected to a water bath that was thermostatically regulating the temperature of the reacting mixture.

#### 2.2.1. Synthesis of the glycerol-enriched CaO

Before starting the transesterification reaction, the synthesis of glycerol-enriched CaO (glycerol-CaO complex) was performed in an airtight three-necked glass reactor as previously mentioned. Measured amount of glycerol (15% by wt% of CaO) was added to the inner bottom surface of the glass reactor. Then, about 70 g of *Jatropha* oil and 10.5 g of non-calcined commercial CaO (15% by wt% of the oil) were added to the reactor and heated to 60°C by vigorously stirring the mixture at 200 rpm for 60 min under ambient pressure. The amount of the glycerol and the temperature used for the synthesis of glycerol-CaO complex was adapted from the previous related works (Avhad et al., 2018; Avhad et al., 2016; Hsiao et al., 2019). The synthesis of glycerol-enriched CaO



was performed in the presence of Jatropha oil, but without adding any butanol to avoid the possibility of the formation of calcium butoxide (Avhad et al., 2018; Avhad et al., 2016; Kouzu et al., 2010).

The reason of adding small amount of glycerol into CaO in the presence of Jatropha oil to synthesize glycerol-CaO complex before adding butanol was to activate the catalyst and speed up the reaction process starting from the beginning. After the activation of CaO with glycerol, the mixture in the glass reactor was heated to the required temperature of a reaction.

### 2.2.2. Transesterification reactions

When the temperature of the mixture in glass reactor (the mixture contained glycerol-enriched CaO) reached at the set temperature, a measured amount of 1-butanol heated separately to the reaction temperature was added to the mixture. This time was taken as the initial time ( $t=0$ ) for the glycerol enriched CaO catalyzed transesterification of Jatropha oil. About 0.5 ml samples of the reacting mixtures were withdrawn at predetermined time intervals (0, 10, 20, 30, 60 and 90 minutes) to follow up the progress of the reaction. At the end of the reaction, the mixture was centrifuged to separate CaO and other components. The butanol in the mixture was also removed through distillation using a rotary evaporator attached to a vacuum pump. The glycerol and fatty acid butyl esters (biodiesel) were separated by decantation using separatory funnel.

### 2.3. Analysis of Samples

The analyses of the reaction samples were performed using a gas chromatography (GC) analyzer (Bruker scion 436 chromatograph), having an autosampler (CP-8400) and a flame ionization detector (FID). A capillary column with 5-phenyl-methylpolysiloxane (DB-5HT column, Agilent Technologies) was used for the analysis. The length, diameter and thickness of GC column were 15m, 0.32mm and 0.10 $\mu$ m, respectively. Helium was used as carrier gas with a flow rate of 1ml min<sup>-1</sup>, and the injection system employed was split-splitless mode. The temperature of the injector and detector were set at 320 and 350 °C, respectively. The temperature of the oven was started from 80 °C and programmed to rise by 10 °C per min until the final temperature of 360 °C was reached. The GC samples were prepared according to AOAC Official Method (2003). Hence, tetradecane was used as the internal standard while pyridine was utilized as a solvent for the GC samples. The analysis was done by injecting 1 $\mu$ l of a sample into the equipment.

From the areas of the chromatogram recorded for a given weight of the sample and the internal standard of the components of the sample, the mass of the components and their molar values were calculated with the help of the standards and the response factors, by employing Eq. (1) and (2) (Avhad et al., 2018).

$$m_{BE} = \frac{m_{is} \times A_{BE}}{R_{BE} \times A_{is}} \quad (1)$$

$$\eta_{BE} = \frac{m_{BE}}{M_{BE}} \quad (2)$$

Where  $m_{BE}$  = mass of butyl ester (g),  $m_{is}$  = mass of internal standard (g),  $A_{BE}$  = peak area of butyl ester,  $R_{BE}$  = response factor of butyl ester,  $A_{is}$  = peak area of internal standard,  $\eta_{BE}$  = number of moles of butyl ester and  $M_{BE}$  = molar mass of butyl ester (g mol<sup>-1</sup>).

Jatropha oil conversion using butanol ( $X_{JOB}$ ) was calculated from the initial moles of the oil ( $\eta_{io}$ ) and the final mole of the oil ( $\eta_{fo}$ ) using Eq. (3).

$$X_{JOB} = (\eta_{io} - \eta_{fo}) / \eta_{io} * 100 \quad (3)$$

The yield of fatty acid butyl esters ( $Y_{FABEs}$ ) obtained was also calculated using Eq. 4 which was also used by Wang et al. (2017).

$$Y_{FABEs} = \frac{FABE (\%)}{TG(\%) + DG(\%) + MG (\%) + FABE(\%) + FAA(\%)} \times 100 \quad (4)$$



Where FABE, TG, DG, MG, and FAA represents fatty acid butyl ester, triglycerides, diglycerides, monoglycerides and free fatty acids, respectively.

## 2.4 Design of the Experiment and Analysis of Data

### 2.4.1 Response surface methodology

Response surface methodology (RSM) involves of a group of statistical and mathematical tools that are useful for the development of models, and the improvement and optimization of a designed process and products (Montgomery 2013; Muriithi et al., 2017; Myers et al., 2004). RSM deals with the analysis and modelling of the functional relationships of a desired response and a number of associated factors, and its main purpose is to optimize the response (Montgomery 2013; Muriithi et al., 2017). According to Muriithi et al. (2017), the major procedures needed in RSM include experimental design with adequate and reliable measurements of the selected responses, developing equations of statistical model with best fittings, obtaining the optimal conditions of the experiment to maximize the responses, and showing the influences of the factors and their interactions using response surface plots.

#### 2.4.1.1. Design of the experiments

The two most frequently used designs for fitting the second-order models using RSM are central composite design (CCD) and Box-Behnken design (BBD). CCD is the most popular class of designs, and generally, it consists of a  $2^k$  factorial runs (experiments),  $2k$  axial or star runs, and some center runs, where  $k$  refers to the number of factors used. BBD design is also formed by combining  $2^k$  factorials with incomplete block designs and the center runs (Montgomery 2013). The number of experiments to be run is less when the BBD is employed compared to that of the CCD, and the former is becoming a more used design as efficient alternative, particularly, when the numbers of factors employed are three and more. Moreover, BBD does not contain combinations where all the factors are at their higher or lower levels, and hence, it may be useful in avoiding experiments under extreme conditions, which might be too expensive or impossible to test because of physical process constraints. However, the BBD may not indicate situations when we would like to know the responses at the extremes, that is, at the vertices of the cube of the design (Montgomery 2013; Sudha et al., 2017).

In the current study, the butanolysis of Jatropha oil using glycerol enriched CaO as catalyst was carried out to determine the effects of the variation of two factors with two levels, reaction temperature (R) and butanol: oil molar ratio (M), on Jatropha oil conversion using butanol ( $X_{JOB}$ ) and the yield of fatty acid butyl esters ( $Y_{FABES}$ ). As the number of varying factors were two and the total number of the experiments to run when CCD is used was only 12 (including the four central point experiments), and we also want to include the response at extreme experimental factors, we have preferred the CCD. Accordingly, the CCD that involved two factors and two levels full factorial ( $2^2$ ) was used to determine the impacts of the factors on the  $X_{JOB}$  and  $Y_{FABES}$ , and to optimize the process.

The design of the experiment contained three stages: factorial (linear) and non-linear stages which consisted of four experiments each as well as the four times replicated center points. Running the replicated center points is important to measure the accuracy of the study, and it is also used to statistically test for the presence or significance of curvature (Montgomery and Sons, 2001). The values of the selected factors and their associated levels for the reactions catalyzed with non-calcined CaO are presented in Table 1. The amount of CaO employed was kept constant at 15% (wt%) of the oil while the glycerol used was 15% (wt%) of the catalyst. The amounts of catalyst and glycerol used were adopted from the results obtained by Avhad et al. (Avhad et al., 2018). The reaction time of the current study was also adjusted to 90 minutes based on results of replicated preliminary experiments carried out at the central point conditions (reaction temperature of 80 °C and butanol: oil molar ratio of 9:1) by taking the reaction samples at predetermined time intervals to determine the progress of the reaction with time. The stirring speed of 200 rpm was also used for all experiments.



**Table 1.** Values of the factors for different levels in the experimental design.

Factors	Levels				
	$-\alpha$	-1	0	1	$\alpha$
Temperature (°C)	65.9	70	80	90	94.10
Molar ratio (-)	4.77	6	9	12	13.23

#### 2.4.1.2. Statistical analysis

The statistical analyses were performed by designing the sets of experiments using CCD by employing Statgraphics Centurion 17 software (Statgraphics Technologies, Inc USA). The analyses enabled us to determine the significances of the influences of the main factors and their interactions on the  $X_{JOB}$  and  $Y_{FABES}$ . The appropriate regression models were also developed to interpret the influences of the factors and their interactions on the response and to estimate the optimum factors needed to maximize the responses (Muriithi et al., 2017).

After running the experiments of factorial and center points (totally eight experiments) and determining the  $X_{JOB}$  and  $Y_{FABES}$  of each experiment, the significances of curvatures in the response surface plots were statistically tested by employing Equations 5–7 (Del Castillo, 2007; Montgomery and Sons, 2001). Then, using the calculated F value, the associated p value was determined to test the significance of curvature ( $p \leq 0.05$ ).

$$SS_{pure\ quadratic} = \frac{n_F n_C (\bar{Y}_F - \bar{Y}_C)^2}{n_F + n_C} \quad (5)$$

$$MS_E = \frac{\sum_{Central\ points} (y_i - \bar{y}_C)^2}{n - 1} \quad (6)$$

$$F = \frac{SS_{pure\ quadratic}}{MS_E} \quad (7)$$

Where:  $SS_{pure\ quadratic}$  is the sum of square for pure quadratic curvature and  $MS_E$  is the mean square error of center points.  $\bar{Y}_F$  and  $\bar{Y}_C$  are the average of responses of factorial and center points, respectively.  $n_F$  and  $n_C$  are number of factorial and center points, respectively.  $y_i$  represents to the responses of the center points while  $n_C - 1$  refers to the degree of freedom for center points. F represents the F-statistic, the test statistic for F-tests.

### 3. RESULTS AND DISCUSSION

#### 3.1 Adjustment of the Reaction Time

The reaction time of the study was made 90 minutes based on results of replicated preliminary experiments carried out at the central points (average reaction conditions), by taking the samples of the reaction mixture at predetermined time intervals (0, 10, 20, 30, 60, 90, 120, 180 and 210 minute) to determine the progress of the reaction with time. From the experiments carried at the average experimental conditions, it was found that the average  $X_{JOB}$  reached around 90% at about 90 minutes. Based on the result from the preliminary experiments, the reaction time was adjusted at 90 minutes for all experiments. Fig. 1 shows the progress of the butanolysis process in terms of  $X_{JOB}$  with the reaction time at the central point conditions.

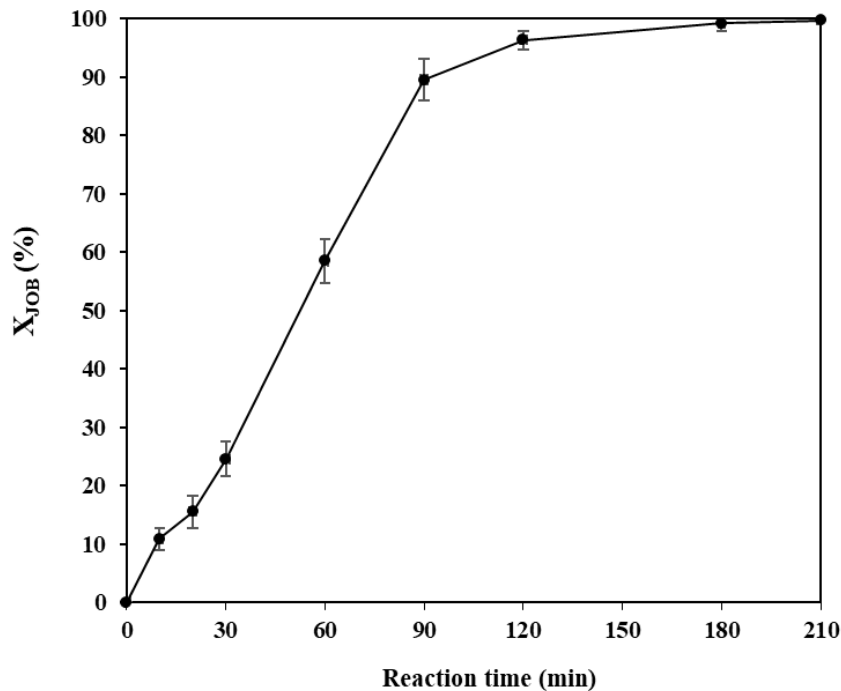


**Fig. 1:** Progress of butanolysis process with reaction time at 80 °C and butanol: oil molar ratio of 9:1

### 3.2 Experiments of different stages and the responses

As previously mentioned, butanolysis of jatropha oil using glycerol enriched CaO as catalyst was carried out to investigate the effects of reaction temperature and butanol: oil ratio and their interaction on X<sub>JOB</sub> and the Y<sub>FABEs</sub>. The CCD with two factors and two levels factorial (2<sup>2</sup>) that consisted of three stages was used to optimize the process. Accordingly, a total of twelve experiments, four experiments for the linear stage, center points and non-linear stage, respectively, were performed randomly, and the responses found were recorded. The natural factors for the reaction temperature (T) and butanol: oil molar ratio (M) and the coded factors for different levels of temperature (X<sub>T</sub>) and butanol: oil molar ratio (X<sub>M</sub>), and the responses obtained for the respective experiments are shown in Table 2.

**Table 2.** Stages of CCD design, Jatropha oil conversion using butsnol (X<sub>JOB</sub>) and yield of fatty acid butyl esters (Y<sub>FABEs</sub>).

Stage/types of experiments	Run	Temperature (T) (°C)	Molar ratio (R)	X <sub>T</sub>	X <sub>R</sub>	X <sub>JOB</sub> (%)	Y <sub>FABEs</sub> (%)
Linear (factorial) stage	1	90	12	1	1	89.70	86.70
	2	90	6	1	-1	96.39	93.13
	3	70	12	-1	1	22.80	9.46
	4	70	6	-1	-1	47.88	45.71
Center point stage	5	80	9	0	0	92.11	85.04
	6	80	9	0	0	87.68	81.73
	7	80	9	0	0	85.44	75.78
	8	80	9	0	0	92.97	88.30
Non-linear stage	9	94.1	9	1.41	0	90.16	86.86
	10	65.9	9	1.41	0	38.16	13.88
	11	80	13.23	0	1.41	94.46	88.87
	12	80,00	4.77	0	-1.41	90.07	84.49



As it is evident from Table 2, the maximum experimental  $X_{JOB}$  (96.39%) and  $Y_{FABEs}$  (93.131%) were obtained when the reaction run at the reaction temperature of 90°C, butanol: oil molar ratio of 6. The smallest  $X_{JOB}$  (22.80%) and  $Y_{FABEs}$  (9.46%) were found when the reaction run at the temperature of 70°C and butanol: oil molar ratio of 12. When the reactions run at 65.9 and 70°C, the oil conversion and biodiesel yields were found to be less than 50% despite of the variation of the values of butanol: oil molar ratio. However, for the reactions that occurred at the average temperatures (80°C) and above, both the oil conversions and biodiesel yields obtained were more than 80% regardless of the differences in the butanol: oil molar ratio. Thus, the results from Table 2 suggested that the impact of reaction temperature on both responses was higher than that of the alcohol: oil molar ratio. Moreover, for all experiments, the values of  $X_{JOB}$  were larger than that of the  $Y_{FABEs}$ , and this might be due to some unreacted diglycerides and monoglycerides remaining in the reaction mixture at the end of the reaction.

### 3.3 Statistical Analysis and Response Optimization

#### 3.3.1 Statistical analysis of the responses

The analysis was performed to determine the influences of the reaction temperature (T) and butanol: oil molar ratio (M), and their interactions (TM) on the responses of the butanolysis process. The influences of the factors and their interactions on the responses were predicted using the Statgraphics Centurion software, and the presence (significance) of curvature ( $p \leq 0.05$ ) in the response surface plot was also tested (Del Castillo, 2007; Montgomery and Sons, 2001). Table 3 shows different parameters obtained from the statistical analysis of the responses.

**Table 3.** Results from the statistical analysis of the experiments

Parameters and types of tests	Responses	
	$X_{JOB}$ (%)	$Y_{FABEs}$ (%)
Main effects and interactions	$\bar{y} = 89.55$	$\bar{y} = 82.71$
	$I_T = 47.23$	$I_T = 56.96$
	$I_R = -6.39$	$I_R = -9.12$
	$I_T^2 = -32.40$	$I_T^2 = -37.23$
	$I_{TM} = 9.19$	$I_{TM} = 14.91$
	$I_R^2 = -4.29$	$I_R^2 = -0.92$
Test for significance of variables (ANOVA test, $p \leq 0.05$ )		
Significant variables	T and T <sup>2</sup>	T and T <sup>2</sup>
R <sup>2</sup> and R <sup>2</sup> adjusted (%)		
R <sup>2</sup> (%)	88.37	93.54
R <sup>2</sup> adjusted (%)	78.68	88.16
Test for significance of curvature		
Mean response (factorial points, $\bar{Y}_F$ )	64.19	58.75
Mean response (center points, $\bar{Y}_C$ )	89.55	82.71
Curvature	-25.35	-23.96
SS <sub>pure quadratic</sub>	1286.19	1148.22
MS <sub>E</sub>	12.87	28.53
F calculated	99.89	40.24
p value	0.0021	0.00094
Significance of curvature ( $p \leq 0.05$ )	ificant	Significant

Where: T refers to temperature, R is butanol: oil molar ratio, and  $I_{TM}$  represents interaction of temperature and alcohol: oil molar ratio and  $R^2$  refers to R-squared.

As is can be seen from Table 3, temperature was found to be the factor with the highest positive impact whereas butanol: oil molar ration had a slight negative effect on the butanolysis process. The positive effect of reaction temperature on the butanolysis process could be due to the improvement of the miscibility and reactivity between



the reactants with rising in temperature (Avhad et al., 2016). The influences of butanol: oil molar ratio ( $I_M$ ) on both responses was negative. However, the interaction of temperature and alcohol: oil molar ratio ( $I_{TM}$ ) was found to have a medium positive impact on both responses. Moreover, the influences of temperature ( $I_T$ ),  $I_M$  and  $I_{TM}$  on the  $Y_{FABEs}$  were higher compared to their respective impacts on  $X_{JOB}$  (Table 3). Furthermore, based on ANOVA test, it was determined that the reaction temperature and its interaction with itself ( $T^2$ ) had a significant effect ( $p \leq 0.05$ ) on the butanolysis process.

The values of R-squared ( $R^2$ ) and  $R^2$ -adjusted for  $X_{JOB}$  and  $Y_{FABEs}$  were found to be 88.37 and 78.68 % and 93.54 and 88.16%, respectively (Table 3). This shows that the estimated models satisfactorily fit the experimental data for both responses. It has been suggested that for a good fit of a model, the  $R^2$  should be at least 80% (Subroto et al., 2015). Moreover, the  $R^2$  and  $R^2$ -adjusted for  $Y_{FABEs}$  were larger than the  $R^2$  and  $R^2$ -adjusted of  $X_{JOB}$ , respectively, and this shows that the fitness of the estimated model to the experimental data in case of  $Y_{FABEs}$  was better than that of  $X_{JOB}$ .

From the calculated parameters to test the presence of curvature, it was found that curvatures are significant ( $p \leq 0.05$ ) for both  $X_{JOB}$  and  $Y_{FABEs}$  (Table 3). Thus, in addition to the linear and the center stages, the non-linear stage of the design of experiments was also taken into consideration to fit the experimental data with a quadratic model.

### 3.3.2 Regression models and optimization of the responses

The natural values of the experimental factors were used to predict the suitable regression models that best described the butanolysis of jatropha oil using glycerol enriched non-calcined CaO as catalyst. As curvatures are significant ( $p \leq 0.05$ ) for both  $X_{JOB}$  and  $Y_{FABEs}$  (Table 3), the second order regression models (quadratic models) were found to be suitable for the optimization of the butanolysis process (Del Castillo, 2007; Montgomery and Sons, 2001). Hence, the suggested quadratic regression models for  $X_{JOB}$  and  $Y_{FABEs}$  under the present experimental ranges are presented in equation 8 and 9, respectively.

$$X_{JOB} = -1035.61 + 26.90T - 9.03M - 0.16T^2 + 0.15TM - 0.23M^2 \quad (8)$$

$$Y_{FABE} = -1148.06 + 30.39T - 20.48M - 0.18T^2 + 0.24TM - 0.051M^2 \quad (9)$$

To show the effects of the interaction of the temperature and butanol: oil molar ratio on the  $X_{JOB}$  and  $Y_{FABEs}$ , the three-dimensional (3D) response surface plots were produced based on the respective regression models presented above. The response surface plot for the effects of the interaction of the two factors on the  $X_{JOB}$  and  $Y_{FABEs}$  are shown in Fig. 2 and Fig. 3, respectively. As it can be seen from Fig. 2 and Fig. 3, generally, raising in the reaction temperature increased both the  $X_{JOB}$  and  $Y_{FABEs}$  until the optimum values (the temperatures at which the maximum responses could be found) would be reached regardless of the amount of butanol: oil molar ratio employed. However, at the lower temperature, raising in the butanol: oil molar ratio highly reduced both the  $X_{JOB}$  and  $Y_{FABEs}$ . As temperature raised from its experimental minimum (65.9 °C) to around the optimum values for both  $X_{JOB}$  (87.35 °C) and  $Y_{FABEs}$  (90.48 °C) (Table 4), the negative impacts of butanol: oil molar ration on both responses rapidly decreased, and then, started to positively contribute to maximize the responses as the optimum amount of butanol: oil molar ratio would approach.

By using the quadratic model equations produced and the RSM, the maximum  $X_{JOB}$  of 98.16% was predicted to be obtained at the optimum temperature and butanol: oil molar ration of 87.35 °C and 9.13:1, respectively. The maximum  $Y_{FABEs}$  of 95.79 % was also estimated to be found at the optimum temperature of 90.48 °C and butanol: oil molar ratio of 13.24:1 (Table 4). Moreover, after the prediction of the optimum conditions for both responses, two experiments were carried out at the optimum conditions estimated for the  $Y_{FABEs}$  (temperature of 90.48 °C and butanol: oil molar ratio of 13.24:1) to compare the average of the experimentally obtained responses with that of the predicted values. The optimum conditions predicted for  $Y_{FABEs}$  were selected to perform the experiments as the  $R^2$  and  $R^2$ -adjusted for  $Y_{FABEs}$  were larger than those of  $X_{JOB}$  (Table 3). Accordingly, the average experimental  $Y_{FABEs}$  of 95.64% was obtained, and this is in excellent agreement with the predicted optimum  $Y_{FABEs}$  (95.79 %).

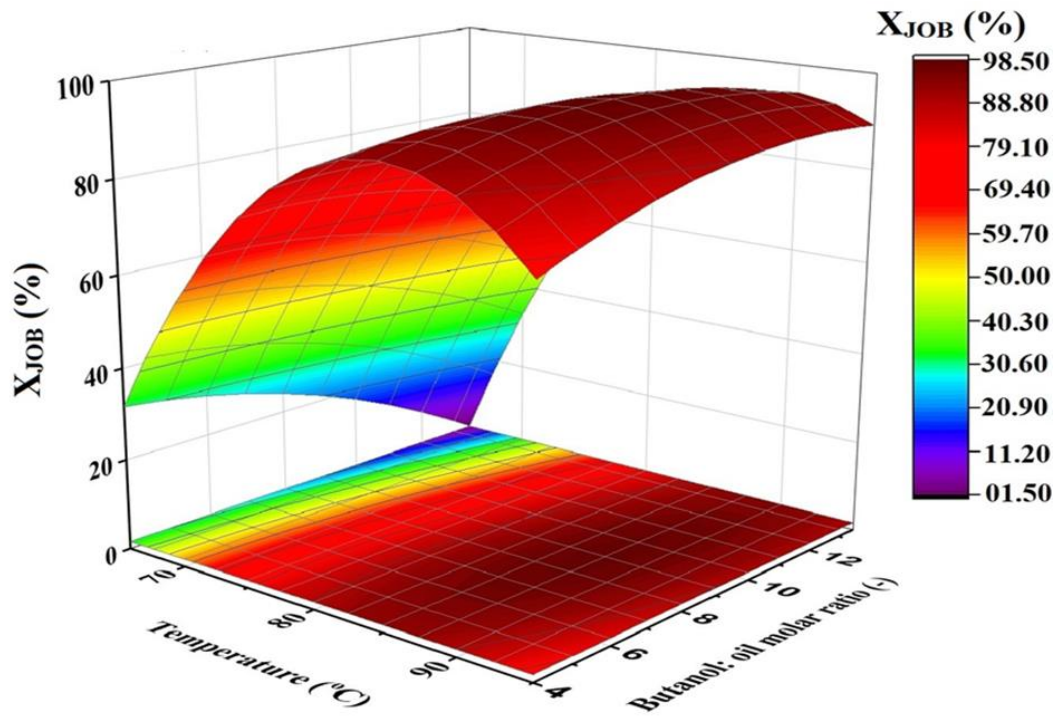


**Fig. 2:** Response surface plot for the effects of reaction temperature and butanol: oil molar ratio on  $X_{JOB}$  at the catalyst amount 15%, 15% glycerol, and stirring speed of 200 rpm (temperature and butanol: oil molar ratio refer to the actual values)

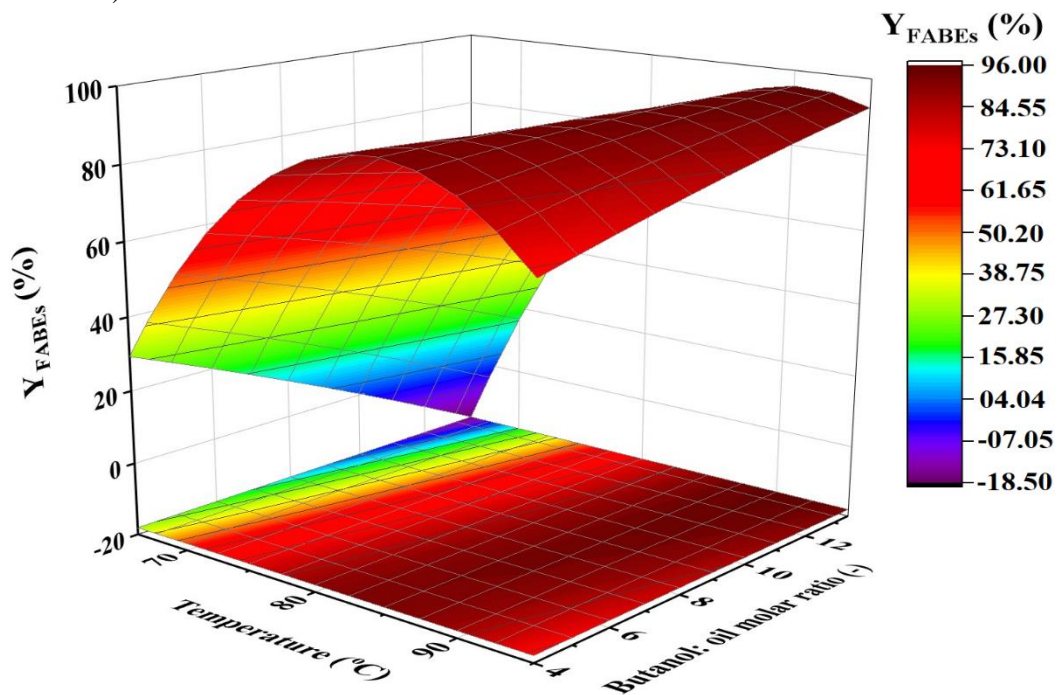


**Fig. 3:** Response surface plot for the effects of reaction temperature and butanol: oil molar ratio on the  $Y_{FABEs}$  at the catalyst amount 15%, 15% glycerol, stirring speed of 200 rpm (temperature and butanol: oil molar ratio refer to the actual values)

**Table 4.** Optimum conditions predicted for maximum  $X_{JOB}$  and  $Y_{FABES}$  and the optimum responses

Factors	Conversion		Yield	
	Optimum factors	Optimum Response (%)	Optimum factor	Optimum Response (%)
Temperature (°C)	87.35	98.16	90.48	95.79
Molar ratio (-)	9.13		13.24	

The maximum  $Y_{FABES}$  (95.64%) found in the current study was in line with the fatty acid butyl ester yield (97%) that was obtained by Navas et al. (Navas et al., 2018) in the reaction of castor oil with butanol using  $MgO/\gamma-Al_2O_3$  as catalyst by applying 5% catalyst, alcohol: oil molar ratio of 6:1, reaction temperature of 80°C and reaction time of 6 h. However, the maximum  $Y_{FABES}$  of the present work was larger than the fatty acid butyl ester yield (85%) that was found by Navas et al. (Navas et al., 2018) in the same study using  $ZnO/\gamma-Al_2O_3$  as catalyst at the previously mentioned reaction conditions.

Fig. 4 (a) and (b) show the plot of the predicted values and experimental results of  $X_{JOB}$  and  $Y_{FABES}$ , respectively. As it can be seen from the graphical presentation, the predicted  $X_{JOB}$  and  $Y_{FABES}$  generally banded around the predicted regression line, and these demonstrate the satisfactory fitness of the values of the predicted and experimental responses. However, some predicted and experimental responses showed relatively less fit, particularly for the lower values of predicted and experimental  $X_{JOB}$ .

The outlier values for  $X_{JOB}$  and  $Y_{FABES}$  (Fig. 4 a and b) were those of the responses with lower values, and the deviation is higher in the case of  $X_{JOB}$ . The outlier values of  $X_{JOB}$  (Fig. 4 a) were the predicted and experimental values of the reactions that were carried out at the temperatures and butanol: oil molar ratios of 70 °C and 12 and 65.9 °C and 9, respectively. The oil conversions and ester yields recorded for the reactions carried out at 65.9 and 70 °C were very low compare to those of the reactions performed at 80 °C and higher temperatures (Table 2). The fitness of the experimental and predicted values of  $X_{JOB}$  for the reactions performed at these two temperatures (65.9 and 70 °C) were also relatively lower as the values showed higher deviation from the regression line (Fig. 4 a). These results suggested that lower temperatures negatively affected both the values of  $X_{JOB}$  and the fitness of the regression model to the experimental  $X_{JOB}$ , and this effect was higher in the case of  $X_{JOB}$  compared to  $Y_{FABES}$ . Moreover, as previously mentioned, the fitness of the regression model of  $Y_{FABES}$  to the experimental data was better than that of  $X_{JOB}$ .

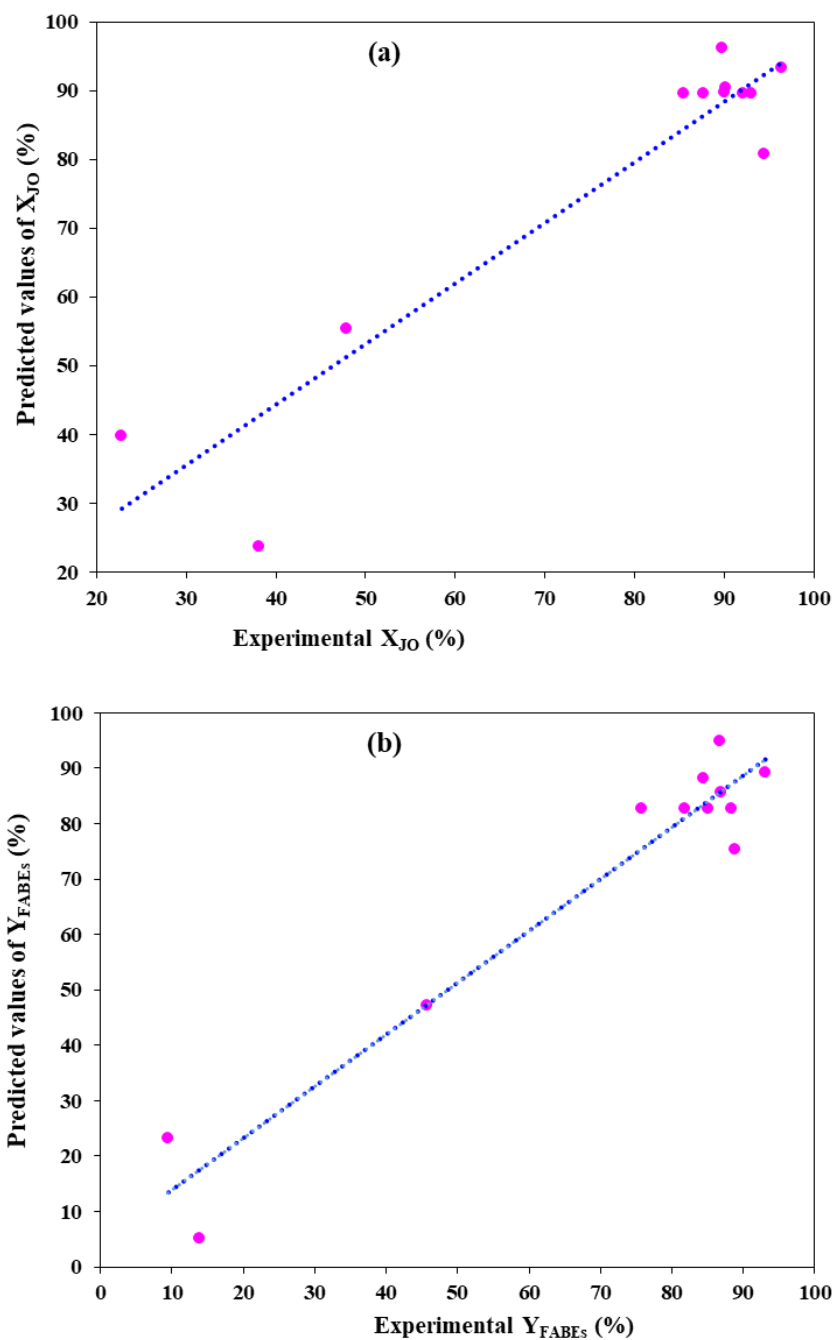


Fig. 4: Predicted versus experimental values of (a)  $X_{JOB}$  and (b)  $Y_{FABEs}$ , respectively

#### 4. CONCLUSION

The present study was carried out to investigate the catalytic butanolysis of Jatropha oil using glycerol enriched non-calcined CaO to determine the influences of reaction temperature and butanol: oil molar ratio on  $X_{JOB}$  and  $Y_{FABEs}$ , and to optimize the responses. Central composite design (CCD) that involved two factors and two levels full factorial ( $2^2$ ) was used to determine the effects of the factors and to optimize the process. From the main factors and their interaction, temperature was found to highly affect both the  $X_{JOB}$  and  $Y_{FABEs}$ . Since curvatures are statistically significant ( $p \leq 0.05$ ), quadratic regression models were found to be more suitable for the optimization process. As  $R^2$  and  $R^2$ -adjusted of the selected quadratic models for  $X_{JOB}$  and  $Y_{FABEs}$  were found to be 88.37 and 78.68% and 93.54 and 88.16%, respectively, both models were suggested to fit adequately to the respective experimental responses to satisfactorily optimize the butanolysis process. Using the models and the response surface methodology, the maximum  $X_{JOB}$  (98.16%) and  $Y_{FABEs}$  (95.79%) were predicted to be found at the optimum temperatures of 87.35 and 90.48 °C and butanol: oil molar ratios of 9.13:1 and 13.24:1, respectively.



Moreover, the maximum  $Y_{FABEs}$  of 95.64% was experimentally obtained at the optimum temperature (90.48 °C) and alcohol: oil molar ratio (13.24:1), and this was in good agreement with the predicted optimum  $Y_{FABEs}$  (95.79%). Based on the results obtained for the experimental ranges used in this experiment, it was suggested that glycerol enriched non-calcined calcium oxide can be used as good alternative catalyst for biodiesel production using butanol. More future studies are also suggested for upscaling the reaction process of the current experiments by using more integrated reaction factors.

## ACKNOWLEDGMENTS

The financial support from the EnPe/NORHED of Norad project entitled "Research and Capacity Building in Clean and Renewable Bioenergy in Ethiopia", Agreement No. 2015/8397 to the Norwegian University of Life Sciences (NMBU), is gratefully acknowledged.

## REFERENCES

- Abbaszaadeh, A., Ghobadian, B., Omidkhah, M.R., Najafi, G. (2012): Current biodiesel production technologies: A comparative review. *Energy Conversion and Management*, 63: 138-148.
- Ahmad, A., Yasin, N.M., Derek, C., Lim, J. (2011): Microalgae as a sustainable energy source for biodiesel production: a review. *Renewable and Sustainable Energy Reviews*, 15(1): 584-593.
- Amiri, H., Karimi, K. (2018): Pretreatment and hydrolysis of lignocellulosic wastes for butanol production: Challenges and perspectives. *Bioresource Technology*, 270: 702-721.
- Atabani, A.E., Silitonga, A.S., Badruddin, I.A., Mahlia, T., Masjuki, H., Mekhilef, S. (2012): A comprehensive review on biodiesel as an alternative energy resource and its characteristics. *Renewable and sustainable energy reviews*, 16(4): 2070-2093.
- Atadashi, I., Aroua, M., Aziz, A.A., Sulaiman, N. (2013): The effects of catalysts in biodiesel production: A review. *Journal of Industrial and Engineering Chemistry*, 19(1): 14-26.
- Avhad, M.R., Gangurde, L.S., Sánchez, M., Bouaid, A., Aracil, J., Martínez, M., Marchetti, J.M. (2018): Enhancing Biodiesel Production Using Green Glycerol-Enriched Calcium Oxide Catalyst: An Optimization Study. *Catalysis Letters*, 148: 1169–1180.
- Avhad, M.R., Marchetti, J.M. (2016): Innovation in solid heterogeneous catalysis for the generation of economically viable and ecofriendly biodiesel: a review. *Catalysis Reviews*, 58(2): 157-208.
- Avhad, M.R., Sánchez, M., Bouaid, A., Martínez, M., Aracil, J., Marchetti, J.M. (2016): Modeling chemical kinetics of avocado oil ethanolysis catalyzed by solid glycerol-enriched calcium oxide. *Energy Conversion and Management*, 126: 1168-1177.
- Boey, P.-L., Maniam, G.P., Hamid, S.A. (2011): Performance of calcium oxide as a heterogeneous catalyst in biodiesel production: A review. *Chemical Engineering Journal*, 168(1):5-22.
- Brahmkhatri, V., Patel, A. (2013): Biodiesel Production over 12-Tungstosilicic Acid Anchored to Different Mesoporous Silica Supports, in: Patel, A. (Ed.), *Environmentally Benign Catalysts for Clean Organic Reactions*, Springer, Panch Tattva Publishers, India, pp. 189-208.
- Calero, J., Luna, D., Sancho, E.D., Luna, C., Bautista, F.M., Romero, A.A., Posadillo, A., Verdugo, C. (2014): Development of a new biodiesel that integrates glycerol, by using CaO as heterogeneous catalyst, in the partial methanolysis of sunflower oil. *Fuel*, 122: 94-102.
- Cho, Y.B., Seo, G., Chang, D.R. (2009): Transesterification of tributyrin with methanol over calcium oxide catalysts prepared from various precursors. *Fuel Processing Technology*, 90(10): 1252-1258.
- Colombo, K., Ender, L., Barros, A.A.C. (2017): The study of biodiesel production using CaO as a heterogeneous catalytic reaction. *Egyptian Journal of Petroleum*, 26: 341–349.
- Dai, Y.-M., Lin, J.-H., Chen, H.-C., Chen, C.-C. (2018): Potential of using ceramics wastes as a solid catalyst in biodiesel production. *Journal of the Taiwan Institute of Chemical Engineers*, 91: 427-433.
- de Rezende, S.M., de Castro Reis, M., Reid, M.G., Silva Jr, P.L., Coutinho, F.M., San Gil, R.A.d.S., Lachter, E.R. (2008): Transesterification of vegetable oils promoted by poly (styrene-divinylbenzene) and poly (divinylbenzene). *Applied Catalysis A: General*, 349(1-2): 198-203.
- Del Castillo, E. (2007): *Process optimization: a statistical approach*, Springer Science & Business Media, New York, USA, pp459.
- Di Serio, M., Cozzolino, M., Giordano, M., Tesser, R., Patrono, P., Santacesaria, E. (2007): From homogeneous to heterogeneous catalysts in biodiesel production. *Industrial & Engineering Chemistry Research*, 46(20): 6379-6384.



- Ferrero, G.O., Almeida, M.F., Alvim-Ferraz, M.C.M., Dias, J.M. (2015): Glycerol-enriched heterogeneous catalyst for biodiesel production from soybean oil and waste frying oil. *Energy Conversion and Management*, 89: 665-671.
- Gupta, A.R., Yadav, S.V., Rathod, V.K. (2015): Enhancement in biodiesel production using waste cooking oil and calcium diglyceroxide as a heterogeneous catalyst in presence of ultrasound. *Fuel*, 158: 800-806.
- Hsiao, M.-C., Chang, L.-W., Hou, S.S. (2019): Study of solid calcium diglyceroxide for biodiesel production from waste cooking oil using a high speed homogenizer. *Energies*, 12(17): 3205.
- Kolesinska, B., Fraczyk, J., Binczarski, M., Modelska, M., Berlowska, J., Dziugan, P., Antolak, H., Kaminski, Z.J., Witonska, I.A., Kregiel, D. (2019): Butanol synthesis routes for biofuel production: trends and perspectives. *Materials*, 12(3): 350.
- Kouzu, M., Kasuno, T., Tajika, M., Yamanaka, S., Hidaka, J. (2008): Active phase of calcium oxide used as solid base catalyst for transesterification of soybean oil with refluxing methanol. *Applied Catalysis A: General*, 334(1): 357-365.
- Kouzu, M., Tsunomori, M., Yamanaka, S., Hidaka, J. (2010): Solid base catalysis of calcium oxide for a reaction to convert vegetable oil into biodiesel. *Advanced Powder Technology*, 21(4): 488-494.
- Kouzu, M., Yamanaka, S.-y., Hidaka, J.-s., Tsunomori, M. (2009): Heterogeneous catalysis of calcium oxide used for transesterification of soybean oil with refluxing methanol. *Applied Catalysis A: General*, 355(1): 94-99.
- Lani, N.S., Ngadi, N., Inuwa, I.M. (2020): New route for the synthesis of silica-supported calcium oxide catalyst in biodiesel production. *Renewable Energy*, 156: 1266-1277.
- León-Reina, L., Cabeza, A., Rius, J., Maireles-Torres, P., Alba-Rubio, A.C., López Granados, M. (2013): Structural and surface study of calcium glyceroxide, an active phase for biodiesel production under heterogeneous catalysis. *Journal of Catalysis*, 300: 30-36.
- Montgomery, D.C. (2013): *Design and Analysis of Experiments*, Eighth edition ed. John Wiley & Sons, Inc., New York, USA.
- Montgomery, D.C. (2001): *Design and analysis of experiments*. John Wiley & Sons, Inc., New York, USA.
- Muriithi, D.K., Koske, J.A., Gathungu., G.K. (2017): Application of Central Composite Design Based Response Surface Methodology in Parameter Optimization of Watermelon Fruit Weight Using Organic Manure. *American Journal of Theoretical and Applied Statistics*, 6(2): 108-116.
- Myers, R.H., Montgomery, D.C., Vining, G.G., Borror, C.M., Kowalski, S.M. (2004): Response surface methodology: a retrospective and literature survey. *Journal of Quality Technology*, 36(1): 53-77.
- Navas, M.B., Lick, I.D., Bolla, P.A., Casella, M.L., Ruggera, J.F. (2018): Transesterification of soybean and castor oil with methanol and butanol using heterogeneous basic catalysts to obtain biodiesel. *Chemical Engineering Science*, 187: 444-454.
- Navas, M.B., Ruggera, J.F., Lick, I.D., Casella, M.L.J.B., *Bioprocessing* (2020). A sustainable process for biodiesel production using Zn/Mg oxidic species as active, selective and reusable heterogeneous catalysts. *Bioresour Bioprocess*, 7(1): 1-13.
- Neupane, D. (2022). *Biofuels from Renewable Sources, a Potential Option for Biodiesel Production*. *Bioengineering*, 10(1), 1-29.
- Pinzi, S., Leiva, D., López-García, I., Redel-Macías, M.D., Dorado, M.P. (2014): Latest trends in feedstocks for biodiesel production. *Biofuels, Bioproducts Biorefining*, 8(1): 126-143.
- Reyero, I., Arzamendi, G., Gandía, L.M. (2014): Heterogenization of the biodiesel synthesis catalysis: CaO and novel calcium compounds as transesterification catalysts. *Chemical Engineering Research and Design*, 92(8): 1519-1530.
- Sánchez-Cantú, M., Reyes-Cruz, F.M., Rubio-Rosas, E., Pérez-Díaz, L.M., Ramírez, E., Valente, J.S. (2014): Direct synthesis of calcium diglyceroxide from hydrated lime and glycerol and its evaluation in the transesterification reaction. *Fuel*, 138: 126-133.
- Sani, Y.M., Daud, W.M.A.W., Aziz, A.A. (2014): Activity of solid acid catalysts for biodiesel production: a critical review. *Applied Catalysis A: General*, 470: 140-161.
- Shibasaki-Kitakawa, N., Honda, H., Kuribayashi, H., Toda, T., Fukumura, T., Yonemoto, T., (2007): Biodiesel production using anionic ion-exchange resin as heterogeneous catalyst. *Bioresource Technology*, 98(2): 416-421.
- Shinde, K., Kaliaguine, S.J.C. (2019): A comparative study of ultrasound biodiesel production using different homogeneous catalysts. *Chem Engineering*, 3(18): 1-10.
- Sosa-Rodríguez, F.S., Vazquez-Arenas, J. (2021): The biodiesel market in Mexico: Challenges and perspectives to overcome in Latin-American countries. *Energy Conversion and Management*, 12: 100149.
- Steen, E.J., Chan, R., Prasad, N., Myers, S., Petzold, C.J., Redding, A., Ouellet, M., Keasling, J.D. (2008): Metabolic engineering of *Saccharomyces cerevisiae* for the production of n-butanol. *Microbial Cell Factories*, 7(1): 36.



- Subroto, E., Manurung, R., Heeres, H.J., Broekhuis, A.A. (2015): Optimization of mechanical oil extraction from *Jatropha curcas* L. kernel using response surface method. *Industrial Crops and Products*, 63, 294-302.
- Sudha, T., Divya, G., Sujaritha, J., Duraimurugan, P. (2017): Review of experimental design in analytical chemistry. *Journal of Pharmaceutical Research*, 7(08): 550-565.
- Sun, S., Guo, J., Duan, X. (2019): Biodiesel preparation from Phoenix tree seed oil using ethanol as acyl acceptor. *Industrial Crops and Products*, 137: 270-275.
- Taufiq-Yap, Y.H., Lee, H.V., Lau, P.L. (2012): Transesterification of *jatropha curcas* oil to biodiesel by using short necked clam (*orbicularia orbiculata*) shell derived catalyst. *Energy Exploration & Exploitation*, 30 (5): 853–866.
- Taufiq-Yap, Y.H., Teo, S.H., Rashid, U., Islam, A., Hussien, M.Z., Lee, K.T. (2014): Transesterification of *Jatropha curcas* crude oil to biodiesel on calcium lanthanum mixed oxide catalyst: Effect of stoichiometric composition. *Energy Conversion and Management*, 88: 1290-1296.
- Uzar, U. (2020): Political economy of renewable energy: Does institutional quality make a difference in renewable energy consumption? *Renewable Energy*, 155: 591-603.
- Vakulchuk, R., Overland, I., Scholten, D. (2020): Renewable energy and geopolitics: A review. *Renewable and Sustainable Energy Reviews*, 122: 109547.
- Verziu, M., Coman, S.M., Richards, R., Parvulescu, V.I. (2011): Transesterification of vegetable oils over CaO catalysts. *Catalysis Today*, 167(1): 64-70.
- Videsh, S., Yamani, R., Rodney, R.J. (2009): Laboratory Scale Production of Biodiesel from Used Vegetable Oil. *The Journal of the Association of Professional Engineers of Trinidad and Tobago*, 38(1): 57-65.
- Wan, Z., Hameed, B.H. (2011). Transesterification of palm oil to methyl ester on activated carbon supported calcium oxide catalyst. *Bioresource Technology*, 102(2): 2659-2664.
- Wang, X., Qin, X., Li, D., Yang, B., Wang, Y. (2017): One-step synthesis of high-yield biodiesel from waste cooking oils by a novel and highly methanol-tolerant immobilized lipase. *Bioresour Technol*, 235: 18-24.
- Welela Meka (2023): Bifunctional Heterogeneous Catalysts for Biodiesel Production Using Low-Cost Feedstocks: A Future Perspective, in: Islam Md Rizwanul, F. (Ed.), *Advanced Biodiesel*. IntechOpen, Rijeka, pp. 1-18.
- Wong, Y.C., Tan, Y.P., Taufiq-Yap, Y.H., Ramli, I., Tee, H.S. (2015): Biodiesel production via transesterification of palm oil by using CaO–CeO<sub>2</sub> mixed oxide catalysts. *Fuel*, 162: 288-293.
- Xie, W., Zhao, L. (2013): Production of biodiesel by transesterification of soybean oil using calcium supported tin oxides as heterogeneous catalysts. *Energy Conversion and Management*, 76: 55-62.
- Yadessa Gonfa, Legesse Adane, Marchetti, J.M. (2021): Effects of Different Extraction Solvents on Oil Extracted from *Jatropha* Seeds and the Potential of Seed Residues as a Heat Provider. *BioEnergy Research*. <https://doi:10.1007/s12155-020-10217-5>



## Implementation of Non-Axisymmetric Moving Heat Source modeling in Disc Geometry and Material Selection

Kejela Temesgen Deressa<sup>1,\*</sup>, Demiss Alemu Ambie<sup>2</sup>

<sup>1</sup>African Railway Center of Excellence, Addis Ababa Institute of Technology, Addis Ababa University, Addis Ababa, Ethiopia

<sup>2</sup>School of Mechanical and Industrial Engineering, Addis Ababa Institute of Technology, Addis Ababa University, Addis Ababa, Ethiopia

\*Corresponding author, e-mail: [kej.tem@gmail.com](mailto:kej.tem@gmail.com); [kejela.temesgen@aait.edu.et](mailto:kejela.temesgen@aait.edu.et)

### ABSTRACT

Railroad vehicles require the use of disc brakes for safety purposes. However, the disc brakes are susceptible to surface damages including fade, wear, squeal, thermal cracks, thermal stress and thermal fatigue, which ultimately shortens their lifespan. Hence, to counteract these negative consequences, and to accurately predict the life of railway disc brakes in thermal load simulations, the availability of a model that considers spatial and temporal variations of temperature and thermal stress is essential. As a result non-axisymmetric moving heat source was successfully developed to address spatial and temporal variations of temperature (Deressa and Ambie in *Urban Rail Transit* 8(3–4):198–216, 2022. 10.1007/s40864-022-00176-9), thermal Stress and Fatigue Analysis of Railway Vehicle Disc Brakes (Deressa and Ambie in *Urban Rail Transit*, 2023). And this study aims to extend this models to test its implementation in pad geometry, disc geometry and disc material selections. Finite element ANSYS parametric design language (APDL) is implemented in coding the variations in thermal loads and the corresponding boundary conditions, both spatially and timely. The simulation is conducted for braking conditions and disc geometry extracted from trailer and motor bogie of Addis Ababa Light Rail Transit (AALRT). Besides, cast iron families (flake, spheroidal and compacted) are implemented in testing the application of the model. The NAMHS model algorithm has proven to be a successful model for accurately and efficiently identifying the optimal pad geometry, disc geometry and disc material through thermal and mechanical analysis. Hence, it is hoped that this finding could influence disc brake manufacturers, researchers and maintenance personnel in disc brake damage investigation.

**Keywords:** ANSYS APDL, Disc brake, disc geometry, disc material, rail vehicle

### 1. INTRODUCTION

Brakes are the most important safety component of the train vehicles in managing speed. But, it could results unfavorable consequences, including fade (Zhang et al., 2019), surface wear (Handa et al., 2020), thermal stress (Rashid & Stromberg, 2012) and thermal fatigue (Xie et al., 2021). To counteract such damaging consequences, accurate prediction or determination of temperature is fundamental during design stage and preventive maintenance.

Appropriate modeling of FE heat input and boundary condition simulation (thermal, structural and life) plays a key role in its design and development of brakes geometries and materials. Since the early development of railway and automotive transportation, braking performance has been improved in three areas of investigations: Model development (Deressa & Ambie, 2022; Deressa & Ambie, 2023), optimum geometry selection (Tirovic & Ali, 2001; Tirovic & Sarwar, 2004) and optimum material selection (Mahmoudi et al., 2015). With a compact size geometry, that could dissipate heat easily to the neighboring areas has been developed to minimize failure and increase service life (Tirovic, 1998). However, the success of these investigations require the further development and implementation of a better FE (Finite element) model in geometry and material selection.

Based on its connection with the bogie, disc brakes' geometries are either friction surface-bolted (Fig. 1.a), or hub-bolted (Fig. 1.b). In the former one, the disc friction surface has holes through which it is tightened to the axle plate or wheel web with bolts. Meanwhile, in the latter one, the friction surface is free from the hole, and the disc is tightened to the axle/wheel by its hub. Three main difference is revealed between them, which could affect disc's service life. Firstly, the pad-disc contact area (and resulting heat input) is low in friction surface-bolted discs. And this could greatly affect the distribution of temperature (Deressa & Ambie, 2022), stress (Deressa & Ambie, 2023), and fatigue life in a significant manner. Secondly, the presence or absence of bolt holes on the

friction surface could significantly influence the development of stress and crack initiation site (X Xie et al., 2021). And finally, the variation in mass could affect the specific heat capacity of the disc. So, to evaluate better disc geometry from both, further investigation with better FE model is mandatory.

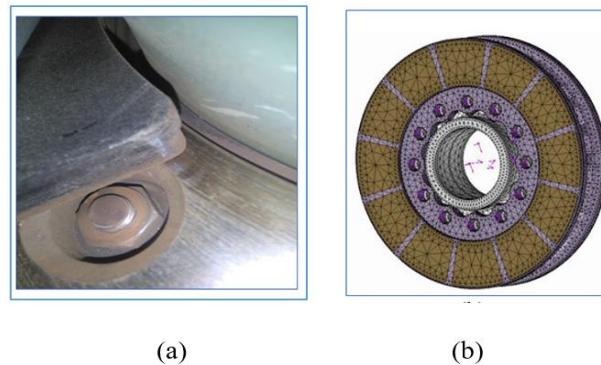


**Fig. 1:** Axle mount disc brake designs: (a) friction surface-bolted [camera view from AALRT] (b) hub-bolted (Jiang et al., 2019)

In contrast, the pad and disc contact area vary depending on pad geometries. And, the variations in contact geometry due to pad types substantially affect the spatial distribution of temperature (Nong et al., 2011). Although various types of pad geometries were seen in the literature, they are mainly classified into two groups: composite and sintered pads. Composite pads are further classified based on their grooves' number and position. The positions of grooves are seen as radial (Yevtushenko et al., 2021), tangential (Belhocine et al., 2016), or both (Benseddiq et al., 1996). Besides, composite pads may have no groove (Kim et al., 2008), one radial groove ((Belhocine et al., 2016) and Fig. 4.b), two radial grooves (Benhassine et al., 2019), and a maximum of four grooves (Goo, 2018). On the other hand, sintered pads are the same in number (18), but vary based on their pin geometries, such as circular, hexagonal, and triangular (Jiguang & Fei, 2015). Hence implementation of reliable FE model in selecting the best geometry plays essential role in design, manufacturing and preventive maintenance of the disc brake.

Recent evidence (Table 1) suggests that optimum geometry selection was conducted through modeling pad structures (Benseddiq et al., 1996; Nong et al., 2011; Jiguang & Fei, 2015). Besides, it was seen performed by geometries around the disc hub (Tirovic & Ali, 2001), hub-disc junction geometry (Tirovic & Sarwar, 2004), the holes around the bolt area (Šamec et al., 2011), disc wall thickness (Luo & Zuo, 2014), and the location and shape of the pillared fins (Grivc et al., 2019).

FE Axisymmetric model is shown as the most widely implemented method in optimum disc and pad geometry selection (Table 1), while uncoupled thermomechanical method is reported rarely used. Because, computational problems (convergence, computational time) have been easily improved, in the former, and not in the latter model (Deressa & Ambie, 2021). Although the disc brake is a three-dimensional model, axisymmetric model assumes the disc as a two-dimensional geometry (Tang et al., 2018). Consequently, previous studies have suffered from shortcomings in managing spatial (radial and tangential) variation of heat input and boundary conditions (Deressa & Ambie, 2021).

For most of the study, optimum geometry was measured by temperature evolution (Luo & Zuo, 2014), or stress and axial deflection (Tirovic & Sarwar, 2004) (Šamec, Oder, et al., 2011). Nonetheless, the optimum geometry in temperature doesn't mean optimum in every aspect. As the maximum temperature and stress developed appeared at different braking times and locations (Oder et al., 2011), any design must be checked for both parameters before being accepted as optimum. Since the maximum stress might be observed at lower temperatures (Oder et al., 2011), geometric design with lower temperatures doesn't mean an acceptable design in structural analysis (stress). Therefore, optimum geometry selection made on only temperature value in any design is not guaranteed in thermal stress and might cause fatigue crack initiation.



Table 1. Disc and pad geometries and implemented models

Studied area	Studied Geometry	Results	Authors & Models
Optimum pads geometry study: composite	Pad backplate thickness and pad groove numbers	Lower temperature was seen registered for the higher number of pad grooves	(Benseddiq et al., 1996) <sup>UTM</sup>
Structure-function dev't for sintered pads geometry	Pads number and distribution	12 cylindrical shapes revealed lowest temperature and stress distribution	(Nong et al., 2011) <sup>A</sup>
Better geometry selection from 5 candidate sintered pad designs	Number, shape, size, distribution	Minimum and thermal stress reported for triangular pad with 10 numbers of blocks	(Jiguang & Fei, 2015) <sup>A</sup>
Disc geometry development	Wheel mounted disc design selection	Disc with two full rings, hubs- bolted to a wheel was developed	(Tirovic, 1998) <sup>A</sup>
Disc hub design development	Disc hub for wheel mounted disc	Flexible/ fingered hub disc design was proposed	(Tirovic & Ali, 2001) <sup>A</sup>
Optimum geometry selected from 30 different disc designs	Wheel hub dimensions varied	Model No.22 was the best balance of hub stresses and disc deflection	(Tirovic & Sarwar, 2004) <sup>UTM</sup>
Disc brake temperature and stress analysis	Bolt hole geometry	New disk geometry around bolt mounting holes was proposed	(Samec, Oder, et al., 2011) <sup>A</sup>
Disc heat transfer study	Disc wall thickness	30% improvement in heat transfer	(Luo & Zuo, 2014) <sup>A</sup>
Optimization of brake disc crown from 280 fins	The location and shape of the fins	A 21% in mass reduction	(Grivc et al., 2019)

<sup>A</sup> Axisymmetric; <sup>UTM</sup> Uncoupled thermomechanical

On the other hand, the disc brakes' required material properties are identified as lower density, lower thermal expansion coefficient, higher thermal conductivity, higher specific heat capacity, higher tensile and compressive strength, and stable friction coefficient (Maleque et al., 2010). Based on these properties, selecting the optimum material is not an easy task, because no material exists that can fulfill all the required properties.

To investigate the relations between materials type and their application in various speed ranges, the study of (Günay et al., 2020) recommends cast steel and ceramic composites for speeds more than 400 kph. Meanwhile, cast iron and aluminum are implemented for low-speed trains (less than 200 kph). Besides, by implementing moving heat source FE model, (Mahmoudi et al., 2015) was reported that using functional graded material (FGM) instead of ductile cast iron improved the safety factor by 59%, while the Al 359 material reported to fall in between the two. In similar way, disc brake materials were investigated on composite (FGM (Bayat et al., 2019), SiC<sub>3D</sub>/Al alloy (Nong et al., 2017), SiC/7075Al (Yu et al., 2012)). However, according to the review conducted by the authors (Deressa & Ambie, 2021), the models implemented were failed to address spatial variations of heat input and boundary conditions. Besides, convergence problem and simulation time explosions were another challenge observed.

An addition, there has been little agreement on the use of cast iron material families, in rolling stock disc brake, based on the shape of the graphite: flake graphite cast iron (FGI) (Samec et al., 2011), spheroidal graphite cast iron (SGI) (Mahmoudi et al., 2015) and compact graphite cast iron (CGI) (Lim & Goo, 2011). This is due to conflicting interest between thermal and mechanical properties, in service life improvement. Wang et al., 2022, for example, found a contradictory relationship between tensile strength and thermal conductivity of cast irons. On the one hand, FGI has the highest thermal performance (due to its thermal conductivity owing to its graphite shape (ASM, 2005)). Next, CGI has better thermal performance than ductile cast iron (ASM, 2005). In this case, FGI is expected to be the best material. On the other hand, the reverse was reported true in tensile stress, displayed FGI as the lowest, SGI as the highest, and CGI as intermediate (ASM, 2005). Eventually, SGI seems the best



material in advancing disc service life. Still debate continues about the best material for disc brakes, from the cast iron families. And this attracts the attention of the researchers, in developing and implementing reliable FE model.

Besides, the preceding literature also revealed inconsistent findings about the thermal fatigue resistance of cast iron families. (Lee, 1995) and (Lee, 1991) showed that CGI provides better thermal fatigue resistance compared to FGI. On the contrary, (Fredriksson et al., 1988) uncovered that FGI has better resistance to thermal fatigue. The contradictory conclusion of the above studies can be explained by the complex thermal fatigue behavior and inhomogeneous structure of cast iron. Hence, there is a surprising paucity of evidence-based scientific literature describing the best material for disc brakes, which require the implementation of reliable FE model.

Based on this foundation, the authors developed the NAMHS model for temperature (Deressa & Ambie, 2022) and stress and life analysis (Deressa & Ambie, 2023). The model was reported successful in managing spatial variation of failure symptoms: temperature, stress, crack initiation sites and disc service life. Nonetheless, what is not yet clear is the extent to which the model contributes to geometry and material selection remains unknown. Hence, this study is to extend the previous investigations (Deressa & Ambie, 2022; Deressa & Ambie, 2023), with the main objective of assessing the implementation of the NAMHS model in disc material and geometry selection, and pad geometry selection. Besides, optimum geometry and material is also selected

To achieve this objective the study is organized in to five sections. The second section introduces the methods of investigation. And thermal and mechanical material properties are summarized in the third section. Then, results and discussions are elaborated in section four. At the end, the fifth section presents conclusions and recommendations.

## 2. MATERIALS AND METHODS

### 2.1. Data Collection

A methodology followed in this study implements both primary and secondary data. The primary data (disc geometry and braking conditions) are collected from AALRT. The actual measurement of disc geometry is conducted carefully by a stainless steel digital vernier caliper, having a measuring range of 0-150mm, within the accuracy of +/- 0.02 mm. GVC-15KD M-type standard slide caliper is also employed in parallel (Fig. 2). Besides, the operation and maintenance manual of AALRT (AALRT, 2013) is crosschecked with measured geometry parameters for the accuracy of measured dimensions. And then, the secondary data collection (review) is accomplished by preferred reporting items for systematic reviews and meta-analyses (PRISMA) statements (Deressa & Ambie, 2021). Particularly, in the areas of optimum material and geometry selections, candidate materials' thermomechanical properties and geometry types are extracted from the literature. This kind of method is also utilized in other investigations (Grzes et al., 2016; Sokolska & Sokolski, 2019). Once all the braking parameters and conditions are extracted, the empirical equations are employed in calculating heat flux and boundary conditions, which is presented in (Deressa & Ambie, 2022) and (Deressa & Ambie, 2023). The NAMHS model applicability for other research areas is tested in two ways: applicability in optimum material and geometry selection.



Fig. 2 Disc and pad dimensional data extractions at AALRT (a) pad (b) disc



## 2.2 Candidate Geometries Selection

The novelty of the NAMHS model encircles around the spatial variation of heat input on the friction surface (Deressa & Ambie, 2022). Consequently, the hub-bolted and friction surface-bolted type discs are purposefully selected, due to three reasons: contact area, mass and stress concentration area variations. These parameters have a significant impact on the spatial distribution of temperature, stress, and fatigue life. In fact, it has been observed that these effects may not be insignificant and could even dominate over other factors (Duzgun, 2012). It is impossible to judge optimum disc geometry from the two, before conducting thermomechanical analysis. Firstly, the reduction in mass on the friction surface-bolted disc may be counterbalanced by the removal of reinforcing structures around the fins in the hub-bolted disc (Fig. 3). Secondly, the presence or the absence of bolt holes on the friction surface may affect the temperature and stress evolution, positively or negatively.

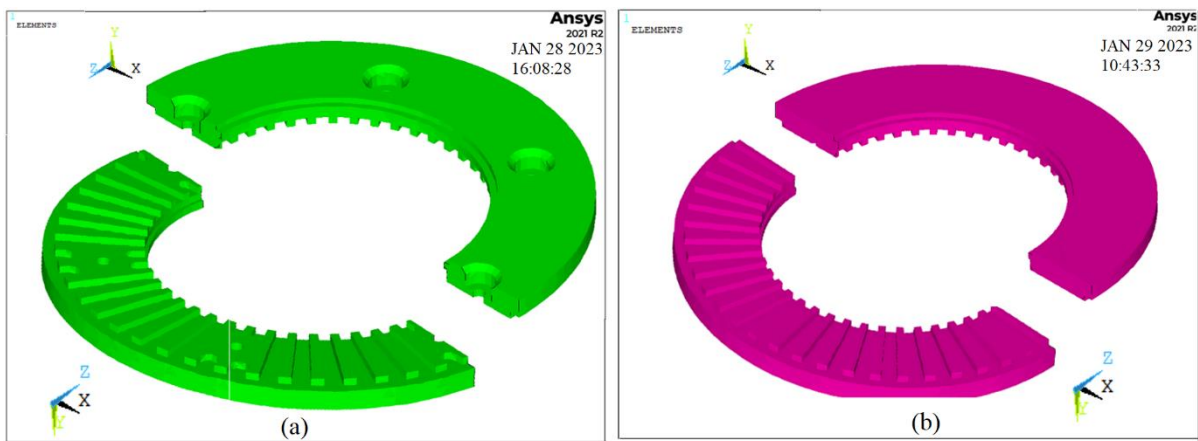


Fig. 3 Disc geometry: (a) Friction surface-bolted and (b) hub-bolted

Due to the unavailability of the hub-bolted disc on AALRT, hub-bolted type design is employed by modifying surface-bolted disc on AALRT trailer bogie (Fig. 3.b), by removing the bolt holes from the friction surface, reinforcing structures around holes from the fins side. But key dimensions are preserved, such as the internal radius, external radius, and thickness (Deressa & Ambie, 2023).

Similarly, it is required to assess the effectiveness of the NAMHS model algorithm in handling the optimum geometry selection of the pads. To do so, only composite pad designs are purposefully selected, as it is representative of all pad geometry designs. Besides, this selection of pad geometry candidates are based on the types of pad geometry found in AALRT: two radial groove without a tangential groove (Fig. 4. a) and one radial groove without a tangential groove (Fig. 4. b). For each of these basic geometries, tangential grooves are varied from 0 (no tangential groove) to two. For these pad geometries, the applied braking power is the same. But, heat flux varies, due to contact area variations. As the number of grooves rises in number (tangentially or radially), applied heat flux increases, due to the reduction of contact area (Deressa & Ambie, 2022). In addition to varying heat application spatially, heat is removed from groove locations.



Fig. 4 Damaged friction surface due to thermal stress: (a) two radial grooves, (b) one radial groove, (camera view from AALRT)



As a result, a total of six pad groove geometries are presented as candidates from which the optimum is selected (Table 2). Since the main objective here is to evaluate the NAMHS model in selecting optimum geometry, increasing additional numbers of grooves (tangentially or radially) might appear not to alter the conclusion drawn here based on selected geometries. Further diversification of the pad geometry is beyond the scope of the study, and cannot disprove the conclusion arrived on the selected geometry.

Table 2. Composite pad geometry variations

Tangential groove variations	Radial groove variations	
	R1	R2
T0	T0R1(AALRT pad)	T0R2 (AALRT pad)
T1	T1R1	T1R2
T2	T2R1	T2R2

Hence, to predict temperature and life at the design stage, and for preventive maintenance, better FE modeling is mandatory. This should be implemented for precise failure prediction by brake manufacturers at the design stage, for timely response in preventive maintenance by maintenance personnel, and for better safety of the whole railway stakeholders.

### 2.3 Candidate Materials Selection

Cast iron material families are purposefully selected to evaluate the efficiency of the NAMHS model in material selection. Firstly, AALRT is a low-speed train (70kph maximum speed). As a result, cast iron fits the scale of the speed according to the literature data (Günay et al., 2020), as well as according to technical data or maintenance manual of AALRT (AALRT, 2013). Secondly, there has been hot debate on the selection of optimum material from its families: FGI, CGI, SGI, which needs further investigation. Both thermal (density, specific heat capacity and thermal conductivity) and mechanical (young’s modulus, poisson’s ratio, tensile stress, yield stress) material properties are carefully extracted from literatures, according to their chemical compositions and microstructures.

### 2.4 FE Simulation

ANSYS Parametric Design Language (APDL) implemented in (Deressa & Ambie, 2022)(Deressa & Ambie, 2023) is utilized here for the simulation of temperature and stress. Simulation is conducted for emergency braking on the trailer bogie of AALRT. FE modeling in terms of meshing and boundary conditions are extracted from (Deressa & Ambie, 2022). And, braking conditions (speed, deceleration, braking time, mass) and non-linear martial properties are extracted from (Deressa & Ambie, 2023). Moreover, only thermal analysis performed on hub-bolted disc seems enough to predict optimal pad geometry. Because, stress follows temperature footstep, according to stress and fatigue evaluations conducted in (Deressa & Ambie, 2023), and other studies also confirm this assumption (W. Nong et al., 2011). In addition, stress and fatigue life simulation for optimum material selection is conducted on friction surface-bolted disc design.

Thermal and mechanical analyses are conducted, sequentially. Instead of calculating thermal fatigue life, stress ratio is used in this study. To generate a comparison ratio, Von Mises equivalent yield criteria is divided for materials’ yield stress (Eq. 1). Material with a lower stress ratio (<1) is assumed to have higher fatigue life, and vice versa. Temperature is extracted, in the first analysis, meanwhile, stress and stress ratio are taken from the structural analysis, as a comparison parameter.

$$\text{Stress ratio} = \frac{\text{von Mises equivalent stress}}{\text{Yield stress}} \quad (1)$$

According to von Mises failure criteria, yield would occur when von Mises stress  $\sigma_e$  equals or exceeds yield stress  $\sigma_y$ , where  $\sigma_x, \sigma_y, \sigma_z$  are component stress: circumferential, axial, and radial stresses (Eq. 2) (Budynas & Nisbett, 2014). When the yield stress is exceeded by the von Mises stress elastic-plastic damage is calculated

from plastic deformation. This type of failure criteria (Von Mises equivalent) has been widely utilized in disc brake failure analysis (Tirovic & Sarwar, 2004).

$$\sigma_e = \left( \frac{(\sigma_x - \sigma_y)^2 + (\sigma_y - \sigma_z)^2 + (\sigma_z - \sigma_x)^2}{2} \right)^{1/2} \geq \sigma_y \quad (2)$$

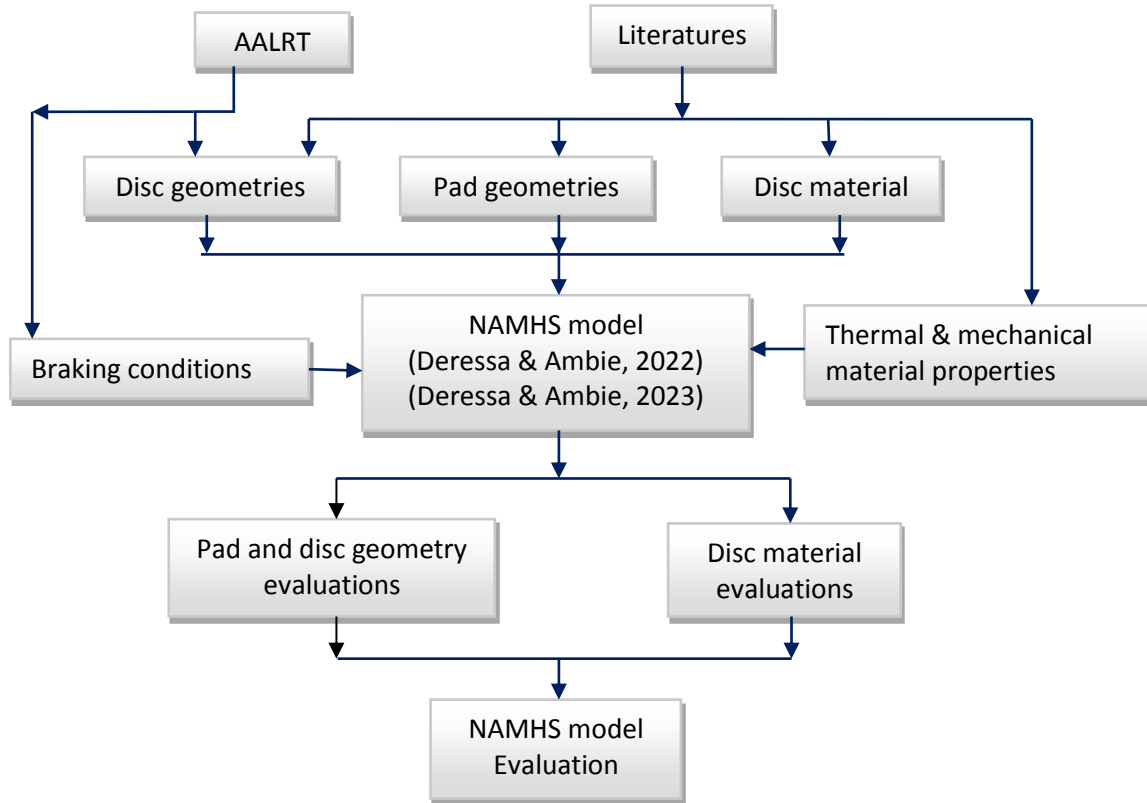


Fig. 5 Flow of information in study methodology

Based on the model developed, the data analysis, discussion, and interpretation have been made. The analysis of the research has been largely quantitative, which has been used to highlight patterns and make the analysis more robust, exploratory, or descriptive, summarizing data in the form of charts, tables, and ratio. Besides, Origin 2018, is utilized in plotting diagrams of temperature, stress, and fatigue life. Finally, by combining the findings of the research with the related literature, ways forward have been proposed. Finally, Fig. 5 depicts the overview of the methodology flow diagram.

## 2.5 The Input Thermal and Mechanical Material Properties

The thermal conductivities of various grades of pearlitic cast iron family are taken from regressional modeling investigated by (Holmgren & Selin, 2010) for three graphite morphologies: Flake, compacted, and spheroidal (Fig. 6.a). And the validity of the predicted property is checked by the ASM international handbook material standard (ASM, 2005). It is revealed to fit the ASM standard within a maximum of 9%, 5%, and 7% variation at 100°C for flake, compacted, and spheroidal cast iron, respectively.

For the specific heat capacity (Fig. 6.b), however, there is no validated unified empirical equation developed, to the best of the author’s knowledge. Hence literature value is taken from the ASM standard, except compacted graphite iron. And, for the compacted graphite iron, (Lim & Goo, 2011) presented specific heat capacity properties in disc brake material up to 300°C, and interpolation is conducted for the remaining temperature.

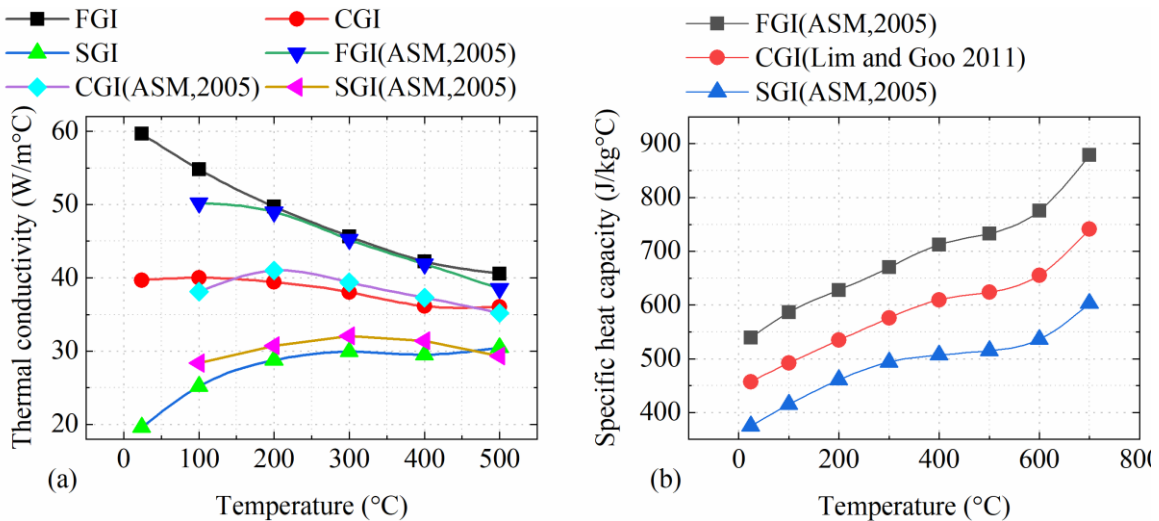


Fig. 6 (a) Thermal conductivity and (b) specific heat capacity of the candidate materials

For flake graphite cast iron, all mechanical properties are extracted from grey cast iron investigated by Pevec et al. 2014 (Pevec et al., 2014) for disc brakes. Young's modulus, yield strength, and thermal expansion coefficient are presented temperature dependent, and highlighted to fall as temperature rises for the first two properties (Fig. 7). Similarly, chemical compositions of spheroidal cast iron used for railway brake discs are taken from tensile strength and low-cycle fatigue (LCF) behavior evaluations conducted by (Samec et al., 2011).

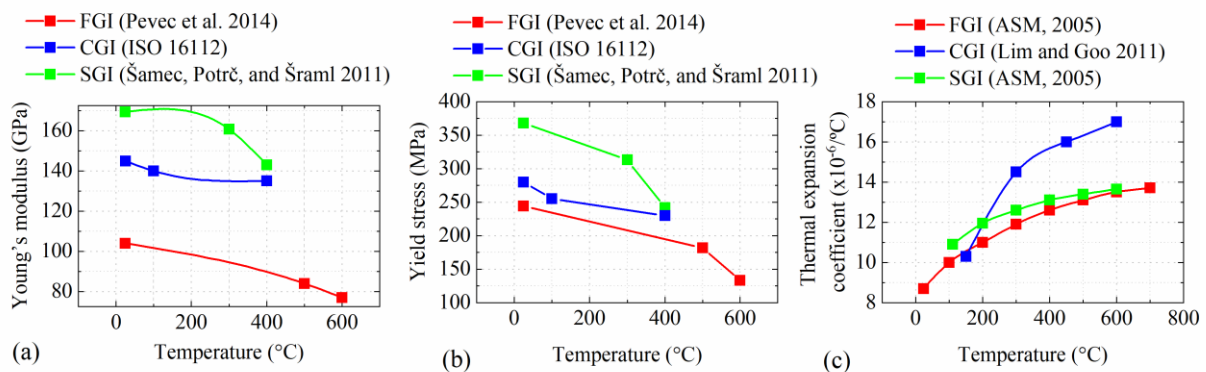


Fig. 7 Mechanical properties: (a) Young's modulus, (b) yield stress, (c) thermal expansion coefficient

From the selected cast iron families in this study, coefficients of thermal expansion for disc brake material were reported only for compacted cast iron. Eventually, the ASM standard properties (ASM, 2005) are implemented for flake and spheroidal cast irons, according to their microstructure matrix (Fig. 7.c).

Finally, compacted cast iron is taken from its development as a railway vehicle disc brake by Lim and Goo 2011 (Lim & Goo, 2011). From three compacted and conventional flake cast iron, material C was seen as the best in fatigue life. Its thermal expansion coefficient is directly implemented in this study (Fig. 7.c). However, since all mechanical properties were not presented in detail, reviewing further literature seems mandatory. The investigated compacted iron material by (Lim & Goo, 2011) has a tensile strength of 445.4 MPa, more similar to the international standard grade of GJV 450, from five grades of ISO 16112 international standard (ISO 16112, 2006). The chemical composition of the studied material also resides within the ranges specified by ISO 16112 for GJV 450 compacted cast iron. So we could have, Young's modulus and yield stress presented in Fig. 7.a-b

Moreover, Poisson's ratio is taken 0.3, and kept constant despite variations in microstructure and temperature, which is also found in the investigation of (Seifert & Riedel, 2010) on cast iron families' material development. Besides, the density of cast iron materials did not seem vary with temperature, and has been observed to have similar values of 7200 kg/m<sup>3</sup> (Duzgun, 2012), 7125 kg/m<sup>3</sup> (Sintercast, n.d.), and 7100 kg/m<sup>3</sup> (Biswas et al., 2016) for flake, compacted and spheroidal, respectively.

To sum up, both mechanical/strength properties and thermal properties of candidate materials revealed conflicting interests in improving stress and fatigue life. Because thermal performance is observed to increase from spheroidal to flake graphite iron (Fig. 6). In contrast, strength or mechanical performance is displayed to decrease from spheroidal to flake graphite iron (Fig. 7). Compacted graphite iron is shown intermediate performance in either case. On the other hand, it has the poorest thermal expansion coefficient (Fig. 7.c). Therefore, thermal stress analysis with the NAMHAS model is tested to reveals the optimum material for railway vehicles' disc brakes.

### 3. RESULTS AND DISCUSSIONS

Two-dimensional graphs of friction surface temperature are presented by NAMHS for temperature and von Mises stress. In addition, contour plots from ANSYS are also reported as additional evidence for spatial variation of temperature and stress. Only thermal analysis and corresponding temperature are observed for pad geometries. Meanwhile, both thermal and mechanical analyses are conducted for material selection.

#### 3.1 Pad Geometry Investigations

The first set of questions aimed to investigate the applicability of the NAMHS model algorithm is its handling spatial variation of heat and boundary conditions due to pad geometry. The analysis is performed for emergency braking of AALRT trailer bogie, with modified geometry. And, the spatial and contour results are extracted at the time when the maximum temperature is recorded, which is 3.5 sec.

As is apparent from Fig. 8 a and c, the rise in the tangential groove from 0 (T0R1) to 2 (T2R1) demonstrates the reduction in temperature by 12.5°C, for constant one radial groove. Besides, for the constant radial groove of two, the rise in the tangential groove from 0 (T0R2) to 2 (T2R2) uncovers the fall of temperature by 17°C, as illustrated in Fig. 9 a and d, respectively. The contour plot is displayed in Fig. 10. a-f witnesses these findings.

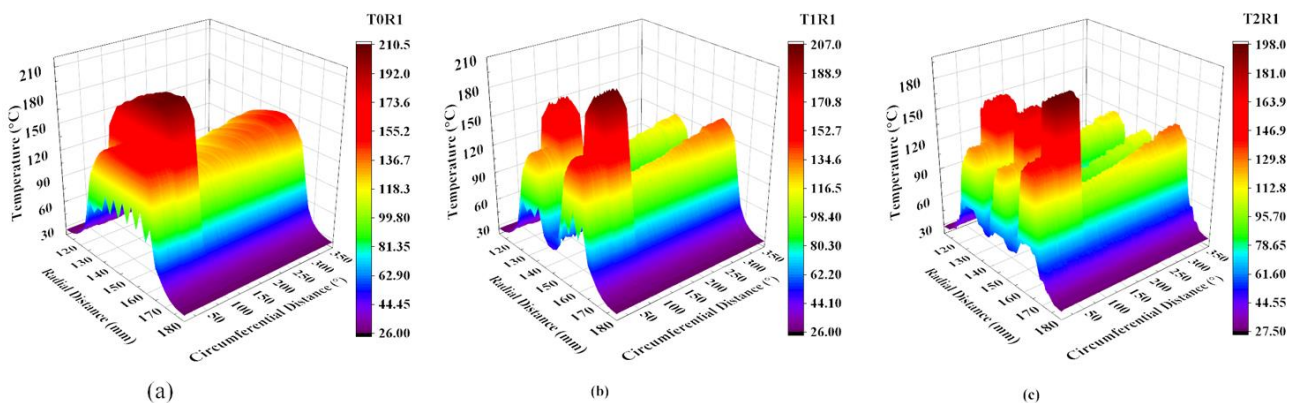


Fig. 8 Maximum temperature distribution for tangential groove variation with one radial groove: (a) T0R1, (b) T1R1, (c) T2R1

Based on these findings, it is reasonable to infer that the number of tangential grooves has more influence at a higher number of radial grooves. And the effect of radial groove is not seen significant, as in the case of tangential groove, which is clearly seen from its enlarged, rotated and tilted plot displayed in Fig. 9 b for T0R2. Another interesting aspect of this graph is the effect of the rising radial groove when the tangential groove is kept constant. It is observed that the temperature slightly rises (3°C) with the increase of radial groove from 1-2 when there is no tangential groove. This is evident by comparing the results displayed in Fig. 8 a and Fig. 9 a.

Likewise, the maximum temperature is raised by 5 °C when one tangential groove is utilized with radial groove variation from 1-2 (Fig. 8 b and Fig. 9 c). Contrary to these expectations, the maximum temperature is seen to drop by 1.5 °C when the radial groove is raised from 1 to 2, for 2 tangential grooves (2T2R) Fig. 8 c & Fig. 9 d. But this is not surprising, as the tangential groove's impact in reducing temperature is significant at its higher number. This implies the temperature-rising capability of the radial groove is counterbalanced by the temperature-reducing effect of the tangential groove. These findings suggested that the presence of a higher number of radial grooves in pad design geometry is not encouraged, as it increases friction surface temperature.

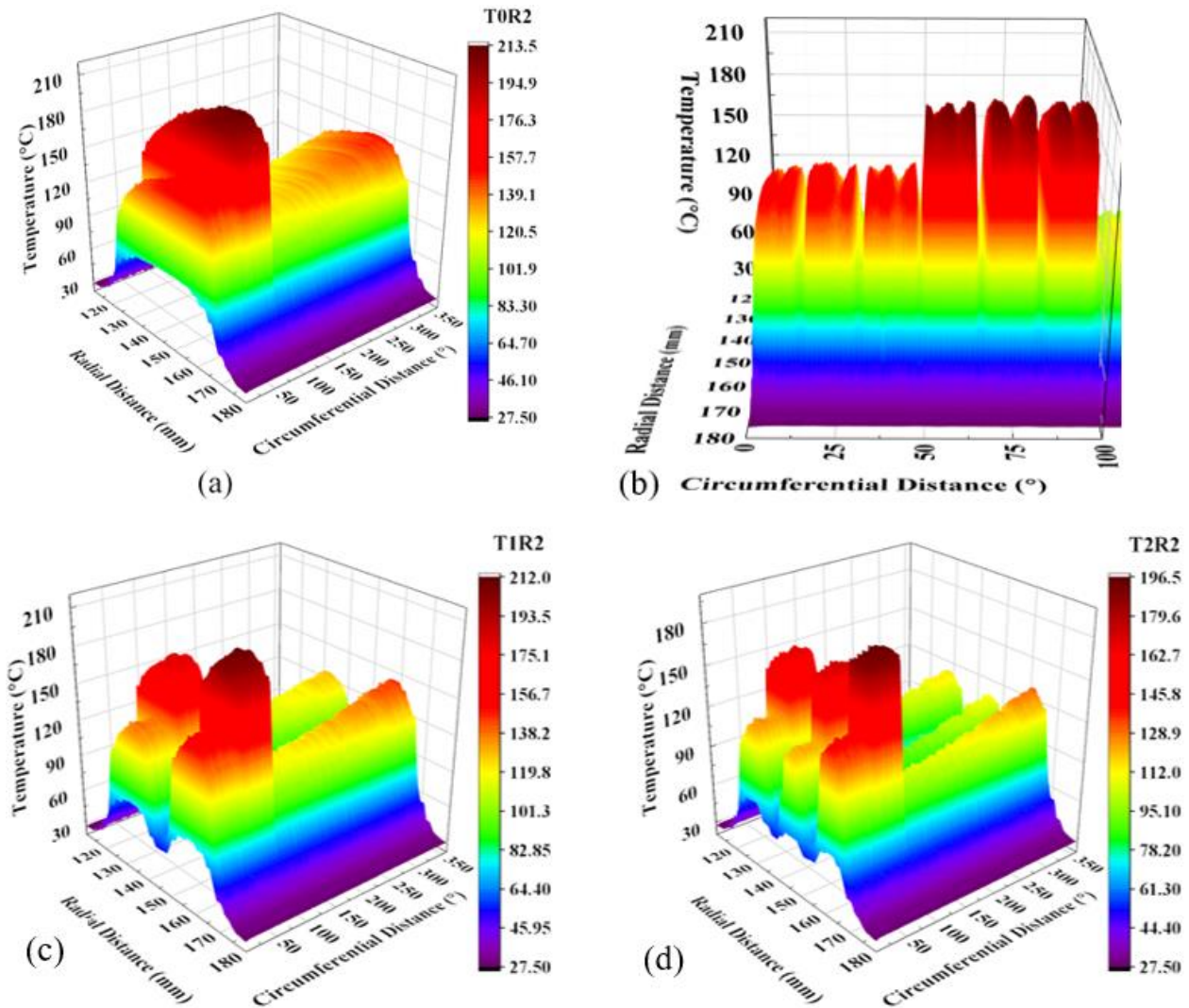


Fig. 9 Maximum temperature distribution for tangential groove variation with two radial grooves: (a) T0R2, (b) TOR2 (enlarged), (c) T1R2, (d) T2R2

The lack of radial grooves in many pad geometries supports this finding (Kim et al., 2008). Even if available, the limitation of its maximum number to one (Yevtushenko et al., 2021) or two in AALRT (Fig. 4.a) agrees with this study. Moreover, Benseddiq et al. 1996 (Benseddiq et al., 1996) reported a reduction in temperature from 1136 to 600°C by varying tangential grooves from 1 to 4.

The finding reported in this study could eventually lead to recommendations for the implementation of the NAMHS model as a broadly applicable approach that can be used in selecting optimum pad geometry selection that could reduce friction surface temperature. The approach presented in the NAMHS model algorithm is seen as suitable for handling spatial heat variation due to pad geometries.

### 3.2 Temperature Results of the Candidate Materials

To demonstrate the NAMHS based optimum material, three critical analysis times are selected: braking time at maximum results (3.8574 sec), end of the braking time (8.2071 sec), and the end of the cooling time (184.2 sec). As can be seen from Table 3, temperature, von Mises stress, and stress ratio are presented for all candidate materials at these critical times. Yield stress at the corresponding time and temperature is calculated from Fig. 7.b by interpolation. Besides, these results are compatible with spatial and contour plots displayed on figures Fig. 12. c-d and Fig. 13. c-d.

From the data in Table 3 and Fig. 11, it is apparent that the temperature is presented higher in SGI, CGI, and FGI, in reducing order, at maximum and end braking time. But this is not surprising, as it can be predicted

easily from thermal properties (Fig. 6). FGI has shown the best thermal performance, as it displays lower temperatures. The same argument is put forward for the remaining materials. Nonetheless, what stands out in this thermal analysis is the rate at which temperature is removed is interestingly higher in SGI, followed by CGI and FGI. This means the temperature is found to drop by 299.15 °C, 228.7 °C, and 183.8 °C respectively in SGI, CGI, and FGI, between cooling time and maximum temperature time (within 180.3426 sec).

One possible explanation for this result might be thermal diffusivity  $\alpha$  (m<sup>2</sup>/s), another significant thermal property (Eq. 3). It is the capability of a material to conduct thermal energy compared to its capability to store thermal energy (Budynas & Nisbett, 2014). Materials of higher  $\alpha$  will reply quickly to variation in temperature through conduction, while materials of lower  $\alpha$  will respond more sluggishly (taking a longer time to reach a new equilibrium condition, Fig. 11. b).

Eventually, for SGI (material with lowest  $\alpha$ ), the temperature is concentrated (accumulated) on the friction surface and no further rise in temperature is expected in disc thickness, for the whole braking time. This is due to its poor thermal diffusivity  $\alpha$ . As braking time (8.2071sec) is completed, convective heat dissipation is applied as a boundary condition on the friction surface (where a higher temperature is found). Consequently, SGI has a higher opportunity to dissipate heat, compared to other candidate materials (FGI, CGI) where temperature is distributed in disc thickness, and no further opportunity to dissipate heat to the atmosphere.

Furthermore, a higher reduction in temperature is also observed between the braking time at maximum results and end braking time (within time variation of 4.3497 sec) for SGI and CGI with a magnitude of 141.2 °C and 110.5 °C, respectively, compared to FGI (88.5 °C). Likewise, the same possible explanation could be proposed for this result is the removal of friction surface concentrated temperature by convection during braking at the location where heat flux is removed (Fig. 12 a-d).

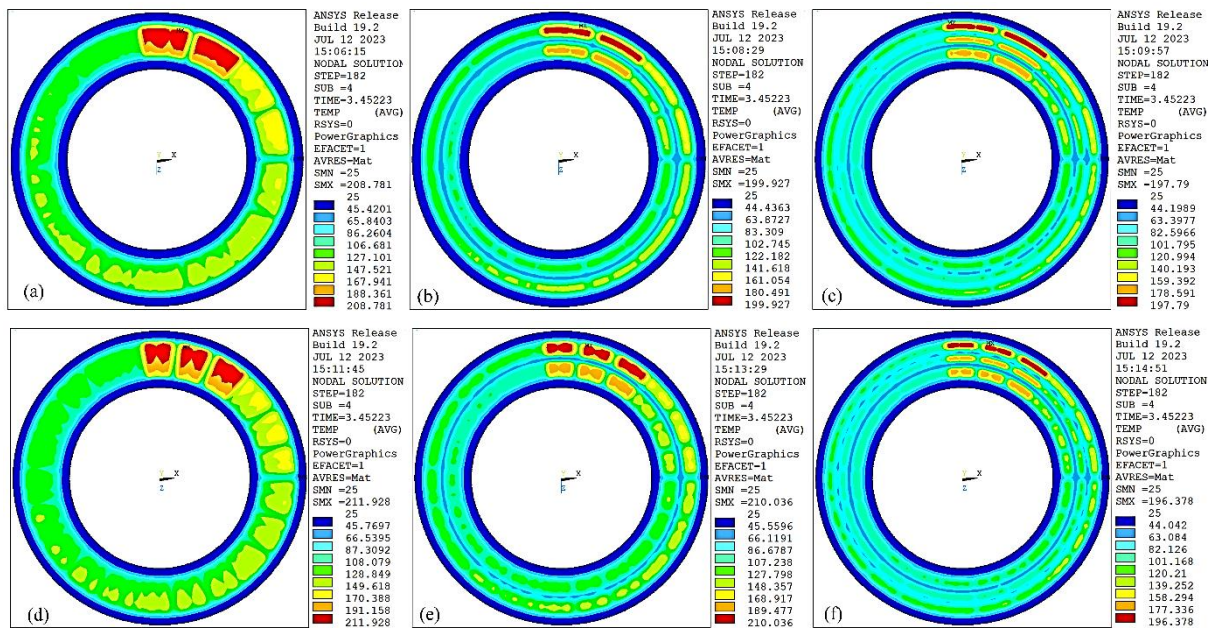


Fig. 10 Friction surface temperature: (a) T0R1, (b) T1R1, (c) T2R1, (d) T0R2, (e) T1R2, (f) T2R2

This result suggests that SGI responds more quickly to friction surface heat spatial variation, followed by CGI and FGI. Hence, it could conceivably be hypothesized that the NAMHS model algorithm spatial variation of heat and boundary condition is more suitable for SGI, followed by CGI and FGI. Application of other traditional methods, like the axisymmetric model couldn't provide these results, because of incapability in varying heat and boundary conditions spatially on the friction surface.

Friction surface temperature spatial variation is presented for CGI and SGI at maximum temperature (3.8574 sec), radially, and circumferentially (Fig. 12 a-b). Besides, the contour plot is depicted for the original disc geometry for both materials (Fig. 12 c-d), and presented in Table 3 for FGI. For these presented results, the heat source is rotating counterclockwise and found within 78° to 128°.

Table 3. Temperature, Von Mise Stress, and Stress ratio of candidate materials at different times

Candidate materials	Comparison Parameters	Braking and cooling times (seconds)		
		3.8574 sec	8.2071 sec	184.2 sec
FGI	Temperature (°C)	246.5	158	62.7
	Von Mise Stress (MPa)	424	482	216
	Yield stress (MPa)	211.95	223.11	235.12
	Stress ratio	2	2.16	0.92
CGI	Temperature (°C)	287	176.5	58.3
	Von Mise Stress (MPa)	620	710	280
	Yield stress (MPa)	241.3	252.35	271.12
	Stress ratio	2.57	2.81	1.03
SGI	Temperature (°C)	358.7	217.5	59.55
	Von Mise Stress (MPa)	872	1050	337
	Yield stress (MPa)	268.91	327.93	362.27
	Stress ratio	3.24	3.20	0.93

$$\alpha = \frac{k_d}{\rho_d c_d}$$

3

This observation may support the hypothesis that SGI should be utilized in repeated braking where enough cooling time is available between consecutive braking. Whereas FGI seems better in braking conditions with lower cooling time observed, including long braking time and drag or continuous braking. CGI is highlighted intermediate between these two extreme results.

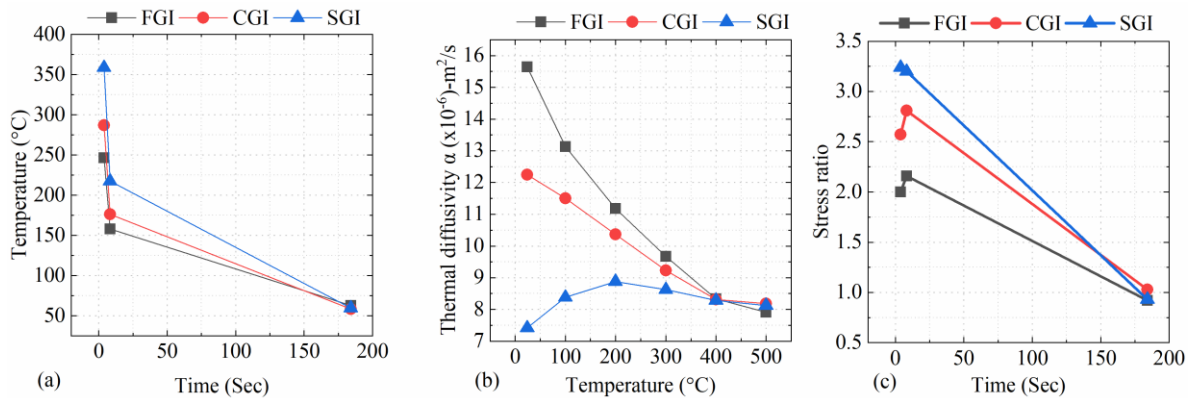


Fig. 11 Candidate materials (a) temperature variation, (b) thermal diffusivity (c) stress ratio

### 3.3 Stress and Stress Ratio Results of the Candidate Materials

The next section of the NAMHS’ study is concerned with stress and its ratio, where the exact comparison of the materials is revealed. Because the contribution of both opposing thermal and mechanical properties in service life evaluation is clearly seen. To do so, stress spatial variation is illustrated in Fig. 13 for CGI and SGI at the end time of braking. For the remaining braking and cooling times, and for the FGI material, still Table is utilized.

It can be seen from the data in Table and Fig. 13 that stress is higher in SGI, at any braking and cooling time, followed by CGI and FGI. These relationships may fully be explained by their corresponding thermal performance.

Spatial variation of stress result is shown fully dominated by disc geometry (holes), compared to the other factors contributing to spatial variations. This is manifested on nodes around bolt holes, due to their proximity to constrained boundary conditions ( $u_x=x_y=u_z=0$ ) and stress concentrations at sharp edges. These nodes are displayed in Fig. 13 every 60°, starting from 0° to 360°.

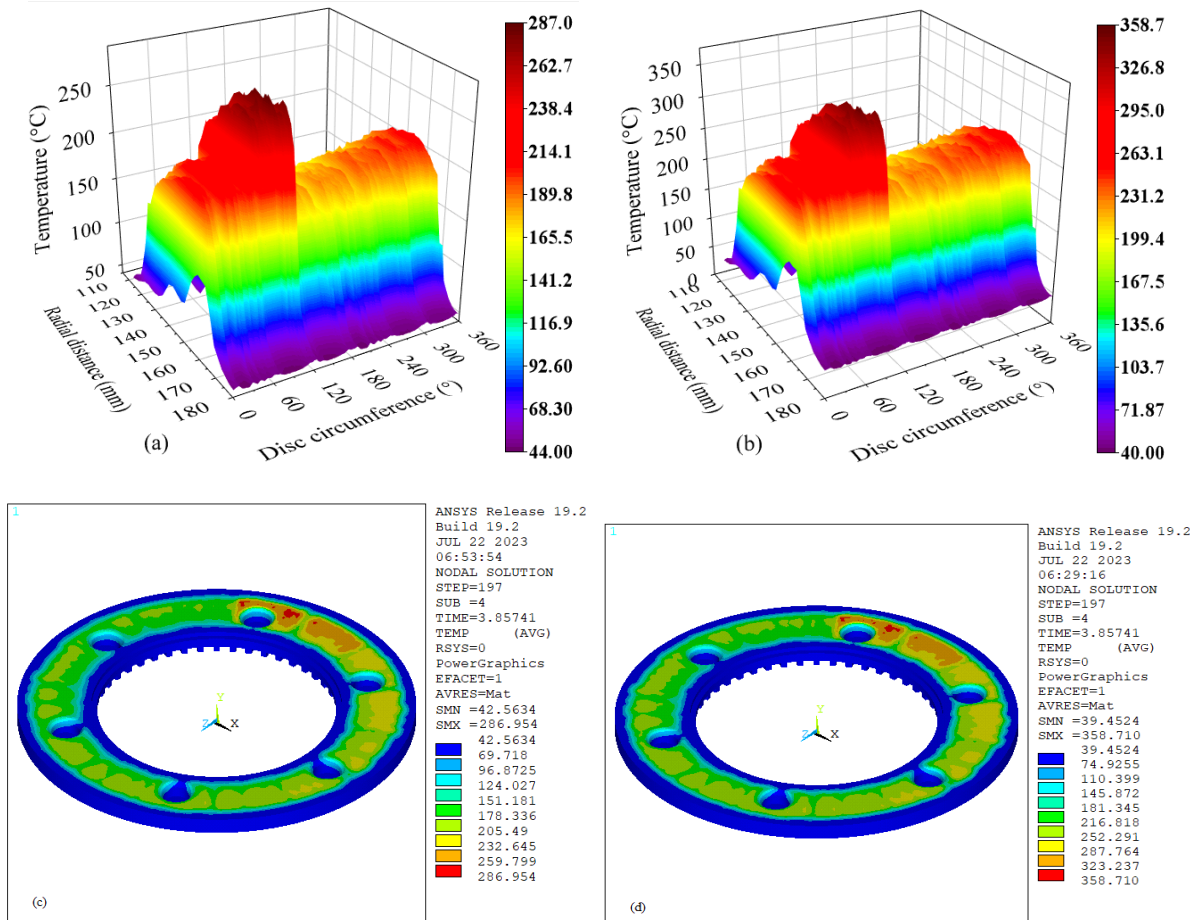


Fig. 12 Spatial maximum temperature (3.8574 sec) distribution: CGI (a,c) and SGI (b,d)

Eventually, stress at these nodes is illustrated as high as 710 MPa and 1050 MPa in CGI and SGI, respectively (Fig. 13 a-b). Despite that, the contour plot displayed in Fig. 13 c-d, unfortunately, reported higher results, 926 MPa and 1320 MPa for CGI and SGI, respectively. This inconsistency is due to the inclusion of nodes residing in the holes (and far from the friction surface), where extensive stress is reported due to constrained boundary conditions.

But, to decide in which material the crack is early initiated is based on comparison with their respective yield stress, through stress ratio (Eq. 1) presented in Fig. 14. Firstly, the yield stress is extracted from mechanical properties presented in Fig. 7.b by interpolation at reported temperature values in Table . And then stress ratio is calculated and presented for friction surface nodes of FGI, CGI and SGI at the end of braking and cooling times (Fig. 14).

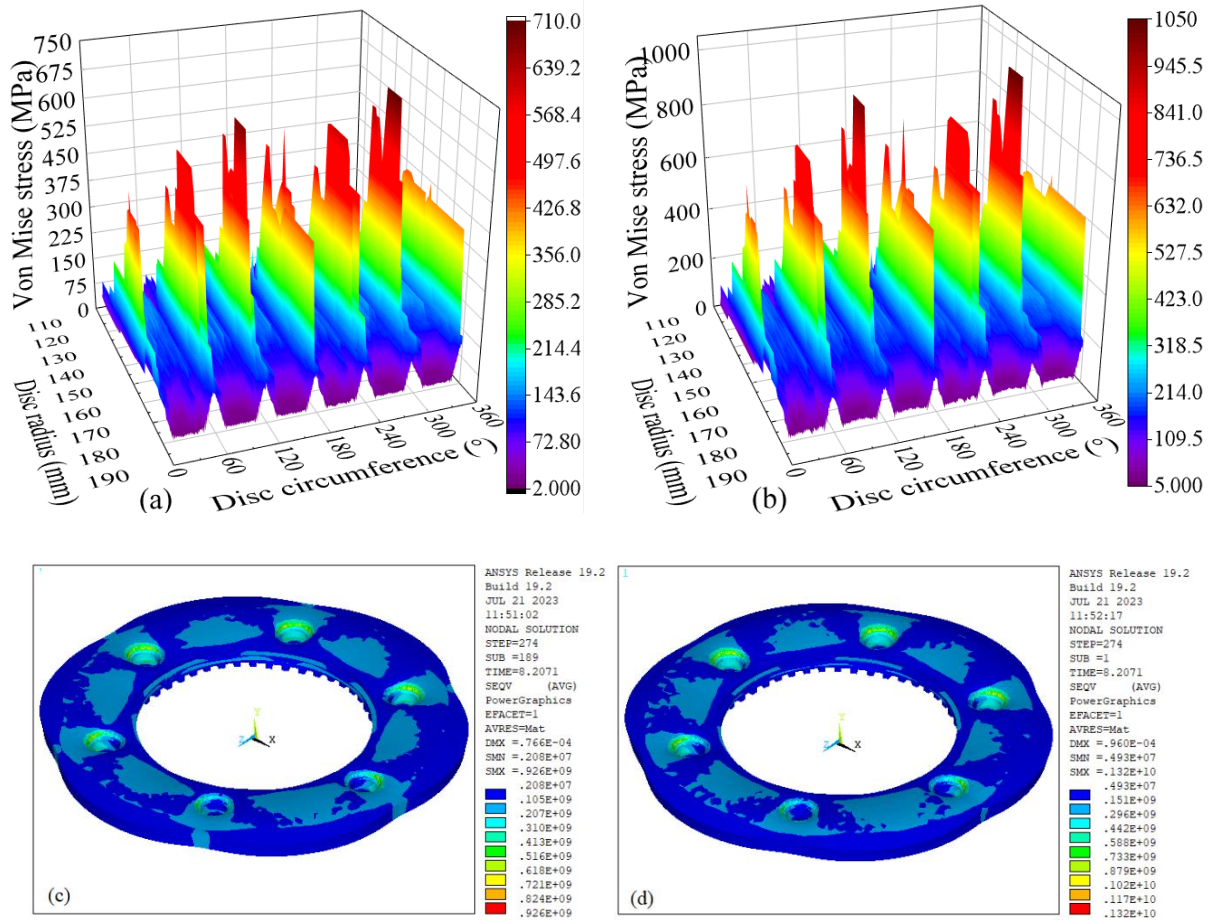


Fig. 13 End braking von Mises stress CGI (a,c), SGI (b,d) station 3

And finally, the stress ratio is summarized and presented in Fig. 11. c for all materials. According to this Figure, we can infer that FGI material is seen as the optimum material throughout braking time. This might seem due to the contribution of its lower Young's modulus and its higher thermal diffusivity (Fredriksson et al., 1988). Nonetheless, this trend is seen overtaken by SGI before 150 sec (within the cooling period). And if cooling time is continued beyond 184 sec, SGI might overtake FGI. This observation may support the hypothesis that the rate of concentrated heat removal is high from the SGI friction surface. And this concentrated heat is appeared due to its poor thermal diffusivity.

Eventually, during and when braking is completed, friction surface with high heat is exposed to convective boundary conditions, leading to a steep reduction in stress ratio (Fig. 11.c). It can thus be suggested that SGI is the optimum material whenever excess cooling time is allowed, and followed by CGI.

On the other hand, CGI is not shown to overpass FGI, at the end of cooling time. This result may be explained by the fact that it has a higher thermal expansion coefficient, which could reduce thermal stress and fatigue (Fredriksson et al., 1988). Therefore, this finding adds to a growing body of evidence that suggests FGI material for drag and long braking time. This type of braking is implemented to maintain constant braking on downhill driving. Besides, these results suggest SGI and CGI for short braking time with long cooling time. This type of braking is observed in emergency braking and frequent or repeated braking stations of light rail transit, including AALRT.

Fredriksson et al. (1988) reported that FGI has better thermal fatigue compared to CGI as well as SGI, in spite of its lower rupture stress. Besides, it was reported that its lower elasticity modulus and its higher heat diffusivity contributed to its success in thermal fatigue. Although their study is in good agreement with this investigation during braking time, they disregarded the effect of convective heat dissipation during cooling time, in which SGI might seem optimum. Furthermore, the disc brake optimum material section was also investigated by 2006 (Sakamoto & Hirakawa, 2006) among different types of steel and cast iron materials.

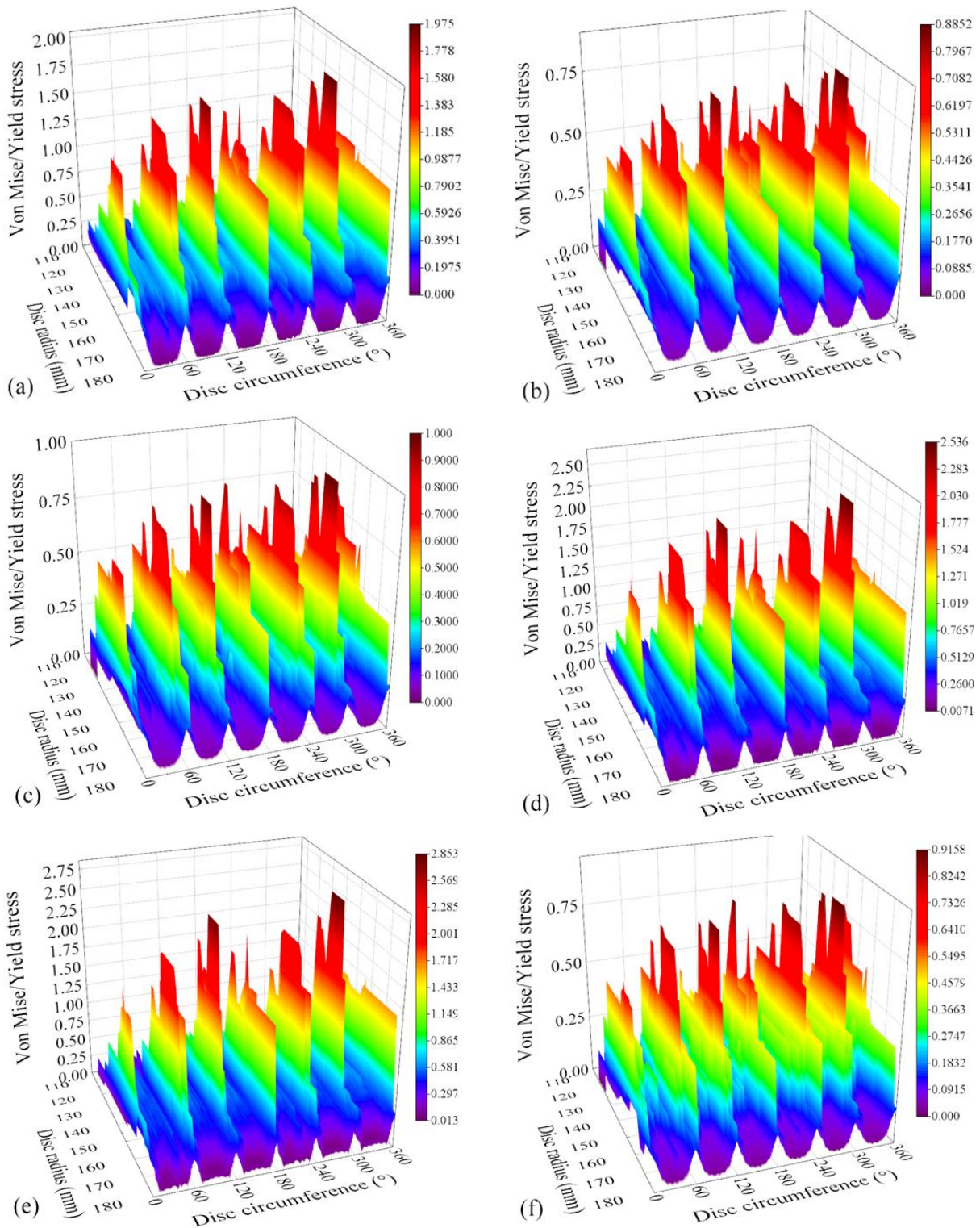


Fig. 14 Spatial stress ratios at end of braking (a,c,e) and cooling (b,d,f) for FGI (a-b), CGI (c-d) and SGI (e-f)

#### 4. CONCLUSION AND RECOMMENDATIONS

The NAMHS model is assessed in optimum pad geometry selections, based on the number and orientation of grooves on the pad friction surface. Thermal analysis is conducted for emergency braking of trailer bogie on AALRT, and the key findings are (1) The NAMHS model algorithm has proven to be a successful method for accurately and efficiently identifying the optimal pad geometry through thermal analysis; (2) Increasing the number of tangential grooves has a greater impact on reducing temperature compared to increasing the number



of radial grooves; (3) Encouraging a higher number of radial grooves in pad design geometry is not advisable, as it leads to an increase in friction surface temperature.

Implementation of the NAMHS model in optimum material selection is also conducted for three cast iron material families having an application in a disc brake. Thermal and mechanical analysis are performed sequentially, resulting in temperature, stress, and stress ratio as comparison parameters. Thermal fatigue is evaluated indirectly by the stress ratio presented as the ratio of von Mises equivalent stress and materials' yield stress. The main findings are:

- The NAMHS model algorithm is observed successful model in identifying the optimum disc material.
- Optimum material selection is based on the length of the cooling and braking time ranges
- In lower braking and cooling time, optimum material is presented in reducing order as follows: FGI, CGI, SGI. Whenever sufficient cooling time is provided between braking frequencies, the selection of optimum material in decreasing order is presented in reversed order as SGI, CGI, and FGI.
- The concentration of maximum temperature on the friction surface, due to poor thermal diffusivity revealed a greater chance to dissipate heat by convection in SGI, followed by CGI and FGI.
- NAMHS' capability in providing convective coefficient and heat flux simultaneously on friction surface served the SGI more, compared to other materials, according to their maximum surface temperature
- Thermal conductivity, thermal expansion coefficients, Young's modulus, and yield stress are identified to affect stress and fatigue life

This study is focused on thermal and mechanical properties variation, in determining the temperature, stress, and stress ratio of the materials. But, many of the properties important for thermal fatigue are influenced by chemical composition, type of matrix, shape, morphology, and fraction of the graphite in cast iron families. Hence, recommendations for future studies should include these parameters accompanied by the NAMHS model, for better selection of optimum materials for rail vehicles disc brake.

## LIST OF SYMBOLS

$\sigma_e$	Mises equivalent stress (MPa)
$\sigma_y$	Yield stress (MPa)
$\sigma_x$	Circumferential stresses (MPa)
$\sigma_y$	Axial stresses (MPa)
$\sigma_z$	Radial stresses (MPa)
$\alpha$	Thermal diffusivity ( $m^2/s$ ),
$k_d$	Thermal conductivity of the disc ( $W/m^{\circ}C$ )
$\rho_d$	Density of the disc ( $kg/m^3$ )
$C_d$	Specific heat capacity of the disc ( $J/kg^{\circ}C$ )

## ABBREVIATIONS

FE	Finite element
NAMHS	Non-axisymmetric moving heat source
FGM	Functional graded material
FGI	Flake graphite cast iron
SGI	Spheroidal graphite cast iron
CGI	Compact graphite cast iron
PRISMA	Preferred reporting items for systematic reviews and meta-analyses
AALRT	Addis Ababa light rail transit
APDL	ANSYS Parametric Design Language
LCF	Low-cycle fatigue
TiRj	i=tangential groove variation (0-2), j=Radial groove variation (1-2)



## ACKNOWLEDGEMENTS

The authors are grateful to Addis Ababa Light Rail Transit personnel and African Railway Center of Excellence staff who contributed to this article.

## REFERENCES

- AALRT. (2013). *Operation and Maintenance Manual for 70% Low Floor Light Rail Vehicle Project in Addis Ababa, Ethiopia*.
- ASM. (2005). *ASM Handbook, Volume 1, Properties and Selection: Irons, Steels, and High Performance Alloys Section* (10th ed.). ASM International.
- Bayat, M., Alarifi, I. M., Khalili, A. A., El-Bagory, T. M. A. A., Nguyen, H. M., & Asadi, A. (2019). Thermo-mechanical contact problems and elastic behaviour of single and double sides functionally graded brake disks with temperature-dependent material properties. *Scientific Reports*, 9(1). <https://doi.org/10.1038/s41598-019-51450-z>
- Belhocine, A., Abu Bakar, A. R., & Bouchetara, M. (2016). Thermal and structural analysis of disc brake assembly during single stop braking event. *Australian Journal of Mechanical Engineering*, 14(1), 26–38. <https://doi.org/10.1080/14484846.2015.1093213>
- Benhassine, N., Haiahem, A., & Bou-Said, B. (2019). A comparative study of the transient thermomechanical behavior of friction of the ceramic brake discs: Temperature field effect. *Journal of Mechanical Science and Technology*, 33(1), 233–240. <https://doi.org/10.1007/s12206-018-1223-4>
- Benseddiq, N., Weichert, D., Seidermann, J., & Minet, M. (1996). Optimization of design of railway disc brake pads. *Proceedings of the Institution of Mechanical Engineers, Part F: Journal of Rail and Rapid Transit*, 210(1), 51–61. [https://doi.org/10.1243/PIME\\_PROC\\_1996\\_210\\_326\\_02](https://doi.org/10.1243/PIME_PROC_1996_210_326_02)
- Biswas, S., Monroe, C., & Prucha, T. (2016). *Analysis of Published Cast Iron Experimental Data BT - Proceedings of the 3rd World Congress on Integrated Computational Materials Engineering (ICME 2015)* (W. Poole, S. Christensen, S. R. Kalidindi, A. Luo, J. D. Madison, D. Raabe, & X. Sun (eds.); pp. 293–303). Springer International Publishing.
- Budynas, R., & Nisbett, K. (2014). *Shigley's Mechanical Engineering Design*. McGraw-Hill Higher Education - VST E+p. <https://books.google.com.et/books?id=B7wivgAACAAJ>
- Deressa, K. T., & Ambie, D. A. (2021). Thermal Load Simulations in Railway Disc Brake: A Systematic Review of Modelling Temperature, Stress and Fatigue. *Archives of Computational Methods in Engineering*, 29(4), 2271–2283. <https://doi.org/10.1007/s11831-021-09662-y>
- Deressa, K. T., & Ambie, D. A. (2022). Non-Axisymmetric Modelling of Moving Heat Source for Spatial and Temporal Investigation of Temperature in Railway Vehicles Disc Brake. *Urban Rail Transit*, 8(3–4), 198–216. <https://doi.org/10.1007/s40864-022-00176-9>
- Deressa, K. T., & Ambie, D. A. (2023). Non-axisymmetric Modeling of a Moving Heat Source for Thermal Stress and Fatigue Analysis of Railway Vehicle Disc Brakes. *Urban Rail Transit*. <https://doi.org/10.1007/s40864-023-00207-z>
- Duzgun, M. (2012). Investigation of thermo-structural behaviors of different ventilation applications on brake discs. *Journal of Mechanical Science and Technology*, 26(1), 235–240. <https://doi.org/10.1007/s12206-011-0921-y>
- Fredriksson, H., Sunnerkrantz, P. A., & Ljubinković, P. (1988). Relationship between structure and thermal fatigue in cast iron. *Materials Science and Technology (United Kingdom)*, 4(3), 222–226. <https://doi.org/10.1179/mst.1988.4.3.222>
- Goo, B. C. (2018). A study on the contact pressure and thermo-elastic behavior of a brake disc-pad by infrared images and finite element analysis. *Applied Sciences (Switzerland)*, 8(9). <https://doi.org/10.3390/app8091639>
- Grivc, U., Deržič, D., & Muhič, S. (2019). Numerical optimisation and experimental validation of divided rail freight brake disc crown. *Journal of Modern Transportation*, 27(1). <https://doi.org/10.1007/s40534-018-0174-x>
- Grzes, P., Oliferuk, W., Adamowicz, A., Kochanowski, K., Wasilewski, P., & Yevtushenko, A. A. (2016). The numerical-experimental scheme for the analysis of temperature field in a pad-disc braking system of a railway vehicle at single braking. *International Communications in Heat and Mass Transfer*, 75, 1–6. <https://doi.org/10.1016/j.icheatmasstransfer.2016.03.017>
- Günay, M., Korkmaz, M. E., & Özmen, R. (2020). An investigation on braking systems used in railway vehicles. *Engineering Science and Technology, an International Journal*, 23(2), 421–431. <https://doi.org/10.1016/j.jestch.2020.01.009>
- Handa, K., Ikeuchi, K., & Morimoto, F. (2020). Temperature-dependent wear of tread-braked railway wheels. *Wear*, 452–453, 203265. <https://doi.org/https://doi.org/10.1016/j.wear.2020.203265>
- Holmgren, D., & Selin, M. (2010). Regression model describing the thermal conductivity of various cast irons. *Materials Science Forum*, 649, 499–504. <https://doi.org/10.4028/www.scientific.net/MSF.649.499>
- ISO 16112. (2006). *Compacted (vermicular) graphite cast irons - Classification*.



- <https://standards.globalspec.com/std/10069310/ISO 16112>
- Jiang, L., Jiang, Y., Yu, L., Yang, H., Li, Z., & Ding, Y. (2019). Thermo-mechanical coupling analyses for Al alloy brake discs with Al<sub>2</sub>O<sub>3</sub>-SiC(3D)/Al alloy composite wear-resisting surface layer for high-speed trains. *Materials*, 12(19). <https://doi.org/10.3390/ma12193155>
- Jiguang, C., & Fei, G. (2015). Temperature field and thermal stress analyses of high-speed train brake disc under pad variations. *Open Mechanical Engineering Journal*, 9(1), 371–378. <https://doi.org/10.2174/1874155X01509010371>
- Kim, D. J., Lee, Y. M., Park, J. S., & Seok, C. S. (2008). Thermal stress analysis for a disk brake of railway vehicles with consideration of the pressure distribution on a frictional surface. *Materials Science and Engineering: A*, 483–484(1-2 C), 456–459. <https://doi.org/10.1016/j.msea.2007.01.170>
- Lee J, L. S. (1995). Thermal fracture endurance of cast irons with application study of pig iron ingot molds. *Metallurgical and Materials Transactions A*, 1431–1440.
- Lee S, W. L. C. (1991). On thermal shock resistance of austenitic cast irons. *Metallurgical and Materials Transactions A*, 22(8), 1821–1831.
- Lim, C.-H., & Goo, B.-C. (2011). Development of compacted vermicular graphite cast iron for railway brake discs. *Metals and Materials International*, 17(2), 199–205. <https://doi.org/10.1007/s12540-011-0403-x>
- Luo, Z., & Zuo, J. (2014). Conjugate heat transfer study on a ventilated disc of high-speed trains during braking. *Journal of Mechanical Science and Technology*, 28(5), 1887–1897. <https://doi.org/10.1007/s12206-014-0336-7>
- Mahmoudi, T., Parvizi, A., Poursaeidi, E., & Rahi, A. (2015). Thermo-mechanical analysis of functionally graded wheel-mounted brake disk. *Journal of Mechanical Science and Technology*, 29(10), 4197–4204. <https://doi.org/10.1007/s12206-015-0914-3>
- Maleque, M. A., Dyuti, S., & Rahman, M. M. (2010). Material selection method in design of automotive brake disc. *WCE 2010 - World Congress on Engineering 2010*, 3, 2322–2326.
- Nong, W., Gao, F., Fu, R., & Yu, Q. (2011). On structure function and the temperature and the thermal stress of brake discs. *Applied Mechanics and Materials*, 80–81, 521–526. <https://doi.org/10.4028/www.scientific.net/AMM.80-81.521>
- Nong, X. D., Jiang, Y. L., Fang, M., Yu, L., & Liu, C. Y. (2017). Numerical analysis of novel SiC3D/Al alloy co-continuous composites ventilated brake disc. *International Journal of Heat and Mass Transfer*, 108, 1374–1382. <https://doi.org/10.1016/j.ijheatmasstransfer.2016.11.108>
- Oder, G., Šamec, B., Lerher, T., & Potrč, I. (2011). Numerical analysis of braking discs for a taurus class locomotive. *Journal of Shanghai Jiaotong University (Science)*, 16(3), 320–323. <https://doi.org/10.1007/s12204-011-1152-1>
- Pevc, M., Oder, G., Potrč, I., & Šraml, M. (2014). Elevated temperature low cycle fatigue of grey cast iron used for automotive brake discs. *Engineering Failure Analysis*, 42(1), 221–230. <https://doi.org/10.1016/j.engfailanal.2014.03.021>
- Rashid, A., & Strömberg, N. (2012). *An Efficient Sequential Approach for Simulation of Thermal Stresses in Disc Brakes*. 1–6.
- Sakamoto, H., & Hirakawa, K. (2006). Fracture analysis and material improvement of brake discs. *JSME International Journal, Series A: Solid Mechanics and Material Engineering*, 48(4), 458–464. <https://doi.org/10.1299/jsmea.48.458>
- Šamec, B., Oder, G., Lerher, T., & Potrč, I. (2011). Numerical analysis of railway brake disc. *Journal of Shanghai Jiaotong University (Science)*, 16(2), 149–151. <https://doi.org/10.1007/s12204-011-1111-x>
- Šamec, B., Potrč, I., & Šraml, M. (2011). Low cycle fatigue of nodular cast iron used for railway brake discs. *Engineering Failure Analysis*, 18(6), 1424–1434. <https://doi.org/10.1016/j.engfailanal.2011.04.002>
- Seifert, T., & Riedel, H. (2010). Mechanism-based thermomechanical fatigue life prediction of cast iron. Part I: Models. *International Journal of Fatigue*, 32(8), 1358–1367. <https://doi.org/https://doi.org/10.1016/j.ijfatigue.2010.02.004>
- Sintercast. (n.d.). Compacted Graphite Iron Compacted Graphite Iron -Material Data Sheet. *Supermetal CGI*, 2–3.
- Sokolska, J., & Sokolski, P. (2019). Thermal evaluation of operation of disc brakes made of selected materials. In *Lecture Notes in Mechanical Engineering*. [https://doi.org/10.1007/978-3-030-04975-1\\_79](https://doi.org/10.1007/978-3-030-04975-1_79)
- Tang, J., Bryant, D., Qi, H., Whiteside, B., & Babenko, M. (2018). Simplified three-dimensional finite element hot-spotting modelling of a pin-mounted vented brake disc: an investigation of hot-spotting determinants. *Proceedings of the Institution of Mechanical Engineers, Part D: Journal of Automobile Engineering*, 232(7), 877–895. <https://doi.org/10.1177/0954407017713080>
- Tirovic, M. (1998). Development of a wheel mounted disc brake for a high-speed train. *Proceedings of the Institution of Mechanical Engineers, Part F: Journal of Rail and Rapid Transit*, 212(2), 113–121. <https://doi.org/10.1243/0954409981530724>
- Tirovic, M., & Ali, G. (2001). Design synthesis of non-symmetrically loaded high-performance disc brakes Part 1.



- Proceedings of the Institution of Mechanical Engineers, Part F: Journal of Rail and Rapid Transit*, 215(2), 101–109. <https://doi.org/10.1243/0954409011531431>
- Tirovic, M., & Sarwar, G. A. (2004). Design synthesis of non-symmetrically loaded high-performance disc brakes part 3: Verification and optimization. *Proceedings of the Institution of Mechanical Engineers, Part F: Journal of Rail and Rapid Transit*, 218(2), 105–115. <https://doi.org/10.1243/0954409041319641>
- Wang, G., Liu, Z., Li, Y., & Chen, X. (2022). Different thermal fatigue behaviors between gray cast iron and vermicular graphite cast iron. *China Foundry*, 19(3), 245–252. <https://doi.org/10.1007/s41230-022-1204-1>
- Xie, X, Li, Z., Domblesky, J. P., Yang, Z., Liu, X., Li, W., & Han, J. (2021). Analysis of deep crack formation and propagation in railway brake discs. *Engineering Failure Analysis*, 128. <https://doi.org/10.1016/j.engfailanal.2021.105600>
- Xie, Xiaodong, Li, Z., Domblesky, J. P., Yang, Z., Liu, X., Li, W., & Han, J. (2021). Analysis of deep crack formation and propagation in railway brake discs. *Engineering Failure Analysis*, 128, 105600. <https://doi.org/10.1016/j.engfailanal.2021.105600>
- Yevtushenko, A., Kuciej, M., Grzes, P., & Wasilewski, P. (2021). Comparative analysis of temperature fields in railway solid and ventilated brake discs. *Materials*, 14(24), 7804. <https://doi.org/10.3390/ma14247804>
- Yu, L., Jiang, Y., Lu, S., Ru, H., & Fang, M. (2012). FEM for brake discs of SiC 3D continuous ceramic reinforced 7075 Aluminum alloy for CRH3 trains applying Emergency Braking. *Applied Mechanics and Materials*, 120, 51–55. <https://doi.org/10.4028/www.scientific.net/AMM.120.51>
- Zhang, P., Zhang, L., Fu, K., Wu, P., Cao, J., Shijia, C., & Qu, X. (2019). Fade behaviour of copper-based brake pad during cyclic emergency braking at high speed and overload condition. *Wear*, 428–429, 10–23. <https://doi.org/https://doi.org/10.1016/j.wear.2019.01.126>



## Synthesis and Characterization of Pores Bioactive Glass Nanomaterials for Bone Tissue Engineering

Fetene Fufa Bakare\*, Tsion Chuni, Tadele Hunde Wondimu

Department of Materials Science and Engineering, Adama Science and Technology University, Adama, Ethiopia, P.O. Box. 1888

\*Corresponding author, e-mail: [fetene.fufa@astu.edu.et](mailto:fetene.fufa@astu.edu.et)

### ABSTRACT

Bioactive glass (BG) is one of the most remarkable biomaterials in the field of biomedical applications due to owing properties such as, bioactivity, biodegradability, biocompatibility and etc., which mainly used for the applications of bone implants, dermal fillers and drug releasing carriers. Bioactive glass materials which contain pores spherical structure are the most predominant materials in the field of biomedical applications due to owing its superior properties such as, large porosity, higher specific surface area and possible applications for bone implants, sealing materials in dentistry and drug releasing carriers. Here we report an easily controllable continuous method to produce pores spherical bioactive glasses (PSBGs) microspheres. We used poly (ethylene glycol) (PEG), to produce pores spherical bioactive glasses (PSBGs) with controlled internal morphology using a spray pyrolysis method. Surface morphologies and inner structures of all bioactive glass (BG) powders were examined by scanning electron microscopy and transmission electron microscopy, respectively. In addition, the *in vitro* bioactivity was examined by SEM after soaking in stimulated body fluid (SBF). The *in vitro* bioactivity of BG powders was determined by evaluating their apatite-forming ability in simulated body fluid (SBF). The results showed that PSBGs possessed the better hydroxyapatite-forming capacity than SBGs. Therefore, the PSBG's have better *in vitro* bioactivity ability is critical for future tissue engineering development.

**Keywords:** bioactive glasses, electron microscopy, pores particles, spray pyrolysis

### 1. INTRODUCTION

Over last few decades' bioactive glasses (BGs) have received special attention in the applications of bone tissue, drug delivery, tooth implants, and dermal fillers (Bo Lei et al., 2011; Lei et al., 2010). Particularly, due to its own superior properties such as, bioactivity, biodegradability, biocompatibility, and osteoconductivity, which stimulate new tissue growth which is similar compositions with in the main inorganic components of human bones (Bakare et al., 2019; Bellucci et al., 2019; Hadush et al., 2019; Kaya & Boccaccini, 2018). Among these properties, the bioactivity have been received special attention extensively to enhance BG's performance (Wu & Chang, 2012). Then, to increase the formation of hydroxyl apatite (HA) factors such as composition, surface area and morphology were the main factors. It is well known that BG has the capability to form hydroxyl apatite (HA) layers once immersed in simulated body fluid (SBF), and the formation of HA is influenced by factors such as compositions (Hench, 2006; Xia & Chang, 2008) and surface areas (Mackovic et al., 2012).

Recently, in the fields of tissue reconstruction, designing biomaterials with multifunctional properties such as injectability, drugs delivery and bioactivity, is one of the most challenging goals (Kretlow et al., 2007; Rottensteiner et al., 2014). To the minimally invasive nature, injectable delivery systems in the fields of drug delivery and tissue engineering, and can fill tissue effects of irregular shape in bone regeneration (Paul & Sharma, 1999). To obtain injectable BGs, the flowability properties of particles are important to be extruded easily by a syringe. To enhanced the flowability properties of micrometer spheres make it easier to extrude BGs particles than irregularly shaped BGs particles (Paul & Sharma, 1999). As compared to irregularly shaped particles, the spherical morphology facilitates procedures of bone tissue regeneration, optimizes drug release and minimizes inflammatory reactions (Xu, Lei, & Yu, 2019). Then, to overcome those limitations and improve bioactivity of BGs particles, hollow spherical bioactive glasses particles have attracted, due to owing superior properties such as, higher specific surface area, lower density and large porosity (Sharma et al., 2015). Therefore, the BGs with hollow spherical particle is critical for future tissue engineering development. So far, several methods have been made to synthesize BG nanoparticles, such as sol-gel, spray drying and spray pyrolysis methods. However, little attention has been paid to synthesis of hollow spherical BG particles, which would be expected to improve their



bioactivity. In this study, we introduce an easy, economical, continuous, and controllable method of preparing hollow spherical bioactive glass using spray pyrolysis method in which the internal morphology of the bioactive glass is controlled using PEG (Ningsih et al., 2021; Shih et al., 2013).

In this work, the SP process was used for the preparation of both solid and pores spherical BG powder, in which PEG were used as pore-forming agent. The resulting powders were characterized by scanning electron microscopy (SEM), transmission electron microscopy (TEM) and the nitrogen adsorption/desorption method (Brunauer-Emmett-Teller (BET) method), for the observation of surface morphology, inner structure and the specific surface area, respectively.

## 2. MATERIALS AND METHODS

### 2.1. Powder Preparation

Two BG powders were synthesized using SP. Initially, BG precursors without pore forming agent were prepared using, Tetraethyl orthosilicate (TEOS,  $\text{Si}(\text{OC}_2\text{H}_5)_4$ , 99.9wt%, Showa, Japan), calcium nitrate tetrahydrate (CN,  $\text{Ca}(\text{NO}_3)_2 \cdot 4\text{H}_2\text{O}$ , 98.5wt%, Showa, Japan), and triethyl phosphate (TEP,  $(\text{C}_2\text{H}_5)_3\text{PO}_4$ , 99.0wt%, Alfa Aesar, USA) were used as the sources for Si, Ca, and P, respectively. The precursor solution was prepared by mixing 37.49 g tetraethyl orthosilicate (TEOS,  $\text{Si}(\text{OC}_2\text{H}_5)_4$ , 99.9 wt %, Showa, Osaka, Japan), 25.50 g calcium nitrate tetrahydrate (CN,  $\text{Ca}(\text{NO}_3)_2 \cdot 4\text{H}_2\text{O}$ , 98.5 wt %, Showa, Osaka, Japan), and 4.37 g triethyl phosphate (TEP,  $(\text{C}_2\text{H}_5)_3\text{PO}_4$ , 99 wt %, Alfa Aesar, Haverhill, MA, USA) into 60.00 g of ethanol with 1.60 g of 0.5 M HCl. Secondly, for PEG-derived BG particles, the precursor solutions were prepared by adding additional polyethylene glycol (PEG, 95.0 wt %, molecular weight of 600g/mol, Showa, Tokyo, Japan) Si, Ca, and P precursor mixture, were dissolved in 60.00g ethanol combined with 1.00g 0.5M HCl and stirred at room temperature for 24h to form the final precursor solution (Bakare et al., 2019).

For the SP process, the precursor solution was dispersed into fine droplets using an ultrasonic nebulizer (King Ultrasonic Co., Taiwan) at a frequency of 1.65 MHz. The droplets went through the thermal treatments of preheating, calcining, and cooling in a tube furnace (D110, Dengyng, Taiwan) at 250 °C, 550 °C, and 350 °C, respectively. The surfaces of the particles were charged by electrons released from tungsten corona wire at high voltage (16kV). After that, the negative-charged powders were neutralized and condensed in an earthed stainless-steel collection. In the SP process, the precursor solution was first atomized into small droplets while an air flow with a controlled flow rate carried the droplets into the heated tubular reactor with three heating zones of 200, 550, and 350 oC. In the reactor the droplets undergo solvent evaporation, solute precipitation, and precursor decomposition to convert into oxide particles. The resulting particles were then collected by a cylindrical electrostatic collector with an applied high-voltage potential of 16 kV.

### 2.2 Characterization

The two precursors were characterized by TGA (TGA, Perkin-Elmer Model TGA-7) under nitrogen flow to examine the decomposition temperature, in which the heating rate was 20 OC/min. BET method was used to measure the specific surface areas of all BG specimens. The specimens were degassed under 200 °C for 3 h and were transferred onto a nitrogen adsorption/desorption device (Novatouch LX2, Quantachrome Instruments, FL, USA) which recorded the isotherms at -196 °C. In addition, surface morphology, and inner structure were carried out by scanning electron microscopy (SEM) and transmission electron microscopy (TEM), respectively. Furthermore, bioactivity was determined by immersing the powders in SBF and evaluating the HA formation. Finally, the formation mechanisms of hollow spherical particles were described. TEM powders were prepared by dispersing the particles in acetone using an ultrasonic bath for around 5 min, and then depositing a drop of suspension onto holey carbon film grids. The solvent on the carbon grids was evaporated at room temperature.

## 3. RESULTS AND DISCUSSION

### 3.1 Thermal Analysis for BG Precursors

The TGA result of PEG, pure BG, and BG-derived PEG precursor were shown in Fig.1. As shown from Fig. 1a, at ~400 °C the sharp peak associated with mass loss for PEG in the particles. For pure BG precursors, as shown



in Fig.1b (inset 1) with the temperature ranges of ~50 to ~200 °C, and 550 to 800 °C can be attributed to dehydration, and formation of calcium oxide, respectively. In addition, Fig. 1b (inset 2) BG-derived PEG precursors showed that some PEG residues might be within particles, even at 400 °C temperature. The second mass loss stages at ~550 °C which is associated with the decomposition of  $\text{Ca}(\text{NO}_3)_2$ , and there is no PEG remaining in the particles at this temperature.

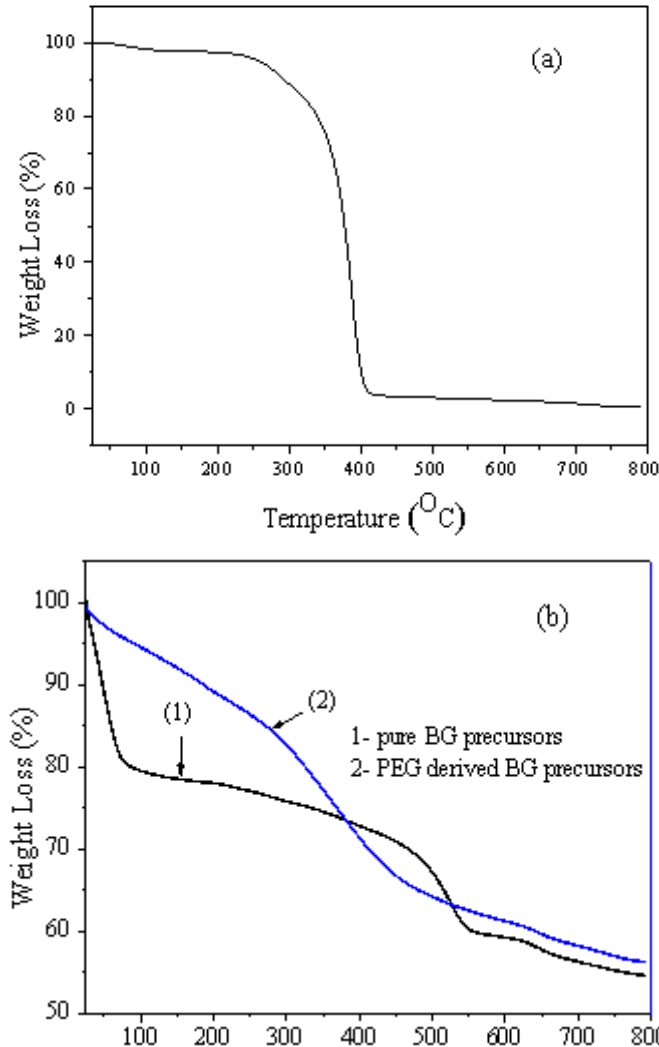


Fig. 1. The TGA data for the (a) PEG and (b) pure BG and BG-derived PEG precursors

Table 1. The specific surface area and pore volume comparison of pure BG and BG derived-PEG

Materials	Specific surface area (m <sup>2</sup> g <sup>-1</sup> )	Pore volume (cm <sup>3</sup> g <sup>-1</sup> )
Pure BG	41.2+0.1	0.22+0.01
BG derived- PEG	92.5+0.3	0.27+0.01

The specific surface area and pore volume for BG derived-PEG powders are 92.5+0.3 and 0.27+0.01 respectively, which are higher than those of pure BG (41.2+0.1 for specific surface area and 0.22+0.01 for pore volume) (Table 1). The surface morphology of both BG powders was observed using SEM images, as shown in Fig. 2. Fig. 2(a) shows that solid spherical BG powder were spherical and smooth surface morphology were obtained. Similarly, the SEM images of the BG derived-PEG powder also exhibited spherical and smooth surface morphology, as seen in Fig. 2(b).

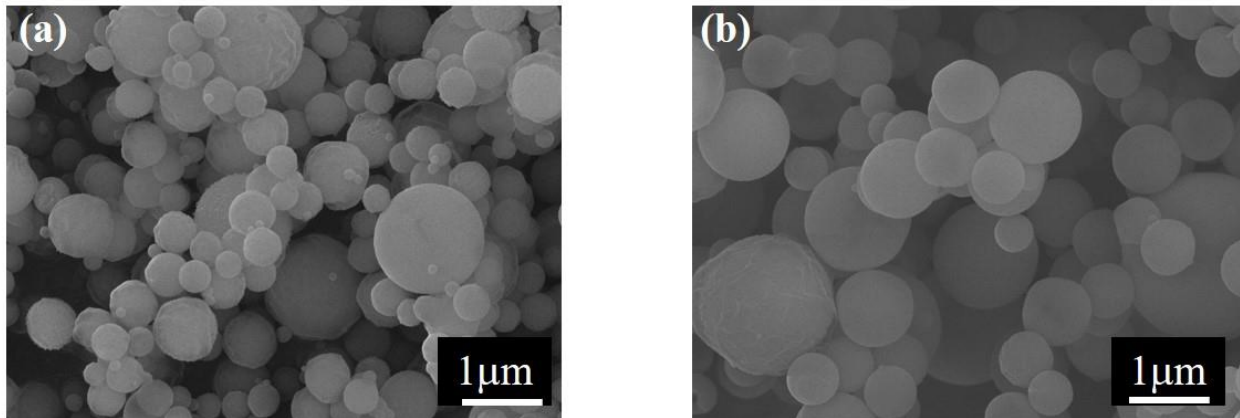


Fig. 2. SEM images of (a) pure BG powder and (b) BG derived-PEG powder

For the inner morphology, Fig. 3 shows the TEM images of both BG particles. For the pure BG powder shown in Fig. 3a, only the particles with continuous contrast were found, which indicates that there is no thickness variation within the particles. Thus, it can be recognized as a solid particle while Fig. 3b, within a hollow sphere that contains a single pore. In summary, by combining both SEM and TEM images, pure BG particles exhibit only one morphology of a solid sphere, whereas the BG derived-PEG particles exhibit of hollow structures.

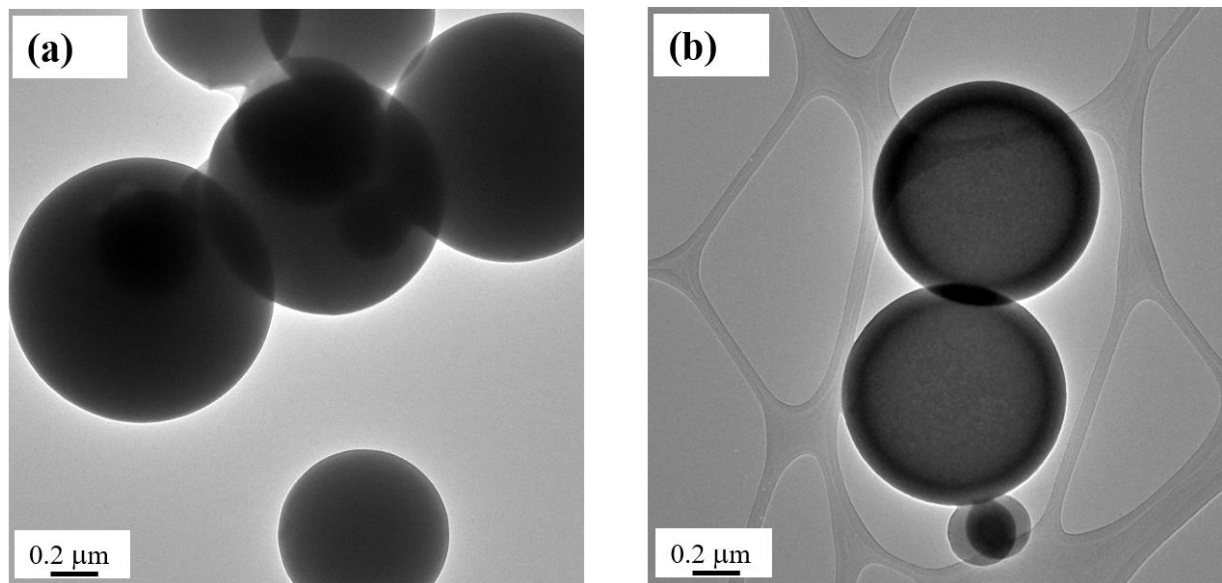


Fig. 3. TEM images of (a) solid BG particles and (b) hollow BG derived-PEG particles

Furthermore, for the evaluations of in vitro bioactivity both BGs powder were carried out after immersing in SBF for 24h. Fig. 4, shows the SEM images of both BG powders after immersing in SBF for 24h. It can be seen from the images that the formation of needle shaped was observed on the surface of each BGs powder. As shown from Fig. 4, (inset) the Ca/P ratio were calculated from SEM-EDS spectra, and the higher Ca/P ratio were obtained for BG derived-PEG powders compared to pure BG powders which induces better invitro bioactivity formation (Bakare et al., 2019).

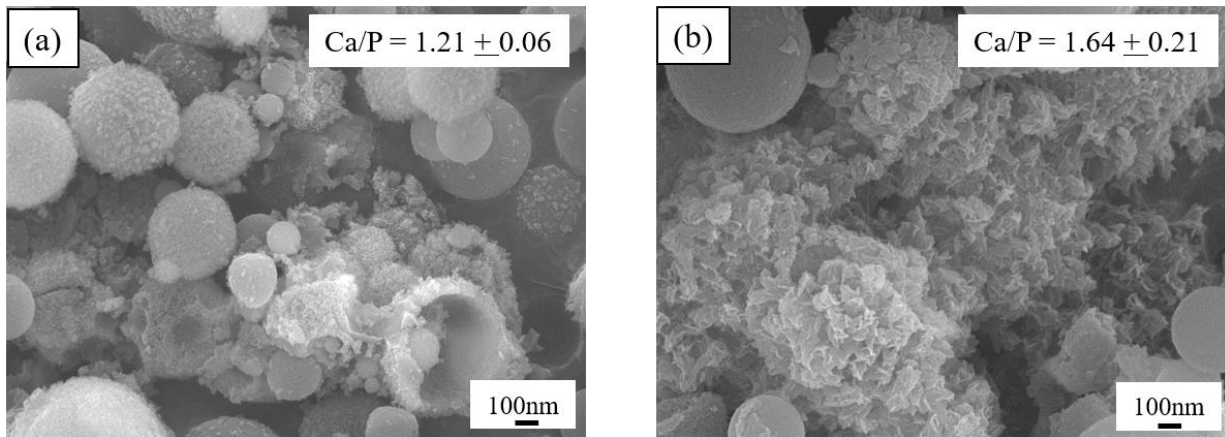


Fig. 4. SEM images of (a) pure BG powder and (b) BG derived-PEG powder after immersed in SBF for 12h

Based on the SEM images of as-prepared BG powders shown in Fig. 2, it has been demonstrated that the particle morphology is spherical for both BG powders. This is due to the typical particle formation mechanism of spray pyrolysis method, similar to the "one-particle per-drop" (Ningsih et al., 2021). Moreover, it can be seen from the TEM prepared BG powders shown in Fig. 3 that pure BG powders exhibit solid whereas BG derived-PEG powders exhibit hollow structures. The mechanism of hollow particle formation is expected to be sequential PEG decomposition, BG particles precipitation. Furthermore, temperature increases which can lead to pyrolysis of the PEG core, leaving the only the BGs shell, as shown in Fig. 5.

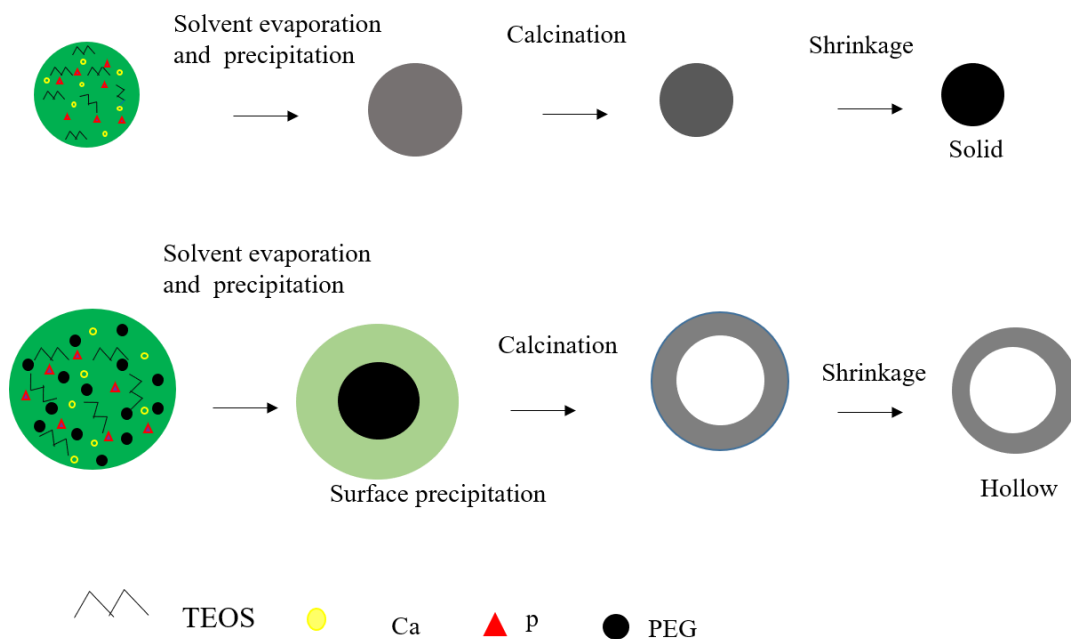


Fig. 5. The schematic diagram of the formation mechanism of the pure BG and BG derived -PEG powders

#### 4. CONCLUSIONS

In this study, hollow spherical BG particles were successfully synthesized by spray pyrolysis. The results showed that by adding pore-forming agent PEG, hollow spherical BG particle's structure were successfully formed within spray pyrolyzed BG nanoparticles. Compared to pure BG, BG derived-PEG powders hold the larger specific surface area and pore volume and performed an enhanced deposition rate of HCA layer. Thus, it can be concluded that BGs with hollow spherical particle is critical for future tissue engineering development. At last, the result also showed a simple method to control the surface reactivity and apatite-forming bioactivity of bioactive glasses for their efficient applications in bone tissue regeneration.



## ACKNOWLEDGMENTS

The authors acknowledge the financial support from Adama Science and Technology University, and National Taiwan University of Science and Technology.

## REFERENCES

- Bakare, F. F., Chou, Y. J., Huang, Y. H., Tesfay, A. H., Moriga, T., & Shih, S. J. (2019). Correlation of Morphology and In-Vitro Degradation Behavior of Spray Pyrolyzed Bioactive Glasses. *Materials (Basel, Switzerland)*, 12(22). doi:10.3390/ma12223703
- Bellucci, D., Salvatori, R., Giannatiempo, J., Anesi, A., Bortolini, S., & Cannillo, V. (2019). A New Bioactive Glass/Collagen Hybrid Composite for Applications in Dentistry. *Materials (Basel, Switzerland)*, 12(13), 2079. doi:10.3390/ma12132079
- Hadush Tesfay, A., Chou, Y.-J., Tan, C.-Y., Fufa Bakare, F., Tsou, N.-T., Huang, E. W., & Shih, S.-J. (2019). Control of Dopant Distribution in Yttrium-Doped Bioactive Glass for Selective Internal Radiotherapy Applications Using Spray Pyrolysis. *Materials (Basel, Switzerland)*, 12(6), 986. doi:10.3390/ma12060986
- Hench, L. L. (2006). The story of Bioglass. *J Mater Sci Mater Med*, 17(11), 967-978. doi:10.1007/s10856-006-0432-z
- Kaya, S., Cresswell, M., & Boccaccini, A. R. (2018). Mesoporous silica-based bioactive glasses for antibiotic-free antibacterial applications. *Materials Science and Engineering: C*, 83, 99-107. doi:https://doi.org/10.1016/j.msec.2017.11.003
- Kretlow, J. D., Klouda, L., & Mikos, A. G. (2007). Injectable matrices and scaffolds for drug delivery in tissue engineering. *Adv Drug Deliv Rev*, 59(4-5), 263-273. doi:10.1016/j.addr.2007.03.013
- Lei, B., Chen, X., & Koh, Y.-H. (2011). Effects of acidic catalysts on the microstructure and biological property of sol-gel bioactive glass microspheres. *Journal of Sol-Gel Science and Technology*, 58(3), 656-663. doi:10.1007/s10971-011-2441-8
- Lei, B., Chen, X., Wang, Y., Zhao, N., Du, C., & Fang, L. (2010). Surface nanoscale patterning of bioactive glass to support cellular growth and differentiation. *J Biomed Mater Res A*, 94(4), 1091-1099. doi:10.1002/jbm.a.32776
- Mackovic, M., Hoppe, A., Detsch, R., Mohn, D., Stark, W., Spiecker, E., & Boccaccini, A. (2012). Bioactive Glass (Type 45S5) Nanoparticles: In Vitro Reactivity on Nanoscale and Biocompatibility. *Journal of Nanoparticle Research*, 14. doi:10.1007/s11051-012-0966-6
- Ningsih, H. S., Bakare, F. F., Liu, Y.-c., & Chou, Y.-J. (2021). Preparation and characterization of spray-pyrolyzed porous SiO<sub>2</sub> nanoparticles for low dielectric constant applications. *Journal of the Australian Ceramic Society*, 57, 1301 - 1307.
- Paul, W., & Sharma, C. P. (1999). Development of porous spherical hydroxyapatite granules: application towards protein delivery. *J Mater Sci Mater Med*, 10(7), 383-388. doi:10.1023/a:1008918412198
- Rottensteiner, U., Sarker, B., Heusinger, D., Dafinova, D., Rath, S. N., Beier, J. P., . . . Arkudas, A. (2014). In vitro and in vivo Biocompatibility of Alginate Dialdehyde/Gelatin Hydrogels with and without Nanoscaled Bioactive Glass for Bone Tissue Engineering Applications. *Materials (Basel, Switzerland)*, 7(3), 1957-1974. doi:10.3390/ma7031957
- Sharma, M. K., Rohani, P., Liu, S., Kaus, M., & Swihart, M. T. (2015). Polymer and Surfactant-Templated Synthesis of Hollow and Porous ZnS Nano- and Microspheres in a Spray Pyrolysis Reactor. *Langmuir*, 31(1), 413-423. doi:10.1021/la5021675
- Shih, S.-J., Chou, Y.-J., & Borisenko, K. B. (2013). Preparation method: structure-bioactivity correlation in mesoporous bioactive glass. *Journal of Nanoparticle Research*, 15(6), 1-9. doi:DOI:101007/s11051-013-1763-6
- Wu, C., & Chang, J. (2012). Mesoporous bioactive glasses: structure characteristics, drug/growth factor delivery and bone regeneration application. *Interface focus*, 2(3), 292-306. doi:10.1098/rsfs.2011.0121
- Xia, W., & Chang, J. (2008). Preparation, in vitro bioactivity and drug release property of well-ordered mesoporous 58S bioactive glass. *Journal of Non-Crystalline Solids*, 354, 1338-1341. doi:10.1016/j.jnoncrysol.2006.10.084
- Xu, C., Lei, C., & Yu, C. (2019). Mesoporous Silica Nanoparticles for Protein Protection and Delivery. *Frontiers in chemistry*, 7, 290-290. doi:10.3389/fchem.2019.00290



## Performance Evaluation of Low-Emission Injera Baking Biomass Gasifier Stove

Assefa Tesfaye Hailu\*

Department of Mechanical Engineering, College of Engineering and Technology, Mattu University, 318, Mettu, Ethiopia

\*Corresponding author, e-mail: [asefaseng2003@gmail.com](mailto:asefaseng2003@gmail.com)

### ABSTRACT

The main goal of this study was to evaluate the performance of the biomass gasifier stove used to bake injera using *Eucalyptus Globulus* wood fuel as a feedstock. Its performance was affected by the wood fuel's physical and thermal properties; like particle size, biochar yield, burning rate, syngas composition, and tar content. The height and diameter of the designed gasifier stove were settled to be 50 cm and 40cm, respectively. The gasifier stove's temperature range for gasification was 657 to 840°C at 100% grate opening. Standard Control Cooking Test procedures were used to evaluate the gasifier stove's performance. The regression analysis was performed by using IDM SPSS software. The largest increase in biochar yield (12% to 19.8%) was obtained by varying biomass particle size from 8 to 30 mm; however, larger particles also triggered tar generation, which peaked at 93g/m<sup>3</sup> syngas at 30-mm biomass particles; in contrast, the hydrogen content and CO composition in syngas was at its lowest at this condition, 2.89% and 11.82%, respectively. The amount of tar present in the syngas was negatively correlated with the combustion temperature. Using 8mm-sized particles, a maximum combustion temperature of 840°C was attained. The burning time in the reactor using 6kg of fuel was 26 minutes. Results showed that heated air is more fuel-efficient for gasification and effective for reducing baking time. The Control Cooking Test indicated that the new gasifier reduces baking time and fuel usage by 32% and 50%, respectively, when compared to a three stone stove.

**Keywords:** air flow rate, gasifier stove, injera, moisture content, particle size

### 1. INTRODUCTION

A thermal process called gasification converts solid biomass fuel into combustible gases in a reactor with sub-stoichiometric air (Erakhrumen, 2012). Consideration of biomass resources for energy to address energy drivers has been promoted by several national and international challenges. Climate change-causing greenhouse gases, sustainability, rising energy prices, and the need for rural diversification are a few of them. Today, gasification has rekindled attention as a method to reduce emissions by functioning as a staged combustor and potentially generating syngas for both energy and chemical feedstock due to rising fuel prices and environmental concerns (Balcha, 2010). It uses a variety of feedstock, including wood, cow dung, charcoal, and agricultural waste to produce syngas. Wastes are also converted into carbon monoxide and hydrogen through a high-temperature reaction with a controlled volume of oxygen and/or air (WHO, 2006). To extract this syngas energy, it uses different types of feedstock such as wood, cow dung, charcoal, and agricultural residue and also converts wastes into carbon monoxide and hydrogen through a high-temperature reaction with a controlled amount of oxygen and/or air (Kamil & Demiss, 2017). Concerns about the release of CO<sub>2</sub> from burning fossil fuels have been made. There are three key reasons why fossil fuel burning needs to be reduced sustainably, environmental protection, climate change mitigation, and energy security. The energetic use of biomass fuel is one strategy to reduce the increasing amount of CO<sub>2</sub> in the atmosphere (Tesfaye & Khader, 2015).

In the new gasifier design, syngas is produced by supplying primary air through the grate hole 2cm in diameter and the liberated syngas will then flow through the cone to mitad support space. It should be efficiently burned with secondary air by supplying through the heated pipe and its sensible heat can be used for injera baking applications (Nega et al., 2022). Biomass can be converted into syngas using thermo-chemical processes such as pyrolysis, gasification, reforming, or combustion. The most efficient method for creating syngas from biomass is gasification (Benti et al., 2021; Negash et al. 2020). The main thermochemical, products of all these processes are divided into volatile fractions, which include tar, gas, and vapor components as well as a carbon-rich solid residue(Benti et al., 2021). At higher temperatures between 500 and 1400 °C (Nega et al., 2022). the gasification process is carried out in the presence of a gasifying agent (for instance, air, pure oxygen, steam, or combinations of these components (Assefa et al., 2022). Biomasses with a moisture content of less than 35% are appropriate



for the gasification process. The use of these feedstock's directly in the gasifier will result in significant energy losses in the entire process for biomass feedstock's with higher moisture contents, in the range of 25–60%. Before being fed into the gasifier, it was advised that the biomasses be preheated or dried to a moisture content of 10% to 20%. An effective method of transforming biomass into clean energy is biomass gasification (Gautam, 2010; Rivas, 2012). To get an appropriate gas product for industrial and power generation purposes, gasification procedures must be optimized. Gasification performance may be impacted by operational characteristics. Gasification parameters that can be changed to enhance gasification performance include biomass properties, gasification agent flow rate, gasification agent type, feed air temperature, reaction temperatures, and gasifier design (Ahmad et al., 2016; Gautam, 2010; Rivas, 2012). Since the water-shift reaction is enhanced at a lower temperature, the temperature drop produces more CO<sub>2</sub>. Because the little increase in H<sub>2</sub> is insufficient to make up for the loss of a substantial amount of CO with an increase in moisture content, the overall result is a fall in the calorific value of syngas (Ahmad et al., 2016; Chhnang, 2009). Specific heat capacity and heating values are impacted by this (Pieratti, 2011).

Traditional open fire stove initially consumes more wood fuel as a result of feeding technique errors and their large support size which requires more wood flame for heating and the flame affects women and men in the kitchen (Gebreegziabher et al., 2018). Hence, we need to design an insulated gasifier to solve this problem. The efficient sizing of the related components of the gasifier and parameters such as biomass feed door, air flow rate controlling part, moisture contents of wood fuel, and insulating are developed to enhance the performance of the gasifier (Assefa et al., 2022). This is selecting a syngas-producing biomass type and adjusting the air flow rate through the grate by the cover, improving the combustion of the gasifier (Manaye et al., 2022; Yosef, 2007). The Ethiopian Energy Studies Research Center created the Mirt injera stove in the early 1990's to decrease or solve this issue. This stove is being advertised and widely distributed in the nation since it is thought to be capable of up to 40% fuel efficiency and a total time reduction of 23% (Gebreegziabher et al., 2018). According to them, the findings of field tests show that an average household using an updated Mirt stove to bake injera saves roughly 570kg of fuel annually. Even though the stove is intended to last for roughly 4-5 years, the payback period for the purchaser is only about 2-3 months. According to the research done by (Assefa et al., 2022), it can reach an efficiency of 33%. The reaction temperature and biochar output were found to be strongly correlated in earlier research (Demirbas, 2004a; Vigouroux et al., 2002).

Researchers conducted pyrolysis studies with waste from tea, corn, and olives, increasing the reaction temperature from 450 °K to 1250 °K (Demirbas, 2004a, 2004b; Setter et al., 2021; Sizirici et al., 2021; Vigouroux et al., 2002). They discovered that when the temperature rose, the output of biochar fell for all types of biomass (Demirbas, 2004a; Murray & Johnels, 2013; Setter et al., 2021; Sizirici et al., 2021). Biomass fuels are used inefficiently in poorly ventilated kitchens resulting in indoor air pollution and consumption of large amounts of wood fuel. Micro-gasification cook stoves can improve fuel use efficiency and reduce indoor air pollution while producing char as a by-product (Gitau et al., 2019; Konieczna et al., 2022). The efficiency of conversion of biomass to biochar is highly dependent on the type of feedstock. The objective of the present study was to design a biomass gasifier stove for injera baking purposes and evaluate its performance. In addition, the effect of the physical and thermal properties of the wood fuel (Eucalyptus tree) on the performance of the gasifier was experimentally investigated.

## 2. MATERIALS AND METHODS

### 2.1. Instrumentation for Measurement

The weight of the wood fuel, the weight of char, and the weight of cooked food were measured using a digital precision balance (WA-2Y Model) made in China by Wan Jun Co., Ltd., with an accuracy of 0.01 grams and a maximum measurement capacity of 100 kg. The tape meter used to measure the size of the Eucalyptus wood chips (mm). It has a total length of 3m, with accuracy of 0.001m. The elemental gas Analyser (Elmer Perkin 2400, PerkinElmer: Waltham, MA, USA) used to measure the carbon, hydrogen, nitrogen, Sulphur, and oxygen values. The device has an accuracy of less than 1%. An infrared thermometer was used to measure the flame temperatures on top of the mitad. This instrument is manufactured by Testo instruments, which is based in Germany, and



precision of 0.5°C. The equipment used for measuring the temperatures on the top and bottom parts of the gasifier stove was the K-type digital thermocouples (made in Germany by Testo instruments), with a temperature range of -50°C-1000°C. The instrument has an accuracy of 0.1°C with proper calibration. The adiabatic bomb calorimeter (IKA-Calorimeter C200, IKA-werke GmbH and co.KG, staufen, Germany) is used for measuring the heating values. Stopwatch used to measure injera baking time from the beginning to the end. Moisture meter used for measuring wood fuel moisture in percentage.

## 2.2 Properties of Eucalyptus Globulus

The type of biomass fuel as a feedstock used for conducting this study was eucalyptus Globulus which is commonly used in most parts of Ethiopia. Figure 1 shows different sizes of Eucalyptus wood chips used to conduct the experimental analysis. Table 1 presents a summary of the main physical and thermal properties of the Eucalyptus Globulus biomass fuel as a feedstock. The ultimate and proximate analysis was conducted to examine the feedstock characteristics. The ultimate analysis was determined in CHNS/O elemental gas Analyser. The measured characteristics were moisture content (ASTM D3173-73), ash content (ASTM D3174-73), volatile matter (ASTM D3175-73), heating values, and bulk density. The fixed carbon value was determined by the percentage difference of Volatile matter. The lower and higher heating values were performed in an adiabatic bomb calorimeter using benzoic acid as a standard. Before loaded biomass fuel into the reactor, its moisture content should be measured by moisture meter. The moisture content should be less than or equal to 14%. The wood fuels are cut into pieces with an average particle size of 4, 8, 17 and 30 mm.



Figure 1. Pictorial representation of eucalyptus chopped fuels

Table 1: Properties of Eucalyptus Globulus

Property	Value
Particle Size (mm)	4-30
Length (mm)	8-60
C (%)	53.24
H (%)	6.36
O (%)	40.14
N (%)	0.12
S (%)	0.14
Moisture Content (%wb.)	14.00
Ash content (%db.)	11.28
Volatile matter (%db.)	59.36
Fixed carbon*(%db.)	16.96
Lower heating value (MJ/kg)	16.93
Higher heating value (MJ/kg)	19.53
Bulk density (kg/m <sup>3</sup> )/average particle size (mm)	207/4, 211/8, 196/17, 192/30

\*calculated by the percentage difference

The calculation of biochar yield, in (%) depends on the weight of the final biochar yield and the biomass weight. Eq. (1) presents the empirical formula of the biochar calculation.



$$\text{Biochar yield (\%)} = \frac{(DWC - MC)}{(DWB - MB)} * 100 \dots\dots\dots (1)$$

Where, *DWC* is the dry weight of biochar (g), *DWB* is the dry weight of biomass (g), *MC* is the moisture in biochar (g) and *MB* is the moisture content in biomass (g).

The burning rate was obtained by dividing the difference between the thermocouples  $T_{C1}$  and  $T_{C2}$  by the time that the peak combustion temperature moved from  $T_{C1}$  and  $T_{C2}$ . The burning rate calculation is presented in Equ. (2).

$$\text{Burning rate } \left(\frac{mm}{min}\right) = D_T / t \dots\dots\dots (2)$$

Where,  $D_T$  is the distance between thermocouple  $T_{C1}$  and  $T_{C2}$ , and  $t$  is the time for the flame to move from thermocouple  $T_{C1}$  to  $T_{C2}$  in minutes.

### 2.3 Experimental Setup

Figure 2 employed the photograph of the performed experiment, the front view, and top views of the gasifier stove. Figure 2 front view shows a biomass gasifier stove (BGS) used for injera baking purposes. The gasifier stove that produces syngas from wood biomass for injera baking applications was developed with a height of 50cm and diameter of 40cm with 1.5mm thick sheet metal. Ash is used as an insulator between the double strip sheets. The gasifier was integrated 60cm diameter of mitad by 12cm support height at the top as shown in Figure 2 front view. The wood biomass is issued through the feed door and it will gasify with primary air which is manually regulated through the grate hole that is integrated at the bottom of the reactor. Secondary air supplies to support space through the pipe burns syngas produced in the reactor. The heat from the wall of the gasifier heats the pipe and secondary air passing through it is also heated. This improves the burning rate of syngas in the support space and the temperature of the cooking mitad. The size of the gasifier was determined based on the average user height and diameter of the injera baking mitad. The total height is the sum of the gasifier leg, reactor, cone height, and mitad support. The volume of the reactor determines the amount of biomass fuel loading, biomass fuel consumption, and energy production. Temperature distribution on the surface of the mitad can be improved by adjusting the cone diameter at the top of the reactor through inspection Figure 2 front view, the diameter of the mitad support is greater than the diameter of the gasifier. The temperatures within the gasifier were measured with thermocouples at the top and bottom, as shown in Figure 2Figure front view. The combustion temperature was defined as the average peak temperature recorded on the two thermocouples. To determine the size of the gasifier, three holes were drilled on the bottom part of the support at an equal circumference distance with the diameter of the secondary air pipe, as shown in Figure 2 top view. As can be seen in Figure 2 top view, the gap between the three holes is the diameter of the reactor which is equal to 40cm. This is the reactor size in a circular shape where biomass was burned on the grate for syngas energy production. When performing the experiment, we should take all necessary precautions, such as avoiding combustible/flammable materials near the gasifier stove, wearing safety shoes, and wearing thick heat-resistant gloves made from cattle skin.

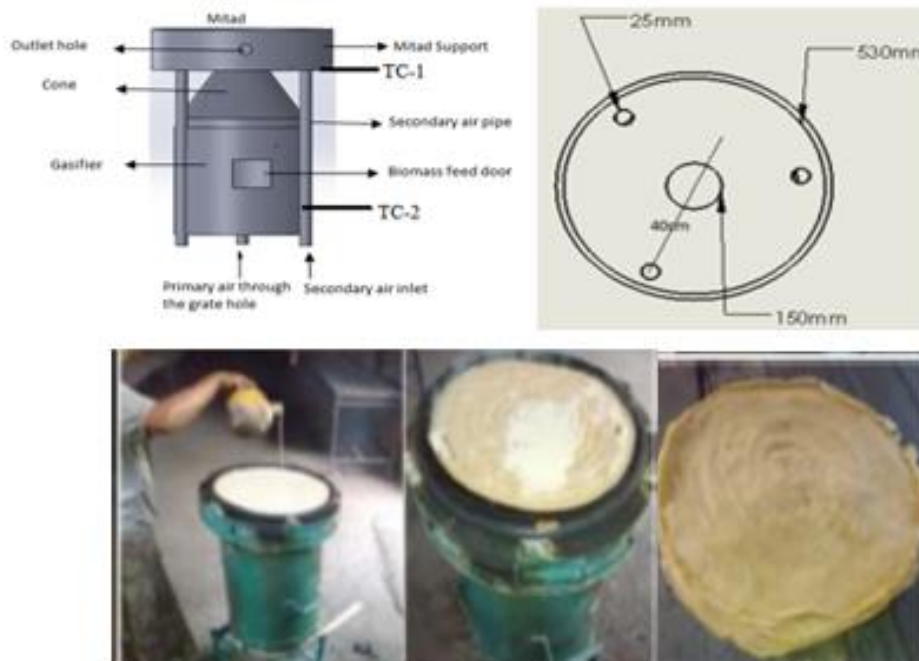


Figure 2. Biomass gasifier stove: front and top views

## 2.4 Air Flow Rate Controller

Primary air entering the reactor is managed manually by the slide grate cover. It is managed by restricting the grate's openings by sliding on the reactor end. At hole openings of 25%, 50%, and 100% (full grate), the impact of the airflow rate was examined. This technique of regulation is also utilized to maintain heat loss via the grate and shorten the gasification period once wood biomass ignition begins. The air-to-fuel ratio for complete combustion of wood fuel  $CH_{1.5}O_{0.69}N_{0.002}$  is 5.8kg/kg, according to the stoichiometric equation 5.8kg of air is needed for the full combustion of 1 kg of wood fuel. For 6 kg of wood fuel,  $5.8 \times 6 = 34.8$  kg/kg of air is required to complete combustion. By adjusting the cover, this quantity of air (5.8kg) will be decreased for the gasification of wood fuel. The mass ratio of the stoichiometric air-fuel mixture at a full grate hole opening is 5.8: 1. This suggests that for complete combustion, 5 kg of access air is needed. Reduce the amount of access air needed for gasification from 5kg to 4kg in a grate hole opening of 75%, 2kg at 50%, and 1kg at 25%. The amount of wood fuel used for the experiment should make the calculated air/fuel ratio below stoichiometric. For 1kg of wood fuel, 5.8kg/kg is stoichiometric. 6kg of wood biomass loaded in the reactor reduced 5.8 kg/kg air-fuel ratio below stoichiometric (that is 0.2). In gasification, the air-fuel ratio is below one.

## 2.5 Control-Cooking Test for Biomass Gasifier Stove

The control cooking test was created to accurately represent how the new gasifier stove performed when using conventional baking techniques. When preparing meals locally, it is utilized to evaluate the performance of the new stove in comparison to conventional stoves. To spot variations in the precise fuel consumption, it analyzes the exact wood consumption of various stoves with that of brand-new stoves while preparing identical amounts of food, components, and fuel (Yosef, 2007).

## 3. RESULTS AND DISCUSSION

### 3.1 The Impact of Biomass Particle Size

The performance of gasification was strongly impacted by biomass particle size. Figure 3 shows that the biochar yield drastically dropped from 19 to 12 % as the particle size rose from an average size of 4 to 8 mm. However, the output of biochar started to rise from 12 to 19.8 % as the particle size increased from 8 to 17 mm. Furthermore, the yield of biochar obtained with a higher particle size of 30 mm (19.9%) was not substantially different from this. It is important to note that the effect of biomass particle size on biochar yield can also be associated with the bulk density of the biomass. Biomass fuel with an average particle size of 4mm presented a



bulk density of 207 kg/m<sup>3</sup>, which increased to 211 kg/m<sup>3</sup> when the particle size was increased to an average of 8 mm. However, larger particle sizes presented decreasing bulk densities as indicated in Table 1. Less biomass fuel was concentrated as the bulk density dropped, and as a result, less fuel was produced during the devolatilization reactions. As a result, the temperatures during combustion dropped.

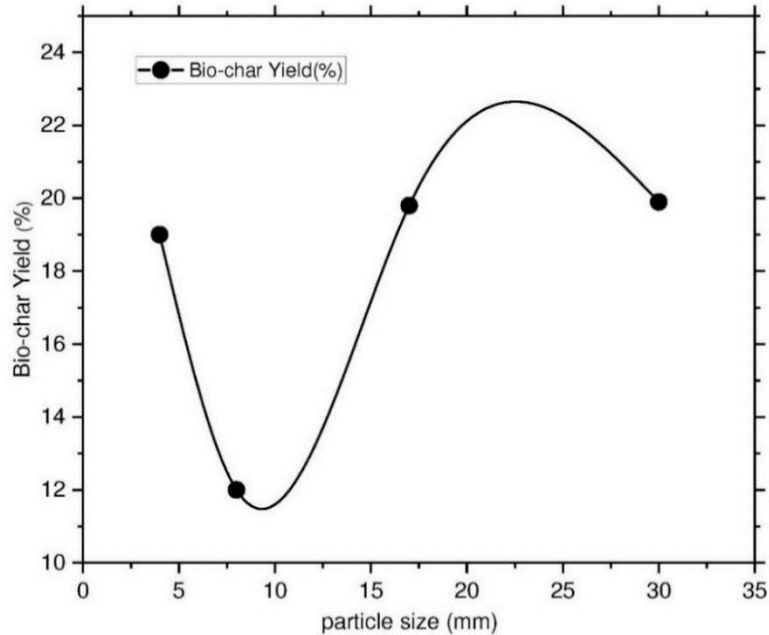


Figure 3. The bio-char yield of eucalyptus biomass fuel at varying particle sizes (moisture content of 14% and  $P < 0.05$ )

Figure 4 demonstrates a change in particle size from 4 to 8 and then 30 mm, the temperature increased from 657°C to 840°C and subsequently decreased to 614°C. It was clear that the production of biochar had a poor correlation ( $R^2 = 0.86$ ) with the temperature of the combustion zone. Although the temperature rose as seen in Figure 4, the burning rate (Figure 5) significantly decreased as the particle size rose from 4 to 8 mm, from 16.6 to 13.2 mm/min.

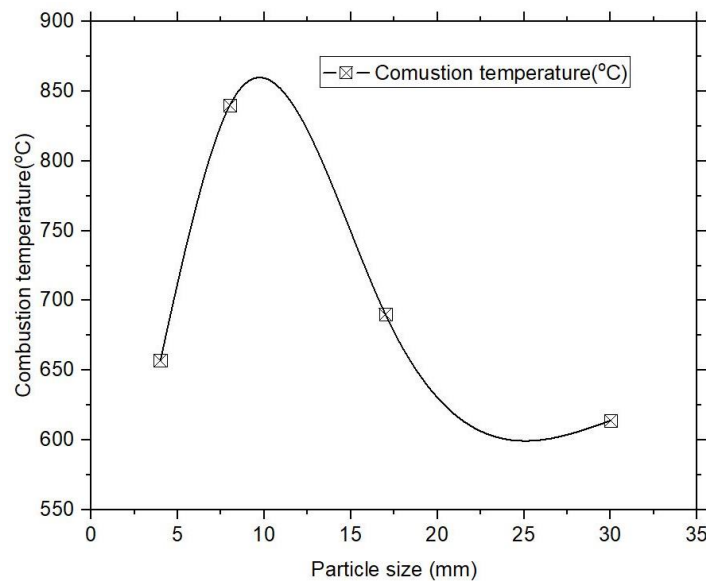


Figure 4. Combustion temperature of eucalyptus biomass fuel at varying particle size (moisture content 14% and  $P < 0.05$ )

When the particle size was further enlarged from (8 to 30 mm), the burning rate, on the other hand, tended to rise, rising from 13.2 to 20.3 mm/min, even though the temperature decreased as the particle size grew. This implied that the burning rate depended on the particle size in addition to the reaction temperature ( $R^2 = 0.54$ ) due to differences in biomass bulk density ( $R^2 = 0.74$ ), which was connected with the fire intensity. If the fire intensity and biomass bulk density are compared, biomass with a lower bulk density has a higher burning rate, whereas biomass with a larger bulk density has a lower burning rate. Additionally, there was an increase in the biochar yield due to the correlation between the biochar yield and burning rate ( $R^2 = 0.79$ ).

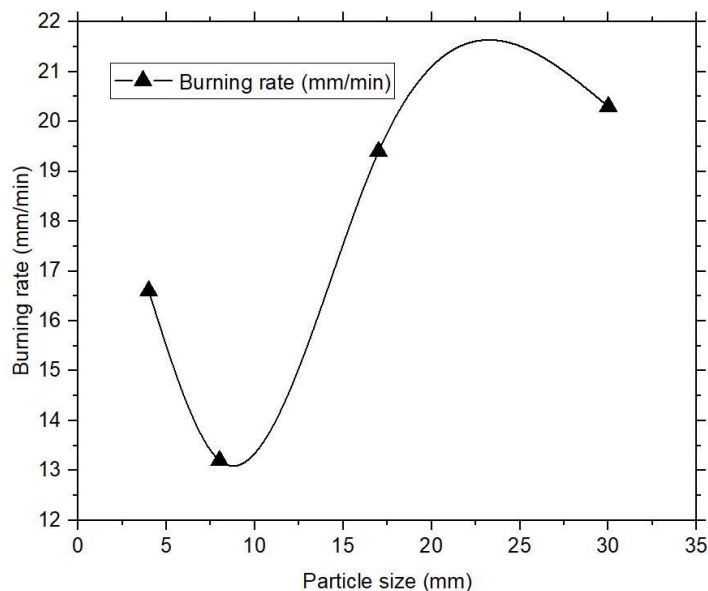


Figure 5. Burning rate of eucalyptus biomass fuel at varying particle sizes (moisture content 14% and  $P < 0.05$ )

The amount of tar in the syngas is depicted in Figure 6 by altering the particle size. The amount of tar in the syngas exhibited a negative relationship ( $R^2 = 0.77$ ) with the combustion temperature. A faster devolatilization resulted in increased tar production since the tar content of syngas was positively connected with the burning rate ( $R^2 = 0.69$ ). The tar concentration considerably decreased from 79.4 to 13 g/cm<sup>3</sup> (Figure 6) when the particle size rose from 4 to 8 mm due to the higher combustion temperature. However, the tar content in the syngas increased from 13 to 93 g/m<sup>3</sup> as the combustion temperature dropped at bigger particle sizes.

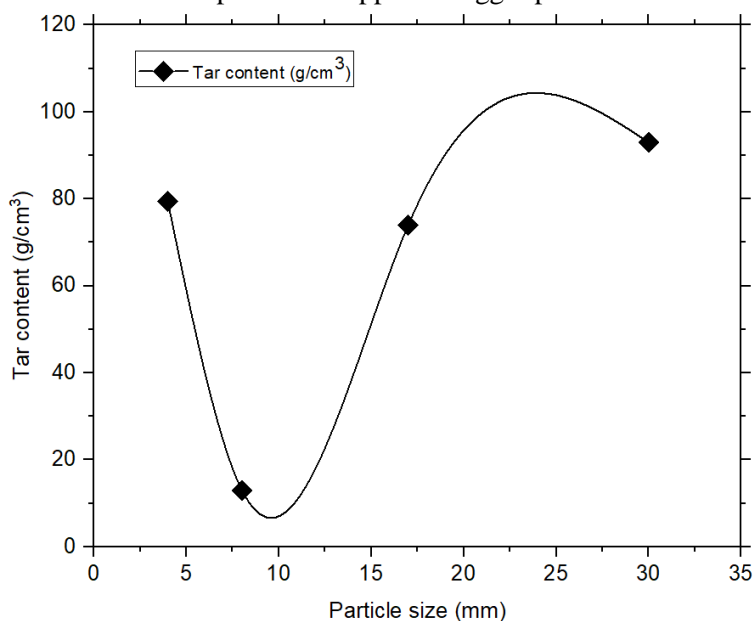


Figure 6. Tar content in syngas at various particle sizes (moisture content 14%,  $P < 0.05$ )



### 3.2 Effect of Particle Size on Syngas Composition

The impact of particle size on syngas composition is shown in Table 2. The hydrogen concentration of the syngas increased from 4.28% to 6.60% when the average particle size grew from 4 to 8 mm. However, there was very little variance in the content of carbon monoxide. Additionally, the content of hydrogen was drastically reduced from 6.60 to 2.88% and the composition of carbon monoxide was decreased from 15% to 11.82% by increasing the particle size from 8 to 30 mm. The greater heating value thus decreased from 3.65 to 2.72 MJ/m<sup>3</sup>.

Table 2. The impact of particle size on the composition of syngas

Particle size	H <sub>2</sub> (% v/v)	CO (%)	CO <sub>2</sub> (%)	CH <sub>4</sub> (%)	N <sub>2</sub> (%)	O <sub>2</sub> (%)	HHV (MJ/m <sup>3</sup> )
4	4.28±0.56	15.01±1.04	12.54±0.37	2.18±0.31	65.01±1.59	1.43±0.15	3.27±0.33
8	6.60±0.33	14.97±0.24	13.58±0.36	2.41±0.09	62.05±0.81	1.54±0.29	3.65±0.21
17	3.58±0.05	12.83±0.25	14.48±0.46	2.21±0.05	66.46±0.43	1.59±0.41	2.98±0.05
30	2.88±0.17	11.82±0.48	14.83±0.53	2.16±0.12	67.64±0.61	1.78±0.25	2.72±0.17

### 3.3 Effect of Airflow Rate on Gasification Temperature

Figure 7 depicts the airflow effect through grate hole openings that are 25, 50 and 100% (full grate hole openings). At a constant moisture content of 14%, the temperature variance in the reactor increases correspondingly when air input through the grate is increased. At 25% grate opening, the air is not sufficient for gasification. At full grate opening air and gasification temperature range 657-840°C, syngas flame was continued and stable in the reactor for 26 minutes. And gasifier produces high calorific value syngas which is easily burned with secondary air. Mitad succeeded temperature of 185°C. To preserve this continuity of syngas in the reactor, control air by cover after baking mitad temperature reach 185°C. As long as syngas continuity is maintained in the reactor, fuel consumption can be reduced (Ishaq & Dincer, 2019; Nega et al., 2022).

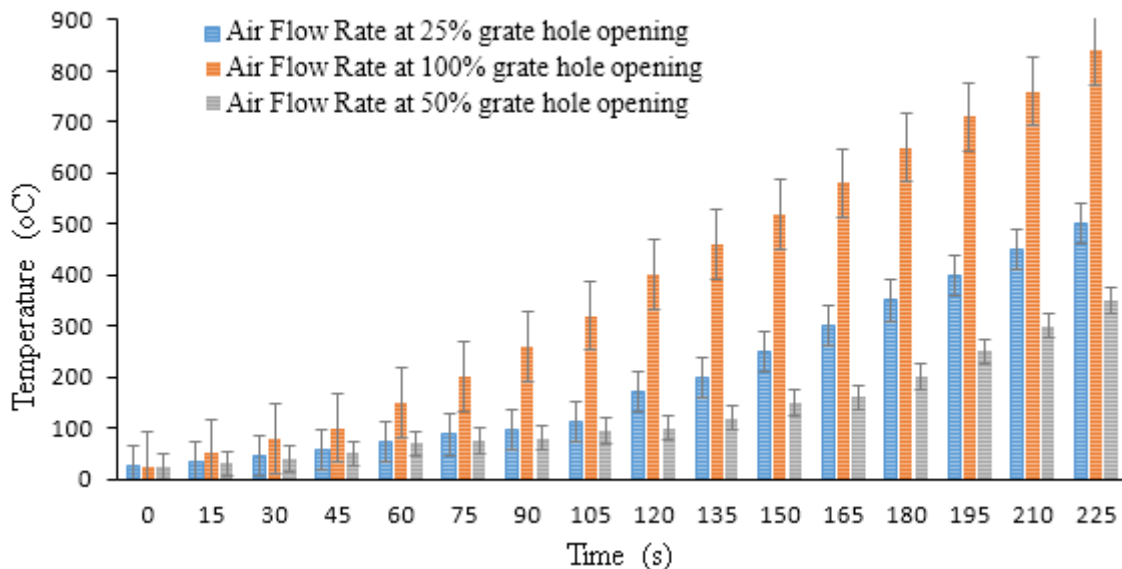


Figure 7. Effect of airflow rate on temperature (14% MC, P<0.05)

### 3.4. Result Validation with Published Literature Data

Table 3 represents the validation of the properties of Eucalyptus Globulus present work experimental values with previously published journals (Getahun et al., 2019; Hailu, 2022; Ishaq & Dincer, 2019). As can be seen in Table 3, the experimental results are in good agreement with previously published literature results for the elemental gas components C, H, O, S, N, and moisture content. The percentage difference between the present work and published work for literature 1 in carbon, hydrogen, oxygen, Sulphur, nitrogen and moisture content are 7.02, 5.66, 5.99, 100, 16.66 and 33.96%, respectively. This percentage difference may take place due to lack



of calibration, experimental irregularity, and Engineering data. The moisture content results for the present study are desirable because they are a little bit smaller compared with the results found in the previous studies.

Table 3. Comparison of the present work with previously published papers

S/N	Present work and literature values	Properties						Thermal Efficiency (%)
		C (%)	H (%)	O (%)	S (%)	N (%)	Moisture Content (%)	
1	Present work	53.24	6.36	40.14	0.14	0.12	14	37.4
2	Ishaq & Dincer (2019)	49.5	6	42.7	0.00	0.1	21.2	29.90
	%difference	7.02	5.66	5.99	100	16.66	33.96	-
3	Getahun et al. (2019)	47.54	5.8	43.23	0.00	0.61	10.00	22.5% for natural draft, 25% for forced draft
	% difference	10.70	8.80	7.69	100	19.3	28.57	-
4	Hailu (2022)	-	-	-	-	-	8.51	32.30±0.30%

### 3.5 Comparison of Baking Time and Fuel Saving of Open Fire Stove and Biomass Gasifier Stove

As seen in Figure 8, open-fire stoves require more time to cook food on average than gasifier stoves, which take 118 minutes. (7,080sec.). This is a result of issues with open fire stoves' wood fuel feeding techniques, flame continuity gaps, and starting time consumption. According to the results of the Control Cooking Test (CCT) in Table 4, the net performance efficiency of gasifier stoves in terms of time and wood fuel savings as compared to open fire stoves is 50% and 32%, respectively. This cost-saving was discovered when the new gasifier and open-fire stove were both burned at their maximum rates of 6 kg per hour for each test's one baking cycle.

Table 4. Results of control cooking Test (CCT) comparing two stoves

CCT results of open-fire stove	Units	Test 1	Test 2	Test 3	Mean	St.Dev.
Total weight of food cooked	g	1,323	1,218	1344	1295	67
Weight of char remaining	g	450	657	600	569	106
Equivalent dry wood consumed	g	1,412	1,390	1,410	1,404	12
Specific fuel consumption	g/kg	2,864	2,760	2,890	2,838	68
Total cooking time	Min.	118	120	116	118	2
CCT Results of new biomass gasifier stove	Units	Test 1	Test 2	Test 3	Mean	St.Dev
Total weight of food cooked	g	1302	1270	1370	1314	51
Weight of char remaining	g	300	350	300	317	29
Equivalent dry wood consumed	g	1911	1752	1911	1858	92
Specific fuel consumption	g/kg	1468	1379	1395	1414	47
Total cooking time	Min.	79	82	79	80	2
Comparison of the two stoves	Units	% difference	T-test	Sig.@95%		
Specific fuel consumption	g/kg	50%	11.81	Yes		
Total cooking time	Min.	32%	8.43	Yes		

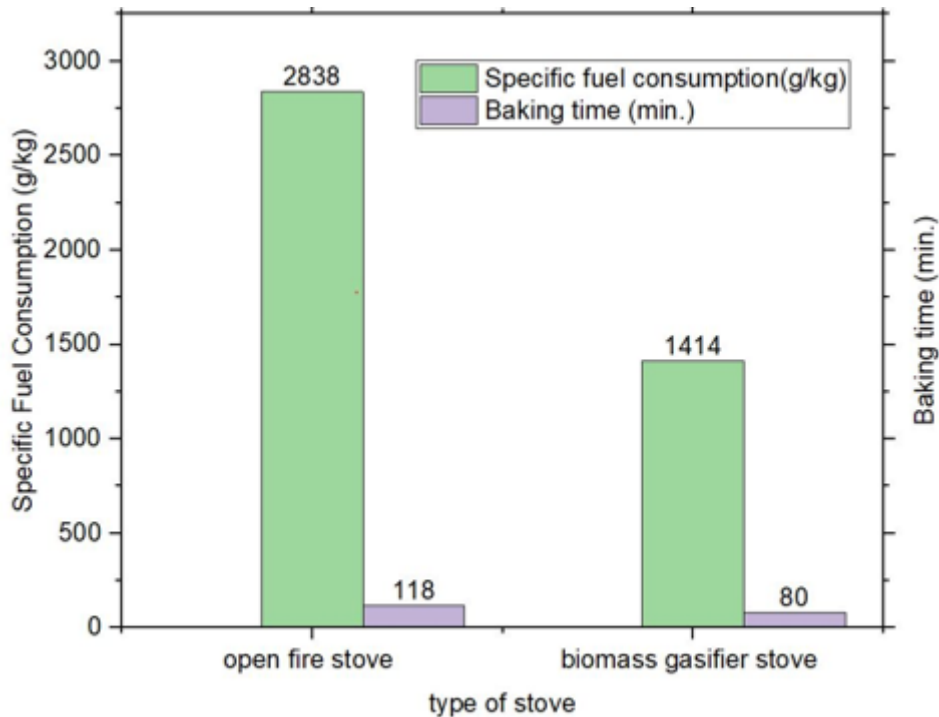


Figure 8. Comparison of time and fuel consumption saving of gasifier and open fire stove

An open-fire stove typically uses 2,838 g/kg of specified fuel, whereas a gasifier uses 1,414 g/kg. By adjusting the air flow rate provided through the grate by the controller, fuel consumption in the gasifier stove was reduced. Once the air-fuel ratio falls below stoichiometric, syngas flame continuity would be maintained, and gasification could be improved. In an open-fire stove, once the wood fuel has begun to burn, a significant amount of continuous airflow bends the fire flame's vertical orientation away from the pot surface. The front of the mitad experiences temperature variations during baking. It is how the flame exits as a loss through outlets and edges. Open fire stoves, therefore, need more wood fuel. The open-fire stove and the gasifier stove's control cooking test results are shown in Table 4.

#### 4. CONCLUSIONS AND RECOMMENDATIONS

A laboratory-scale biomass gasifier stove for injera baking purposes was designed, manufactured, and evaluated for its performance. Biomass fuel such as the eucalyptus tree was used as a feedstock. The gasifier stove's performance was found to be influenced by the wood's particle size, moisture content, burning rate, and syngas composition. The gasifier stove was developed with a height and diameter of 50cm and 40cm respectively. The gasifier was integrated 60cm diameter of mitad by 12cm support height at the top. The performance of the gasifier stove was determined using standard Control cooking test (CCT) methods using eucalyptus as a feedstock. At full grate opening air, the range of gasification temperature of the gasifier stove was 657-840°C. At a larger particle size of 30mm, a higher biochar yield of 19.9% was obtained. Additionally, tar production peaked at 93 g/cm<sup>3</sup> syngas due to larger particles. The biomass's addition of moisture resulted in a slower rate of combustion, which increased the use of carbon and reduced the generation of biochar. The moisture content also greatly reduced the amount of tar in the syngas due to reforming and cracking reactions that were helped by the excess water and abundant carbon in the reactor. In comparison to typical gasification processes, the examined injera baking process produced syngas with significantly lower hydrogen gas and carbon monoxide levels. When compared to the existing open-fire stove, it has been shown that the new gasifier reduces baking time and fuel consumption by 32% and 50%, respectively. The effect of the insulator on gasification temperature change is suggested to be done as further work.

**NOMENCLATURE**

BGS	Biomass Gasifier Stove
CCT	Control Cooking Test
CO	Carbon Monoxide (% v/v)
CO <sub>2</sub>	Carbon Dioxide (% v/v)
H <sub>2</sub>	Hydrogen Molecule (% v/v)
CH <sub>4</sub>	Methane Molecule (% v/v)
N <sub>2</sub>	Nitrogen Molecule (% v/v)
db.	dry bulb (%)
wb.	wet bulb (%)
R <sup>2</sup>	Correlation Coefficient
P	Significance Level
ASTM	American Standard of Testing and Materials

**REFERENCE**

- Ahmad, A. A., Zawawi, N. A., Kasim, F. H., Inayat, A., & Khasri, A. (2016). Assessing the gasification performance of biomass: A review on biomass gasification process conditions, optimization and economic evaluation. *Renewable and Sustainable Energy Reviews*, 53, 1333-1347.
- Balcha, D. A. (2010). Numerical Modeling of Small-scale Biomass Straw Gasifier. Retrieved from <https://books.google.com.et/books?id=bt0sngEACAAJ>
- Benti, N. E., Gurmesa, G. S., Argaw, T., Aneseyee, A. B., Gunta, S., Kassahun, G. B., . . . Asfaw, A. A. (2021). The current status, challenges and prospects of using biomass energy in Ethiopia. *Biotechnology for Biofuels*, 14(1), 209. Retrieved from <https://doi.org/10.1186/s13068-021-02060-3> doi:10.1186/s13068-021-02060-3
- Chhngang, K. (2009). Promotion of the Efficient Use of Renewable Energies in Developing Countries.
- Demirbas, A. (2004a). Effects of temperature and particle size on bio-char yield from pyrolysis of agricultural residues. *Journal of analytical and applied pyrolysis*, 72(2), 243-248. Retrieved from
- Demirbas, A. (2004b). Effects of temperature and particle size on bio-char yield from pyrolysis of agricultural residues. *Journal of analytical and applied pyrolysis*, 72(2), 243-248.
- Demirbaş, A. (2004). Effects of Temperature and Particle Size on Bio-Char Yield From Pyrolysis of Agricultural Residues. *Journal of Analytical and Applied Pyrolysis*, 72, 243-248. doi:10.1016/j.jaap.2004.07.003
- Erakhrumen, A. A. (2012). Biomass Gasification: Documented Information for Adoption/Adaptation and Further Improvements toward Sustainable Utilisation of Renewable Natural Resources. *ISRN Renewable Energy*, 2012, 536417. Retrieved from <https://doi.org/10.5402/2012/536417> doi:10.5402/2012/536417
- Gautam, G. (2010). *Parametric study of a commercial-scale biomass downdraft gasifier: experiments and equilibrium modeling*.
- Gebreegiabher, Z., Beyene, A., Bluffstone, R., Martinsson, P., Mekonnen, A., & Toman, M. (2018). Fuel Savings, Cooking Time and User Satisfaction with Improved Biomass Cookstoves: Evidence from Controlled Cooking Tests in Ethiopia. *Resource and Energy Economics*, 52. Retrieved from doi:10.1016/j.reseneeco.2018.01.006
- Getahun, E., Tessema, D., & Gabbiye, N. (2019). Design and development of household gasifier cooking stoves: natural versus forced draft. *Advances of Science and Technology: 6th EAI International Conference, ICAST 2018, Bahir Dar, Ethiopia, October 5-7, 2018, Proceedings* 6, 298-314. Retrieved from
- Gitau, J. K., Sundberg, C., Mendum, R., Mutune, J., & Njenga, M. (2019). Use of Biochar-Producing Gasifier Cookstove Improves Energy Use Efficiency and Indoor Air Quality in Rural Households. *Energies*, 12(22), 4285. Retrieved from <https://www.mdpi.com/1996-1073/12/22/4285>
- Hailu, A. (2022). Development and performance analysis of top lit updraft: natural draft gasifier stoves with various feed stocks. *Heliyon*, 8(8), e10163. Retrieved from <https://www.sciencedirect.com/science/article/pii/S2405844022014517> doi:<https://doi.org/10.1016/j.heliyon.2022.e10163>
- Ishaq, H., & Dincer, I. (2019). Design and performance evaluation of a new biomass and solar based combined system with thermochemical hydrogen production. *Energy Conversion and Management*, 196, 395-409. Retrieved from doi:10.1016/j.enconman.2019.05.100



- James Rivas, A. M. C. (2012). The effect of biomass, operating conditions, and gasifier design on the performance of an updraft biomass gasifier. Retrieved from
- Kamil Dino, A., & Demiss Alemu, A. (2017). Performance and emission reduction potential of micro-gasifier improved through better design. *AIMS Energy*, 5(1), 63-76. Retrieved from <https://www.aimspress.com/article/doi/10.3934/energy.2017.1.63> doi:10.3934/energy.2017.1.63
- Konieczna, A., Mazur, K., Koniuszy, A., Gawlik, A., & Sikorski, I. (2022). Thermal Energy and Exhaust Emissions of a Gasifier Stove Feeding Pine and Hemp Pellets. *Energies*, 15(24), 9458. Retrieved from <https://www.mdpi.com/1996-1073/15/24/9458>
- Manaye, A., Amaha, S., Gufi, Y., Tesfamariam, B., Worku, A., & Abrha, H. (2022). Fuelwood use and carbon emission reduction of improved biomass cookstoves: evidence from kitchen performance tests in Tigray, Ethiopia. *Energy, Sustainability and Society*, 12(1), 28. Retrieved from <https://doi.org/10.1186/s13705-022-00355-3> doi:10.1186/s13705-022-00355-3
- Murray, S., & Johnels, E. (2013). *Performance Evaluation of the FirePipe Cookstove with focus of its Product Development*. (Independent thesis Basic level (degree of Bachelor) Student thesis), Retrieved from <http://urn.kb.se/resolve?urn=urn:nbn:se:kth:diva-123948> DiVA database.
- Nega, T., Habtu, N. G., Tesfaye, A., Melesse, G. T., & Aswossie, E. (2022). Biomass energy conversion in a gasifier for injera baking mitad application. *Heliyon*, 8(12), e12128. Retrieved from <https://www.sciencedirect.com/science/article/pii/S2405844022034168> doi:<https://doi.org/10.1016/j.heliyon.2022.e12128>
- Nega, T., Tesfaye, A., & Paramasivam, P. (2022). Design and CFD modeling of gasifier stove combined with heat exchanger for water heating application. *AIP Advances*, 12(4), 045121. Retrieved from doi:10.1063/5.0081001
- Negash, D., Abegaz, A., & Smith, J. (2020). Environmental and Financial Benefits of Improved Cookstove Technologies in the Central Highlands of Ethiopia. *SSRN Electronic Journal*. Retrieved from doi:10.2139/ssrn.3751276
- Pieratti, E. (2011). *Biomass gasification in small scale plants: experimental and modelling analysis*. University of Trento,
- Setter, C., Ataíde, C. H., Mendes, R. F., & de Oliveira, T. J. P. (2021). Influence of particle size on the physico-mechanical and energy properties of briquettes produced with coffee husks. *Environ Sci Pollut Res Int*, 28(7), 8215-8223. Retrieved from doi:10.1007/s11356-020-11124-0
- Sizirici, B., Fseha, Y. H., Yildiz, I., Delclos, T., & Khaleel, A. (2021). The effect of pyrolysis temperature and feedstock on date palm waste derived biochar to remove single and multi-metals in aqueous solutions. *Sustainable Environment Research*, 31(1), 9. Retrieved from <https://doi.org/10.1186/s42834-021-00083-x> doi:10.1186/s42834-021-00083-x
- Strategy, E. R. B. S.-s. March 2003. Ethiopian Rural Energy Development and Promotion Center. *Biomass Technology Group BTG. BV*. Retrieved from
- Tesfaye, A., Habtu, N. G., & Wang, Q. (2022). Fabrication and Performance Evaluation of Solar Tunnel Dryer for Ginger Drying. *International Journal of Photoenergy*, 2022, 1-13. Retrieved from <https://doi.org/10.1155/2022/6435080> doi:10.1155/2022/6435080
- Tesfaye, A., & Khader, M. A. (2015, 14-17 Sept. 2015). *Strategies for promoting the use of renewable energy in Ethiopia*. Paper presented at the AFRICON 2015.
- Tesfaye, A., Workie, F., & Kumar, V. S. (2022). Production and Characterization of Coffee Husk Fuel Briquettes as an Alternative Energy Source. *Advances in Materials Science and Engineering*, 2022, 9139766. Retrieved from <https://doi.org/10.1155/2022/9139766> doi:10.1155/2022/9139766
- Vigouroux, R., Sjöström, K., & Björnbom, E. (2002). Rapid Pyrolysis of Agricultural Residues at High Temperature. *Biomass and bioenergy*, 23, 357-366. Retrieved from doi:10.1016/S0961-9534(02)00061-2
- WHO, G. (2006). Fuel for life: household energy and health.
- Yosef, A. (2007). Assessing environmental benefits of mirt stove with particular reference to indoor air pollution (Carbon Monoxide & Suspended Particulate Matter) and energy conservation. *Unpublished Msc thesis, Addis Ababa University*.



## Syndicate 2



## Steady State Experimental Study on the Advanced Stationary Engine Combustion Mode Operation (RCCI)

Habtamu Deresso Disassa<sup>1,\*</sup>, Venkata Ramayya Ancha<sup>2</sup>, Ramesh Babu Nallamothu<sup>1</sup>

<sup>1</sup>Department of Mechanical Engineering, Adama Science and Technology University, Adama, Ethiopia

<sup>2</sup>Department of Mechanical Engineering, Jimma University Institute of Technology, Jimma, Ethiopia

\*Corresponding author, e-mail: [habtamu.deresso@astu.edu.et](mailto:habtamu.deresso@astu.edu.et)

### ABSTRACT

To improve engine combustion efficiency and reduce emissions, numerous low-temperature combustion (LTC) methods have been put forth. The RCCI combustion mode favored lower oxide of nitrogen and PM emissions by controlling the ignition and combustion process, but it had not yet found the optimal answer. For RCCI operations, the intake system is adjusted to use port injection for emissions, combustion phasing, and in-cylinder charge reactivity control. In this work, an experimental inquiry is conducted on a dual blended port-injected RCCI engine that runs on port-injected mixes of gasoline-ethanol, with direct injection of diesel fuel. The results of the G10E10-RCCI engine operation mode have a maximum cylinder pressure of 70.8 bars at 2300-RCCI and a minimum of 59.84 bars at 2700 rpm on baseline fuel. The maximum HRR of the engine is 66 J/CA at the engine speed of 2700-RCCI and a minimum at baseline with an HRR of 8.58 J/deg. The maximum normalized pressure (NVP) of the engine is 72.3 bar at the engine speed of 2300-RCCI and a minimum of 59.65 at 2700 baseline. The brake power of the engine is maximum at both speeds of the RCCI engine and lower in both baselines. The brake torque is maximum at 2300-RCCI which is 15.23N-m with the engine running with a G10E10-RCCI engine and minimum (14.16N-m) at a speed of 2300 baseline. At 80% engine load operation, the baseline engine had better thermal efficiency (28.94%), and minimum at the speeds of 2700-RCCI (26%) brake thermal efficiency. NO<sub>x</sub> and CO<sub>2</sub> increase in all cases of a diesel engine operating and minimum in the cases of RCCI and both speed cases and the reverse for HC and CO in all baseline and G10E10-RCCI engine combustion modes.

**Keywords:** LTC, NO<sub>x</sub>, PFI, RCCI, Speed

### 1. INTRODUCTION

Worldwide, strict laws are being implemented to restrict engine emissions in an effort to lessen the pollution they cause to the environment. The development of after treatment systems and the reduction of engine-out emission are the two main strategies that the automotive scientific community is concentrating on in order to lessen engine pollution. In an effort to lower engine-out emissions, scientists are developing novel combustion theories [1]. A possible low temperature combustion (LTC) idea to provide extremely clean and effective combustion is called RCCI [2]. The efficiency of diesel combustion technologies from an ecological standpoint and in light of the energy crisis are the driving motivations behind this research [3, 4]. LTCs, such as ignition through pre-mixed charge compression (PCCI) [5, 6], partially pre-mixed charge ignition (PPCI) [7], and homogenous charge compression ignition (HCCI) [8] have been proposed to increase combustion efficiency and lower the emissions. The ratio of the two fuels with flexible reactivity one is port injected, and the other is directly injected is controlled by the reactivity-control compression ignition (RCCI) engine [9] in order to regulate the combustion process [10, 11]. Compression ignition engines often have greater compression ratios (CR) [12], leaner charges [13], and lower throttle losses [14, 15] as compared to spark ignition engines. On the other hand, emissions of NO<sub>x</sub> and particulate matter (PM) were significantly elevated by compression ignition engines. According to both existing and upcoming legislation, reviews of RCCI engine management vehicles must adhere to strict criteria for both pollution and fuel efficiency [4]. Due to these issues, sophisticated internal combustion engine technology as well as fuel alternatives to fossil fuels that can lower pollutants were developed [16]. Several frontline techniques have been studied to reduce emissions in a cylinder while preserving thermal efficiency [17, 18]. Most current techniques fall within the category of LTC engines [19, 20].

It showed that NO<sub>x</sub> and PM emissions from RCCI engine combustion are low, but further research is still needed to fully understand these emissions in order to achieve the higher recommended emission efficiencies. Most previous RCCI research exclusively tested low reactivity fuels (LRFs) such as ethanol, methanol, gasoline,

NG, and CNG. For direct injection (DI) in an engine that has been upgraded RCCI, high reactivity fuel (HRF) such as diesel and biodiesel fuel is utilized. However, a study is necessary because previous research using only gasoline or premixed alcohol has shown substantial CO and UHC emissions [20, 21]. The unique port-injected fuel RCCI testing findings shown that ultra-low engine-out emissions (NO<sub>x</sub> and PM) may be achieved simultaneously, despite higher CO and UHC emissions. Consequently, it is critical to evaluate ethanol-gasoline blends (EGB) in a current RCCI LTC concept that permits injection into the intake manifold. This study looks into the emissions, performance, and combustion of a diesel engine running on diesel direct injection and port-injected EGB. Diesel fuel is immediately pumped into the intake manifold together with a combined gasoline and ethanol fuel supply to boost fuel responsiveness. The study also aims to lower NO<sub>x</sub> and PM by replacing fossil fuels with sustainable ethanol and to find the operating conditions for optimized CO and HC [20, 22].

## 2. MATERIALS AND METHODS

### 2.1. Test Rig Engine Arrangement

As seen in Fig.1 baseline and advanced test rig engines are equipped with a data collecting system connected to a dynamometer with a detailed interpretation. The baseline experiment is performed using a CT100.23 CT110 horizontally mounted, naturally aspirated, water-cooled, single-cylinder, DI diesel engine of 0.309 liters and the specification listed in Table 1. The same engine converted to an advanced (RCCI) engine was used in the second experiment. PFI control is done by a microcontroller on Arduino board. Table.1 also illustrates the physiochemical characteristics of the gasoline, diesel, and ethanol fuels utilized in the experiment. Diesel fuel is supplied to the engine via direct injection, while low reactivity (ethanol-gasoline blended) fuel is injected into the intake manifold using port fuel injection to lengthen the reaction time. In the process of investigating combustion, performance, and emissions, the 80% maximum load, two speeds, and fuel ratios are used as variables to identify the combustion phase, at which efficiency is optimal and emission is minimal.

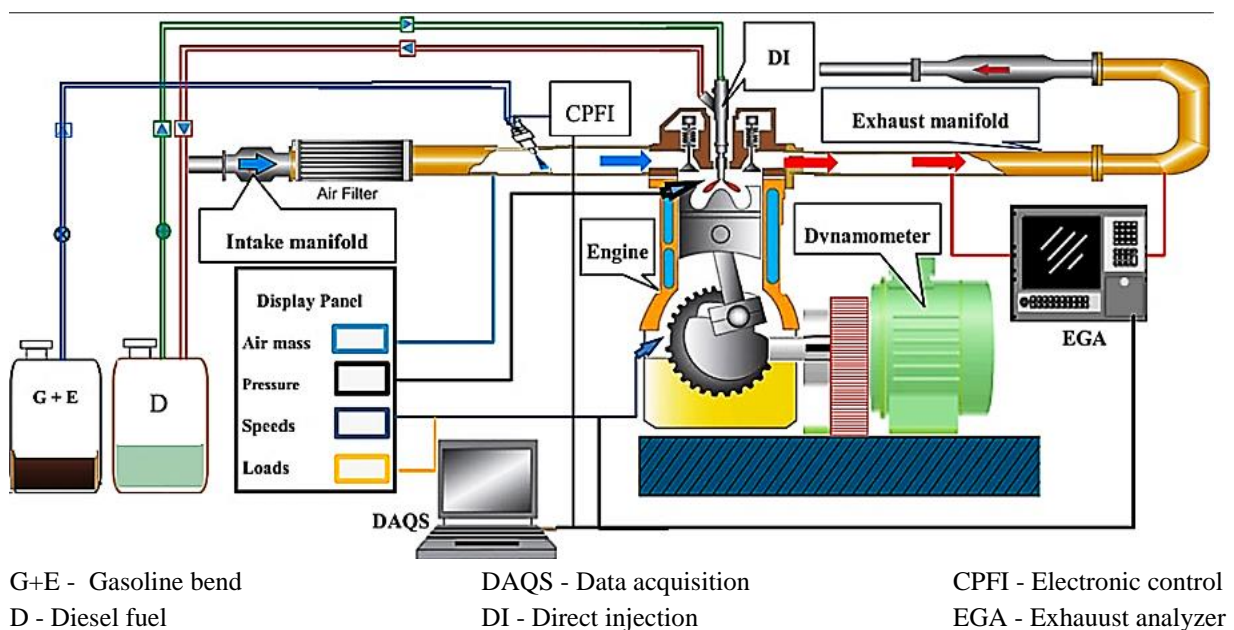


Figure 1: Experiment engine test rig

One-stage injection fuel delivery was used to investigate 80% of direct injected diesel fuel and 20% of mixed port injected fuel was used. Utilizing cylinder pressure vs engine crank-angle data during the engine's compression and power strokes, quantitative insights into the combustion process are derived. Using the single zone model, the heat release rate (HRR), also known as the rate of fuel burning, is calculated from the cylinder pressure data by using Equation (1). The rate at which fuel energy is released during a diesel engine's combustion is measured using data [23].



Table 1: Engine specification and physio-chemical properties of the fuels used

Engine type, Company	EA300-E2-NB, Kubota	Properties	Ethanol	Gasoline	Diesel
No cylinder	1	Auto ignition temp(°C)	420	300	210
Engine, stroke	Diesel, 4-stroke	Flashpoint (°C)	13	45	93
Bore	75.0 mm	Final boiling point (°C)	78.5	70	369.8
stroke	70.0 mm	Density at 15°C	0.79	0.720	0.840
Power at 3,000rpm	5.1 KW	Adiabatic FT @(25°C)	2234	2289	2600
Swept volume:	309cm <sup>3</sup>	Molecular weight	46	105	198
Connecting rod ratio	0.25	Reid Vapor pres. KPa	17	41-65	-
Noise level	95 dB(A)	Cetane Number	7	17	54.6
Speed 1 <sup>st</sup>	2300	Latent HOV (KJ/kg)	904	410	904
Speed 2 <sup>nd</sup>	2700	RON	106	Min 92	-
Compression ratio	23	MON	89	85	-
Injection	Direct	LHV(MJ/kg)	26.8	42.4	42.5
Engine position	Horizontally mounted	Final boiling point in °C	-	Max 225	380

$$HRR(\theta) = \left( \frac{\gamma}{\gamma - 1} * P(\theta) * dV(\theta) \right) + \left( \frac{1}{\gamma - 1} * V(\theta) * dP(\theta) \right) \quad (1)$$

Where V is the instantaneous chamber volume, P is the cylinder pressure, and  $\theta$  is the crank position;  $\gamma$  is the ratio of specific heats (cp/cv), with 1.35 that is suitable for diesel heat-release study. Specifically, it is anticipated that the heat-release analysis of a diesel engine will produce values that match air temperatures at the end of the compression stroke ( $\approx 1.35$ ) [24]. In both RCCI and baseline combustion, experiments are carried out with constant engine loads, injection time, varied blended fuel ratios, and speeds. Equation (2)[25] defines the premixed fuel ratio (rp) as the ratio of port fuel injection (PFI) energy to the total fuel (PFI+DI) energy injected[26].

$$R_p = \frac{m. LHV(GE)}{M. LHV(D) + m. LHV(B)} \quad (2)$$

Where LHV is the lower heating value of each fuel and M and m are the mass flow rates of the primary and secondary fuels, respectively. The primary and secondary fuels are denoted by the subscripts D (diesel) and B (gasoline-ethanol blended fuel; Rp=G10E10), respectively; for baseline compression ignition combustion, rp = 0. The diesel fuel's SOI timing was kept constant at all experiments at 14°CA (bTDC). Fig. 2 depicts the overall conceptual framework for the experimental research and validation. Table 2 lists the instruments used to measure the cylinder pressure, emissions, cooling water temperature, heat in the exhaust gas, speed, load, and uncertainty associated with each material.

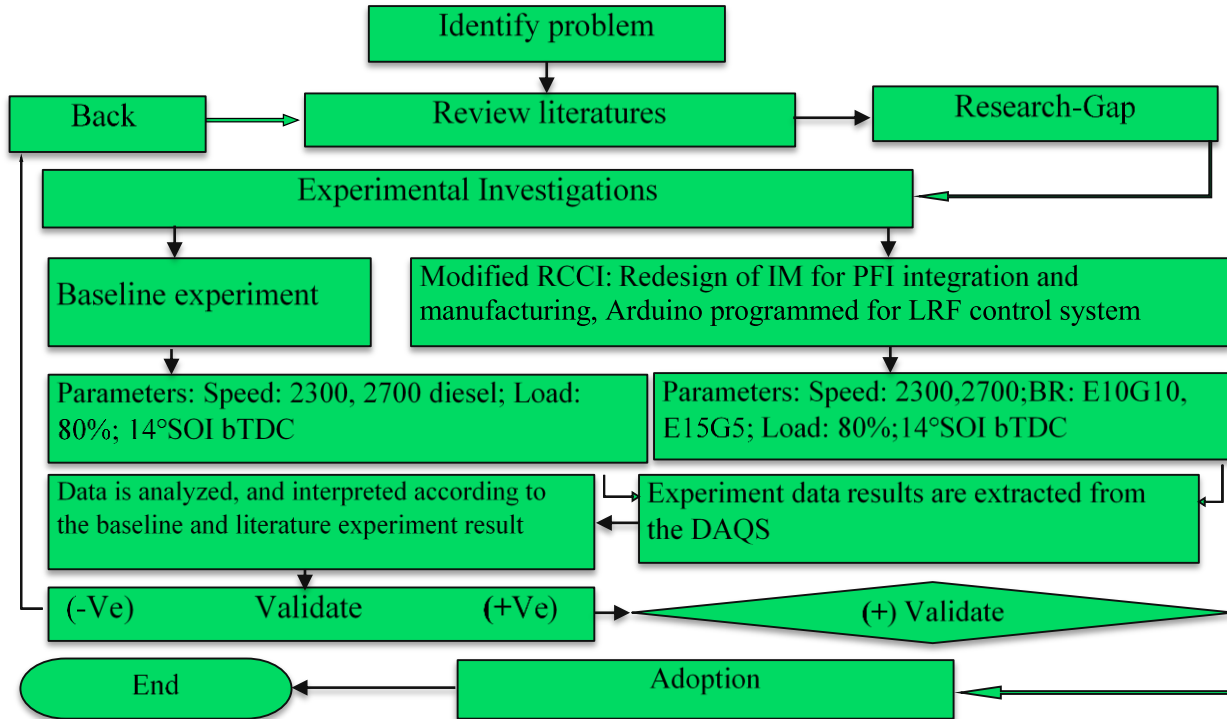


Figure 2: Conceptual frame work for investigation

## 2.2 Uncertainty Analysis

The instrument, testing environment, calibrations, data collecting, instrumentation, the procedures used, and random errors are the main causes of uncertainty in findings. Errors are often present in experimental testing when measuring various test data. Therefore, in order to get precision, uncertainty analysis was done to address the errors and deviations that happened throughout the experimental effort. The accuracy with the measuring instruments, shown in Table 2 indicates the maximum mean percentage uncertainty ( $\bar{U}_{max}$ ) estimated concerning the engine emissions and the engine performance of the base equation as shown in (Eq.3), uncertainty equation (Eq.4), and maximum percentage uncertainty (Eq.5).

$$P_b = \frac{2\pi NT_b}{60,000} \quad (3)$$

$$\text{Uncertainty}(U) = cT_b\Delta N + cN\Delta T_b \quad (4)$$

$$\text{Maximum uncertainty}(U_{max})\% = \left[ \frac{\Delta N}{N} + \frac{\Delta T_b}{T_b} \right] \times 100 \quad (5)$$

Table 2: Instrument accuracy and measurement uncertainties

Instrument	Emissions	Measuring range	Accuracy	$\bar{U}_{max}\%$
Kane AUTO plus gas analyzer	NOx	0 - 5000ppm	± 12 PPM	21.2
	CO	0-10% vol	± 0.06% vol	10.3
CT 159.02 EG-Analyzer	CO <sub>2</sub>	0-20% vol	± 0.1% vol	2.9
	HC	0-2500ppm	± 3 ppm	7.1
CT 100.23	N	0-5000rpm	± 12 ppm	0.51
	Pb	-	± 0.1	2.87
	Tb	-	± 0.20	1.89
	TFC	-	± 0.05cm <sup>3</sup>	2.43

TFC-total fuel consumption;  $\bar{U}_{max}\%$  - maximum mean percentage uncertainty



### 3. RESULTS AND DISCUSSION

#### 3.1 Combustion

*Cylinder pressure (bar):* A binary low-reactivity blended fuel (gasoline-ethanol) technique, which uses premixed blend ratios and diesel fuel, was employed in the experimental study on the baseline and modified diesel engines. At two engine speeds of 2300 and 2700 RCCI, the cylinder pressure is 70.8 and 67.3 respectively. When the engine is operating at 2300 and 2700rpm using baseline, the low cylinder pressures are 60.34 and 59.85 bar, respectively. Based on the findings, the engine operating on diesel fuel at the speeds shown in Fig. 3 has the lowest cylinder pressure, whereas the maximum is found at both speeds of E10G10-RCCI. When compared to the baseline trial, the fuel reactivity starts at the intake manifold, which lengthens the time required for the air-fuel mixture to homogeneously mix in the combustion chamber, which explains why the engine operating with the G10E10 advanced engine at 2300-RCCI has 15% higher than the minimum cylinder pressure at 2700 baseline engine operation[27].

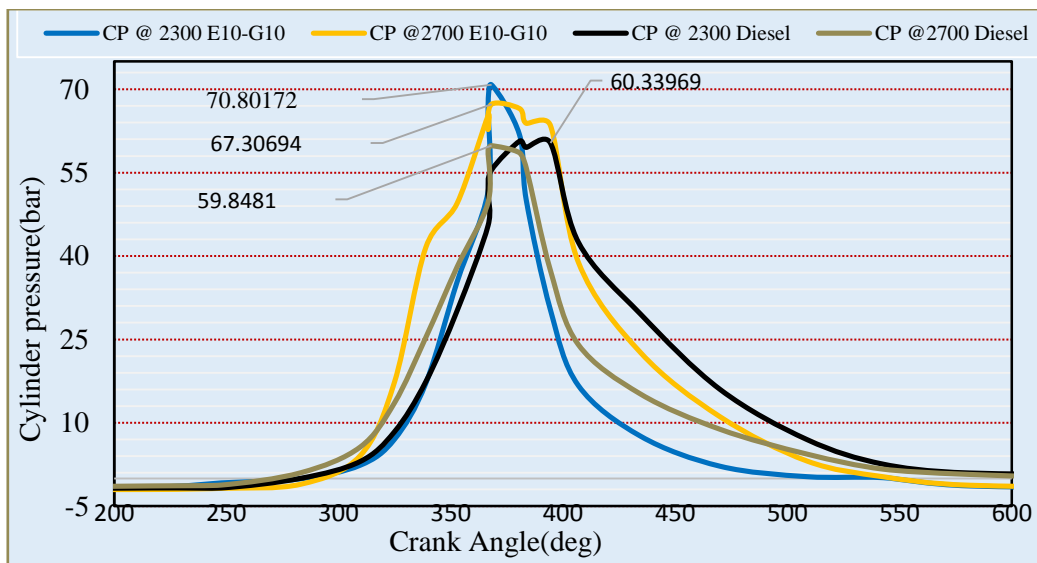


Figure 3: Cylinder pressure (bar)

*Normalized volume:* A diesel engine operates using the diesel cycle, which consists of four processes: two isentropic processes for compression and expansion; two isobaric processes; and one isochoric process ( $Q_{in}$ ,  $Q_{out}$ ). Process 1-2: The air that is drawn in from the surroundings is compressed isentropic. The system's job ( $W_{in}$ ) in this process is to compress the air. Process 2-3: This is the isobaric process and the injection point for diesel. Here, the high pressure and temperature cause the fuel to burn. Engine heat is produced in this process ( $Q_{in}$ ). This is the power stroke (process 3–4). The process of expansion is isentropic. This piece is titled  $W_{out}$ . Process 4-1: This process is isochoric. In this stage, the engine produces all of the combustion process' exhaust gasses. Additionally, some heat is lost to exhaust gasses ( $Q_{out}$ ). During the experiments, a diesel engine (baseline) operates on the diesel and advanced RCCI engine cycle, as depicted in Figs 4. a, b, c, and d.

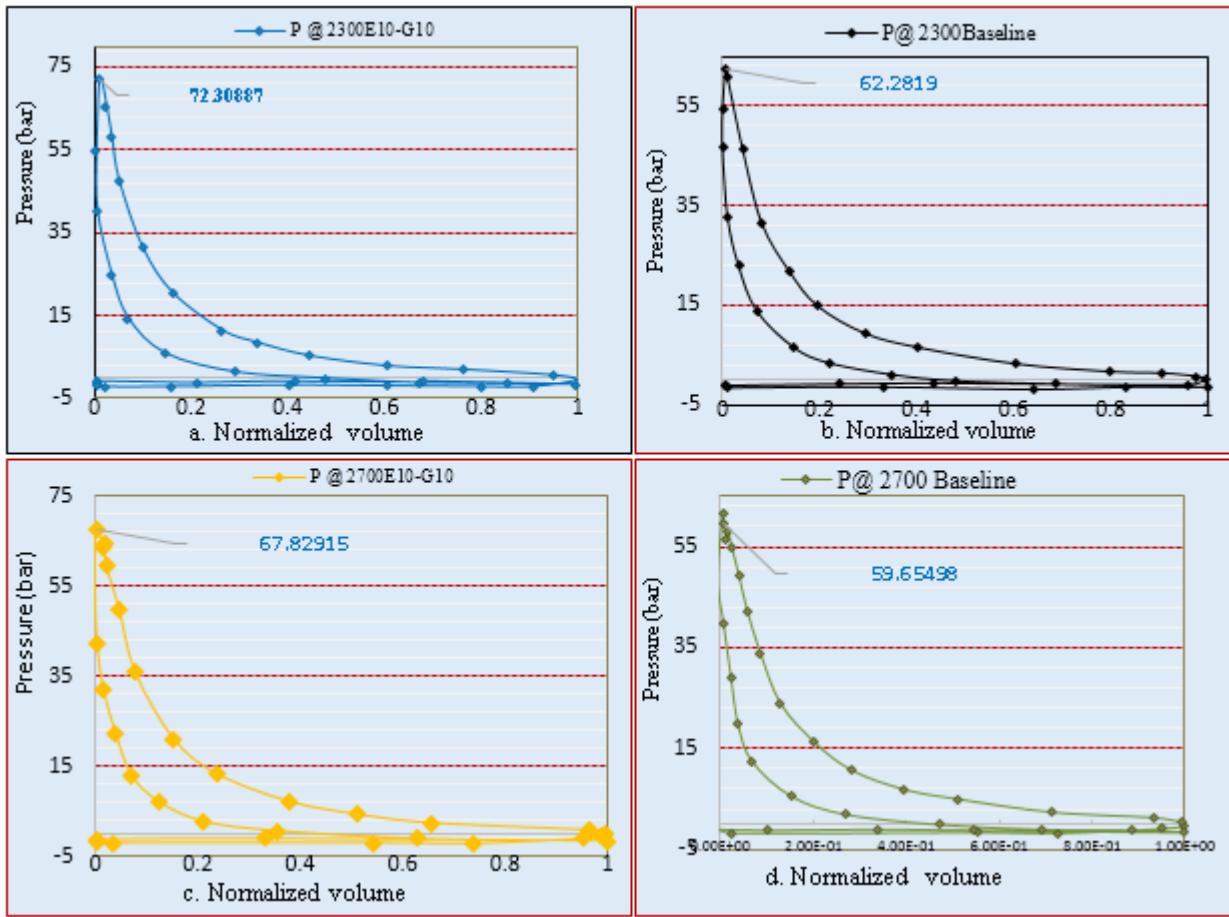


Figure 4: a, b, c and d, normalized pressure at each speed

**Heat Release Rate (J/CA):** Heat release rate was 66.85 at the maximum engine speed of 2700 and E10-G10-RCCI, and 30.3J/CA at diesel fuel combustion. The heat release rate is 8.58J/CA baseline and 48.9 at 2300-E10G10-RCCI. As a result, in both engine speed cases, the peak heat release rate is at the engine operating with 2700-E10G10-RCCI which is 27% more than 23-E10G10-RCCI while the lower heat release rate is found at the baseline as it is in-lined with[28]. As illustrated in Fig.5, the engine operating on the premixed fuel ratio of G10E10 RCCI has a maximum heat release rate at engine speeds of 2700 and a minimum at 2300 rpm of the base fuel.

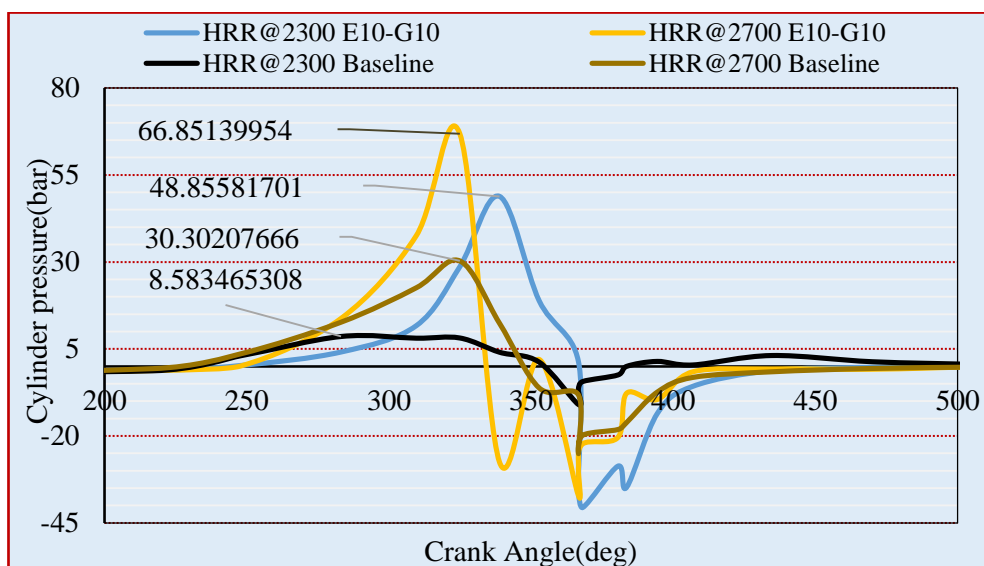


Figure 5: Heat release rate (J/CA)



### 3.2 Engine Performances

Brake power is the amount of power that an engine can produce at crankshaft. When referring to IC engines, brake power is the engine's power output that remains after different mechanical losses like friction and auxiliary drives are taken into consideration. An engine dynamometer is used to measure it. It loads the engine and records the torque and rotational speed. It's also critical to keep in mind that the engine's operational parameters, like the air/fuel ratio, engine speed, and external environment, can affect brake power. The brake power versus engine at 2300 and 2700 rpm and the two fuels of G10E10 and baseline are investigated. The experiment result showed that the brake power of the engine running at the baseline fuel with speeds of 2300 and 2700 had low engine power of 3.35kW. The power from the engine at both speeds with the modified G10E10 port injected RCCI engine was 4kW as it is shown in Fig.6.

$$P_b = T_b \omega (kW) \quad (6)$$

Where:  $(\frac{2\pi N}{60}) 10^{-3}$  is the average angular speed, N is the rotational speed in rpm

The torque that an engine produces at its crankshaft or output shaft is brake torque. It is a measurement of the twisting force produced by the motor or engine and is commonly given in Newton-meters (Nm) of measurement. Brake torque in Fig.6 showed the brake torque versus engine speed at different fuel ratios and engine speeds. The results showed a higher 15.23 Nm with the G10E10 RCCI at the speed of 2300rpm and the lower brake torque value was at 2700 RCCI and 2300 baseline fuel and intermediate at 2700 baseline which is 14.16.

$$T_b = \frac{(W + S)}{1000} (Nm) \quad (7)$$

Where (W+S) is the total weight applied.

Brake thermal efficiency is a measure of the efficiency with which an engine converts the energy contained in the fuel into useful work. It represents the ratio of the brake power output to the energy input from the fuel. In the context of internal combustion engines, brake thermal efficiency is typically expressed as a percentage and calculated using the equation (8). The BTE calculated how effectively heat was converted into useful work. The brake thermal efficiency purely depends on the engine design, type of fuel, and engine application. Fig.6 shows the variation of brake thermal efficiency for different blends and pure diesel fuel. Among the different blends, the calorific values of ethanol, gasoline, and diesel fuel used are 26800, 42400, and 42500 J/kg respectively. After computing the calorific values of G10E10-RCCI, and diesel fuel, which are 40,920J/kg, and 42,500 J/kg, respectively.

$$\eta_{b.th} = \frac{P_b}{mf \times Q_{LHV}} \times 100\% \quad (8)$$

Where  $Q_{LHV}$  is the lowest heating value of the fuel in J/Kg and mf is the mass flow rate of fuel flow in kg/sec. The brake thermal efficiency of the engine running with the baseline at a higher speed has better thermal efficiency and is lower at G10E10RCCI as shown in Fig 6.

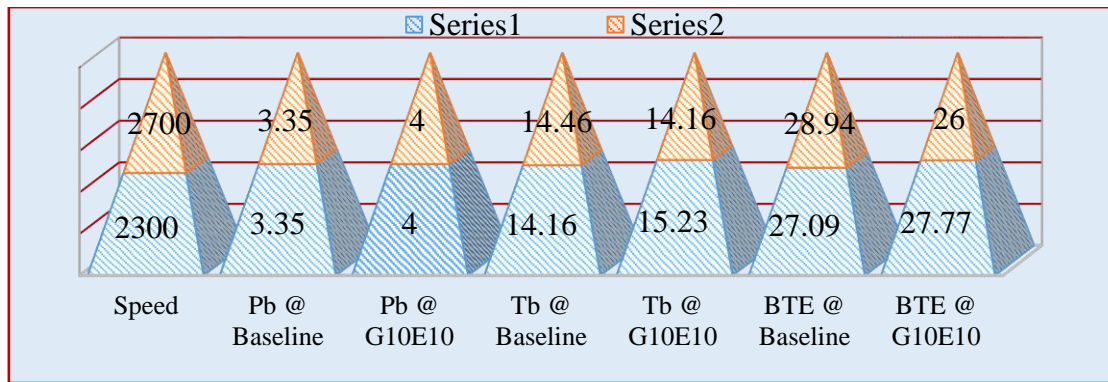


Figure 6: Engine performances (Pb, Tb, BTE)

*Brake-specific fuel consumption (BSFC)*: is the ratio between the engine's effective power outputs at the engine crankshaft to the rate of fuel consumption. Fig.7 pinpoints the brake-specific fuel consumption (BSFC) characteristics versus engine speed. The investigation's result expressions indicate a minimum brake-specific fuel consumption at the baseline experiment and a maximum at G10E10 premixing fuel. Nevertheless, as the speed increases; brake-specific fuel consumption is decreased until the maximum engine speed of 2700 rpm. The brake-specific fuel consumption is minimum for the diesel fuel and maximum for the G10E10 but average for G10E10-RCCI as shown in Fig.7.

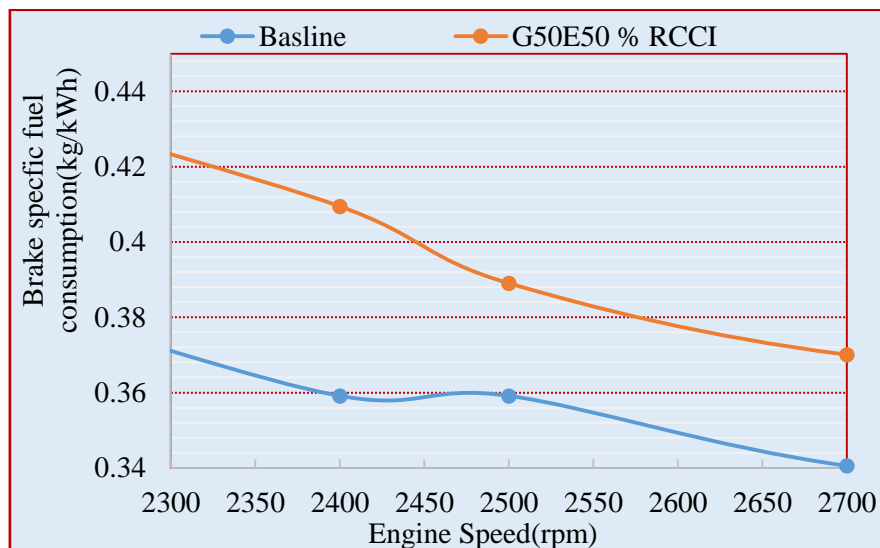


Figure 7: Brake-specific fuel consumption

### 3.3 Engine Emission

The emissions that need attention from the diesel engine are oxides of nitrogen and particulate matter. Unburned hydrocarbons and carbon monoxide are the emissions from the RCCI-diesel operation. Nitrogen oxide emissions from the engine with the percentage of ethanol (G10E10-RCCI) are the lowest at all engine speed ranges and highest at the engine running with the baseline diesel fuel engine combustions. The G10E10 premixed blend ratio-fueled RCCI engine has a lower value, which is an acceptable targeted result according to the study's purposes. The nitrogen oxide and CO<sub>2</sub> reduced due to the cooling effect of the ethanol content as shown in Fig.8.

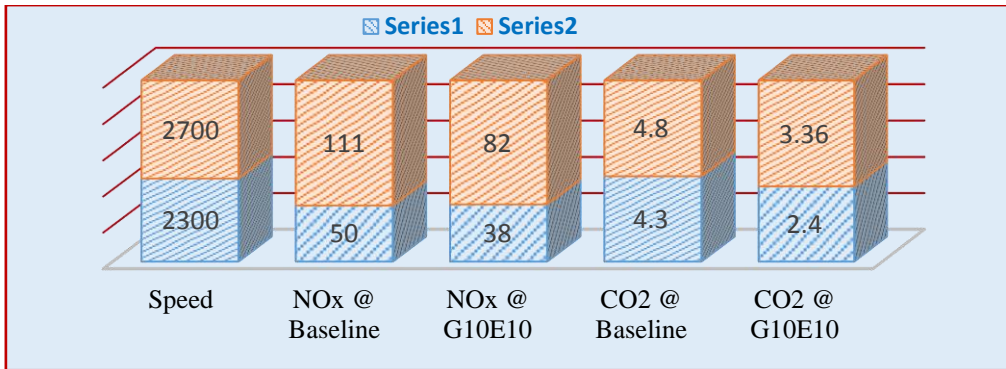


Figure 8: NO<sub>x</sub> and CO<sub>2</sub> emission

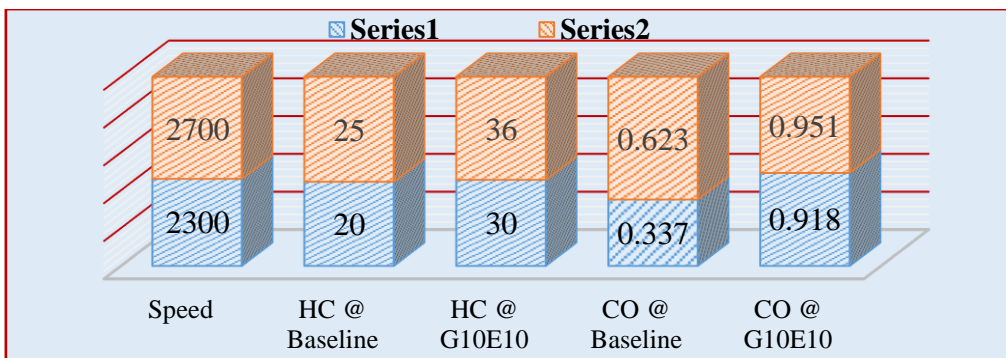


Figure 9: HC and CO emission

The CO<sub>2</sub> at the engine speeds of 2300rpm and 2700rpm-RCCI is lower and maximum in CDC at all engine speeds. Because of the nature of the lean operations of the diesel engine, engine emissions of carbon monoxide in percentage volume and unburnt hydrocarbon in ppm versus engine speed were lowest when the engine run with conventional diesel combustion. The CO and UHC emissions of the diesel engines running with the G10E10 are maximum and lower for the engine operating with the baseline. The carbon monoxide and unburned hydrocarbon emission results from the experiment indicate that the RCCI engine operation mode has more CO and UHC emissions but low carbon dioxide emissions when compared to the CDC engine in all engine speed ranges, as shown in Fig.9. The carbon dioxide emissions in percent volume at all speed ranges are maximum with conventional diesel combustion. The percentage improvement depending on the speed and fuel blend ratio of the experiment results are clearly stated in Table 3.

Table 3 Percentage improved

Speed	NOx at Baseline	NOx at G10E10-RCCI	Percent
2300	50	38	24
2700	111	82	26.13
Percent	54.9	53.7	
Speed	CO <sub>2</sub> at Base	CO <sub>2</sub> at G10E10-RCCI	Percent
2300	4.3	2.4	44
2700	4.8	3.36	30
Percent	10.4	28.6	

#### 4. CONCLUSIONS

In the current work, an experimental investigation of a blended port injected fuel of gasoline-ethanol with diesel direct injected RCCI engine running is conducted. Accordingly, the following conclusions are drawn:

G10E10-RCCI engine operation mode has a maximum cylinder pressure of 70.8 bars at 2300-RCCI and a minimum of 59.84 bars at 2700 rpm on baseline fuel. The maximum HRR of the engine is 66 J/CA at the engine



speed of 2700-RCCI and a minimum at baseline with an HRR of 8.58 J/deg. The maximum normalized pressure (NVP) of the engine is 72.3 bar at the engine speed of 2300-RCCI and a minimum of 59.65 at 2700 baseline.

The brake power of the engine is maximum at both speeds of the RCCI engine and lower in both baselines. The brake torque is maximum at 2300-RCCI which is 15.23N-m with the engine running with a G10E10-RCCI engine and minimum (14.16N-m) at a speed of 2300 baseline. At 80% engine load operation, the baseline engine had better thermal efficiency (28.94%), and minimum at the speeds of 2700-RCCI (26%) brake thermal efficiency. NO<sub>x</sub> and CO<sub>2</sub> increase in all cases of a diesel engine operating and minimum in the cases of RCCI and both speed cases and the reverse for HC and CO in all baseline and G10E10-RCCI engine combustion modes.

## ACKNOWLEDGMENT

The authors would like to express gratitude to Adama Science and Technology University for their fund Grant number ASTU/SP-R/ 097121, material support and their valuable assistance. The authors also would like to express their gratitude to Jimma University Institute of Technology (JiT) Center of Excellence for their permission to use the research facilities.

## REFERENCES

- [1] J. M. Desantes, R. Payri, A. Garcia, and J. Monsalve Serrano, "Evaluation of Emissions and Performances from Partially Premixed Compression Ignition Combustion using Gasoline and Spark Assistance," presented at the SAE Technical Paper Series, 2013.
- [2] Hu Wanga, Xumin Zhaoa, Laihui Tongb, and M. Yaoa, "The effects of DI fuel properties on the combustion and emissions characteristics of RCCI combustion," *Fuel*, 2018.
- [3] J. Li, D. Wang, C. Zhuang, S. Gong, and S. J. P. Li, "Numerical Investigation of the Knocking Combustion Characteristics of the N-Butanol/N-Octanol RCCI Engine," vol. 10, no. 10, p. 2142, 2022.
- [4] D. Splitter, R. Reitz, R. J. S. I. J. o. F. Hanson, and Lubricants, "High efficiency, low emissions RCCI combustion by use of a fuel additive," vol. 3, no. 2, pp. 742-756, 2010.
- [5] G. D. Neely, S. Sasaki, and J. A. J. S. t. Leet, "Experimental investigation of PCCI-DI combustion on emissions in a light-duty diesel engine," pp. 197-207, 2004.
- [6] Y. Zhao, E. Weibo, T. Niu, and J. He, "Study on combustion processes of a premixed charge compression ignition (PCCI) engine fueled with DME/diesel," in *Journal of Physics: Conference Series*, 2021, vol. 1732, no. 1, p. 012154: IOP Publishing.
- [7] H. S. Juneja and S. S. Sandhu, "Experimental Investigation of PPCI Engine fuelled with Ethanol," in *IOP Conference Series: Materials Science and Engineering*, 2019, vol. 691, no. 1, p. 012059: IOP Publishing.
- [8] N. Komninos, C. J. R. Rakopoulos, and S. E. Reviews, "Modeling HCCI combustion of biofuels: A review," vol. 16, no. 3, pp. 1588-1610, 2012.
- [9] U. Ž. Baškovič, S. R. Oprešnik, T. Seljak, and T. J. F. Katrašnik, "RCCI combustion with renewable fuel mix–Tailoring operating parameters to minimize exhaust emissions," vol. 311, p. 122590, 2022.
- [10] J. S. Rosa, M. E. S. Martins, G. D. Telli, C. R. Altafini, P. R. Wander, and L. A. O. J. F. Rocha, "Exploring the effects of diesel start of injection and water-in-ethanol concentration on a reactivity controlled compression ignition engine," vol. 281, p. 118751, 2020.
- [11] J. Li, W. Yang, D. J. R. Zhou, and S. E. Reviews, "Review on the management of RCCI engines," vol. 69, pp. 65-79, 2017.
- [12] K. K. Sadabadi, *Modelling and control of combustion phasing of an rcci engine*. Michigan Technological University, 2015.
- [13] J. Benajes, S. Molina, A. García, E. Belarte, and M. J. A. T. E. Vanvolsem, "An investigation on RCCI combustion in a heavy duty diesel engine using in-cylinder blending of diesel and gasoline fuels," vol. 63, no. 1, pp. 66-76, 2014.
- [14] T. D. Nguyen, T. T. Anh, V. T. Quang, H. B. Nhat, and V. N. J. A. E. Duy, "An experimental evaluation of engine performance and emissions characteristics of a modified direct injection diesel engine operated in RCCI mode," vol. 8, no. 6, 2020.
- [15] E. Uherek *et al.*, "Transport impacts on atmosphere and climate: Land transport," vol. 44, no. 37, pp. 4772-4816, 2010.
- [16] M. Mofijur, M. M. Hasan, T. Mahlia, S. A. Rahman, A. Silitonga, and H. C. J. E. Ong, "Performance and emission parameters of homogeneous charge compression ignition (HCCI) engine: a review," vol. 12, no. 18, p. 3557, 2019.
- [17] T. Li, "A High Efficiency and Clean Combustion Strategy for Compression Ignition Engines: Integration of Low Heat Rejection Concepts with Low Temperature Combustion," 2017.



- [18] S. L. Kokjohn, R. M. Hanson, D. A. Splitter, and R. D. J. S. I. J. o. E. Reitz, "Experiments and modeling of dual-fuel HCCI and PCCI combustion using in-cylinder fuel blending," vol. 2, no. 2, pp. 24-39, 2010.
- [19] B. Tekgül *et al.*, "Large-eddy simulation of split injection strategies in RCCI conditions," vol. 26, no. 3, pp. 590-611, 2022.
- [20] F. Zhao, T. N. Asmus, D. N. Assanis, J. E. Dec, J. A. Eng, and P. M. Najt, "Homogeneous charge compression ignition (HCCI) engines," 2003.
- [21] S. Pan *et al.*, "Experimental study on the cyclic variations of ethanol/diesel reactivity controlled compression ignition (RCCI) combustion in a heavy-duty diesel engine," *Energy*, vol. 237, 2021/12// 2021.
- [22] Gharehghani, A. Salahi, M. M. Andwari, A. M. Mikulski, M. Könnö, and J. J. Energy, "Reactivity enhancement of natural gas/diesel RCCI engine by adding ozone species," p. 127341, 2023.
- [23] M. Gad, Z. He, A. El-Shafay, and A. I. J. C. S. i. T. E. EL-Seesy, "Combustion characteristics of a diesel engine running with Mandarin essential oil-diesel mixtures and propanol additive under different exhaust gas recirculation: Experimental investigation and numerical simulation," vol. 26, p. 101100, 2021.
- [24] J. B. Heywood, *Internal combustion engine fundamentals*. McGraw-Hill Education, 2018.
- [25] V. B. Pedrozo, X. Wang, W. Guan, and H. J. I. J. o. E. R. Zhao, "The effects of natural gas composition on conventional dual-fuel and reactivity-controlled compression ignition combustion in a heavy-duty diesel engine," vol. 23, no. 3, pp. 397-415, 2022.
- [26] M. Mikulski and C. Bekdemir, "Understanding the role of low reactivity fuel stratification in a dual fuel RCCI engine – A simulation study," *Applied Energy* 191 (2017) 689–708, 2017.
- [27] D. Splitter, M. Wissink, S. Kokjohn, and R. D. Reitz, "Effect of Compression Ratio and Piston Geometry on RCCI Load Limits and Efficiency," presented at the SAE Technical Paper Series, 2012.
- [28] M. Yıldız and B. A. J. F. Ceper, "A comparative study on gasoline/diesel-fueled RCCI combustion at different premixed ratios and high-EGR diesel CI combustion in an IC engine under low load conditions," vol. 324, p. 124596, 2022.
- [29] N. T. Nghia, N. X. Khoa, W. Cho, and O. J. E. Lim, "A study the effect of biodiesel blends and the injection timing on performance and emissions of common rail diesel engines," vol. 15, no. 1, p. 242, 2021.
- [30] R. Hanson, S. Curran, R. Wagner, and R. J. S. I. J. o. E. Reitz, "Effects of biofuel blends on RCCI combustion in a light-duty, multi-cylinder diesel engine," vol. 6, no. 1, pp. 488-503, 2013.



# Sustainable Advanced Composites Materials from Waste: Fabrication, Properties, and Deployment

Belay Taye Wondmagegnehu \*

College of Engineering and Technology, Department of Mechanical and Automotive Engineering, Dilla University, P.O. Box 419, Dilla, Ethiopia

\*Corresponding author, e-mail: [belaytaye1@gmail.com](mailto:belaytaye1@gmail.com)

## ABSTRACT

Advanced composite materials are lightweight, robust, and designed materials made of toughened polymeric matrix with high-performance reinforcing fibers incorporated in them. Multiscale microparticle reinforcements in the composite were determined a significant variation in mechanical, physical, and microstructure properties through developed by various particle sizes and weights of content. The particles are processed through an easy-to-use mold configuration and impregnated with epoxy resin. A homogenous material should have a higher density. The density of composite was found the highest under category S3, sample designation S34 that is 1.58 g/cm<sup>3</sup> and 3.84% void contents. Tensile, flexural, moduli, hardness, and moisture properties are measured. Fly ash weight fractions and particle size play a major role in enhancing the mechanical and physical characteristics of polymer matrix composites; thus, a decrease in particle size in the composite materials seems to improve mechanical strength and physical properties while increasing the weight of the contents, decreasing the mechanical properties, and increasing water absorption. The highest tensile strength, modulus, and flexural strength were shown smallest particle size and content in the designation. The flexural rigidity was increased with increased ash particle size and contents. The ash particle size and contents increase in composite was found to increase void content. The hardness value of a composite was showed nonlinear property with various weight content of bagasse ash. Bagasse ash size and loading in composites were statistically significant, which means less than a P-value of 0.05. A scanning electron microscope and optical microscope are used to characterize the morphology of the composite. This innovative understanding drives the efficient use of fly ash and offers long-term, and sustainable solutions for their practical implementation. With continued research and development, sustainable composites have the potential to become a mainstream material choice, promoting a more sustainable future.

**Keywords:** microstructure, polymer, reinforcement, technology, waste

## 1. INTRODUCTION

Sustainable composites can exhibit a range of properties depending on the type of waste materials used and the fabrication process. By diverting waste from landfills and incorporating recycled materials, sustainable composites offer a lower environmental footprint. Natural fibers like wood, bamboo, or hemp can provide lightweight reinforcement, making these composites suitable for applications in transportation and construction. Depending on the waste materials used, sustainable composites can achieve good tensile strength, flexural strength, and impact resistance. Sugarcane is an agricultural product. Sugarcane bagasse ash is the waste from incineration for energy generation. Fly ash, the fine particles carried by flue gases, contains a significant amount of silicon dioxide (SiO<sub>2</sub>). Studies have shown high SiO<sub>2</sub> content in various biomass sources like sugarcane bagasse (up to 71.5%, Chemical Composition of Bagasse Ash and Extracted Bio-SiO<sub>2</sub>), rice husk (86.8%), and wood byproducts (55%) (Baloyi et al., 2021; Rachniyom & Srisittipokakun, 2019), compared to coal fly ash (44.7-61.8%) (Ovcacikova et al., 2022). Ethiopia's year-round sugarcane production, except for maintenance breaks, further increases bagasse ash generation. Fortunately, regeneration techniques can help reduce this solid waste. Almost all of the product of its ash was sent to landfills. In 2012, the UK was utilized at 50%. Fly ash, while containing potentially harmful heavy metals (Tiwari et al., 2020), can offer some advantages in construction. Bagasse fly ash (BFA), specifically, has been shown to improve strength due to its silica content (Chuewangkam et al., 2022) and is comprised of various metal oxides (Rauf et al., 2017). Studies have found BFA useful in mortars and pastes, increasing viscosity (Jimenez-Quero et al, 2013; Castaldelli et al., 2016). Epoxy resin is a common choice for composites due to its strength properties, but it can be brittle (Tiwari et al., 2020, p. 2).



Researchers are exploring ways to improve epoxy by incorporating fillers like BFA to create nanocomposites, a promising area of study. Multi-scale composites are composite materials that incorporate reinforcing elements from various size scales (i.e., macro, micro, and/or nano) (Rana et al., 2012a; 2017; Díez-et al., 2014)..

Composite materials are engineering marvels that combine the best of various worlds, offering a remarkable combination of properties: lightweight construction with high strength and strength-to-weight ratio (Keya, 2019), excellent resistance to corrosion and high impact (Habibie, 2021), along with the freedom for design flexibility and part consolidation. They also exhibit dimensional stability, are nonconductive, and have low thermal conductivity (Habibie, 2021), making them ideal for a wide range of applications. The size of particles influences in HDPE composite (25 and 5 $\mu$ m) and volume (0, 20, 35, and 50 wt%) of micro silica filler particles on mechanical strength showed a decrease in tensile strength, ductility, elastic modulus on size 25 $\mu$ m, and toughness (Siraj et al., 2022). A first-time recycled and fresh fly ash composite was developed by variation of particle size (50-90, 90-150 and 150-250  $\mu$ m) and determined a tensile strength and young's modulus. To decrease the strength due to bigger fly ash particles, smaller fly ash particle batter performed composites (Alghamdi, 2021). In epoxy composites, sugarcane bagasse/fly ash/carbon nanotube reinforced tubes were examined and found that fly ash volume increased yield strength, while young's strength decreased while tensile strength increased (Gopalan et al., 2021).

This study investigated how the size of bagasse ash particles affects the mechanical strength and physical properties of a composite material made with glass fiber in an epoxy matrix. They found that bagasse ash, a waste product from the sugar industry. Overall, this research demonstrates the potential to transform industrial waste into valuable products. The properties are analyzed based on an analysis of variance (ANOVA), which is performed to obtain the significant factors for tensile and flexural strength. The ash powder sizes are at four levels (600-300, 300-150, 150-75 and 75-25 $\mu$ m) and the percentage ash weight is at four levels (10, 15, 20, and 25 wt.%). The percentage of reinforcement is not more than 50% in the matrix due to the fiber not being fully wetted with the resin (Ismail et al., 2022).

## 2. MATERIALS AND METHODS

### 2.1. Materials Used

In composite incorporated materials are epoxy resin, E-glass fiber, and sugarcane bagasse ash, the ash density 1.18 g/cm<sup>3</sup>. Particle size was determined by a sieve analyzer based on ASTM E11, which has sieve designations of #30, #50, #100, #200, and #500. The retained sample was retained on five consecutive sieves corresponding to 600-300 $\mu$ m, 300-150 $\mu$ m, 150-75 $\mu$ m, and 75-25 $\mu$ m size fractions. The experiment was conducted at the Vellore Institute of Technology (VIT), India. Sugarcane bagasse ash is prepared (details likely in Fig. 1) and then incorporated into a composite material using a conventional hand lay-up technique. The bagasse ash contents set 10, 15, 20, and 25 wt.% of the powders. Epoxy resin with hardener was mixed in a ratio of 10:1 (Vijayan, Subramanian, & Sankaranarayanan, 2020) by weight percentage. Subsequently, the mixtures were prepared by combining epoxy with bagasse, and a mixture was stirred for 5 minutes with a hand drill machine (1.2 kg) in an added blender on the tip of the drill bit. The E-glass fiber (36mm length) set (25 wt.%) in a wood mold having the dimensions of 250 $\times$ 200 $\times$ 10mm was used for composite fabrication based on designation shown in Table 1.

### 2.2 Characterization

#### 2.2.1 Determination of Density

This study measured the density of composites consisting of matrix, fiber, and particulate filler. The actual density ( $\rho_{ct}$ ) was determined using the ASTM D792-91 standard, while the theoretical density based on weight fraction was calculated with equation (1). Density is a key parameter influencing the properties of polymer composites (Moritzer et al., 2021; Ji et al., 2022). Distilled water used to measure the density of a composite material and then applied equation (2) to determine the volume fraction of voids, or empty spaces, within the composite.

$$\rho_{ct} = \frac{1}{(W_f / \rho_f) + (W_m / \rho_m) + (W_p / \rho_p)} \quad (1)$$

$$V_v = \frac{\rho_{ct} - \rho_{ce}}{\rho_{ct}} \quad (2)$$

Where, suffix f, m, p, and ct stand for fiber, matrix, ash particle and composite.  $\rho$  and  $W$  are density and weight fraction respectively.

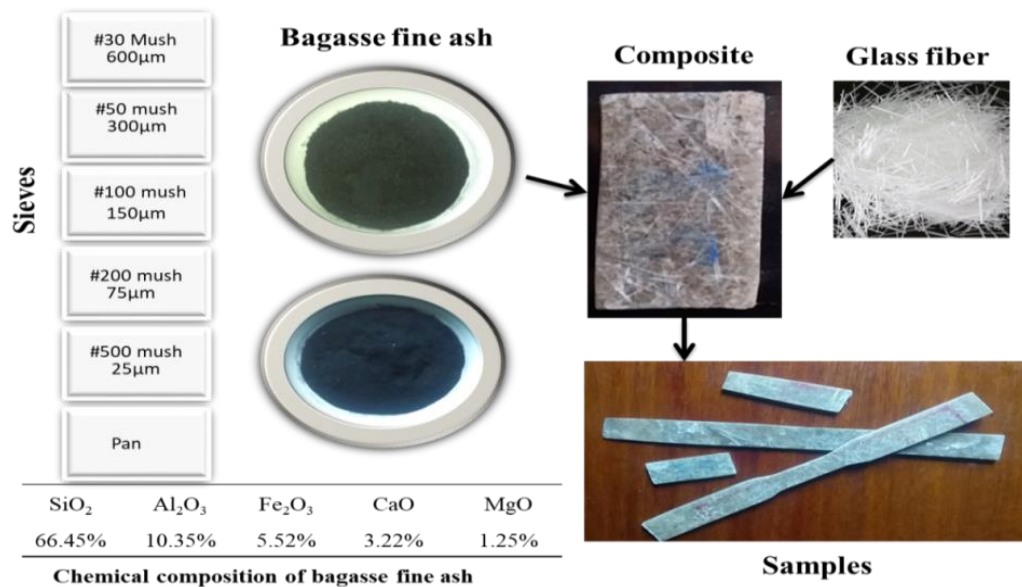


Figure 1: Preparation of designed materials and samples

### 2.2.2 Water absorption and thickness swelling test

The samples were submerged in water for 312 hours at room temperature (25°C). Three 20 x 20 x 3 mm specimens were prepared for each composite type, followed ASTM D570. Water absorption was calculated using Equation 3 (Dever et al., 2013), and thickness swelling (TS) was determined using Equation 4. The results were then analyzed through the graphical presentation in Figure 3.

$$\text{Mass change, \%} = \frac{W_i - W_b}{W_b} \times 100 \quad (3)$$

$$\text{Thickness Swelling (TS)} = \frac{T_i - T_o}{T_o} \times 100\% \quad (4)$$

The current specimen mass ( $W_i$ ), baseline specimen mass ( $W_b$ ), initial thickness ( $T_o$ ), and final thickness ( $T_i$ ) after 24 hours of water immersion can be used to calculate a value

### 2.2.3 Tensile strength test

Composite samples with dimensions of 25 mm width, 3.2 mm thickness and 150 mm gauge length were prepared according to ASTM D3039 and tested for tensile strength using a Universal Testing Machine at a speed of 5 mm/min. The average tensile strength and elongation were calculated from up to three measurements on five specimens per composite type.

### 2.2.4 Flexural strength test

The experiment examined the elasticity of a material by measuring its strain under a three-point load following ASTM D790 standards. Specimens with specific dimensions (127 x 12.7 x 3.2 mm) were



tested on a support span 16 times their thickness. Deflection and flexural properties were then calculated using Equation (5).

$$\text{Flexural Strength} = \frac{3PL_o}{2W_o t^2} \quad (5)$$

In engineering mechanics, the central load (P in KN), span length (Lo in mm), width (Wo in mm), and thickness (t in mm) of a specimen influence the maximum deflection (D in mm) of its center. This relationship can be expressed through an equation that considers the interplay of these dimensions and material properties.

### 2.2.5 Hardness test

Hardness was assessed following the ASTM D785 standard, which utilizes a Rockwell hardness tester. In this test, a weighted indenter penetrates the material, and the material's hardness is determined by the depth of this indentation. The test begins with a minor load of 10 kg to set the indenter, the dial is then zeroed, and a major load of 60 kg is applied to measure the indentation depth.

### 2.2.6 Scanning electron microscope (SEM)

Scanning Electron Microscopy (SEM) is a technique used to examine the morphology of composite specimens. The process involves placing a conductive specimen in a chamber and irradiating it with an electron beam. The emitted electrons provide information about the surface features of the composite (Hossain, 2012). The glass fiber distribution in the matrix was observed using optical microscopy.

## 3. RESULTS AND DISCUSSION

### 3.1 Density and Void Content Analysis

A study investigated the effect of bagasse ash filler content on the density of composites, since density and moisture absorption are known to influence dimensional stability (Chandrika et al., 2022). According to Archimedes' principle (Robert et al., 2019) theoretical density determined assuming no pores or defects.

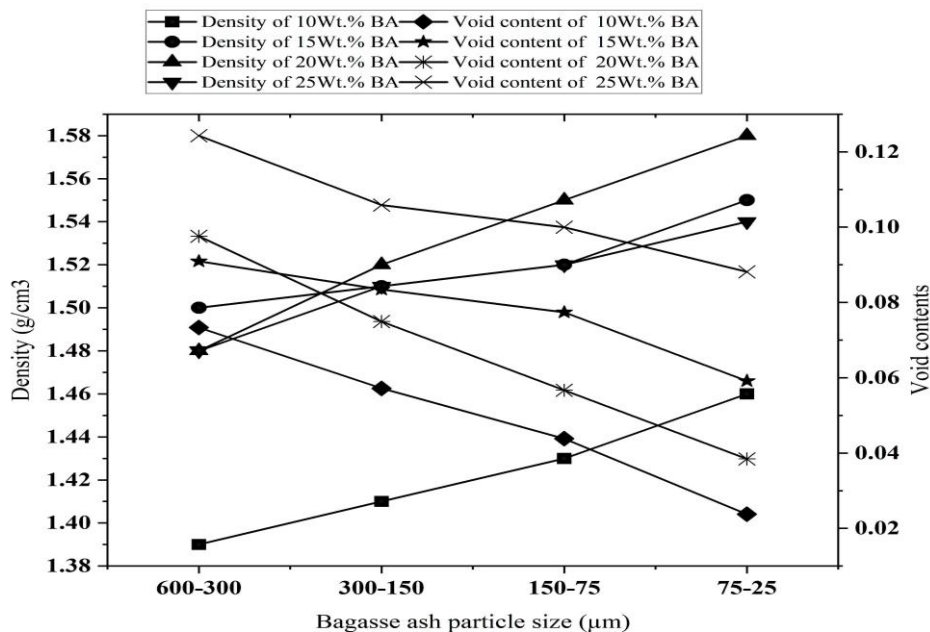


Figure 2: Composites density versus void content plot

A homogenous material should have a higher density. The breakage and pore generation result from the difference between the theoretical density and the experimental density. Since the production processes and conditions were optimized for the wettability (Jian-jun et al., 2021; Ruya Shi, et al., 2022) of the composite, it was possible to minimize or not greatly differ between them. Actually, manufactured composite gives rise to a



certain number of voids within the composite body. As shown in Fig. 2, an increase in content and a decrease in particle size in the composite decreased the density and increased the void contents. The density increased by 5.04% with a decrease in the particle size from 600-300 to 75-25  $\mu\text{m}$ , and similarly, the void content decreased by 68% in 10 wt.%.

### 3.2 Water Absorption and Thickness Swelling Analysis

A study investigated the effect of bagasse fly ash content and particle size on the moisture absorption of composites. Composites with increased fly ash loading and larger particles absorbed more water at a faster rate, with the highest absorption observed in a composite containing 25 wt.% of 600-300  $\mu\text{m}$  fly ash.

Table 1: Physical analysis of designed composite samples

Category	Label	Bagasse ash particle size ( $\mu\text{m}$ )	Bagasse ash contents (Wt.%)	Glass fiber contents (Wt.%)	Composites density	Void content
S1	S11	600-300	10	25	1.39	0.073
	S12	300-150	10	25	1.41	0.057
	S13	150-75	10	25	1.43	0.044
	S14	75-25	10	25	1.46	0.024
S2	S21	600-300	15	25	1.5	0.091
	S22	300-150	15	25	1.51	0.083
	S23	150-75	15	25	1.52	0.077
	S24	75-25	15	25	1.55	0.059
S3	S31	600-300	20	25	1.48	0.098
	S32	300-150	20	25	1.52	0.075
	S33	150-75	20	25	1.55	0.057
	S34	75-25	20	25	1.58	0.038
S4	S41	600-300	25	25	1.48	0.124
	S42	300-150	25	25	1.51	0.106
	S43	150-75	25	25	1.52	0.100
	S44	75-25	25	25	1.54	0.088

Previous studies found that too many fillers clump together (Asyraf, et al., 2022; Badaruzzaman, et al., 2022), creating voids that weaken the material and increase water absorption. Researcher concluded the balancing of mechanical performance and water resistance is crucial for reducing water absorption, as a composite's density and void content are strongly linked to its water absorption rate (Atiqah et al., 2017). When the loading of 25 wt.% of BA with 600-300 $\mu\text{m}$  size particles was observed, the composite had the highest void content (0.124) and a lower density (1.48g/cm<sup>3</sup>). Similar strands were observed in other composites consisting of 20 wt.% BA with 75-25 $\mu\text{m}$  particle size, the highest density (1.58 g/cm<sup>3</sup>), and a lower void content (0.038), which revealed Fig. 3 lower water absorption.

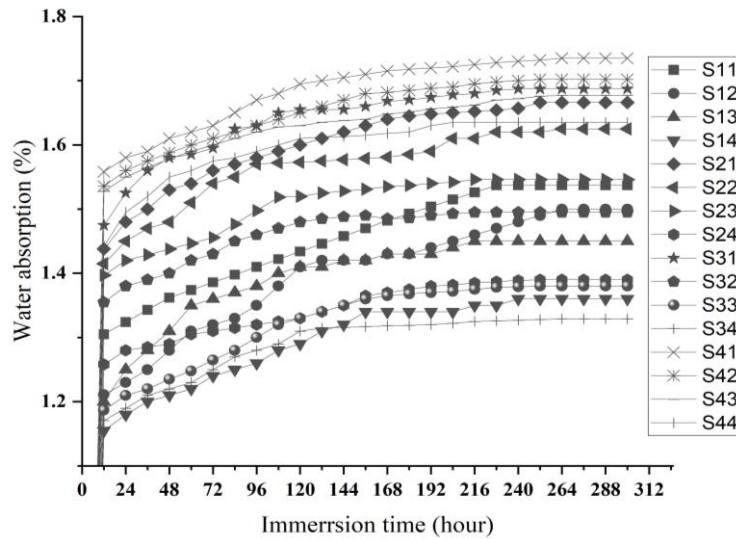


Figure 3: Water absorption of designed samples

The research found that thickness in the composite increased with time, BA content, and particle size. This is because more bagasse fly ash makes the composite panels more susceptible to swelling, possibly due to poor adhesion between the filler and the matrix polymer (Jawaid et al., 2019). As shown on Fig. 4, the S1 composite with the least amount of fly ash showed the least swelling, while S6 with the most fly ash showed the most swelling.

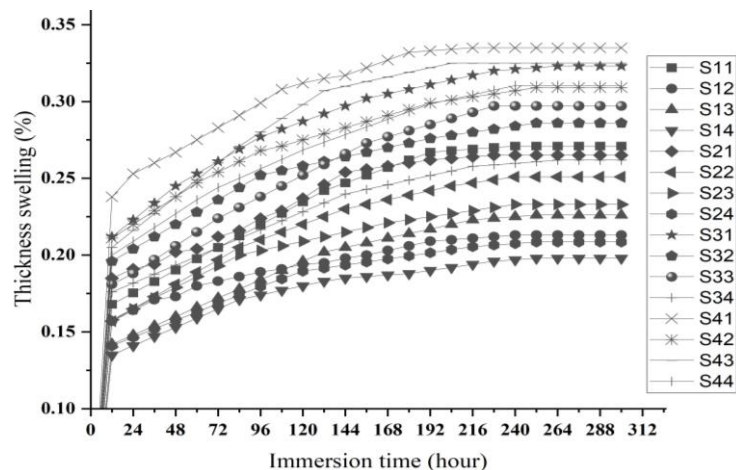


Figure 4: Thickness swelling of designed samples

### 3.3 Tensile Strength Analysis

The highest tensile strength in designation S14 was 185 MPa, which is the lowest void content, and the highest tensile modulus value in designation S41 was 320 MPa, which is the highest void content. Tensile strength was shown in Fig. 5a to rise from the findings, with a particle size reduction of BA from 600-300 $\mu$ m to 75-25 $\mu$ m, which may be related to excellent particle dispersion and strong polymer/filler interface adhesion for effective stress transmission, as reported by another researcher (Devendra & Rangaswamy, 2013). The loading of BA increased from 10 wt.% to 25 wt.% in composites, decreasing the tensile strength as shown in Fig. 5c.

The study found that the Young's modulus, a measure of stiffness, of the composites increased with increasing BA content (25 wt%) as shown in Fig. 5b and 5d. This is because the stiffer BA filler strengthens the polymer matrix, enhancing its resistance to deformation under load. This trend is exemplified by designations S11, S21, S31, and S41, which have progressively higher strengths (260.61, 245.45, 189.47, and 320 MPa respectively) with increasing BA content.

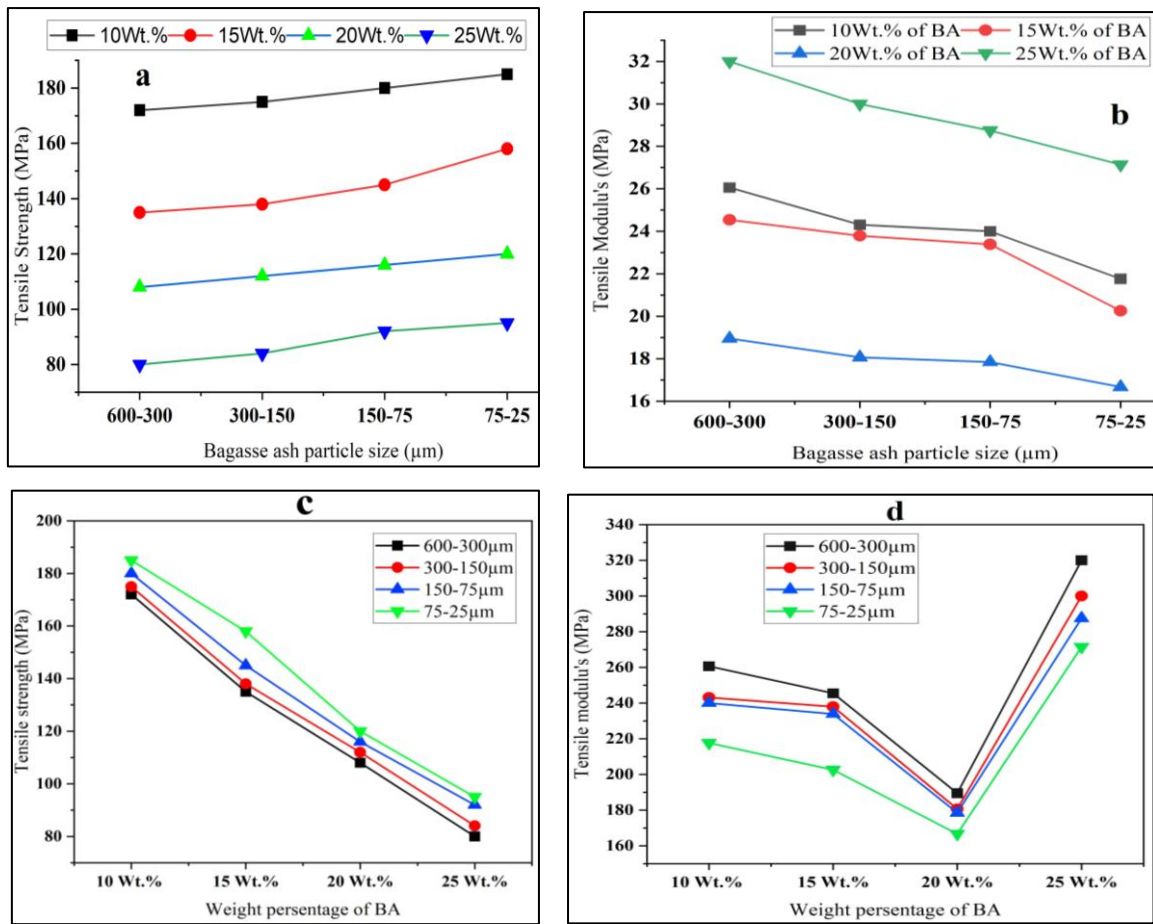


Figure 5: Tensile strength and modulus’s analysis; a and b) BA particle size and c and d) BA content on tensile and modulus’s strength analysis plots, respectively

### 3.4 Flexural Strength Analysis

While adding bagasse ash (BA) to a composite initially improves its flexural strength due to better wetting of the filler by the resin, further increases in BA concentration have a negative impact (Fig. 6). This is because excess BA creates cross-links within the resin, making it more rigid but also more brittle (Fig. 6c). Additionally, the small size of the BA particles can disrupt the bonding between the resin and reinforcing fibers, further reducing overall strength. Similar results were found with oil palm nano filler/kenaf/epoxy hybrid nanocomposites in other studies (Saba et al., 2016). The highest flexural strength was found in the designation of S24 composite at 86.4 MPa with 75-25μm particle size. Flexural strength increases with particle size as a result of the greater wettability of chopped particles by epoxy resin (small interface region), which causes an increase in transferring stresses from epoxy to chopped particles. Furthermore, tiny chopped particle sizes increase the boundary grains of chopped composite material, which increases the flexural strength of composite materials. These results are comparable with references (Ahmed, 2018).

A study by El-Shekeil et al. (2019) found that incorporating fillers increased the flexural modulus of composites, especially with higher fiber loadings and larger particle sizes (Figure 6c). This is because fillers are stiffer than the surrounding matrix. As expected from the definition of flexural modulus (ratio of force to elastic deflection), higher moduli correspond to increased particle size and filler content, as observed in the 600-300μm particle size with 25% loading for filled BA samples. These findings align with polypropylene composites with coconut shell particles prior research (Obasi et al., 2021).

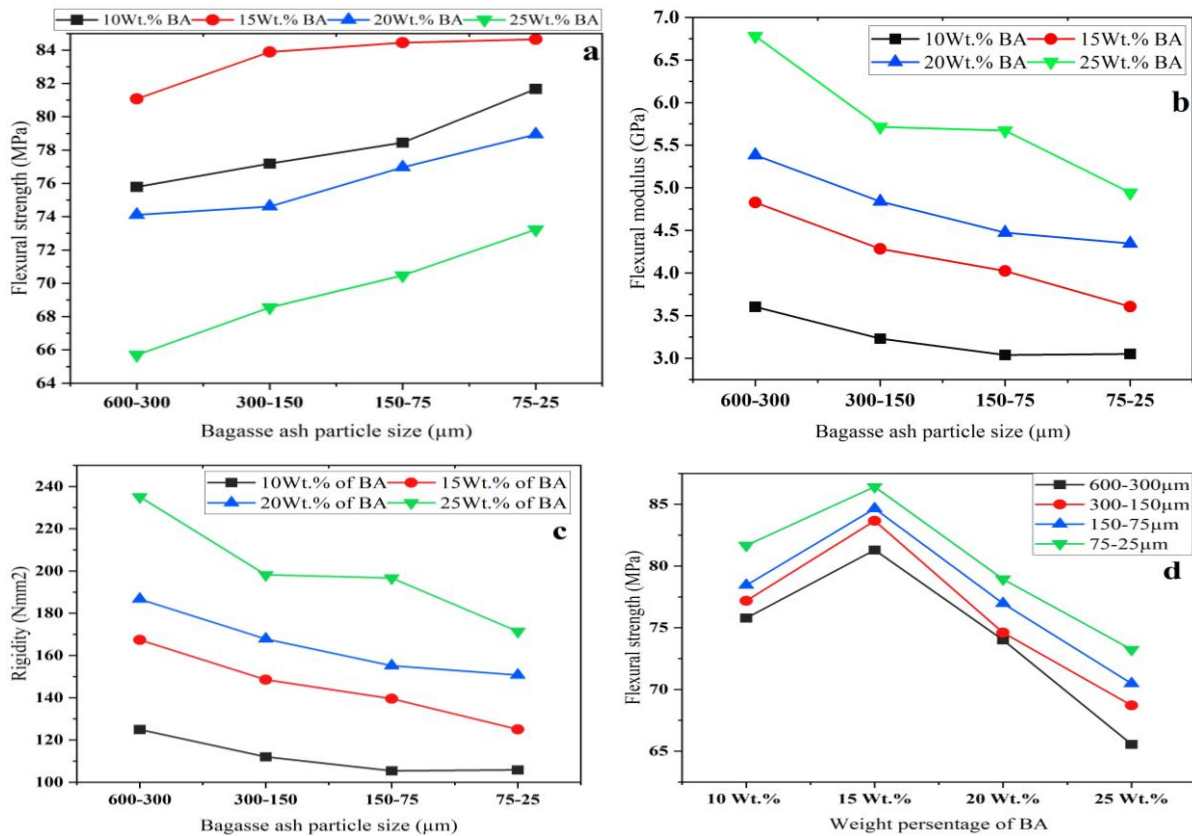


Figure 6: Flexural strength and modulus test; a and b) BA particle size factor on flexural strength and modulus, c) BA particle size factor on flexural rigidity, and d) content of BA with flexural strength plot

### 3.5 Hardness test analysis

Adding more bagasse ash to the composite didn't directly make it harder, even though the ash particles got smaller (Figures 7a and b). This is because the ash particles clumped together. The best hardness came from a mix with particle sizes between 75 and 25 microns. Similar results were found with limestone and wood particles in other studies (Anirudh et al., 2022; Vinayagamorthy, 2020). There's a trade-off between hardness and tensile strength, because making the composite harder with smaller particles also makes it more brittle (less elastic and bendy). This is shown in Fig. 5a and 7b, where higher hardness corresponds to lower tensile strength.

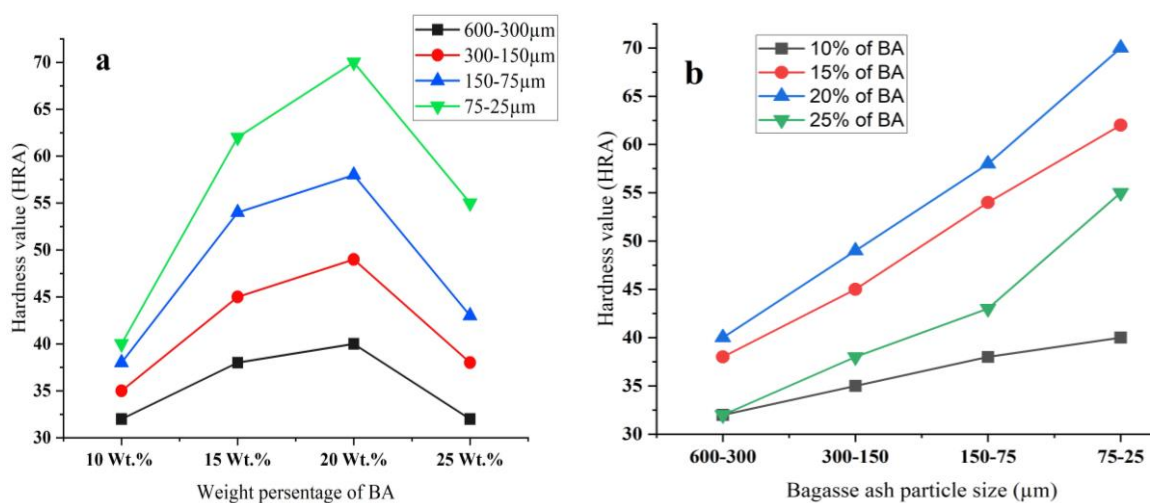


Figure 7: Hardness value test analysis with a) weight percentage and particle size of BA plot



### 3.6 Hypothesis analysis

The ANOVA technique was used to assess the influence of process parameters on performance measures. Results from Table 2 show that content and particle size have a significant effect ( $p < 0.05$ ) and a positive impact on tensile strength, flexural strength, and hardness. Although Table 3 compares the significance level of these factors using the Turkey method, any means sharing a letter are not statistically different.

Table 2. ANOVA analysis factors of bagasse ash particle size and contents

ANOVA analysis for tensile strength						
Source	DF	Adj SS	Adj MS	F-Value	P-Value	
BFA particle size ( $\mu\text{m}$ )	3	575.7	191.90	28.28	0.000	
BFA contents (Wt.%)	3	18150.2	6050.06	891.72	0.000	
Error	9	61.1	6.78			
Total	15	18786.9				

ANOVA analysis for flexural strength						
Source	DF	Adj SS	Adj MS	F-Value	P-Value	
BFA particle size ( $\mu\text{m}$ )	3	58.11	19.371	14.20	0.001	
BFA contents (Wt.%)	3	404.57	134.856	98.83	0.000	
Error	9	12.28	1.365			
Total	15	474.96				

ANOVA analysis for hardness value						
Source	DF	Adj SS	Adj MS	F-Value	P-Value	
BFA particle size ( $\mu\text{m}$ )	3	650.2	216.73	3.95	0.047	
BFA contents (Wt.%)	3	769.7	256.56	4.67	0.031	
Error	9	494.1	54.90			
Total						

ANOVA: analysis of variance; DF: degrees of freedom; Adj SS: adjusted sum of squares; Adj MS: adjusted mean squares

Table 3. Grouping information using the Tukey Method and 95% confidence

	Tensile Strength				Flexural Strength			
	N	Mean	Grouping		N	Mean	Grouping	
Weight percentage of BA content	10	4	178.00	A	15	4	83.5138	A
	15	4	144.00	B	10	4	78.2726	B
	20	4	114.00	C	20	4	76.1319	B
	25	4	87.75	D	25	4	69.4882	C
Particle size of BA	(75-25 $\mu\text{m}$ )	4	139.50	A	(75-25 $\mu\text{m}$ )	4	79.5719	A
	(150-75 $\mu\text{m}$ )	4	133.25	B	(150-75 $\mu\text{m}$ )	4	77.6329	A B
	(300-150 $\mu\text{m}$ )	4	127.25	C	(600-300 $\mu\text{m}$ )	4	75.5413	B C
	(600-300 $\mu\text{m}$ )	4	123.75	C	(300-150 $\mu\text{m}$ )	4	74.6604	C

### 3.7 Morphology Analysis

Examining the material under a scanning electron microscope (SEM) revealed uneven distribution of bagasse ash and glass fibers (Fig. 8 & 9). Higher filler content resulted in poor interaction between fibers and the matrix, creating voids and holes (Fig. 8c). This suggests that the increased filler overwhelmed the matrix's ability to coat it properly, leading to the observed cavities, micro-holes, and clumping.

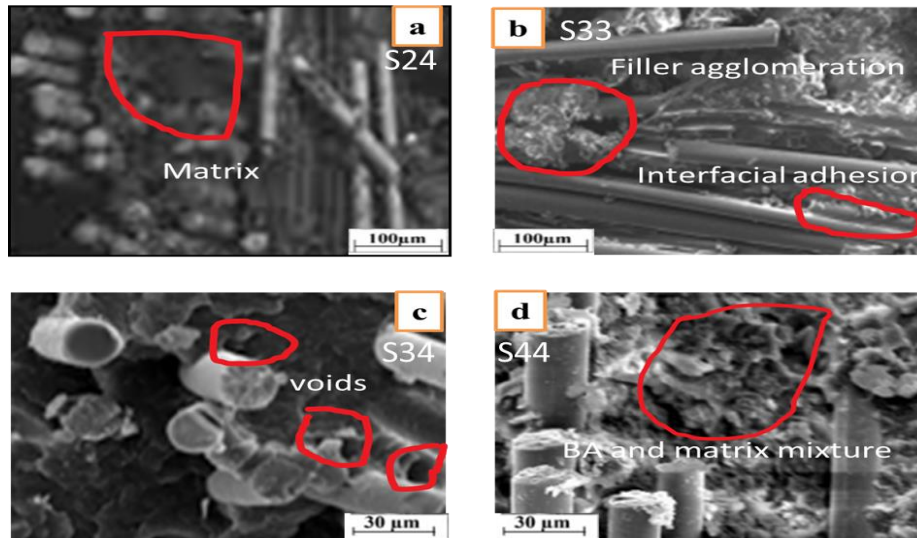


Figure 8: Microscopic images of SEM

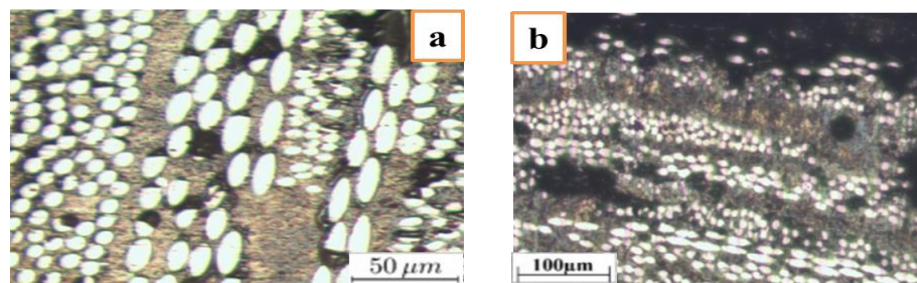


Figure 9: Optical microscopic images (etched by ethanol (CH<sub>3</sub>CH<sub>2</sub>OH) with HCl (50:1))

#### 4. CONCLUSIONS AND RECOMMENDATIONS

The mechanical and physical characteristics of hand-layup-molded bagasse finest ash polymer composite microparticles were effectively investigated. Smaller particle sizes demonstrated superior qualities as compared to bigger particle sizes. The agglomeration of filler particles in the polymer matrix influences the saturation level as filler loading increases. The density of the composite increased with particle size decreases, while void contents decreased. The water absorption of composites was increased at the initial stage but, over time, reached saturation point. The highest tensile strength and modulus in the designation S14 were 185 MPa and 320 MPa, respectively. The highest flexural strength was found in the designation of S24 composite at 86.4 MPa with 75-25µm particle size. The hardness of a composite is not linearly increased with BA loading. The ANOVA technique revealed that the effect of content and particle size appears insignificant as its  $P > 0.05$ . However, these two factors have a positive effect on the properties considered. The SEM observed weak wetting between filler, fiber, and matrix, as indicated by the presence of filler agglomeration and pores in the picture. Optical microscopy revealed that the spreading of bagasse ash particles and glass fiber was clearly observed.

The recommendations for future work are: (1) Investigate methods to improve filler-matrix interaction for better bonding; (2) Explore surface modification techniques for the bagasse ash particles to enhance their compatibility with the polymer matrix; (3) Analyze the long-term behavior of the composites, including water absorption and mechanical properties over time. Overall, Sustainable Advanced Composite Technologies via Waste Products hold significant promise. Further research and development are needed to improve process efficiency, optimize material properties, and ensure cost-effectiveness for widespread industrial adoption.

#### REFERENCE

Ahmed, S. J. (2018). Effect of Particle Size on Mechanical Properties of the Recycling Compact Disks Reinforced Epoxy. *Engineering and Technology Journal*, 36(6), 641-645.



- Alavudeen, A., Rajini, N., Karthikeyan, S., Thiruchitrabalam, M., & Venkateshwaren, N. (2015). Mechanical properties of banana/kenaf fiber-reinforced hybrid polyester composites: Effect of woven fabric and random orientation. *Materials & Design*, 66, 246-257.
- Alghamdi, M. (2021). Effect of Filler Particle Size on the Recyclability of Fly Ash Filled HDPE Composite. *Polymers*, 13(16).
- Anirudh, V., Krishna, S. A., Akshat, A., Venkatachalam, G., & Loganathan, T. (2022). Virtual fatigue analysis of epoxy based composite reinforced with sugarcane fibre, fly ash and carbon nano tubes. *Materialwissenschaft und Werkstofftechnik*, 53(1), 56-67.
- Asyraf, M., Ishak, M., Syamsir, A., Nurazzi, N., Sabaruddin, F., Shazleen, S., et al. (2022). Mechanical properties of oil palm fibre-reinforced polymer composites: A review. *Journal of Materials Research and Technology*, 17(4), 33–65.
- Atiqah, A., Jawaid, M., Ishak, M., & Sapuan, S. (2017). Moisture absorption and thickness swelling behaviour of sugar palm fibre reinforced thermoplastic polyurethane. *Procedia engineering*, 184, 581-586.
- Baloyi, R., Ncube, S., Moyo, M., & Nkiwane, L. a. (2021). Analysis of the properties of a glass/sisal/polyester composite. *Scientific Reports*, 11(1), 1-10.
- BaniHani, S., L-Oqla, F. M., & Mutawe, S. (2021). Mechanical performance investigation of lignocellulosic coconut and pomegranate / LDPE biocomposite green materials. *Journal of the Mechanical Behavior of Materials*, 30, 249–256.
- Castaldelli, V., Moraes, J., Akasaki, J. L., Melges, J., Monzó, J., Borrachero, M., et al. (2016). Study of the binary system fly ash/sugarcane bagasse ash (FA/SCBA) in SiO<sub>2</sub>/K<sub>2</sub>O alkali-activated binders. *Fuel*, 174, 307-316.
- Chandrika, V., Anamika, A., Jeeva, C., Perumal, B., Kumar, S., Roseline, J., et al. (2022). Natural Fiber Incorporated Polymer Matrix Composites for Electronic Circuit Board Applications. *Advances in Materials Science and Engineering*, 2022, 9.
- Chuewangkam, N., Nachaithong, T., Chanlek, N., Thongbai, P., & Pinitsoontorn, S. (2022). Mechanical and Dielectric Properties of Fly Ash/Geopolymer/Sugarcane Bagasse Ash Composites. *Polymers*, 14(6).
- Devendra, K., & Rangaswamy, T. (2013). Strength Characterization of E-glass Fiber Reinforced Epoxy Composites with Filler Materials. *Journal of Minerals and Materials Characterization and Engineering*, 1, 353-357.
- Dever, J., Nathal, M., & DiCarlo, J. (2013). Research on high-temperature aerospace materials at NASA Glenn Research Center. *Journal of Aerospace Engineering*, 26(2), 500-514.
- Díez-Pascual, A. M., Naffakh, M., Marco, C., Gómez-Fatou, M. A., & Ellis, G. J. (2014). Multiscale fiber-reinforced thermoplastic composites incorporating carbon nanotubes: A review. *Current Opinion in Solid State and Materials Science*, 18(2), 62-80.
- Elkington, M., Ward, C., Chatzimichali, A., & Potter, K. (2015). Studying effects of preshearing on hand layup. *Advanced Manufacturing: Polymer & Composites Science*, 1(2), 80-93.
- El-Shekeil, Y., AL-Oqla, F., & Sapuan, S. (2019). Performance tendency and morphological investigations of lignocellulosic tea/polyurethane bio-composite materials. *Polym Bull*, 1-14.
- GOPALAN, V., VYAS, R., GOSWAMI, I., SHAH, A., & PRAGASAMA, V. (2021). Tensile behaviour of sugarcane fiber/fly ash/carbon nano tubes reinforced epoxy composites. *U.P.B.Sci.Bull., Series D*, 83(1), 181-192.
- Hossain, M. K. (2012). Scanning Electron Microscopy Study of Fiber Reinforced Polymeric Nanocomposites. In V. Kazmiruk, *Scanning Electron Microscopy*. IntechOpen.
- Ibrahim, I., Sadiku, E., Jamiru, T., Kupolati, W., Agwuncha, S., Fasiku, V., et al. (2017). Hybrid Natural/Synthetic Fiber Biocomposites. In A. Shahzad (Ed.), *Biocomposites. Properties, Performance and Applications* (p. 27). USA: Nova Science.
- Ipilakyaa, T. D., Tuleun, L. T., & Sule, J. T. (2019). Influence of The Variation Of Particle Size And Content on The Mechanical Properties of Coconut Husk Ash (Cha)-Reinforced Polyester Composite. *European Journal Of Materials Science And Engineering*, 4(4), 212-220.
- Ismail, A. S., Jawaid, M., Hamid, N. H., Yahaya, R., Sain, M., & Sarmin, S. N. (2022). Dimensional stability, density, void and mechanical properties of flax fabrics reinforced bio-phenolic/epoxy composites. *Journal of Industrial Textiles*, 52, 1–22.
- Jawaid, M., Thariq, M., & Saba, N. (2019). *Mechanical and Physical Testing of Biocomposites, Fibre-Reinforced Composites and Hybrid Composites*. Sawston, UK; Cambridge, UK: Woodhead Publishing.
- Ji, Y., Lei, W., Huang, Y., Wu, J., & Yu, W. (2022). Influence of Resin Content and Density on Water Resistance of Bamboo Scrimber Composite from a Bonding Interface Structure Perspective. *Polymers*, 14(9), 1856.
- Jian-jun SHA, Zhao-zhao LÜ, Ru-yi SHA, Yu-fei ZU, Ji-xiang DAI, Yu-qiang XIAN, et al. (2021). Improved wettability and mechanical properties of metal coated carbon fiber-reinforced aluminum matrix composites by squeeze melt infiltration technique. *Trans. Nonferrous Met. Soc. China*, 31(2), 317–330.



- Jiménez-Quero, V., León-Martínez, F., Montes-García, P., Gaona-Tiburcio, C., & Chacón-Nava, J. (2013). Influence of sugar-cane bagasse ash and fly ash on the rheological behavior of cement pastes and mortars. *Construction and Building Materials*, 40, 691-701.
- Keya, K. N. (2019). Natural fiber reinforced polymer composites: history, types, advantages and applications. *Materials Engineering Research*, 1(2), 69-85.
- Ku, H., Wang, H., Pattarachaiyakoop, N., & Trada, M. (2011). A review on the tensile properties of natural fiber reinforced polymer composites. *Composites Part B: Engineering*, 42(4), 856-873.
- Moritzer, E., Elsner, C. L., & Schumacher, C. (2021). Investigation of metal-polymer composites manufactured by fused deposition modeling with regard to process parameters. *Polymer Composites*, 42(11), 6065-6079.
- Obasi HC, Mark UC, Mark U. (2021). Improving the mechanical properties of polypropylene composites with coconut shell particles. *Composites and Advanced Materials*, 30. doi:10.1177/26349833211007497
- Ovčáčíková, H., Velička, M., Vlček, J., Topinková, M., & Klárová, M. a. (2022). Corrosive Effect of Wood Ash Produced by Biomass Combustion on Refractory Materials in a Binary Al–Si System. *Materials*, 15(16), 579-586.
- R Vinayagamorthy. (2020). Effect of particle sizes on the mechanical behaviour of limestone-reinforced hybrid plastics. *Polymers and Polymer Composites*, 28(6), 410–42.
- Rachniyom, W., & Srisittipokakun, N. a. (2019). Comparative study of SiO<sub>2</sub> in biomass ashes at different temperatures. *Interdisciplinary Research Review*, 14(3), 12-15.
- Radhakrishnan, G., & Mathialagan, S. (2022). Effect of fiber orientation on mechanical behavior of glass fiber reinforced polyethylene terephthalate foam sandwich composite. *Materials Today: Proceedings*, 62(2), 624-628.
- Rana, S., Alagirusamy, R., & Joshi, M. (2012a). *Carbon Nanomaterial Based Three Phase Multi-functional Composites: Three Phase Multi-functional Composites*. Germany: LAP LAMBERT Academic Publishing GmbH & Co. KG.
- Rana, S., Parveen, S., & Fangueiro, R. (2017). Advanced Carbon Nanotube Reinforced Multiscale Composites. In E. Bafekrpour (Ed.), *Advanced Composite Materials: Properties and Applications* (pp. 545-578). de Gruyter.
- Rauf, N., Damayanti, M., & Pratama, S. (2017). The Influence of Sugarcane Bagasse Ash as Fly Ash on. *AIP Conference Proceedings*, 1801, 1-3.
- Robert, U. W., Etuk, S. E., & Ebuka, A. O. (2019). Modified Water Displacement Method and Its Use for Determination of Bulk Density of Porous Materials. *Journal Renewable Energy & Mechanics*, 01(01), 1-16.
- Ruya Shi, Dongdong Ye, Ke Ma, Wenhan Tian, Yan Zhao, Hongbo Guo, et al. (2022). Understanding the Interfacial Adhesion between Natural Silk and Polycaprolactone for Fabrication of Continuous Silk Biocomposites. *ACS Appl. Mater. Interfaces*, 14(41), 46932–46944.
- Saba, N., Tahir, P. M., Abdan, K., & Ibrahim, N. A. (2016). Physical, structural and thermomechanical properties of oil palm nano filler/kenaf/epoxy hybrid nanocomposites. *Materials Chemistry and Physics*, 184, 64-71.
- Siraj, S., Al-Marzouqi, A., Iqbal, M., & Ahmed, W. (2022). Impact of Micro Silica Filler Particle Size on Mechanical Properties of Polymeric Based Composite Material. *Polymers*, 14(22).
- Sudirman Habibie, N. S. (2021). Prospect of Ramie Fiber Development in Indonesia and Manufacturing of Ramie Fiber Textile-based Composites for Industrial Needs, an Overview. *International Journal of Composite Materials*, 11(3), 43-53.
- Tiwari, S., Srivastava, K., CL, G., & Srivastava, D. (2020). Epoxy/Fly ash from Thermal Power Plant/Nanofiller Nanocomposite: Studies on Mechanical and Thermal Properties: A Review. *Int J Waste Resour*, 10(1).
- Vijayan, S., Subramanian, N., & Sankaranarayanan, K. (Eds.). (2020). *Trends in Manufacturing and Engineering Management: Select Proceedings of ICMechD 2019* (illustrated ed.). Springer Natural Singapore.
- Wan Badaruzzaman, W., Dabbagh, N., Salleh, K., Saharuddin, E., Mat Radzi, N., Azham, M., et al. (2022). Mechanical Properties and Water Absorption Capacity of Hybrid GFRP Composites. *Polymers*, 14(7), 1394.



# Fatigue life assessment of Electric Multi-Unit High-Speed Train Wheel Tread Considering Structural flexibility

Awel Momhur<sup>1,2,\*</sup>, Y.X Zhao<sup>1</sup>, Abrham Gebre<sup>2,3</sup>

<sup>1</sup>School of Mechanical Engineering, Southwest Jiao tong University, Chengdu 10031, China

<sup>2</sup>Addis Ababa University Addis Ababa Institute of Technology, Africa Railway Center of Excellence,

<sup>3</sup>Addis Ababa University Addis Ababa Institute of Technology, School of Civil and Environmental Engineering

\*Corresponding author, e-mail: [awel.mohammedseid@aait.edu.et](mailto:awel.mohammedseid@aait.edu.et)

## ABSTRACT

A vehicle system dynamic model with flexible wheelsets was constructed using the wheelset of the CRH2A high-speed train. To investigate the fatigue life of wheels, the finite element approach and the Palmgren Miner rule were employed. Initially, the wheelset finite element model and its substructure model were developed using ANSYS finite element software. Second, the time history of loads and the dynamic response applied to the wheelset are obtained by utilizing the multibody dynamics software SIMPACK to create a rigid-flexible coupling dynamic model of the vehicle system, which incorporates three selected vehicles. The findings were compared with the vehicle system dynamic models integrated with track irregularity. At last, the fatigue life of the wheel was examined using the Palmgren Miner rule and nominal stresses. The outcomes demonstrate the increased accuracy of the temporal history of dynamic loads applied to the wheels acquired by the vehicle system dynamic model with flexible wheelsets. Moreover, the fatigue life prediction of wheel tread and the overall train safety, and performance considering the track irregularity has a significant effect.

**Keywords:** Fatigue life, Finite element method, Flexible wheelset, Rigid-flexible dynamic model

## 1. INTRODUCTION

The development of EMUs trains in China has been accelerating. The Chinese high-speed EMUs, which serve as a characteristic vehicle, have extended the highest commercial speed in the world at 350 km/h. China's future rail transit system is an important research project featuring different-gauge high-speed EMUs traveling at 400 km/h. The reactions of high-speed EMUs are becoming more difficult and complex due to the increased operational vehicle speed and robust and lightweight construction. High-speed EMUs may experience fatigue due to these amplified responses, frequently observed with severe, unusual vibrations, resonance, and even higher dynamic loads [1]. In each structure project, fatigue life is one of the most important factors for a solid design [2-4]. These days, the evaluation of fatigue life is becoming more and more crucial for both highly sensitive systems and mass production. Peixoto and de Castro [5] studied the formation of fatigue cracks in a high-speed train wheel. Christodoulou et al. [6] examined the behavior of the material's fatigue and damage tolerance. Alongside stereoscopic and fractographic examination of broken specimens, they conducted tests for fatigue, fracture toughness, and fatigue crack propagation. Edel and Boudnitski [7] using the linear elastic fracture mechanics (LEFM) approach analyzed the fatigue behavior of reusable solid railway wheels made of old wheel steel. Because of the recurrent contact stress created by rolling motion, the fatigue issue with train wheels is sometimes referred to as rolling contact fatigue [8]. Analysis of high-cycle fatigue typically uses a stress-based methodology. Empirical equivalent stress, stress invariants, average stress, and critical plane stress are the four categories into which the stress-based techniques can be separated. There are further reviews available [9-12].

The service life of railroad tracks is significantly shortened as a result of damage accumulation brought on by wear, plastic deformation, and fatigue. Wheel/rail contact forces have lately grown due to faster trains and larger axle loads. Rolling contact fatigue is another name for the issue of railroad wheels wearing down [8]. By applying an accepted fatigue damage analysis technique for complex mechanical components, Yongming Liu et al. [13] solve the problem of wheel/rail rolling contact fatigue. Wheel-rail rolling contact fatigue was investigated experimentally by S. Zhang et al. [14]. Liu and Mahadevan [15] presented and used experimental data from bending-torsional fatigue to verify a critical-plane-based model for fatigue damage arising from multiaxial modeling. To improve the interaction between the wheel and the rail, I.Y. Shevtsov [16] looked into a technique



for designing a wheel profile that takes rolling contact fatigue into account while decreasing wear. G. Zhou et al. hypothesized the lateral stress-induced fatigue degradation mechanism of railway wheels [17]. The fatigue life of wheelsets is determined by utilizing field testing carried out by Michele Maglio [18]. Reza Masoudi Nejad investigated railway wheel specimens subjected to cyclic stress in terms of fatigue properties [19]. The effective cyclic elastoplastic rolling contact was proposed by K. A. Meyer et al. [20] using a 3D finite element model.

Reliability engineering has therefore been more well-known over the last few decades as a technique for producing goods with essential reliability and the greatest design. Numerous assessments are in place [21, 22].. Sakalo et al. have released an algorithm for fatigue damage accumulation processes and wear modeling in railway wheels induced by rolling contact [23]. Seo et al. [24] and Lansler and Kabo [25] investigated the subsurface crack formation deflections of railway wheels under rolling contact situations. The essential crack sizes and development parameters for the wheels and rails of train cars were found [26]. A high-speed train wheel's fatigue fracture propagation was studied by Peixoto and de Castro [5]. Wheel fatigue and damage tolerance behavior were studied by Christodoulou et al. [6].

A recent study largely focuses on measuring fatigue life and the dynamic behavior of a single vehicle of multi-body dynamics (rigid and flexible) to analyze the dynamic response in terms of performance, safety, ride comfort, fatigue, and reliability. Furthermore, at this time, there is no research on the multi-body dynamics combined with track irregularity and wheel structural flexible bodies (wheelset, rail, and slab track) for fatigue life assessment under novel approaches.

## **2. MATERIALS AND METHODS**

The multibody dynamic simulation (MBS) method was chosen for this study because it is an affordable solution to assess wheel fatigue life analysis in railway vehicles. As seen in Figure 1, MBS permits the use of experimental techniques to examine a range of operational and fault scenarios that are commercially impractical.

The present research includes the following main sections. First, Flexible wheelset, rail developed based on finite element Method, and the flexible track established based on Programming language FORTRAN. Second, developed Multi body system dynamics by using SIMPACK. Third, established the track irregularity. Fourth, coupling of rigid and flexible body that helps to present the dynamic response result input to Fatigue life assessment. Finally, the fatigue life and damage analysis software is used. The detailed research work methodology is presented in Figure 1.

According to the above method, the structural flexible and track defect influence studied the vehicle load and deliberately considered the speed. Besides, the impact on the dynamic safety and performance of vehicle components will investigate. Moreover, in order to verify the present research work previous studies reported in the literature used. After validating the model, a series of simulations are performed, based on the dynamic impact load, and dynamic stress/strain, under consideration of selected vehicle. Finally, the fatigue life assessment of electric multi-unit vehicle (EMUs) of wheel tread can be examined.

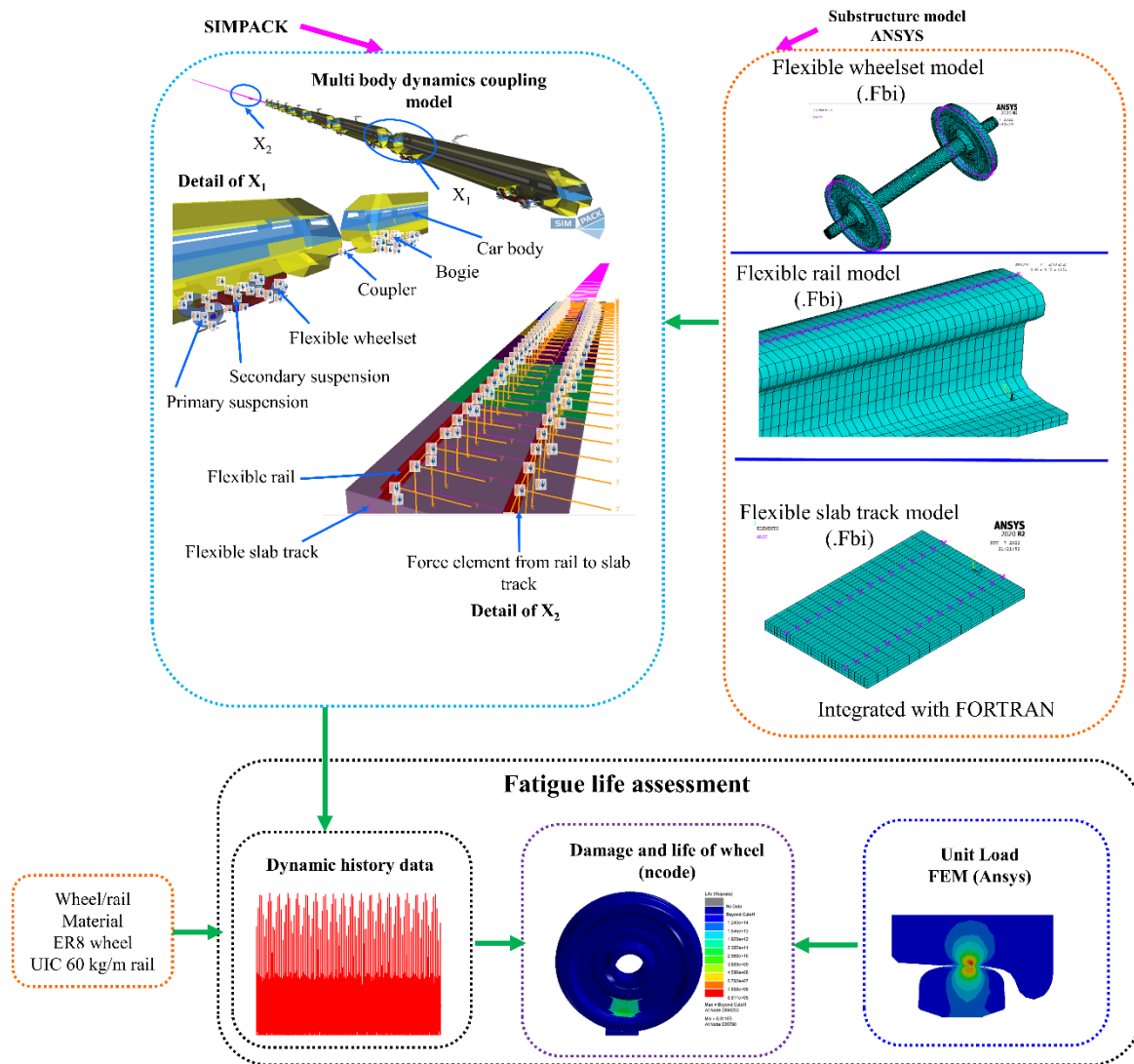


Figure 1. Fatigue life assessment of present research work methodology

### 3. VEHICLE/TRACK COUPLED MODEL

To take into consideration the maximum impact loads and the dynamic performance of the train caused by track irregularity, as well as to measure the fatigue life, a coupled vehicle/track model integrating the flexible slab and rail, the wheel/rail interaction, and the flexible wheelset model is developed.

#### 3.1 Vehicle Dynamic Model

This investigation provided a typical train on China's CRH2A high-speed rail line. The structural parameters of the CRH2A type, which consists of eight car bodies, 32 wheelsets, and 16 bogies, are used to build the coupling vehicle dynamic model see Figure 2. Awel Momhur et al. [27] also presented a detailed vehicle/track model equation in their previous work. As a result, the single-vehicle dynamic model is given 35 degrees of freedom.

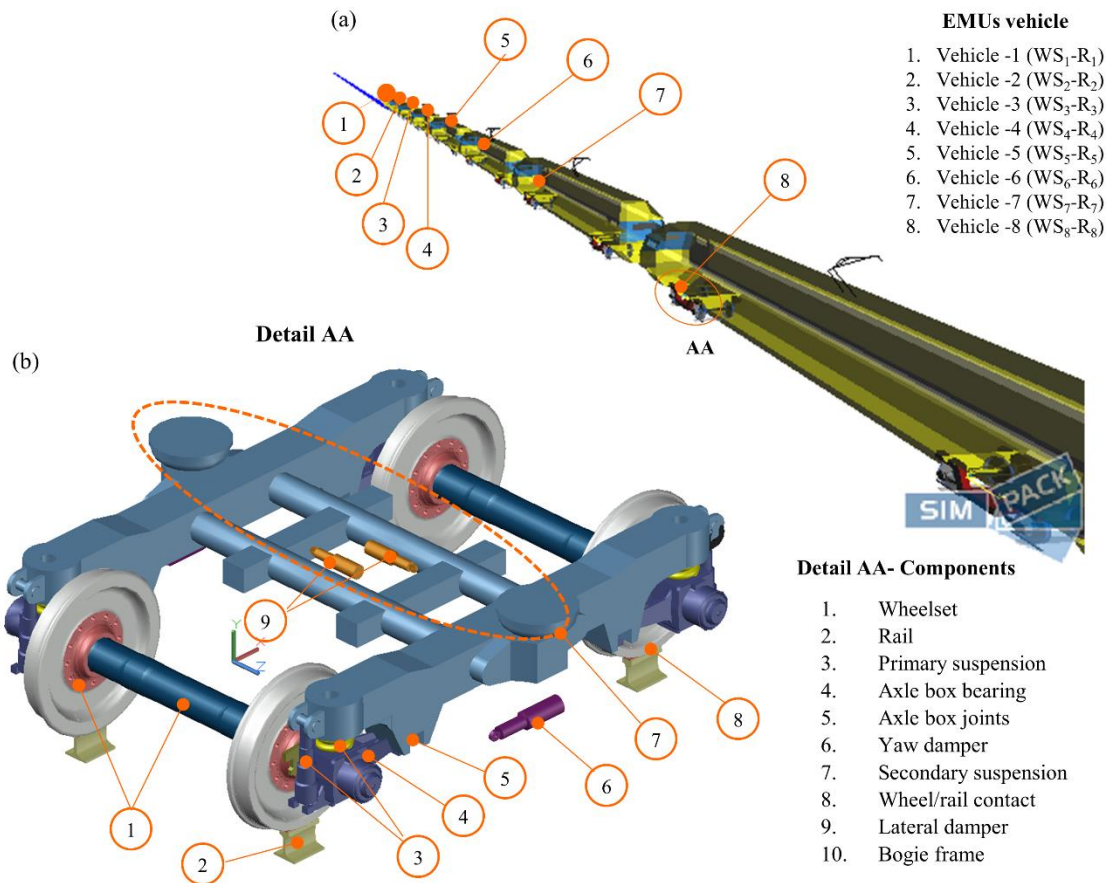


**Figure 2.** Railway vehicle-track dynamic model. (a) Eight coupled vehicles, (b) Detail of the bogie components

Figure 2 (a) shows the fully loaded couple multi-body system dynamics and Figure 2 (b) detail of the bogie components. The dynamic motion equation of a vehicle with a wheel-rail interaction model is expressed in the form of a submatrix.

$$\begin{bmatrix} M_v & 0 \\ 0 & M_r \end{bmatrix} \begin{Bmatrix} \ddot{D}_v \\ \ddot{D}_r \end{Bmatrix} + \begin{bmatrix} C_v & 0 \\ 0 & C_r \end{bmatrix} \begin{Bmatrix} \dot{D}_v \\ \dot{D}_r \end{Bmatrix} + \begin{bmatrix} K_v & 0 \\ 0 & K_r \end{bmatrix} \begin{Bmatrix} D_v \\ D_r \end{Bmatrix} = \begin{Bmatrix} F_v \\ F_r \end{Bmatrix} \quad (1)$$

where the subscripts 'v' and 'r' intend the vehicle dynamics and track of the subsystem, correspondingly; M, C, and K refer to the subsystem matrices of collection, stiffness, and damping separately; and D and F represent the longitudinal vehicle movement and external force employed on the system, respectively.

### 3.2 Structural Flexibility Model

To develop a flexible body structure, the authors of this study expanded on their earlier research [28]. They have also introduced a flexible track to the system dynamics to accommodate straight and curved tracks. At this point, mass, stiffness, damping, and modal matrices are analyzed by FE software. Since the slab and rail model must be built as a superelement in ANSYS before it can be entered into SIMPACK, a substructure analysis must be completed first. The substructuring method enables the element, as shown in Figure 4-6, to be reduced in size to a single unit represented as a matrix, called the superelement. As shown in Figure 3, the maximum frequency level that occurred during the multibody system integration simulation was determined by analyzing the modal frequency of the structure flexibility for the wheelset, rail, and slab track.

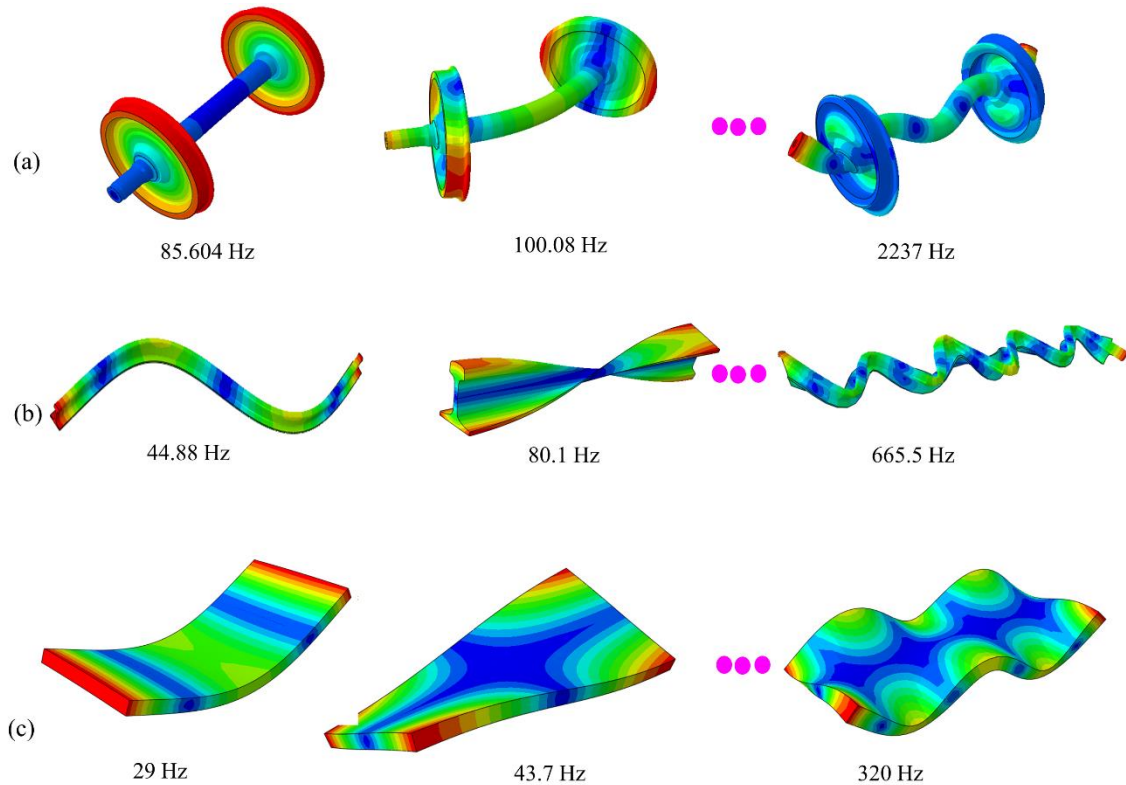


**Figure 3.** Modal frequency of the structural flexibility: (a) wheelset, (b) rail, and (c) slab track

### 3.2.1 Flexible wheelset

Figure 4 shows that the flexible wheelset model was generated using the finite element method to assess the high-frequency wheelset vibration and the wheelset axle dynamic stress caused by the wheel damage. Equation 2 can be used to show the location of any point M on the wheelset.

$$\vec{X}^0(t) + P^{XM} + X^f(X^M, t) \quad (2)$$

$\vec{x}^M$  is the vector denoting the restricted (local) coordinates of a general independent variable on the wheelset, and  $P = P(\varphi)$  is the transformation matrix resulting from the rotation of a rigid body  $\vec{\varphi} = [\varphi(t), x(t), \psi(t)]$ .

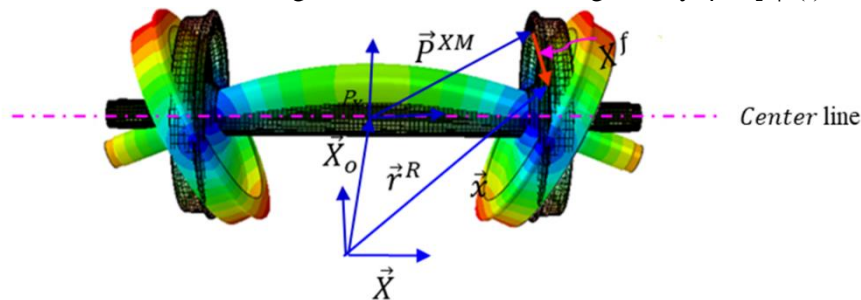


**Figure 4.** Deformed and undeformed wheelset model for construction of mathematical equation

The movement of the wheelset centre as a rigid body is represented by  $X^0(t)$ . The flexibility of the system allows for the consideration of the movement of the  $\vec{x}^f(\vec{x}^M, t)$  point  $\vec{x}^M$  and the modification of  $\vec{x}^f$  following the many flexible modes of the wheelset formula 16 express as.

### 3.2.2 Flexible rail

Deformable rails can be represented using a floating reference frame of design [29] in simulations of multi-body rail dynamics, as shown in Figure 5. The flexible section detail equation and relations for the rail, slab track, and wheelset are also presented in the author's earlier work [28].

The technique gives the overall location of any point  $Q_r$  on a deformable track.

$$r^{Q_r} = r^R + b^r (d_r^{Q_{or}} + d_r^{Q_r}) \quad (3)$$

where  $r^R$  is the vector location of the origin of the frame structure  $X_r Y_r Z_r$  concerning the overall (global) frame  $G_f$ -XYZ,  $b^r$  the rotation matrix necessary to change the components of a vector from the rail to the global frame,  $\vec{d}_r^{Q_{or}}$  the vector location of the point Q, the equation below can be used to obtain the vector  $\vec{d}_r^{Q_r}$ .

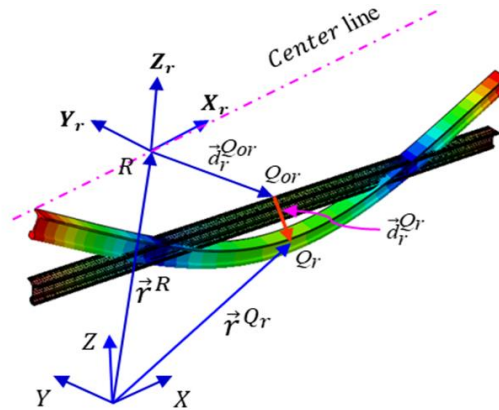


Figure 5. Deformed and undeformed rail model for construction of mathematical equation

### 3.2.3 Flexible slab track

Under each wheel, the floating track frame encounters rail deformation, as shown in Figure 6. The floating track frame is  $G_f$ -XYZ, while the entire train-track system's inertial reference frame is  $G_f$ -XYZ. The track initial frame is  $S_0$ - $X^{s0} Y^{s0} Z^{s0}$  and  $S$ - $X^s Y^s Z^s$ . A 3D model of the slab track structure is provided in this study, which deliberates the behaviors of the rails, fasteners, track slabs, and subgrade. The location vector of the selected point  $Q_s$  on the rails can be written [30], as shown in Figure 6.

$$r^{Q_s} = r^S + b^r (\vec{d}_s^{Q_{os}} + b^{sr} \vec{d}_s^{Q_s}) \quad (4)$$

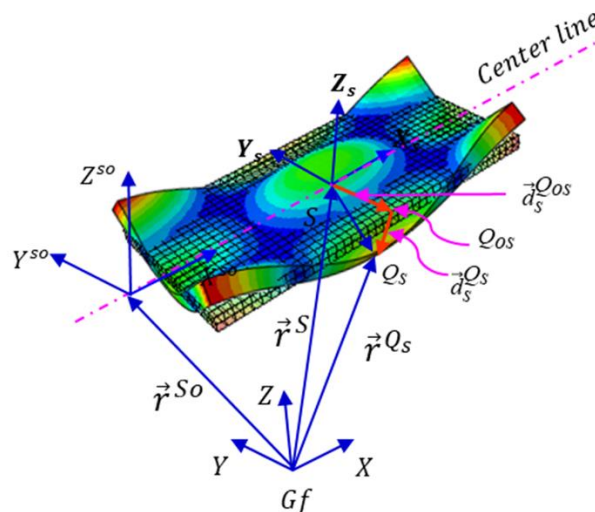


Figure 6. Deformed and undeformed slab track model for construction of mathematical equation

where  $r^S$  is the location vector of the source of the body frame ( $X_s Y_s Z_s$ ) regarding the global frame XYZ,  $b^r$  the rotation essential matrix to convert the elements of a vector from the rail to the global frame,  $b^{sr}$  the direction of the matrix of the trajectory frame regarding the coordinate rail system,  $\vec{d}_s^{Q_{os}}$  the location vector of the point  $Q_{os}$

regarding the body frame when the flexible body is undeformed and  $\vec{d}_s^{Q_s}$  the movement of the point  $Q_s$  by the effect of deformation

#### 4. NUMERICAL MODEL

##### 4.1 Verification of Multi-Body System Dynamic Model

Our earlier research [28] and [31] sufficiently validated the suggested multi-body system dynamics model when combined with uncertainty parameters and finite elements. Figure 7(a-d) illustrates the time domain acceleration. The time history correlation analyses, as shown in Figure 7(a-d), demonstrate a good agreement between the current model and reference [31]. On the vertical rail, lateral rail, vertical slab, and slab lateral acceleration, the relative errors of the two models are 7.69, 5.13, 4.78 and 4.02%, respectively.

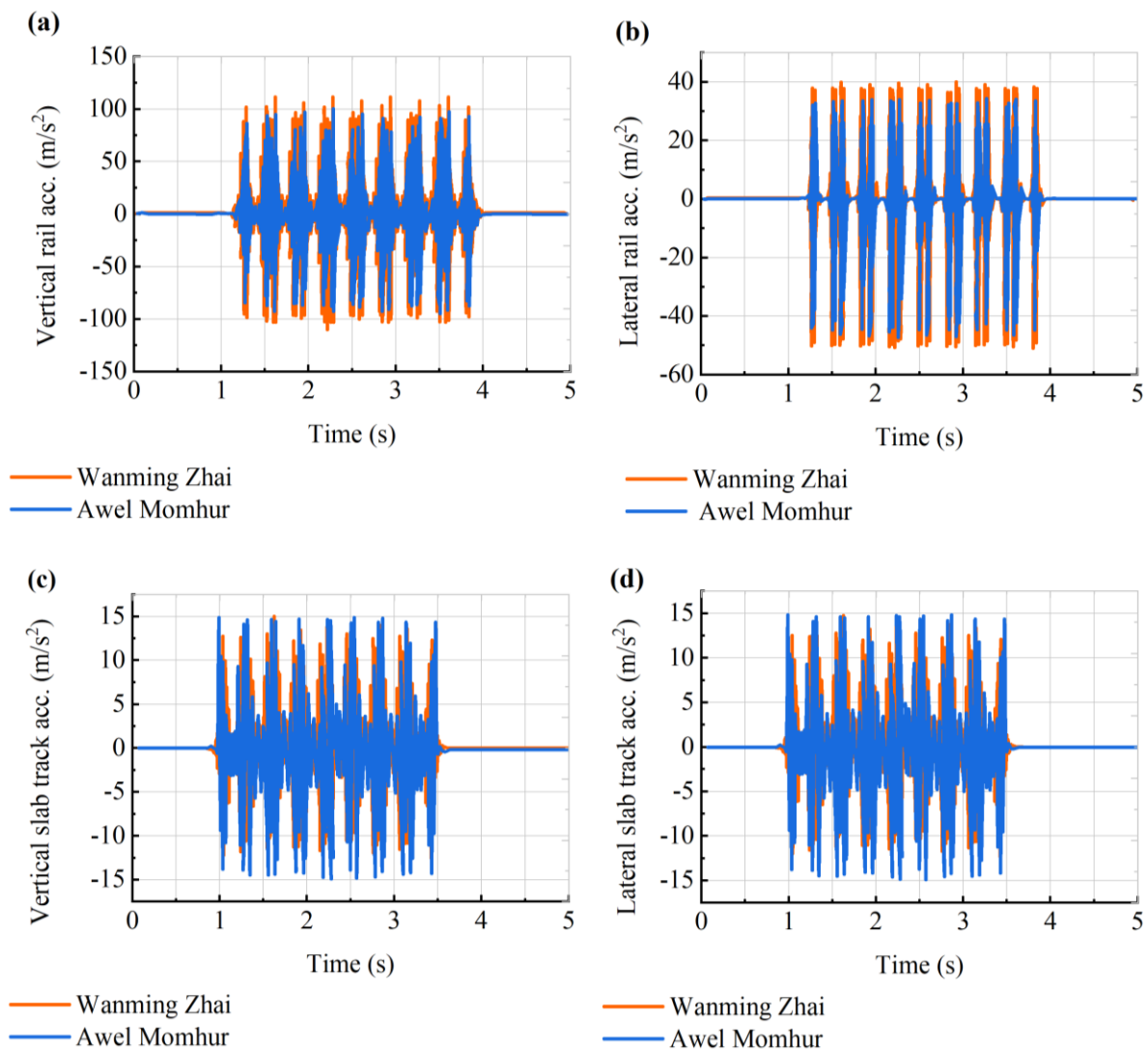


**Figure 7.** Validation of the multi-body system dynamics model: (a) vertical rail acceleration, (b) lateral rail acceleration, (c) vertical slab track acc., and (d) lateral slab track acc.

It was clear from Figure 7 that the new method yields results that are almost strictly comparable to those of the reference and enables the dynamic examination of structures that are challenging to describe theoretically, such as flexible wheelsets, vehicle bodywork, and so forth.

##### 4.2 Vehicle Dynamic Response

The flexible-rigid multi-body dynamics model (FRMBD) is used by SIMPACK software to capture dynamic responses, and 200-300 km/h is the operating speed on a straight line.

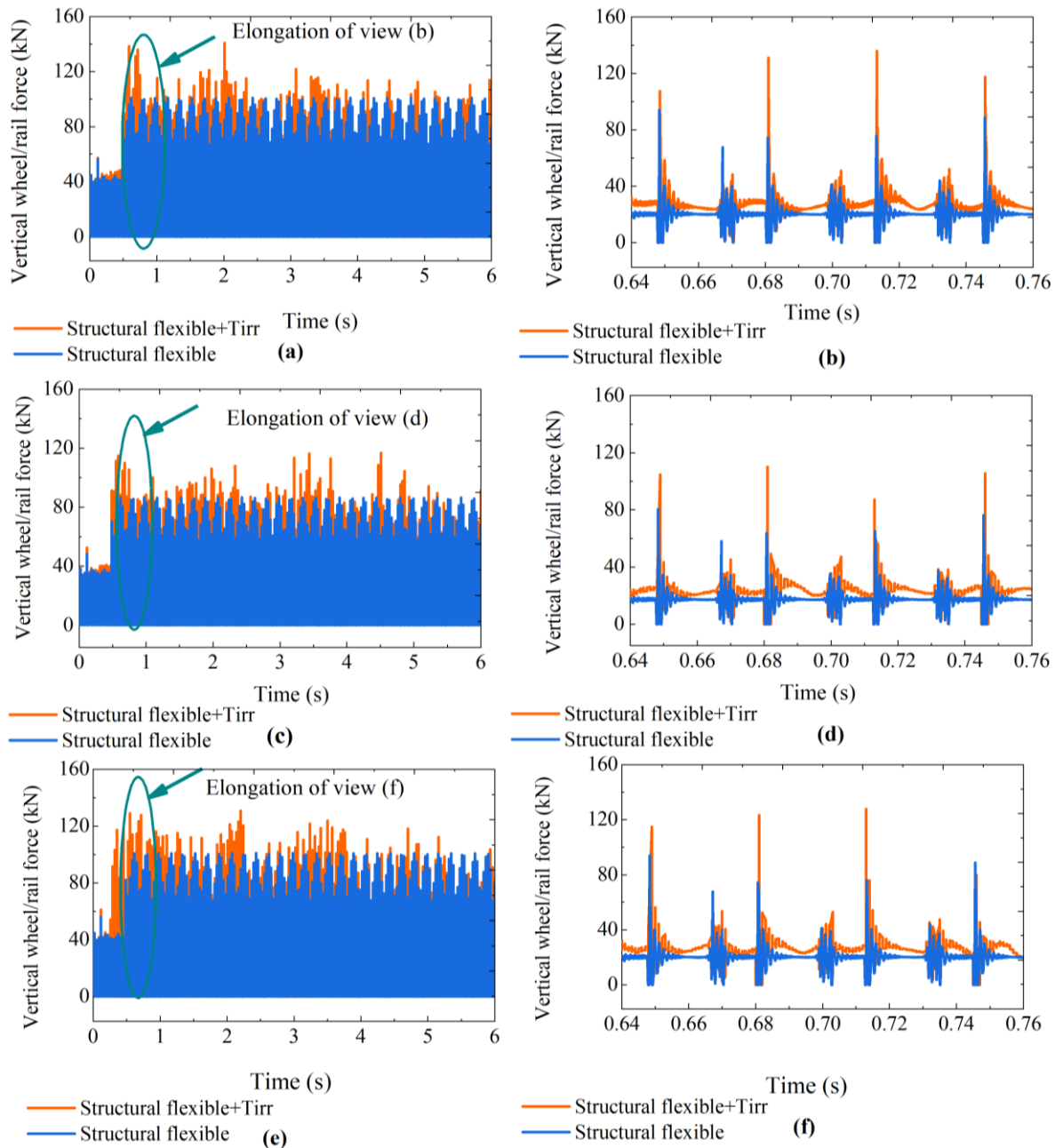


Figure 8: Dynamic response of vertical wheel/rail contact force structural flexibility and track irregularity with vehicle speed ( $v=200$  km/h): (a, c, and e) leading, middle, and rear vehicle, (b, d, and f) elongation

The vibration amplitude is more important than the average value under cyclic operating circumstances. The selected sample, leading, middle, and rear vehicles, are effectively studied to assess the dynamic response of flexible body integrated with and without track irregularity. Figure 8 (a, c, and e) illustrate the dynamic impact of three selected vehicle models, and Figure 8 (b, d, and f) indicates the elongation view of the response. Figure 8 shows the vertical dynamic response of flexible wheel/rail contact with track irregularity (Tirr) of the leading, middle, and rear vehicles are about 140 kN, 120 kN, and 130 kN, respectively. Similarly, the vertical dynamic response of flexible wheel/rail contact without track irregularity of the selected vehicles are about 105 kN, 90 kN, and 100 kN, respectively. Consequently, the track irregularity and flexible body introduced to the system dynamics significantly affect the vehicle system. Therefore, the relative variation of vertical force with and without track irregularity are for the leading vehicle 28.57 %, middle vehicle 28.1 %, and rear vehicle 26 %, respectively.

### 4.3 Influence of Dynamic Stress and Strain

The dynamic von Mises equivalent stress responses of the component are shown in Figure 9-11. Figure 9-11 (a) demonstrates the dynamic von-misses stress of wheel/rail contact with and without uncertainty parameters (UP). Figure 9-11 (b) also indicates the elongation view of dynamic von Mises stress.

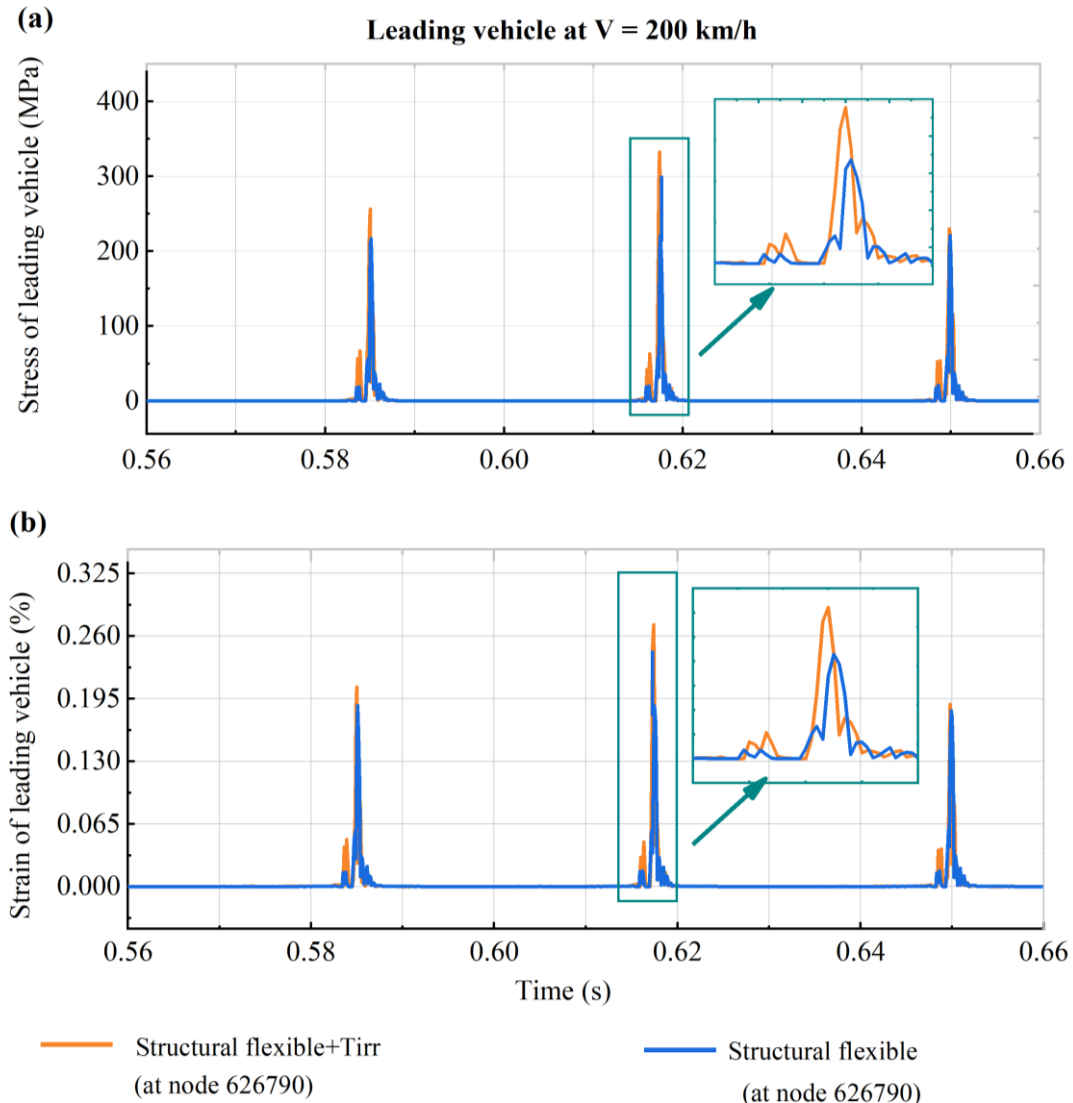


Figure 9: Leading vehicle of dynamic response of vertical wheel/rail contact force structural flexibility and track irregularity with vehicle speed ( $v=200$  km/h): (a) leading vehicle, (b) elongation view of (a), and (c) elongation of view of (b)

The dynamics of von-misses stress amplitude of the leading, middle, and rear vehicle in the absence of track irregularity are about 300 MPa, 240 MPa, and 250 MPa compared with 340 MPa, 270 MPa, and 290 MPa in the presence of uncertainty parameters, the relative variation in percentage for leading vehicle 12.5 %, for middle vehicle 11.76 %, and rear vehicle 14.76 %.

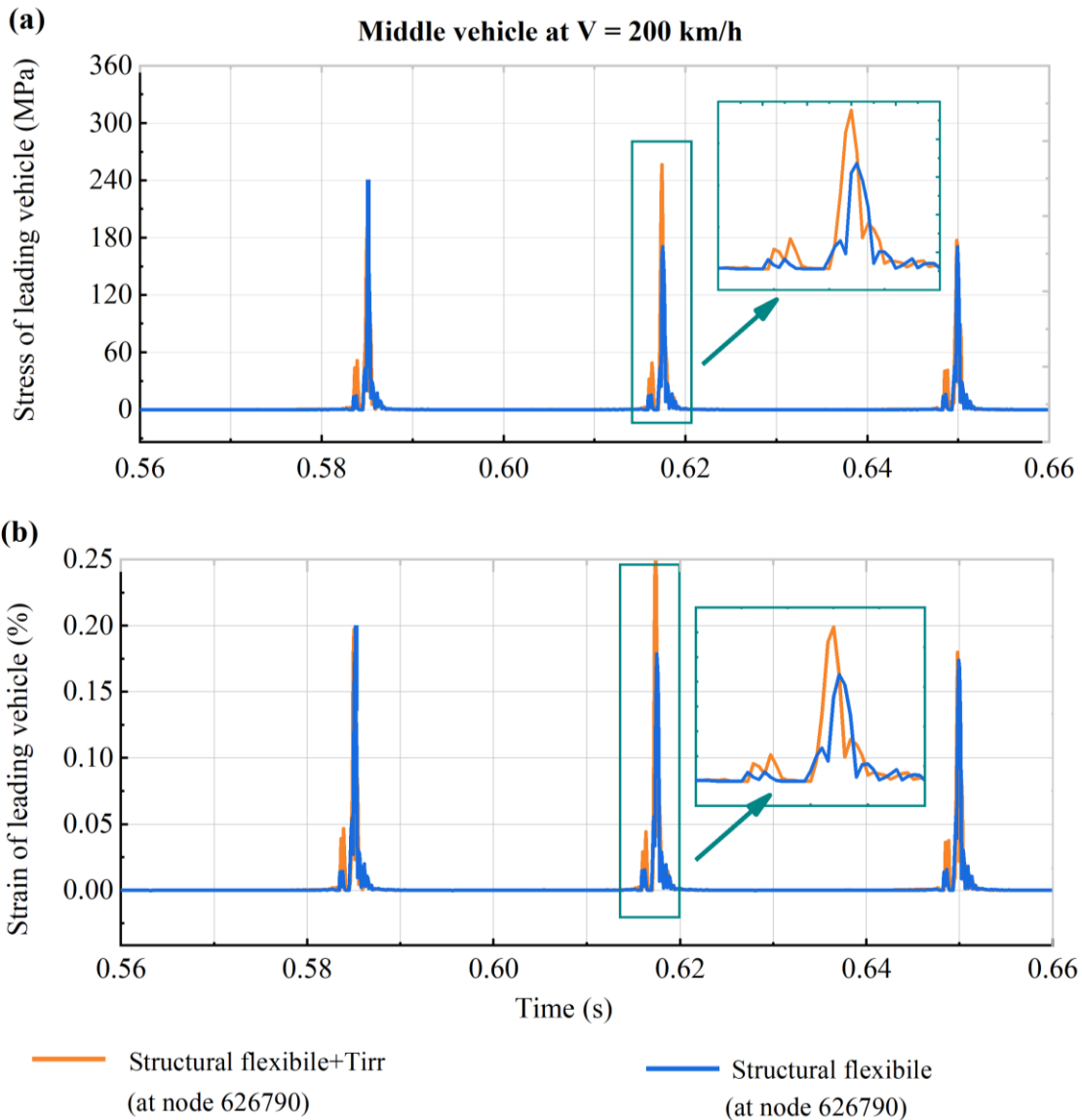


Figure 10: Middle vehicle of dynamic response of vertical wheel/rail contact force structural flexibility and track irregularity with vehicle speed ( $v=200$  km/h): (a) leading vehicle, (b) elongation view of (a), and (c) elongation of view of (b)

It means the random dynamic behavior with wheel flat damage and uncertainty parameters have significant differences on the dynamic von-mises stress of the wheel/rail contact. Therefore, the maximum von Mises equivalent stress should be observed as significantly higher than the wheel yield stress (540 MPa), which may lead to local plastic deformation of the wheel.

Additionally, based on such analyses, it can be found that the random dynamic has a significant effect on the leading and rear. Still, the middle vehicle has a relatively slight impact on dynamic response. Thus, the random behavior, wheel flat damage, and flexible body should be carefully considered for the fatigue life assessment.

Figure 9-11 (c) shows the dynamic von-mises strain of wheel/rail contact with and without uncertainty parameters (UP). Figure 9-11 (d) also indicates the elongation view of dynamic von Mises stress. The vertical dynamics of von-mises strain amplitude of the leading, middle, and rear vehicle in the absence of track irregularity are about 0.245 %, 0.22 %, and 0.23 % compared with 0.28 %, 0.25 %, and 0.27 % in the presence of uncertainty parameters, the relative variation in percentage for leading vehicle 13.3 %, for middle vehicle 12.76 %, and rear vehicle 16 %. It means the dynamic behavior with track irregularity and structural flexibility has significantly differ on the dynamic von Mises stress and strain of the wheel/rail contact.

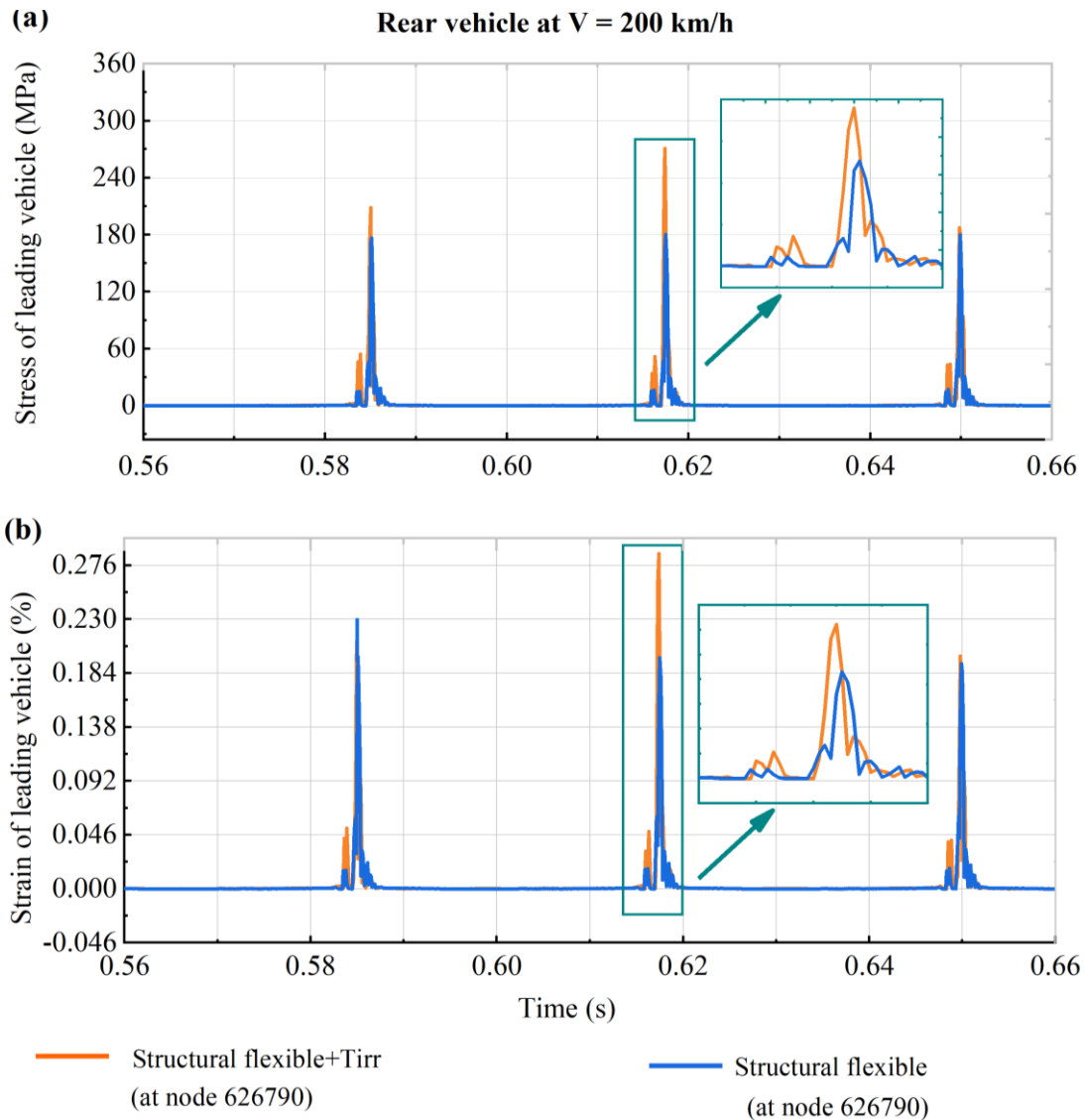


Figure 11: Rear vehicle of dynamic response of vertical wheel/rail contact force structural flexibility and track irregularity with vehicle speed ( $v=200$  km/h): (a) leading vehicle, (b) elongation view of (a), and (c) elongation of view of (b).

#### 4.4 Fatigue Life Assessment Of ER8 Wheel

To get around the wheelset, non-conservative assessment under extrapolation changing amplitude loads, the relative Miner's rule [32] is used. According to the relative Miner's rule, the severe cumulative damage  $D^c$  ( $D^c = 1$ ) is taken into account by using the conventional Miner's rule with a safety factor  $q^{sf}$  ( $q^{sf} < 1$ ). Thus, a component's service life can be calculated in cumulative fatigue damage  $D$ .

$$D = \frac{1}{N} \tag{5}$$

For simplicity in the present investigation, Miner's rule, a linear damage accumulation rule, is employed. Miner's rule is described in general by Equation (6).

$$D = \sum_{i=1}^K D_i = \sum_{i=1}^K \frac{n_i}{N_i} \tag{6}$$

where  $K$  is the number of loading blocks,  $i$  the  $i$ th applied loading cycle.



The wheel/rail contact point is where the maximum cumulative damage positions are placed, according to Figure 12. Figure 12 (a) illustrates the fatigue life of the three selected vehicles. Their minimum fatigue life is  $8.811e^5$  for the leading,  $2.02e^6$  for the middle, and  $1.302e^6$  for the rear vehicle in the presence of track irregularity and similarly, Figure 12 (b) shows that  $4.288e^6$  for the leading,  $9.841e^6$  for the middle, and  $5.513e^6$  for the rear vehicle without track irregularity. The duration for the load spectrum selected in the calculation process is 90 s, and the travelling distance is about 6.1 km. Therefore, from this condition, the total mileage that the wheelset can run during the fatigue life of the leading, middle, and rear vehicles in the presence of track irregularity is about 5.37, 12.32, and 7.94 million kilometres, respectively. Similarly, without track irregularity is about 26.15, 60.03, and 33.6 million kilometres, separately. Consequently, the CRH2A EMUs China high-speed train runs 800,000 kilometres per year. Therefore, based on this travelling history data, the fatigue life of the leading, middle, and rear vehicles with track irregularity is about 6.71, 15.4, and 9.9 years, respectively. Similarly, without track irregularity, the fatigue life for the selected vehicle is 26.15, 60.03, and 33.6 years, correspondingly.

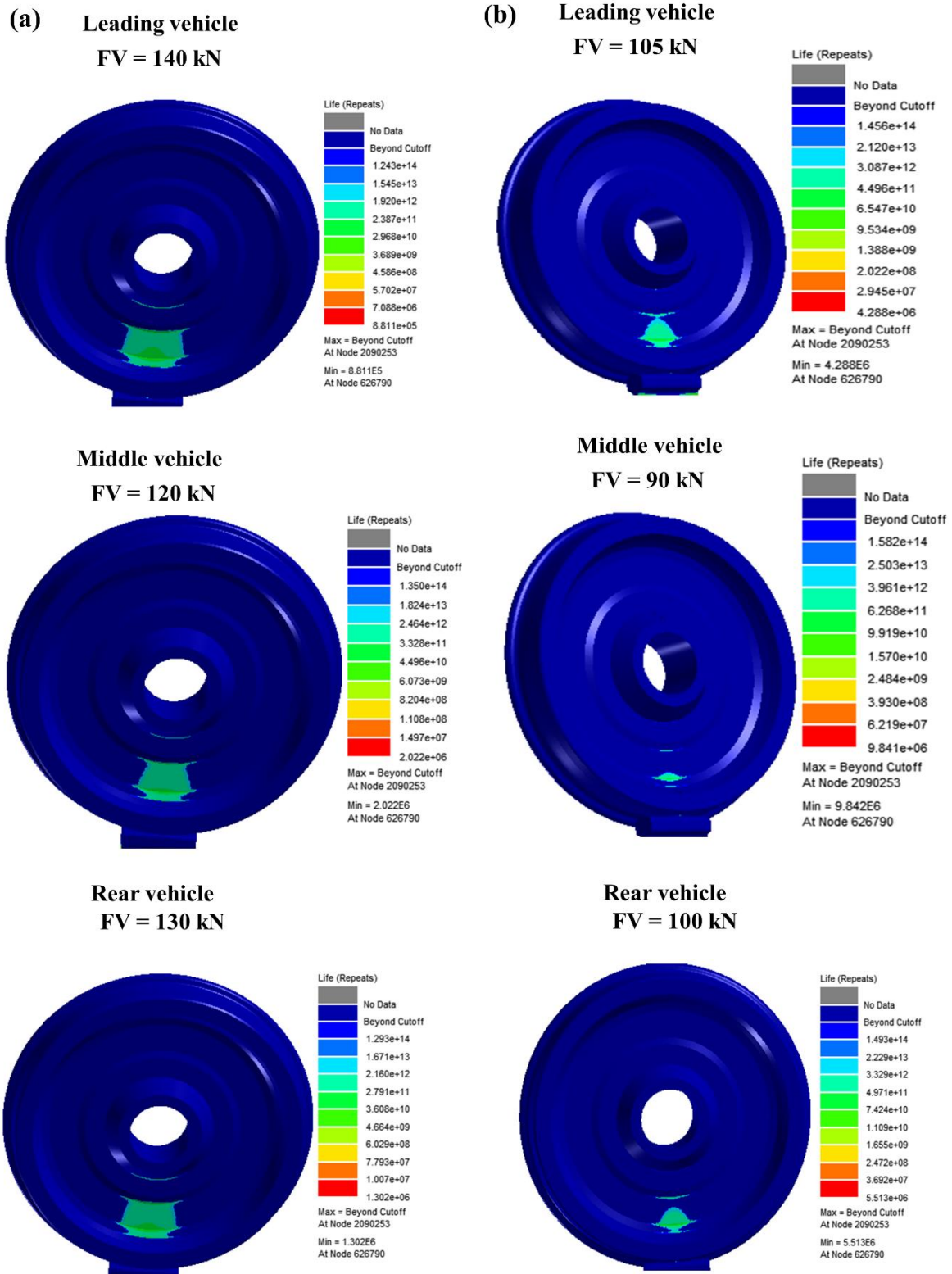


Figure 12: The fatigue life of wheelset: (a-c) with UP+FR+wf (leading, middle, and rear vehicle), (d-f) without UP+FR+wf (leading, middle, and rear vehicle), at the wheel flat length 50 mm, vehicle speed 300 km/h

## 5. CONCLUSIONS

The present research work mainly focused on assessing the fatigue life of the EMUs wheel. A numerical model investigates the fatigue life of the CRH2A train based on Palmgren Miner rule, finite element model, and integrated with fully loaded eight coupled vehicles of system dynamics under consideration of flexible body (wheelset, rail, and slab track). The fatigue life assessment based on the cumulative damage at the hot spot position



of the wheel/rail contact is then calculated and compared with track irregularity and without track irregularity. From the foregoing studies; the following conclusion can be drawn.

- 1) A Multi-body system dynamics integrated with structural flexibility is developed to extract the influence of dynamic impact load, dynamic stress/strain, wheel damage can be considered effectively.
- 2) The fully loaded eight-vehicle multi-body system dynamic result indicates the influence of vertical impact load, dynamic von-mises stress, and dynamic von-mises strain high in the leading, rear, and middle vehicles.
- 3) According to fatigue life assessments, simulation result indicates that the fatigue life of the leading, middle, and rear vehicles with track irregularity is about 6.71, 15.4, and 9.9 years, respectively. Similarly, without track irregularity, the fatigue life for the selected vehicle is 26.15, 60.03, and 33.6 years, correspondingly. From this can be understood that the random dynamic behaviour and the wheel defect significantly reduced the life period of the wheel. Moreover, regular maintenance is mandatory to improve train performance, safety, reliability, ride comfort, and fatigue life.
- 4) It is critically recommended that the flexible body (wheelset, rail, and slab track) developed in this study should be considered in the dynamic system when a numerical framework evaluates the fatigue life of the wheel based on vehicle system dynamics (VSD) and finite element (FEM)

## REFERENCE

- [1] W. Zhai, P. Liu, J. Lin, and K. Wang, "Experimental investigation on vibration behaviour of a CRH train at speed of 350 km/h," *International Journal of Rail Transportation*, vol. 3, no. 1, pp. 1-16, 2015.
- [2] R. Branco, J. D. Costa, L. Borrego, F. Berto, N. Razavi, and W. Macek, "Comparison of different one-parameter damage laws and local stress-strain approaches in multiaxial fatigue life assessment of notched components," *International Journal of Fatigue*, vol. 151, p. 106405, 2021.
- [3] X.-Y. Fang, W. Huang, X.-F. Yang, and J.-G. Wang, "Effects of temperature on fatigue cracks initiation and propagation for a high-speed railway wheel rim steel," *Engineering Failure Analysis*, vol. 109, p. 104376, 2020.
- [4] E. Mortazavian, Z. Wang, and H. Teng, "Repair of light rail track through restoration of the worn part of the railhead using submerged arc welding process," *The International Journal of Advanced Manufacturing Technology*, vol. 107, pp. 3315-3332, 2020.
- [5] D. F. Peixoto and P. M. de Castro, "Fatigue crack growth of a railway wheel," *Engineering failure analysis*, vol. 82, pp. 420-434, 2017.
- [6] P. Christodoulou, A. Kermanidis, and G. Haidemenopoulos, "Fatigue and fracture behavior of pearlitic Grade 900A steel used in railway applications," *Theoretical and Applied Fracture Mechanics*, vol. 83, pp. 51-59, 2016.
- [7] K.-O. Edell and G. Boudnitski, "Fracture mechanical fatigue analysis of railway wheels with rolling defects," in *European Structural Integrity Society*, vol. 22: Elsevier, 1997, pp. 125-133.
- [8] K. Johnson, "The strength of surfaces in rolling contact," *Proceedings of the Institution of Mechanical Engineers, Part C: Mechanical Engineering Science*, vol. 203, no. 3, pp. 151-163, 1989.
- [9] Y. Garud, "Multiaxial fatigue: a survey of the state of the art," *Journal of Testing and Evaluation*, vol. 9, no. 3, pp. 165-178, 1981.
- [10] I. V. Papadopoulos, P. Davoli, C. Gorla, M. Filippini, and A. Bernasconi, "A comparative study of multiaxial high-cycle fatigue criteria for metals," *International journal of fatigue*, vol. 19, no. 3, pp. 219-235, 1997.
- [11] Y.-Y. Wang and W.-X. Yao, "Evaluation and comparison of several multiaxial fatigue criteria," *International Journal of Fatigue*, vol. 26, no. 1, pp. 17-25, 2004.
- [12] B.-R. You and S.-B. Lee, "A critical review on multiaxial fatigue assessments of metals," *International Journal of Fatigue*, vol. 18, no. 4, pp. 235-244, 1996.
- [13] Y. Liu, B. Stratman, and S. Mahadevan, "Fatigue crack initiation life prediction of railroad wheels," *International journal of fatigue*, vol. 28, no. 7, pp. 747-756, 2006.
- [14] S. Zhang *et al.*, "Experimental study on wheel-rail rolling contact fatigue damage starting from surface defects under various operational conditions," *Tribology International*, vol. 181, p. 108324, 2023.
- [15] Y. Liu and S. Mahadevan, "Multiaxial high-cycle fatigue criterion and life prediction for metals," *International Journal of Fatigue*, vol. 27, no. 7, pp. 790-800, 2005.
- [16] I. Shevtsov, V. Markine, and C. Esveld, "Design of railway wheel profile taking into account rolling contact fatigue and wear," *Wear*, vol. 265, no. 9-10, pp. 1273-1282, 2008.
- [17] G. Zhou, C. He, G. Wen, and Q. Liu, "Fatigue damage mechanism of railway wheels under lateral forces," *Tribology International*, vol. 91, pp. 160-169, 2015.
- [18] M. Maglio, E. Kabo, and A. Ekberg, "Railway wheelset fatigue life estimation based on field tests," *Fatigue & Fracture of Engineering Materials & Structures*, 2022.



- [19] R. M. Nejad and F. Berto, "Fatigue fracture and fatigue life assessment of railway wheel using non-linear model for fatigue crack growth," *International Journal of Fatigue*, vol. 153, p. 106516, 2021.
- [20] K. A. Meyer, R. Skrypnik, and M. Pletz, "Efficient 3d finite element modeling of cyclic elasto-plastic rolling contact," *Tribology International*, vol. 161, p. 107053, 2021.
- [21] D. Kim, K. Park, K. Kim, C.-S. Seok, J. Lee, and K. Kim, "A method for predicting the delamination life of thermal barrier coatings under thermal gradient mechanical fatigue condition considering degradation characteristics," *International Journal of Fatigue*, vol. 151, p. 106402, 2021.
- [22] M. Yamamoto, "Non-parametric optimization of railway wheel web shape based on fatigue design criteria," *International Journal of Fatigue*, vol. 134, p. 105463, 2020.
- [23] V. Sakalo, A. Sakalo, A. Rodikov, and S. Tomashevskiy, "Computer modeling of processes of wear and accumulation of rolling contact fatigue damage in railway wheels using combined criterion," *Wear*, vol. 432, p. 102900, 2019.
- [24] J. W. Seo, S. J. Kwon, H. K. Jun, and D. H. Lee, "Effects of residual stress and shape of web plate on the fatigue life of railway wheels," *Engineering Failure Analysis*, vol. 16, no. 7, pp. 2493-2507, 2009.
- [25] E. Lansler and E. Kabo, "Subsurface crack face displacements in railway wheels," *Wear*, vol. 258, no. 7-8, pp. 1038-1047, 2005.
- [26] K.-O. Edel, "Allowable crack sizes for railway wheels and rails," *Theoretical and Applied Fracture Mechanics*, vol. 9, no. 2, pp. 75-82, 1988.
- [27] A. Momhur, Y. Zhao, L. Quan, S. Yazhou, and X. Zou, "Flexible-Rigid Wheelset Introduced Dynamic Effects due to Wheel Tread Flat," *Shock and Vibration*, vol. 2021, 2021.
- [28] M. Awel and Z. YongXiang, "The random dynamic performances of EMUs with polygonal damages," *Vehicle System Dynamics*, pp. 1-26, 2023.
- [29] A. Shabana, *Dynamics of multibody systems*. Cambridge university press, 2020.
- [30] R. Chamorro, J. L. Escalona, and M. González, "An approach for modeling long flexible bodies with application to railroad dynamics," *Multibody System Dynamics*, vol. 26, no. 2, pp. 135-152, 2011.
- [31] J. Luo, S. Zhu, and W. Zhai, "An advanced train-slab track spatially coupled dynamics model: Theoretical methodologies and numerical applications," *Journal of Sound and Vibration*, vol. 501, p. 116059, 2021.
- [32] W. Schütz, "The prediction of fatigue life in the crack initiation and propagation stages—a state of the art survey," *Engineering fracture mechanics*, vol. 11, no. 2, pp. 405-421, 1979.



# Single Fiber Characterization in Light of Micromechanical Analysis and Mechanical Modeling of Enset Plant Fiber and Its Composite

Ababayehu Abdela<sup>1,\*</sup>, Bart Buffel<sup>2</sup>, Belete Sirahbizu<sup>3</sup>, Frederik Desplentere<sup>2</sup>

<sup>1</sup>Ethiopian Institute of Technology-Mekelle, Mekelle University, Mekelle, Ethiopia

<sup>2</sup>Department of Materials Engineering, ProPoLiS research group, KU Leuven, Bruges campus, Bruges, Belgium

<sup>3</sup>College of Engineering, Addis Ababa Science and Technology University, Addis Ababa, Ethiopia

\*Corresponding author, e-mail: [abexmesc@yahoo.com](mailto:abexmesc@yahoo.com)

## ABSTRACT

The investigation of tensile properties at the fiber level is crucial for conducting micromechanical analyses and mechanical modeling of materials and their composites. Yet, there is a research gap when it comes to Enset fiber. To bridge this gap, a study was conducted to characterize single Enset fibers, with a primary focus on measuring fiber diameter, determining density, assessing single fiber tensile strength and stiffness, and conducting relevant analyses. JMP 13 Pro and Python programming were employed for experiment design and analysis. The measurement of strain, strength, and stiffness, along with subsequent correlation, was carried out using digital image correlation technique. The finding revealed that, Enset fiber has a density of  $1.38\text{gcm}^{-3}$ , signifying its suitability for feasibility in lightweight applications. Also, its notable strength, capable of reaching 1000Mpa, coupled with its good stiffness, makes it as a promising substitute with commendable capacity for bearing mechanical loads while also presenting environmental advantages. In conclusion, Enset fiber demonstrates the necessary qualities to be considered a viable alternative for various lightweight industrial applications. This positions it as a competitive fiber, contingent upon careful extraction, proper treatment, and efficient processing. The utilization of Enset fiber in industrial settings, coupled with value addition, would yield be a win-win scenario for both industries and farmers, offering the later with a much-needed additional source of income.

**Keywords:** Enset, Enset fiber, processing, strength, lightweight application

## 1. INTRODUCTION

The characteristics of the natural fiber reinforced composite are dependent on the attributes of the fibers used; the fiber properties helps to estimate the properties of the resulting material. Specially, the tensile tests of fibers serve as a means to ascertain the mechanical properties of the fibers and helps to determine the fiber's mechanical properties before using them as a reinforcement (Abdela et al., 2021; Cline et al., 2018; B. Sanborn & Weerasooriya, 2015; Brett Sanborn et al., 2015) (Andersons, n.d.; Depuydt et al., 2017; Kim et al., 2015; B. Sanborn & Weerasooriya, 2015). This approach is preferred in situations where there is a limited material during the material development phase (Andersons, n.d.; Cline et al., 2018; Brett Sanborn et al., 2015). Understanding the tensile properties of fibers is essential for conducting micromechanical analyses and mechanical modeling of these materials and their composites (Abdela et al., 2021; Cline et al., 2018; Depuydt et al., 2017). While manufacturers usually offer fiber properties for synthetic fibers, datasheets are often lacking for natural fibers. Due to unavailability of data for natural fibers, when testing new materials, the need to characterize plant fibers' tensile characteristics is inevitable (Karimah et al., 2021; Monteiro et al., 2010; Saadati et al., 2019).

Alternatively, literatures reveal a wider range of the measured properties of one plant fiber. There are a number of reasons for this variation (Analysis, 2016; Kiflie, 2019; Monteiro et al., 2010; Teli & Terega, 2017). A part of this variation can be attributed to the inherent variability in plant nature, test samples and associated error; but this is unlikely to be a complete explanation (Alves Fidelis et al., 2013a; Brandt et al., 2020). There is a need for a consistent fiber testing method where the variation is only a function of the material variability and not of the testing setup (Depuydt et al., 2017). Thus, proper method to conduct single fiber tensile test is needed; and digital image correlation is one of the preferred methods for such application (Abdela et al., 2021; Depuydt et al., 2017). There are some challenges when testing plant fibers' tensile characteristics that can lead to a wide range of results (Depuydt et al., 2017; Kim et al., 2015). Hence, it is important to identify the determinants that affect the test result and mitigate.



The guiding principle during such measurement is that the tensile strength depends on the applied load and the cross-sectional area of the fiber (Kumar & Anbumalar, 2015; Monteiro et al., 2010; B. Sanborn & Weerasooriya, 2015). Cross-sectional area depends of the diameter while diameter also depends on the density of the fiber under consideration and other related factors (Abdela et al., 2021; Cline et al., 2018). There are, also, other factors related to the testing machine and digital image correlation facilities and software thereof (Kim et al., 2015; Brett Sanborn et al., 2015). Hence, the diameter of the fiber needs to be carefully measured and estimated so as to identify the fiber strength measurement accurate.

Considering every important determinants, in this regard, it is possible to estimate the tensile strain, strength and stiffness of single natural fiber (Andersons, n.d.; Cline et al., 2018; Kim et al., 2015; Salih et al., 2020). And, the result can be used as an input for micromechanical characterization and mechanical modeling of their composite. Enset fiber is used as a case study and the experiments are designed and the results are analyzed using JMP 13 Pro and Python programming. As a result, this investigation focused on the correct methods for carrying out single fiber tensile analysis and suggested ways to improve the accuracy of findings as well as opportunities for enhancing precision.

## 2. MATERIALS AND METHODS

### 2.1. Material

Enset fibers were sourced from Ethiopian indigenous plant (*Ensete ventricosum*) from Kokosa, Oromia, Ethiopia, found at an altitude of 2627 m with min and max annual average temperatures of 12 and 18°C, respectively (Abdela et al., 2023). Manually, using in house developed technique, extracted fibers from plants with 3 diverse ages (1, 2, and 3 years after the pulp is ready for 1<sup>st</sup> round of extraction).



Figure 1: (A) Enset Plant (B) Enset Plant (C) Manual Extraction (D) Extracted Fiber

Steel fibers with a diameter of 30  $\mu\text{m}$ , and a known stiffness of 193 GPa. This is used to validate the method using a material with known diameter and tensile properties comparing against the measured value using digital image correlation.

### 2.2 Methods

The diameters of fibers were measured using Laser Microscope (*Keyence*) on 25 spot across the 10 cm length. As this device is limited to measuring the external diameter, and natural fibers contain an internal cavity, it is essential to consider additional aspects. The fiber's lumen cannot extend along its axial length, and its distribution is not uniform throughout the length. Thus, an additional methodology is required to evaluate the density of a substance and subsequently deduce the estimated diameter, as this is a critical factor that determines the tensile strength based on the *Equation 1* provided below.

$$\text{Density } \rho = \frac{m}{v} \quad \text{But, } V = AL = \frac{\pi d^2}{4}L \quad \text{thus, } d = \sqrt{\frac{4m}{4\rho l}} \quad (1)$$

Where;  $m$ ,  $\rho$  and  $l$  are mass, density and length, respectively.

Density is measured using Quanta-chrome Helium Gas Pycnometry and the detail of the method is given here below. The fibers were cut to a length of 10 cm, dried for 24 hrs at 60 °C and later cooled using desiccator without absorbing moisture. In the latter state, the mass of the fibers was measured using analytical balance with accuracy to 10<sup>-5</sup>g; *Mettler AT 261 Delta Range*. And, fibers are cut to different length (*powder*, 1 mm, 3 mm, 5 mm and 10 mm) to measure the density.

To determine density, each fiber samples are weighed and are recorded on the machine using the data input interface. Then, the samples are put in to the *Pycnometer* being in the selected volume cell. The system is calibrated using the two standard spheres with known volume of 56.5592 cm<sup>3</sup> and 2.145 cm<sup>3</sup>. In this process, all the three available volume cells are considered; their volume of 147.3974 cm<sup>3</sup>, 27.216 cm<sup>3</sup> and 11.4285 cm<sup>3</sup> for the large, small and micro respectively. Also, effects of the uniformity of purging duration has been checked by altering the three purging duration (5, 10 and 15 min).

The tensile test is done using the following methods and standards. To check the reliability of the method, result from steel fibers with known stiffness measured using the same method was used as a benchmark (Depuydt et al., 2017). The fiber was glued onto paper frame using a double-sided glue roller (*Permanent Pritt glue roller, Henkel*) and adhesive (*SICO MET 8300*). Fig 2A shows the paper frame for a test gauge length of 50 mm and the position of the fiber in this frame. The frame facilitates sample mounting and fiber alignment. Tensile tests were performed on an Instron 5943 equipped with a 100N load cell according to the ASTM C1557-14 standard in a conditioned environment at 50% RH and 21 °C. The frame was pneumatically gripped with a gripping force of 200N. A pre-load of maximum 0.01N was applied to the fiber to straighten it. Fiber straightness is critical when the strain is to be derived from the crosshead displacement, especially for comparison of the result with Digital Image Correlation (DIC). The crosshead displacement rate was chosen according to the ASTM C1557-14 standard, which suggests achieving fracture within 30s of testing. For the investigated fibers, this translates to a crosshead displacement rate of 1mm/min.

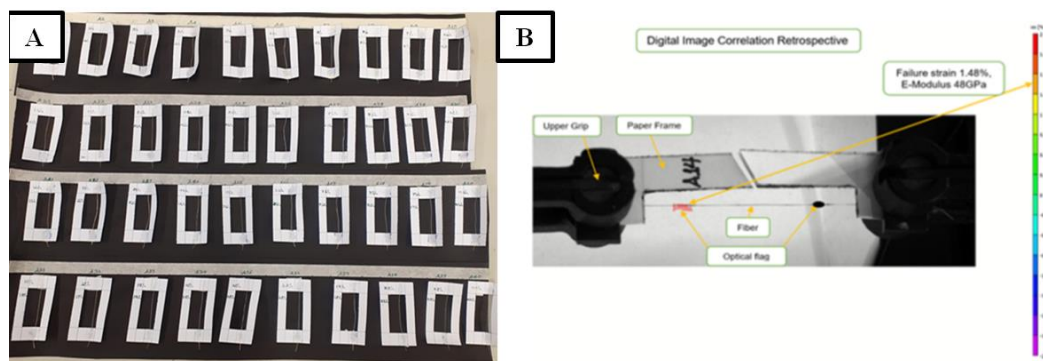


Figure 2: A) Specimen Preparation for SFTT B) Digital Image Correlation

*Gluing* - potent glue is used to fully make the fiber rigid around grip. Double side glue is used to straighten the fiber at the contact point of fiber and paper and SICO MET 8300 is used.

*Optical Flag and speckle formation* - Optical flag is prepared using TIPEX followed by speckle formation and dot making using the tick marker to make visible spot on the fiber.

*Fiber straightness* - Fiber straightness during attaching and gripping is critical; it affects the strain value estimation on both methods because the straightening stage itself is considered as elongation. Hence the fiber has been straightened by using of a preload less than 0.01N.

*Digital Image Correlation* - During digital image correlation process, images before elongation starts and after failure have been filtered, first. Initial guess have also been conducted to check whether it is possible to correlate before starting the analysis and assist the correlation process if required. In case the initial guess face problems while correlating, going to the picture where the correlation stops and assisting with the possible options available is required.

### 3. RESULT AND DISCUSSION

#### 3.1 Optimal Experiment Design

The experiments have been designed using JMP 13 pro software. The DOE platform is considered. The main effect and the interaction effect with 2-level has been taken into account in the process. Constraints are also set to make the experiment more real replica of the situation. The minimum number of experiment recommended by JMP has been taken with extra experiments, depending on importance, for boosting the certainty of the result as it is tabulated on Table 1.

Table 1: Optima Number of Experiment

Test Type	Categories	Min. test	Test considered
Single fiber test	Category 1	24	40
	Category 2	24	40
	Category 3	24	40

Table 1 illustrates that an additional 16 tests are incorporated for each individual fiber test, aiming to improve the accuracy of the results and enhance their representativeness. The diameter of each fiber within the categories indicated above has been estimated, leading to the result discussed on section 3.2 below.

#### 3.2 Diameter Estimation

The measurement of Enset fiber diameter is conducted through the utilization of a laser microscope, while the lumen size is estimated based on information obtained from literature. The sample of the image diameter measured using the laser microscope is illustrated in Fig 3.

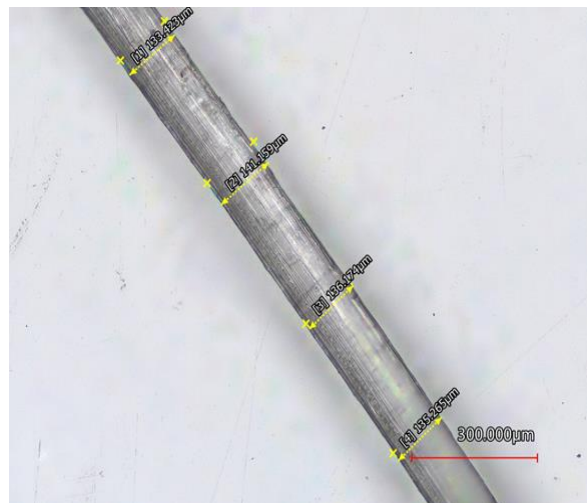


Figure 3: Microscopic image of Enset fiber diameter

Upon completion, the obtained result is validated by estimating the Fiber density utilizing Helium gas Pycnometry, followed by a back-calculation procedure employing the relationship between density and diameter as illustrated in Equation 1.

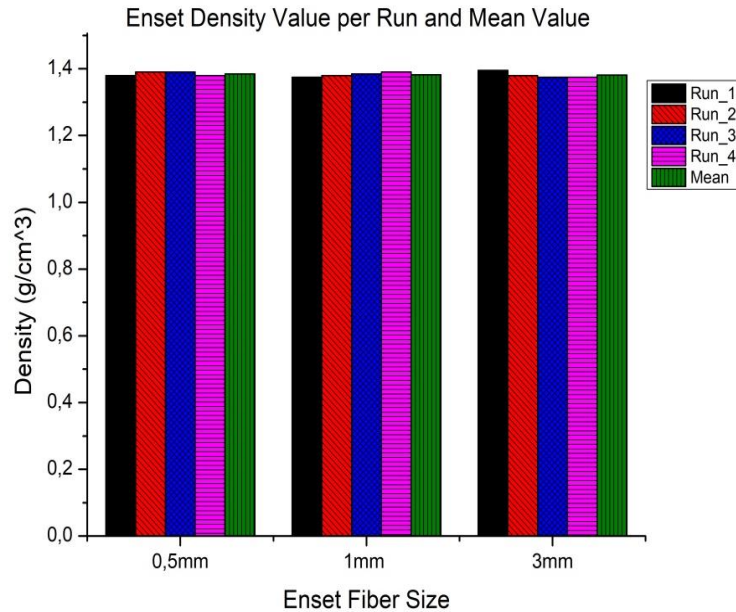


Figure 4: Enset fiber density estimation results

Fig 4 illustrates the density of Enset for various sizes, with an average density measurement of  $1.38\text{gcm}^{-3}$ . This particular value is utilized jointly with the Equation 2 for each fiber, where the cross-sectional areas are computed by taking into account the diameter and then documented using the universal testing machine

The Enset fiber diameter is measured at a length of 10 cm to determine the cross-sectional area of the fiber. The smallest diameter measured using laser microscope is  $50.1\mu\text{m}$  while the average and large fiber diameter are  $163.7\mu\text{m}$  and  $298\mu\text{m}$  respectively. In order to conduct a thorough study, 40 fiber samples were carefully selected and subjected to examination. Yet, 97.8% of the fibers fall in the range between  $70\mu\text{m}$  and  $240\mu\text{m}$ ; while 85% of fibers diameter falls between  $90\mu\text{m}$  -  $210\mu\text{m}$ . The diameters are utilized in determining the cross-sectional area of individual fibers subjected to the load, with the resultant areas being inputted into the tensile testing machine. The preloads applied to straighten the fiber are elaborated upon in section 3.3.

### 3.3 Preloads Considerations

The result found from the universal tensile testing setup analog data revealed that the preload used to straighten the fiber is in acceptable range as shown on the Fig 5. After the finishing of the test, the result has been used as an input to the simulated correlation system.

It is clear from the data presented in Fig 5 that 72.5% of the testing was conducted with a preload of less than 0.00025KN. Given the minimum strength observed of nearly 200MPa, this accounts for less than 0.05% of the final strength achieved. The applied load has a minimal effect on strength, with only a small percentage being insignificant (Depuydt et al., 2017; Kim et al., 2015). Preloads of 87.5% are below 0.0003KN, and 95% of preloads are less than 0.0004KN. The use of smaller preloads ensures the reliability of test results. However, no tests have been conducted with preloads exceeding 0.0005KN.

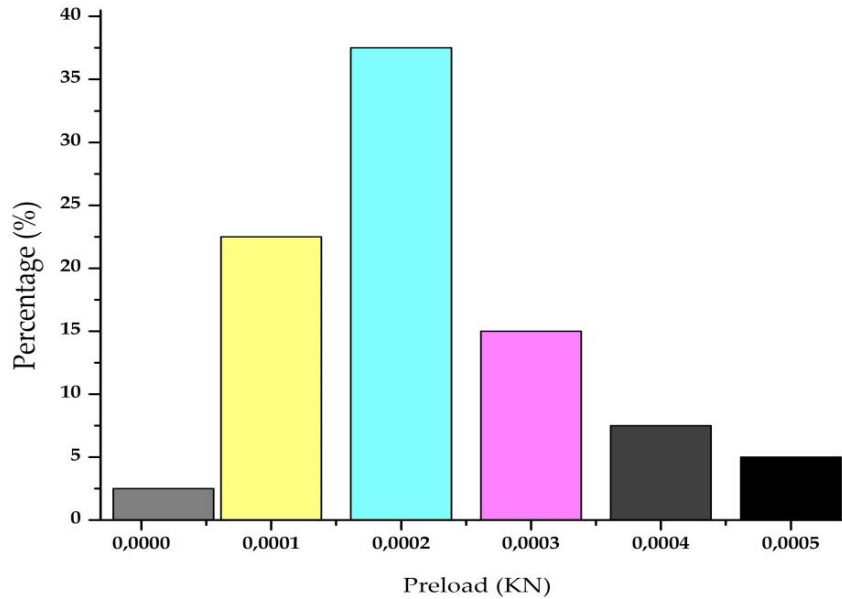


Figure 5: Ranges of the preloads applied

The preloads fall within the acceptable range, prompting the need to investigate the failure spot. The failure spot of the fiber plays a crucial role in determining the fiber's attribute during a single fiber tensile test. Failures occurring near the grip may be attributed to either the gripping load or the adhesive applied at the attachment point of the fiber to the paper. The findings related to the failure spot are illustrated in Fig 6. The data presented in Fig 6 indicates that 82.5% of fiber failures occurred at the midpoint, suggesting that these failures are primarily due to the applied load rather than issues with gripping. Conversely, the remaining 17.5% of failures were located around the grip and are not considered in the subsequent analysis due to their association with failure at grip.

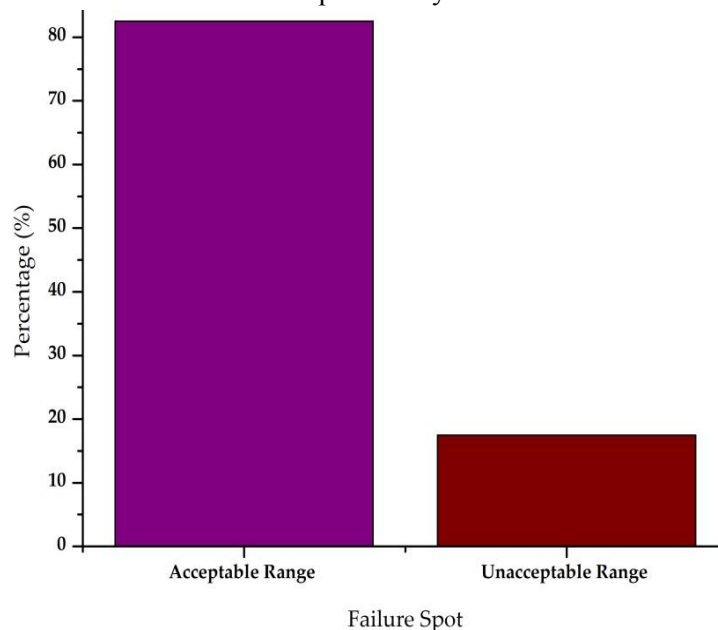


Figure 6: Acceptable failure spot of fibers

The evaluation of the fiber's strength reveals that it falls within the acceptable range, as demonstrated in Fig 6. Consequently, an investigation into the tensile strength of each individual fiber was conducted. Furthermore, a comprehensive analysis of the failures occurring at the acceptable spot and under the allowable preloads, as indicated above, was undertaken. Fig 7 presents a graphical representation of the range of tensile strength exhibited by a single Enset fiber.

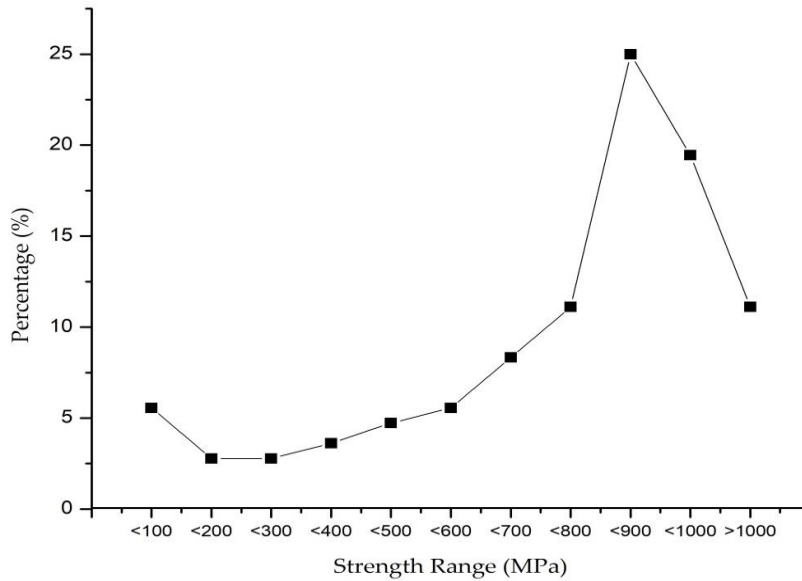


Figure 7: Tensile strength of single Enset fiber

Initially, it was observed that approximately 5% of the fibers experienced failure before attaining strength of 100MPa. This value deviates significantly from the average strength. The study reveals that only 14.72% of the fibers possess strength below 500MPa. Consequently, it is recommended to disregard the premature failure as it does not accurately represent the properties of the fibers. On the contrary, a significant 69.44% of the fibers fall within the strength range of 500-1000MPa. Therefore, the 5% of fibers failing before reaching strength of 100MPa is not indicative of the overall scenario. The most probable reason for this premature failure is the damage caused during the manual extraction process, which involves indentation loading. Furthermore, the storage conditions may also contribute to this premature failure.

The findings of this investigation revealed that a significant proportion of the fibers, specifically 25%, exhibited a strength falling within the range of 800MPa to 900MPa. Conversely, the majority of the fibers, constituting approximately 70%, displayed a strength surpassing 500MPa. Moreover, more than 30% of the fibers demonstrated a strength exceeding 900MPa, while 11% achieved the highest possible strength of over 1000MPa. It is important to note that there were also instances where fibers with the smallest diameters reached a strength of 1000MPa, albeit infrequently. These results are consistent with the existing literature on the subject (Alkbir et al., 2016; Alves Fidelis et al., 2013b; Depuydt et al., 2017; Monteiro et al., 2010; Teli & Terega, 2017). The following Fig 8 summarized the possibility of reaching above 1000MPa of strength.

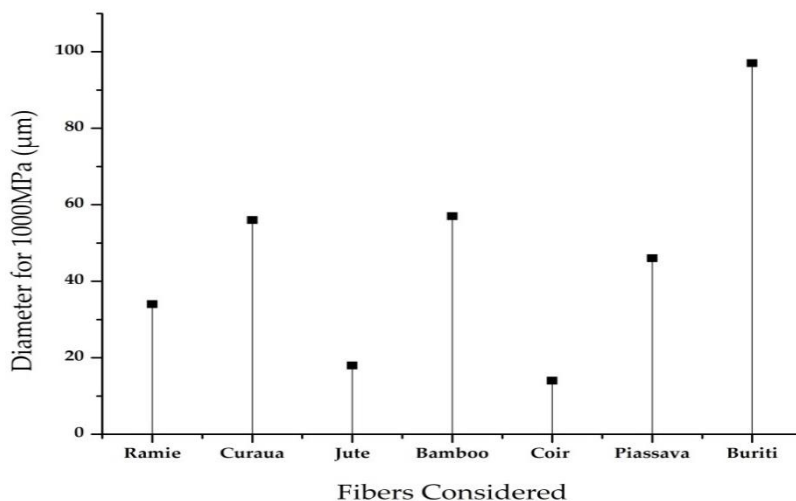


Figure 8: The diameter of natural fibers that produces a strength of 1000MPa



All fibers shown on Fig 8, except Buriti fiber, exhibit 1000MPa strength for a diameter less than 60µm. For Jute and coir fibers, this threshold is below 20 µm. The relationship between diameter and strength is characterized by an inverse and square relationship; as strength is inversely related to the square of the cross-sectional area, leading to a hyperbolic relationship. The relationship between Enset fiber strength and diameter can be expressed by the equation derived from the analysis of all individual test results.

$$\sigma(d) = 0.02243553d^2 - 8.6359d + 1379.96 \tag{2}$$

The correlation established using Vic2D software ensures that the acceptable error range, which is below 5% (0.05), is maintained for all data points and tests. By analyzing the displacement in the images and calculating the corresponding strain, the tensile strength and tensile modulus of Enset fiber can be accurately determined. The comprehensive results of the tensile properties for various test categories conducted under tension, including strength and modulus are presented below.

Table 2: Tensile Characteristics of Enset Fiber

Categories	Properties	Minimum	Maximum	Mean
Category 1	Strength	41	723	541
	Modulus	35	65	40
Category 2	Strength	51	821	618
	Modulus	46	68	45
Category 3	Strength	67	923	647
	Modulus	12	69	46

The minimum strength limits observed in the displayed data can be attributed to various factors. One primary factor is the manual fiber extraction method, which has the potential to cause damage to the fiber. This damage can lead to early breakage during loading, resulting in lower strength values. Another subset of fibers exhibiting low strength failed either at the clamp or in close proximity to it, potentially causing damage that affects the Poisson ratio. Thus, enhancing the extraction means to preserve the fiber during extraction will minimize breakage and increase the strength as a result.

Due to the hydrophilic relationship shown on equation 2 above, the fiber may perform relatively less compared to other petrochemicals, even though it can be mitigated using different technics of coating. Nevertheless, Enset fiber exhibits promising characteristics that make it a viable alternative to other natural fibers. This assertion is supported by a thorough examination of the properties of different natural fibers documented in relevant literature, as well as the outcomes of this study which highlight the favorable properties of Enset fiber (Andersons, n.d.; Ilankeeran et al., 2012; Salih et al., 2020). Examination of flax fiber, a natural fiber widely used in various applications, demonstrated a young’s modulus of 31 GPa and a strength of 305 ± 120 MPa when tested using a 75mm Gauge and a testing speed of 1 mm/min in the green flax test. Similarly, bamboo fiber exhibited a young’s modulus of 33.37 MPa and a strength of 639 MPa when tested across different gauges of 5, 15, 25, 35, and a testing speed of 1 mm/min in the steam explosion test. Yield of 43MPa young’s modulus and 775 MPa of strength has been test for different gauges of 5, 10, 25, 40, with 1 mm/min, mechanical extraction [19]. Hence, the outcome can be likened to that of other natural fibers, indicating that Enset fiber holds promise as a potential natural fiber for various nonstructural lightweight applications.

#### 4. CONCLUSION

The mechanical properties of Enset fiber, a potential material for natural fiber reinforced composites, were effectively characterized in this study. The inverse and quadratic relationship between tensile strength and fiber diameter leads to a significant difference in strength value when there is a slight underestimation or overestimation of the diameter. Therefore, the method utilized in this investigation, which strengthens the microscopic measurement of diameter with density estimation via helium gas Pycnometry, elevates the precision of the



diameter and in turn of the tensile strength of the fiber. However, in contrast to the direct measurement technique that calculates strain by analyzing crosshead movement, the approach utilized in this investigation (DIC) produces notably better results owing to its enhanced ability to account for slippage effects. In general, the implementation of the digital image correlation method in this study offers several advantages over the direct method, and the findings can contribute valuable insights to the micromechanical analysis and mechanical modeling of Enset fiber and its composite. Furthermore, the results indicate that Enset fiber holds promise as a potential fiber for future research, particularly in relation to specific applications.

## ACKNOWLEDGMENTS

We are very grateful to Mekelle University (Ethiopian Institute of Technology-Mekelle), KU Leuven and Addis Ababa Science and Technology University (AASTU) for privileging us with lab facilities for different tests we have conducted. In line, we are thankful to all lab technicians in these institutions together with MSc and PhD students working in the laboratory we are using for their unreserved cooperation and help

## REFERENCE

- Abdela, A., Buffel, B., & Desplentere, F. (2021). Determinants of Single Natural Fiber Stiffness Estimation Accuracy and Enhancement Possibilities. *Proceedings of the International Conference on Industrial Engineering and Operations Management*, 1495–1502.
- Abdela, A., Vandaele, M., Haenen, S., Buffel, B., Sirahbizu, B., & Desplentere, F. (2023). *Moisture Absorption Characteristics and Subsequent Mechanical Property Loss of Enset – PLA Composites*. 1–12.
- Alkbir, M. F. M., Sapuan, S. M., Nuraini, A. A., & Ishak, M. R. (2016). Fibre properties and crashworthiness parameters of natural fibre-reinforced composite structure: A literature review. *Composite Structures*, 148, 59–73. <https://doi.org/10.1016/j.compstruct.2016.01.098>
- Alves Fidelis, M. E., Pereira, T. V. C., Gomes, O. D. F. M., De Andrade Silva, F., & Toledo Filho, R. D. (2013a). The effect of fiber morphology on the tensile strength of natural fibers. *Journal of Materials Research and Technology*, 2(2), 149–157. <https://doi.org/10.1016/j.jmrt.2013.02.003>
- Alves Fidelis, M. E., Pereira, T. V. C., Gomes, O. D. F. M., De Andrade Silva, F., & Toledo Filho, R. D. (2013b). The effect of fiber morphology on the tensile strength of natural fibers. *Journal of Materials Research and Technology*, 2(2), 149–157. <https://doi.org/10.1016/j.jmrt.2013.02.003>
- Analysis, M. (2016). *Lignocellulose*. 5(2), 139–151.
- Andersons, J. (n.d.). *Tensile strength of single fibers : test methods and data analysis*. 2, 1.
- Brandt, S., Spring, A., Hiebsch, C., McCabe, J. T., Tabogie, E., Wolde-Michael, G., Yntiso, G., Shigeta, M., & Tesfaye, S. (2020). The “ Tree Against Hunger ” “ Tree Against Hunger. *Advancement Of Science*, July 2016, 56. <http://www.aaas.org/international/africa/enset/>
- Cline, J., Wu, V., & Moy, P. (2018). *Assessment of the Tensile Properties for Single Fibers*. Cline, J.,.
- Depuydt, D., Hendrickx, K., Biesmans, W., Ivens, J., & Van Vuure, A. W. (2017). Digital image correlation as a strain measurement technique for fibre tensile tests. *Composites Part A: Applied Science and Manufacturing*, 99, 76–83. <https://doi.org/10.1016/j.compositesa.2017.03.035>
- Ilankeeran, P. K., Mohite, P. M., & Kamle, S. (2012). Axial Tensile Testing of Single Fibres. *Modern Mechanical Engineering*, 02(04), 151–156. <https://doi.org/10.4236/mme.2012.24020>
- Karimah, A., Ridho, M. R., Munawar, S. S., Adi, D. S., Ismadi, Damayanti, R., Subiyanto, B., Fatiasari, W., & Fudholi, A. (2021). A review on natural fibers for development of eco-friendly bio-composite: characteristics, and utilizations. *Journal of Materials Research and Technology*, 13, 2442–2458. <https://doi.org/10.1016/j.jmrt.2021.06.014>
- Kiflie, Z. (2019). Lignocellulose Chemical and Morphological Analysis of Enset ( Ensete). *Lignocellulose*, 5(2), 139–151. <https://www.researchgate.net/publication/334284412>
- Kim, J. H., Heckert, N. A., Mates, S. P., Seppala, J. E., McDonough, W. G., Davis, C. S., Rice, K. D., & Holmes, G. A. (2015). Effect of fiber gripping method on the single fiber tensile test: II. Comparison of fiber gripping materials and loading rates. *Journal of Materials Science*, 50(5), 2049–2060. <https://doi.org/10.1007/s10853-014-8736-8>
- Kumar, S. S., & Anbumalar, V. (2015). Selection and Evaluation of Natural Fibers – A Literature Review. *International Journal of Innovative Science, Engineering & Technology*, 2(11), 929–939.
- Monteiro, S. N., Satyanarayana, K. G., Ferreira, A. S., Nascimento, D. C. O., Lopes, F. P. D., Silva, I. L. A., Bevitori, A. B., Inácio, W. P., Bravo Neto, J., & Portela, T. G. (2010). Selection of high strength natural fibers. *Revista Materia*, 15(4),



488–505. <https://doi.org/10.1590/S1517-70762010000400002>

- Saadati, Y., Chatelain, J. F., Lebrun, G., & Beauchamp, Y. (2019). Comparison of density measurement methods for unidirectional flax-epoxy polymer composites. *European Conference on Multifunctional Structures*, 1–6. <https://doi.org/10.23967/emus.2019.014>
- Salih, A. A., Zulkifli, R., & Azhari, C. H. (2020). Tensile Properties and Microstructure of Alkali Treatment. *Fibers*, 8(26), 1–10.
- Sanborn, B., & Weerasooriya, T. (2015). Tensile Properties of Dyneema SK76 Single Fibers at Multiple Loading Rates Using a Direct Gripping Method. *Conference Proceedings of the Society for Experimental Mechanics Series*, 65(VOLUME 1), 1–4. [https://doi.org/10.1007/978-3-319-06995-1\\_1](https://doi.org/10.1007/978-3-319-06995-1_1)
- Sanborn, Brett, DiLeonardi, A. M., & Weerasooriya, T. (2015). Tensile Properties of Dyneema SK76 Single Fibers at Multiple Loading Rates Using a Direct Gripping Method. *Journal of Dynamic Behavior of Materials*, 1(1), 4–14. <https://doi.org/10.1007/s40870-014-0001-3>
- Teli, M. D., & Terega, J. M. (2017). Chemical , Physical and Thermal Characterization of Ensete ventricosum Plant Fibre. *International Research Journal of Engineering and Technology*, 04(12), 67–75.



## Evaluation of Waste Glass Powder as Partial Replacement for Mineral Filler in Asphalt Concrete Mixes

Destaw Kifile<sup>1,\*</sup>, Emer T. Quezon<sup>2</sup>, Abel Tesfaye<sup>3</sup>

<sup>1</sup>Civil Engineering Department, Debretabor University, Debretabor, Ethiopia

<sup>2</sup>Construction Technology & Management Department, Ambo University, Ambo, Ethiopia

<sup>3</sup>Faculty of Civil & Environmental Engineering Department, Jimma University, Jimma Ethiopia

\*Corresponding author, e-mail: [destkif@dtu.edu.et](mailto:destkif@dtu.edu.et)

### ABSTRACT

The research study provided an attempt to evaluate the effect of waste glass powder as a partial replacement of conventionally used filler material in hot mix asphalt concrete. For this purpose, three different asphalt concrete samples were produced using crushed stone dust (CSD) in different percentages (5, 6.5 and 8%) as mineral filler with five different bitumen content (4, 4.5, 5, 5.5 and 6%). From the series of asphalt content, 6.5% crushed stone dust filler was selected, which provided the highest stability waste glass powder (WGP). The content of crushed stone dust (CSD) filler was replaced with a rate of 0, 25, 50, 75 and 100%. The samples were tested with a marshal stability test to obtain the Optimum Bitumen Content (OBC) and optimum filler content. A total of sixty (60) mix specimens were prepared, forty-five (45) of these compacted at each percentage of CSD filler and bitumen content to determine the OBC and optimum filler content. The remaining samples were used to find out the optimum replacement rate of waste glass powder (WGP). Results showed a 75% replacement of crushed stone dust with waste glass powder at 5.10% bitumen content, the Marshall stability was 12.0KN, Flow was 2.84mm, air void was 4.0%, VFB was 72.3%, and bulk density was 2.360g/cm<sup>3</sup>. From these results, the mixture of 75% WGP passed the ERA and Asphalt Institute Standard Specifications. It observed that for heavily trafficked roads, waste glass powder was 75% of the weight of CSD or 4.875% of the total aggregate weight. Also, it may solve the significant disposal problem of waste glass to save the environment.

**Keywords:** filler, hot mix asphalt, marshal stability, waste glass powder

### 1. INTRODUCTION

Disposing of various waste products from various industries is a major issue. Global trash output of various forms has increased dramatically as a result of the expansion of numerous businesses and population development (Isa Olowosulu eta Joel, 2018). The removal of waste materials such as blast furnace slag, fly ash, silica fume (obtained from the power plant), recycled aggregate (from the demolition of the site), solid waste, plastic waste (domestic waste), and rubber waste (commercial waste). glass, metal, rubber, plastic, etc that large quantity of waste especially non-decaying waste materials becomes a problem of great concern in developed as well as in developing countries (Ahmed, Othman eta Mahmoud, 2006). Municipal solid waste is a problem for local governments. Recycling is one of the best ways to dispose of this waste. With the increasing cost of materials, there has been a renewed interest in reusing waste materials in construction (Haddad eta Khedaywi, 2023).

In recent years, the reclaiming, reuse, and recycling of wastes in place of virgin materials have become a recurring theme of growing importance (Choudhary, Kumar eta Gupta, 2021). A lot of research has been done on using solid waste as raw materials in the production of Hot Mix Asphalt Concrete (HMAC). There are three ways to incorporate waste material into HMAC. One is to use solid waste as raw materials as a modifier for the asphalt binder. These types of additives have also been used to improve the mechanical properties of bitumen and asphalt concrete, which are usually added to the bitumen (Taherkhani, 2016). Studies have shown that when asphalt binder is modified with crumb rubber and styrene-butadiene rubber (D. Khan, Ali, *et al.*, 2023), polymer (Paul, Suresh eta Pal, 2021; Khan, 2023), and other waste materials, HMAC has better properties. The second advancement is solid waste material used as a replacement for conventional filler and aggregates in HMAC like bottom ash (Jattak, Hassan eta Mohd Satar, 2021), corn cob ash (Endashaw, 2023), sugarcane waste molasses (Le, 2021), coal bottom ash (Kamran *et al.*, 2023), marble dust (D. Khan, Khan, *et al.*, 2023) cinder, and natural sand (N. Khan *et al.*, 2023). Conclusions from several studies confessed the importance of the filler used in asphalt concrete (Al Qadi *et al.*, 2021; M. Haddad eta Khedaywi, 2023). Furthermore, it is globally accepted that natural



filler can be replaced with any suitable material either natural or artificial (Rashwan, 2016). The third method is to use additives such as polymers and fibers to HMAC in addition to the binders and aggregates. The application of polyethylene in HMA asphalt has been studied by (Thiam, Fall et al., 2021). The performance of HMAC with Polyethylene Terephthalate (PET) and High-Density Polyethylene (HDP) in stone mastic asphalt was tested in many studies (Fayissa, Gudina et al., 2020). The results reveal that the replacement or addition makes the mix better.

With the rapid economic growth and continued increased consumption, a large number of waste materials are generated (Tahmoorian *et al.*, 2017; Olukanni, Oyedepo et al., 2021). If a large amount of waste or by-product materials is generated and used instead of natural materials in construction projects, there would be three benefits: conserving natural resources, disposing of waste materials (which are often unsightly), and freeing up valuable land for other uses. Among them, waste glass material is an important part (Pasandín et al., 2014; Kifile *et al.*, 2023). Glass is a common product found in different forms such as bottles, jars, windows and windshields, bulbs, cathode ray tubes, etc (Choudhary, Kumar et al., 2021). These products have a limited lifetime and must be used to avoid environmental problems related to their stockpiling or landfills. Since glass is a nonmetallic inorganic material that cannot be decomposed or burned, landfills do not provide an environmentally friendly solution. Hence, there is a dire need to use waste glasses. One solution to this crisis is recycling waste into useful products (Simone *et al.*, 2019). According to (Cheru, 2016) the proportion of glass waste in the domestically generated waste in Addis Ababa city is estimated to be around 11.8% (978 tons per year) of the total solid waste of about 8313 tons per year. Thus, this glass can either be reused for other, but limited purposes or be sent to a landfill. Due to the limited landfill space in urban areas and the increasing cost of landfilling, the process of recycling and reuse of waste material is trending these days. On the other hand, one of the main problems in the construction of highway pavement is the deficiency of the amount of mineral fillers from crushing rocks (Saltan, Öksüz et al., 2015; Isa, Olowosulu et al., 2018; Al Qadi *et al.*, 2021). The shortage is to be made up by importing materials from other locations (blasting of more quarry areas). This may result in the deterioration or depletion of naturally available materials like sand and rock to produce the required amount of mineral fillers. So, it is advisable to preserve and curtail the use of natural materials and to think about how to reuse and recycle waste products that are suitable to replace natural materials. Previous kinds of literature observed that glass powder is notorious for causing stripping in asphalt mixes, and hence the glass powder is incorporated not only as filler but also in the form of glass hydrated lime composite filler. Glass hydrated lime as filler was prepared with an intention of avoiding the possibility of formation of the moisture-sensitive mix due to high silica content in glass by adding a nominal amount of hydrated lime as an antistripping agent. Therefore, the use of waste glass powder as a partial replacement for conventionally used filler material in hot mix asphalt concrete production is one option that can alleviate the waste glass disposal problem and significantly save natural construction materials. The overall objective of this study is to maximize the utilization of waste glass powder in asphalt concrete mixes as filler without compromising with the engineering, economical, and environmental suitability of asphalt mixes. This study's primary objective is to carry out a laboratory investigation into the effects of waste glass powder as a partial replacement for conventionally used filler material in hot mix asphalt concrete.

## 2. MATERIALS AND METHODS

### 2.1 Material

The materials, used for this study, are CSD and WGP as a filler material, crushed stone as a coarse and fine aggregate, and 85/100 penetration grade of bitumen as binder material. The waste glass was collected from Addis Ababa glass and bottles Shear Company's waste stockpile. Aggregates and CSD filler were obtained from International First Highway (IFH) Engineering Private Limited Company (PLC) construction quarry site. The asphalt cement of 85/100 penetration grade was also obtained from IFH engineers PLC batching plant. The glass powder was produced by crushing waste glass bottles and jars. The crushed stone and glass powder were sieved to obtain the desired particle size distribution. The bitumen was then heated to the desired temperature. The crushed stone dust, glass powder, aggregates, and bitumen were mixed to produce the hot mix asphalt concrete. The hot mix asphalt concrete was then compacted and cooled to produce the final product.



## 2.2 Methods

This study is based on laboratory testing as the main procedure to achieve study goals. All the testing is conducted using equipment and devices available in International First Highway (IFH) Engineering laboratory. Laboratory tests are divided into several steps, which begin with an evaluation of the properties of used materials such as mineral filler (crushed stone dust and waste glass powder), mineral aggregates, and bitumen. Aggregate quality test performed, including Los Angeles abrasion, sand equivalent, flat and elongated particles. Sieve analysis is carried out for each aggregate and filler type to obtain the grading of aggregate sizes. Then the aggregate blending calculation was performed to obtain the asphalt binder course gradation curve used to prepare the asphalt mix. Select the appropriate asphalt cement grade based on the type and climate condition of the mixture design. Then after selecting the range of mixing and compaction temperatures from the temperature-viscosity graph. After that, samples were prepared using CSD 5%, 6.5%, and 8% by weight of aggregate and five different bitumen content 4.0% to 6.0% with 0.5% increment by weight of the total mix. Three samples were prepared for each of the bitumen contents. These samples were tested under the Marshall Stability test to determine the optimum bitumen content for asphalt mixes based on maximum Marshall Stability. Then, the value of the optimum bitumen content is used to prepare the replaced asphalt mixes with four various percentages of waste glass powder. After that Marshall tests were utilized to evaluate the properties of these replaced mixes. Finally, laboratory test results are obtained and analyzed. Fig. 1 shows the overall research and laboratory design employed.

## 2.3 Material Property Test Result

### 2.3.1 Physical properties of mineral filler

Fillers play a great role in the engineering properties of bituminous paving mixes (Khedaywi, Haddad eta Alyaseen, 2023). Mineral fillers are finely ground inert material passing the No.200 sieve (Ahmed, Othman eta Mahmoud, 2006; Maurana eta Sani, 2015; Fayissa, Gudina eta Yigezu, 2020; Khedaywi, Haddad eta Alyaseen, 2023). Mineral fillers added to asphalt mixtures serve a dual purpose. Asphalt cement binder mixes with mineral filler (finer than the thickness of asphalt film) to form mortar which leads to improved stiffening of the mix (Taherkhani, 2016; Mohd Shukry et al., 2018). The fillers used in the current study namely crushed stone dust (CSD) and waste glass powder (WGP). Laboratory tests have been conducted to evaluate the physical properties of each type types of filler, which consist of the gradation parameters, plasticity index, and apparent specific gravity. Table 1 illustrates the physical properties of each type of filler.

Table 1 shows all types of filler are passing sieve #200 which conformed with the range specified by ASTM D242. Both crushed stone dust and waste glass powder are non-plastic (NP), with the apparent specific gravity of crushed stone dust being 2.70 and that of waste glass powder 2.60. The test results indicated that the particle size distributions for the two mineral fillers are similar. The apparent specific gravity of the waste glass powder sample is slightly lower than the crushed stone dust.

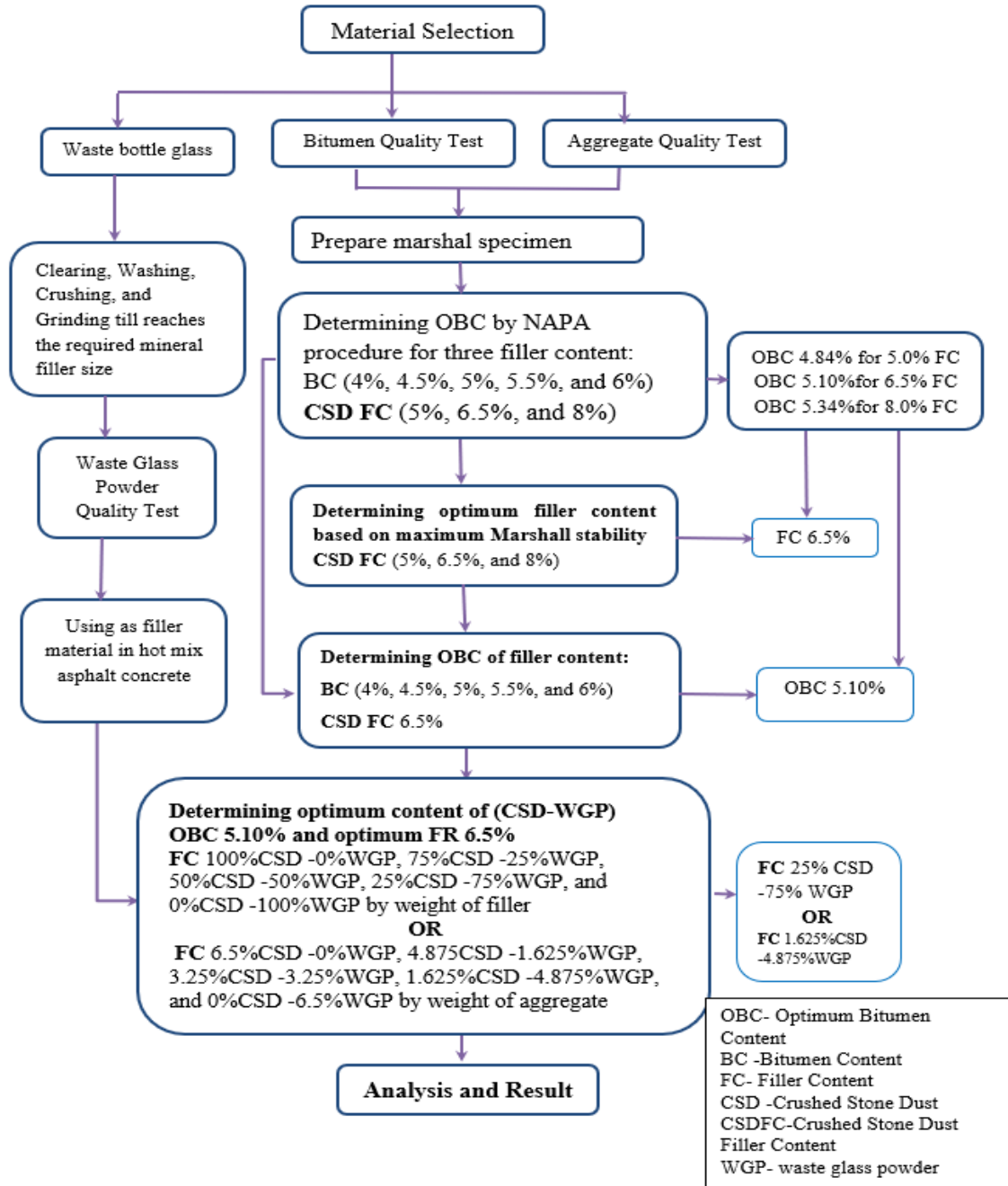


Fig. 1: Research design flow chart

Table 1: Physical properties of used mineral filler

Sieve No.	% Passing		ASTM D242
	Waste Glass Powder	Crushed Stone Dust	
No. 30	100	100	100
No. 50	96	98	95-100
No. 200	80	89	70-100
Plasticity Index	NP	NP	Max 4
Absorption (%)	0.2	1.2	Max 2
Apparent specific gravity	2.60	2.70	2.5 - 3.0



### 2.3.2 Aggregate physical properties

The quality of aggregates plays a great role in the performance and long-term economy of the road structure (Mohammed, 2017; Simone *et al.*, 2019). The coarse aggregates should have good abrasion value, impact value, and also crushing strength. The function of coarse aggregates is to bear the stresses due to wheels. The function of Coarse aggregates is also to resist wear due to abrasion (Saltan, 2015; Taherkhani eta Bayat, 2022). To investigate the physical properties of the aggregates and their suitability in road construction, various lab tests were conducted on aggregate including sieve analysis, specific gravity, and Los Angeles abrasion tests. Specific gravity test results are shown table 2. While the abrasion or wear percentage of aggregate after 500 revolutions in the Los Angeles abrasion test is 13%. Table 2 summarizes the physical properties of the aggregate samples. The results indicate that all aggregate materials conform to specifications.

Table 2: Physical properties of aggregate

Test	Test Method	Test Result		Specification
		Coarse Aggregate	Fine Aggregate	
Specific Gravity (Bulk)	AASHTO T 85-91	2.76	2.58	--
Sand Equivalent, %	AASHTO T176	73.9	--	Min 40
Water absorption %	BS 812, Part 2	0.9	1.9	Max 2
Flakiness Index	BS 812 Part 105	21	--	Max 45
Apparent S. G	AASHTO T 85-91	2.71	2.77	--
ACV, %	BS:812 Part 110	16	--	Max 25
LAA %	AASHTO T 96	15	--	Max 30

### 2.3.3 Combined gradation of Miniral aggregates

The asphalt-concrete mixture is formed from aggregates and asphalt and is widely used in the surface layer of flexible pavement roads (Sargin *et al.*, 2013; Bindu, 2014). The aggregates are expected to provide a skeleton to resist the repeated traffic load applications and the asphalt provides adhesive action among aggregate particles and contributes viscous-elastic properties to the mixture. Aggregates are usually classified by their size when blending aggregate proportions in the mixture. Available aggregate materials, coarse aggregate, fine aggregate and filler, were integrated to get the proper gradation within the allowable limits according to ASTM D3515 specifications using the mathematical trial method. Table 3 shows the final proportion of aggregate material in the asphalt binder and the proposed aggregate gradation curve is found to satisfy ASTM D3515 specifications for asphalt binder course gradation.

Table 3: Mix composition and sieve analysis of aggregates and specification criteria based on ASTM D3515 for nominal size 19 mm

Sieve Size (mm)	Graduation for three different filler percentage			ASTM D3515 Specification
	5.0%	6.5%	8.0%	
25	100	100	100	100
19	94.5	94.5	94.5	90-100
12.5	77.8	77.8	77.8	71-88
9.5	67.5	67.5	67.5	56-80
4.75	47.4	47.4	47.5	35-65
2.36	32.8	32.9	34.3	23-49
1.18	22.2	22.8	24.3	15-37
0.6	14.7	15.7	17.2	10-28
0.3	9.8	11.1	12.6	5-19
0.15	7.2	8.6	10.1	4-13
0.075	5.0	6.5	8.0	2-8

Fig. 2 demonstrates the proposed aggregates gradation curve found to satisfy ASTM D3515 specifications for asphalt binder course gradation. Based on the specification for gradation indicated in the above table and figure, for this research, a nominal size of mix aggregate is selected to be 19 mm.

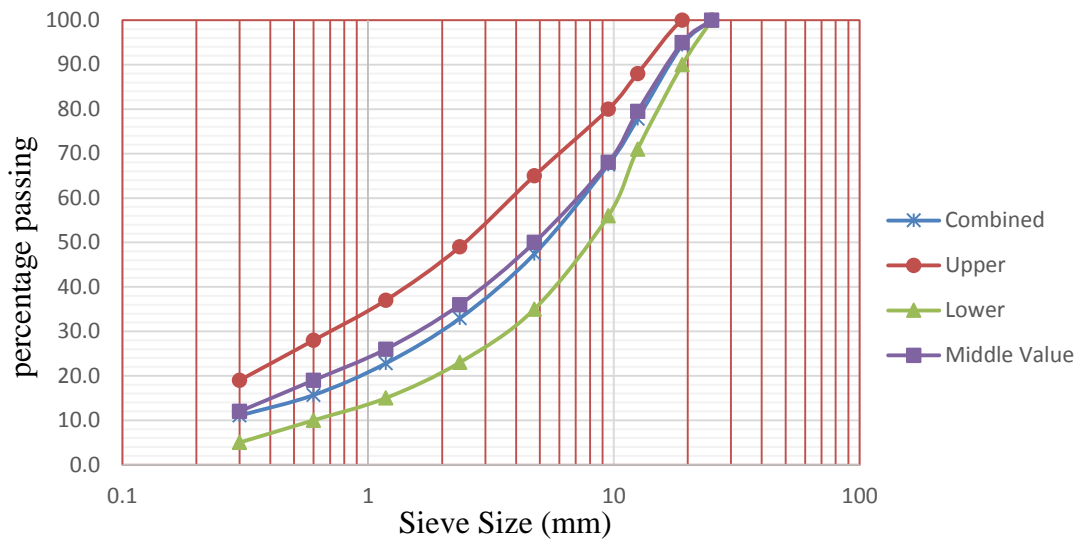


Fig. 2: Combined aggregate gradation for 6.5% Mix

Fig. 2 demonstrates the proposed aggregates gradation curve found to be satisfying ASTM specification for asphalt binder course gradation. Based on the specification for gradation indicated in the above table and figure, for this research or thesis a nominal size of mix aggregate is selected to be 19 mm.

**2.3.4 Asphalt binder properties**

A series of bitumen quality tests were conducted before the start of the mix design. Table 4 presents the summary of the various properties of the 85/100 penetration grade binder.

Table 4: Properties of the 85/100 Penetration Grade Bitumen

Property	unit	Test Method (AASHTO)	Test Result	Recommended Specification ERA for 85/100
Penetration (25°C, 100g, 5sec)	(0.1mm)	T 49	90.7	85-100
Softening point	(°C)	T 53	48.8	42-51
Ductility(25°C)	(cm)	T 51	105	>100
Solubility	(%)	T 44	99.74	>99%
Specific gravity at (25 <sup>0</sup> C)	(g/cm <sup>3</sup> )	T 228	1.017	1.01-1.06

**3. RESULTS AND DISCUSSION**

**3.1 Analysis of Asphalt Mixture Properties**

Asphalt mixes were designed as per the Marshall mix design procedure, in which binder content corresponding to 4% air voids is considered OBC (Choudhary, Kumar eta Gupta, 2021; Permeh, Lau eta Tansel, 2021). In the Marshall Method, the resistance to plastic deformation of compacted cylindrical specimen of asphalts mixture is measured when the specimen is loaded diametrically at a deformation rate of 50mm per minute (Ethiopian road authority (ERA) asphalt pavement roads manual, 2013). The Marshall stability of the mix is defined as the maximum load carried by the test specimen at a standard test temperature of 60 °C (Endashaw, 2023). The results of Marshall Properties of specimens prepared with 5%, 6.5%, and 8% of crushed stone dust as filler by weight of aggregate with varying bitumen contents. A total of 45 samples each one of which weighs 1200 grams, were



prepared using five different bitumen contents (4.0, 4.5, 5.0, 5.5, and 6.0% of total weight) to determine the optimum bitumen content. Tables 5, 6 and 7 show the Marshall test results of mixtures with 5.0%, 6.5%, and 8 % crushed stone dust as filler and the corresponding values of marshall properties such as stability, flow value, air voids (VIM), voids in mineral aggregates (VMA), voids filled with asphalt (VFA), and bulk density at different bitumen contents respectively. According to (Ethiopian road authority (ERA) asphalt pavement roads manual, 2013) marshall design criteria for heavy traffic, minimum stability must be 7 kN at 60°C, flow value must be ranged between 2 to 4mm, percentage of air voids must be ranged between 3 to 5%, minimum VMA related to 4% air voids and nominal maximum particle size of 19 mm must be 13 and VFB must be ranged between 65 to 75%.

Table 5: Average volumetric properties of the asphalt concrete with 5.0% CSD filler

Volumetric properties	Symbol (Unit)	Mix Design Volumetrics					OBC (%)
Bitumen Content	BC (%)	4	4.5	5	5.5	6	
Bulk density	$\rho_A$ (g/cm <sup>3</sup> )	2.32	2.348	2.354	2.359	2.351	
Air voids	VIM (%)	6.5	4.7	3.8	2.8	2.5	
Voids in mineral aggregate	VMA (%)	14.9	14.3	14.5	14.8	15.5	4.48
Voids filled with asphalt	VFA (%)	56	67	74.1	80.8	84.1	
Stability	S (kN)	7.9	8.6	8.7	9	7.9	
Flow	F (mm)	2.73	3.08	3.38	3.75	4.12	

Table 6: Average volumetric properties of the asphalt concrete with 6.5% CSD filler

Volumetric properties	Symbol (Unit)	Mix Design Volumetrics					OBC (%)
Bitumen Content	BC (%)	4	4.5	5	5.5	6	
Bulk density	$\rho_A$ (g/cm <sup>3</sup> )	2.311	2.328	2.356	2.373	2.377	
Air voids	VIM (%)	7.5	6.1	4.2	2.8	2.1	
Voids in mineral aggregate	VMA (%)	15.2	15	14.4	14.3	14.6	5.1
Voids filled with asphalt	VFA (%)	50.8	59.4	70.8	80.5	85.3	
Stability	S (kN)	8.2	10.6	11.1	9.9	9.6	
Flow	F (mm)	3.02	2.64	3.31	3.37	3.44	

Table 7: Average volumetric properties of the asphalt concrete with 8.0% CSD filler

Volumetric properties	Symbol (Unit)	Mix Design Volumetrics					OBC (%)
Bitumen Content	BC (%)	4	4.5	5	5.5	6	
Bulk density	$\rho_A$ (g/cm <sup>3</sup> )	2.301	2.326	2.343	2.355	2.363	
Air voids	VIM (%)	8	6.3	4.9	3.7	2.6	
Voids in mineral aggregate	VMA (%)	15.6	15.1	14.9	14.9	15.1	5.34
Voids filled with asphalt	VFA (%)	48.9	58.6	67.5	75.6	82.8	
Stability	S (kN)	7.9	8.6	9.9	9.7	9.4	
Flow	F (mm)	2.12	2.92	2.58	2.73	2.56	

Fig. 3 shows that the unit weight for total mix and stability value increases with the increase of the bitumen content up to a maximum and then gradually decreases, whereas the VFA and flow value increases with an increase of bitumen content. Besides, the percent VMA decreases to the minimum value and then increases with increasing bitumen content. The NAPA mix design method requires the mix to have 4% air voids at the optimum binder content. Using this criterion, the optimum bitumen content was found equal to 5.10 % by weight of the total mix.

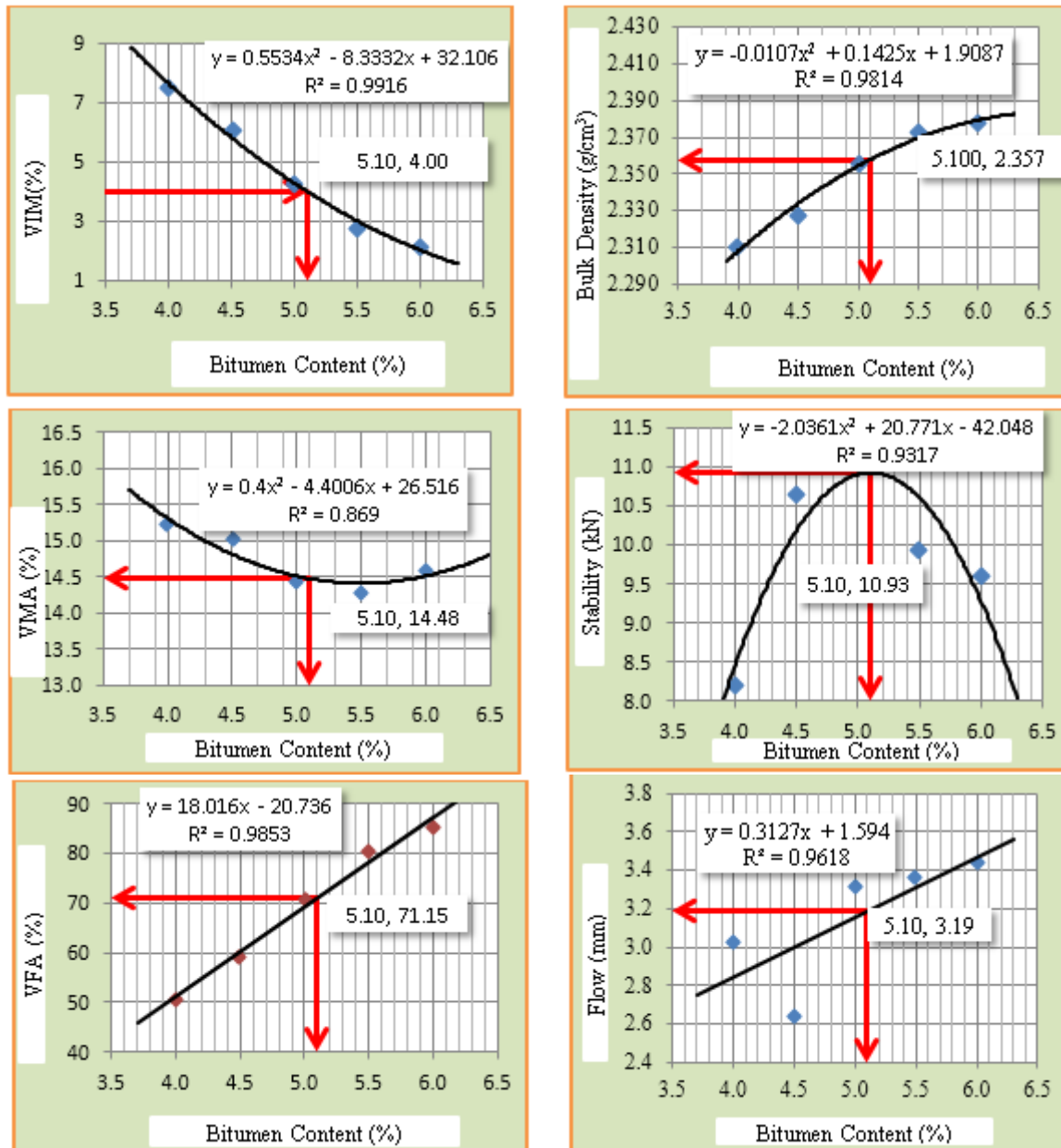


Fig. 3: OBC and the properties of mixtures with 6.5% CSD filler

### 3.2 Determining Optimum Bitumen Content

Marshall test was used to examine the specimens of asphalt mixture with different percentages of bitumen content which were (4.0, 4.5, 5.0, 5.5, and 6.0%) to obtain the optimum bitumen content. The optimum bitumen content is determined by the method of the National Asphalt Pavement Association (NAPA) which suggests preparing the plots contained in Fig. 3. The optimum bitumen content is determined by first finding the bitumen content that corresponds to the median air void content (4 percent) of the specification (ERA asphalt pavement roads manual, 2013). That bitumen content is then used to determine the values for Marshall Stability, flow, VMA, VFA, and percent of voids filled from each of the plots in Fig. 3. Each value is compared against the specified value for that property and if all are within the specified range, the bitumen content at 4 percent air voids is the optimum bitumen content. Based on the result, the optimum bitumen content is 4.84, 5.10, and 5.34 percent at 4 % air voids for 5.0%, 6.5%, and 8 % of CSD filler respectively.



### 3.3 Effect of Waste Glass Powder on Volumetric Properties of Asphalt Mix

The effects of replacing various proportions of the primarily used filler with the WGP on Marshall Stability, flow, and volumetric properties of a typical binder course asphalt concrete have been evaluated. Based on determining the amount of optimum bitumen content (5.10%) and optimum filler content (6.0%), crushed stone dust filler was replaced at 4 incremental percentages 25, 50, 75, and 100% by weight of CSD filler with waste glass powder filler. Hot mix asphalt mix with no waste glass powder served as the control mixture for the subsequent studies. The obtained asphalt concrete specimens with the waste glass powder were denominated by using the RAC abbreviation, formed by the initials “Replaced Asphalt Concrete”. The samples were numbered from RAC 1 to RAC 4 based on percentage values, starting from 25%, and with 100% WGP. Table 8 shows the mix proportion of asphalt concrete mixtures prepared by using different filler content and their proportions of used aggregate.

Table 8: Mix proportion of asphalt concrete mixtures prepared by using different filler content and their proportions of used aggregate

Samples Name	Coarse aggregate	Fine aggregate	Waste Glass	Crushed Stone
	14-20mm	0-3mm	Powder (%)	Dust (%)
Control Sample	32.5	70	0 (0%)	6.5 (100%)
RAC 1	32.5	70	1.625 (25%)	4.875 (75%)
RAC 2	32.5	70	3.25 (50%)	3.25 (50%)
RAC 3	32.5	70	4.875 (75%)	1.625 (25%)
RAC 4	32.5	70	6.5(100%)	0 (0%)

Marshall Properties of asphalt mixes with WGP at a constant bitumen content of 5.10% are summarized in Table 9. A total of 15 Marshall specimens of mixture each one of them weighing 1200 gm were prepared using five glass powder content (0, 25, 5, 75, and 100%) by the weight of crushed stone dust filler and 5.10% bitumen content by the weight of the total mix. Table 9 shows the asphalt mixtures laboratory test results with different filler content and the corresponding values of Marshall Properties at a constant bitumen content (5.10%). The properties of the asphalt mixtures with varying content of glass powder will be discussed in subsequent sections.

Table 9: Average Marshall Properties of Asphalt Mixes with WGP at OBC of 5.10%

% of replacement	%	0%	25%	50%	75%	100%
Content CSD & WGP filler	CSD and WGP	6.5% CSD; 0% WGP	4.875% CSD; 1.625% WGP	3.25% CSD; 3.25% WGP	1.625% CSD; 4.875% WGP	0% CSD; 6.5% WG
Bulk density	ρA	2.35	2.352	2.356	2.36	2.355
Air voids	VIM (%)	4.2	4.3	4.1	4	4.2
Voids in mineral aggregate	VMA (%)	14.8	14.7	14.6	14.4	14.6
Voids filled with asphalt	VFA (%)	71.3	70.8	71.8	72.3	71.1
Stability	S (kN)	10.1	10.4	11.0	12.0	10.3
Flow	F (mm)	3.26	2.96	3.12	2.84	3.1

### 3.4 Effect of Glass Powder Content on Marshall Stability of Asphalt Mix

The maximum load carried by the test specimen at a specified test temperature of 60 °C is known as Marshall stability (Khedaywi, Haddad eta Alyaseen, 2023; Kifile *et al.*, 2023). Fig. 4 shows that all values of stability with the replacement of WGP filler content have achieved the specification requirements. Fig. 4 indicates that as the Marshall stability value of the mixtures increases as the glass powder content increases until it reaches the maximum stability of 12.0kN at 75% glass powder content, then it starts to decline and is consistent with the findings of (Taherkhani, 2016; Kifile *et al.*, 2023). This result may be explained by that the increase in glass powder content made the mix flexible so it became strong to resist loads.

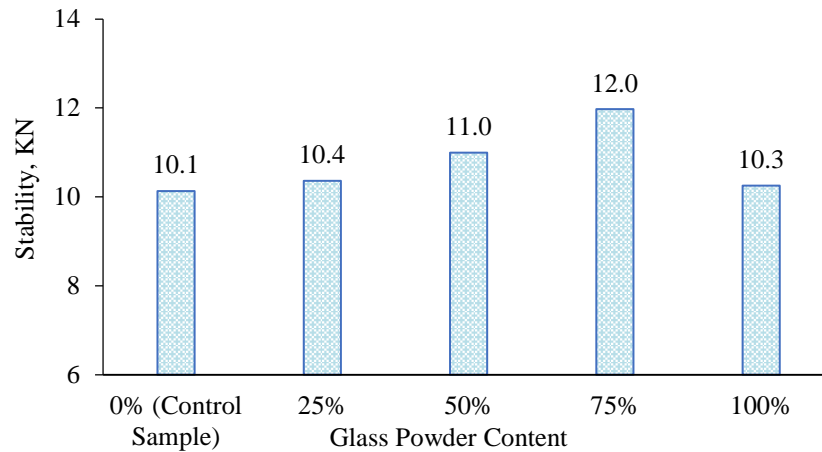


Fig. 4: Effect of glass powder content on Marshall Stability of asphalt mix

### 3.5 Effect of Glass Powder Content on Flow Value of Asphalt Mix

The flow value is the total deformation of the Marshall Test specimen at the maximum load, expressed in mm units (Sargin *et al.*, 2013). According to (ERA asphalt pavement roads manual, 2013), the flow value limit must be a minimum of 2 mm and a maximum of 4 mm for heavy traffic. The results of the flow values test for different glass powder contents are presented in Fig. 5. The flow of replacing mixes around the value of the control mix which is 3.26 mm and still in the range of ERA Pavement Design Manual specifications at all replacement rates. When considering Fig. 5 lowest flow value was obtained at the point of 2.84 mm for samples prepared with 75% WGP (1.625% CSD filler and 4.875% WGP), a maximum flow value which is 3.26 mm for the sample prepared with 0% WGP (6.5% CSD and 0% WGP). However, flow values are located within the required specification (Ethiopian road authority (ERA) asphalt pavement roads manual, 2013) range of 2 to 4mm.

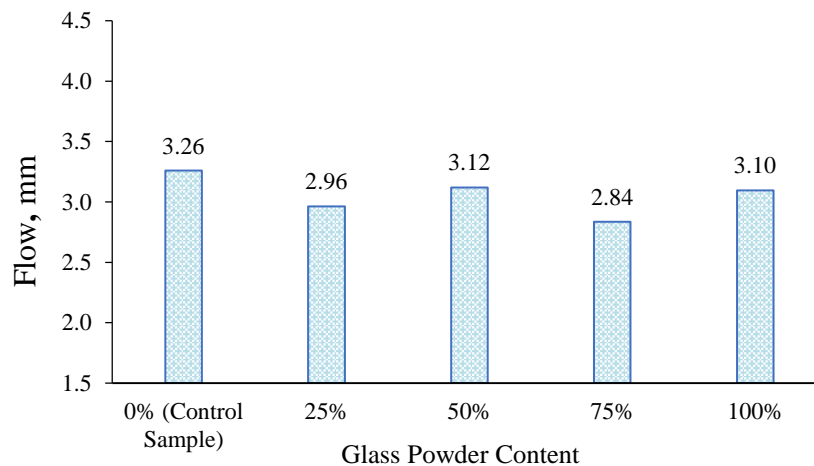


Fig. 5: Effect of glass powder content on flow value of asphalt mix

### 3.6 Effect of Glass Powder Content on Bulk Density of Asphalt Mix

The relationships between different glass powder contents and bulk density are illustrated in Fig. 6. The same trend of the results of stability values was observed in the bulk density value increases with increased waste glass powder content until it reaches the maximum bulk density at 75% glass powder content, then it starts to decline. The maximum bulk density is (2.360 g/cm<sup>3</sup>) at 75% glass powder content and the minimum bulk density is (2.350 g/cm<sup>3</sup>) at 0% glass powder content, which is consistent with the results of previous studies (Olutaiwo eta Owolabi, 2015; Endashaw, 2023).

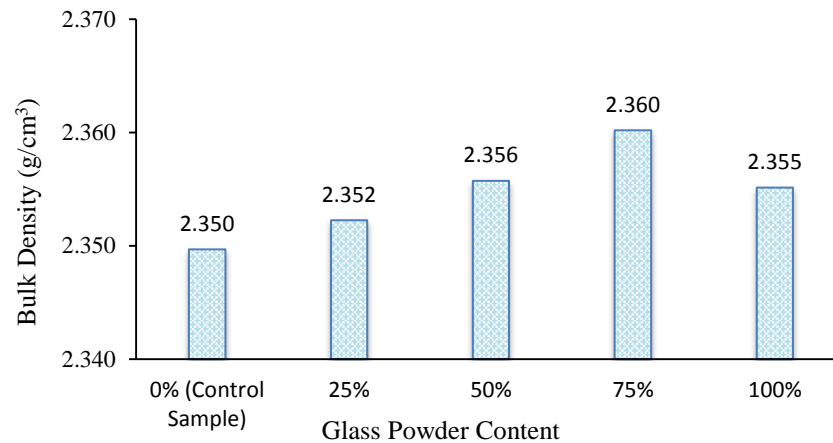


Fig. 6: Effect of glass powder content on bulk density of asphalt mix

### 3.7 Effect of Glass Powder Content on Air Voids of Asphalt Mix

Air voids ( $V_a$ ) it should be emphasized that the design range of air voids (3-5%) is a level desired after several years of traffic (Taherkhani, 2016). The mixes that ultimately consolidate to less than 3% can be expected to rut and shove, similarly, problems like brittleness and premature cracking can occur if the final air void content is above 5% (ERA asphalt pavement roads manual, 2013; Pasandín eta Pérez, 2014). Fig. 7 shows that at 75% glass powder content the air voids percentage was 4% which is the median value of local and international specification. Ethiopian Road Authority asphalt pavement roads manual (Ethiopian road authority (ERA) asphalt pavement roads manual, 2013) requires a minimum and maximum air void content of 3 and 5%, respectively, for binder coarse, which is satisfied by all the mixtures.

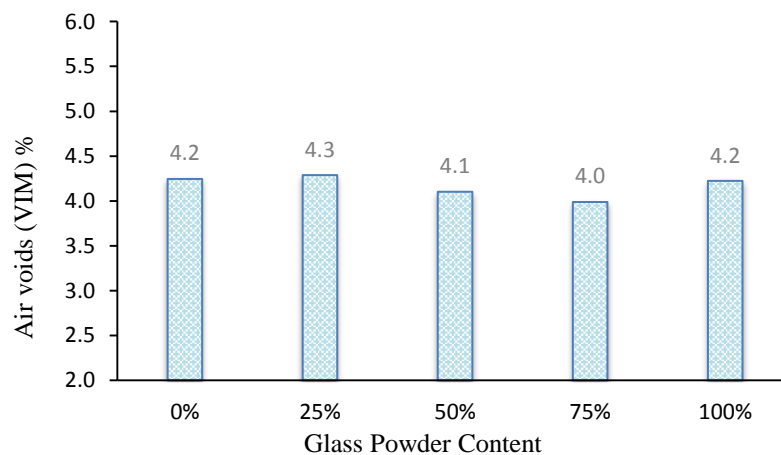


Fig. 7: Effect of glass powder content on air voids of asphalt mix

### 3.8 Effect of Glass Powder Content on Voids in Mineral Aggregates of Asphalt Mix

The relationship between glass powder content and voids in mineral aggregates is shown in Fig. 8. It is noticed that the voids in mineral aggregates decrease with increased glass powder content up to a minimum value, then increase at higher content glass powder. The minimum VMA value is 14.4% of asphalt samples prepared with 1.625% CSD and 4.875% WGP. A minimum VMA value of 13% is required by the specification in Ethiopian Road Authority asphalt pavement roads manual (Ethiopian road authority (ERA) asphalt pavement roads manual, 2013) for the asphalt concrete with a nominal size of mix aggregate of 19 mm, which is satisfied by all of the mixtures.

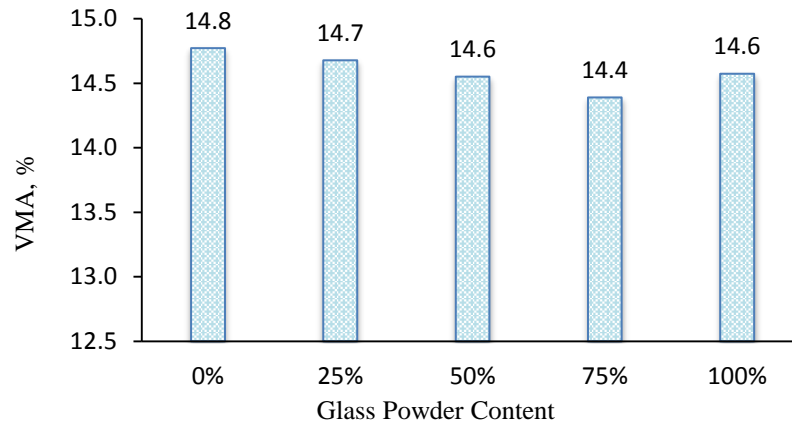


Fig. 8: Effect of glass powder content on voids in mineral aggregates of asphalt mix

### 3.9 Effect of Glass Powder Content on Percent Voids Filled with Asphalt of Asphalt Mix

The relationship between glass powder content and voids filled with asphalt is shown in Fig. 9. Voids filled with asphalt value increase with an increased replacement rate of glass powder till they reach the highest VFA value at 75% WGP. It is noticed that the VFA for replaced mixes with 0% - 100% glass powder was all within the range of 65% - 75% specified by (Ethiopian road authority (ERA) asphalt pavement roads manual, 2013). At a 75% replacement rate of glass powder content, the VFA in the mix is higher indicating the lowest air void for the mix. The VFA for the control mix is lower than 75% of the replaced mix. This was because more effective bitumen content was present in the mix to fill available voids between the intergranular spaces.

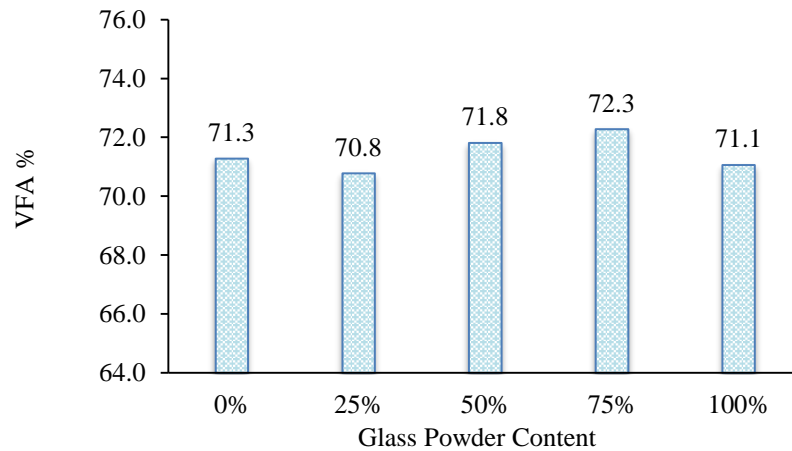


Fig. 9: Effect of glass powder content on percent voids filled with asphalt of asphalt mix

Table 10: Marshall Properties of Asphalt Mixes with different WGP filler content

Property	Percentage of Glass Powder				
	0%	25%	50%	75%	100%
% of Bitumen	5.10	5.10	5.10	5.10	5.10
Stability (kN)	10.1	10.4	11.0	12.0	10.3
Flow (mm)	3.26	2.96	3.12	2.84	3.10
Bulk Density (gm/cm <sup>3</sup> )	2.35	2.352	2.356	2.36	2.355
% of Va %	4.2	4.3	4.1	4.0	4.2
% of VMA	14.8	14.7	14.6	14.4	14.6
% of VFB	71.3	70.8	71.8	72.3	71.1



Table 10 indicates that each Marshall's stability, bulk density, and VFA increase as the glass powder increases. Flow values, air voids, and voids in mineral aggregates decrease as the glass powder content increases.

### 3.10 Determination of Optimum Replacement Rate of Waste Glass Powder

Asphalt mix with optimum content satisfies the Maximum stability, Maximum bulk density, and Va % within the allowed range of specifications (ERA asphalt pavement roads manual, 2013). From Fig. 4 it's noticed that all values of Marshall Stability for various glass powder content satisfy the local and international specifications which are a minimum of 7.0kN and 8.006kN respectively. However, the maximum stability corresponding to 75% of glass powder content is 12.0kN. Fig. 6 represents the values of bulk density at various glass powder content and the maximum bulk density was obtained at 75% glass powder content. It was also noticed in Fig. 7 that all the values of air voids percentage at various glass powder content and 75% WGP filler content the corresponding air voids value was 4.0% which is the median air voids in the specifications. The mix obtained using 25% CSD and 75% WGP meets the standard specified in terms of Maximum stability, Maximum bulk density, and Va % within the allowed range of specifications, at an optimum bitumen content of 5.10%. Hence 75% was adopted as the optimum content of glass powder.

### 3.11 Comparison of Properties of Asphalt Mix at Optimum WGP with Standard Specifications

The comparison of Marshall and volumetric properties of asphalt mix at optimum glass powder content (75 % by weight of optimum crushed stone dust filler) with local and international specifications. All the results are within the required specification range. Table 11 illustrates a comparison of the Marshall properties of the asphalt mix containing 75% glass powder content with the local specifications (ERA asphalt pavement roads manual, 2013).

Table 11: Comparison of properties of asphalt mix optimum WGP with specification

Marshall Method Mix Criteria	(75%) replaced asphalt mix	International Spec. ( <i>Asphalt Institute</i> )		Remark
		Traffic Heavy		
		Min	Max	
No. of blows	2*75	2*75		
Stability (kN)	12.0	8.006	-	Satisfied
Flow, (mm)	2.84	2	3.5	Satisfied
VIM, %	4.0	3	5	Satisfied
VFA, %	72.3	65	75	Satisfied
VMA, %	14.4	13	-	Satisfied

As shown in Table 9 the asphalt mix with optimum glass content of 1.5% CSD and 4.5% WGP by weight of the aggregates (or 75% by weight of crushed stone dust filler) satisfied the requirements of (ERA asphalt pavement roads manual, 2013) specifications, and asphalt institute specifications for all tested properties. According to the results of all tests conducted for this laboratory investigation, the best outcomes were obtained at 75% WGP by weight of crushed stone dust filler or 4.5% by weight of aggregate.

## 4. CONCLUSIONS AND RECOMMENDATIONS

The study focused on the effects of waste glass powder on volumetric properties of asphalt mix. Based on the results of the research the following conclusions are drawn.

- The laboratory test result for WGP gives gradation parameters and plastic index, satisfying the specification for using filler in hot asphalt concrete production.
- It was observed that 6.0% filler content of CSD had shown maximum Marshall stability for 5.10% bitumen content.



- Bulk density and stability values increased with the increase of glass powder content until it reached the maximum, then it started to decline in the asphalt mix.
- At 75% replacement of crushed stone dust by glass powder, the mixtures give maximum stability, maximum bulk density, and % of Va within the permissible range of specifications.
- Thus, 75% glass powder content by weight of CSD filler or 4.5% by weight of aggregate is recommended as optimum content for heavy traffic.
- The problem of disposal of industrial waste can be reduced by using these waste materials.

In conclusion, this article makes two key contributions to the field of asphalt mix research. First, it provides a comprehensive review of the literature on the topic of asphalt concrete. This paper provides a valuable resource for researchers who are new to the field or who are looking for an overview of the latest research. Second, the article proposes a new framework for understanding the asphalt mix, which is based on the concept of a cognitive hierarchy. This framework provides a useful way of thinking about the asphalt mix and its potential applications.

From the above finding, it is evident that waste glass powder can be used as a filler in asphalt concrete mix and the result is good, so the client should use this material as filler. Based on the recent research studies and experiments relating to the performance of waste glass powder in asphalt concrete mix, the need for further research and studies has been indicated. The proposed future recommendations will conduct further research in various proportions of waste glass powder content in asphalt concrete mix production; will evaluate the effect of using waste glass powder on the pavement using different penetration grades of bitumen; and will investigate the characteristics of Marshall on the use of waste glass powder to asphaltic binder courses for heavy-trafficked roads.

## ACKNOWLEDGEMENTS

The authors wish to thank the IFH engineering laboratory staff for their cooperation, encouragement, and guidance in completing this study.

## REFERENCES

- Ahmed, H.Y., Othman, A.M. eta Mahmoud, A.A. (2006) Effect of Using Waste Cement Dust As a Mineral Filler on the Mechanical Properties of Hot Mix Asphalt, Assiut University Bulletin for Environmental Researches. Available at: <https://doi.org/10.21608/auber.2006.150251>.
- Bindu, C.S. (2014) Influence of Additives on the Drain Down Characteristics of Stone Matrix Asphalt Mixtures, International Journal of Research in Engineering and Technology. Available at: <https://doi.org/10.15623/ijret.2014.0307014>.
- Cheru, M. (2016) «Solid Waste Management in Addis Ababa: A new approach to improving the waste management system», or. 71.
- Choudhary, J., Kumar, B. eta Gupta, A. (2021) «Utilization of Waste Glass Powder and Glass Composite Fillers in Asphalt Pavements», Advances in Civil Engineering, 2021. Available at: <https://doi.org/10.1155/2021/3235223>.
- Endashaw, D.K. (2023) «Influence of Corn Cob Ash as a Filler Material in Asphalt Concrete Mixes», International Journal of Pavement Research and Technology, 16(5), or. 1217–1225. Available at: <https://doi.org/10.1007/s42947-022-00191-w>.
- Ethiopian road authority (ERA) asphalt pavement roads manual (2013) Federal Democratic Republic Of Ethiopia Ethiopian Roads Authority Pavement Design Manual Volume 1, Flexible Pavements. Available at: [www.era.gov.et](http://www.era.gov.et).
- Fayissa, B., Gudina, O. eta Yigezu, B. (2020) «Application of Sawdust Ash as Filler Material in Asphaltic Concrete Production», Civil and Environmental Engineering, 16(2), or. 351–359. Available at: <https://doi.org/10.2478/cee-2020-0035>.
- Haddad, M. eta Khedaywi, T. (2023) «Investigating the Effect of Olive Husk Ash on Dynamic Creep of Asphalt Concrete Mixtures», Journal of Engineering Science and Technology, 18(2), or. 931–948.
- Haddad, M.A. eta Khedaywi, T.S. (2023) «Moisture Resistance of Olive Husk Ash Modified Asphalt Mixtures», Annales de Chimie: Science des Matériaux, 47(3), or. 141–149. Available at: <https://doi.org/10.18280/acsm.470303>.
- Isa, N., Olowosulu, A. eta Joel, M. (2018) «Mechanistic evaluation of the effect of calcium carbide waste on properties of asphalt mixes», Nigerian Journal of Technological Development, 15(1), or. 20. Available at: <https://doi.org/10.4314/njtd.v15i1.4>.



- Jattak, Z.A., Hassan, N.A. et al. Mohd Satar, M.K.I. (2021) «Moisture susceptibility and environmental impact of warm mix asphalt containing bottom ash», *Case Studies in Construction Materials*, 15(March), or. e00636. Available at: <https://doi.org/10.1016/j.cscm.2021.e00636>.
- Kamran, M. et al. (2023) «Experimental Evaluation of Hot Mix Asphalt Using Coal Bottom Ash As Partial Filler Replacement», *Roads and Bridges - Drogi i Mosty*, 22(2), or. 167–179. Available at: <https://doi.org/10.7409/rabdim.023.008>.
- Khan, D. (2023) «Effect of Recycled Aggregates and Polymer Modified Bitumen on the Marshall Properties of Hot Mix Asphalt- A Case Study», *Quaid-e-Awam University Research Journal of Engineering, Science & Technology*, 21(1), or. 16–26. Available at: <https://doi.org/10.52584/qrj.2101.03>.
- Khan, D., Ali, B., et al. (2023) «Effects of crumb rubber and styrene-butadiene rubber additives on the properties of asphalt binder and the Marshall performance properties of asphalt mixtures», *Budownictwo i Architektura*, 22(4), or. 147–161. Available at: <https://doi.org/10.35784/bud-arch.5499>.
- Khan, D., Khan, R., et al. (2023) «Performance of hot-mix asphalt using polymer-modified bitumen and marble dust as a filler», *Journal of Traffic and Transportation Engineering (English Edition)*, 10(3), or. 385–398. Available at: <https://doi.org/10.1016/j.jtte.2022.12.002>.
- Khan, N. et al. (2023) «Effect of Fine Aggregates and Mineral Fillers on the Permanent Deformation of Hot Mix Asphalt», *Sustainability (Switzerland)*, 15(13). Available at: <https://doi.org/10.3390/su151310646>.
- Khedaywi, T., Haddad, M. et al. Alyaseen, S. (2023) «Effect of Filler Materials on Marshall Properties and Rutting of Asphalt Mixtures Using Wheel Tracking Test: a Comparative Study», *Journal of Engineering Science and Technology*, 18(4), or. 1915–1935.
- Kifile, D. et al. (2023) «Evaluation of Maize Cob Ash as Filler in Hot-Mix Asphalt Concrete Production», *International Journal of Pavement Research and Technology*, 16(3), or. 592–605. Available at: <https://doi.org/10.1007/s42947-021-00150-x>.
- Le, V.P. (2021) «Performance of asphalt binder containing sugarcane waste molasses in hot mix asphalt», *Case Studies in Construction Materials*, 15(March), or. e00595. Available at: <https://doi.org/10.1016/j.cscm.2021.e00595>.
- Mohd Shukry, N.A. et al. (2018) «Effect of various filler types on the properties of porous asphalt mixture», in *IOP Conference Series: Materials Science and Engineering*. Institute of Physics Publishing. Available at: <https://doi.org/10.1088/1757-899X/342/1/012036>.
- Murana, A. et al. Sani, L. (2015) «Partial Replacement of Cement with Bagasse Ash in Hot Mix Asphalt», *Nigerian Journal of Technology*, 34(4), or. 699. Available at: <https://doi.org/10.4314/njt.v34i4.5>.
- Olukanni, E.O., Oyedepo, O.J. et al. Ajani, A.M. (2021) «Performance and Microstructural Evaluation of Asphalt Concrete Produced with Hydrated Lime, Glass Powder and Cement Modifiers», *Nigerian Journal of Technological Development*, 18(4), or. 296–301. Available at: <https://doi.org/10.4314/njtd.v18i4.5>.
- Olutaiwo, A. et al. Owolabi, A. (2015) «Investigation of the Effects of Partial Replacement of Coarse Aggregate with Graded Palm Kernel Shell in Asphaltic Binder Course», *British Journal of Applied Science & Technology*, 10(3), or. 1–13. Available at: <https://doi.org/10.9734/bjast/2015/18785>.
- Osuya, D.O. et al. Mohammed, H. (2017) «Evaluation of sawdust ash as a partial replacement for mineral filler in asphaltic concrete», *Ife Journal of Science*, 19(2), or. 431. Available at: <https://doi.org/10.4314/ijss.v19i2.23>.
- Pasandín, A.R. et al. Pérez, I. (2014) «Mechanical properties of hot-mix asphalt made with recycled concrete aggregates coated with bitumen emulsion», *Construction and Building Materials*, 55, or. 350–358. Available at: <https://doi.org/10.1016/j.conbuildmat.2014.01.053>.
- Paul, D., Suresh, M. et al. Pal, M. (2021) «Effect of CENEX polymer on the performance of bituminous concrete and dense bituminous macadam of pavement», *Case Studies in Construction Materials*, 15, or. e00558. Available at: <https://doi.org/10.1016/j.cscm.2021.e00558>.
- Perme, S., Lau, K. et al. Tansel, B. (2021) «Moisture and ion mobilization and stratification in post-tensioned (PT) grout during hydration», *Case Studies in Construction Materials*, 15(August), or. e00644. Available at: <https://doi.org/10.1016/j.cscm.2021.e00644>.
- Al Qadi, A.N.S. et al. (2021) «Investigating the effect of olive husk ash on the properties of asphalt concrete mixture», *Annales de Chimie: Science des Matériaux*, 45(1), or. 11–15. Available at: <https://doi.org/10.18280/acsm.450102>.
- Rashwan, N.K. (2016) «Hot Mix Asphalt (HMA) Performance as Affected by Limestone Powder Filler Content», *World Applied Sciences Journal*, 34(2), or. 237–244. Available at: <https://doi.org/10.5829/idosi.wasj.2016.34.2.15656>.
- Saltan, M., Öksüz, B. et al. Uz, V.E. (2015) «Use of glass waste as mineral filler in hot mix asphalt», *Science and Engineering of Composite Materials*, 22(3), or. 271–277. Available at: <https://doi.org/10.1515/secm-2013-0135>.



- Sargin, Ş. et al. (2013) «Evaluation of rice husk ash as filler in hot mix asphalt concrete», *Construction and Building Materials*, 48, or. 390–397. Available at: <https://doi.org/10.1016/j.conbuildmat.2013.06.029>.
- Simone, A. et al. (2019) «Experimental application of waste glass powder filler in recycled dense-graded asphalt mixtures», *Road Materials and Pavement Design*, 20(3), or. 592–607. Available at: <https://doi.org/10.1080/14680629.2017.1407818>.
- Taherkhani, H. (2016) «Investigating the Effects of Nanoclay and Nylon Fibers on the Mechanical Properties of Asphalt Concrete», *Civil Engineering Infrastructures Journal*, 49(2), or. 235–249. Available at: <https://doi.org/10.7508/cej.2016.02.004>.
- Taherkhani, H. eta Bayat, R. (2022) «Investigating the properties of asphalt concrete containing recycled brick powder as filler», *European Journal of Environmental and Civil Engineering*, 26(8), or. 3583–3593. Available at: <https://doi.org/10.1080/19648189.2020.1806932>.
- Tahmoorian, F. et al. (2017) «Evaluation of mechanical properties of recycled material for utilization in asphalt mixtures», *Applied Sciences (Switzerland)*, 7(8). Available at: <https://doi.org/10.3390/app7080763>.
- Thiam, M., Fall, M. eta Diarra, M.S. (2021) «Mechanical properties of a mortar with melted plastic waste as the only binder: Influence of material composition and curing regime, and application in Bamako», *Case Studies in Construction Materials*, 15(May), or. e00634. Available at: <https://doi.org/10.1016/j.cscm.2021.e00634>.



## Jute Reinforced PLA Bio-composite for Production of Ceiling Fan Blades

Neway Seboka\*

Textile and garment industry research and development center, Addis Ababa, Ethiopia

\*Corresponding author, e-mail: [contny@gmail.com](mailto:contny@gmail.com) or [neway\\_seb@yahoo.com](mailto:neway_seb@yahoo.com)

### ABSTRACT

*This project aims at replacing the conventional aluminum ceiling fan blades. Hence, jute fabric is used as reinforcement and PLA (poly lactic acid) film is the matrix by which composites are made by stacking of number of fabric layers in between the PLA films. For surface modification of the jute fabrics, different chemical treatments are carried out such as alkali, acetylation, silane treatment and treatment with maleic anhydride. Compression molding machine is used for composite making. Based on the tensile strength test result performance, Alkali + Silane treated fabrics are used for making of the composite samples. Composite blades with 50:50 fibre volume fractions and having a weight of 75g and a thickness of 2mm is found to be the lightest and shows a tensile strength value of 47.1 MPa, which is half of the value of the aluminum alloy and having an ILSS (Inter-laminar shear strength) value of 8.88MPa has been chosen as the composite blades. Using Digimizer software, the pitch angles of the composite blades are measured and average pitch angles of 10.13° and 12° are found. Test results show the composite blades have a higher air velocity than the Usha fans. However, due to the higher blade surface of Usha fans i.e 0.5ft<sup>2</sup>, the air delivery for the composite blades is calculated to be lower having a blade surface area of only 0.3ft<sup>2</sup>. With the use of the composite blades, an average power savings of 15.65Watt has been achieved while the fan is operating at the maximum speed, which is 20% power reduction.*

**Keywords:** composite blades, compression molding, Jute fabric, PLA, power savings, surface modification

### 1. INTRODUCTION

In order of importance, jute fibre is second to cotton hence it is cheaper. Its main constituent parts are cellulose and lignin. Since lignin is the hardest part for decomposing, it makes the plant fibre to be tough (Berhanu et al., 2014). Jute fibre stiffness comes because of the cellulose. It also gives strength and stability. But due to the hydrophilic properties of cellulose, compatibility with that polymer matrix is difficult because they have hydrophobic nature. For this basic reason different surface modification methods has to be there for the jute fibre so that the interfacial adhesion can be improved (Khan et al., 2015). To ensure better mechanical properties for the composite materials to be made, the jute fibre has to be surface treated (Nam et al., 2012).

While reinforcing the fibre with the matrix material, the cellulosic hydroxyl groups on the fibre surfaces make both the physical and chemical bonds. To say that bond between fibre and the matrix is good, number and strength of bonds between the two materials has to be better (Zafar et al., 2016). For improving the surfaces of the fibres, which in turn helps for better bonding with the matrix, adhesion agents have been made and their properties are also being studied that they bring improvements (Mitra et al., 1998). Jute fibre has impurities and oils. For removal of it caustic soda treatment helps and hence increment of bonding with the matrix will be there (Mwaikambo, 2009). Two mechanical properties which show increments on the surface treated jute fibres are: tensile strength and stiffness properties (Liu et al., 2007). While treating the fabric, we may use catalyst chemicals. In order to avoid occurrence of hydrolysis, weak mineral acids and acid salts are used (Bledzki et al., 2008).

The other chemical treatment of jute fibre, which is silane treatment with acid solution, brings an increment in mechanical properties of the fibre. Jute fabric is treated with Alkali, Silane, Maleic anhydride and acetic acid. Besides the observations in color changes after treatments, the fabric treated with Alkali & Silane in combination shows a higher tensile strength and Young's modulus values. Compared to the traditional polymers (Polypropylene, polystyrene & polyethylene), PLA has better mechanical properties like: tensile strength, tensile young's modulus, flexural strength, etc. besides the stated better mechanical properties, it has also its own drawbacks like poor toughness property and for those applications which need Plastic deformation this poor property limits its use. (Hamadi et al., 2015).

In addition, its higher price, fast physical aging and water sensitivity it creates an issue for industrial applicability. (Ashok et al., 2014). The tensile properties of PLA film are dependent on its orientation and it has



good wicking property besides it can be recycled by hydrolysis to lactic acid. (Gruber & O’Brien, 2002). The influence of chemical modifications on jute fibres has been studied and reported in different works. Amongst them are: latex coating, alkali treatment, monomer grafting, silane treatment, isocyanate treatment, permanganate treatment, acetylation, and so on. With the stated modification methods, improvements have been seen on the fibre matrix adhesion of the composites. Usually the need for modifications is for improvements on wettability and making compatible the reinforced fibre with the resin material so that the produced composite is going to be strong and durable (Gon, et al., 2012).

It is reported that the bending strength for jute fabric reinforced thermoplastic composites was 115MPa and the figure is comparable with that of glass fabric reinforced thermoplastic composites made with 20 % by weight of long fibre. (Katayama et al., 2006). Earlier mild steel were used for fan blades but it was having more weight and replaced with Aluminum alloy. But still it weighs. So as to mitigate the weight and increase efficiency of the blades, glass fibre-epoxy composite materials can be used. (NagaKiran et al., 2015). It seems that ceiling fans consumes less power. But due to continuous running, their power consumption will get higher. But if the proper material is selected for making of the blades, the consumption can be reduced along with the manufacturing costs. Composite materials can be a good choice for this (Comfortson et al., 2014).

The main aim of ceiling fan manufacturers is to produce fans having an input of 60W, but actually their fans consume between 72W to 83.8W, which is extra payment (Department of Consumer affairs, January 2012). So in this research, it is studied that the higher energy consumption of fans is caused by the heavier weight of aluminum ceiling fan blades and to mitigate the problem jute fabric is used as a substrate and PLA as a matrix/resin since it is thought that composite materials have lower density and they are lighter in weight also. Based on this fact, in this research it is tried to make lighter weight jute-PLA composite ceiling fan blades having better air-delivery & lower power consumptions in comparison with the existing aluminum ceiling fan blades.

## 2. MATERIALS AND METHODS

### 2.1. Materials and Chemicals

Woven Jute fabric (1/1 plain fabric) and PLA (poly lactic acid) film were used. The following chemicals were used for chemical treatments and preparation of composites: NaOH, HCl, Acetic acid, Ethyl acetate, H<sub>2</sub>SO<sub>4</sub>, Amino propyl trimethoxysilane, Maleicanhydride, Acetone solvent, and Araldite epoxy. Compression moulding machine, LCD Wind Speed Gauge Meter Anemometer & Thermometer, 4 In1 Digital Meter AC (80-260V/20A) Ammeter/Voltmeter/Power Meter/energy Meter are the equipment used for making of the composite blades and for testing the performance parameters.

### 2.2 Methods

#### A. Jute fabric surface treatments

The characteristics of the jute fabric is shown in Table 1.

Table 1 Characteristics of untreated jute fabric

Ends/inch	Picks/inch	GSM	Density (g/cm <sup>3</sup> )
10	9	251	1.42

#### Alkali treatment

5% w/w NaOH solution is prepared using sodium hydroxide pellets and distilled water. Then the fabric is dipped in NaOH solution for 1hour separately. After 1 hour, fabric is washed with 1% HCl solution for neutralization. Finally, it is washed with distilled water. Fabric is then kept in hot air oven for 3 hours at 70°C to hinder the water content (Singhal & Tiwari, 2014).

#### Alkali treatment + Acetylation

The alkali treated jute fabric is then treated with acetic acid for 1hour at room temperature and then thoroughly washed with distilled water and dried.



#### Alkali treatment + Silane treatment

A solution of 0.5 wt% silane coupling agent [3-(2-aminoethyl amino) propyl trimethoxysilane] is prepared in acetone. Then, the Alkali treated jute fabric is immersed in the solution for 45 min. After that, the fabric is removed from the solution and get dried in oven at 65<sup>o</sup>c for 1h. Finally, the fabric gets washed with water to remove chemical residues until a pH of 7 is obtained and then dried at room temperature (Ramamoorthy, et al 2015).

#### Alkali treatment + Maleic anhydride treatment

In maleic anhydride treatment, the alkali treated jute fabrics were surface treated for 5 min with 1% solution of maleic anhydride dissolved in toluene solvent at 55<sup>o</sup>C. After treatment, fabrics were washed in toluene to remove extra MA. The fabrics were then dried for 6 h followed by oven drying at 60<sup>o</sup>C (Singhal and Tiwari, 2014).

#### Composite fabrication

Composites were prepared on a compression moulding machine. Plies of jute fabrics were stacked between PLA films of the same dimension with the fabrics. The composites are processed at three different fibre volume fractions. Moulding is carried out under vacuum condition of 15 bar, at a moulding temperature of 190<sup>o</sup>c for 8 min. After moulding, the composites are air-cooled at laboratory temperature.

#### Composite Blade Fabrication with 70:30 Volume Fraction

Weight of the blades to be produced = 150g, so to get the weight fraction of the fabric and the matrix the following formula has been used;

$$W_{\text{fibre}} = \left[ 1 + \frac{1}{\left( \frac{V_f}{1 + V_f} \right) \left( \frac{\rho_{\text{fibre}}}{\rho_{\text{resin}}} \right)} \right]^{-1}$$

$$W_{\text{fibre}} = [1 + 1 / (2.33 * 1.15)]^{-1}$$

$$W_{\text{fibre}} = 73 \text{ \& therefore } W_{\text{matrix}} = 27$$

Therefore with this fibre volume fraction to produce 150g of the blade we need to have: 0.73\*150 = 109.5 g of fabric and the remaining 40.5 g will be the matrix. The composite blade is supposed to have a size of 4\*10 in<sup>2</sup> and one layer of the jute fabric having the same dimension weights about 6.7g therefore for 109.5 g we need to have about 16 fabric layers and 17 matrix layers. The figure below shows composite blade made with sixteen fabric layers.



Fig. 1 composite blade (made with sixteen fabric layers and fibre volume fraction: 70%)

#### Composite Blade Fabrication with 50:50 Volume Fraction

With this fibre volume fraction composite blades weighing 150g and 75g have been produced. Weight of the blades to be produced is 150g. Similarly, to get the weight fraction of the fabric and the matrix the above formula has been used;



$$W_{\text{fibre}} = [1 + 1 / (1 * 1.15)]^{-1}$$
$$W_{\text{fibre}} = 53 \text{ \& therefore } W_{\text{matrix}} = 47$$

Therefore with this fibre volume fraction to produce 150g of the blade we need to have,  $0.53 * 150\text{g} = 79.5\text{g}$  of fabric and the remaining 70.5g will be the matrix.

The composite blade is supposed to have a size of  $4 * 10 \text{ in}^2$  and one layer of the jute fabric having the same dimension weights about 6.7g therefore for 79.5g we need to have about 12 fabric layers and 13 matrix layers. Weight of the blades to be produced = 75g. So using the above formula we have:  $W_{\text{fibre}} = [1 + 1 / (1 * 1.15)]^{-1}$

$$W_{\text{fibre}} = 53 \text{ \& therefore } W_{\text{matrix}} = 47$$

To produce composite blades weighing 75g,  $0.53 * 75\text{g} = 40 \text{ g}$  of fabric and  $0.47 * 75\text{g} = 35\text{g}$  of matrix will be needed. The composite blade is supposed to have a size of  $4 * 10 \text{ in}^2$  and one layer of the jute fabric having the same dimension weights about 6.7g therefore for 40g we need to have about 6 fabric layers and 7 matrix layers. Stacking of the jute and PLA layers are shown in Fig. 2.



Fig. 2 Jute fabric layer and PLA film stacking for making composite blade

### B. Characterization Techniques

#### Evaluation of tensile properties of fabrics

Breaking strength and elongation of fabrics were tested on Universal testing machine following ASTM D 5035:1995 using load cell of 1000N. Five specimens were tested for each sample. The testing conditions are:

Width: 5cm; Thickness: 2mm; Length: 20cm; Gauge length: 7.5cm; Loading rate: 300mm/min.

#### Evaluation of tensile properties of composites

Tensile stress (MPa) and breaking extension of composites were tested on a Zwick tensile testing machine following ASTM D 3039. A load cell of 50 KN was used. The testing conditions are: Width: 25mm, 20mm; Thickness: 2mm, 3mm, 4mm & 5mm; Length: 175mm; Gauge length: 100mm; Cross head speed: 2mm/min. Fig. 3 shows a composite specimen ready for tensile strength testing.



Fig. 3 Specimen preparation and testing on Zwick composite tensile testing machine

#### *Testing of Inter-laminar shear strength of composite*

By using Zwick/Z010 shear strength tester, inter-laminar shear strength of composite specimens was tested following ASTM D2344/D2344M – 16 using load cell of 5KN. The testing details are: Thickness: 2 mm; Width: thickness\*2= 4mm; Length: thickness\*10= 20mm; Span length: thickness\*4= 8mm; Cross head speed: 2 mm/min. The figure below shows testing of specimen for shear strength on Zwick/Z010 shear strength tester.



Fig 4 Specimen testing on Zwick/Z010 shear strength tester

#### *Measurement of air velocity of fans*

The Figure 5 indicates An LCD wind speed gauge Anemometer used for measuring the air velocity (ft/min) of fans (both Usha and the composite blade) running at different speeds starting from the minimum to the maximum. Readings were taken at the tip (edge) part of the blades, where maximum air velocity is there and to get the actual readings data has been recorded just after completion of 3 minutes.



Fig. 5 LCD Wind Speed Gauge Meter Anemometer

*Measurement of power consumption of fans*

Power consumptions of fans were measured using 4 in 1 Digital meter AC (80-260V/20A) as indicated in figure 6. By using the wiring diagram at the back of the meter, 1<sup>st</sup> and 4<sup>th</sup> terminals of the meter are loaded to the power conductors of the fan’s regulator switch and through 20 A load current, 2<sup>nd</sup> and 3<sup>rd</sup> terminals of the meter are connected to the voltage supply of the regulator switch. Finally, the fan regulator has been switched on and readings are taken at different speeds.



Fig. 6 In1Digital Meter AC (80-260V/20A) Ammeter/Voltmeter/Power Meter/energy Meter

**3. RESULTS AND DISCUSSION**

**3.1 Tensile Properties of Jute Fabrics**

The tensile strength and young’s modulus of un-treated and chemically treated fabrics are given and compared in Fig 7. The breaking extension (%) at maximum breaking load has been compared for the differently treated and untreated jute fabrics and the result shows jute fabrics treated with Maleic anhydride and Acetic acid exhibits highest breaking extension (%) and this is due to the fact that many constituent fibres in the fabric slips rather than catastrophic failure when breaking load is applied on the fabric and do not contribute for the load sharing, and hence, the fabrics show a lower breaking strength and tensile strength values. On the contrast, Alkali+Silane treated jute fabrics show the lowest breaking extension (%) value because of the catastrophic failure of the constituent fibres which in turn contributes for the load sharing and hence a highest breaking strength and tensile strength values.

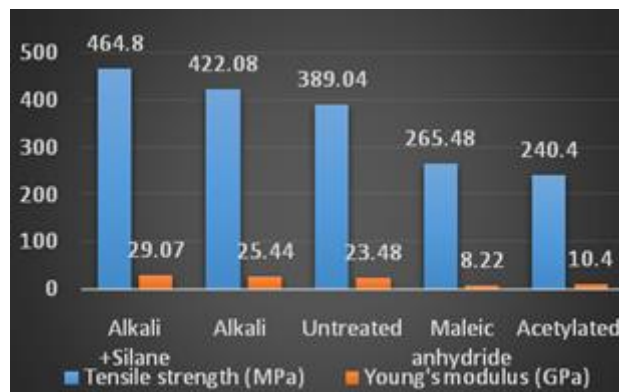


Fig 7 Tensile properties of untreated and treated fabrics



Alkali+Silane treated jute fabrics exhibits a higher tensile strength and Young's modulus followed by alkali only treated jute fabrics (Fig.7). So for making of composite specimens with different fibre volume fractions and weights, jute fabrics treated with Alkali+Silane were only considered.

### 3.2 Mechanical Characterization of Composite Samples

Three composite specimens made from Alkali + Silane treated jute fabrics as reinforcement by 60:40 fibre volume fraction to matrix volume fraction and with five layers of jute fabrics have been tested and results are compared with that of aluminum alloy 1050 H14, which is a potential candidate for making ceiling fan blades. Figures 8 – 12 show load – extension graphs of composite specimens made with different numbers of fabric layers & fibre volume fractions.

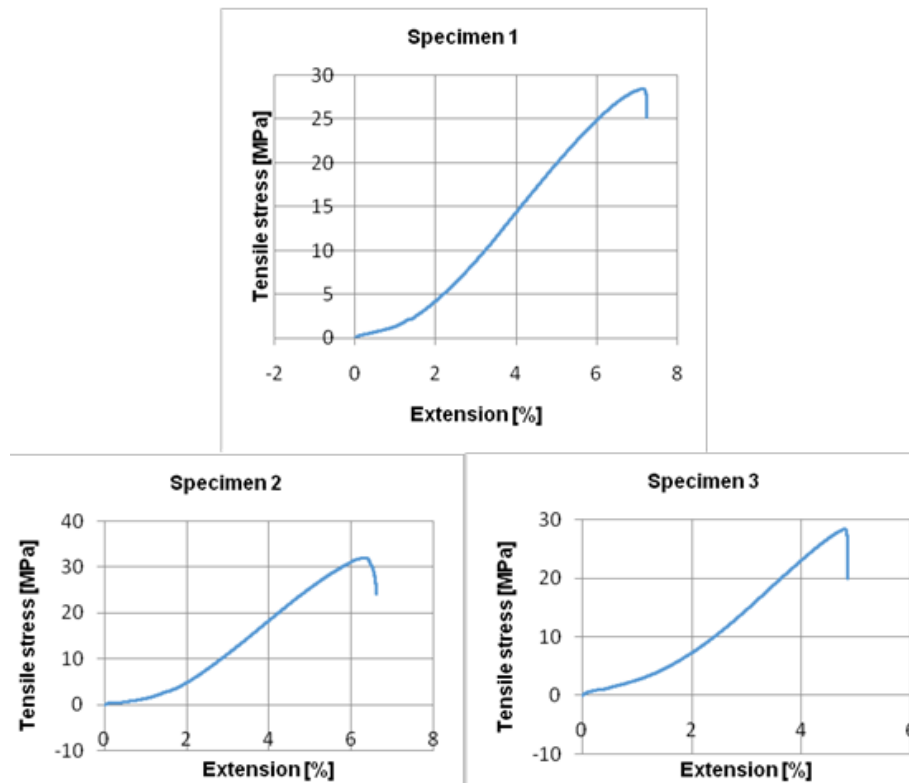


Fig 8 Load-extension graphs of composites with five fabric layers (fibre volume fraction: 60%)

Another four specimens of composites having the same volume fractions but only increasing the number of fabric layers to ten have been tested and compared.

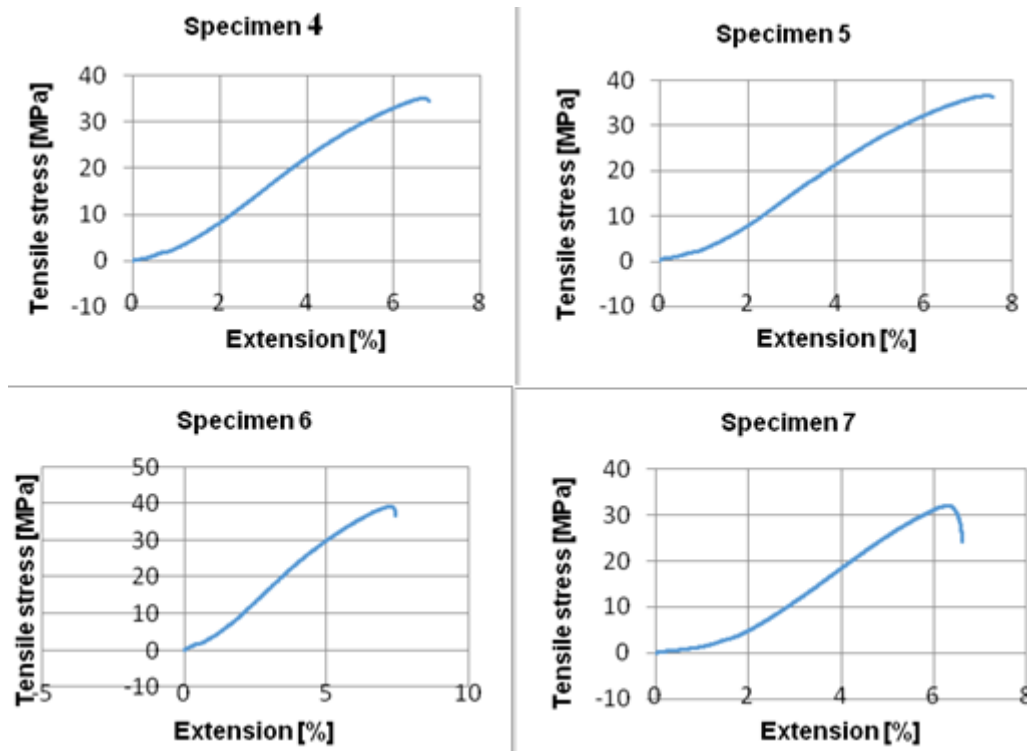


Fig. 9 Load-extension graphs of composites with ten fabric layers (fibre volume fraction: 60%)

Below is a table showing the tensile properties of aluminum alloy, which is widely used for making of ceiling fan blades.

Table 2 Tensile Properties of Aluminum Alloy 1050 H14

Material	$\rho$ (g/cc)	E (GPa)	Tensile strength (MPa)
Aluminium Alloy 1050 H14	2.8	70	105-145

### 3.3 Tensile Test of Composite Blades (70% Fibre Volume Fraction & sixteen fabric layers)

Composite specimens which are used for producing 150 g weighing composite blade are made from Alkali + Silane treated jute fabrics as reinforcement by 70:30 fibre volume fraction to matrix volume fraction and with sixteen layers of jute fabrics are tested and results are compared with that of aluminum alloy 1050 H14, which is a potential candidate for making ceiling fan blades.

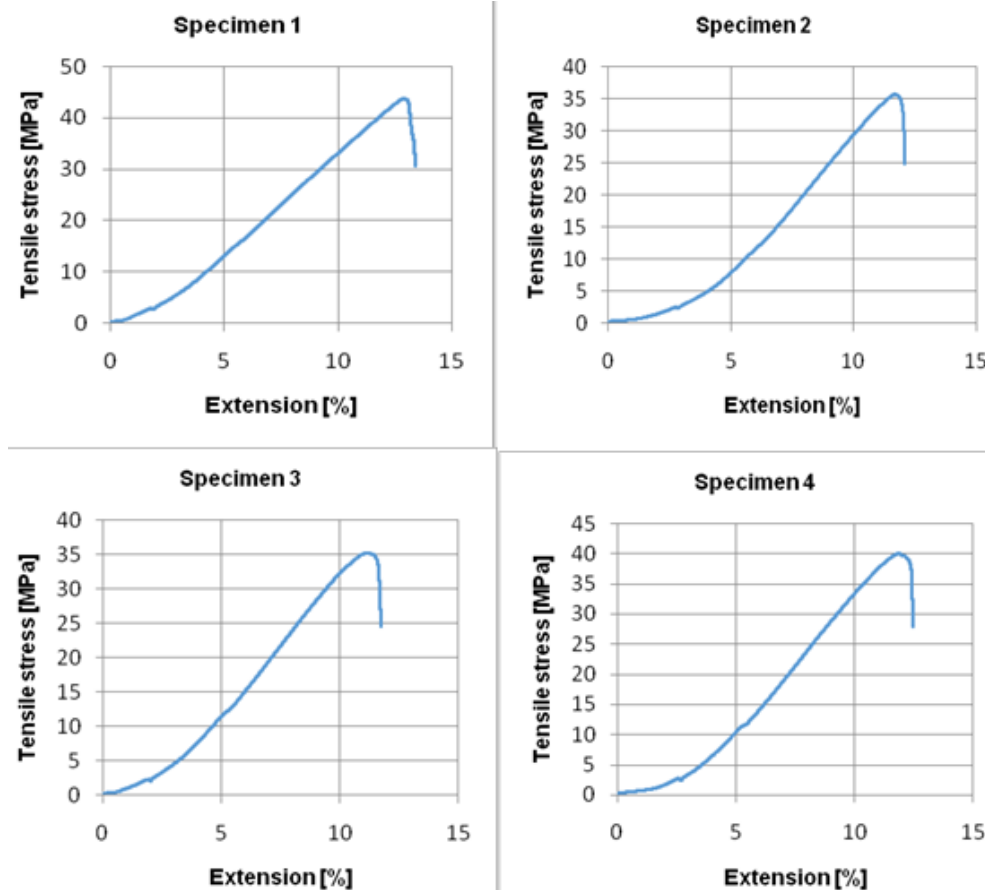


Fig 10 Load-extension Graphs of composites with sixteen fabric layers (fibre volume fraction: 70%)

### 3.4 Tensile Test of Composites (50% Fibre volume fraction & twelve fabric layers)

Composite specimens which are used for producing 150 g weighing composite blade are made from Alkali + Silane treated jute fabrics as reinforcement by 50:50 fibre volume fraction to matrix volume fraction and with twelve layers of jute fabrics are tested and results are compared with that of aluminum alloy 1050 H14, which is a potential candidate for making ceiling fan blades.

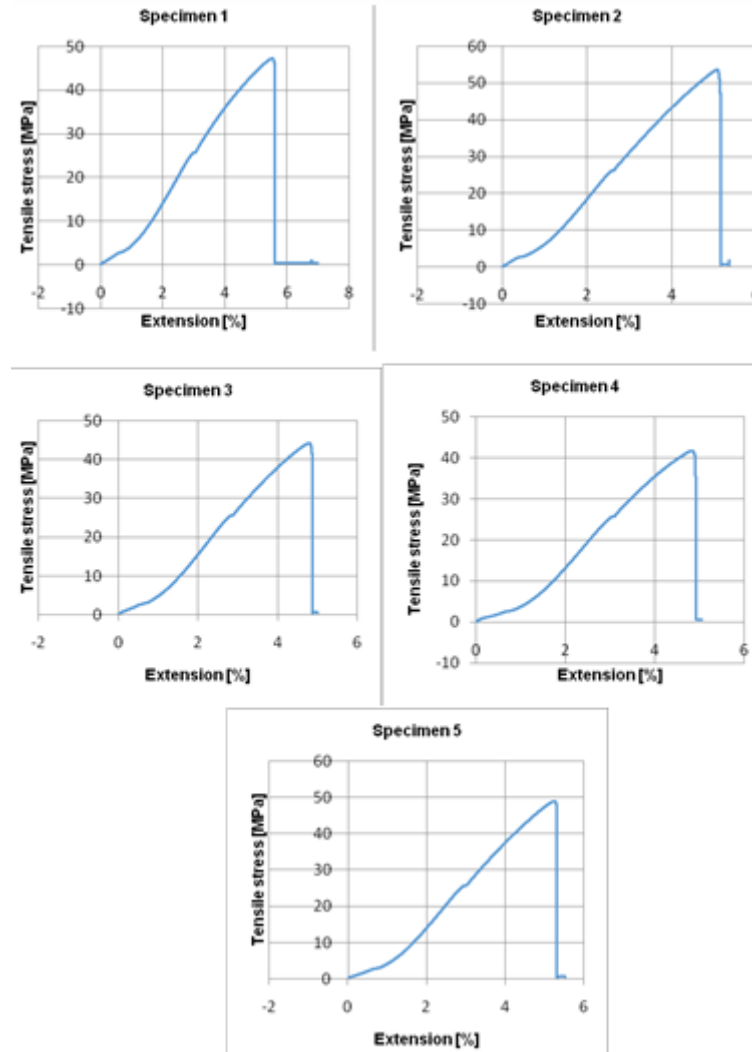


Fig 11 Load-extension graphs of composites with twelve fabric layers (fibre volume fraction: 50%)

### 3.5 Tensile Test of Composites (50% Fibre Volume Fraction and Six Fabric layers)

Composite specimens which are used for producing 75g weighing composite blade are made from Alkali + Silane treated jute fabrics as reinforcement by 50:50 fibre volume fraction to matrix volume fraction and with six layers of jute fabrics are tested and results are compared with that of aluminum alloy 1050 H14, which is a potential candidate for making ceiling fan blades.

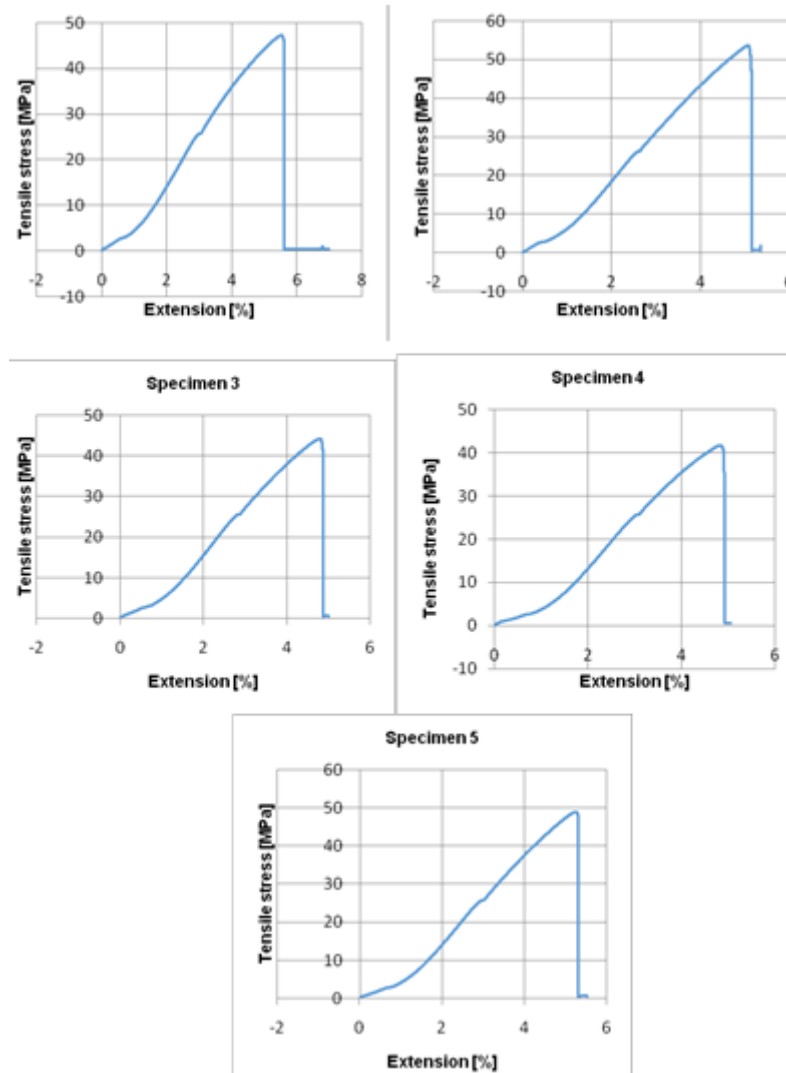


Fig. 12 Load-extension graphs of composites with six fabric layers (fibre volume fraction: 50%)

Referring from table 3 below, tensile strength achieved for composite blades made with 50:50 fibre volume fraction weighing 150g is most comparable with the Aluminum alloy 1050 H14 but it is still heavier blade so composite blades made with 50:50 fibre volume fraction weighing 75g has been chosen as the composite blades because it is lightest one although it has a tensile strength value which is half of that of the aluminum alloy.

Table 3 Summary of comparisons of tensile strength of composites with Aluminum blade

S/No.	Material	Tensile strength (MPa)	Strain at failure (%)	Br. Load (N)
1	Composite blade with 60:40 fibre volume fraction	36.075	7.1	2167.5
2	Composite blade with 70:30 fibre volume fraction	38.7	12.4	3870
3	Composite blade with 50:50 fibre volume fraction weighing 150g	99.12	8.26	7929.6
4	Composite blade with 50:50 fibre volume fraction weighing 75g	47.1	5.1	1886
5	Aluminium Alloy 1050 H14	105-145	-	-



### 3.6 Short Beam Shear Strength Tests for Composite Blades Made with 50:50 Fibre Volume Fraction Weighing 75g

With the use of short beam shear tests, we can see the effects of jute fibre surface treatments and compare the bonding strength with that of the untreated fabric. A total of 9 composite specimens made from both treated (Alkali+Silane) and untreated jute fabrics having the same dimensions have been tested and results are also compared (referred to Tables 4 & 5).

Table 4 Summary of short beam shear strength tests for Alkali+Silane treated jute fabric composites with six fabric layers (fibre volume fraction: 50%)

S/no.	Thickness, t (mm)	Width, w (mm)	Max. load, P <sub>max</sub> (N)	Displacement (mm)	Short beam strength, F <sup>sbs</sup> (MPa) F <sup>sbs</sup> = 0.75*(P <sub>max</sub> /t*w)
1	2	4	101.19	2.01	9.48
2	2	4	95.5	1.45	8.95
3	2	4	99.72	1.53	9.35
4	2	4	90.86	1.34	8.52
5	2	4	86.55	2.45	8.11
Average	2	4	94.764	1.756	8.88

Table 5 Summary of short beam shear strength tests for untreated jute fabric composites with six fabric layers (fibre volume fraction: 50%)

S/no.	Thickness (mm)	Width (mm)	Max. load, P <sub>max</sub> (N)	Displacement (mm)	Short beam strength, F <sup>sbs</sup> (MPa) F <sup>sbs</sup> = 0.75*(P <sub>max</sub> /t*w)
1	2	4	79.52	1.8	7.45
2	2	4	68.77	1.45	6.45
3	2	4	76.01	1.42	7.13
4	2	4	67.61	1.58	6.34
Average	2	4	73	1.56	6.84

So from the test results given in the Tables (4&5) the composite specimens made with Alkali+Silane treated jute fabrics shows higher ILSS (inter-laminar shear strength) of 8.88 MPa and composite specimens made with untreated jute fabrics shows a lower value of 6.84 MPa. A 23 % improvement on the shear strength is observed, because of the treatments.

So, based on the above stated mechanical characterizations of the different composite blades the one that shows the comparatively better properties and lightest one has been chosen and below in table 6 the weight and dimensions has been compared with the existing Usha fan blades.

Table 6 Comparison of weights and dimensions of existing (Usha) fan and the composite blades made with 50:50 volume fractions

Weight of each blade (g)		Width (in.)		Length (in.)		Thickness (mm)	
Existing (Usha fan)	Composite blade	Existing (Usha fan)	Composite blade	Existing(Usha fan)	Composite blade	Existing (Usha fan)	Composite blade
250	75	5	4	18.8	10	1	2

In Table 7, the air velocity and air delivery of the composite blades made with 2 pitch angles has been compared with the conventional Usha fan blades. Here, the air velocity is found to be higher for the composite blades. But due to the lower surface areas of the composite blades, their air delivery is also found lower. Accordingly, for measuring the pitch angles of each composite blade, software called Digimizer is used by which



angles are measured from their pictures. The figures below shows pitch angle measurements for the composite blades.

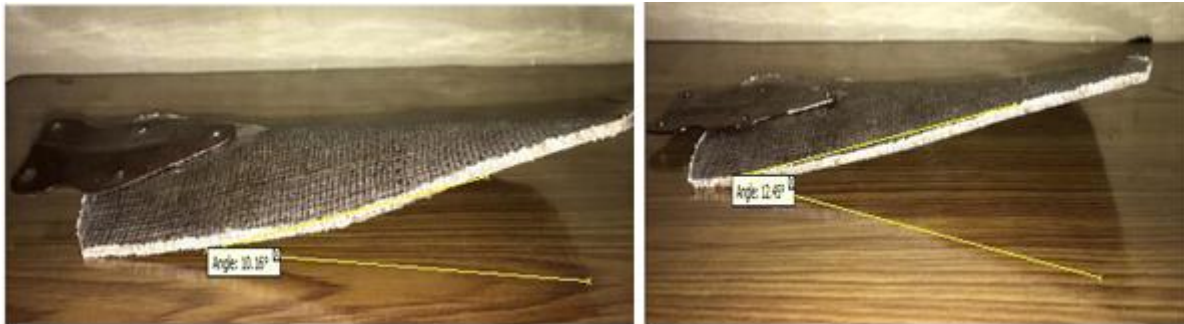


Fig. 13 measuring of pitch angles for the Composite blades

Table 7 Summary of air velocity (ft/min) and air delivery (cfm) at maximum speed for composite blades (with six fabric layers & fibre volume fraction: 50%)

Speed	Air velocity (ft/min)		Air delivery (CFM)		Blade surface area (ft <sup>2</sup> )	
	Usha fan blades weighing 250g	Composite blades weighing 75g	Usha fan blades weighing 250g	Composite blades weighing 75g	Usha fan blades weighing 250g	Composite blades weighing 75g
5	713	836 846	357	251 254	0.5	0.3

Figures 14 – 16 show power consumptions measured while the fan is operating from speed 1 – 5 & it clearly shows that there is power savings while using the composite blades than the conventional Usha fan blades.



Fig. 14 power consumption of Usha fan blades at different speeds



Fig. 15 power consumption of composite fan blades (six fabric layers & 50 % Volume fraction) at different speeds and pitch angle of 12<sup>0</sup>



Fig. 16 Power consumption of composite fan blades (six fabric layers & 50% Volume fraction) at different speeds and pitch angle of 10.13<sup>0</sup>

Table 8 summarizes the comparisons of power consumptions and depicts that there is an average power savings of about 20% while performing the blades at a maximum speed of 5.

Table 8 Comparisons of power consumption of Usha fan blade and the composite blade (with six fabric layers & fibre volume fraction of 50%)

Speeds	Power consumption (Watt)			Average Power savings (W)	Average % age power reduction
	Usha fan blades weighing 250g	Composite blades weighing 75g			
		10.13 <sup>0</sup>	12 <sup>0</sup>		
1	14.4	14	13.6	0.6	-
2	34.8	36	35.8	-	-
3	52.5	45.8	45.7	6.75	13
4	57.8	58	56.3	0.65	-
5	77.8	60.6	63.7	15.65	20

### 3.7 Bonding of the Composite Blades with the Metal Plate

For joining of the blades with the metal plate, which is connected with the disc material under which the motor is enclosed in it, adhesive joining has been preferred over that of mechanical joining due to the different comparative advantages achieved in adhesion bonding. Figures 17 & 18 shows joining of the composite blades with the metal plate & fabricated composite blades made with different pitch angles.



Fig 17 Joining of the metal plate with the composite blades using Araldite epoxy



Fig 18 Jute-PLA composite blades made with different pitch angles

Figure 19 shows the composite blades while they are in operation.



Fig 19 the composite blades fan while in operation

So from Table 9, service values for the composite blades are a little bit lower than the Usha fan blades due to the lower air delivery values of the composite blades & that is because of the lower surface area of the blades.

Table 9 Comparisons of service value (cfm/watt) of Usha fan blade and the composite blade (with six fabric layers & fibre volume fraction of 50%) at maximum speed

Speed	Service value (cfm/watt)					
	Usha fan blades weighing 250g	Composite blades weighing 75g				
5	4.58	<table border="1"> <tr> <td>10.13<sup>0</sup></td> <td>12<sup>0</sup></td> </tr> <tr> <td>4.14</td> <td>4</td> </tr> </table>	10.13 <sup>0</sup>	12 <sup>0</sup>	4.14	4
10.13 <sup>0</sup>	12 <sup>0</sup>					
4.14	4					



#### 4. CONCLUSION

For the production of jute fabric reinforced PLA composite, chemical modifications of the fabrics were carried out as, alkalization, acetylation, silane and maleic anhydride treatments. The differently treated fabrics have been characterized. Jute fabrics treated with 5 % alkali followed by 0.5 % Silane treatment shows the highest tensile strength, young's modulus, specific tensile strength and specific young's modulus followed by fabrics treated with 5 % alkali only.

So, composite blades were prepared from jute fabrics treated with Alkali+Silane on a compression molding machine at a temperature of 190<sup>o</sup>c, with a pressure of 15 bars for 8 minutes followed by air cooling at room temperature. The samples were tested for tensile-and shear-strength as per ASTM standards and also compared with the existing aluminum blade, Aluminum Alloy 1050 H14. Composite blades with 50:50 fibre volume fractions and having a weight of 75g and a thickness of 2mm was found to be the lightest and showed a tensile strength of 47.1 MPa, which is half of the value of the aluminum alloy and having an ILSS (Inter-laminar shear strength) value of 8.88MPa has been chosen as the composite blades. The composite blades are made with average pitch angles of 10.13<sup>o</sup> and 12<sup>o</sup>. An air velocity of 836 and 846 ft/min and an air delivery of 251 and 254 CFM were achieved for the composite blades with the pitch angles of 10.13<sup>o</sup> and 12<sup>o</sup> respectively. An average power savings of 15.65Watt has been achieved with the use of the composite blades while operating at the maximum speed of 5, which is about 20% power savings.

#### ACKNOWLEDGEMENTS

I want to thank Natur-tec India pvt. Ltd company for providing me the PLA films free of any charges. I am also thankful to all my friends for being so supportive and helpful in every possible ways.

#### REFERENCE

- A.K. Bledzki, et al. (2008): The effects of acetylation on properties of flax fibre and its polypropylene composites. EXPRESS Polymer Letters, 2(6): 413–422.
- Amazing Comfortson S, et al. (2014): Glass Fibre Reinforced Polymer Composite Ceiling Fan Blade. International Journal of Emerging Technology and Advanced Engineering, 4(11): 174-179.
- B. Ashok, et al. (2014): Tensile and Thermal Properties of Poly (lactic acid)/ Eggshell Powder Composite Films. International Journal of Polymer Analysis and Characterization, 19(3): 245-255.
- B. C. Mitra, et al. (1998): Studies on jute-reinforced composites, its limitations, and some solutions through chemical modifications of fibers. Journal of Applied Polymer Science, 67: 1093 – 1100.
- Debiprasad Gon, et al. (2012): Jute Composites as Wood Substitute. International Journal of Textile Science, 1 (6): 84-93.
- Department of Consumer affairs, (January 2012): Ceiling Fans: Revolving Faster. [Online], <http://consumeraffairs.nic.in/consumer/writereaddata/Ceilingfans>.
- Giuseppe Cristaldi, et al. Composites Based on Natural Fibre Fabrics. University of Catania – Department of Physical and Chemical Methodologies for Engineering, Catania Italy.
- G.M. Arifuzzaman Khan, et al. (2015): Effect of chemical treatments on the physical properties of non-woven jute/PLA bio composites. Jute/PLA composite, Bio Resources, 10(4): 7386-7404.
- Gruber P & O'Brien M. (2002): Polylactides Nature Works TM PLA. Weinheim:Wiley-VCH, 4: [ISBN 3-527-30225-5] 235-249.
- K. Hamadi, et al. (2015): Properties and medical applications of polylactic acid. EXPRESS Polymer Letters, 9(5): 435–455.
- Leonard Y. Mwaikambo, (2009): Tensile properties of alkalis jute fibres. Bio-resources.com, 4(2): 566-588.
- M.NagaKiran, et al. (2015): Finite element analysis of axial flow fan. International journal of innovative research in science, engineering and technology, 4(8): 7633-7647.
- Mohammad Tahir Zafar, et al. (2016): Effect of surface treatment of jute fibers on the interfacial adhesion in poly (lactic acid)/jute fiber bio composites. Fibers and Polymers, 17(2): 266-274.
- PriyaSinghal and S.K. Tiwari, (2014): Effect of various chemical treatments on the damping property of jute fibre reinforced composite. International Journal of Advanced Mechanical Engineering, 4(4): 413-424.
- Sunil Kumar Ramamoorthy, et al. (2015): Effect of alkali and silane surface treatments on regenerated cellulose fibre type (Lyocell) intended for composites. Springer Science & Business Media, 22: 637-654.



- T. Katayama, et al. (2006): Compression moulding of jute fabric reinforced thermoplastic composites based on PLA non-woven fabric. WIT Transactions on the built environment, WIT press, 85: 159-167.
- Temesgen Berhanu, et al. (2014): Mechanical Behaviour of Jute Fibre Reinforced Polypropylene Composites. Science direct.com, 402-411.
- Tran Huu Nam, et al. (2012): Mechanical and thermal properties and water absorption of jute fiber reinforced poly (butylene succinate) biodegradable composites. Advanced Composite Materials, 21(3): 241–258.
- X. Y. Liu & G. C. Dai, (2007): Surface modification and micromechanical properties of jute fiber mat reinforced polypropylene composites. EXPRESS Polymer Letters, 1(5): 299–307.



# Experimental Investigation of $(\text{Ba}_{(1.6-3/2x)}\text{Sr}_{2.4}\text{Na}_2\text{Nb}_{10}\text{O}_{30}:x\text{Ho}^{3+})$ Ferroelectric Nanomaterials by Solid State Reaction Methods for Optoelectronic Applications

Solomon H. D\*, Menberu M.W., Nebiyu G. D.

Physics Department, Jimma University, Jimma, Ethiopia

\*Corresponding author, e-mail: [solomon.didu@ju.edu.et](mailto:solomon.didu@ju.edu.et)

## ABSTRACT

This paper presents rare earth Holmium ion additive Barium Strontium Sodium Niobate ( $\text{Ba}_{(1.6-3/2x)}\text{Sr}_{2.4}\text{Na}_2\text{Nb}_{10}\text{O}_{30}:x\text{Ho}^{3+}$ ) tungsten bronze structured ferroelectric nanomaterial by conventional solid state reaction routes using Barium carbonate ( $\text{BaCO}_3$ ), Strontium carbonate ( $\text{SrCO}_3$ ), Sodium carbonate ( $\text{Na}_2\text{CO}_3$ ) 99.90% NICE, and Niobium oxide ( $\text{Nb}_2\text{O}_5$ ) and Holmium oxide ( $\text{Ho}_2\text{O}_3$ ) 99.99% Sigma-Aldrich as starting materials under normal stoichiometric ratio synthesis approach. The X-ray diffraction (XRD), the scanning electron microscopy (SEM), energy dispersive x-ray spectroscopy (EDS), Fourier transform-infrared spectroscopy (FTIR), UV-Vis Spectroscopy and PL (Photoluminescence) Spectrophotometer were used to study the structure, surface morphology/ microstructure, elemental composition/mapping, finger print functional groups identification, absorption and emission respectively. The XRD pattern revealed Tetragonal Tungsten Bronze structured crystallite phase that best match with the JCPDS card number -00-039-1453 having space group of  $p4bm$  and lattice parameters of  $a = 12.33 \text{ \AA}$ ,  $b = 12.33 \text{ \AA}$  and  $c = 3.93 \text{ \AA}$ . The average crystallite size of the synthesized sample obtained at the prominent peak (311) for position at  $2\theta = 32.32^\circ$  is 67.52 nm. The SEM images showed that surface microstructures have random and nearly uniform distribution of nanoparticles with different shapes and size on the surface. It is also nearly nonporous surface microstructure that is promising for enhancing optical properties having more particles on the surface. EDS analysis confirmed the presence of all the constituent elements with their right ratios of Wt. % and At%. EDS experimental results best fit with theoretically calculated values. For the pure metal oxide the FTIR results showed the bond vibration mode at wavenumber of  $540.60 \text{ cm}^{-1}$ , having only single collective metal oxide intense peak without impurities. When  $\text{Ho}^{3+}$  ions with concentration of 0.05 and 0.10 % added additional peaks were observed at  $429.92 \text{ cm}^{-1}$  &  $415.77 \text{ cm}^{-1}$  respectively; confirming the existence of Ho-O bond vibration modes. Nice absorption was obtained at 205 nm having maximum intensity for 0.03%  $\text{Ho}^{3+}$  ions concentration. The PL value for 0.03%  $\text{Ho}^{3+}$  ions is unique and highly intensified.

**Keywords:** Bronze structure, FTIR, Holmium ion, Nanomaterial, SEM, Tetragonal Tungsten, XRD

## 1. INTRODUCTION

In the last three decades, the production of nanostructured materials has attracted much attention due to their great diversity, excellent, interesting and unique properties and various possible applications [1-4]. Holmium oxide ( $\text{Ho}_2\text{O}_3$ ) is one of the most attractive rare earth oxides due to its special, excellent and unique optical and electrical properties, as well as several applications in wavelength calibration devices and pyrolysis catalysts, as well as improved optical properties for transition temperature control of ferroelectric nanomaterials when used as an additive [5, 6].

A ferroelectric material is a material that has a spontaneous polarization in the absence of an electric field that can be reversed by applying an electric field. Ferroelectric materials have unique dielectric, pyroelectric, piezoelectric and electro-optical properties [7]. These properties have several applications in capacitors, dielectric resonators, sensors, transducers, actuators, and ferroelectric nonvolatile memories, dielectric memories, optical waveguides, displays, microelectromechanical systems (MEMS), miniature mechanical and electromechanical elements [8-13]. Based on their special properties, ferroelectric materials have been used to produce active elements of various devices [14, 15].

The structure of Tetragonal Tungsten Bronze (TTB) consists of corner-sharing octahedral that are joined to form triangle, square and pentagonal areas. A structure is called a filled TTB if all square and pentagonal sites are filled; a classic example of this is  $\text{Ba}_2\text{NaNb}_5\text{O}_{15}$  (BNN), where the octahedra are filled with Nb, the square sites with Na, and the pentagonal sites with Ba [16-18]. Ferroelectric tetragonal tungsten bronzes (TTB) are the second largest group of ferroelectric oxides after perovskites [19]. The crystal structure of TTB is similar to the



perovskite structure in that it consists of corner-sharing  $\text{BO}_6$  octahedral; however, the unit cell of the prototype TTB is approximately 10 times larger than the perovskite cell [7]. In a filled TTB, the triangular channels are empty, while the square and pentagonal channels are fully occupied, and the general formula can be written as  $\text{A}_2\text{A}_1\text{B}_2\text{O}_{10}$  [20]

The tetragonal tungsten bronze structure has been discussed by Magneli and Blomberg [21, 22] Wadsley [23], Francombe [24] and by Jamieson et al.[17]. The structural flexibility of tungsten bronze oxides offers more opportunities for exploiting new P b-free ferroelectric materials. The tetragonal tungsten bronze structure is composed of ten distorted octahedral sharing corners in such a way that three different interstices (2 tetragonal A1, 4 pentagonal A2, and 4 triangle C) are available for cations in the general formula  $(\text{A}1)_2(\text{A}2)_4(\text{C})_4(\text{B}1)_2(\text{B}2)_8\text{O}_{30}$  [17].

One of the most effective ways in the synthesis of composite materials composed of ferroelectric material and ferromagnetic phases that allow a wide range of ferroelectric/piezoelectric and magnetic properties are that the material pairs with both good ferroelectric and good ferromagnetic properties [25-29]. Such a crystal structure with a large number of cationic and anionic sites allow synthesis of various compounds and doping, resulting in excellent control and great progress functional properties of the synthesized material [30-33].

Again, the high toxicity of lead-based chemical compounds and the high pressure level of the process, which causes serious environmental problems, direct the attention of researchers to lead-free material. A promising way to solve this problem is to develop lead-free electro-ceramics to reduce lead contamination. Tungsten bronze compound is one of them. Recently, due to increasing demand, several studies have focused on the availability of high-quality lead-free materials [34, 35].

The nobility of this work is that we use a new design in addition to rare earth ions addition, to control the transition temperature of the system to be close to the room temperature and to obtain enhanced ferroelectric property. As recently reported work revealed by adding impurities such as La, Nd, Sm, Dy, and Y ions,[36], the possibility to control the transition temperature of ferroelectric materials were observed. However,  $\text{Ho}^{3+}$ -doped nanomaterials had unique properties, for instance, ferroelectric measurements show that the ferroelectric curie temperature  $T_c$  increases with decreasing ionic radius (R) size, thus showing a direct relationship between  $T_c$  and the tetragonal ionic radius of R [37]. For smaller rare earth ions, the  $T_c$  is above ambient and the non-centrosymmetric space group  $\text{P}4\text{bm}$  is appropriate.

In the synthesis of rare earth ion ( $\text{Ho}^{3+}$ ) additive tungsten bronze structured ferroelectric nanomaterials via conventional high temperature solid state reactions methods, we used carbonates and oxides as precursors. All raw materials were mixed by normal stoichiometric equation ratios. Digital electronic balance was used to measure the mass of each powder samples with the desired significant digits. Then the powder was grinded using Grey Black Agate Mortar and pestle, size 6 inch in diameter for 3 hr. before furnace. The grinded samples were placed in a high standard platinum crucible and subsequently fired at  $1100^\circ\text{C}$  for 4 hour at the heating rate of  $5^\circ\text{C}$  per minute. Finally this sufficient time of grinding results complete interactions and diffusion process which have an outcome of fine powder taken to furnace. To make it very confined and refined powder nanoparticles with miniaturized nanosize, we had also grinded the powder after furnace for additional 2 hrs. Then pure white powders obtained become ready for characterization.

In this paper, we reported the synthesis and characterization of Holmium ion additive Barium Strontium Sodium Niobate via solid state reaction route. The structural analysis was studied using X-ray diffractometer (XRD). The surface morphology and microstructure was examined by SEM. The elemental composition identification and mapping have done by EDS. The absorption properties were analyzed by UV-Vis spectroscopy near UV. The different stretching modes were also analyzed using Fourier transform infrared spectroscopy (FTIR).

## 2. MATERIALS AND METHODS

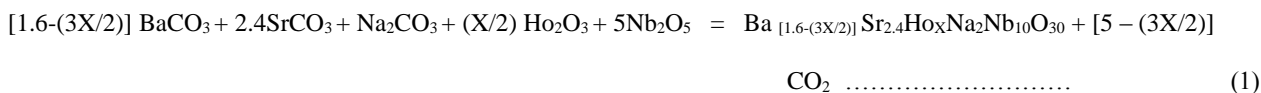
### 2.1. Synthesis

Rare earth metal Holmium ( $\text{Ho}^{3+}$ ) ion doped Barium Strontium Sodium Niobate tungsten bronze structured ferroelectrics  $(\text{Ba}_{(1.6-3/2X)}\text{Sr}_{2.4}\text{Na}_2\text{Nb}_{10}\text{O}_{30}:x\text{Ho}^{3+})$  powder nanomaterials which was synthesized via high



temperature solid state reaction route using calcium carbonate (CaCO<sub>3</sub>) 99.90%, Strontium carbonate (SrCO<sub>3</sub>) 99.99%, Sodium oxide (Na<sub>2</sub>O) 99.99%, Holmium Oxide (Ho<sub>2</sub>O<sub>3</sub>) 99.99% and Niobium Oxide (Nb<sub>2</sub>O<sub>5</sub>) 99.99% taking as a starting materials were successfully synthesized and characterized according to their stoichiometric ratio for various values of dopants concentration (x), (x= 0.00, 0.01, 0.03, 0.05, 0.07, 0.10, % Ho<sup>3+</sup>). Then the powder was milled thoroughly for 3 hour using Grey Black Agate Mortar and pestle, size 6 inch in diameter. Then all the grinded samples were placed in a platinum crucible and subsequently fired at 1100 °C for 4 hour at the heating rate of 5 °C per minute. Finally, pure white powders were obtained after cooling down the programmable furnace.

The chemical reaction process is given as follows:



The solid state reaction occurs at high temperature (1100 °C) and all CO<sub>2</sub> burned out. The desired product with normal stoichiometric equation obtained at the end of this process. The diffusion of ions also occurred during the grinding and solid state reaction process.

**2.2 Characterization**

The structure and phase formation of Ba<sub>(1.6-3/2X)</sub>Sr<sub>2.4</sub>Ho<sub>x</sub>Na<sub>2</sub>Nb<sub>10</sub>O<sub>30</sub> nanocomposites were identified by using XRD Phillips XPERT-PRO Model: X-ray powder diffractometer using Cu-Kα radiation (λ=1.5406 Å) at 40.0 KV, 30 mA) and the data were collected over the range (2θ = 10 to 80°). SEM/EDS results were obtained from (OXFORD INSTRUMENTS ;( The Business of Science) model SS230862, ZEISS. The images obtained from scanning electron microscopy (SEM) showed morphology and microstructure clearly with high quality images. The elemental composition and mapping of the powder samples were measured using energy dispersive x-ray spectroscopy (EDS). EDS spectroscopy was used as complementary and a standard procedures for determining and quantifying elemental composition of sample area as small as a few nanometers to micrometers. Chemical bonds present in Ba<sub>(1.6-3/2X)</sub>Sr<sub>2.4</sub>Ho<sub>x</sub>Na<sub>2</sub>Nb<sub>10</sub>O<sub>30</sub> were identified by FTIR spectra analysis with the help of Shimadzu IR Prestige-21 FT-IR Spectrometer. We use FTIR transmittance spectroscopy for investigating the functional group (4000 to 400 cm<sup>-1</sup>) of the Ba<sub>(1.6-3/2X)</sub>Sr<sub>2.4</sub>Ho<sub>x</sub>Na<sub>2</sub>Nb<sub>10</sub>O<sub>30</sub> ferroelectric nanomaterial samples by direct use of as- prepared powder sample.

**3. RESULTS AND DISCUSSION**

**3.1. XRD Analysis**

The XRD of Ba<sub>(1.6-3/2X)</sub>Sr<sub>2.4</sub>Ho<sub>x</sub>Na<sub>2</sub>Nb<sub>10</sub>O<sub>30</sub> nanomaterials were identified by using XRD Phillips XPERT-PRO Model: X-ray powder diffractometer using Cu-Kα radiation (λ=1.5406 Å) at 40.0 KV, 30 mA) with Bragg’s angle (2θ) range from 10°-80° with scanning rate of 0.033 °C per second as shown in figure 1. The smooth and sharp peaks can confirm the crystalline nature of the samples in the XRD pattern, and all the samples are pure tetragonal tungsten bronze structures ferroelectric nanomaterials.

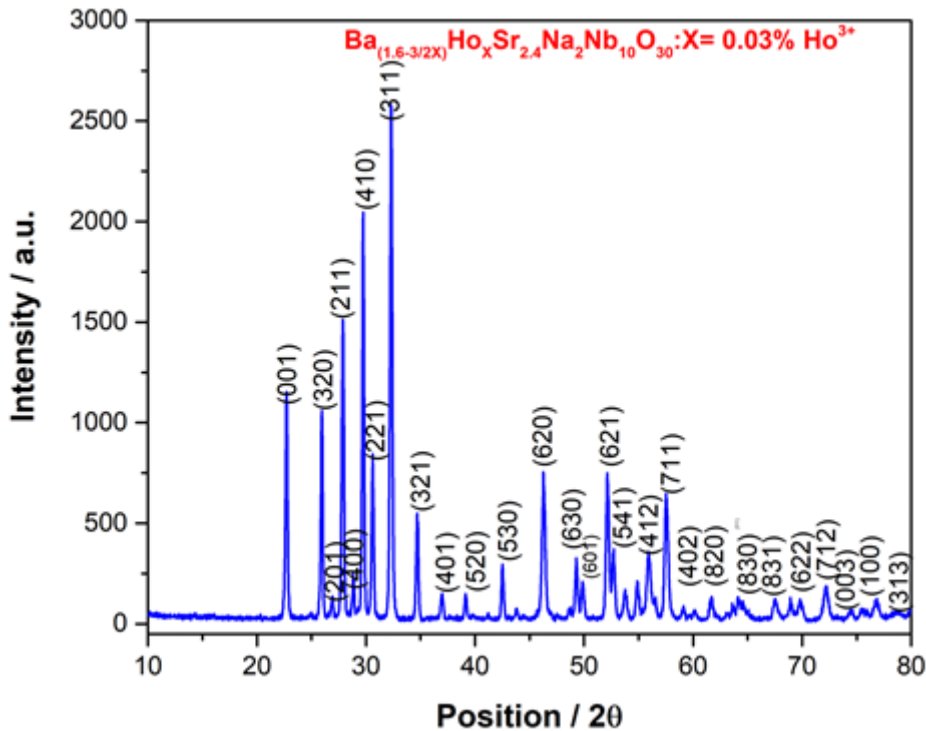


Figure: 1. XRD pattern of Holmium ion doped Barium Strontium Sodium Niobate Tungsten Bronze Structured Ferroelectrics nanomaterials for (x= 0.03 % Ho<sup>3+</sup>)

The typical XRD patterns of  $Ba_{(1.6-3/2x)}Sr_{2.4}Ho_xNa_2Nb_{10}O_{30}$ , tungsten bronze structured ferroelectric nanomaterial is shown in Figure 1 [38]. The respective plane’s diffraction lines were compared with the standard JCPDS card number 00-039-1453 [39] for confirmation. Using the sharp peak (311) in Bragg’s formula gives the values of interplanar spacing [40, 41]. The value of the lattice parameters is calculated using [37, 42]. The calculated values of our TTBs structured crystal lattice parameters are, a=b= 12.33 Å<sup>0</sup> and c=3.93 Å<sup>0</sup>, having Group space of P4bm.

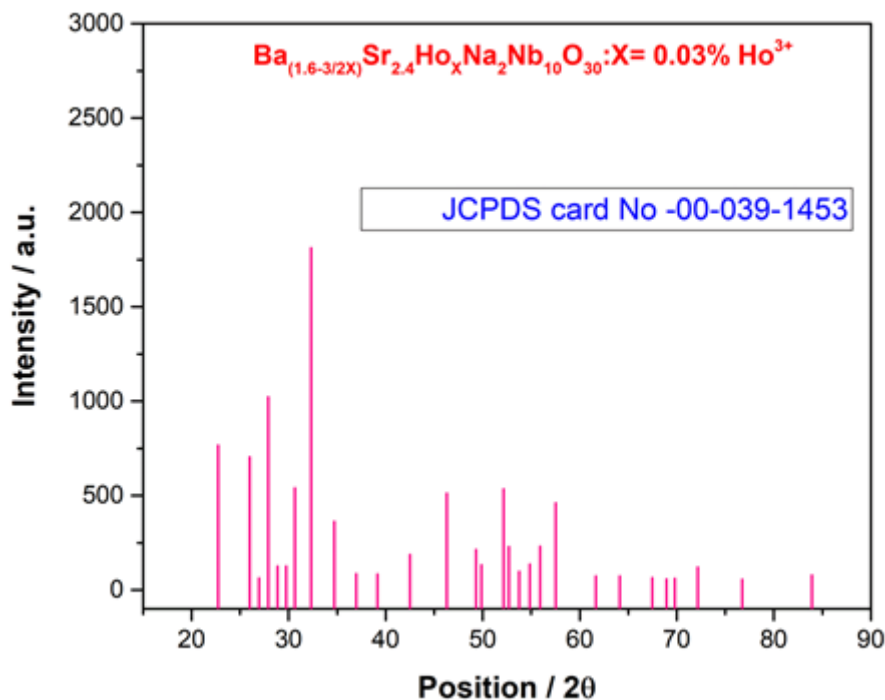


Figure 2. XRD pattern of Holmium ion doped Barium Strontium Sodium Niobate Tungsten Bronze Structured Ferroelectrics nanomaterials JCPDS card match for x=0.03 % Ho<sup>3+</sup>

The significant effect of the dopants was also clearly observed from the XRD pattern. The experimental results showed the highest intensity (1845 a.u.) of the XRD pattern optimum value obtained for  $x=0.05$  %  $\text{Ho}^{3+}$  ion concentration without phase change (TTBs). The results were in good agreement with recent reports of rare earth ions doped system [21].

Smooth and sharp XRD pattern peaks were also obtained for all different amounts of dopants concentrations consistently without phase change. It was consistent for entire  $x=0.01 - 0.10$  %  $\text{Ho}^{3+}$  ions variation in concentrations. The prominent peak with maximum intensity (1845 a.u.) was found for  $x=0.05$  %  $\text{Ho}^{3+}$  ions concentration at angle ( $2\theta=32.3342^\circ$ ) (Figure 3).

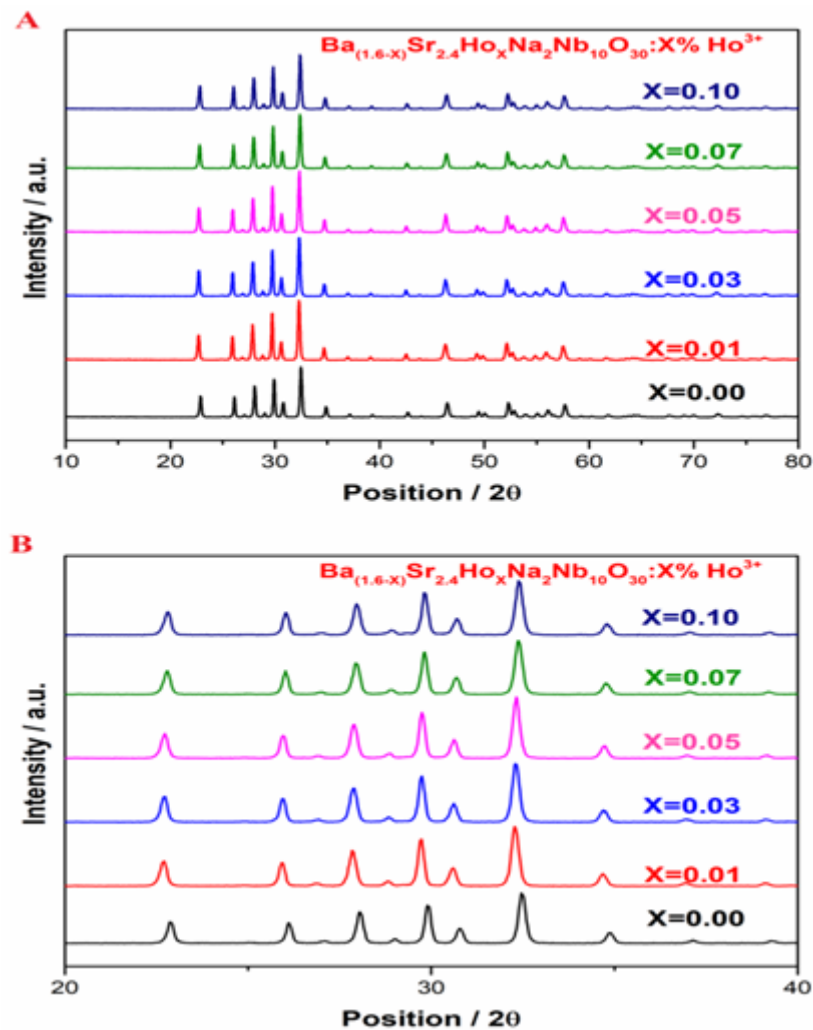


Figure: 3. XRD pattern of Holmium ion doped Barium Strontium Sodium Niobate Tungsten Bronze Structured Ferroelectrics nanomaterials for ( $x=0.00 - 0.10$  %  $\text{Ho}^{3+}$ ), A) normal B) zoomed

As Magneli and Blomberg [21] reported similar results that were obtained and checked with JCPDS standard card number for tetragonal tungsten bronze structure phase. The result obtained from our sample was also in good agreement with others recently reported works and standard card number (JCPDS 00-039-1453) that was confirmed from the XRD patterns match.

There is slight shift of peaks to lower angle from the reference point ( $x=0.00$ ) to dopants having concentrations of 0.01, 0.03 and 0.05%  $\text{Ho}^{3+}$ . Then again it slightly shifts to higher angle for the increment of concentrations from  $x=0.07$  to  $x=0.10$ . This is due to ionic radius difference of Holmium ion which substitute some amount of the Barium ion which have different ionic radius ( $\text{Ho}^{3+}$ : 1.02 and  $\text{Ba}^{2+}$ : 1.42 see Table 1) that in turn expected to improve the ferroelectrics property of the system since it depends on the ionic radii difference of A1 and A2 site atoms.

For prominent peak (311), using Debye–Scherer formula, the average crystallite size (D) of the Ba<sub>(1.6-3/2X)</sub>Sr<sub>2.4</sub>Nb<sub>2</sub>Nb<sub>10</sub>O<sub>30</sub>:xHo<sup>3+</sup> ferroelectrics tungsten bronze structured crystal is calculated as (67.52) nm. Debye–Scherer formula is represented as follows:

$$D = K\lambda/\beta\cos\theta \dots\dots\dots (2)$$

where K is the Scherer constant having value 0.94, λ is wavelength of incident X-ray (λ = 1.5406 Å), β = FWHM (Full Width Half Maximum) of the peaks and θ = corresponding Braggs diffraction angle [43, 44].

Table 1: Ionic Radius of elements: (CN=8, Alkali, Rare Earth and Transition) metals (Source: Shannon Radii)

Atomic Number	Name	Symbol	Ionic Radius (Å)
56	Barium	Ba	Ba <sup>2+</sup> : 1.42
38	Strontium	Sr	Sr <sup>2+</sup> : 1.26
11	Sodium	Na	Na <sup>1+</sup> : 1.26
39	Yttrium	Y	Y <sup>3+</sup> : 1.019
67	Holmium	Ho	Ho <sup>3+</sup> : 1.02
57	Lanthanum	La	La <sup>3+</sup> : 1.16
60	Neodymium	Nd	Nd <sup>3+</sup> : 1.109
62	Samarium	Sm	Sm <sup>3+</sup> : 1.079
63	Europium	Eu	Eu <sup>3+</sup> : 1.25
66	Dysprosium	Dy	Dy <sup>3+</sup> : 1.027
41	Niobium	Nb	Nb <sup>5+</sup> : 0.74

Figure 4 showed the crystal structure of tetragonal tungsten bronze compound with formula (A1)<sub>2</sub>(A2)<sub>4</sub>(B1)<sub>2</sub>(B2)<sub>8</sub>(C)<sub>4</sub>(X)<sub>30</sub> (where X = oxygen and A, B, C are metal cations) constructed by using the XCRYSDEN and VESTA (*visualization for electronic structural analysis*) software’s respectively.

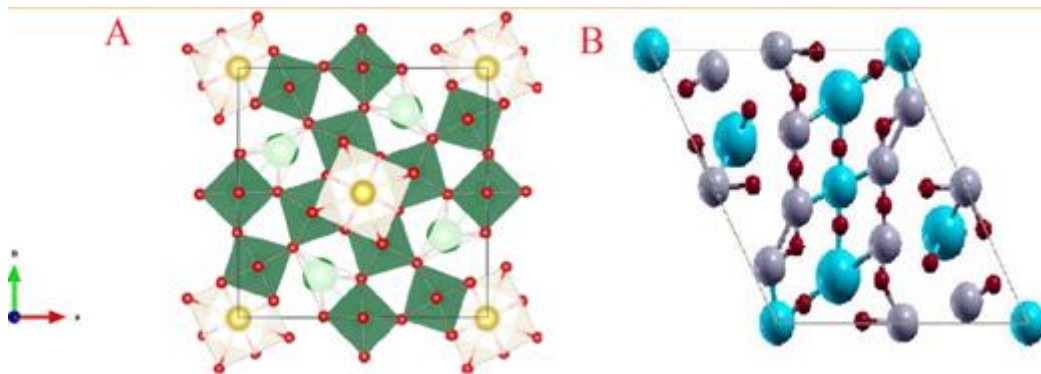


**Figure 4:** Crystal Structure of Tetragonal Tungsten Bronze Structure using VESTA (A) and XCRYSDEN (B)



Table 2: XRD pattern data with different dopant concentration of Ba<sub>(1.6-3/2x)</sub>Sr<sub>2.4</sub>Na<sub>2</sub>Nb<sub>10</sub>O<sub>30</sub>: xHo<sup>3+</sup>: tungsten bronze structured nanomaterials (For the three strongest peaks)

S. No	Quantity	Concentration					
		0.00	0.01	0.03	0.05	0.07	0.10
1	Crystallite Size (D) nm	66.68	61.09	60.13	66.82	75.18	75.24
2	Interplanar Distance (d) Å <sup>0</sup>	2.75313	2.76898	2.76729	2.76649	2.76104	2.76002
		2.9829	3.00148	2.99962	2.99866	2.99217	2.99111
		3.17526	3.19776	3.19519	3.19381	3.18652	3.18523
3	2θ (Degree)	32.4954	32.3043	32.3246	32.3342	32.3998	32.4121
		29.9309	29.7416	29.7604	29.7702	29.8363	29.8471
		28.0794	27.8778	27.9007	27.9130	27.9782	27.9897
4	Intensity (Counts)	1541	1830	1813	1845	1664	1669
		1162	1415	1372	1371	1251	1278
		931	1027	1023	1009	927	917
5	FWHM	0.21580	0.22340	0.21820	0.21090	0.22130	0.22350
		0.19100	0.18780	0.18820	0.18770	0.19160	0.19190
		0.20940	0.22290	0.22490	0.21780	0.22350	0.21840
6	-	Average Lattice Parameter: a= 12.33 Å <sup>0</sup> , b=12.33 Å <sup>0</sup> and c=3.93 Å <sup>0</sup>					
	-	Average Volume of the unit cell = 597.47 Å <sup>(0)3</sup>					
	-	Average Density = 5.16					
	-	Space Group = P4bm					

### 3.2. Scanning Electron Microscopy (SEM)

The images obtained from scanning electron microscopy (SEM) showed morphology and microstructures as shown in Figure 5 & Figure 6. We used SEM to examine the morphology of samples, since the luminescence characteristics of nanoparticles depend on the morphology of the particles such as size, shape, size distribution, and defects so on. The scanning of SEM was performed in the ranges of 200 nm to 5µm dimension and 1000 to 50,000 times magnifications to see all aspects which demonstrate the clear morphology of (Ba<sub>(1.6-3/2x)</sub>Sr<sub>2.4</sub>Na<sub>2</sub>Nb<sub>10</sub>O<sub>30</sub>:xHo<sup>3+</sup>) TTBs (Figure 5 & 6).

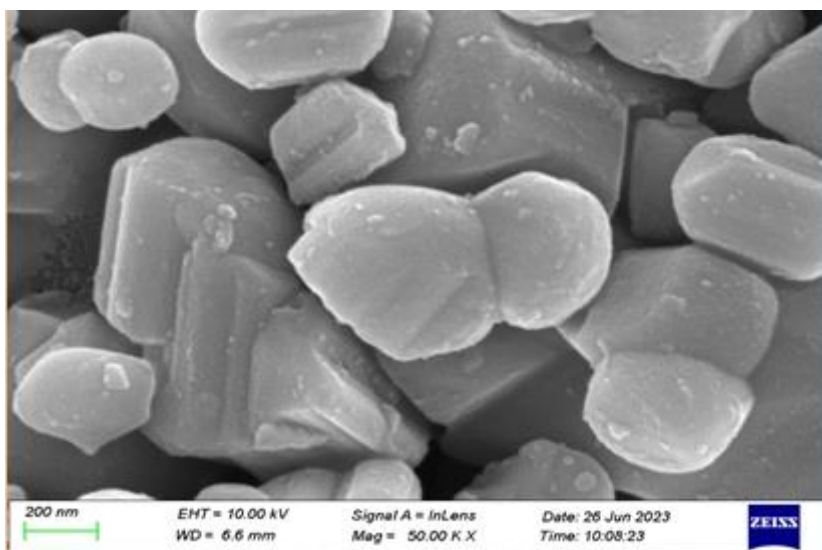


Figure 5: SEM image of (Ba<sub>(1.6-3/2x)</sub>Sr<sub>2.4</sub>Na<sub>2</sub>Nb<sub>10</sub>O<sub>30</sub>:xHo<sup>3+</sup>): x=0.00 % Ho<sup>3+</sup> for (A=5µm, B=200 nm) dimension. From the SEM image result, it was observed that the surface morphology of the particles distributions were nearly non-uniform and random for large dimensions and separate particles with different shape, size and size

distributions are observed in nanometer dimensions. And they were aggregated tightly with each other. It was also clearly observed that the surface is less porous with different size and shape. It looks suitable and promising for different optical properties like a good absorption having more charge carriers available on the dense surface.

The surface morphology of 200 nm dimension was presented in figure 5. The image clearly showed that separate particles with different shape, size and distributions. Moreover, using ImageJ software, we have estimated the average particle size of randomly chosen 30 particle (from scanned SEM image) to be 97.83 nm. This is in line with the result obtained from XRD analysis.

Figure 6 with different dimensions and magnifications showed the possible types of the surface morphology of the system with and without dopants in comparison ( $x=0.00\%$ ,  $0.05\%$  and  $0.10\%$ ) concentrations. Figure 6 also showed the clear difference in surface morphology having the same dimension and magnification but with and without dopants; demonstrating the significant effects of dopants with different concentrations.

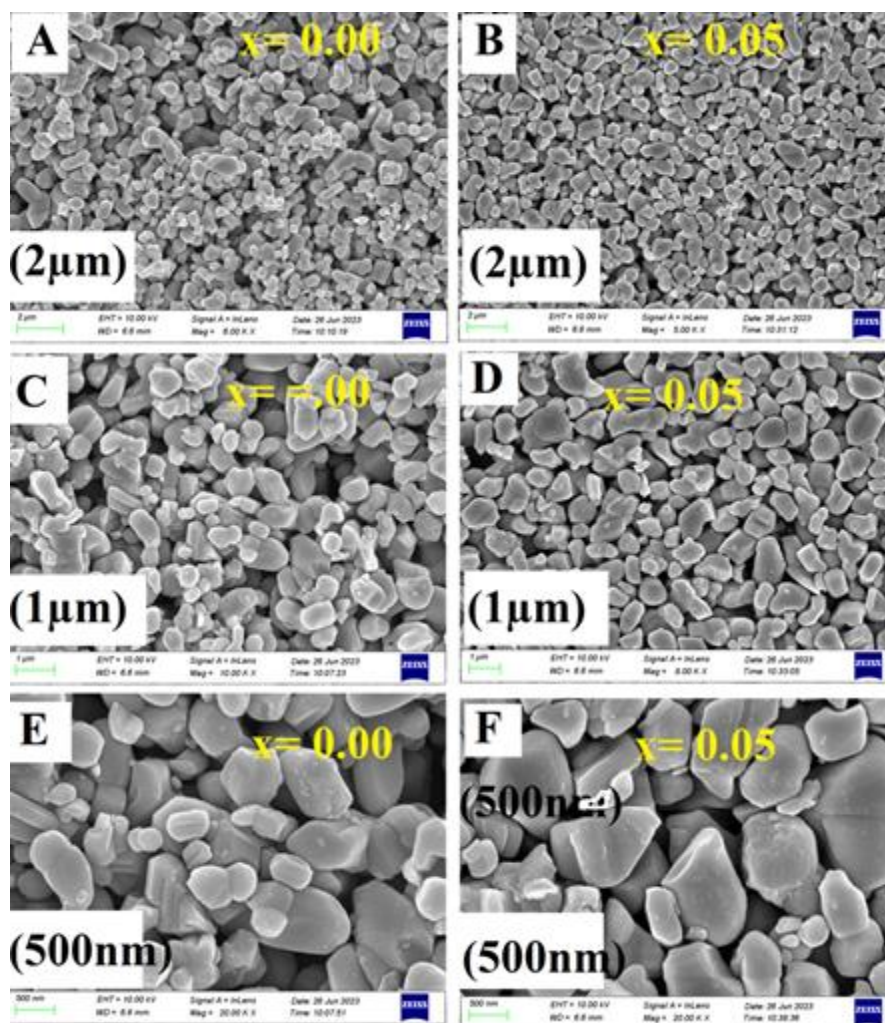


Figure 6. SEM Image of  $(Ba_{(1.6-3/2X)}Sr_{2.4}Na_{2}Nb_{10}O_{30}:xHo^{3+})$ : A, C, E,  $x=0.00\%$   $Ho^{3+}$  and B, D, F  $x=0.05\%$   $Ho^{3+}$  for  $2\mu m$ ,  $1\mu m$  &  $500\text{ nm}$  top down respectively

### 3.3 Energy Dispersive X-ray Spectroscopy (EDS)

The EDS spectra confirms the standard stoichiometric combination of nanocomposite system of  $(Ba_{(1.6-3/2X)}Sr_{2.4}Na_{2}Nb_{10}O_{30}:xHo^{3+})$  as shown in Figure 7 and Table 3. The elemental composition and mapping of the powder samples were measured using energy dispersive x-ray spectroscopy (EDS). Since EDS spectroscopy is complementary and standard procedures for determining and quantifying elemental composition of sample area as small as a few nanometers to micrometers; we have used it to identify all constitute elements of the as-prepared samples. The existence of Holmium ( $Ho^{3+}$ ) ion in the corresponding EDS mapping was also clearly observed

especially when we add more dopants (0.10 %). As we expected apart from Barium (Ba), Strontium (Sr), Sodium (Na), Niobium (Nb) and oxygen (O) in  $Ba_{(1.6-3/2x)}Sr_{2.4}Na_2Nb_{10}O_{30}:xHo^{3+}$ , there were no other emission observed in the EDS mapping of the Barium Strontium Sodium Niobate doped with Holmium ion (see Figure 7). The existence of Ba, Sr, Na, Nb, O and Ho, intense peaks are preliminarily indicates the formation of  $Ba_{(1.6-3/2x)}Sr_{2.4}Nb_{10}O_{30}:xHo^{3+}$  Tetragonal Tungsten Bronze Structured nanomaterial as shown in (Figure 7).

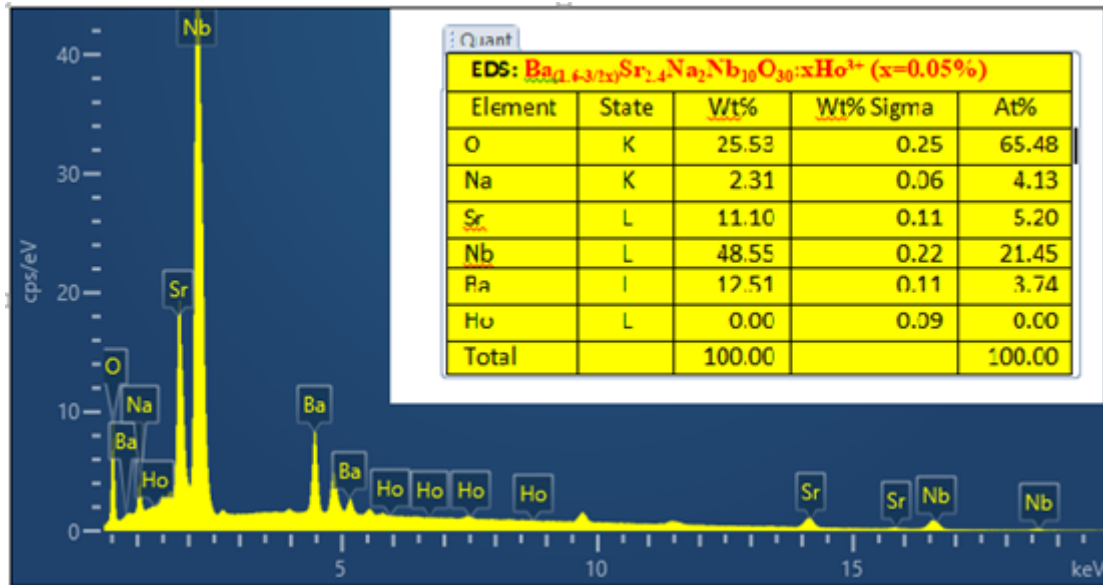


Figure 7: EDS Mapping of  $(Ba_{(1.6-x)}Sr_{2.4}Na_2Nb_{10}O_{30}:xHo^{3+})$ : For  $x = 0.05\% Ho^{3+}$

Figure 7 revealed and confirmed that all the constitute elements are available within exact range of proportion in accordance with our standard stoichiometric equation (see Fig 7 & table 3). Moreover, it further confirmed that there were no impurities added during our samples preparation. The EDS Layered image confirmed also that all the components (barium, strontium, sodium, oxygen and niobium and dopant holmium) of the TTBs are available in the nanocomposite materials. This is also another way of confirming the quality synthesis procedures used with uniform distribution of nanoparticles within the system of the samples.

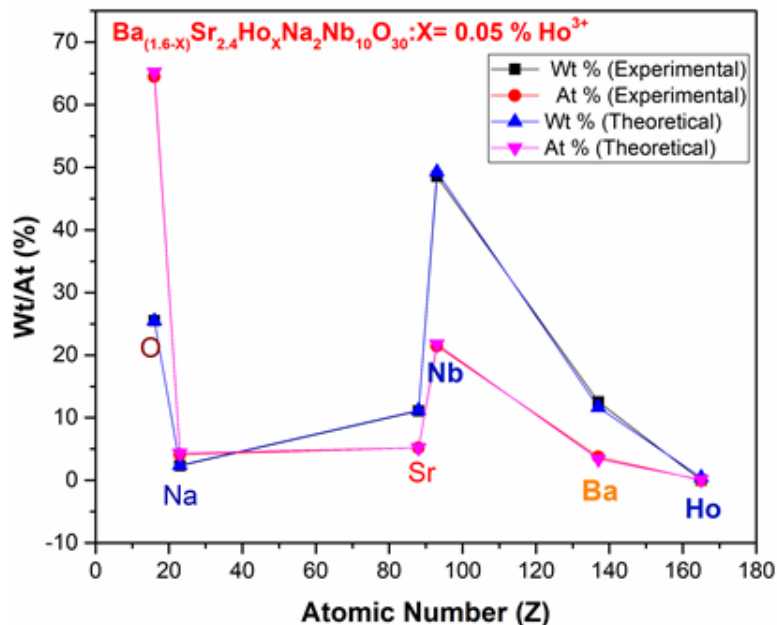


Figure 8: EDS Elemental Composition in Wt/At % for  $(Ba_{(1.6-3/2x)}Sr_{2.4}Na_2Nb_{10}O_{30}:xHo^{3+})$  for Experimental and Theoretical calculated Values

Figure 8 is the energy dispersive x-ray spectroscopy (EDS) result of the as prepared ( $\text{Ba}_{(1.6-3/2x)}\text{Sr}_{2.4}\text{Na}_2\text{Nb}_{10}\text{O}_{30}:\text{xHo}^{3+}$ ) nanocomposite. The results further revealed that the experimental values of each constitute elements percentage molecular weight (Wt%) and atomic (At%) are in good agreement with the theoretically calculated values from the standard stoichiometric equations (See Figure 8 & Table 3). Again this showed that advanced measuring instruments i.e. both EDS and digital electronic balance are well calibrated. The coincidence of experimental and theoretical calculated values of both molecular and atomic percentage values confirmed that during the experiment all carbonates and oxides of the samples burned out well at 1100 °C temperature for 4 hrs duration in the furnace.

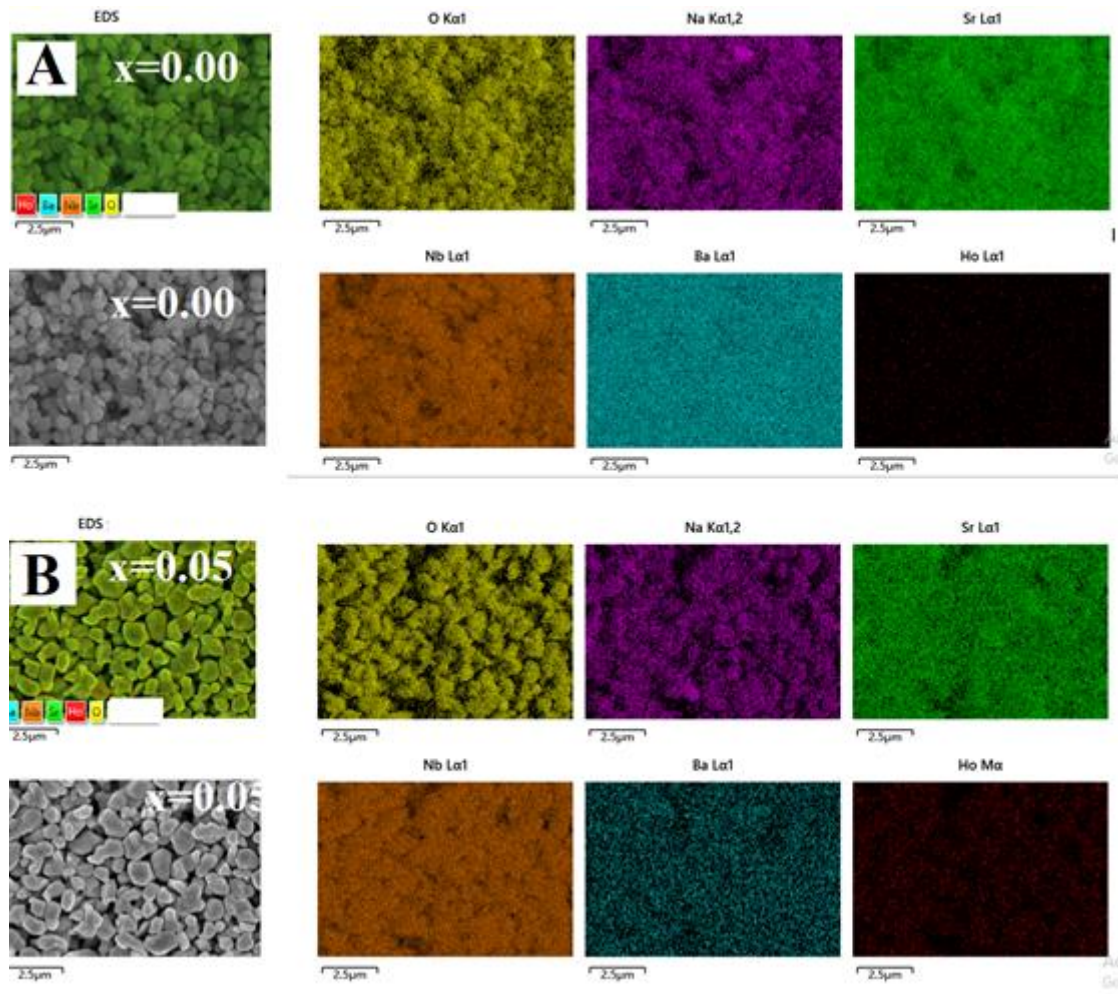


Figure 9. EDS Mapping of Barium Strontium Sodium Niobium Oxygen & Holmium ( $\text{Ba}_{(1.6-3/2x)}\text{Sr}_{2.4}\text{Na}_2\text{Nb}_{10}\text{O}_{30}:\text{xHo}^{3+}$ ): A)  $x=0.00$  %  $\text{Ho}^{3+}$  , B)  $x=0.05$  %  $\text{Ho}^{3+}$  (Map sum Spectrum).

Figure 9 showed comparative analysis of the samples with and without dopants. Figure 9 A left sides color and black is the composite nanomaterial without dopants while the right sides are the separate constitute all five elements (Barium Strontium Sodium Niobium and Oxygen) with different colors. Again it confirmed that only the expected elements were found without any additional impurities. Figure 9 B showed the same but in this case the dopant element availability was indicated clearly both in the left and right side images. This is another way of confirming we successfully added the dopant Holmium ion in the system in correct proportion as indicated with detail numerical figure in Table 3.



Table 3: Constitute Elements Composing from EDS of Ba<sub>(1.6-3/2X)</sub>Sr<sub>2.4</sub>Na<sub>2</sub>Nb<sub>10</sub>O<sub>30</sub>:xHo<sup>3+</sup>

Concentration (%)	Elements	Experimental		Theoretical	
		wt%	At%	wt%	At%
x = 0.00	O	24.59	64.61	25.46	65.22
	Na	2.13	3.96	2.44	4.35
	Sr	10.96	5.26	11.16	5.22
	Nb	48.98	22.16	49.29	21.74
	Ba	13.34	4.08	11.66	3.48
	Ho	0	0	0	0
	Total	100	100	100	100
x = 0.05	O	25.53	64.48	25.46	65.22
	Na	2.31	4.13	2.44	4.35
	Sr	11.1	5.2	11.16	5.22
	Nb	48.55	21.45	49.29	21.74
	Ba	12.51	3.74	11.66	3.37
	Ho	0	0	0.44	0.107
	Total	100	100	100	100
x = 0.10	O	28.75	69.46	25.46	65.12
	Na	2.02	3.39	2.44	4.35
	Sr	10.52	4.64	11.16	5.22
	Nb	44.6	18.56	49.29	21.74
	Ba	13.72	13.86	11.29	3.26
	Ho	0.38	0.09	0.88	0.22
	Total	100	100	100	100

### 3.4. Fourier Transforms Infrared Spectroscopy (FTIR)

The Fourier transform infra-red spectroscopy (FTIR) spectrum has been widely used for the identification of organic and inorganic compounds. The FTIR spectra were recorded in the range of (4000 cm<sup>-1</sup> to 400 cm<sup>-1</sup>) to obtain the figure print results. (FTIR) is also an essential characterization technique to identify the compositional elements of the material and to analyze the chemical bonding and functional groups present in the material. FTIR spectra (Figure 10 A, B) of the samples calcined at 1100°C showed collective metal - oxygen band vibration modes at 540.60 cm<sup>-1</sup> for (x= 0.00% Ho<sup>3+</sup>) without dopant or pure host nanocomposite. But we observe additional band vibration modes at 429.92 for (x= 0.05% Ho<sup>3+</sup>) cm<sup>-1</sup> with slight variation in wavenumber that may be due to ionic radius difference of the Barium, other metal ions and Barium substituted Holmium ions, having an additional peaks which indicates the existence of Ho – O, stretching band vibration modes since it was observed when we add the dopant ion only.

The FTIR results on Figure 10 B and C indicated that in terms of two frequencies vibrations and stretching U<sub>1</sub> at (500-600 cm<sup>-1</sup>), U<sub>2</sub> at (400-450) cm<sup>-1</sup>. We observed also as concentrations of dopants vary from 0.05 % to 1.0% we obtained more intense peaks with slight shift of the position to lower wavenumber position, except this we observed similar results for all dopants concentrations values consistently. The FTIR results also confirmed that the samples spectrum of holmium ion doped barium strontium sodium niobate powders calcined at 1100 °C in (Figure 10 B and C) absence of external impurities, which is also in a good agreement with literature values that in turn confirming the nanocomposite samples are pure i.e. without any impurities or defects [5].

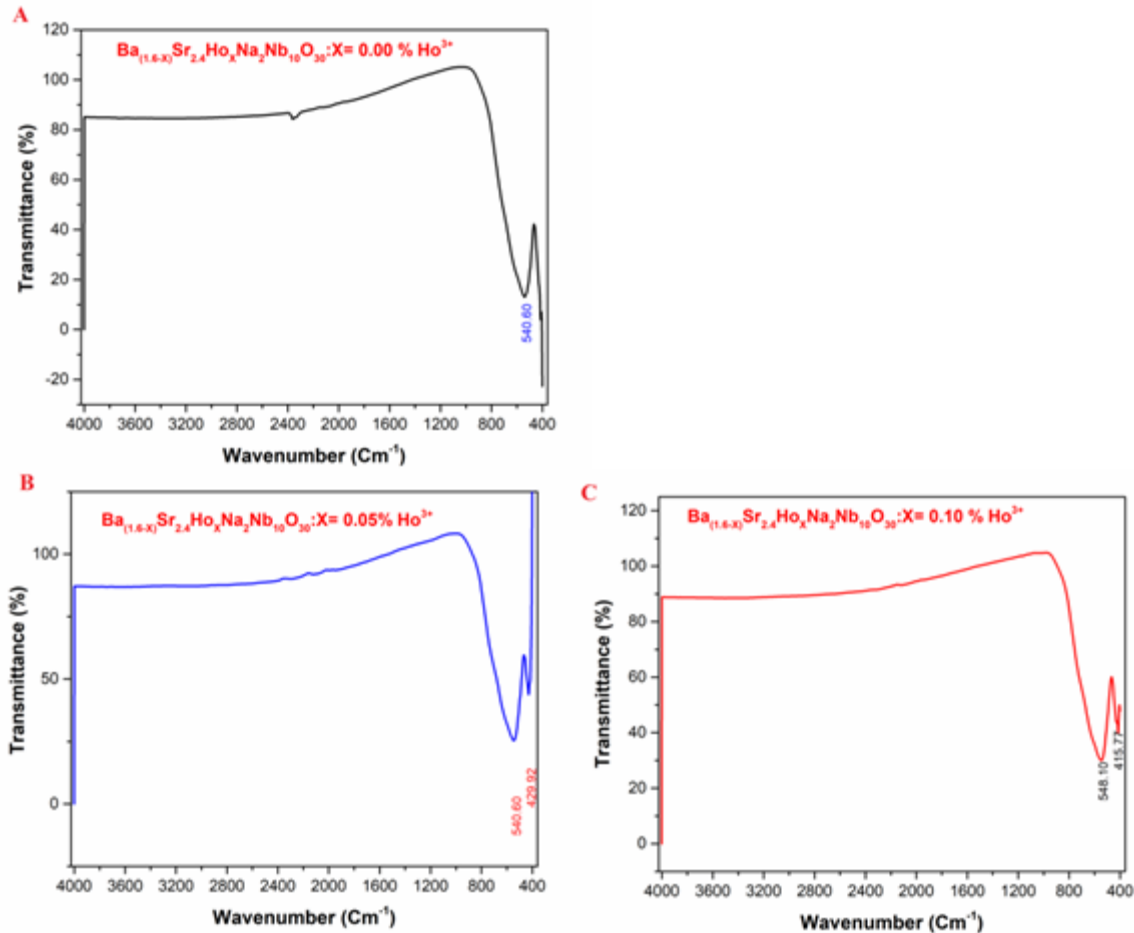


Figure 10: FTIR Spectra of ( $Ba_{(1.6-3/2X)}Sr_{2.4}Na_2Nb_{10}O_{30}:xHo^{3+}$ ): A)  $x=0.00\% Ho^{3+}$ , B)  $x=0.05\% Ho^{3+}$  and C)  $x=0.10\% Ho^{3+}$

### 3.5. UV-Vis Spectroscopy

The detailed information on some crucial optical entities such as the optical transitions, band structure, and band gap energies can be scrutinized from the UV-VIS-NIR absorption spectra. Comparatively, the edges of absorption for crystalline materials are typically very sharp while the absorption edge in an amorphous material unveiled finite slope.

Figure 11 Showed the typical UV-Vis spectra of  $Ba_{(1.6-3/2X)}Sr_{2.4}Nb_{10}O_{30}:xHo^{3+}$  ferroelectric nanomaterial near UV. Figure 11 also displays that the absorption edges of all kinds of  $Ba_{(1.6-3/2X)}Sr_{2.4}Nb_{10}O_{30}:xHo^{3+}$  ferroelectric nanomaterial are at the same wavelength region of approximately 205 nm. From this we observed that  $Ho^{3+}$  doping has significant effects on the peaks (intensity): when we vary the dopants concentration from 0.00% to 0.10% the absorption intensity become increasing with increasing concentration from 0.00-0.03%  $Ho^{3+}$  ions, and then it tends to decrease when we keep on increasing from 0.05-0.10 %  $Ho^{3+}$  ions concentration. Moreover, we observed the optimum absorption intensity obtained at  $x=0.03\% Ho^{3+}$  ions concentration and no peaks at two extremes (0.00 & 0.10 %  $Ho^{3+}$ ) ions concentrations.

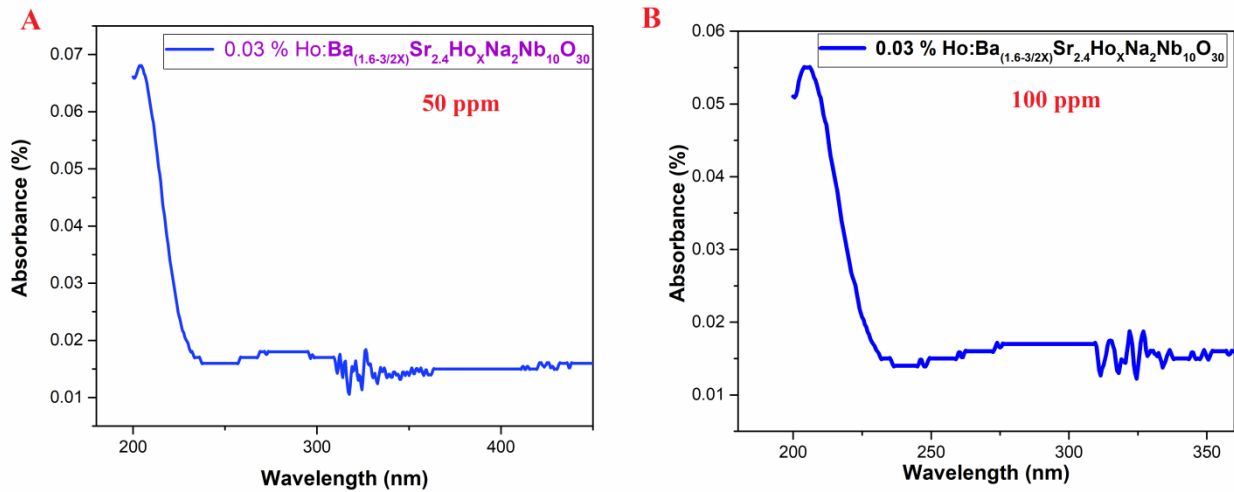


Figure 11. UV-Vis absorption spectra of Ba<sub>(1.6-3/2X)</sub>Sr<sub>2.4</sub>Nb<sub>10</sub>O<sub>30</sub>: xHo<sup>3+</sup> ferroelectric nanomaterials

The band-gap energy (*E*) can be calculated by the following equation [45]

$$E = \frac{1240}{\lambda} \dots\dots\dots (3)$$

where  $\lambda$  is the wavelength in nanometers [46]. The calculated band-gap energy (*E*) corresponding to the 205 nm light wave is ~ 6.05 eV.

Doping and coating nanostructured materials with rare earths can be an effective way to enhance many interesting properties. Because rare earths act as good luminescence centers due to their narrow and intense emission lines arising from 4f internal transitions [47], moreover, rare earths are very reactive and tend to form oxides very easily [48]. Among the rare earths, Holmium was selected as a promising element because it fluoresces in the visible and near-infrared regions and is promising for communication window and solid-state lasers [49].

The effects of Holmium ion doping revealed in the experiments are: i) from the XRD analysis the highest intensity was obtained at 0.05% Ho<sup>3+</sup> with (1845 a.u.). The crystallinity of the system was also confirmed by the lattice parameters a= 12.33 Å, b=12.33 Å and c=3.93 Å. The average density = 5.16, average Volume of the unit cell = 597.47 Å<sup>3</sup>, the average dislocation density = 2.19 x 10<sup>-4</sup>/nm<sup>2</sup> and space group = P4bm that confirmed Tetragonal Tungsten Bronze structured nanomaterials [37]. The SEM result further confirmed that by excess concentration (0.10 % Ho<sup>3+</sup>) the surface morphology changed to non-uniform and more porous. The FTIR results revealed also the dopant enhance the absorption in near infrared region with 0.05% Ho<sup>3+</sup>. The UV-Vis showed also optimum value obtained at wavelength of 205 nm with concentration of 0.03 % Ho<sup>3+</sup> that in turn signified the effect of Holmium dopant where no absorption peaks were observed at two extreme concentrations (0.00 & 0.10 % Ho<sup>3+</sup>).

### 3.6. Photoluminescence (PL)

When the single rare earth ion doped (Ba<sub>(1.6-x)</sub>Sr<sub>2.4</sub>Na<sub>2</sub>Nb<sub>10</sub>O<sub>30</sub>: xHo<sup>3+</sup>) ferroelectric nanomaterials was excited at 285 nm, the emission peak was observed at 572 nm arising from the radiative emission transition from F orbital to the various H orbitals. Specifically the emission spectra at 572 nm (yellow) is ascribed to 4F<sub>9/2</sub> → 6H<sub>13/2</sub> transitions. This is also ascribed to the electric dipole transitions (i.e. a hypersensitive transition) [50, 51].

To inspect the luminescence traits of rare earth ions amalgamated oxide, it is crucial to detect the right excitation wavelength. Figure 12 these spectra emit, peaking at 572 nm accredited to 4F<sub>9/2</sub> → 6H<sub>13/2</sub> (yellow) transition, and at 652 nm accounted to 4F<sub>9/2</sub> → 6H<sub>11/2</sub> (red) transition with maximum intensity for x=0.03% Ho<sup>3+</sup> content with drastically made red shift. The yellow emission, credited to 4F<sub>9/2</sub> → 6H<sub>13/2</sub> transition is a forced electric dipole (ED) transition following ΔL=2, ΔJ=2 golden rule. This transition was found to be hypersensitive and is usually influence by the local environment [52, 53]. Furthermore, the interrelation between emission

hierarchy and  $\text{Ho}^{3+}$  doping content was also deliberated. Apparently, the intensity of the emitted light upsurges with growth in the  $\text{Ho}^{3+}$  ions fraction up to 0.3 mol % and diminishes at 0.5 mol %. The observed decrement is ascribed to the quenching in dopant contents via resonant energy transfer (RET) between  $\text{Ho}^{3+}$  -  $\text{Ho}^{3+}$  ions, thus clarifying self-quenching phenomenon and cross relaxation mechanism [54].

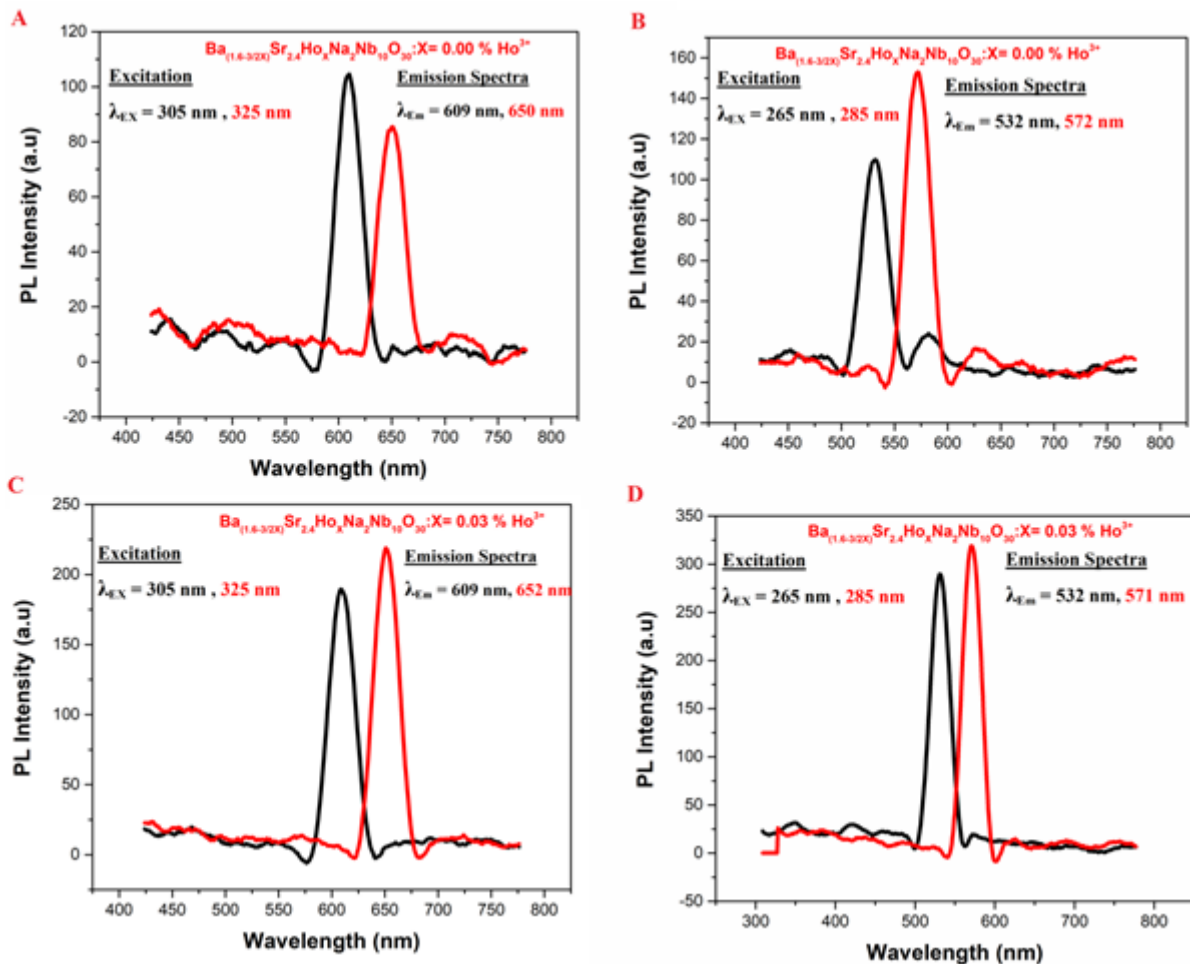


Figure: 12 Photoluminescence spectra of 0.03 %  $\text{Ho}^{3+}$  doped BSNN: xH excited from 265 nm to 325 nm wavelength ranges

#### 4. CONCLUSION

XRD analysis of Holmium doped Barium Strontium Sodium Niobate ferroelectrics nanomaterials revealed Tetragonal Tungsten Bronze structured nanomaterial successfully synthesized through conventional high temperature synthesis route. The identified crystal phase has an average crystallite size of 67.52 nm and particle size of 97.83 nm, having space group of p4bm and lattice parameters of  $a = 12.33 \text{ \AA}$ ,  $b = 12.33 \text{ \AA}$  and  $c = 3.93 \text{ \AA}$ . The XRD pattern obtained showed also a best match with JCPDS card number-00-039-1453. Further analysis of XRD result indicated the highest intensity value (1845 a.u.) was obtained for the concentration of 0.05 %  $\text{Ho}^{3+}$  ions. SEM and EDS analysis of surface morphology and elemental compositions of Holmium doped Barium Strontium Sodium Niobate ferroelectrics Tetragonal Tungsten Bronze structured nanomaterial showed clear and high quality surface morphology, microstructure and elemental mapping which is promising to enhance absorption. The SEM images have also shown separate nanoparticles with different shapes, size and size distributions with random distributions. Moreover the micro level dimension showed relatively uniform distribution of particles and less porosity of the surface.

Over all, surface morphology is promising for enhancing optical properties of the system because of its homogeneous surface microstructure having dense nanoparticles distributions. The EDS results confirmed that all the constitute elements are found in correct proportion to the standard stoichiometric ratios. In addition it



further confirmed that there were no impurities added during the synthesis and characterization which in turn confirming high quality synthesis procedures were employed. The experimental and theoretical molecular weight and atomic percentage coincidence also indicating that the composites made in high quality and proportion synthesis approach. The FTIR analysis result indicated also the collective metal oxide single peak for the bond vibration at wave number of  $540.60\text{ cm}^{-1}$  as expected since in the finger print of FTIR values of metal oxides were commonly found  $400 - 600\text{ cm}^{-1}$  and the Holmium oxygen bond vibration modes at (0.05%  $\text{Ho}^{3+}$ ),  $415.77$  (0.10 %  $\text{Ho}^{3+}$ )  $429.92\text{ cm}^{-1}$  which was not seen for the system without dopant. UV-Vis displays that the absorption edges of all kinds of  $\text{Ba}_{(1.6-3/2x)}\text{Sr}_{2.4}\text{Nb}_{10}\text{O}_{30}: x\text{Ho}^{3+}$  ferroelectric nanomaterial are at the same wavelength region of approximately 205 nm. The single rare earth ion doped ( $\text{Ba}_{(1.6-x)}\text{Sr}_{2.4}\text{Na}_2\text{Nb}_{10}\text{O}_{30}: x\text{Ho}^{3+}$ ) ferroelectric nanomaterials was excited at 285 nm, and then the emission peak was observed at 572 nm arising from the radiative emission transition from F orbital to the various H orbitals.

## REFERENCES

- [1] S. Chavan, P. Sastry, A. Tyagi, Combustion synthesis of nano-crystalline Nd-doped ceria and Nd<sub>2</sub>O<sub>3</sub> and their fractal behavior as studied by small angle X-ray scattering, *Journal of alloys and compounds*, 456 (2008) 51-56.
- [2] N. Mir, M. Salavati-Niasari, Effect of tertiary amines on the synthesis and photovoltaic properties of TiO<sub>2</sub> nanoparticles in dye sensitized solar cells, *Electrochimica Acta*, 102 (2013) 274-281.
- [3] S. Zinatloo-Ajabshir, M. Salavati-Niasari, Novel poly (ethyleneglycol)-assisted synthesis of praseodymium oxide nanostructures via a facile precipitation route, *Ceramics International*, 41 (2015) 567-575.
- [4] M. Zawadzki, Microwave-assisted synthesis and characterization of ultrafine neodymium oxide particles, *Journal of alloys and compounds*, 451 (2008) 297-300.
- [5] G.A. Mekhemer, Surface acid–base properties of holmium oxide catalyst: in situ infrared spectroscopy, *Applied Catalysis A: General*, 275 (2004) 1-7.
- [6] K. Shafiq, M. Aadil, W. Hassan, Q. Choudhry, S. Gul, A. Rais, A.A. Fattah, K.H. Mahmoud, M.Z. Ansari, Cobalt and holmium co-doped nickel ferrite nanoparticles: synthesis, characterization and photocatalytic application studies, *Zeitschrift für Physikalische Chemie*, 237 (2023) 1325-1344.
- [7] I.-E. Nylund, N.S. Løndal, J. Walker, P.E. Vullum, M.-A. Einarsrud, T. Grande, Cation Disorder in Ferroelectric Ba<sub>4</sub>M<sub>2</sub>Nb<sub>10</sub>O<sub>30</sub> (M= Na, K, and Rb) Tetragonal Tungsten Bronzes, *Inorganic Chemistry*, 61 (2022) 15540-15546.
- [8] J.F. Scott, J.F. Scott, Frequency dependence, *Ferroelectric Memories*, (2000) 145-147.
- [9] H. Fan, G.T. Park, J.J. Choi, H.E. Kim, Preparation and Characterization of Sol–Gel-Derived Lead Magnesium Niobium Titanate Thin Films with Pure Perovskite Phase and Lead Oxide Cover Coat, *Journal of the American Ceramic Society*, 85 (2002) 2001-2004.
- [10] G. Anand, P. Kuchhal, P. Sarah, The structure and complex impedance spectroscopy of Sr<sub>1-x</sub>Ca<sub>x</sub>Bi<sub>4</sub>Ti<sub>4</sub>O<sub>15</sub> (x= 0, 0.2, 0.4, 0.6, 0.8) ceramics, *Procedia Materials Science*, 10 (2015) 533-541.
- [11] G. Anand, A. James, P. Sarah, Dielectric and Polarization Studies of Ca Substituted in Bi<sub>4</sub>SrTi<sub>4</sub>O<sub>15</sub> Ceramics, *Integrated Ferroelectrics*, 116 (2010) 137-144.
- [12] D. Bao, X. Yao, K. Shinozaki, N. Mizutani, Crystallization and optical properties of sol–gel-derived PbTiO<sub>3</sub> thin films, *Journal of Physics D: Applied Physics*, 36 (2003) 2141.
- [13] G. Anand, P. Kuchhal, P. Sarah, AC and DC Conductivity Studies on Lead-Free Ceramics: Sr<sub>1-x</sub>Ca<sub>x</sub>Bi<sub>4</sub>Ti<sub>4</sub>O<sub>15</sub> (x= 0, 0.2, 0.4, 0.6, 0.8), *Particulate Science and Technology*, 33 (2015) 41-46.
- [14] S. Sakka, *Sol-Gel Science and Technology: Topics in Fundamental Research and Applications* (4 Volume Set), Taylor & Francis US, 2002.
- [15] G. Anand, A. James, T.R. Krishna, P. Sarah, Synthesis and characterisation of strontium bismuth titanate ceramics via high-energy mechanical milling, *DEFENCE SCIENCE JOURNAL-NEW DELHI*, 57 (2007) 29.
- [16] S. Wemple, M. DiDomenico Jr, I. Camlibel, Relationship between linear and quadratic electro-optic coefficients in LiNbO<sub>3</sub>, LiTaO<sub>3</sub>, and other oxygen-octahedra ferroelectrics based on direct measurement of spontaneous polarization, *Applied Physics Letters*, 12 (1968) 209-211.
- [17] P. Jamieson, S. Abrahams, J. Bernstein, Ferroelectric tungsten bronze-type crystal structures. II. Barium sodium niobate Ba(4+ x)Na(2- 2x)Nb<sub>10</sub>O<sub>30</sub>, *The Journal of Chemical Physics*, 50 (1969) 4352-4363.
- [18] J. Scott, Ferroelectrics go bananas, *Journal of Physics: Condensed Matter*, 20 (2007) 021001.



- [19] M.E. Lines, A.M. Glass, Principles and applications of ferroelectrics and related materials, Oxford university press, 2001.
- [20] R. Neurgaonkar, W. Cory, J. Oliver, E. Sharp, G. Wood, G. Salamo, Growth and optical properties of ferroelectric tungsten bronze crystals, *Ferroelectrics*, 142 (1993) 167-188.
- [21] A. Magnéli, B. Blomberg, Contribution to the knowledge of the alkali tungsten bronzes, *Acta chem. scand.*, 5 (1951) 372-378.
- [22] J.B. Felder, W. Wong-Ng, R.A. Qabbani, R.S. Roth, B.H. Toby, J.Y. Chan, Structural investigation of the "triple-tetragonal-tungsten-bronze" phases  $\text{Sr}_2\text{M}_{10-x}\text{O}_{27-y}$  (M= Nb, Ta), *Polyhedron*, 170 (2019) 359-363.
- [23] A. Wadsley, Crystal chemistry of non-stoichiometric compounds, (1955).
- [24] M. Francombe, The relation between structure and ferroelectricity in lead barium and barium strontium niobates, *Acta Crystallographica*, 13 (1960) 131-140.
- [25] C.-W. Nan, M. Bichurin, S. Dong, D. Viehland, G. Srinivasan, Multiferroic magnetoelectric composites: Historical perspective, status, and future directions, *Journal of applied physics*, 103 (2008).
- [26] M.-L. Hicks, A.C. Pakpour-Tabrizi, R.B. Jackman, Diamond Etching Beyond 10  $\mu\text{m}$  with Near-Zero Micromasking, *Scientific Reports*, 9 (2019) 15619.
- [27] J. Ma, J. Hu, Z. Li, C.W. Nan, Recent progress in multiferroic magnetoelectric composites: from bulk to thin films, *Advanced materials*, 23 (2011) 1062-1087.
- [28] N.J. Vickers, Animal communication: when i'm calling you, will you answer too?, *Current biology*, 27 (2017) R713-R715.
- [29] R. Gao, X. Qin, Q. Zhang, Z. Xu, Z. Wang, C. Fu, G. Chen, X. Deng, W. Cai, A comparative study of the dielectric, ferroelectric and anomalous magnetic properties of  $\text{Mn}_{0.5}\text{Mg}_{0.5}\text{Fe}_2\text{O}_4/\text{Ba}_{0.8}\text{Sr}_{0.2}\text{Ti}_{0.9}\text{Zr}_{0.1}\text{O}_3$  composite ceramics, *Materials Chemistry and Physics*, 232 (2019) 428-437.
- [30] M. Josse, O. Bidault, F. Roulland, E. Castel, A. Simon, D. Michau, R. von Der Mühl, O. Nguyen, M. Maglione, The  $\text{Ba}_2\text{LnFeNb}_4\text{O}_{15}$  "tetragonal tungsten bronze": Towards RT composite multiferroics, *Solid state sciences*, 11 (2009) 1118-1123.
- [31] W. Abbass, M.I. Khan, S. Mourad, Experimentation and predictive models for properties of concrete added with active and inactive  $\text{SiO}_2$  fillers, *Materials*, 12 (2019) 299.
- [32] M.I. Josse, P. Heijboer, M. Albino, F. Molinari, F. Porcher, R. Decourt, D. Michau, E. Lebraud, P. Veber, M. Velazquez, Original crystal-chemical behaviors in  $(\text{Ba}, \text{Sr})_2\text{Ln}(\text{Fe}, \text{Nb}, \text{Ta})_5\text{O}_{15}$  tetragonal tungsten bronze: Anion-driven properties evidenced by cationic substitutions, *Crystal growth & design*, 14 (2014) 5428-5435.
- [33] L.-J. Gao, X.-L. Liu, J.-Q. Zhang, S.-Q. Wang, J.-F. Chen, Grain-controlled barium titanate ceramics prepared from high-gravity reactive precipitation process powder, *Materials chemistry and physics*, 88 (2004) 27-31.
- [34] T. Mitsui, W.B. Westphal, Dielectric and X-Ray Studies of  $\text{Ca}_x\text{Ba}_{1-x}\text{TiO}_3$  and  $\text{Ca}_x\text{Sr}_{1-x}\text{TiO}_3$ , *Physical Review*, 124 (1961) 1354.
- [35] G. Distler, V. Konstantinova, Y.M. Gerasimov, G. Tolmacheva, Interaction of defect and domain structures of triglycine sulphate crystals in ferroelectric and paraelectric states, *Nature*, 218 (1968) 762-765.
- [36] J. Gardner, F.D. Morrison, A-site size effect in a family of unfilled ferroelectric tetragonal tungsten bronzes:  $\text{Ba}_{4-x}\text{R}_x\text{Nb}_{10}\text{O}_{30}$  (R= La, Nd, Sm, Gd, Dy and Y), *Dalton transactions*, 43 (2014) 11687-11695.
- [37] M. Rashid, W. Hassan, M. Aadil, H. Somaily, N.M. Mahdi, R. Lataef, A.G. Taki, K. Srithilat, D.F. Baamer, S.M. Albukhari, Solar-light-driven and magnetically recoverable doped nano-ferrite: an ideal photocatalyst for water purification applications, *Optical Materials*, 135 (2023) 113192.
- [38] S.Y. Mulushoa, M.T. Wegayehu, G.T. Aregai, N. Murali, M.S. Reddi, B.V. Babu, T. Arunamani, K. Samatha, Synthesis of spinel  $\text{MgFe}_2\text{O}_4$  ferrite material and studying its structural and morphological properties using solid state method, *Chemical Science*, 6 (2017) 653-661.
- [39] S.Y. Mulushoa, C.V. Kumari, V. Raghavendra, K.E. Babu, B. Murthy, K. Suribabu, Y. Ramakrishna, N. Murali, Effect of Zn-Cr substitution on the structural, magnetic and electrical properties of magnesium ferrite materials, *Physica B: Condensed Matter*, 572 (2019) 139-147.
- [40] B. Madhavalatha, D. Parajuli, K. Jayadev, C. Komali, N. Murali, V. Veeraiah, K. Samatha, Effect of Cu substitution on magnetic properties of  $\text{Co}_{0.6}\text{Ni}_{0.4}\text{Fe}_2\text{O}_4$  nanoferrites, *Biointerface Res. Appl. Chem*, 12 (2022) 1899-1906.
- [41] M. Aadil, T. Kousar, M. Hussain, H. Somaily, A.K. Abdulla, E.R. Muhammad, E.A. Al-Abbad, M.A. Salam, S.M. Albukhari, D.F. Baamer, Generation of mesoporous npn ( $\text{ZnO-CuO-CeO}_2$ ) heterojunction for highly efficient photodegradation of micro-organic pollutants, *Ceramics International*, 49 (2023) 4846-4854.



- [42] K. Chandramouli, B. Suryanarayana, P.P. Varma, V. Raghavendra, K. Emmanuel, P. Taddesse, N. Murali, T.W. Mammo, D. Parajuli, Effect of Cr<sup>3+</sup> substitution on dc electrical resistivity and magnetic properties of Cu<sub>0.7</sub>Co<sub>0.3</sub>Fe<sub>2-x</sub>CrxO<sub>4</sub> ferrite nanoparticles prepared by sol-gel auto combustion method, *Results in Physics*, 24 (2021) 104117.
- [43] H. Klung, L. Alexander, X-ray diffraction procedures, John Wiley & Sons, New York, 1 (1962) 974.
- [44] T. Li, M. Aadil, S. Zulfiqar, A. Anwar, S.M. Yakout, N.M. Panduro-Tenazoa, S. Mubeen, Synthesis of doped and porous CuO with boosted light-harvesting features for the photocatalytic mineralization of azo dyes, *Ceramics International*, 49 (2023) 27827-27836.
- [45] M. Pudukudy, A. Hetieqa, Z. Yaakob, Synthesis, characterization and photocatalytic activity of annealing dependent quasi spherical and capsule like ZnO nanostructures, *Applied surface science*, 319 (2014) 221-229.
- [46] Z. Liu, W. Xu, J. Fang, X. Xu, S. Wu, X. Zhu, Z. Chen, Decoration of BiOI quantum size nanoparticles with reduced graphene oxide in enhanced visible-light-driven photocatalytic studies, *Applied Surface Science*, 259 (2012) 441-447.
- [47] J. Petersen, C. Brimont, M. Gallart, G. Schmerber, P. Gilliot, C. Ulhaq-Bouillet, J.-L. Rehspringer, S. Colis, C. Becker, A. Slaoui, Correlation of structural properties with energy transfer of Eu-doped ZnO thin films prepared by sol-gel process and magnetron reactive sputtering, *Journal of applied physics*, 107 (2010).
- [48] K. Fabitha, M.R. Rao, Ho<sup>3+</sup>-doped ZnO nano phosphor for low-threshold sharp red light emission at elevated temperatures, *JOSA B*, 34 (2017) 2485-2492.
- [49] S. Babu, Y. Ratnakaram, Emission characteristics of holmium ions in fluoro-phosphate glasses for photonic applications, in: *AIP Conference Proceedings*, AIP Publishing, 2016.
- [50] J. Zhang, Q. Guo, L. Liao, Y. Wang, M. He, H. Ye, L. Mei, H. Liu, T. Zhou, B. Ma, Structure and luminescence properties of La<sub>6</sub>Ba<sub>4</sub>(SiO<sub>4</sub>)<sub>6</sub>F<sub>2</sub>: Dy<sup>3+</sup> phosphor with apatite structure, *RSC advances*, 8 (2018) 38883-38890.
- [51] D. Singh, J. Kaur, N. Suryanarayana, R. Shrivastava, V. Dubey, Synthesis and luminescent behavior of UV induced Dy<sup>3+</sup> activated LaAlO<sub>3</sub>, *Journal of Materials Science: Materials in Electronics*, 28 (2017) 2462-2470.
- [52] M.R. Babu, N.M. Rao, A.M. Babu, N. Jaidass, C.K. Moorthy, L.R. Moorthy, Effect of Dy<sup>3+</sup> ions concentration on optical properties of lead borosilicate glasses for white light emission, *Optik*, 127 (2016) 3121-3126.
- [53] I. Kashif, A. Ratep, Cool white light emission from Dy<sup>3+</sup>-doped SiO<sub>2</sub>-Bi<sub>2</sub>O<sub>3</sub>-Ga<sub>2</sub>O<sub>3</sub>-B<sub>2</sub>O<sub>3</sub>-GeO<sub>2</sub>-TeO<sub>2</sub> glasses: Structural and spectroscopic properties, *Materials Science and Engineering: B*, 275 (2022) 115488.
- [54] M. Mariyappan, K. Marimuthu, Concentration dependent spectroscopic properties of Dy<sup>3+</sup> ions doped boro-phosphate glasses, in: *AIP Conference Proceedings*, AIP Publishing, 2016.



## Assessment of Compatibility and Work Rate of Tractors and Implements at Wonji Shoa Sugar Estate

Cherinet Gosaye<sup>1,\*</sup>, Tsegaye Dinku<sup>2</sup>

<sup>1</sup>Ethiopian Sugar Industry Group, Research and Training

<sup>2</sup>Wonji Shoa Sugar Factory, Wonji, Ethiopia

\*Corresponding author, e-mail: [cherinet22@gmail.com](mailto:cherinet22@gmail.com)

### ABSTRACT

A study was conducted at Wonji Shoa Sugar Estate to assess compatibility of tractors and implements as well as work rates for major tillage operations. Before this study, it was not clear as to which tractor - implement combinations were compatible and whether they were achieving standard work rates, thus leading to low knowledge about their overall profitability. Thus, there was a need to scientifically evaluate compatibility and work rates. List of machinery and related data were sourced from the sugar estate. Implement draft, drawbar power requirement, expected tractor drawbar power under Wonji soil condition, as well as expected work rates were determined by using ASAE standard procedures and equations. Tractor power and implement power requirements were compared. Computed and actual work rates were also compared. The results showed that among the evaluated 18 tractor – implement combinations, only 3 were compatible. The remaining 15 combinations showed that the tractors had excess power ranging from 10 - 70 % than needed to operate the implement. Most combinations also showed work rates less than the standard with gaps as high as 2.7 ha/h. By rectifying these problems, the estate could save as high as ETB 1277.46 per operation. Thus, recommendations were given to rectify all incompatible combinations either by changing the tractor or the implement. Until machinery replacements are made, combinations with the least amount of unused power should be selectively used. Efforts should be made to increase work rates by giving practical training to operators and enforcing minimum work rates.

**Keywords:** ASAE Standards, compatibility, work rate

### 1. INTRODUCTION

In modern day agriculture, farm machinery requires a major financial investment and its use is one of the causes of high costs of production. As a result, current farming economics reinforce the importance of efficient farm tractor operation. Efficient farm tractor operation on the other hand, requires proper selection and deployment of matching tractors and implements. Tractor and implement selection is an important part of machinery management. A well matched tractor and implement allow efficient use of resources; reduces production costs and increases profitability.

Selecting a tillage system best suited to a particular farming situation is an important decision and it starts with machine selection and sizing. Machine selection and sizing in turn, requires an estimate of draft requirements of the implement. Draft is the major component of forces acting on an implement being drawn by a tractor. It acts in a parallel direction to the soil surface and to the direction of travel (Ishak et al., 1993). It is an important consideration in selecting implements, in getting tillage systems and tractor sizes that are compatible with the operations.

Conventionally, seedbed preparation in Wonji Shoa sugar estate is accomplished using a series of tillage operations, viz., uprooting, subsoiling, ploughing, harrowing, planning, and furrowing. Tractors and implements of different sizes and shapes are used for these operations. The use of incompatible tractors and implements will incur higher production costs or reduce work quality. When purchasing tractors and implements used in the estate, no systematic study was made to determine and match their sizes. Although a previous study was conducted in 2011 to evaluate tractor and implement matching status at the estate, several of the machinery tested back then were replaced (Cherinet and Zewdu, 2011). As a result, it is not known whether the implements currently in use by the estate are compatible with their power units or not. It is not clear as to which machine combinations are better in terms of utilization of available power from the tractor. Therefore, there is a need to evaluate the compatibility of power units and implements.



In addition, the work rate being accomplished by the machines has never been scientifically evaluated as to whether it is within an acceptable range to the standard work rate expected from the machines under the given circumstances in which they are operated. Thus, there is also a need to scientifically estimate expected work rates from the machinery used in tillage operations. The general objective of the research was to increase productivity and reduce cost of production by ensuring tractor – implement compatibility and working at acceptable work rates. To realize this the operational steps were (1) to assess the compatibility of tractors and implements by determining the power requirement of tillage implements analytically and comparing it with the power output of tractors and (2) to evaluate status of farm machinery work rates as compared to the expected standard rates.

## 2. MATERIALS AND METHODS

### 2.1. Description of the Study Area

The study was conducted at Wonji Shoa Sugar Estate which is located at about 108 km South of Addis Ababa in the Great Rift Valley of Ethiopia at a latitude and longitude of 8031’N and 39012’E, respectively. Average elevation is 1550 m.a.s.l. The area has a mean minimum and maximum temperature of 15.3 °C and 26.9 °C, respectively with annual rainfall of 800 mm. According to Ambachew and Abiy (2009), the estate has the soil properties of sand % ranges from 13 – 51 with an average of 26%, silt % ranges from 8 – 49 with an average of 22% and clay % ranges from 16 – 78 with an average of 52%.

### 2.2 Tractors, Implements and Materials Used

The experiment was carried out by making use of the existing tractors and implements as used conventionally by the estate. The list of land preparation machinery and their data were collected from the sugar estate as indicated in Table 1.

Table 1. Evaluated tractor – implement combinations

Operation	Prime mover			Implement				Working speed (km/h)	Work rate (ha/h)	Work rate (h/ha)
	Name	Model	HP	Name	No. of bottoms	Width (m)	Depth (cm)			
Uprooting	John Deere	9310	310	Heavy duty disc harrow	36” x 16	2.80	20 - 25	5.0	0.90	1.11
	John Deere	9410	410	Heavy duty disc harrow	36” x 16	2.80	20 - 25	5.5	1.00	1.00
Subsoiling	John Deere	9310	310	5 -shank subsoiler	5	3.20	60 - 70	6.00	0.80	1.25
	John Deere	9410	410	5 -shank subsoiler	5	3.20	60 - 70	6.00	0.90	1.11
Ploughing	John Deere	9310	310	3 bottom mouldboard plough	3	1.40	35 - 50	3.00	0.50	2.00
	John Deere	9410	410	3 bottom mouldboard plough	3	1.40	35 - 50	4.00	0.55	1.82
	John Deere	9310	310	Heavy duty disc harrow	42” x 16	2.80	35	5.00	1.00	1.00
	John Deere	9410	410	Heavy duty disc harrow	42” x 16	2.80	35	5.00	1.10	0.91
	YTO	1804	180	3 bottom mouldboard plough	3	0.60	35	2.00	0.30	3.33
	John Deere	9310	310	Disc harrow	24” x 48	3.50	25	7.50	4.50	0.67
Harrowing	John Deere	9410	410	Disc harrow	24” x 72	5.60	25	8.00	1.75	0.57
	John Deere	9310	310	Heavy duty disc harrow	36” x 16	2.80	25	6.00	1.10	0.91
	John Deere	9410	410	Heavy duty disc harrow	36” x 16	2.80	25	6.50	1.20	0.83
	John Deere	9310	310	Planner		5.00		9.50	0.80	1.25
Planning	John Deere	9410	410	Planner		5.00		10.00	0.85	1.18



Furrow- ing	YTO	1804	180	4 bottom furrower	4	4.35	25 - 30	7.00	2.00	0.50
	YTO	1804	180	3 bottom furrower	3	2.90	25 - 30	8.00	1.40	0.71
	YTO	1804	180	3 bottom furrower	3	2.90	25 - 30	6.00	1.35	0.74
	URSUS		140	3 bottom furrower	3	2.90	25 - 30	8.0	1.40	0.71

### 2.3 Methods

The procedure used in evaluating the compatibility of tractors and implements is as follows:

- Recommended speed of operation figures were collected from ASAE standards.
- Based on these speeds, the implement draft, drawbar power requirement of the implements were determined.
- Considering the field condition and tractor configurations, the drawbar power developed by the tractors were determined.
- The implement power demand and the drawbar power available from the tractor were compared.
- For work rate evaluations, theoretical and effective field capacities were determined analytically.
- Actual work rate data for all operations were collected from the factory.
- Comparisons were made between actual work rates and expected standard work rates.

#### 2.3.1 Recommended operation speed

The American Society of Agricultural Engineers have put forward the recommended speed for all major operations. It is a well-known fact that draft generally increases as speed of tillage operation increases (Al-Janobi et. al. 1998). Table 2 shows the recommended speed of different tillage operations.

Table 2. Recommended field efficiency and field speed extracted from ASAE 2000

Tillage implement	Field efficiency		Field speed
	Range (%)	Typical (%)	Range (km/h)
Mouldboard plough	70-90	85	5.0 - 10.0
Heavy duty disc	70-90	85	5.0 - 10.0
Tandem disc harrow	70-90	80	6.5 - 11.0
Field cultivator	70-90	85	8.0-13.0
Row crop cultivator	70-90	80	5.0 - 11.0
Fertilize spreader	60-80	70	8.0-16.0

#### 2.3.2 Determination of implement draft and drawbar power requirement

There are two methods of determining draft and power – experimental and analytical. In experimental methods, the implement draft is measured using appropriate equipment such as draft dynamometers. In analytical methods, the draft is determined analytically by making use of already developed standard procedures as described in the ASAE (2000) and ASAE (2003). Validation studies conducted to determine feasibility of using analytical methods of determining machinery performance found that the ASAE equations are valid and could be used as a substitute in cases where actual field data measurement is not possible (Mai, 2009).

##### 2.3.2.1 Implement draft

The American Society of Agricultural Engineers issued the standard (ASAE, 2000), for estimating implement draft requirements at different working conditions as follows:

$$D = Fi [ A + B (S) + C (S)^2 ] WT$$

Where: D = implement draft, N;

F = a dimensionless soil texture adjustment parameter (Annex 1, Table 1);

i = soil factor and it is = 1 for fine, 2 for medium and 3 for coarse texture soils;

A, B & C = machine – specific parameters referred from table (Annex 1, Table 1);



S = forward speed, km/h;  
 W = machine working width, m (Annex 1, Table 1);  
 T = tillage depth (cm) for major tools; =1(dimensionless) for minor tillage tools and seeding implements.

### 2.3.2.2 Drawbar power

After determining implement draft, drawbar power required to power the implement was determined using the following formula obtained from (ASAE, 2003) and as used by Mai (2009). Travel speed was taken as recommended speed by ASAE for the specific operation.

$$P_{db} = \frac{D \times S}{3.6}$$

Where:  $P_{db}$  = drawbar power (kW)  
 D = Implement draft (kN)  
 S = travel speed (km/ h)

### 2.3.3 Tractor drawbar performance determination

Drawbar performance of tractors depends primarily on engine power, weight distribution on drive wheels, type of hitch, and soil surface. Due to losses in the drive train, all the power generated by the engine does not reach the drive wheels to do the job. Similarly, all the power that reaches the drive wheels is not entirely used because of losses due to slippage and surface conditions. Throughout the drive train, power at a given location can be used to estimate power at another location by using the mechanical power performance chart (Fig. 1).

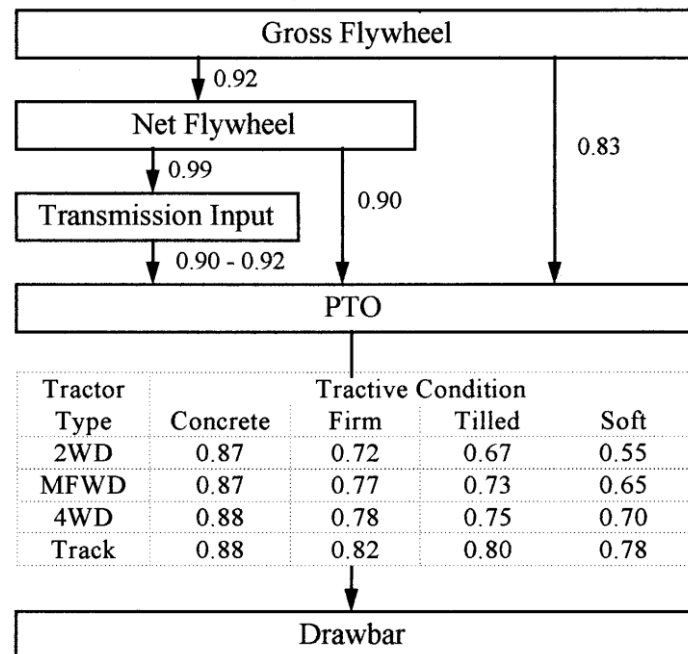


Fig. 1. Maximum mechanical power performance expected from tractors (Source: ASAE, 2000)

### 2.3.4 Theoretical field capacity

The theoretical field capacity (TFC) of land preparation operations were determined by using recommended standard working speeds and the following formula:

$$TFC \left( \frac{ha}{hr} \right) = \frac{Speed \left( \frac{km}{hr} \right)}{10} * width (m)$$

Where: TFC = Theoretical field capacity



Speed = working speed of the tractor implement combination under consideration

Width = width of implement

### 2.3.5 Determination of effective field capacity (EFC)

Farm machinery are not operated at their theoretical field capacity. They are rather operated at a lesser capacity due to the existence of different sources downtime during operation. Thus, the theoretical field capacity is reduced by the amount of field efficiency (FE). Recommended field efficiencies for all operations were obtained from international standards and the effective field capacities were determined by the following formula:

$$EFC \left( \frac{ha}{h} \right) = \frac{Speed \left( \frac{km}{hr} \right)}{10} * width (m) * FE (%)$$

Where: EFC = Effective field capacity (ha/h)

Speed = Working speed of the machine (km/h)

Width = Width of implement (m)

### 2.3.6 Collected data

The collected data include the following:

- Tractor type and power rating
- Implement type and working width
- Actual work rate of the tractor – implement combination
- Tillage depth
- Recommended standard speed of operation (from ASAE data)

### 2.3.7 Data analysis

Based on the obtained data, the following parameters were calculated or derived:

- Implement draft and drawbar power requirement of implements
- Maximum drawbar power developed by the tractor
- Theoretical field capacity and effective field capacity

After determining the power requirement of the implement and available power from the tractor, comparison was made among the two parameters to determine compatibility.

## 3. RESULTS AND DISCUSSIONS

### 3.1 Compatibility Evaluation

The results of the tractor – implement compatibility evaluations are summarized in Table 3. Out of the evaluated 18 combinations all but 3 combinations were found to be in an overpowered condition where by the tractors produced more power than what is actually used / needed by the implement. The unused power available from the tractors reached as high as 70%, thus indicating that the power use was not efficient.

Generally it is advisable to rectify the incompatibility problems as soon as possible by replacing either the tractors or the implements. Until such rectification is made, it is advisable to use combinations with less unused power more often than those with big unused power. This way we can systematically reduce the cost of land preparation.

- For example for uprooting operation, using John Deere 9310 tractor results in only 37.7% unused power whereas using John Deere 9410 tractor results in 53% unused power. Thus, using John Deere 9310 tractor will result in less cost of uprooting.
- Similarly for subsoiling operation using John Deere 9310 tractor results in less cost of operation.
- For ploughing operation using John Deere 9310 tractor with 2.8 m harrow resulted in the least unused power and hence this combination should be favored over the others.
- For harrowing operation using John Deere 9410 tractor with 5.6 m harrow resulted in the least unused power and hence this combination should be used as often as possible.



- For planning operation using John Deere 9310 tractor with the 5 m planner was found to be more or less compatible and hence should be used more often.
- For furrowing operation using URSUS tractor with 3 bottom furrower was found to be more compatible and hence should be favored. Next to that is using YTO tractor with 4 bottom furrower should be used.

Table 3. Summary of results on power unit and implement matching

Operation	Prime mover			Implement Name	Width (m)	Drawbar power required (kW)	Max. drawbar power (kW)	Used power (%)	Excess power available (%)
	Name	Model	HP						
Uprooting	John Deere	9310	310	Heavy disc harrow	2.80	101.2	162.26	62.3	37.7
	John Deere	9410	410	Heavy disc harrow	2.80	101.2	214.81	47	53
Subsoiling	John Deere	9310	310	5 -shank subsoiler	3.20	139.58	156.02	89	11
	John Deere	9410	410	5 -shank subsoiler	3.20	139.58	206.55	68	32
Ploughing	John Deere	9310	310	3 bottom mouldboard	1.40	120.32	156.02	77	23
	John Deere	9410	410	3 bottom mouldboard	1.40	120.32	206.55	58	42
	John Deere	9310	310	Heavy disc harrow	2.80	141.75	156.02	90	10
	John Deere	9410	410	Heavy disc harrow	2.80	141.75	206.55	69	31
	YTO	1804	180	3 bottom mouldboard	0.60	51.56	90.67	57	43
Harrowing	John Deere	9310	310	Disc harrow	3.50	77.25	156.02	49.5	50.5
	John Deere	9410	410	Disc harrow	5.60	123.6	206.52	60	40
	John Deere	9310	310	Heavy disc harrow	2.80	61.8	156.02	40	60
	John Deere	9410	410	Heavy disc harrow	2.80	61.8	206.52	30	70
Planning	John Deere	9310	310	Planner	5.00	161.1	156.02	103	-3
	John Deere	9410	410	Planner	5.00	161.1	206.52	78	22
Furrowing	YTO	1804	180	4 bottom furrower	4.35	97.44	90.67	107	-7
	YTO	1804	180	3 bottom furrower	2.90	73.08	90.67	80.6	19.4
	URSUS		140	3 bottom furrower	2.90	73.08	70.52	104	-4

Remark: the highlighted rows show compatible, whereas all the remaining are overpowered

### 3.2 Assessment of Work Rate

One of the objectives of this experiment was to determine the expected work rates of the evaluated operations and compare the results with the estates work rates. The work rate parameters are presented in Table 4.

Table 4. Work rate parameters

Operation	Prime mover			Implement Name	Width, m	Suggest- ed speed, km/h	TFC, ha/h	Expected field capacity, %	EFC, ha/h	EWR, ha/h	EFC - EWR, ha/h
	Name	Model	HP								
Uprooting	John Deere	9310	310	Heavy disc harrow	2.80	7	1.96	70	1.37	0.90	0.47
	John Deere	9410	410	Heavy disc harrow	2.80	7	1.96	70	1.37	1.00	0.37
Subsoiling	John Deere	9310	310	5 -shank subsoiler	3.20	6	1.92	70	1.34	0.80	0.54
	John Deere	9410	410	5 -shank subsoiler	3.20	6	1.92	70	1.34	0.90	0.44
Ploughing	John Deere	9310	310	3 bottom mouldboard	1.40	7	0.98	70	0.69	0.50	0.19
	John Deere	9410	410	3 bottom mouldboard	1.40	7	0.98	70	0.69	0.55	0.14
	John Deere	9310	310	Heavy disc harrow	2.80	7	1.96	70	1.37	1.00	0.37
	John Deere	9410	410	Heavy disc harrow	2.80	7	1.96	70	1.37	1.10	0.27
	YTO	1804	180	3 bottom mouldboard	0.60	7	0.42	70	0.29	0.30	-0.01
Harrowing	John Deere	9310	310	Disc harrow	3.50	8	2.8	70	1.96	4.50	-2.54



Operation	Prime mover			Implement	Width, m	Suggested speed, km/h	TFC, ha/h	Expected field capacity, %	EFC, ha/h	EWR, ha/h	EFC - EWR, ha/h
	Name	Model	HP								
	John Deere	9410	410	Disc harrow	5.60	8	4.48	70	3.14	1.75	1.39
	John Deere	9310	310	Heavy disc harrow	2.80	8	2.24	70	1.57	1.10	0.47
	John Deere	9410	410	Heavy disc harrow	2.80	8	2.24	70	1.57	1.20	0.37
Planning	John Deere	9310	310	Planner	5.00	10	5	70	3.50	0.80	2.7
	John Deere	9410	410	Planner	5.00	10	5	70	3.50	0.85	2.65
Furrowing	YTO	1804	180	4 bottom furrower	4.35	8	3.48	60	2.09	2.00	0.09
	YTO	1804	180	3 bottom furrower	2.90	8	2.32	60	1.39	1.40	-0.01
	URSUS		140	3 bottom furrower	2.90	8	2.32	60	1.39	1.40	-0.01

### 3.3 Expected Financial Benefit

By implementing the findings of this research work, very high financial savings could be achieved. The costs of land preparation operations could be highly reduced by properly matching the tractor – implement combinations in use. Potential cost saving to be gained by properly matching tractors and implements is estimated in table below as a percentage of the entire cost of operation based on the assumption that power savings are directly proportional to cost savings.

Table 5. Expected financial benefits by properly matching tractors and implements

Operation	Prime mover		Implement	Cost of operation (Birr/ha)	Expected cost saving as % of operation cost	Expected Cost saving Birr/ha
	Name	Model				
Uprooting	John Deere	9310	Heavy disc harrow	2410.30	37.7	908.68
	John Deere	9410	Heavy disc harrow	2410.30	53	1277.46
Subsoiling	John Deere	9310	5 -shank subsoiler	2759.62	11	303.56
	John Deere	9410	5 -shank subsoiler	2759.62	32	883.08
Ploughing	John Deere	9310	3 bottom mouldboard	2350.86	23	540.70
	John Deere	9410	3 bottom mouldboard	2350.86	42	987.36
	John Deere	9310	Heavy disc harrow	2350.86	10	235.09
	John Deere	9410	Heavy disc harrow	2350.86	31	728.77
	YTO	1804	3 bottom mouldboard	2350.86	43	1010.87
Harrowing	John Deere	9310	Disc harrow	891.70	50.5	450.31
	John Deere	9410	Disc harrow	891.70	40	356.68
	John Deere	9310	Heavy disc harrow	891.70	60	535.02
	John Deere	9410	Heavy disc harrow	891.70	70	624.19
Planning	John Deere	9310	Planner	2679.05	0	0
	John Deere	9410	Planner	2679.05	22	589.39
Furrowing	YTO	1804	4 bottom furrower	510.59	0	0
	YTO	1804	3 bottom furrower	510.59	19.4	99.05
	URSUS		3 bottom furrower	510.59	0	0

By properly matching tractors and implements, theoretically cost savings ranging from 10 - 70% of the value of the operation cost could be achieved. The highest cost saving per operation per operation was estimated to be Birr 1277.46 which could be obtained for uprooting operation.

### 4. CONCLUSIONS AND RECOMMENDATIONS

The results have shown that among the evaluated 18 tractor – implement combinations, only 3 were found to be more or less properly matched (compatible). The remaining 15 combinations showed situations where the tractors had more excess power than what was actually needed by the implement. The available unused power from the tractors ranged from 10 - 70 %. Had the tractor power been properly used to the full capacity, reduced



cost of production could have been achieved. The presence of excess (unused) power available incurs high cost and reduces competitiveness of the company. Utilizing farm machinery to their maximum capacity and efficiency will reduce production costs and increase profits.

Regarding work rates, most of the combinations showed work rates which are less than the expected standard work rate. The work rate gaps reached as high as 2.7 ha/h with the highest values being observed on planning operation. Three combinations in furrowing operation and one combination in harrowing operation showed work rates which were comparable to the standard expected work rate. This practice should be encouraged and the experiences should be adapted to the remaining operations where significantly high work rate gaps were observed. The major cause of low work rates is the below standard working speed. All tractor implement combinations should be operated as per the recommended standard working speeds. Following the recommended working speeds could significantly improve the work rates.

Finally, based on the findings of this work, the following recommendations are forwarded:

- All incompatible tractor – implement combinations should be rectified by either changing the tractor or the implement as much as possible as per discussions made under each tractor implement combination.
- Until future machinery replacements are made, combinations which showed the least amount of unused power should be favored (selectively used) by the estate.
- Efforts should be made to increase the low work rates and make them close to the standard as much as possible. This could be achieved by giving practical training to the operators and also by enforcing minimum expected work rates per shift or per day.
- Future machinery replacements should be made based on detailed analysis of compatibility.

## REFERENCES

- Al-Janobi, A. A., and Al-Suhaibani, S. A. 1998. Draft of Primary Tillage Implements in Sandy Loam Soil. Applied Engineering in Agriculture published by American Society of Agricultural Engineers Vol. 14(4): pp 343-348.
- Ambachew, D. and Abiy, F. 2009. Assessment of Some Physicochemical Properties of Soils of Wonji – Shoa, Metahara and Finchaa Sugarcane Plantations. Annual Research Report 2009, Ethiopian Sugar Development Agency Research Directorate, P.O. Box 15, Wonji, Ethiopia. pp 118 – 131.
- ASAE 2000. ASAE Standards D497.4 Agricultural Machinery Management Data. In: ASAE Standards 2000, (372-380) St. Joseph, MI.
- ASAE 2003. ASAE Standards EP 496.2 Agricultural Machinery Management. In ASAE Standards 2003, (366-372). St. Joseph, MI.
- Cherinet G. and Zewdu A. 2011. Investigation into Technical and Economical Tractor and Implement Matching, the Case of Wonji Shoa Sugar Estate. MSc. Thesis. Adama Science and Technology University
- Mai, M.A. 2009. Evaluation of Some Standards for Tillage Implement's Draft Requirements in Soba Area, Khartoum State, Sudan. M.Sc. Thesis. Department of Agricultural Engineering, University of Khartoum.
- Ishak, W., Ismail, W. and Burkhardt, T.H. 1993. Draft and Fuel Requirements Measurement Using Tractor On-Board Data Acquisition System. *Pertanika Journal of Science & Technology* 1(1): 51-64 (1993) ISSN: 0128-7680, © University Pertanian Malaysia Press.



## Syndicate 3



## Chromium Speciation in Water Using Paper-Based Devices with Online Oxidation

Abdellah Muhammed<sup>1</sup>, Ahmed Hussien<sup>2</sup>, Takashi Kaneta<sup>3,\*</sup>

<sup>1</sup>Department of Chemistry, Wollo University, Dessie, Ethiopia. [abdellahm1434@gmail.com](mailto:abdellahm1434@gmail.com)

<sup>2</sup>Center for Environmental Science, Addis Ababa University, Addis Ababa, Ethiopia

<sup>3</sup>Department of Chemistry, Okayama University, Okayama, Japan

\*Corresponding author, e-mail: [kaneta@okayama-u.ac.jp](mailto:kaneta@okayama-u.ac.jp)

### ABSTRACT

Speciation of chromium has been a growing interest particularly in drinking water because of the different toxicological relevance of Cr(III) and Cr(VI) species. In this study, speciation of chromium (Cr) was demonstrated using microfluidic paper-based analytical devices ( $\mu$ -PADs) that permit the colorimetric determination of hexavalent chromium (Cr(VI)) and trivalent chromium (Cr(III)) via online oxidation. The  $\mu$ -PADs consist of left and right channels that allow the simultaneous measurements of Cr(VI) and total Cr based on the colorimetric reaction of Cr(VI) with 1,5-diphenylcarbazide (DPC). For the determination of Cr(VI), a sample solution was directly reacted with DPC in the left channels whereas total Cr was determined in the right channels, which permitted online oxidation in the pretreatment zone containing cerium (IV) (Ce(IV)) followed by a colorimetric reaction with DPC. We found that the online oxidation of Cr(III) proceeded 100% whereas Ce(IV) inhibited the reaction of Cr(VI) with DPC. Therefore, speciation can be achieved by measuring the Cr(VI) and total Cr in the left and right channels followed by the subtraction of Cr(VI) from total Cr. The limits of detection and quantification were 0.008 and 0.02 mg L<sup>-1</sup> for Cr(VI), 0.08 and 0.1 mg L<sup>-1</sup> for Cr(III), and 0.07  $\mu$ g and 0.1 mg L<sup>-1</sup> for total Cr. The linear dynamic ranges were 0.02–100 mg L<sup>-1</sup> and 0.1–60 mg L<sup>-1</sup> for Cr(VI) and Cr(III), respectively. The RSDs were less than 7.5%. The results obtained using  $\mu$ -PADs were in good agreement with those obtained via ICP-OES with recoveries of 92–108% for Cr(III) and 108–110% for Cr(VI) using  $\mu$ -PADs, and 106–110% for total Cr using ICP-OES. Thus, the  $\mu$ -PADs could potentially be utilized for the speciation of chromium in developing countries where environmental pollution and the availability of sophisticated instruments are significant problems.

**Keywords:** Cr(III), Cr(VI), Online oxidation, Paper-based device, Speciation

### 1. INTRODUCTION

The current high level of interest in chromium (Cr) speciation has arisen from its applications in industrial activities such as leather tanning, electroplating, chrome plating, dye and pigment production, wood preservation, and metallurgy (Lin et al., 2016; Onchoke and Sasu, 2016). Although Cr exists in oxidation states ranging from -2 to +6 (Dayan and Paine, 2001, Lazo, 2009), only trivalent chromium (Cr(III)) and hexavalent chromium (Cr(VI)) are biologically and environmentally stable (Onchoke and Sasu, 2016; Ducros, 1992).

It is well known that Cr has both beneficial actions and potential risks for humans, depending on the oxidation states. Cr(III) has a low level of human toxicity (Sheehan et al., 1991) and is an essential nutrient for maintaining lipid, insulin, and glucose metabolism (Onchoke and Sasu, 2016). Cr(VI), on the other hand, is extremely toxic and poses risk for diseases ranging from dermatitis to lung and kidney cancers (Liu and Wang, 2013; Martone et al., 2013; Korshoj et al., 2015). Both Cr species are present in drinking water due to the use of corrosion inhibitors in water pipes and containers, or from contamination of underground water due to leaching from sanitary landfills (Zhitkovich, 2011). Consequently, fast and reliable speciation of Cr is an important requirement for drinking water, particularly in remote areas and in developing countries.

Because of the risk to humans, interest in the development of highly sensitive and selective spectroscopic, electrochemical and chromatographic analytical methods for the speciation of Cr has grown exponentially over the past few decades (Yang and Fan, 2012; Markiewicz et al., 2015; Bobrowski et al., 2004). These analytical methods are highly sensitive and selective, but they require expensive and complex instruments as well as professional personnel (Marques et al., 2000) that are complex, tedious, and time-consuming operations.

Microfluidic paper-based analytical devices ( $\mu$ -PADs) have tremendous potential to address the demands for simplicity, expeditiousness, portability, and easy operation that will permit use in remote areas and developing countries (Martinez et al., 2009). Several research groups have reported the colorimetric detection of Cr(VI) using



$\mu$ -PADs based on the specific reaction with 1,5-diphenylcarbazide (DPC) (Wang et al., 2014; Alahmad et al., 2018, Zhai et al., 2020). Although some of the previous methods achieved low detection limits for both Cr(III) and Cr(VI), Cr speciation was accompanied by a preconcentration technique as well as offline oxidation of Cr(III) to Cr(VI) prior to detection by  $\mu$ -PADs, which resulted in additional complexity, cost, and time.

In the present study, we report simpler, cheaper, and faster colorimetric assays for Cr(III) and Cr(VI) using  $\mu$ -PADs in which the oxidation of Cr(III) to Cr(VI) was achieved online. Without the need for tedious separation techniques, the proposed colorimetric  $\mu$ -PAD permits the speciation of Cr at limits of detection that are lower than the maximum contaminant levels (MCL) of Cr in drinking water ( $0.05 \text{ mg L}^{-1}$ ) established by the World Health Organization (WHO) (Edition, 2011) and MCL of Cr(VI) at  $0.010 \text{ mgL}^{-1}$  set by the California Environmental Protection Agency (CEPA, 2011).

## 2. MATERIALS AND METHODS

### 2.1. Apparatus

A wax printer (ColorQube 8580N, Xerox, CT, USA) was used to print the design of the  $\mu$ -PADs on a sheet of filter paper ( $200 \times 200 \text{ mm}$ , Chromatography Paper 1CHR, Whatman™, GE Healthcare Lifesciences, UK). The printed sheets were heated using a drying machine (ONW-300S, AS ONE, Tokyo, Japan) to penetrate wax to the backside of the sheets. A desktop scanner (Canon MG 6300 Series, Tokyo, Japan) was employed to capture images of the  $\mu$ -PADs that were dried before scanning. The total Cr was also determined by inductively coupled plasma-optical emission spectrometry (ICP-OES) (Model VISTA-PRO, Seiko Electronics, Tokyo, Japan).

### 2.2 Chemicals

All reagents used in this study were of analytical grade and were used without further purification. All solutions were prepared with deionized water purified by means of an Elix water purification system (Millipore Co., Ltd., Molsheim, France). Potassium dichromate ( $\text{K}_2\text{Cr}_2\text{O}_7$ ) and DPC were obtained from Nacalai Tesque (Kyoto, Japan). Ammonium cerium(IV) nitrate ( $\text{Ce}(\text{NH}_4)_2(\text{NO}_3)_6$ ) and chromium (III) nitrate nonahydrate ( $\text{Cr}(\text{NO}_3)_3 \cdot 9\text{H}_2\text{O}$ ) were obtained from Wako Pure Chemical Industries (Osaka, Japan). Methanol was obtained from Sigma-Aldrich (MO, USA). Nitric acid (6 M) was obtained from Junsei Chemical Co., Ltd. (Tokyo, Japan). A mineral water sample was purchased from a local store at Okayama University, Japan. Tapwater samples were obtained from an outlet at the Analytical Chemistry Group, Department of Chemistry, Graduate School of Natural Science and Technology, Okayama University, Okayama, Japan. All samples were analyzed for Cr(III) and Cr(VI) levels by the proposed method, and total Cr was determined via ICP-OES.

### 2.3 Design and Fabrication of the $\mu$ -PAD

The pattern for the  $\mu$ -PAD was drawn using Microsoft Office PowerPoint 2010. Each  $\mu$ -PAD consisted of an independent control zone and a sample reservoir that was connected to six flow channels featuring pretreatment and detection zones on the left and right sides (Fig. 1a). The  $\mu$ -PAD has a height of 25 mm and a width of 30 mm with an 8 mm sample reservoir in the shape of a circle at the center. The pretreatment and detection zones had diameters of 4 mm. The sample reservoirs were connected to the pretreatment and detection zones by channels with widths of 2 mm and lengths of 6 mm. The pretreatment zones in the left channels had no depositing reagents to control the flow rate in both the left and right channels, whereas the pretreatment zones in the right channels were used for online oxidation via Ce(IV). The  $\mu$ -PADs were printed on sheets of filter paper followed by heating at  $120 \text{ }^\circ\text{C}$  for 2 min in a drying machine to melt the wax in order to create hydrophobic barriers (Carrilho et al., 2009). The backside of the printed paper was covered with a clear packing tape to prevent leakage of the solutions through the bottoms of the  $\mu$ -PADs during the assay. The three detection zones on both sides of each  $\mu$ -PAD gave triplicate measurements for Cr(VI) and total Cr.

### 2.4 Colorimetric Assay

The fabrication and operation protocols of the  $\mu$ -PADs are shown in Fig. 1b. All detection zones were prepared by adding  $0.5 \text{ }\mu\text{L}$  of 50mM DPC twice and  $0.5 \text{ }\mu\text{L}$  of  $0.1\text{M HNO}_3$  once. In the pretreatment zones of the right

channels, 0.5  $\mu\text{L}$  of 0.5 M  $\text{HNO}_3$  and 0.5  $\mu\text{L}$  of 8  $\text{mg mL}^{-1}$   $\text{Ce(IV)}$  dissolved in 0.5M  $\text{HNO}_3$  were deposited once to oxidize  $\text{Cr(III)}$  to  $\text{Cr(VI)}$ , but no reagent was added to the pretreatment zones of the left channels. After drying the devices, 20  $\mu\text{L}$  of either a sample or a standard solution was introduced into the sample reservoir. When the solution reached the detection zones by capillary action, the immediate appearance of a purple color was visible to the naked eye. The original amount of  $\text{Cr(VI)}$  reacted with 1,5-DPC to form a colored complex in the left channels (Cate et al., 2014; Carrilho et al., 2009; Mentele et al., 2012) whereas the total  $\text{Cr(IV)}$ , which included additional  $\text{Cr(VI)}$  that originated from the online oxidation of  $\text{Cr(III)}$  by  $\text{Ce(IV)}$ , produced a purple color in the right channels.

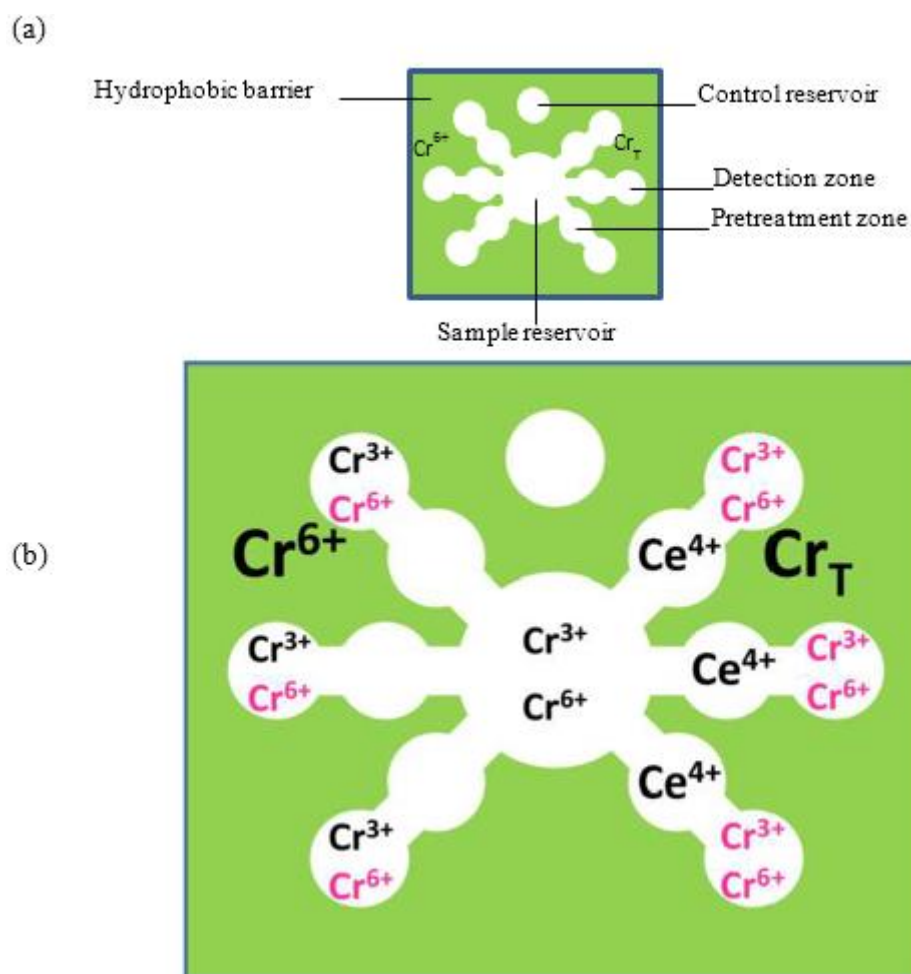


Figure 1: Design, fabrication, and operation of the  $\mu$ -PADs: (a) Design and roles of the zones, (b) Fabrication and operation protocols

After the introduction of a sample, a desktop scanner captured images of the  $\mu$ -PADs that were dried at room temperature (21–22  $^{\circ}\text{C}$ ) for 6 min. The time taken for the entire process from printing of the  $\mu$ -PADs to color image analysis was roughly 20 min. Colorimetric methods using  $\mu$ -PADs frequently employ color intensity (Mentele et al., 2012) and hue (Cantrell et al., 2010). In the present study, the mean color intensity was measured using ImageJ software according to a method reported by Henry's group (Mentele et al., 2012). R statistical package software (R-3.3.2-win version) was used for statistical data analysis.

### 3. RESULTS AND DISCUSSION

#### 3.1 Effect of pH on Mean Color Intensity

The solution containing chromate and reagent need to be acidified as the complex forms and is stable only in an acidic environment (Mulaudzi et al., 2002, Stancheva et al., 2012). Therefore, 1 mL of 10  $\text{mg L}^{-1}$   $\text{Cr(VI)}$



solutions consisting of 0.1 mL of different solutions of acetate buffer, acetic acid as well as different concentrations of nitric acid were investigated separately. Acetate buffer solutions with pH ranging from 3.99 to 5.6 and subsequently different concentrations of acetic acid alone (pH 1.61-2.45) were studied and acidified 10 mg L<sup>-1</sup> Cr(VI) solutions were loaded on the sampling zone. As shown in Fig. 2, the mean color intensity of Cr-DPC complex increased to pH 1.95 of the acidifying solution and then decreased with increasing pH of acidifying solution.

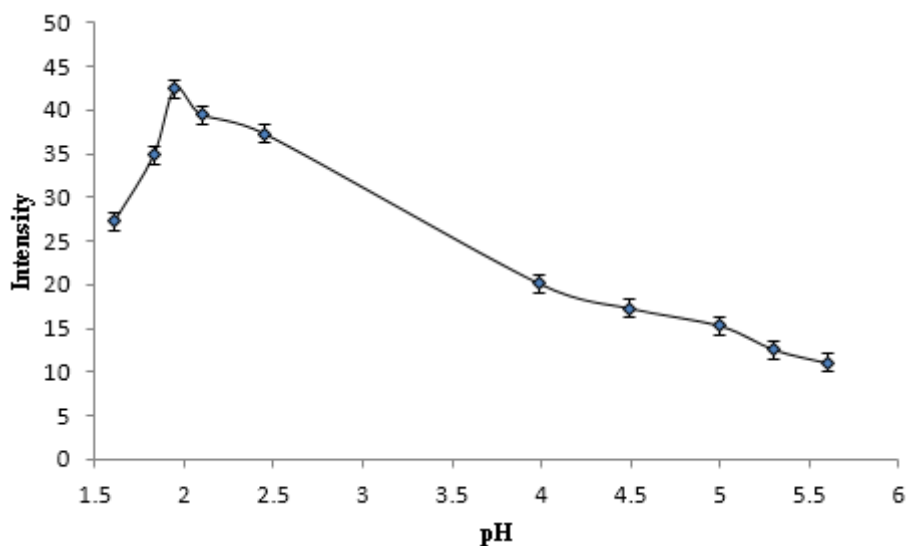


Figure 2: Effect of pH of acetate buffer and acetic acid solution on mean color intensity of Cr-DPC complex.

Some acids were employed for the complex formation of Cr(VI) with DPC. To accomplish the formation, Zhai et al. (2020) used 7 M phosphoric acid (Zhai et al., 2020) while de Andrade et al. (1984) recommend nitric acid (HNO<sub>3</sub>) to enhance the yield of the Cr complex since the formation of the Cr-DPC complex is more complete with nitric acid as a medium (de Andrade et al., 1984). In the present study, therefore, 1 mL of 10 mg L<sup>-1</sup> Cr(VI) solutions containing 0.1 mL of different concentrations of HNO<sub>3</sub> ranging from 0.005 to 0.5 M were employed and studied to evaluate the effect on mean color intensity. The resulted solution was loaded on sampling zone and results are presented in Fig. 3. Higher mean color intensity than those of the aforementioned acetate buffer and acetic acid solutions were obtained and the mean color intensity of Cr-DPC complex increased with increasing concentrations of HNO<sub>3</sub> up to 0.1 M but decreased as concentration increasing. The highest mean color intensity was observed at 0.1 M and hence concentration of 0.1 M HNO<sub>3</sub> was chosen for subsequent experiments.

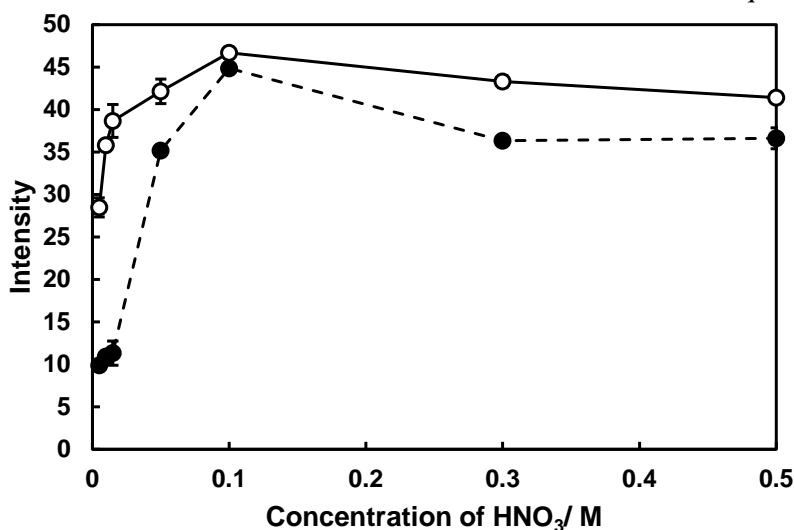


Figure 3: Effect of nitric acid concentration on the mean color intensity of the Cr-DPC complex. Open circle; nitric acid is added to the detection zones (0.5  $\mu$ L of different concentrations of HNO<sub>3</sub> loaded into detection zones), closed circle; nitric acid is added to the sample solutions



In order to evaluate the effect of loading site,  $\text{HNO}_3$  concentrations ranging from 0.005 to 0.5M were loaded on detection zones at different  $\mu$ -PADs without acidifying standard solutions. The results of solutions loaded on detection zones are shown in Fig. 3. In a similar trend with deposition of acidified standard solution on sampling zone, the mean color intensity of Cr-DPC complex increased with increasing concentrations of  $\text{HNO}_3$  up to 0.1 M but decreased as concentration increasing higher than 0.1 M. The mean color intensities observed when  $\text{HNO}_3$  solutions (0.5  $\mu\text{L}$ ) loaded on detection zones were considerably greater than those of  $\text{HNO}_3$  solutions loaded on sampling zones blended with standard solutions and particularly the effect was more pronounced at lower concentrations. Consequently, loading 0.1M  $\text{HNO}_3$  solution on detection zone after DPC drying was chosen for the upcoming experiments.

### 3.2 Effect of DPC Concentration on Intensity

Diphenylcarbazide (DPC) is an organic ligand which has long been used for the colorimetric determination of Cr as the reaction between Cr(VI) and DPC is inherently highly sensitive, highly selective, and simple (USEPA, 1992, Cate et al., 2014, Mulaudzi et al., 2002, Pflaum and Howick, 1956, Rattanarat et al., 2013). Furtherly, optimized amount of DPC solution should be used to achieve maximum sensitivity for Cr speciation. Thereby DPC concentrations in methanol ranging from 0.5 to 50 mM were investigated. The mean color intensity gradually increased with an increase in the concentration of DPC up to 40 mM and then plateaued at concentrations higher than 40 mM. In a previous publication, the concentration of DPC deposited in the detection zones was 50 mM (Rattanarat et al., 2013), which is consistent with this study. Therefore, 50 mM of DPC was added to the detection zones in this study.

### 3.3 Online oxidation of Cr(III) to Cr(VI) on $\mu$ -PADs

In Cr assays using  $\mu$ -PADs, the total Cr was determined by oxidizing Cr(III) to Cr(VI) using an appropriate oxidizing agent before the reaction with DPC. Therefore, Ce(IV) was used and optimized as an oxidant for online oxidation of Cr(III) to Cr(VI) as shown in Fig. 4.

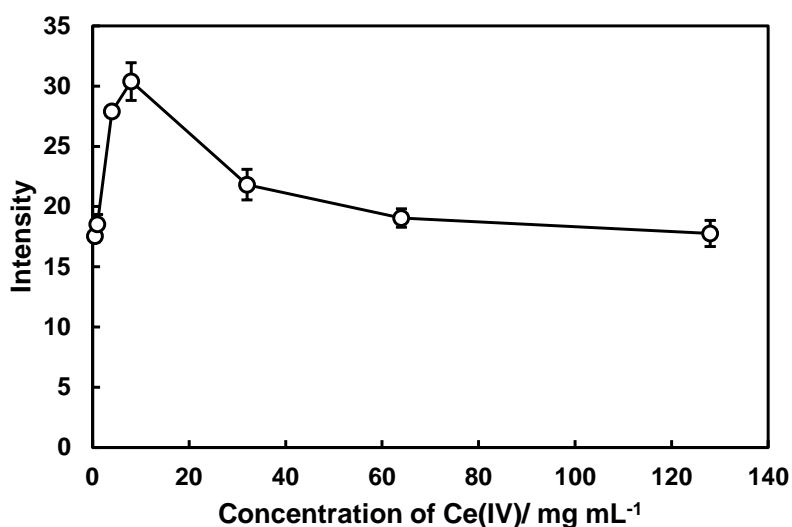


Figure 4: Effect of Ce(IV) concentration on the mean color intensity of the Cr-DPC complex obtained by online oxidation of Cr(III)

Concentrations of Ce(IV) ranging from 0.5 to 128 mg mL<sup>-1</sup> (0.0025-0.64 g in 5 mL of 0.1 M  $\text{HNO}_3$ ) were studied to evaluate the oxidation efficiency of Cr(III) to Cr(VI) via the mean color intensity of the detection zones. As shown in Fig. 4, the mean color intensity increased with increasing in the concentration of Ce(IV) to 8 mg mL<sup>-1</sup> and then decreased at higher concentrations.



The concentration of HNO<sub>3</sub> also influenced the oxidation reaction by Ce(IV). Therefore, concentrations of HNO<sub>3</sub> ranging from 0.05 to 6 M were furtherly investigated as a solvent for Ce(IV) salt in order to enhance the oxidation of trivalent Cr using Ce(IV). Intensity increased with increasing concentration of HNO<sub>3</sub> and reached climax at 0.5 M (Fig. 5). Tuazon suggested that Ce(IV) hydrolyses into Ce(NO<sub>3</sub>)(OH)<sup>2+</sup> species in medium HNO<sub>3</sub> concentrations (Tuazon, 1959). Thus the decrease in the mean color intensity at concentrations higher than 0.5 M could be attributed to the hydrolysis of Ce(IV) while the acidity would be insufficient at concentrations lower than 0.5 M. Thus for a test solution, Ce(IV) was dissolved in 0.5 M HNO<sub>3</sub> because the optimum concentration of HNO<sub>3</sub> proved to be 0.5 M, which represents the mean for maximum color intensity (Fig. 5).

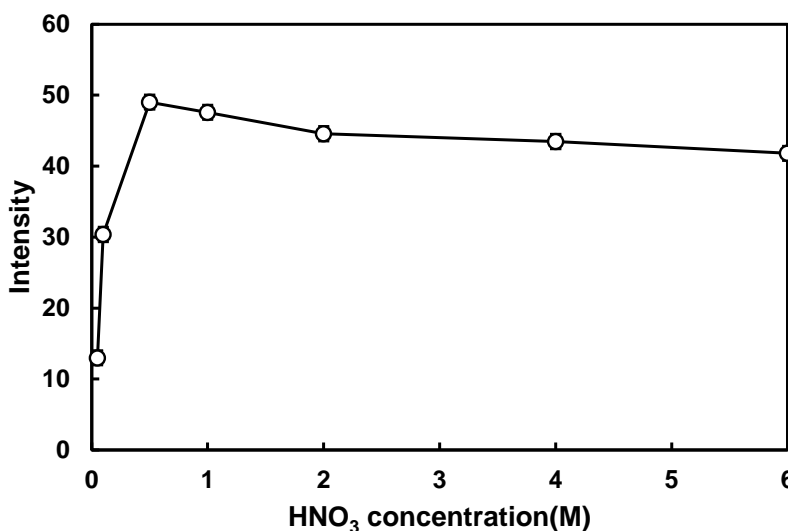


Figure 5: Effect of HNO<sub>3</sub> concentration in the sample solution on the mean color intensity of the Cr-DPC complex obtained by online oxidation

To evaluate the yield of the oxidation reaction, the standard solutions of Cr(III) and Cr(VI) were measured independently using the  $\mu$ -PADs. Thus a  $\mu$ -PAD equipped with two types of channels was used: one channel directly measured Cr(VI) via a colorimetric reaction with DPC; the other measured total Cr via online oxidation of Cr(III) to Cr(VI) followed by colorimetric reaction with DPC. The developed approach for the conversion of Cr(III) to Cr(VI) via online oxidation with Ce(IV) achieved simultaneous determinations of Cr(VI) and total Cr using a  $\mu$ -PAD.

### 3.4 Analytical Features

To evaluate the analytical features of the method, series of standard solutions for Cr(VI) (0.01, 0.1, 0.5, 1, 5, 10, 30, 50, 70, and 100 mg L<sup>-1</sup>) and for Cr(III) (0.01, 0.1, 0.5, 1, 5, 10, 20, 30, 40, 50, and 60 mg L<sup>-1</sup>) were prepared and analyzed to construct the calibration curves. Experimental conditions briefly; as per optimized conditions 0.5  $\mu$ L of 50 mM DPC was deposited on detection zone two times and subsequently 0.5  $\mu$ L of 0.1M HNO<sub>3</sub> was deposited one time on the detection zone, 0.5  $\mu$ L of 0.5M HNO<sub>3</sub> and 0.5  $\mu$ L of 0.8% Ce(IV) solution were deposited on pretreatment zone of right channels one time and finally 20  $\mu$ L sample/standard solution was loaded on sampling zone. The devices were allowed to air dry and images developed on  $\mu$ -PADs were captured using scanner and image mean color intensities were analyzed using imageJ software. The logarithms of the mean color intensities showed linear relationships against the logarithms of the Cr(VI), Cr(III), and total Cr concentrations. The correlation coefficients were 0.997 for Cr(VI) in the absence of Ce(IV), 0.997 for Cr(VI) in the presence of Ce(IV), 0.999 for Cr(III), and 0.999 for total Cr. The linear dynamic ranges were 0.02-100 mg L<sup>-1</sup> and 0.1-60 mg L<sup>-1</sup> for Cr(VI) and Cr(III), respectively.

The limits of detection (LODs) and quantification (LOQs) were calculated from the concentrations determined from 3 $\sigma$  plus the mean and 10 $\sigma$  plus the mean of the color intensity, respectively, where  $\sigma$  was the standard deviation of the mean color intensity for a blank solution (n = 3). The LODs and LOQs were estimated at 0.008



and 0.02 mg L<sup>-1</sup> for Cr(VI) and 0.08 and 0.1 mg L<sup>-1</sup> for Cr(III). The reproducibility of the proposed method was also evaluated using the relative standard deviation (%RSD) for six replicate measurements of a standard solution at a concentration of 10 mg L<sup>-1</sup>. The RSD was less than 5.2 and 7.5% for Cr(VI) and Cr(III), respectively.

Table 1 compares the analytical parameters obtained using the present method with the reported values. The LODs for Cr(VI) and Cr(III) in the present study were lower than those found in studies that employed no preconcentration method. Moreover, the linear dynamic ranges were wide in the present study. The reaction between Cr(VI) and DPC is highly selective without interferences of metal ions in the  $\mu$ -PADs. For example, Rattanarat et al. have found no interference for the determination of Cr in the presence of Mg, Mn, Zn, Al, Ba, V, Co, Cu, Fe, and Ni in metal:Cr ratios of 1:1 and 4:1 (Rattanarat et al., 2013). Li et al. also reported that Na(I), Co(II), Mg(II), Ca(II), Cd(II), Mn(II), Fe(III), Ni(II), Cu(II), Al(III), and Zn(II) showed no interference in the determination of Cr(VI) using DPC in the  $\mu$ -PADs (Li et al., 2019). Therefore, the speciation of Cr should experience no interference from any of these metal ions. However, even though DPC and cerium(IV) are standard reagents commonly used in the speciation of chromium they are light-sensitive (Li et al., 2015, Tuazon, 1959). Therefore, further study is required to improve their stability and hence the shelf life of the paper device.

Table 1: Comparison of the analytical features between the present method and other paper-based studies for chromium speciation

Study	Limits of detection, mgL <sup>-1</sup>		Linear dynamic range, mgL <sup>-1</sup>		RSD (%)	Technique used
	Cr(III)	Cr(VI)	Cr(III)	Cr(VI)		
Present	0.08	0.008	0.1-60	0.02-100	<7.5	Reagent optimization
Alahmad et al. (2018)		0.003		0.01-0.09	<6	Liquid phase microextraction
Asano & Shiraishi (2018)		30		40 – 400	< 8.7	Photolithographic fabrication
Alahmad et al. (2019)	0.001	0.0007	0.003-0.03	0.003-0.07	<7	Electromembrane microextraction
Zhai et al. (2020)	0.0146	0.0104	0.0484-0.312	0.0348-0.260	<7.9	Field amplified stacking
Alahmad et al. (2016)	0.020		0.05–1		<6.5	Chemiluminescence detection system

### 3.5 Speciation of Cr(III) and Cr(VI) in Spiked Water Samples

The results obtained by the proposed method were validated by ICP-OES and showed no significant difference in the results for the spiked samples. The present method showed content recoveries of 92-108% for Cr(III) and 108-110% for Cr(VI) by the  $\mu$ -PADs, and 106-110% for total chromium measured by ICP-OES. The two sets of  $\mu$ -PADs and ICP-OES results were in good agreement, as a paired t-test indicated no significant differences. Thus, the proposed method permits the speciation of Cr(III) and Cr(VI) in water samples.

## 4. CONCLUSIONS

In this study, simple, cheap, fast, and portable  $\mu$ -PADs were developed for Cr speciation with online oxidation of Cr(III) by Ce(IV). This study is the first to demonstrate the speciation of Cr by online oxidation of Cr(III) to Cr(VI) using  $\mu$ -PADs. The proposed  $\mu$ -PADs showed performance sufficient to evaluate the safety of drinking water and environmental pollution in developing countries. ICP-OES validated the analytical results obtained by the  $\mu$ -PADs. The results of the study demonstrated that  $\mu$ -PAD detection system has the potential to complement conventional analytical methods for environmental monitoring, particularly in resource-limited settings.



## ACKNOWLEDGEMENTS

The authors thank Addis Ababa University Thematic Research Fund for supporting the project titled "Developing Innovative Microfluidic Paper-Based Analytical Devices ( $\mu$ -PADs): Viable solution for Environmental Monitoring in Ethiopia" at the Center for Environmental Science. The authors gratefully thank Division of Instrumental Analysis, Department of Instrumental Analysis & Cryogenics, Advanced Science Research Center, Okayama University for the ICP-OES measurements.

## REFERENCES

- Alahmad, W., Tungkijanansin, N., Kaneta, T., & Varanusupakul, P. (2018): A colorimetric paper-based analytical device coupled with hollow fiber membrane liquid phase microextraction (HF-LPME) for highly sensitive detection of hexavalent chromium in water samples. *Talanta*, 190, 78-84.
- Alahmad et al. (2016): A miniaturized chemiluminescence detection system for a microfluidic paper-based analytical device and its application to the determination of chromium (III). *Analytical Methods*, 8, 5414-5420.
- Alahmad et al. (2019): Chromium speciation using paper-based analytical devices by direct determination and with electromembrane microextraction. *Analytica Chimica Acta*, 1085, 98-106.
- Asano, H., & Shiraishi, Y. (2018): Microfluidic paper-based analytical device for the determination of hexavalent chromium by photolithographic fabrication using a photomask printed with 3D printer. *Analytical Sciences*, 34, 71-74.
- Cate et al. (2014): Rapid detection of transition metals in welding fumes using paper-based analytical devices. *Annals of Occupational Hygiene*, 58, 413-423.
- CEPA. (2011): Environmental health hazard assessment, public health goal for hexavalent chromium (Cr(VI)) in drinking water, California Environmental Protection Agency.
- Korshoj, L. E., Zaitouna, A. J., & Lai, R. Y. (2015): Methylene blue-mediated electrocatalytic detection of hexavalent chromium. *Analytical Chemistry*, 87, 2560-2564.
- Li, F., Hu, Y., Li, Z., Liu, J., Guo, L., & He, J. (2019): Three-dimensional microfluidic paper-based device for multiplexed colorimetric detection of six metal ions combined with use of a smartphone. *Analytical and Bioanalytical Chemistry*, 411, 6497-6508.
- Rattanarat et al. (2013): A microfluidic paper-based analytical device for rapid quantification of particulate chromium. *Analytica Chimica Acta*, 800, 50-55.
- Wang et al. (2014): Paper based three-dimensional microfluidic device for monitoring of heavy metals with a camera cell phone. *Analytical and Bioanalytical Chemistry*, 406, 2799-2807.
- Wu et al. (2013): Colorimetric determination of hexavalent chromium with ascorbic acid capped silver nanoparticles. *Analytical Methods*, 5, 560-565.
- Yang, B. & Fan, Z. (2012): Speciation analysis of chromium in natural water samples by electrothermal atomic absorbance spectrometry after separation/preconcentration with nanometer zirconium phosphate. *Journal of Analytical Chemistry*, 67, 443-447.
- Zhai et al. (2020): Colorimetric speciation of Cr on paper-based analytical devices based on field amplified stacking. *Talanta*, 210, 120635.
- Zhitkovich, A. (2011): Chromium in drinking water: sources, metabolism, and cancer risks. *Chemical Research in Toxicology*, 24, 1617-1629.



## Efficiency of Slow Sand Filtration in Removing Bacteria and Turbidity From Drinking Water in Central Ethiopia

Ephrem Guchi<sup>1,\*</sup>, Seyoun Leta<sup>2</sup>, Eline Boelee<sup>3</sup>

<sup>1</sup>Department of Biology, College of Natural and Computational Science, Samara University, Ethiopia

<sup>2</sup>Department of Biology, Addis Ababa University, Ethiopia

<sup>3</sup>Water Health, Amsterdam, the Netherlands

\*Corresponding author, e-mail: [ephremg21@gmail.com](mailto:ephremg21@gmail.com)

### ABSTRACT

Approximately over one billion people world-wide lacks access to adequate amounts of safe water and rely on unsafe drinking water sources. This study was aimed at Efficiency of slow sand filtration (SSF) in removing total and thermotolerant/faecal coliforms (TC and TTC/FC) and turbidity (TR) from drinking water. Triplicate water samples in two-week interval were collected to determine the presence of TC and TTC/FC and turbidity. Membrane filtration and epifluorescence microscope methods were used for TC and TTC/FC analysis, and turbidity was measured using Turbidimeter. Mean analyses of water samples for TC, TTC/FC and TR from influent and effluent of SSF for spring users showed that average TC from influent was 888.9 cfu/100\_ml where as from effluent it was 5.5 cfu/100\_ml. Moreover, average TTC/FC from influent was 289.4 cfu/100\_ml where as from effluent it was 2.5 cfu/100\_ml. Similarly, average TR from influent was 9.0 NTU and from effluent it was 0.9 NTU. The study showed that average removal efficiency of SSF from spring users were 97.4 % and 96.9 % for TC and TTC/FC, respectively, while the removal efficiency for TR was 92.9 %. Similarly, mean analyses of water samples for TC, TTC/FC and TR from influent and effluent of SSF for river users showed that average TC from influent was 824.0 cfu/100\_ml where as from effluent it was 4.8 cfu/100\_ml. In addition, average TTC/FC from influent was 267 cfu/100\_ml, and from effluent it was 2.0 cfu/100\_ml. Coliform removal efficiencies of SSF in clay pots from river users were 97.9 % and 96.6 % for TC and TTC/FC respectively, where as TR reduction of 93.1 % was obtained. Water analyses from the effluent of SSF in clay pot showed that it is safe for drinking purpose from bacteriological point of view. It is recommended that dissemination of SSF to other poor rural areas of Ethiopia is required.

**Keywords:** Coliform, Drinking water, Rural water supply, Slow sand filter

### 1. INTRODUCTION

Approximately over one billion people world-wide lacks access to adequate amounts of safe water and rely on unsafe drinking water sources from lakes, rivers and open well. Nearly all of these people live in developing countries, especially in rapidly expanding urban fringes, poor rural areas, and indigenous communities (Gundry et al., 2015; Bartram et al., 2016). Much of the global population now consumes untreated, non piped drinking water, usually consisting of small volumes <40 lpcd (liter per capita per day) collected and stored in the home by users (WHO, 2014).

The greatest risk associated with the ingestion of water is the microbial risk due to water contamination by human and/or animal feces. The effects of drinking contaminated water result in thousands of deaths every day, mostly in children under five years of age in developing countries (WHO, 2012a). Diseases caused by consumption of contaminated water, and poor hygiene practices are the leading causes of death among children worldwide, after respiratory diseases (WHO, 2012a).

In Ethiopia, over 60 % of the communicable diseases are due to poor environmental health conditions arising from unsafe and inadequate water supply and poor hygienic and sanitation practices (Abebe Legesse, 2011). About 80 % of the rural and 20 % of urban population have inadequate and unsafe water supply of 3-4 liter per capita per day that is fetched from a distance of 3-8 km with human power (WHO, 2012a). Three-fourth of the health problems of children in the country are communicable diseases arising from the environment, especially water and sanitation (IWSC, 2009). Forty six percent of the mortality rate of less than five years of age is due to diarrhea in which water related diseases occupy a high proportion. The Ministry of Health of Ethiopia estimated that 6000 children died each day from diarrhea and dehydration (MoH, 2010).



Indicator organism's are microbes that are routinely found in faeces, survive longer than intestinal pathogens, and are relatively easy to detect and enumerate. It is impractical to attempt the routine isolation of pathogens because they are present in relatively small numbers compared with other types of microorganism. Moreover, there are many types of pathogen and each requires a unique microbiological isolation technique. The approach that has been adopted is to analyse for indicator organisms that inhabit the gut in large numbers and are excreted in human faeces. The presence of these indicator organisms in water is evidence of faecal contamination and, therefore, of a risk that pathogens are present. The coliforms are in the family *Enterobacteriaceae* and include the genera *Escherchia*, *Citrobacter*, *Klebsiela*, and *Enterobacter*. *Escherchia coli* are almost exclusively faecal microorganisms and constitute over 90% of the coliform flora of the human intestine. It is easily distinguished from other coliforms on the basis of its growth at 44<sup>o</sup>c on media normally used for coliform determination. The faecal coliform test must therefore taken as the most sensitive, reliable and specific indicators of faecal pollution. The overall concepts adopted for microbiological quality is that no water intended for human consumption shall contain *E.coli* in 100ml sample (WHO, 2012b).

The mapping of water resources in the study area in the central Highlands of Ethiopia-Yubudo-Legebatu Pessant Association in Dendi woreda-showed that the community had access to 28 water sources including rivers and springs distributed unevenly across three land types: upland, mid-slopes and bottomlands. Most of these sources were found unsuitable for human consumption as livestock has open access to all the sources at any point in time. Analyses of water for coliform count showed that, during the main rainy season most of the water sources were contaminated for human consumption (Eline and Abiy Assefa, 2014). The situation was worse on bottomland and mid-slopes where no source of clean (potable) water was available during the main rains. The reason was that human feces, animal dung and urine were washed down the slopes and deposited directly into the water sources. In addition washing/watering served to initiate and replenish organic contamination (Eline and Abiy Assefa, 2014). Community or municipal water treatment systems are frequently impractical and often unaffordable in these settings. At the present time, inexpensive household water treatment such as slow sand filtration provides a reasonable alternative for many of these people.

In order for a household water treatment technology such as SSF to achieve widespread sustainable use among the poor, it must meet the criteria of the poor (Duke and Baker, 2015). Slow sand filters can be constructed from local materials, mainly from properly graded sand/gravel, concrete/clay, and standard piping, can operate without the use of specialized equipment, and is much less labor intensive than rapid filters. Also slow sand filters operate under gravity flow conditions, and energy, its on-going energy demand is minimal. Thus, SSF is an attractive treatment alternative for local communities. Therefore, this paper reports the efficiency of SSF in clay pots in removing coliform bacteria and turbidity from drinking water for household use in the central highlands of Ethiopia.

## 2. MATERIALS AND METHODS

### 2.1. Description of the Study Area

The study was conducted in West Shoa, Dendi district, Ginch town, Yubudo-Legebatu Peasant Association (YLPA) (Fig. 1). YLPA is located at about 80 km west of Addis Ababa in the Dendi district of Oromia region. The Peasant Association is located at about 20 km from the district town Ginchi. The study area has uneven topography with upland, mid-slopes and bottom lands. It receives mean annual rainfall ranging from 800-1172.2 mm and has an average temperature of between 9.3 °C and 23.8 °C. The altitude of the area ranges between 1600 and 3268 meter above sea level. Total population in YLPA is 5614 and the number of households in upland and bottom land of YLPAs is 796). The survey of water resources in YLPAs showed that the community had access to 28 water sources including rivers and springs distributed unevenly across different land types; upland, mid-slopes and bottom lands (Source: Agricultural Office, Dendi Wereda, 2014).

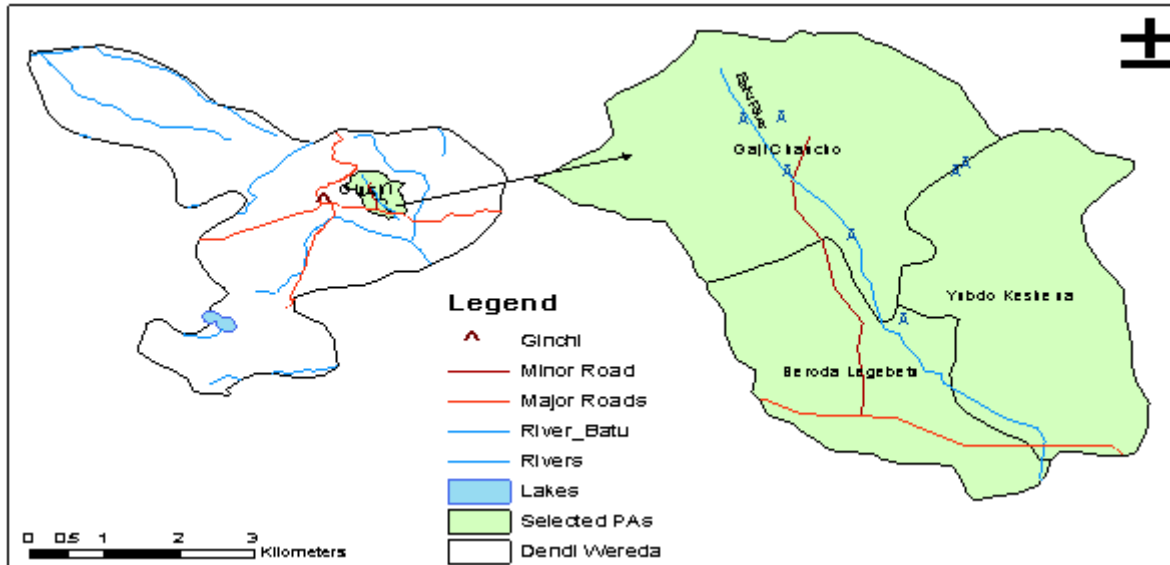


Fig. 1. Map of the study area, Dendi Wereda, Ginchi town, Yubudo-Legebatu PA

## 2.2. Design of the Study

The study had different components. The field work consisted of analyses of drinking water quality for indicator bacteria, such as TC and TTC/FC and for turbidity from the influent and effluent of slow sand filtration in clay pots (Fig. 2) from intervention groups. Moreover, the field work comprised of interviewing 40 intervention households who used a SSF in clay pots to record the perceptions of the users with regard to water quality from the filter, ease of use, and level of satisfaction with the filter to assess sustainability using questionnaires and observations.

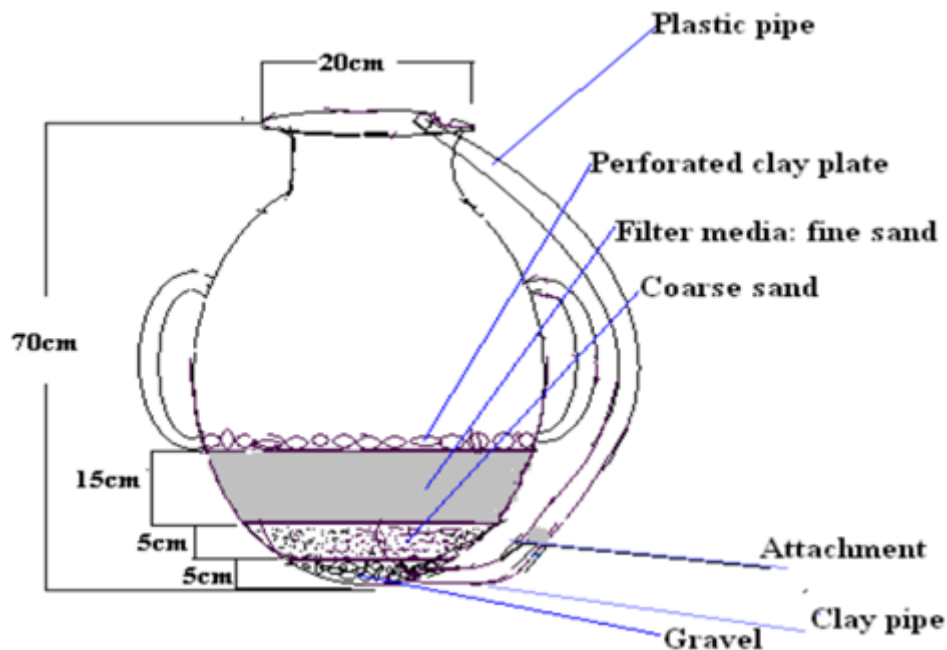


Fig. 2. Schematic drawing of slow sand filtration in clay pot

The basic components of a slow sand filter shown above are: perforated clay plate, sand bed (clean fine sand and clean coarse sand), clean round gravel and outlet hose (plastic pipe). The perforated clay plate reduces splashing of sand when influent or flow water is added. Sand is the usual filter medium because of its low cost, durability and availability.



The sand has a relatively fine grain size (effective size 0.15 to 0.3mm). The gravel provides an unobstructed passage for treated water from the filter bed, which prevents sand from clogging the under-drain piping and supports the filter sand bed. The plastic pipe is attached to the protrude clay pipe and the filtered water is passed through plastic pipe. After taking water, the plastic pipe is attached to the top of the clay pot. Bed depth of the filter media is 25cm (15cm fine sand, 5cm coarse sand and 5cm gravel). Water percolates slowly through the porous sand medium and organic and inorganic particulate matter and pathogenic microorganisms are removed by physical filtration and biological degradation in the sand bed.

### 2.3. Water Samples and Sampling Points

Forty households were selected for this study where 40 households were intervention groups who used slow sand filtration in clay pot comprised of spring users (20) and river users (20). Water sample were collected from the influent and effluent of slow sand filtration in clay pots. Samples were taken at two-week interval using a sterile 200ml glass bottle, labeled and kept in cool ice box during transportation to Applied Microbiology Laboratory, Department of Biology, Addis Ababa University. The appropriate tests were undertaken within 8 hours of collection to avoid the growth or death of organisms in the sample.

### 2.4. Samples Analyses

All samples were analyzed for TC, TTC/FC and turbidity in Applied Microbiology Laboratory, Department of Biology, Addis Ababa University (Fig. 3). To determine the presence of TC and TTC/FC in the water samples, standard membrane filtration methods were used as described in membrane filtration techniques (APHA, 1998). Turbidity was measured using Turbidimeter (HACH- 2100P model Turbidimeter, German).



Fig. 3. Sample water quality analyses in the laboratory

Drinking water was analyzed by filtering 100 ml, or by filtering replicate smaller sample volumes. Using sterile forceps, a sterile membrane filter paper (0.45 $\mu$ m pore sizes, 47mm in diameter, sterile and gridded were from WAGTECH) was placed on the membrane filter support assembly (from WAGTECH). The funnel unit was placed carefully over the filter support assembly and locked in place. The samples were mixed thoroughly by shaking for about 30 minutes and poured in to the funnel assembly. Then the entire volumes of samples were filtered through the membrane-filter by using a vacuum pump. Funnel and membrane-filter assembly were rinsed by sterile dilution water to avoid contamination between water samples.

Up on completion of the filtration process, the vacuum was disengaged, unlocked and using a sterile forceps, membrane paper were removed immediately and placed on rehydrated Difco M-Endo Agar (LES) (No.0736) with a rolling motion to avoid entrapment of air in glass Petri dish. Finally the prepared culture dish were inverted and incubated for 22 to 24h at 35 $\pm$ 0.5  $^{\circ}$ C. Up on completion of the incubation period, typical coliform colonies (pink to dark red color with sheen) were seen on the surface of the membrane filter paper. Colony counts on the filter paper were determined using a low-power (10 to 15 x magnifications) binocular wide-field-dissecting microscope, with a cool white fluorescent light source for optimal viewing of sheen. Then total coliforms per



100ml of sample were calculated. This meets the objectives on determination of total coliforms from influent and effluent of slow sand filtration.

Membrane filter papers were placed on rehydrated M-FC agar with rosolic acid (to increase specificity of medium). Culture dishes were inverted and incubated for  $24 \pm 2$ h at  $44.5 \pm 0.2^\circ$  C. Up on completion of the incubation period; blue colored colonies on the surface of the filter paper were counted. Then TTC/FC colonies per 100 ml of sample were calculated. Verification tests were done by transferring growth from each colony and placed in lauryl tryptose broth; incubating the lauryl tryptose broth at  $35 \pm 0.5^\circ$ C for 48 hours. Gas formed in lauryl tryptose broth within 48h verifies the colony as a coliform. Inclusion of EC broth inoculations for  $44.5 \pm 0.2^\circ$ c incubation verifies the colony as faecal coliforms (APHA, 1998). Generally, in the present study, the efficiency of SSF in clay pot in removing TC, TTC/FC and turbidity were tested. A total of 240 (40 x 2 (inf. & effl.) x 3) water samples were collected from the influent and effluent of slow sand filtration in clay pot taking triplicate water samples from each point. All samples were analyzed for bacteriological qualities and turbidity.

## 2.5. Total and Thermotolerant/Faecal Coliform Colonies Identification



Fig. 4. Total coliform colonies in membrane filtration (a) and Faecal coliform colonies in membrane filtration (b)

Bacterial colonies were identified using membrane filtration techniques. Colors of total coliform bacterial colonies were pink to dark red with sheen, using a low-power (10 to 15 x magnifications) binocular wide-field-dissecting microscope, with a cool white fluorescent light source for optimal viewing of sheen as shown in Fig. 5 (a). Where as colors of thermotolerant/ faecal coliform bacterial colonies were blue as shown in Fig. 5 (b).

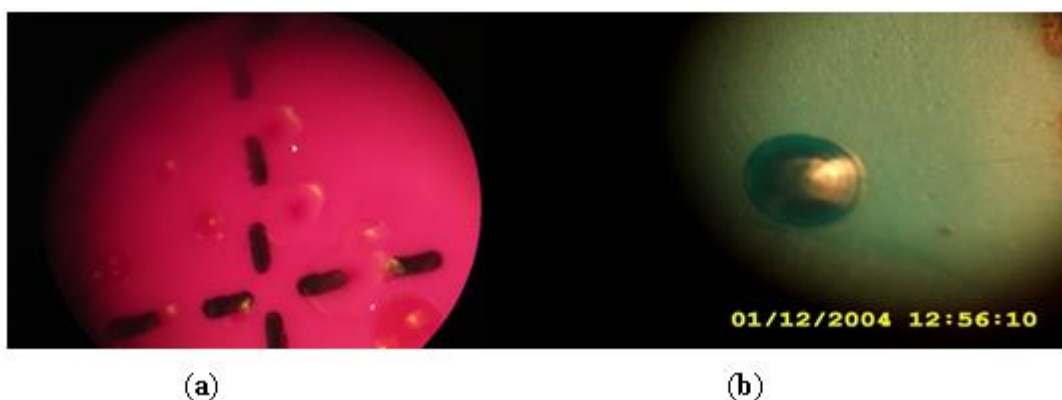


Fig. 5. Total coliform colonies (a) and Faecal coliform colonies (b) with (10 to 15 x) microscope magnification

Further identification of total and thermotolerant/ faecal coliform was made by examining the colonies under an epifluorescence microscope (Olympus BX51, Japan) attached to a CCD camera. Analyses Docu soft-ware (cc12 Docu, Germany) was used for image acquisition of the respective colonies as shown in Fig. 6(a) and 6(b).

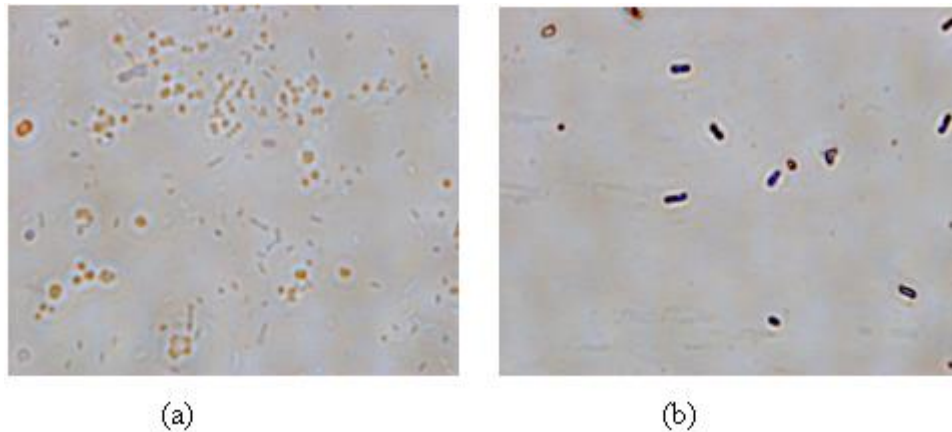


Fig. 6. Epifluorescence microscopic examination of Total coliform bacteria (a) and thermotolerant/ faecal coliform bacteria (b)

## 2.6. Statistical Analyses of Data

The 40 households with SSF in clay pots were selected by ILRI in collaboration with the peasant association. All 40 households with a clay pot filter were included in the study, representing 5 % of the 796 households in the area. Half of these, 20 households were located in the highland part of the area, using a spring as their major water source. The other 20 were located in the low land part and used a river. Results of water analyses were compared against standards set by World Health Organization and Federal Democratic Republic of Ethiopia, Ministry of Water Resources for drinking water qualities (WHO, 2012b). The data were analyzed using the statistical software SPSS version 20 for windows. Removal efficiency of SSF was calculated using Microsoft Excel.

## 2.7. Ethical Consideration

Informed consent was obtained from the concerned offices and community leaders before implementing the actual study. Sampling of water was carried out with full consent of the head of the households. Before each sampling, the study objectives were clearly explained to the households, that the aim of the study was neither to evaluate the performance of the individual nor to blame any one for weakness, but to gather information that might lead to eventual improvement in the situation. Each household was assured that the information provided would be confidential and used only for the purpose of research.

## 3. RESULTS

### 3.1. Total Coliform (TC), Thermotolerant/Faecal Coliform (TTC/FC) and Turbidity (TR) Removal by SSF in Clay Pots

Table 1 shows mean analyses of water samples for TC, TTC/FC and turbidity from influent and effluent of SSF in clay pot for spring users. The results revealed that average TC from influent was 888.9 cfu/100\_ml while from effluent was 5.5 cfu/100ml. Moreover, average TTC/FC from influent was 289.4 cfu/100ml where as from effluent it was 2.5 cfu/100ml. Similarly, average turbidity from influent was 9.0 NTU and from effluent it was 0.9 NTU.

The effectiveness of SSF in clay pot in removing microbial pathogens from water was based on TC and TTC/FC colony counts from the influent water samples versus samples taken from the effluent. Table 2 shows removal efficiencies for each SSF in clay pot for spring users. The result showed that an average removal efficiency of SSF in clay pot were 97.4 and 96.9 % for TC and TTC/FC bacteria, respectively, while the removal efficiency for turbidity was 92.9 % were found.



Table 1. TC, TTC/FC and Turbidity (TR) from influent and effluent of SSF in clay pots for spring users (n = 20)

H H. No	Influent TC	Effluent TC	Influent FC	Effluent FC	Influent TR	Effluent TR
1	780.7	11.3	256.0	4.7	6.0	0.8
2	1016.3	12.3	260.0	4.3	6.3	0.7
3	1030.3	13.3	340.0	5.7	4.7	1.0
4	926.0	7.3	176.0	6.7	4.7	0.8
5	803.0	5.3	340.0	3.0	11.0	1.0
6	706.7	11.7	283.0	7.0	6.3	1.3
7	1036.0	13.7	360.0	4.7	4.3	1.0
8	773.7	11.0	256.0	5.7	6.7	0.7
9	810.0	4.0	290.0	7.3	6.3	0.8
10	1013.0	5.6	210.0	6.0	6.3	0.7
11	780.7	7.7	280.0	1.7	5.3	1.0
12	956.0	12.7	240.0	4.7	8.0	0.5
13	970.3	2.3	376.0	3.0	6.3	1.0
14	933.0	10.7	300.0	7.3	4.0	0.8
15	770.7	2.3	273.0	7.3	6.7	0.8
16	863.0	2.0	360.0	5.0	6.0	0.8
17	1020.0	2.3	176.0	8.3	6.0	1.0
18	763.3	11.7	296.0	2.7	7.0	0.8
19	893.3	7.3	456.0	1.0	5.7	0.8
20	933.7	7.0	260.0	5.7	6.7	1.0
<b>Mean</b>	<b>888.9</b>	<b>5.5</b>	<b>289.4</b>	<b>2.5</b>	<b>9.0</b>	<b>0.9</b>
<b>S.D</b>	<b>339.2</b>	<b>0.9</b>	<b>49.4</b>	<b>0.4</b>	<b>1.5</b>	<b>0.2</b>

Table 2. Removal efficiencies of each SSF in clay pots for TC, TTC/FC and Turbidity, per 100 ml of water samples for spring users (n =20)

HH No.	Removal efficiency (%)		
	TC	TTC/FC	TR
1	99.0	97.5	84.6
2	98.7	98.3	84.5
3	97.9	98.4	98.3
4	94.3	93.2	81.9
5	99.3	99.3	85.0
6	98.5	95.5	97.1
7	93.0	98.4	95.0
8	93.5	96.4	82.6
9	99.3	97.4	86.2
10	96.3	94.7	89.0
11	99.1	99.2	96.9
12	95.7	97.8	93.7
13	99.7	99.3	82.9
14	98.8	97.5	99.4
15	96.3	95.0	87.7
16	97.2	98.2	96.1
17	99.7	95.1	82.5
18	98.5	93.1	87.3



19	99.2	97.8	94.2
20	94.1	97.7	84.1
<b>Mean</b>	<b>97.4</b>	<b>96.9</b>	<b>92.9</b>
<b>S.D</b>	<b>15.9</b>	<b>15.8</b>	<b>15.2</b>

Table 3 shows mean results of analyses of water samples for TC, TTC/FC and turbidity from influent and effluent of SSF in clay pots for river users. The result revealed that average TC from influent was 824.0 cfu/100ml where as from effluent it was 4.8 cfu/100\_ml. In addition, average TTC/FC from influent was 267 cfu/100ml, and from effluent it was 2.0 cfu/100ml. Similarly, average turbidity from influent was 8.4 NTU and from effluent it was 0.9 NTU. Again the results of TC, TTC/FC and turbidity from effluent of SSF in clay pot are at acceptable level which meets the standards set by the World Health Organization and the Federal Democratic Republic of Ethiopia Ministry of Water Resources (WHO, 2012b).

Table 3. TC, TTC/FC and Turbidity (TR) from influent and effluent of SSF in clay pots for river users (n =20)

HH No	Influent TC	Effluent TC	Influent FC	Effluent FC	Influent TR	Effluent TR
1	850.0	7.0	156.7	2.3	7.3	0.8
2	756.7	11.7	200.0	5.3	6.0	0.8
3	876.7	3.0	153.3	3.7	4.3	0.5
4	1126.7	16.3	160.0	7.3	8.3	0.5
5	716.7	5.7	276.7	7.7	7.3	1.0
6	796.7	5.3	333.3	3.0	9.3	1.7
7	613.3	8.7	396.7	5.3	6.7	1.2
8	730.0	8.7	353.3	8.7	7.0	1.3
9	980.0	11.3	276.7	3.0	6.3	1.3
10	800.0	10.7	360.0	8.7	6.7	0.7
11	1020.0	7.0	296.7	8.3	5.7	1.3
12	756.7	5.7	236.7	4.3	6.7	1.0
13	833.3	7.0	163.3	1.7	7.0	1.2
14	480.0	4.0	286.7	5.3	6.0	1.3
15	766.7	10.0	313.3	9.0	5.3	0.8
16	876.7	14.0	243.3	10.7	6.7	0.7
17	870.0	6.3	330.0	3.0	5.0	0.8
18	876.7	10.7	313.3	9.0	4.0	0.7
19	906.7	9.0	256.7	1.0	6.7	1.2
20	846.7	11.7	233.3	3.0	6.0	0.8
<b>Mean</b>	<b>824.0</b>	<b>4.8</b>	<b>267.0</b>	<b>2.0</b>	<b>8.4</b>	<b>0.9</b>
<b>S.D</b>	<b>140.5</b>	<b>0.8</b>	<b>45.5</b>	<b>0.3</b>	<b>1.4</b>	<b>0.2</b>

Table 4 shows removal efficiencies for each SSF in clay pots for river users. The result showed that an average removal efficiency of SSF in clay pots were 97.9 and 96.5 % for TC and TTC/FC bacteria, respectively, while the removal efficiency for turbidity was 93.1 %.



Table 4. Removal efficiencies of each SSF in clay pots for TC, TTC/FC and TR, per 100 ml of water samples, for river users (n =20)

HH No.	Removal efficiency (%)		
	TC	TTC/FC	TR
1	99.1	98.6	88.2
2	96.4	96.9	95.4
3	99.6	97.4	87.8
4	99.1	95.4	93.9
5	99.2	93.5	86.3
6	95.4	98.9	81.9
7	98.5	98.3	81.9
8	98.3	97.5	99.7
9	98.8	94.9	97.9
10	98.7	97.2	90.3
11	97.2	97.1	95.2
12	98.9	93.5	84.7
13	99.1	98.5	80.3
14	93.2	96.6	97.5
15	98.6	95.7	80.2
16	98.4	95.6	99.8
17	99.3	98.5	83.3
18	94.7	94.5	90.6
19	98.9	95.8	82.5
20	98.3	97.4	84.6
<b>Mean</b>	<b>97.9</b>	<b>96.5</b>	<b>93.1</b>
<b>S.D</b>	<b>16.7</b>	<b>16.4</b>	<b>15.9</b>

Fig. 7 shows the distribution of water samples in each range of TC and TTC/FC from influent and effluent of SSF in clay pot for both spring and river users. The results in Fig. 7 revealed that 16(40 %) of water sample taken from the influent had 1 to 10 TC (cfu/100ml) which is ‘a reasonable quality’, 14(35 %) had 11 to 100 TC (cfu/100ml) found in the ‘polluted’ range, 5(12.5 %) tested 101 to 1000 TC (cfu/100ml) which is ‘dangerous’ range, while 5(12.5 %) were over 1000 TC (cfu/100ml) which is found in ‘a very dangerous’ range according to the standards set by the World Health Organization and the Federal Democratic Republic of Ethiopia, Ministry of Water Resources (WHO, 2004b). Similarly, 18(45 %) of water sample taken from the influent had 1 to 10 TTC/FC (cfu/100ml) which is ‘a reasonable quality’, 9(22.5 %) tested between 11 to 100 TTC/FC (cfu/100ml) found in ‘polluted’ range, 11(27.5 %) tested 101 to 1000 TTC/FC (cfu/100ml) ‘dangerous’ range, while 2(5 %) were over 1000 TTC/FC (cfu/100ml) which is found in ‘a very dangerous’ range. Whereas 19(47.5%) of water sample taken from the effluent had Zero TC (cfu/100ml) which is ‘safe water’ and 21(52.5%) tested 1 to 10 TC (cfu/100\_ml) ‘a reasonable quality’. In addition, 18(45%) of water sample taken from the effluent had Zero TTC/FC (cfu/100ml) ‘safe water’ and 22(55%) tested 1 to 10 TTC/FC (cfu/100ml) which is ‘a reasonable quality’ range according to the standards set by the World Health Organization and Federal Democratic Republic of Ethiopia, Ministry of Water Resources (WHO, 2012b).

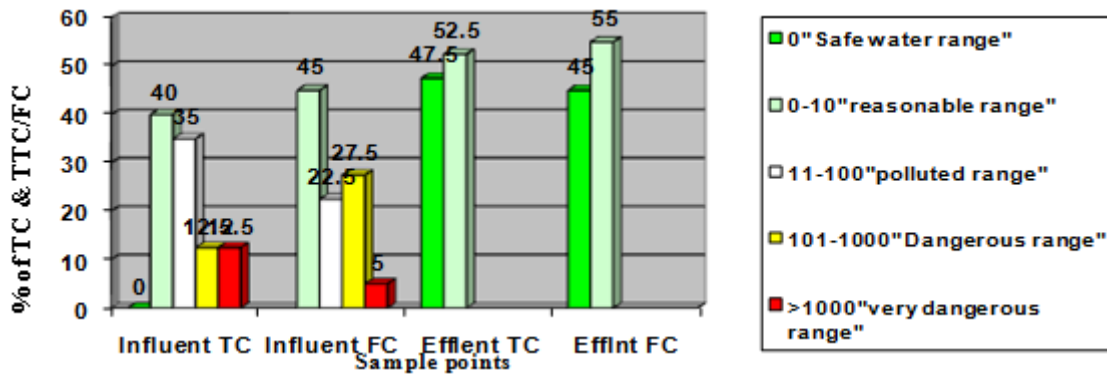


Fig. 7. Ranges of TC and TTC/FC from influent and effluent of SSF in clay pots

### 3.2. Perception and Observations

In addition to water quality analysis, the field work consisted of interviews and observations to record overall satisfaction of filter users. The following results were obtained:

In 37 of the households, the filtered water was used only for drinking. None of the households treated the water with chlorine and boiling after filtering. In 38 of the households, they poured the source water directly in to the slow sand filter, not allowing time for sedimentation or settling. All of the households reported that the filter was easy to use, and that the children who were old enough to lift the bucket could use the filter. In 39 of the households said that the filter produced enough water for the entire household. All of the households responded that they liked the filters, 39 households stated that the treated water had better taste, smell and appearance and gave health protection and 38 said the system worked well. Thirty nine households responded that they would recommend the filter to others.

In 3 of the 40 households reported that they had had problems with slow flow rates and two said that they had to obtain assistance from Community Development to correct the problem. In all of these cases, the problem was blocking of the filter due to impurities and suspended solids in the water. All were easily corrected by a simple cleaning procedure.

Results of observations indicated that in 39 of the cases the filters appeared to be clean and well-maintained and were functioning at the time of the unannounced first visit. The filters were found to be durable with a few observed to be having minor problems such as cracked lids or diffuser plates. One of the filters was found to have a crack near the lip of the filter above the spout, but it was still being used and seemed to function well and seven other filters was found to have been broken near the lip of the filter, a place where an outlet hose become attached, during transportation to the home. For all of these it was replaced by a new one. At the time of the second visit, in all of the cases, the filters were found to be well-maintained, functioning properly and sustainable, implying regular use.

## 4. DISCUSSION

Health is determined by many factors, including income, environmental conditions like access to adequate sanitation and safe drinking water supplies, behavioral change and availability of health services. More than half of the world’s population lives in villages in rural areas and most of those without access to safe drinking water supply or basic sanitation are rural dwellers (Howaard et al., 2013).

Several qualitative studies on the evaluation of the effectiveness of SSF in removing coliform bacteria and reduction of turbidity have been carried out in various countries; however, this is the first report on the evaluation of the effectiveness of SSF in clay pot in removing TC, TTC/FC and of turbidity from drinking water in rural areas of Ethiopia.

In the present study, the result of TC, TTC/FC and turbidity from effluent of SSF in clay pot is in a reasonable water quality range according to the standards set by the World Health Organization and the Federal Democratic Republic of Ethiopia, Ministry of Water Resources (WHO, 2012b). The analyses of water samples from influent and effluent of SSF for total and faecal coliforms and turbidity conducted in rural district of Chikwana in southern



Malawi (Huisman and Wood, 2014). The result showed that analyses from effluent of SSF for all parameters 6.5 cfu/100ml, 3.0 cfu/100ml and 0.8 NTU were found, which meets the standards of World Health Organization while from influent of SSF were not met, which is found to be similar with the present study. A study on analyses of water quality from influent and effluent of SSF for faecal coliforms and turbidity conducted by Huisman and Wood showed that analyses from effluent of SSF were 2.5 cfu/100ml and 0.8 NTU, which meets the standards of World Health Organization (Hijnen, 2014; Kuypers, 2014; Grice et al., 2014; Rittmann, 2015; Wooley, 2015; Zhu, 2015).

In a study of the performance of a low cost household slow sand filtration system carried out in Haiti, it was reported that the system achieved 95.8% removal of coliform bacteria and a reduction on turbidity from 11.2 to 0.9 NTU (Duke and Baker, 2015), which is found to be similar with the present findings. In agreement to the present study, a study conducted in The Hague, Netherlands, suggested that SSF can achieve between 99 and 99.9 % reduction of coliform bacteria (Van Dijk and Ooman, 2013). However, removal efficiencies may be somewhat site specific as there is some variation in the findings from several authors. The variation in bacteria removals can be attributed to differences in source water quality conditions and filter operational conditions. In the present study, SSF in clay pots was efficient due to increased biological maturity of the filters. This resulted in a stable effluent quality. In addition, the increase is because of physical and biological layers in slow sand filtrations which are responsible for removal of microorganisms. The biological layer, known as biofilm, is mainly responsible for the removal of microorganisms from raw water. The growth of the biofilm increased the 'stickiness' of the filter medium and the specific bed surface, and thus raised the filtration efficiency value. Among the several biological processes occurring within slow sand filter beds, predatory action, maturity of sand bed, and biofilm development are very important for water purification.

Turbidity is one of the very important quality parameters. Turbidity may not have a direct health impact, but is more associated with the social acceptance of water. In the present study, water sources which are found in the study area especially produced water with high turbidity levels due to suspended particles. The filters under study were found very excellent in terms of turbidity removal. The water quality standards of the World Health Organization emphasize to have the turbidity of drinking water below 5 NTU (WHO, 2012b); thus, results of the clay pot filters meet the standards.

## 5. CONCLUSIONS AND RECOMMENDATIONS

The improvement of water quality is closely associated with man-environment relationships. There should be a dialogue between all stakeholders and the community when undertaking water and sanitation activities. Water analyses from the effluent of slow sand filtration in clay pot showed that it is safe for drinking purpose from bacteriological point of view. In light of results obtained so far, following conclusions are drawn:

- The study findings indicated that slow sand filtration in clay pot was found to be excellent to have a significant average removal efficiency of 97.4 % and 96.9 % for TC and TTC/FC bacteria, respectively, while the removal efficiency for turbidity was 92.9 % for spring users.
- Moreover, slow sand filtration in clay pot was found to have a significant average removal efficiency of 97.9 % and 96.6 % for TC and TTC/FC bacteria, respectively, while the removal efficiency for turbidity was 93.1 % for river users.
- Perceptions of the householders regarding: (a) the taste, smell and appearance of the filtered water, (b) ease of use of the filter, (c) health protection, and (d) sufficient quantity of water produced by the filter for the entire family, indicate high levels of overall satisfaction.
- Observations revealed that the filters were durable, and that most were well-maintained, and functioning properly.
- The study findings suggest that when considering the development and protection of any water source, improvement of environmental sanitation and hygiene promotion program should be one of the issues to be considered as top priority.
- It is recommended that dissemination of SSF to other poor rural areas of Ethiopia is required.



- Finally, the baseline information generated from this study may contribute to develop similar programs and also pave the way for further studies.

## REFERENCES

- Abebe Legesse. (2011): Hygienic water quality; its relation to health and the testing aspects in Tropical conditions, Department of Civil Engineering, Tempere University, Finland. 5-36.
- APHA (American Public Health Association). (1998): Standards methods for the examination of water and waste water, 20<sup>th</sup> ed. American Public Health Association, Washington DC, 9: 56-66.
- Bartram, J., Lewis, K., Lenton, R. and Wright, A. (2015): Focusing on improved water and sanitation for health. *Lancet*, 365: 810-812.
- Duke, W. and Baker, D. (2015): The use and performance of the biosand filter in the Artibonite valley of Haiti: a field study of 107 households. *Rural & Remote Health*, 6: 570-579.
- Eline, B. and Abiy Assefa. (2014): Preliminary study on slow sand filtration in removing indicator bacteria from drinking water in rural communities. Unpublished data ILRI, Addis Ababa, Ethiopia.
- Grice, E., Kong, H., Renaud, G., Young, A. and Bouffard, G. (2014): A diversity profile of the human skin microbiota. *Genome Research*, 18:1043–1050.
- Gundry, S., Wright, J. and Conroy, R. (2015): A systematic review of the health outcomes related to household water quality in developing countries. *Journal of water & Health*, 2(1): 1-13.
- Hijnen, W., Dullemeent, Y., Schijven, J., Hanzens-Brouwer, A., Rosielle, M. and Medema G. (2014): Removal and fate of cryptosporidium parvum, clostridium perfringens and small-sized centric diatoms (*stephanodiscus hantzschii*) in slow sand filters. *Journal of Water & health*, 3(2): 7-16.
- Howaard, G., Ince, M. and Smith, M. (2013): Rapid Assessment of Drinking water Quality: A Handbook for Implementation- Joint Monitoring for water supply and sanitation. WEDC, Loughborough University.
- Huisman, L. and Wood, W.E.(2014): Slow Sand Filtration. World Health Organization, Geneva, Switzerland. 1-89.
- IWSC (International Water and Sanitation Center). (2009): Guidelines for Hygiene Education in Community water supply and Sanitation. Occasional paper series 5. The Netherlands.
- Kuypers, M. (2014): Sizing up the uncultivated majority. *Science*, 317: 1510–1511.
- MoH (Ministry of Health, Ethiopia). (2010): Knowledge, Attitude and Practice of water supply, Environmental Sanitation and hygiene practice in selected Woredas of Ethiopia.
- Rittmann, B. (2015): Environmental Biotechnology in Water and Wastewater Treatment. *Journal of Environmental Engineering*, 136: 348–353.
- Van Dijk, J.C. and Ooman, J.H.C. (2013): Slow sand filtration for community water supply in developing countries: a design and construction manual. WHO International Reference Center for Community Water Supply, The Hague, Netherlands.
- WHO (World Health Organization). (2014): International Standards for drinking water. 3<sup>rd</sup> guidelines for drinking water quality. Health criteria and other supporting information. Geneva, World Health Organization 2.
- WHO (World Health Organization). (2012a): World Health Report: Geneva, World Health Organization. 1: 1-540.
- WHO (World Health Organization). (2012b): WHO guidelines for drinking water quality. 3<sup>rd</sup> ed. Geneva, World Health Organization, 143.
- Wooley, J.C., Godzik, A. and Friedberg, I. (2015): A Primer on Metagenomics. *PLoS Computational Biology*, 6: 1–13.
- Zhu, B., Wang, X. and Li, L. (2015): Human gut microbiome: the second genome of human body. *Protein & Cell*, 1: 718–725.



## Analysis of Cyprus Papyrus Wastewater Treatment Efficiency in Glass Fiber Constructed Wetland under Different Density

Abere Amogn<sup>\*1</sup>, Ayalew Wondie<sup>2</sup>, Derege Tsegaye<sup>3</sup>

<sup>1</sup>Department of Natural Resource Management, College of Agricultural Sciences, Arba Minch University, P.O. Box 21, Arba Minch, Ethiopia

<sup>2</sup>College of Agricultural and Environmental Sciences, School of Aquatic Ecology and Wetland Management, Bahir Dar University, bahir Dar, Ethiopia

<sup>3</sup>Department Of Natural Resource Management, College of Agricultural and Environmental Sciences, Bahir Dar University, Bahir Dar, Ethiopia

\*Corresponding author, e-mail: [amogn.abere@gmail.com](mailto:amogn.abere@gmail.com)

### ABSTRACT

Unsafe industrial and domestic waste disposal causes surface water contamination and different health problems in many developing countries like Ethiopia. To tackle the pollution problem research based mitigation method is highly needed. Therefore, this study was aimed to analysis Cyprus papyrus wastewater treatment efficiency in glass fiber constructed wetlands under different density. Total 12 glass fiber wetlands were constructed with dimensions of 1.5m length, 1.5m width and 0.8m depth. Four treatments unplanted (control), planted with low (61), medium (84) and high (125) density of Cyprus papyrus with three replication were used under the same gravel and sand substrate. The data were analyzed using SPSS version 20. The treatment beds were irrigated with wastewater sourced from Bahardar city administration. The result showed that the average above ground dry biomass of Cyprus papyrus in low, mid and high density treatment beds were 9.0ton/ha, 12.27ton/ha and 15.82ton/ha in 14 weeks growing period respectively. Except temprature, the analysis of variance showed a significant difference at ( $p < 0.01$ ) among the treatments. The removal efficiency of high density Cyprus papyrus BOD, TSS, TDS, turbidity, TA, SC,  $PO_4^{3-}$ ,  $NO_3^-$  and ammonia were 68.4%, 63.7%, 19.9%, 83.5%, 34.2%, 36.2%, 75.6%, 21.2% and 88.5%, respectively during five days duration of wastewater in the glass fiber constructed wetland had significant difference at 0.01. And also the removal efficacy of heavy metals Cu, Cr, and Zn were 66%, 45.8%, and 66.1% respectively in effluent from high density Cyprus papyrus had significant difference at 0.01. Density of plant directly proportional to pH and DO and inversely proportional to other parameters whereas, temperature was found under oscillation relationship. Thus, Cyprus papyrus reduced substantially the concentrations of most physicochemical parameters and heavy metals. Finally, wastewater treatment by using Cyprus papyrus could be encouraged in Ethiopia.

**Keywords:** constructed wetland, Cyprus papyrus, heavy metals, nutrients, wastewater

### 1. INTRODUCTION

Wastewater is any water that has been adversely affected in quality by anthropogenic influence (Abdel *et al.*, 2010). Currently used traditional treatment options like activated sludge, most often, do not provide adequate treatment as they completely fail to eradicate pathogenic organisms from wastewater (Ibrahim *et al.*, 2020). In Bahir Dar City sixty-four percent of the respondents discharge their wastewater in to the streets and open fields and the inadequacy of sanitation services resulted in defecating in open fields and discharging of raw wastewater into inappropriate places and these, in turn, have created serious environmental problems (Fesseha Hailu, 2012). Farms are irrigated with water from the lake and river waters that are heavily contaminated by waste disposal from different sides of the cities. With the increase in the urban population and industrialization, these water sources have now become further contaminated with various pollutants, among which are heavy metals (Mekonnen Getahun & Yihenew G. Selassie, 2013). However, gradual availability and uptake of heavy metals by plants is major concern as it may enter to humans through food web (FAO, 2006).

Based on Wu *et al.* (2016) Constructed wetland (CW) is a system engineered for treating wastewaters by using plants, soil and microorganisms, to improve the water quality and is an effective treatment system alternative where suitable land is available at low cost. *Cyprus papyrus* (papyrus) is a large herbaceous sedge commonly found in waterlogged environments in the African tropics. Such wetland ecosystems provide ecological and socio-economic services related to the harvesting of aerial biomass, wastewater treatment, hydrological functions and



climate modification (Güereña *et al.*, 2015). Papyrus can have very high C: N: P ratio (Boar, 2006) in comparison to temperate wetland plants; a characteristic that provides an indication of its high nutrient efficiency and during processing, organic substances present in wastewater and undergo a process of oxidation of organic or inorganic compounds in the form of ions such as  $\text{NO}_3^-$ ,  $\text{NH}_4^+$  and so can be absorbed by Papyrus.

Unsafe industrial and domestic waste disposal causes surface water contamination in many developing countries like Ethiopia. This is particularly true in towns and the rural hinterland villages downstream of cities that are dependent on rivers passing through an industrialized area like Bahir Dar City and soundings. Especially discharge of untreated industrial waste is a major problem for many communities dwelling near rivers basins through causing different health problems (Arega Shumetie and Molla Alemayehu, 2014). Many wetlands receive and reduce nutrients and pollutants, as a result they are sometimes described as "the kidneys of the landscape" and as "biological supermarkets" because of the extensive food webs and rich biodiversity they support (Mitsch and Gosselink, 2007). Wastewater treatment using natural plants (*Cyprus papyrus*) has been considered the most environmental friendly method. In addition to the above reason to select *Cyprus papyrus* for wastewater treatment it is also native in Ethiopia and is not invasive species.

Many researchers studied wastewater treatment efficiency and growth of aquatic macrophyte species (*Cyprus papyrus*) etc., under constructed wetlands. However they lack of consider plant density, constructed wetlands from cement and metals which react with wastewater and also without replication of the treatment beds. *Cyprus papyrus* planted in the surrounding of few wastewater disposal of the study area like Bahir Dar University but they did not done laboratory analysis. Untreated wastewater disposal water scarcity and problem of wastewater reuse, wetland degradation surrounding Lake Tana and river Abay is visible problem in the study area Therefore construction and restoration of wetland, determination of plant density and study wastewater treatment potential of *Cyprus papyrus* helps to propose solutions. Hence this research was intended to fill the research gap on wastewater treatment potential of *Cyprus papyrus* under different density with in glass fiber constructed wetlands (did not react with wastewater).

The overall objective of this study was to analysis *Cyprus papyrus* wastewater treatment efficiency in glass fiber constructed wetlands under different density. Bahir Dar City Ethiopia. The specific objectives of this study were to: (1) assess plant biomass production and nutrient storage of *Cyprus papyrus* under different density; (2) analysis physical and chemical characteristics of wastewater influent and effluent under different treatment; and (3) examine selected wastewater heavy metal removal efficiency of *Cyprus papyrus*

## 2. MATERIALS AND METHODS

### 2.1. Description of the Study Area

This study was conducted in Amhara regional state, Bahir city specifically Bahir Dar university in Peda compass, 37°23'57" East and 11° 34' 24" North with 1794 m above sea level (Figure 1). Bahir Dar, the capital of Amhara National Regional State, is situated on the southern shore of Lake Tana, the source of Blue Nile River, approximately 565 kms northwest of Addis Ababa.

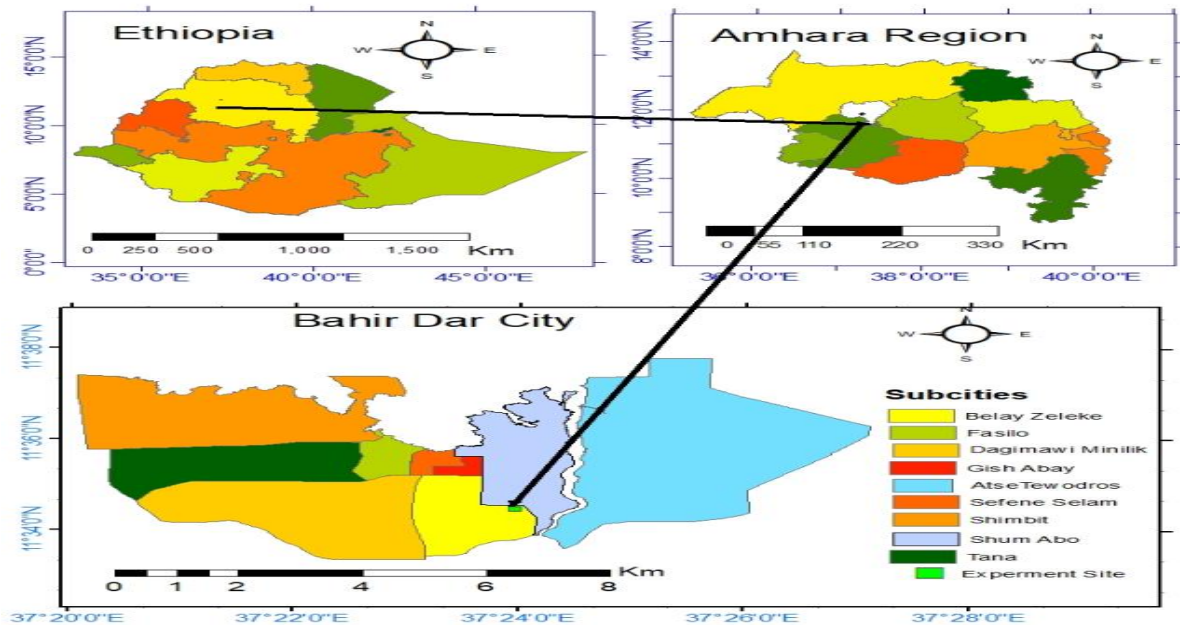


Figure 1: Map of the study area

## 2.2 Sources of Data

The main primary sources of data were the growth characteristics survey data, plant dry biomass and physicochemical characteristics both in the field and laboratory. The sources of secondary data were from literatures, organization departmental reports, journal, magazine, Internet and reports which contain related information on liquid waste treatment and *Cyprus papyrus*.

## 2.3 Experimental Design

Twelve wetlands CW1, CW2, CW3, up to CW12 of 1.5m Length\* 1.5 m width\* 0.8 m depth each were constructed using Glass fiber tanks (Figure 2). The system consists of four treatment beds with three replication aligned in parallel was designed. The steam density of *Cyprus papyrus* 0, 12, 24 and 36 per bed initial density of *Cyprus papyrus* respectively in 14 weeks growing period with total surface area of each glass fiber tanks (2.25m<sup>2</sup>). Coarse and fine gravel and sand were used as a substrate 15 to 30mm size except one in the out let with 40-80 mm gravel to prevent clogging which was the recommended gravel size by USEPA (2000).The substrate was filled to a height of 45 cm. Rhizomes carrying young shoots of *C. papyrus* plants average 10 cm height in the planting time.

## 2.4 Data Collection from the Treatment Beds

### 2.4.1 Measurement of the growth parameters of the plants

Plant density in the treatment bed, plant height, stem diameter and biomass were considered growth parameters of the young plants and Plant density by counting, plant height by meter tab, stem diameter by caliper were measured every two weeks. AGB of papyrus was determined by harvesting (0.3 m x 0.3 m) quadrats in each plantedbeds in the 14<sup>th</sup> weak. Fresh weight was determined for the harvested materials (above- ground parts) then were oven dried to until a constant weight at 105°C and dry weight was determined by sensitive balance.

### 2.4.2 Measurement of plant nutrient content

Prior to nutrient analysis; leaf and stem samples were pulverized and made into fine powder by grinder. The powder of each sample was used in the analysis for total nitrogen (TN), total phosphorus (TP) in the laboratory. The concentration of N in plant tissues was determined using the Kjeldahl method, while P was measured by the molybdate ascorbic acid method and amount of C sequestration also determined by, amount of above ground dry biomass \* 43.5% for herbaceous plants (Ma *et al.*, 2018).



Figure 2. Installation (a), plantation day (b), after eight weeks (c) and after fourteen weeks (d)

### 2.5 Analysis and Measurement of Physico-chemical Parameters of Water Quality

Three samples from influent( before treatment) and 12 samples from treated wastewater effluent coming out of treatment beds were taken in one sampling time for with in seven sampling times so, the total samples were 105 in seven sampling time. Samples were taken after acclimation period for seven times with one week interval after established plants grew fully. The physicochemical parameters such as pH, temperature (T°), specific conductance (SC), dissolved oxygen (DO) were measured on site by using YSI DO meter, total dissolved solids (TDS) by using TDS Sensor/Meter, total suspended solid (TSS) by using filter paper, turbidity by turbidometer, biological oxygen demand (BOD<sub>5</sub>) by using dilution and BOD<sub>5</sub> bottle, alkalinity is determined by simple titration in presence of phenolphthalein and methyl orange indicators. Nitrate, phosphate, ammonia, heavy metals (Cu, Cr, Zn) were measured by using Palintest Photometer 7100 systems (precise, modern means of water analysis) with ±1.0% accuracy. The removal efficiency of the treatment beds for each wastewater quality parameter was calculated using the following formula:

$$\text{Removal Efficiency (\%)} = [(C_i - C_e)/C_i] \times 100 \dots\dots\dots 1$$

Where, C<sub>i</sub> is the concentration of the waste material in the influent (before treatment) and C<sub>e</sub> is the concentration of the waste material in the effluent after treatment (Yezbie and Seyoum, 2014).

### 2.6 Statistical analysis

The data were analyzed through one-way analysis of variance (ANOVA) at 95% confidence level to compare the performance efficiency of each treatment bed with respect to nutrient removal and also above ground biomass production and nutrients storage of *Cyprus papyrus* under deferent density using Statistical Package for Social Sciences (SPSS) software, Version 20.0.



### 3. RESULTS AND DISCUSSION

#### 3.1. Biomass Production, Growth and Nutrient Storage of *Cyprus Papyrus* under Different Density

##### 3.1.1 Biomass production and growth of *Cyprus papyrus* under different density

From the density of 12/36, 8/24, and 4/12 rhizome fragments and shoots respectively per 2.25 m<sup>2</sup>, 125, 84, and 61 plants were obtained respectively in high, medium and low density of *Cyprus papyrus* after 14 weeks growing period in the glass fiber tanks constructed treatment beds during which the system was continuously fed with domestic wastewater. The plant growth rate of *Cyprus papyrus* in high, mid and low density *Cyprus papyrus* fed by wastewater were estimated 1.91 cm/day, 1.93cm/day and 1.96 cm/day average plant height growth figure 3.1 and 0.23mm/day, 0.24mm/day, 0.27mm/day average plant diameter respectively. As indicated in Table 4.1 plant density had significant change above ground biomass. The above ground biomass in low, mid and high density were 9.0ton/ha, 12.27ton/ha and 15.82ton/ha respectively in 14 weeks growing period. In addition to this from the wet biomass the average moisture content of the plant were above 81%. In herbaceous plants, water normally constitutes 70- 90% of fresh weight, although in rare cases it can be less than 70% (Dimitrakopoulos & Bemmerzouk, 2003).

##### 3.1.2 Nutrient storage of *Cyprus papyrus* under different density

*Cyprus papyrus* had higher average plant nitrogen concentration (2.44%) than phosphorus (0.14%). The total phosphors (TP) from average above ground dry biomass *Cyprus papyrus* were 0.013ton/ha, 0.017ton/ha and 0.022ton/ha and the total nitrogen (TN) 0.22ton/ha, 0.3 ton/ha, and 0.39ton/ha and also sequestered carbon 3.91ton/ha, 5.33ton/ha and 6.88 ton/ha respectively low, medium and high density of *Cyprus papyrus* in 14 weeks growing period (Table 1). The high biomass and nutrient contents of the plants may have been caused by the high nutrient levels in the surrounding water. Nitrogen is considered to be the most important nutrient, and plants absorb more nitrogen than any other element (Näsholm et al., 2009).

Table 1. Mean AGDB, nutrient storage, carbon sequestration and moisture content of *C.papyrus*

Treatment	Unit	High density	Mid density	Low density	P value
		Mean	Mean	Mean	
Density	Steam/m <sup>2</sup>	55 <sup>a</sup>	37 <sup>b</sup>	27 <sup>c</sup>	**
AGB	ton/ha	15.82 <sup>a</sup>	12.27 <sup>b</sup>	9.00 <sup>c</sup>	**
TP	ton/ha	0.022 <sup>a</sup>	0.017 <sup>b</sup>	0.013 <sup>c</sup>	**
TN	ton/ha	0.39 <sup>a</sup>	0.3 <sup>b</sup>	0.22 <sup>c</sup>	**
C	ton/ha	6.88 <sup>a</sup>	5.33 <sup>b</sup>	3.91 <sup>c</sup>	**
MC	%	81.71	81.88	81.86	ns

The means, followed by the same letter in a row are not statistically different at (P<0.05).

\*\* The mean difference is significant at the 0.01 level.

Ns= the mean difference is not significance both at 0.01 and 0.05 level.

#### 3.2 Physical and Chemical Characteristics of Influent and Effluent Wastewater under Different Treatment

##### 3.2.1 Total dissolved solid and Turbidity

The influent TDS value were 699 mg/L, reduced into 652.5mg/L, 608 mg/L, and 598 mg/L and 559.3mg/L (Table 3.2) with removal efficiency of 6.6%, 13%, 14.4% and 19.9% ( Table 3.3) in unplanted, low, medium and high density *Cyprus papyrus* treatment beds respectively. Turbidity of influent 32.99 NTU reduced into effluent 21.16NTU, 17.35NTU, 9.63NTU and 5.43NTU with removal efficiency of 35.8%, 47.4%, 70.8% and 83.5% in control (no plant), low, medium and high density of *Cyprus papyrus* treatment beds respectively. Theophile *et al.* (2011) conclude that TDS influent, reduced into 7.1% and 28.9% in unplanted and planted of *Cyprus papyrus* value respectively.



### 3.2.2 Specific conductance and total alkalinity

In the current study the specific conductance of influent 1482.8 $\mu$ S/cm reduced into effluent 1361.7 $\mu$ S/cm, 1279 $\mu$ S/cm, 1040 $\mu$ S/cm and 945.6  $\mu$ S/cm (Table 3.2) with removal efficiency of 8.1%, 13.7%, 29.8% and 36.2% (Table 3.3) in control (no plant), low density, medium density and high density of *Cyprus papyrus* treatment beds respectively. In this study the alkalinity value of influent 303.65 mg/l reduced in to effluent 266.6 mg/l, 238 mg/l, 229mg/l and 199.67 mg/l (Table 3.2) with removal efficiency of 12.1%, 21.6%, 24.5%, and 34.2% (Table 3.3) in control (no plant), low, medium and high density of *Cyprus papyrus treatment beds* respectively.

### 3.2.3 Biological oxygen demand

The influent concentration of BOD 88.2 mg/l reduced to 65.22, 56.37, 36.06 and 27.86 mg/L (Table 2) with removal efficiency values of 26%, 36%, 59.1% and 68.4 % ( Table 3) in control, low, mid and high density of *Cyprus papyrus* treatment beds respectively with in five day detention time. It had significance difference at 0.01 value of p with in treatment beds. Yadav *et al.* (2018) concluded that a BOD<sub>5</sub> removal efficiency 71.38% were achieved through constructed wetlands planted with *Cyprus papyrus* with gravel.

Table 2 physicochemical characteristic of the effluent monitored at the inlet and the outlets

Parameters	Influent Values (before treatment)	Effluent Values( after treatment)							
		Un planted (control)	Planted with <i>Cyprus papyrus</i>			p value	CV %	LSD	
			Low density	Mid density	High density			0.01	0.05
TDS (mg/l)	699.00	652.5 <sup>a</sup>	608 <sup>ab</sup>	598 <sup>ab</sup>	559.3 <sup>b</sup>	**	4.8	80.1	55.11
BOD (mg/l)	88.20	65.22 <sup>a</sup>	56.37 <sup>b</sup>	36.06 <sup>c</sup>	27.86 <sup>d</sup>	**	3.9	4.9	3.4
TSS (mg/l)	800.43	577.60 <sup>a</sup>	528.8 <sup>a</sup>	391.1 <sup>b</sup>	290.0 <sup>c</sup>	**	4.9	60.4	41.5
DO(mg/l)	1.16	1.17 <sup>b</sup>	1.990 <sup>a</sup>	1.993 <sup>a</sup>	2.34 <sup>a</sup>	**	6.5	0.33	0.23
Turbidity(NTU)	32.99	21.16 <sup>a</sup>	17.35 <sup>b</sup>	9.63 <sup>c</sup>	5.43 <sup>d</sup>	**	4.7	1.74	1.19
Temperature(°C)	22.67	22.48	22.60	21.98	22.32	Ns	2.1	1.28	0.88
TA(mg/l)	303.65	266.6 <sup>a</sup>	238 <sup>ab</sup>	229 <sup>ab</sup>	199.67 <sup>b</sup>	**	8.5	55.8	38.4
SC( $\mu$ S/cm)	1482.83	1361.7 <sup>a</sup>	1279 <sup>a</sup>	1040 <sup>b</sup>	945.60 <sup>b</sup>	**	4.5	144	99.5
pH	6.27	6.51 <sup>b</sup>	6.77 <sup>ab</sup>	6.80 <sup>a</sup>	6.83 <sup>a</sup>	**	1.4	0.27	0.18
NO <sub>3</sub> <sup>-</sup> (mg/l)	1.46	1.38 <sup>a</sup>	1.31 <sup>ab</sup>	1.31 <sup>ab</sup>	1.15 <sup>b</sup>	**	5.4	0.19	0.13
Ammonia (mg/l)	38.54	19.70 <sup>a</sup>	9.87 <sup>b</sup>	8.19 <sup>b</sup>	4.42 <sup>c</sup>	**	9.2	2.68	1.84
PO <sub>4</sub> <sup>3-</sup> (mg/l)	4.15	3.30 <sup>a</sup>	1.86 <sup>b</sup>	1.12 <sup>c</sup>	1.01 <sup>c</sup>	**	10	0.53	0.36

\*\* The mean difference is significant at the 0.01 level.

Ns= the mean difference is not significance both at 0.01 and 0.05 level.

CV= Coefficient of variance

LSD=least significant difference

The means Values followed by the same letter on the same row are not statistically significantly different at  $p < 0.01$

### 3.2.4 Total suspended solid

In the current study, the average TSS value in the influent wastewater was 800.43 mg/L (Table 2). Following treatment in, TSS reduced to 27.8% (577.6 mg L-1) in control bed, 33.9% (528.8 mg L-1) in low density bed and reduction rate increased to 51.1% (391.1 mg L-1) and 63.7%(290 mg L-1) in mid and high density treatment beds respectively. This result indicates that when the plant density increase the TSS removal efficiency also increase. It had significance difference at 0.01. TSS greater proportional decrease with the addition of Plant density (Erina and Wiyono, 2012). Dewedar *et al.* (2018) also conclude that the removal efficiency of TSS was 51% by *Cyprus Papyrus*



Table 3. Percentages removal efficiency of Physicochemical Parameters of the effluent in the planted and the unplanted glass fiber Constructed Wetlands

Parameters	Effluent Values % removal efficiency			
	Planted with <i>Cyprus papyrus</i>			Unplanted(control)
	High density	Mid density	Low density	
	Mean	Mean	Mean	Mean
BOD	68.4	59.1	36	26
DO (increase)	50.4	41.8	41.7	0.8
TSS	63.7	51.1	33.9	27.8
Turbidity	83.5	70.8	47.4	35.8
TDS	19.9	14.4	13	6.6
TA	34.2	24.5	21.6	12.1
SC	36.2	29.8	13.7	8.1
pH(increase)	8.1	7.7	7.3	3.6
NO <sub>3</sub> <sup>-</sup>	21.2	10.9	10.2	5.4
Ammonia	88.5	78.7	74.3	48.8
PO <sub>4</sub> <sup>3-</sup>	75.6	73	55.1	20.4

### 3.2.5 Ammonia

The value of ammonia in the influent was 38.54 mg/L and decreased gradually to 19.7 mg/L, 9.87 mg/L, 8.19 and 4.42 mg/L (Table 2) with removal efficiency 48.8, 74.3, 78.7, and 88.5% (Table 3) in control (unplanted), low, mid and high density of *Cyprus papyrus* treatment beds respectively. Analytical results of ANOVA and least significant difference (LSD) value confirmed that values of Ammonia had statistically significant differences at (p<0.01) between planted and unplanted treatment beds. These results were also in agreement with Abou-Elela *et al.* (2013) who reported that nitrogen and phosphorus uptake by *Cyprus Papyrus* was better than other plants evaluated.

### 3.2.6 Nitrate

The NO<sub>3</sub><sup>-</sup> treatment potential of control, low, medium and high density *Cyprus papyrus* were 5.4, 10.2, 10.9 and 21.2%. It had significant difference planted from unplanted at P<0.01(Table 2). This reflects that conditions existed for nitrification (García-Avila *et al.*, 2019). During processing, organic substances present in wastewater and undergo a process of oxidation of organic or inorganic compounds in the form of ions such as NO<sub>3</sub><sup>-</sup>, NH<sub>4</sub><sup>+</sup> and so can be absorbed by Papyrus. The result showed that even if NO<sub>3</sub><sup>-</sup> was produced by nitrification process but lower than the NO<sub>3</sub><sup>-</sup> absorbed by Cyprus papyrus. Based on Negisa *et al.* (2019) *Cyprus papyrus* Municipal Wastewater removal efficiency of NO<sub>3</sub><sup>-</sup> were 22%. Another studies on nitrogen removal treatment have confirmed that unplanted treatment had lower nitrogen removal compared with planted treatment (Yang *et al.*, 2001 and Lin *et al.*, 2002).

### 3.2.7 Phosphate

ANOVA and Post Hoc LSD tests indicated that statistically significant differences (p<0.01) in removal of PO<sub>4</sub><sup>3-</sup> between planted and control treatment beds and also among planted treatment beds. All of the planted treatment beds had better efficiency in the removal of PO<sub>4</sub><sup>3-</sup> compared to unplanted treatment bed. The PO<sub>4</sub><sup>3-</sup> removal efficiency of unplanted, low, mid and high density of Cyprus papyrus treatment beds were 20.4, 55.1, 73 and 75.6% respectively (Table 3). Wiyono (2012) reported that Papyrus showed higher phosphorus removal efficiency (83.2%) than Miscanthidium (48.4%).

### 3.2.8 Temperature, pH and DO

Analysis of Varian’s and LSD test showed that temperature had non-significance difference between unplanted and planted treatment beds (Table 2). Hydrogen ion concentration (pH) of the effluent 6.83, and 6.80, in high and



medium density treatment beds had significant difference from control 6.51 but low density was not significant at  $P < 0.01$  (Table 2). The dissolved oxygen (DO) influent value 1.16 mg/l increase in the treatment beds 1.17, 1.99, 1.993 and 2.34 mg/l in unplanted, low, medium and high density treatment beds respectively (Table 4). pH increase 7.2 to 7.8 and DO also increase 0.28 to 1.3 respectively influent and effluent from *Cyprus papyrus* treatment beds (Dewedar et al., 2006).

### 3.3 Heavy Metal Removal Efficiency of *Cyprus papyrus*

#### 3.3.1 Copper (Cu)

The Copper (Cu) in the influent was 0.56mg/L and decreased gradually to 0.39, 0.27, 0.22 and 0.19mg/L (Table 4) with removal efficiency 30.3, 51.7, 60.7, and 66% (Table 5) in control (unplanted), low, mid and high density of *Cyprus papyrus* respectively. Cu was accumulated into plants as an essential micronutrient (Zabotto et al., 2020).

Table 4 selected heavy metals characteristics of the effluent monitored at the inlet and the outlets

Parameters	Influent Values (inlet)	Effluent Values ( out let)							LSD	
		Un Planted (control)	planted with Cyperus papyrus					CV		
			Mean	Low density	Mid density	High density	P value			
Cu (mg/l)	0.56	0.39 <sup>a</sup>	0.27 <sup>b</sup>	0.22 <sup>b</sup>	0.19 <sup>c</sup>	**	11.8	0.08	0.059	
Cr (mg/l)	0.24	0.22 <sup>a</sup>	0.18 <sup>ab</sup>	0.15 <sup>b</sup>	0.13 <sup>b</sup>	**	10.3	0.06	0.042	
Zn (mg/l)	0.62	0.50 <sup>a</sup>	0.41 <sup>b</sup>	0.24 <sup>c</sup>	0.21 <sup>c</sup>	**	9.2	0.05	0.034	

\*\* The mean difference is significant at the 0.01 level.

CV= Coefficient of variance

LSD=least significant difference

The means Values followed by the same letter on the same row are not statistically significantly different at  $p < 0.01$

Table 5 Percentages Reduction selected heavy metal (Cu, Cr and Zn) of the Effluent

Parameters	Effluent Values % removal efficiency			
	Planted with Cyperus papyrus			Unplanted(control)
	High density	Mid density	Low density	
Cu	66	60.7	51.7	30.3
Cr	45.8	37.5	25	8.3
Zn	66.1	61.2	33.8	19.3

#### 3.3.2 Chromium (Cr)

The influent concentration of Cr 0.24 mg/l reduced into 0.22 mg/l & 8.3%, 0.18 mg/l & 25 %, 0.15 mg/l & 37.5% and 0.13mg/l & 45.8% effluent concentration and removal efficiency in control, low, medium and high density *Cyprus papyrus* treatment beds respectively (Table 4 & 5). Cr value of Planted *Cyprus papyrus* treatment beds had significant difference compare from control at  $P < 0.01$ . Several plant species including *Cyprus papyrus* and *Phragmites australis* have been shown to accumulate high levels of various heavy metals (Deng et al., 2004).

#### 3.3.3 Zinc (Zn)

In the current study, the average Zinc (Zn) value in the influent wastewater was 0.62 mg/L (Table 4.4). Following treatment in constricted wetlands Zn concentration reduced by 19.3% (0.50mg/L) in control bed, 33.8% (0.41mg/L) in low density treatment beds and reduction rate increased to 61.2% (0.24mg/L) and 66.1% (0.21 mg/L) in mid and high density bed respectively (Table 4 & 5). The Zn removal increased with increasing the



number of plant stems and reached a maximum value (83%) (Hamad, 2020). Microbial symbionts such as mycorrhizae could influence the accumulation of metals in the wetland (Sheoran and Sheoran, 2006).

### 3.4 Correlation of Plant Density with Wastewater Removal Efficiency *Cyprus papyrus*

Plant density positively correlated with wastewater treatment efficiency of *Cyprus papyrus*. Such as BOD (0.926), TSS (0.793), TDS (0.807), NO<sub>3</sub><sup>-</sup> (0.686), NH<sub>3</sub> (0.886), PO<sub>4</sub><sup>3-</sup> (0.922) Turbidity (0.936), SC (0.946), Cu (0.864), Cr (0.756), and Zn (0.831). Because when the plant density increase the nitrification, nutrient absorption rate also increase. A greater ratio of plant biomass to wetland volume can enhance the contact between plant roots and wastewater resulting in a greater nutrient removal (Zhu and Ketola, 2011).

### 3.5 Compression of Treated Wastewater from EPA 2012 Recommended Irrigation Water Reuse Standards

The effluent value of most parameters in high density *Cyprus papyrus* treatment beds were under EPA 2012 guide line maximum limit for irrigation of agriculture, garden and aquaculture except row eaten crop the EPA recommended BOD value less than 10 mg/l (Table 6). The use of reclaimed water for irrigation is allow irrigation of food crops with reclaimed water only if the crop is to be processed and not eaten raw (EPA 2012). This indicates that wastewater treated by high density of *Cyprus papyrus* was very important for irrigation purpose.

Table 6. Comparison of high density treated wastewater with EPA 2012 standard recommended for irrigation water reuse maximum limit

Parameter	High density treated effluent value	EPA (2012) standard recommended for irrigation water reuse maximum limit
BOD	27.86 mg/l	30 mg/l
DO	2.34 mg/l	>2mg/l
SC	945.60 μS/cm	1000 μS/cm
PH	6.83	6.5-8.4
NO <sub>3</sub> <sup>-</sup>	1.15 mg/l	5mg/l
Ammonia	4.42 mg/l	10 mg/l
Cu	0.19mg/l	0.2mg/l
Zn	0.21 mg/l	2mg/l
Cr	0.13 mg/l	0.1 mg/l

## 4. CONCLUSION

Progressive increase above-ground dry biomass with increase the plant density. It was observed that *Cyperus papyrus* planted from the glass fiber tanks constructed wetlands significantly influenced the rate of removal of nutrients in wastewater. *Cyprus papyrus* wetlands had the ability to absorb nutrients and sequester significant amounts of carbon. It effectively reduced the concentrations of most physicochemical parameters and heavy metals. The result of the present work also revealed that *Cyprus papyrus* were hopeful for accumulating heavy metals. Generally density of plant directly proportional to pH and DO and inversely proportional to other parameters whereas, temperature was found under oscillation relationship. The analysis showed that most measured parameters in the high density *Cyprus papyrus* treated wastewater effluent value were under the EPA 2012 recommended maximum limits for irrigation.

## ACKNOWLEDGMENTS

I would like to say thanks ministry of education and Arba Minch University sponsored to learn this program. I would also like to say thanks the IUC project and Bahir Dar University for arrangement of financial support for my research work. And also grateful thanks to Bahir Dar University College of agriculture and environmental science, Natural resource management department staffs and faculty of civil and water resource engineering,



chemical engineering, laboratory technician and main campus installation workers for their support in laboratory works and installation activities of experimental constructed wetland system.

## REFERENCES

- Abdel, M. E., Wahid M. Y., and Moneim M., (2010). Chemical, physicochemical and physical properties of wastewater from the Sudanese fermentation industry (sfi). Fourteenth International Water Technology Conference, IWTC, Cairo, Egypt.
- Abou-Elela, S. I., Golinielli, G., Abou-Taleb, E. M., & Hellal, M. S. (2013). Municipal wastewater treatment in horizontal and vertical flows constructed wetlands. *Ecological engineering*, 61, 460-468.
- Arega Shumetie and Molla Alemayehu 2014. Source and Determinants of Water Pollution in Ethiopia: Distributed Lag Modeling Approach Journal of Intellectual Property Rights. *Open Access*.
- Boar, R. R. (2006). Responses of a fringing *Cyperus papyrus* L. swamp to changes in water level. *Aquatic Botany*, 84(2), 85-92.
- Deng, H., Ye, Z. H., & Wong, M. H. (2004). Accumulation of lead, zinc, copper and cadmium by 12 wetland plant species thriving in metal-contaminated sites in China. *Environmental pollution*, 132(1), 29-40.
- Dewedar, A., Ismail, A., Khafagi, I., El-Shatoury, S., & Talaat, M. (2006). Efficiency of the biological waste water treatment system in pollution control and wastewater management. *International Journal of Agriculture and Biology (Pakistan)*.
- Dewedar, A., Khafagi, I., Abu-Seadah, A., & Rashad, A. E. D. (2018). Comparative Efficiency of *Cyperus papyrus* and *Phragmites australis* for Bioaccumulation of Heavy Metals. *Catrina: The International Journal of Environmental Sciences*, 1(2), 37-42.
- Dimitrakopoulos, A. P., & Bemmerzouk, A. M. (2003). Predicting live herbaceous moisture content from a seasonal drought index. *International Journal of Biometeorology*, 47(2), 73-79.
- Erina, R., & Wiyono, E. (2012). Domestic Wastewater Treatment using Constructed Wetland as a Development Strategy of Sustainable Residential. In *International Conference on Environment, Energy and Biotechnology* (Vol. 33, p. 3).
- FAO. (2006). Guidelines for soil description, Food and Agriculture Organization of the United Nation, Rome (4th Ed.).
- Fesseha Hailu. 2012.). Liquid waste management: the case of Bahir Dar, Ethiopia. *Ethiopian Journal of Health Development*, 26(1), 49-53.
- García-Ávila, F., Patiño-Chávez, J., Zhinín-Chimbo, F., Donoso-Moscoso, S., Del Pino, L. F., & Avilés-Añazco, A. (2019). Performance of *Phragmites Australis* and *Cyperus Papyrus* in the treatment of municipal wastewater by vertical flow subsurface constructed wetlands. *International Soil and Water Conservation Research*, 7(3), 286-296.
- Güereña, D. T., Lehmann, J., Thies, J. E., Enders, A., Karanja, N., & Neufeldt, H. (2015). Partitioning the contributions of biochar properties to enhanced biological nitrogen fixation in common bean (*Phaseolus vulgaris*). *Biology and fertility of soils*, 51(4), 479-491.
- Hamad, M. T. (2020). Comparative study on the performance of *Typha latifolia* and *Cyperus Papyrus* on the removal of heavy metals and enteric bacteria from wastewater by surface constructed wetlands. *Chemosphere*, 260, 127551.
- Ibrahim, S., El-Liethy, M. A., Abia, A. L. K., Abdel-Gabbar, M., Al Zanaty, A. M., & Kamel, M. M. (2020). Design of a bioaugmented multistage biofilter for accelerated municipal wastewater treatment and deactivation of pathogenic microorganisms. *Science of the Total Environment*, 703, 134786.
- Lin, Y. F., Jing, S. R., Wang, T. W., & Lee, D. Y. (2002). Effects of macrophytes and external carbon sources on nitrate removal from groundwater in constructed wetlands. *Environmental pollution*, 119(3), 413-420.
- Ma, S., He, F., Tian, D., Zou, D., Yan, Z., Yang, Y., & Fang, J. (2018). Variations and determinants of carbon content in plants: a global synthesis. *Biogeosciences*, 15(3), 693.
- Mekonnen Getahun & Yihene G. Selassie 2013. Pollution of Water, Soil and Vegetables: Challenges to Growing Cities of Bahir Dar and Kombolcha, Amhara Region, Ethiopia. *Journal of Agricultural Science*, 5(9), 22.
- Näsholm, T., Kielland, K., & Ganeteg, U. (2009). Uptake of organic nitrogen by plants. *New phytologist*, 182(1), 31-48.
- Sheoran, A. S., & Sheoran, V. (2006). Heavy metal removal mechanism of acid mine drainage in wetlands: a critical review. *Minerals engineering*, 19(2), 105-116.
- Theophile, F., Sako, I. B., Martin, L., Fabrice, M. T., & Akoa, A. (2011). Potential of *Cyperus Papyrus* in Yard-Scale Horizontal Flow Constructed Wetlands for Wastewater Treatment in Cameroon. *Universal Journal of Environmental Research & Technology*, 1(2).
- USEPA (2000). Manual Constructed Wetlands Treatment of Municipal. Wastewaters Office of Research and Development Cincinnati, Ohio. United States Environmental Protection Agency (USEPA).



- Wu, H., Lin, L., Zhang, J., Guo, W., Liang, S., & Liu, H. (2016). Purification ability and carbon dioxide flux from surface flow constructed wetlands treating sewage treatment plant effluent. *Bioresource technology*, 219, 768-772.
- Yadav, A., Chazarenc, F., & Mutnuri, S. (2018). Development of the «French system» vertical flow constructed wetland to treat raw domestic wastewater in India. *Ecological Engineering*, 113, 88-93.
- Yang, L., Chang, H. T., & Huang, M. N. L. (2001). Nutrient removal in gravel-and soil-based wetland microcosms with and without vegetation. *Ecological engineering*, 18(1), 91-105.
- Zabotto, A. R., França, W. S., Domingos, M., Rinaldi, M. C. S., Kanashiro, S., Ferreira, M. L., & Tavares, A. R. (2020). Copper Accumulation and Distribution in Two Arboreal Species of the Atlantic Forest. *Floresta e Ambiente*, 27(1)
- Zabotto, A. R., França, W. S., Domingos, M., Rinaldi, M. C. S., Kanashiro, S., Ferreira, M. L., & Tavares, A. R. (2020). Copper Accumulation and Distribution in Two Arboreal Species of the Atlantic Forest. *Floresta e Ambiente*, 27(1).
- Zhu, L., Li, Z. and Ketola, T. (2011). Biomass accumulations and nutrient uptake of plants cultivated on artificial floating beds in China's rural area. *Ecol. Eng.* 37:1460–1466.



# Application of SCADA and IoT for Efficient Management of Urban Water Supply Systems

Bahar Adem Beker<sup>1,\*</sup>, Mitthan Lal Kansal<sup>2</sup>

<sup>1</sup>Water Resources engineering Department, School of Civil Engineering and Architecture (IWRIE\_CoE), Adama science and technology university, Ethiopia

<sup>2</sup>Water Resources Development & Management, Indian Institute of Technology, Roorkee, 247667, Uttarakhand, India

\*Corresponding author, e-mail: [baharwsee@gmail.com](mailto:baharwsee@gmail.com)

## ABSTRACT

The demand for urban water supply in developing countries like Ethiopia is increasing exponentially while the supply is decreasing due to various anthropogenic activities. The migration of people to urban centers and the expansion of cities have increased pressure on the existing water supply, and efficient supply management is needed to reduce the supply and demand gap. An urban water supply system is a complex system composed of many different operational components, including pipes, pumps, motors, flow meters, sensors, and control valves. This system requires supervision, monitoring, and control from a central location through artificial intelligence. This paper presents the application of SCADA (Supervisory Control and Data Acquisition) and the Internet of Things (IoT) for urban water supply systems (WSS) to monitor, collect, and analyze data from remote locations in real-time. The study propose the SCADA system, different kinds of IoT-based water sensors, along with the workflow WSS in Ethiopian cities (Addis Ababa and Dire Dawa). The methodology is illustrated with the help of a real-time WSS in Addis Ababa and Dire Dawa cities of Ethiopia. The significant problems in Addis Ababa and Dire Dawa's water supply systems are accessibility, connectivity, reachability, unaccounted water, quality, and irregular timing of water distribution, among others. The study shows how the implementation of SCADA and IoT can help in better management of such utilities under normal and abnormal conditions. Furthermore, it highlights the application of digital technologies in a complex WSS for efficient management by reducing the impact and severity of component failures and efficient preventive and curative maintenance. Generally, this study suggests that the adoption of SCADA and IoT can provide better management of the urban water supply system in Ethiopia, leading to improved water distribution and conservation

**Keywords:** Addis Ababa, Dire Dawa, IoT, real-time monitoring, SCADA, water supply system

## 1. INTRODUCTION

Next to air, potable water and food are the basic requirements for every human being. Water plays a significant role in both economic and social development. The availability of adequate and safe water and sanitation is inextricably related to public health and better living standards for any society. Lack of sufficient wholesome water and poor sanitation services leads to the spread of diseases responsible for the deaths of millions of people worldwide, particularly in developing countries like Ethiopia (Toubkiss, 2006). According to a study, around 80% of all infections and one-third of all fatalities in developing countries are water-born or water-related. One-tenth of each person's adequate time has been spent coping with water-related diseases (WHO and UNICEF, 2017).

The water distribution system (WDS) is one of the crucial urban infrastructures. It is used to deliver water to the consumer with sufficient quantity and quality. WDS consists of many interconnected pipes, pumps, reservoirs, valves, and other hydraulic equipment that transport water from supply areas to demand nodes at sufficient pressure to deliver reliable customer service. It must ensure water supply continuity, water quality control, and monitoring and control of technological process parameters. Further, water utilities must be cost-effective to function efficiently. This entails limiting energy expenses, minimizing water losses, and enhancing the water supply system's reliability (Lenzi, et al., 2013; Shirzad and Tabesh, 2016). These needs necessitate continuous monitoring system development. The hydraulic conditions of WSS operation and the quality of transferred water and energy usage are all monitored (Carrico, et.al. 2014; Stanczyk, and Burszta-Adamiak, 2019)

Population increases, urbanization, and aging infrastructure challenge water systems' operational and controlling approaches. The development of intelligent water networks is one of the most recent achievements in



water system engineering. These intelligent networks handle the management and operational issues of pressure, flow, and water quality changes in the WDS. It also minimizes the time to detect pipe bursts and leaks (Joseph, K., et.al, 2022). Implementing advanced intelligent technology, mainly SCADA and IoT systems, which provides continuous monitoring of the system's characteristics and optimal control of the pump stations, allows for adequate water supply monitoring, management, and control.

SCADA (Supervisory Control and Data Acquisition) systems are centralized computer-controlled/based systems often used in industry to monitor and control whole processes and plants. The implementation of a SCADA system for real-time monitoring of drinking water quality and quantity parameters allows for continuous monitoring, control, and data storage, which aids in the evaluation of long-term changes in water quality, the identification of existing or emerging water quality, and water loss problems, and the detection of water leaks. It is currently a state-of-the-art area for research (Liemberger & Marin, 2006; Carteado-fatima and Vermerschmichel, 2016)

IoT has appeared as the natural choice for smart water management applications, even though the integration of numerous technologies needed to make it operate easily in practice is still not complete. The rise of the Internet of Things is due to a confluence of factors, including low-power wireless technologies, low-cost devices, cloud data centre, availability for storage and processing, high-performance computing resources in commodity platforms, management frameworks for dealing with unstructured data from social networks, and computational intelligence algorithms to deal with this massive amount of data. IoT can be considered the next-generation Internet. Like SCADA, IoT is also a recent state-of-the-art area for research.

Currently, the application of automation of WSS in urban areas (through SCADA and IoT) is rare in developing countries, especially in Ethiopia's WSS. More than 99% of the WSS in Ethiopia is monitored and controlled manually, which cannot monitor the entire water distribution system due to the practical limitation, high cost, and inability to provide many of the required data timely. Through SCADA and IoT water sensors which are installed at various locations in the water system, it is possible to improve urban water management. Such research is necessary to properly manage urban water in developing countries where equitable water distribution remains challenging, and the water loss is very high (Bahar and Kansal, 2021; 2022). The present study focuses on applying SCADA and IoT in urban WSS based on the above limitation. It proposes thus a system for Addis abba and Dire Dawa city of Ethiopia, to alleviate the problem of urban WSS management in Ethiopia, particularly in Addis Ababa and Dire Dawa, that did not study yet is both necessary and timely.

A general layout of an urban water supply scheme from the source (surface water) to the distribution of the treated water to the consumers is shown in Fig. 1. A typical urban water supply scheme consists of four essential components: a collection of water, conveyance of water, treatment and purification of water, and a water distribution system. The collection works are used for collecting the raw water from the water source, and it consists of an intake structure and sump well. Conveyance is meant for transmitting raw water from the source to the treatment plant. Water treatment plant is used for treating the raw water, and it consists of different subcomponents. The distribution system is the main component of WSS for supplying treated (potable) water to consumers, mainly consisting of the pumping station, service reservoir, and distribution piping. Further, the sensors that convert parameters and component information the main control system is installed in all elements of WSS as shown in Fig. 1.

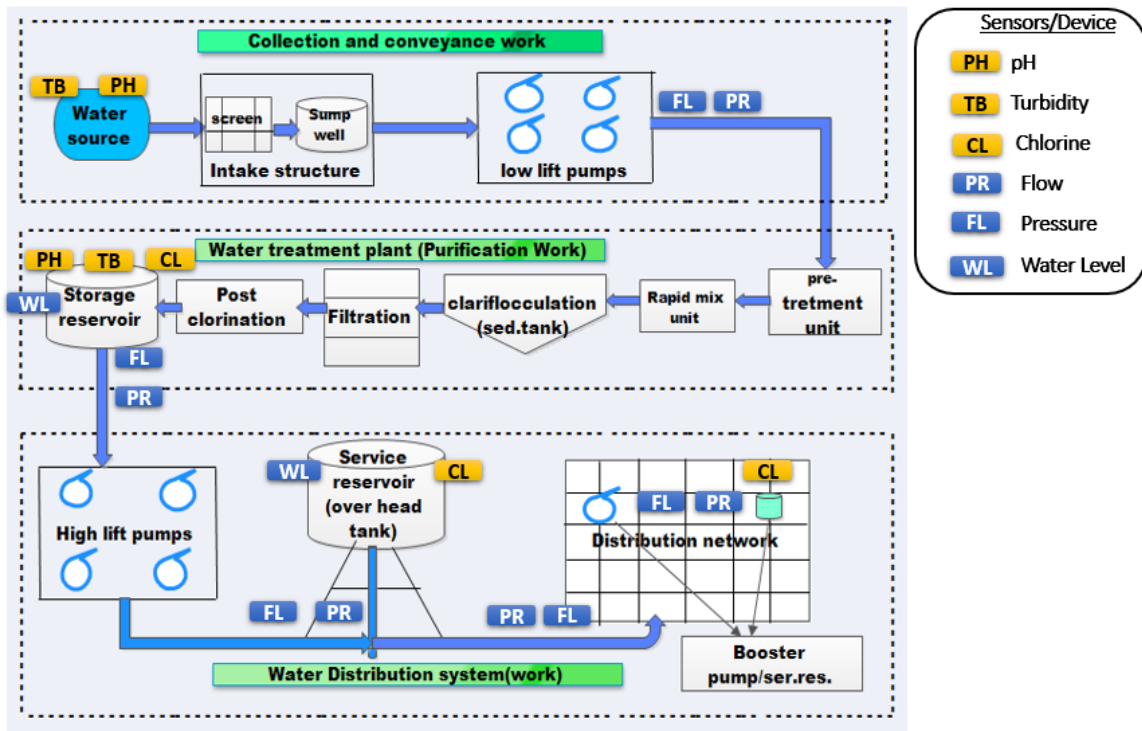


Fig. 1 Layout of typical urban WSS and location of Sensors

The SCADA system is a computer-based system that gathers and analyses the period knowledge to trace, monitor, and manage industrial equipment across numerous industries. SCADA system can support higher-level operational improvement applications and is used mainly for management and automation across numerous sectors like wattage, water & waste product, oil & gas, transportation, telecommunication, water supply system, etc. The primary use of the SCADA system in water supply networks includes sSecurity monitoring Energy management, monitoring equipment activities allows you to plan maintenance, repair, and replacement ahead of time, sub-metering utility usage, detecting alert situations and detection of leaks in transmission pipes.

The SCADA system has four essential components: sensors, SCADA Interference unit, communication, and SCADA master/ Station. Those components of the SCADA system are shown in Fig. 2.

- Sensors and Controllers** - Sensors (digital or analog) and control relays directly communicate with the management system. Water meter, water level, pressure detectors, water quality detectors (mainly chlorine, pH, and turbidity) installed in BH, pump, moters, Tanks/reservoirs, pipelines, valves, etc.
- SCADA Interface Units** - The majority of SCADA systems for WSS use one or more types of SCADA interface units. The remote terminal unit (RTU), the programmable logic controller (PLC), and the intelligent end device are examples of these (IED). The brains of a SCADA system are the Remote Terminal Units.
- Communications Network**- It's utilized to connect the SCADA system's control master to the SCADA interface units and sensors. The system connects and shares information and dates through the internet, such as LAN and wife.
- SCADA Master/Station**. "It is Larger computer consoles serve as the central processor for the SCADA system. Master units provide a human interface to the system (HIM)and automatically regulate the managed system response to sensor input." The master station flow charts is shown in Fig. 3.

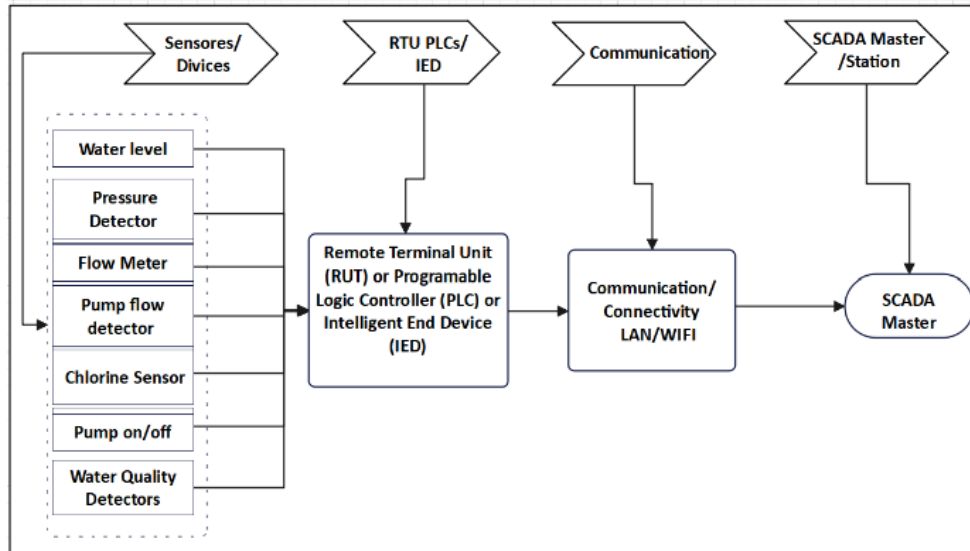


Fig. 2: SCADA System components

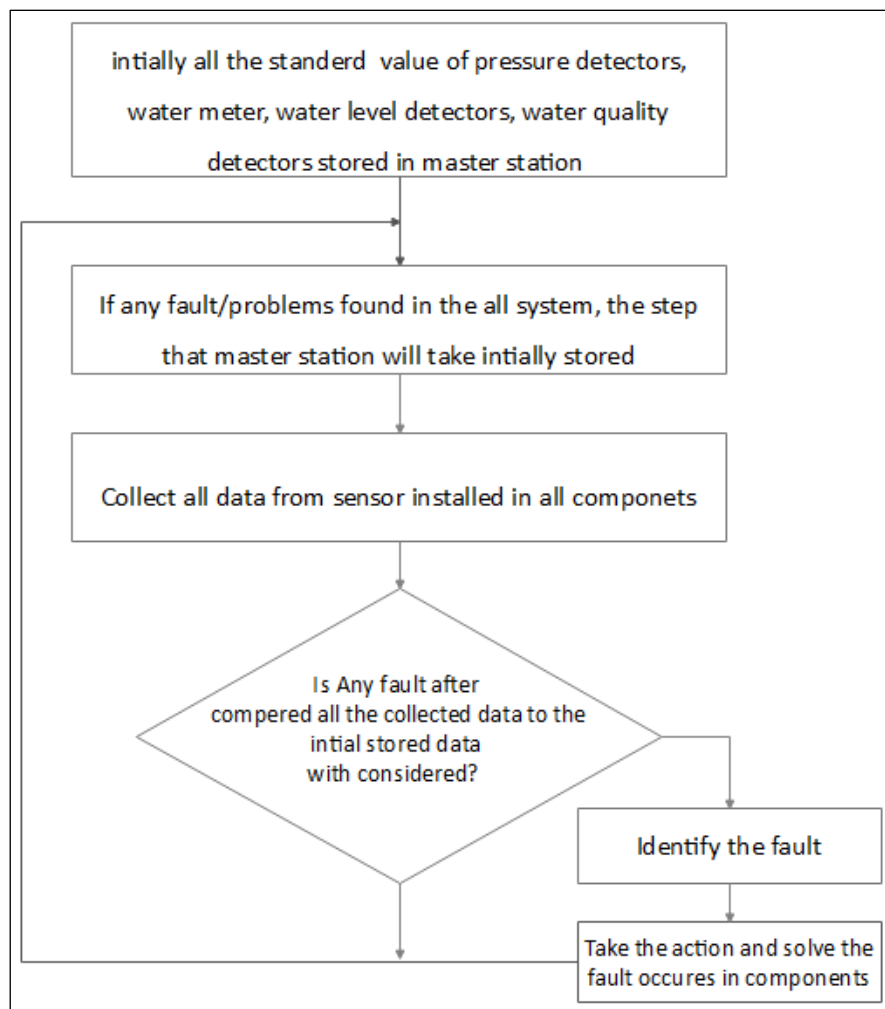


Fig. 3: Flowchart of the Master station

IoT is a giant connection system where people and machines generate, collect, and share information with each other and among each other whenever and wherever with the help of internet access. The IoT is considered as one of the most up-to-date approaches and is still in its beginning stage. It is estimated that 20 billion devices

to be connected to the internet by 2020 (Vermesan and Friess, 2014). IoT can be considered as the next-generation Internet. The ultimate goal of applying IoT is to save time and money and boost efficiency

It is predicted that by 2025, nearly half of the urban population will live in water-stressed areas as this valuable resource becomes increasingly scarce (WHO and UNICEF, 2017). As a result, IoT intelligent water management solutions are required to avoid an unanticipated water shortage. IoT water sensors are placed at various points across the IoT water system to detect any leaks or other defects, ensuring greater smart water management. IoT smart water management approaches are expected to reduce water expenses by up to 20%, resulting in higher profits at lower costs. It also allows communities to save money on building, maintenance, and other operating costs (WHO and UNICEF, 2017). A typical complete IoT system comprises sensors, connectivity, data processing, and a user interface, as shown in Fig. 4.

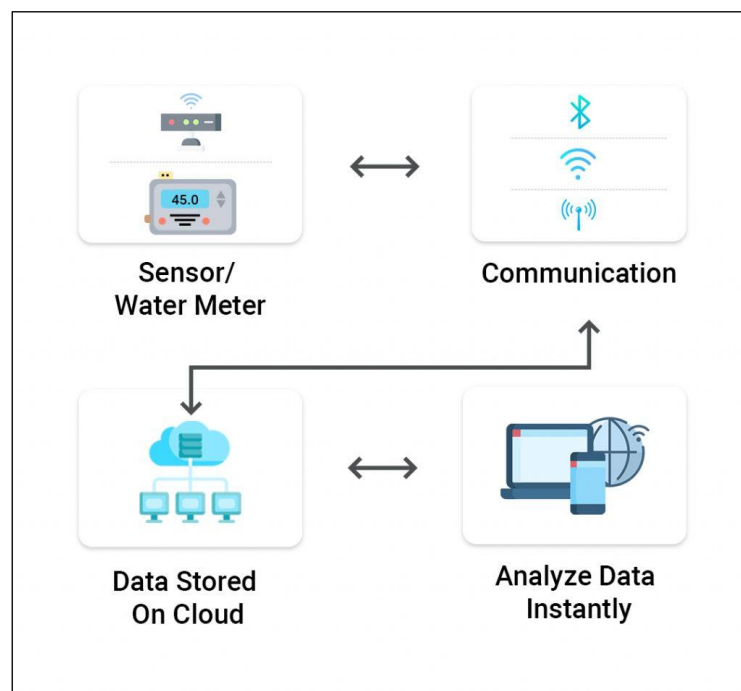


Fig. 4: Workflow of complete IoT system

Most urban water distribution systems need computerization to manage under various uncertainties. More than 30-60% water loss from WSS in sub-Sahara Africa, like Ethiopia (Macharia et.al, 2022). The absence of a centralized monitoring and control system network leads to frequent failure of water supply scheme components and is responsible for unaccountable water/water loss. Using SCADA and IoT can help restore normal conditions and management under various uncertainties. This can also help identify vulnerable locations and booster pumps and chlorination stations to provide safe and adequate drinking water to the masses in various cities.

Despite Ethiopia being touted as one of the fastest developing countries in the world, it ranks very low in regard to providing safe drinking water and improved sanitation services to its people. The main challenges of the municipal WSS in Ethiopian cities include urbanization, high water demand and mismanagement, shrinking water supply, water quality deterioration, low functionality of the existing WSS components (technical problems), limitation in institutional capacity, and lack of proper water management strategy. Additionally, the entire experiences of Ethiopian Water utility have been focused only on achieving the hardware (expansion works such as pipes, tanks, pumps, wells, etc.). In contrast, the software components have not been adequately developed to solve operation & maintenance challenges using innovative technology like SCADA and IoT systems. The WDN has not been controlled and monitored using this system entirely; for instance, in the city of Addis Ababa (the capital of Ethiopia) water loss and water pollution will be seen in this section. Further, the other main problem in Ethiopian city WSS is the presence of high-water loss



Water loss is a problem that can happen in any water supply system. More than 30% of drinking water is lost through pipelines worldwide, with high pressure and lack of water management in the WDN being the major cause of water loss (Duan, 2020). Its magnitude highly varies from place to place. The major reason for water loss is leakage. More than 87 percent of actual water loss is due to leakage in WDS caused by a pipe failure, excessive pressure, improper fitting and pipe installation, and water hammer (Annus et al, 2020). Excessive use or inappropriate use can also be termed as a loss. Other reasons for water loss are unmeasured use and incorrect meter. Unaccounted for water (UFW) can be defined as "the percentage of the water produced from the raw water source which is not accounted for (Welday, 2005)

In Addis Ababa, about 38 percent of produced water is lost before reaching consumers (Kitessa et al. 2021). There are many reasons for this high level of water loss. The magnitude of loss is affected by the age of pipes, ground elevation difference, metering error, and lack of rapid detection of leakage in WSS. For instant, in Addis Ababa, about half of the city's pipe network was installed more than 25 years ago. Due to the city's topography, considerable elevation differences exist between different settlement areas that receive water from the same reservoir. The amount of leakage loss is greatly influenced by these elevation differences. Until recently, the city's water utility did not examine customers' meters unless they specifically requested it. On the other hand, customers are more likely to apply when the meter is over registered rather than underreported. In general, water-related difficulties can account for more than this for all urban WSS in Ethiopia; hence Ethiopia's average non-revenues water (NRW)/water loss is nearly 43%, substantially more significant than that of other cub-Saharan African countries cities, except for Tanzania, Nigeria, and Guinea Bissau, as presented in Fig. 5. Leakage management solutions, including automation of WSS through SCADA and IoT should be used to reduce NRW as much as possible.

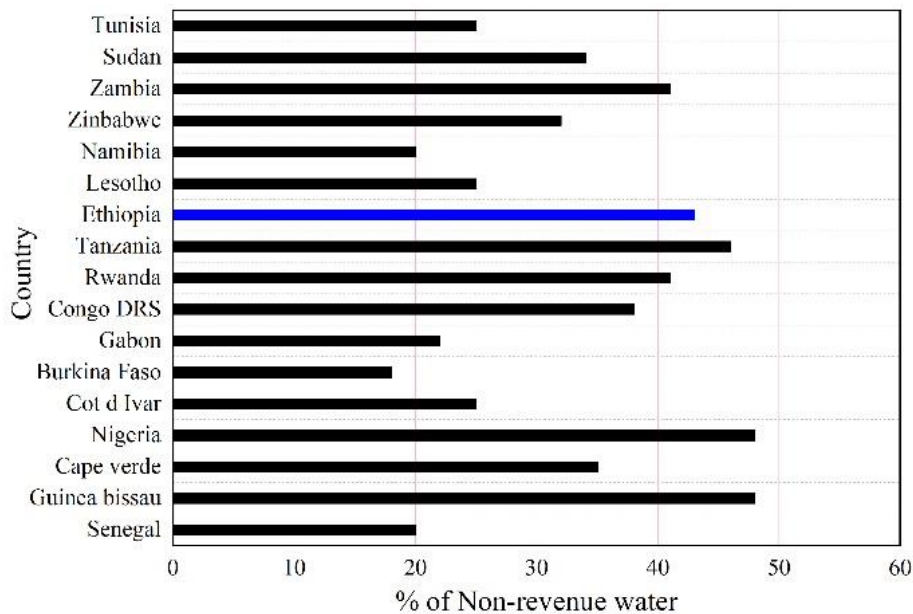


Fig. 5: Percentage NRW for selected countries in Sub Sahar Africa

## 2. MATERIALS AND METHODS

### 2.1 The Case Study Description

Ethiopia, a landlocked country in the Horn of Africa, has a landmass of 1.13 million km<sup>2</sup> and is Africa's second-most populous country after Nigeria, with a population of 120.8 million people, 77.8% of whom live in rural areas and 22.2 percent in urban areas in 2021, and ranks twelfth globally (UN/DESA. 2019). Two major Ethiopian cities were chosen for this study based on population, urbanization rate, water scarcity, and the complexity of the water distribution network (WDN). Addis Ababa and Dire Dawa are the cities chosen for investigation based on these characteristics. Furthermore, these two cities are home to more than 22% of Ethiopia's urban population. Hence they might be represented as big Ethiopian cities (UN/DESA., 2019).



Addis Ababa (38.73°E and 9.17°N) is Ethiopia's capital city, home to more than 20% (5,060,000) of the country's urban population and one of Africa's fastest-growing cities (UN/DASA, 2018). As indicated in Fig. 6(a), the city's entire size is 540 km<sup>2</sup>, with elevations ranging from 2,000 to 3,000 meters above mean sea level (amsl). AA accounts for half (50%) of the entire national gross domestic product (GDP), which is growing at a rate of 14% each year (World Bank, 2015). The total amount of water extracted from surface and groundwater is around 460 million liters per day, which is supplied to consumers by pumping and gravity (Kitessa Badane. et.al. 2021).

Dire Dawa is another Ethiopian city that has been chosen for this research. It is divided into nine districts (kebeles) with a total size of 85 km<sup>2</sup>. The city is 458 kilometres far to the east of Addis Ababa, positioned between 41.768° and 41.891° latitude and 9.571° to 9.643° longitudinal direction (Fig. 6(b)). Its elevation varies between 1130 and 1335 amsl. The city's population was predicted to be 4,26,000 in 2021 (UN/DASA 2019). The city's water source is groundwater from three wellfields (Sabian, Boren, and Tome) and deep wells within a 3-km radius of the city, with a total production capacity of 39.42 MLD.

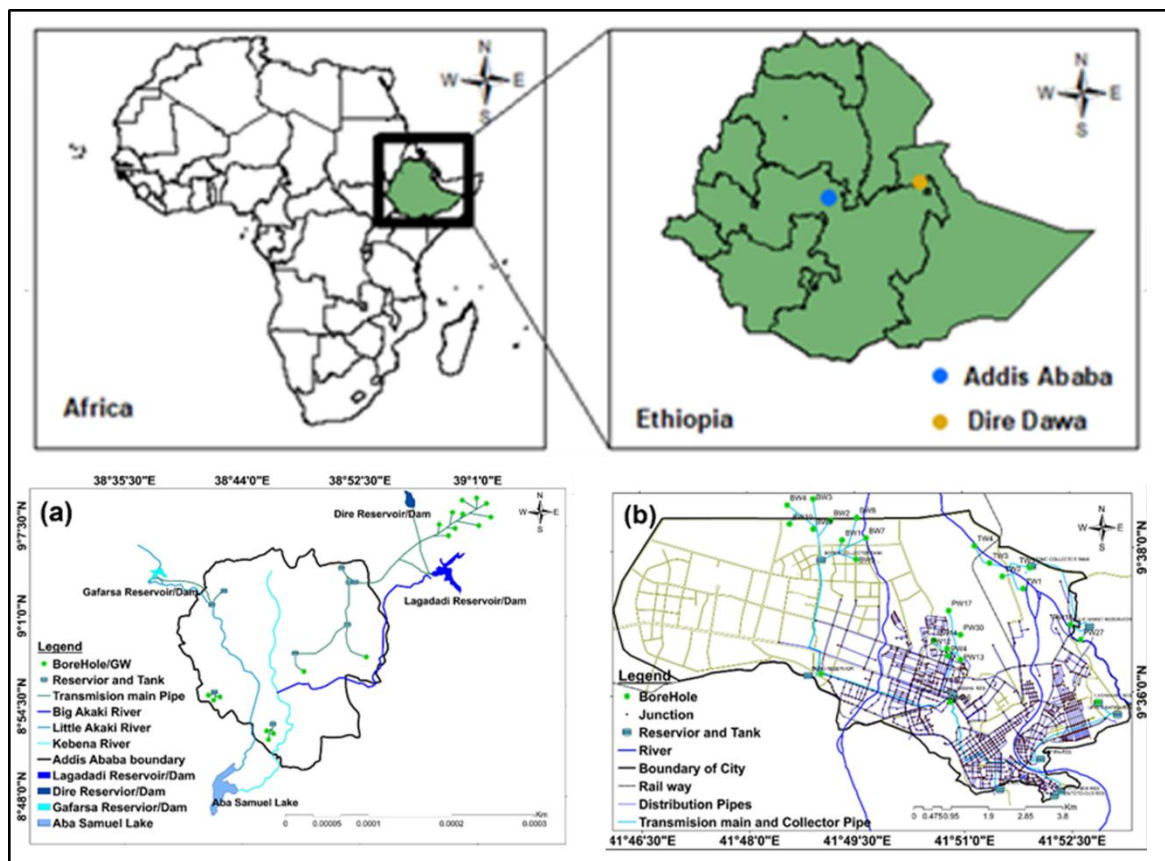


Fig. 6: Details of the urban water supply systems of a case study

## 2.2 Data Collection, Analysis of Existing SCADA System, and Proposed Sensors

Both primary and secondary data were collected from various sources for this study. Field observations of the study area, including water source, reservoir, pumping station, and tanks, were performed. Further, interviews with selected water users, experts (engineers, operation and maintenance workers), and decision-makers (managers of water utility) were conducted to assess the status and various problems related to WSS in case studies. The secondary data sources included published articles, books from the internet and journals, various reports and design documents from water utilities that are published or unpublished, and government publications. For this study, the latest versions of ArcMap 2021, ArcGIS 10.8, EdrawMax 11.5, and OriginPro 2021 are used for modeling, drawing graphs, and data analysis.

The water supply system of Dire Dawa city has the SCADA systems that were installed in 2018, but the system is only to manage and control the bulk water supply (I.e, the system is not installed in a pipe network). Further,

the SCADA system in Dire Dawa WSS should be expanded to all systems, including distribution pipes and valves. The sensors can be installed to measure pressure, water flow, and chlorine residual at the selected node and pipes. Due to network complexities and economic limitations, it is impossible to locate sensors in every nodes and pipe. For this study that the following criteria should be considered to select the critical location of proposed sensors in the networks: (1) type of demand at the nodes (Social-economic Importance), (2) Types of Pipes (i.e., whether the pipes are primary, secondary or tertiary pipe), (3) age of pipes. Based on the above criteria, the location of sensors will be selected, whereas the number of sensors depends on the economic condition of the water utility.

### 3. RESULTS AND DISCUSSION

Most urban water supply systems need computerization to manage under various uncertainties. More than 30-60% water loss in developing countries like Ethiopia from WDN (Bahar Adem and Mithan Lal, 2023). The absence of a centralized monitoring and control system network leads to frequent failure of water supply scheme components. The use of SCADA and IoT can help in the restoration of normal conditions and management under various uncertainties. This can also help in the identification of vulnerable pipes and node locations and booster pumps, and chlorination stations so as to provide safe and adequate drinking water to the masses in various cities.

#### 3.1 Analysis of SCADA System in Dire Dawa WDS

The existing SCADA system in WSS of Dire was installed in a new expansion project in 2018. The SCADA system is controlled and monitored from the common station through the SCADA master, located at Sabian station (Fig. 7). The system controls real-time tracking of water supply components such as boreholes, pumping stations, reservoirs, and the tanks. Various components are located in different sections of the network as shown in Fig. 7. The existing SCADA system in the city is limited to main components. The system is not controlling at lower levels due to lack of sensors at different levels.

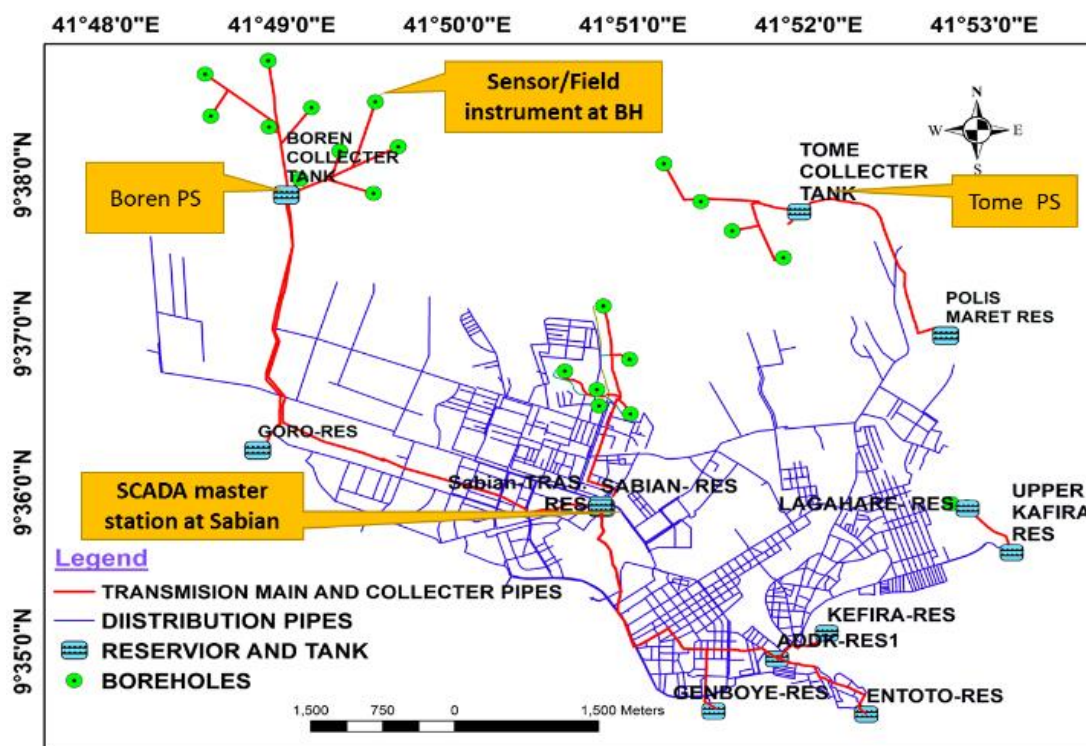


Fig. 7: The SCADA system of the Dire Dawa water supply network

Fig. 9 shows the online (real-time) overall SCADA system generated at 03:22 Pm, 07/25/2018, from SCADA master dispatches. The results indicated overall real-time tracking of all components. Further, the presented Fig. 8 indicated the details of WSS components' hydraulic and mechanical parameters values (water level in tank and reservoirs, discharge rate of pumps, totalized flow, pressure, pumping capacity pumps, status of components,



etc.). The sensor that measures all parameters are installed at Boreholes, tanks and reservoirs, and pumping stations. Furthermore, the results generated from the master station for groundwater sources (mainly boreholes) of the Dire Dawa WSS are shown in Fig. The results indicate the water level in BH water produced from each BH, the status of BHs (working or not), etc., taken at 09:05 am on 11-14-2018 (Fig.9).

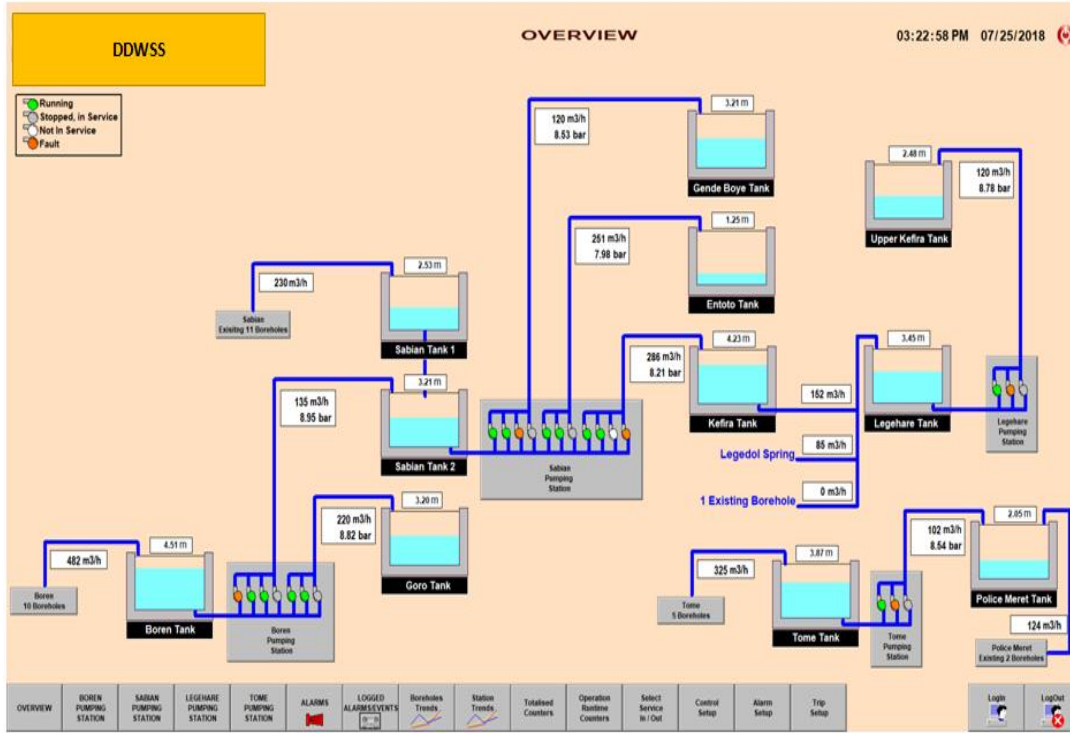


Fig. 8: Real-time output of SCADA display in the main control room for overall WDS system of DD

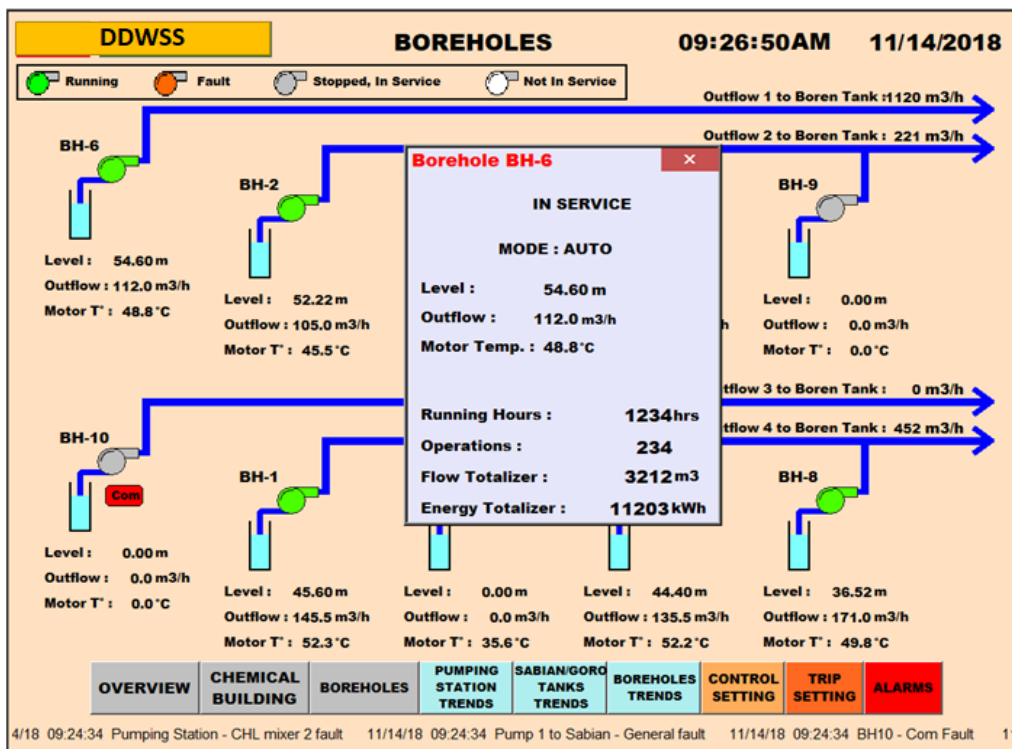


Fig. 9: Real-time output of SCADA display in the main control room for (a) Boren and (b) Tome Boreholes

### 3.2 Tank/Reservoirs and Pump Station in Dire Dawa SCADA

A water tank is a storage container for water ready to be sent to the city. This water tank should be kept at a height where the water's speed and pressure are sufficient to reach the highest point of a large structure. Fig. 10 indicates a real-time output of the SCADA display in the main control room for Boren and Sabian pumping stations, including tanks, reservoirs, and pump control. There are two sensors in the tank. These sensors measure the water level and send the information to the main master and control stations. The central control station immediately starts the pump when the water level is very low. The pump station starts the pump after receiving power from the main control station and a start signal from the control station. Also, the water should flow from the reservoir to the tank. A pressure detector and a sensor are installed in the reservoir. These are used to detect the water level and amount of water, and the data is subsequently communicated to the master station through telemetry media via the substation.

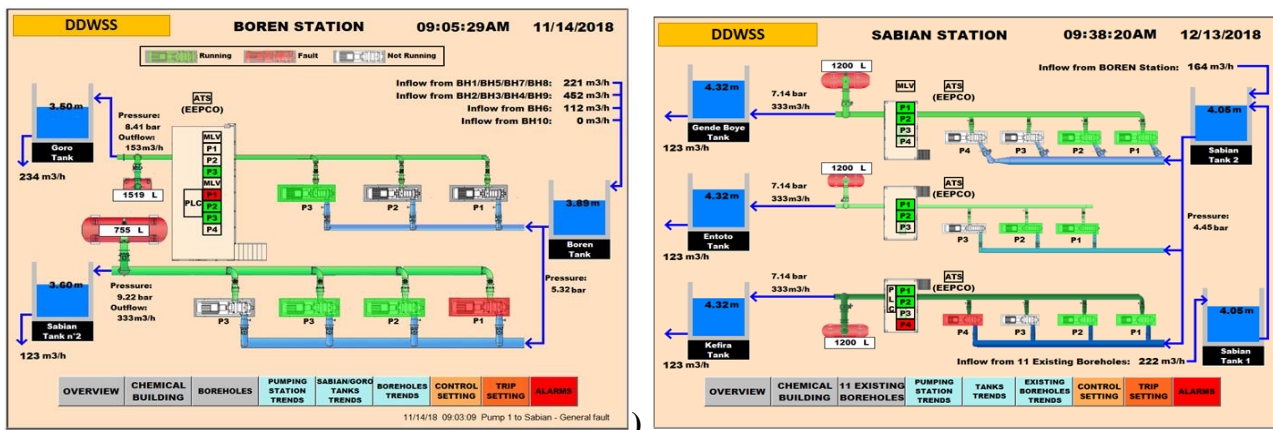


Fig. 10: Real time output of SCADA display in main control room for (a) Boren and (b) Sabian pumping station

### 3.3 Proposed IoT for Dire Dawa and Addis Ababa WDS

The previous sections present the challenges of Addis Ababa water supply management and how the new technology, IoT works. The IoT-based water supply management model will be proposed in this section to address these challenges, specifically water quality monitoring and water level, and pressure control. In Addis Ababa, the manual methods for water quality monitoring are not only of high cost but also unable to provide much of the required data timely. It shows a clear need for continuous online water quality monitoring using advanced sensor technologies.

Monitoring water levels and water conservation from loss is critical for a given water supply system. This study proposes one of the good models provided by a recent report (Patawala, et.al. 2020). This proposed model's components are two solenoid valves, ultrasonic sensors for level measurement, flow rate sensors, water quality sensors like pH, chlorine residual, and conductivity, a microcontroller, and a Wi-Fi module. The block diagram of the model is given in Fig. 11.

This proposed system can be implemented on the city's service reservoirs for safe and waste less drinking water use. When water is supplied to service reservoirs, the chlorine residual level will be checked. The pH level of the water will be examined if it falls within the specified range. The conductivity of the water will be tested if it also falls within the required range. If the water's residual chlorine level, pH, or conductivity are not within safe limits, the water will not be provided to domestic tanks, and the valves will be stopped. Until the water is at a safe range, a similar procedure will be performed. If the tanks are full after an acceptable water quality check, the tank valves will be opened, and water will be distributed. The water flow rate is assessed during distribution to ensure that it is distributed evenly. Finally, all of this information will be transmitted through Wi-Fi to a Web page, allowing the system to be accessed remotely from a computer. Water delivery quality and flow will be monitored via a web page that can be accessed from anywhere on the internet. The method is very adaptable. Other water

quality parameters can only be monitored by replacing the related IoT sensors and modifying the required software applications. The flow chart of the system is shown in Fig. 12.

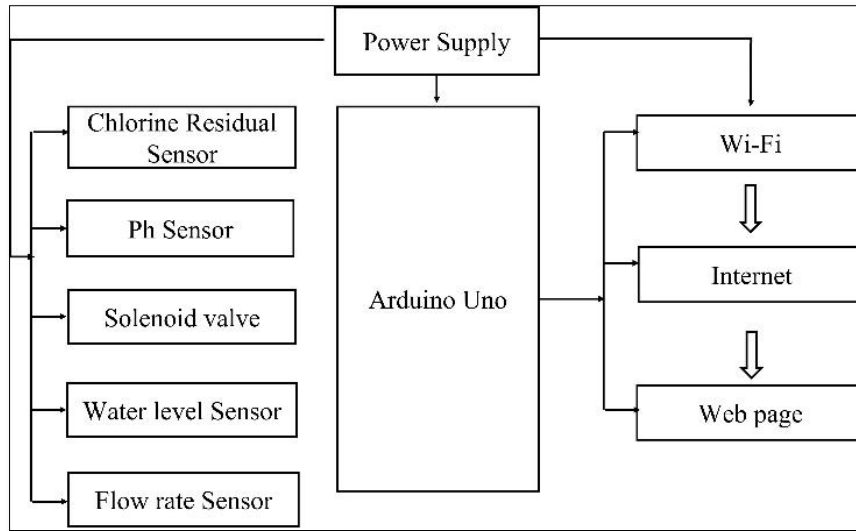


Fig. 11: Block diagram for a proposed system

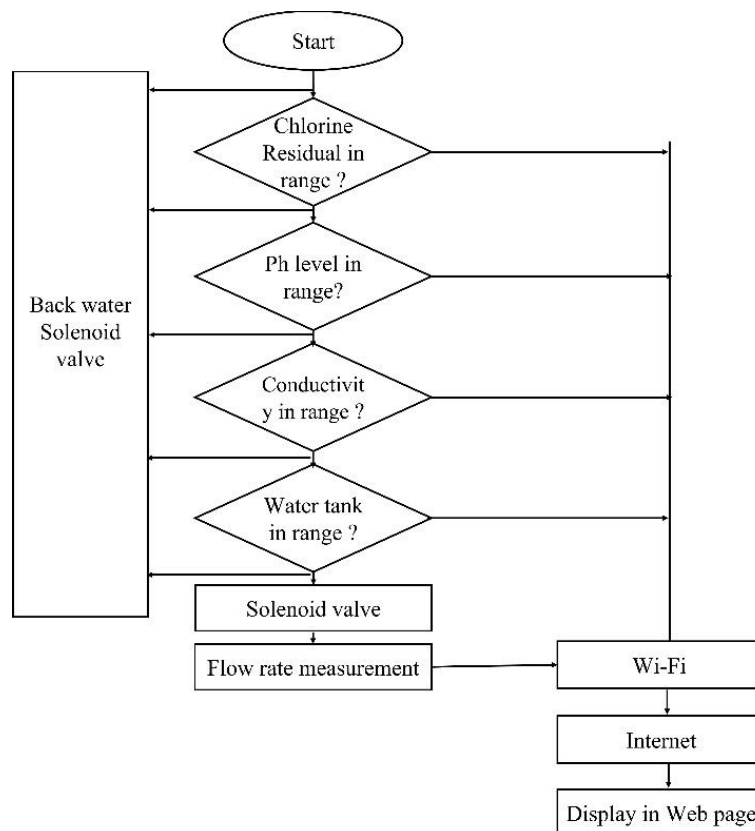


Fig. 12: Flow chart for the proposed system

#### 4. CONCLUSIONS

This paper presents the application of the SCADA system for monitoring and control components of the Addis Ababa and Dire Dawa water supply system, which will allow the optimum functioning of the Bore holes, motor, pumping system, reservoir, tanks, etc. Lack of advanced monitoring and control can be the main problem of failures in water supply components. It is important to apply the SCADA and IoT system for sustainable management of the Ethiopian city water supply scheme, especially in Addis Ababa and Dire Dawa.



The IoT-based urban water supply system is efficient and effective in water operation, maintenance, and management. It can monitor water quality automatically in real-time base, and it is inexpensive and does not necessitate the presence of personnel. As a result, water quality monitoring is expected to be more cost-effective, convenient, and quick. The Internet of Things has the potential to cut water bills by up to 20%. One reason is that new battery-powered networking technologies are becoming available for inexpensive IoT sensors. This Lower tech solution prices allow utilities to "light up" bigger areas of their networks, enhance the consumer experience, and lower operating and maintenance expenses.

Smart water meter has an enormously vast advantage. It can enable the water distribution system for early detection of a leak, supply customers with information to reduce water use, provide more accurate water rates, reduce meter reading costs, improve billing accuracy and improve cash flow, improve outage information and response, help detect theft of service, allow remove/virtual turnoff of water.

## ACKNOWLEDGMENTS

The authors are thankful to the Dire Dawa Water Supply and Sewerage Authority (DWSSA), DWSAA and Addis Ababa Water Supply and Sewerage Authority (AAWSSA) in Ethiopia for providing necessary data.

## REFERENCES

- Annus, I., Vassiljev, A., Kändler, N., & Kaur, K. (2020). Determination of the corresponding roughness height in a WDS model containing old rough pipes. *Journal of Water Supply: Research and Technology-AQUA*, 69(3), 201-209.
- Bahar. A., & Kansal, M. L. (2021). Use of WaterGEMS for Hydraulic Performance Assessment of Water Distribution Network: A Case Study of Dire Dawa City, Ethiopia. In *Advances in Energy and Environment* (pp. 151-162). Springer, Singapore.
- Bahar.A., & Kansal, M. L. (2022). Fuzzy logic-based integrated performance evaluation of a water distribution network. *AQUA—Water Infrastructure, Ecosystems and Society*, 71(3), 490-506.
- Bahar.A, Kansal, M.L. Complexities of the urban drinking water systems in Ethiopia and possible interventions for sustainability. *Environ Dev Sustain* 26, 4629–4659
- Carrico, N., Covas, D., Alegre, H., & do Céu Almeida, M. (2014). How to assess the effectiveness of energy management processes in water supply systems. *Journal of Water Supply: Research and Technology—AQUA*, 63(5), 342-349.
- Duan, H. F. (2020). Development of a TFR-based method for the simultaneous detection of leakage and partial blockage in water supply pipelines. *Journal of Hydraulic Engineering*, 146(7), 04020051
- Carteado-fatima, E. F., & Vermersch-michel, E. M. (2016). Apparent water losses and revenue collection ratio: review, assessment and recommendations.
- Kitessa, B. D., Ayalew, S. M., Gebrie, G. S., & Teferi, S. T. (2021). Long-term water-energy demand prediction using a regression model: a case study of Addis Ababa city. *Journal of Water and Climate Change*, 12(6), 2555-2578
- Lenzi, C., Bragalli, C., Bolognesi, A., & Artina, S. (2013). From energy balance to energy efficiency indicators, including water losses. *Water Science and technology: water supply*, 13(4), 889-895.
- Joseph, K., Sharma, A. K., & van Staden, R. (2022). Development of an Intelligent Urban Water Network System. *Water*, 14(9), 1320.
- Liemberger, R., & Marin, P. (2006). *The Challenge of Reducing Non-Revenue Water in Developing Countries--How the Private Sector Can Help: A Look at Performance-Based Service Contracting*.
- Macharia, P., Kreuzinger, N., & Kitaka, N. (2020). Applying the Water-Energy Nexus for Water Supply—A Diagnostic Review on Energy Use for Water Provision in Africa. *Water*, 12(9), 2560.
- Patawala, A.H., Bansode, N.P., Bhong, Y.P., & Zadbuke, A.S.(2017). *Advance Research, Ideas and Innovations in Technology. 'IOT Based Water Management System for Smart City'*. 3(2), 379-382.
- Shirzad A, Tabesh M (2016) New indices for reliability assessment of water distribution networks. *J Water Supply Res Technol AQUA* 65(5):384–395
- Stańczyk, J., & Burszta-Adamiak, E. (2019). The Analysis of Water Supply Operating Conditions Systems by Means of Empirical Exponents. *Water*, 11(12), 2452
- Toubkiss, J. (2006). *Costing MDG target 10 on water supply and sanitation, comparative analysis obstacles and recommendations* (No. 33364 Caja (535)). World Water Council.
- Welday, B.D.(2005) *Water supply coverage and water loss in distribution system the case of Addis Ababa* (Unpublished master's thesis). ITC, Netherland.



- WHO and UNICEF (2017). Progress on Sanitation and Drinking Water: 2015 Update and MDG Assessment. WHO/Unicef, Geneva: [http://apps.who.int/iris/bitstream/10665/177752/1/9789241509145\\_eng.f](http://apps.who.int/iris/bitstream/10665/177752/1/9789241509145_eng.f).
- World Bank, (2015) Enhancing Urban Resilience in Addis Ababa: Resilient Cities Program; Document Number 100980, World Bank Group, Addis Ababa, Ethiopia, 2015
- Vermesan, O., & Friess, P. (Eds.). (2014). Internet of things-from research and innovation to market deployment (Vol. 29). Aalborg: River publishers.
- UN/DESA. (2019). World urbanization prospects: The 2018 revision. Retrieved from <https://population.un.org/wup/Publications/Files/WUP2018-Report.pdf>.



# Enhancing Deforestation Detection: Remote Sensing Approach Using Satellite Imagery in Gambella National Park, Ethiopia

Gizatie Desalegn Taye\*

Department of Computer Science, Gafat Institute of Technology, Debre Tabor University, Debre Tabor, Ethiopia

\*Corresponding author, e-mail: [gizades@dtu.edu.et](mailto:gizades@dtu.edu.et)

## ABSTRACT

Deforestation within protected areas poses a significant threat to the environment, contributing to climate change, biodiversity loss, and habitat destruction. Despite its impact, monitoring these activities is often inadequate. To address this, we propose a solution utilizing deep learning-based semantic segmentation models on high-resolution Sentinel-2 satellite images of the Gambella National Park. Our approach involves pixel-level land cover classification before detecting Anti-Deforestation activities. We constructed the U-Net architecture and enhanced its encoder with state-of-the-art Convolutional Neural Network (CNN) architectures, including Vgg-16 and ResNet-50. By ensemble the U-Net models, we achieved F1-Scores of 86.69%, 88.08%, 91.28%, and a final ensemble model with 92.12%. This approach offers a robust method for detecting and mapping anti-deforestation activities in regions with heterogeneous land cover within small areas.

**Keywords:** Deforestation, Gambella National Park, Satellite Images, Semantic Segmentation, U-Net

## 1. INTRODUCTION

Forests are vital to the environment, providing critical ecosystem services and livelihood to people and shelter to wild life. They are very important to balance the weather condition of the environment by reducing greenhouse gas emissions. They can also have high contribution in reducing global warming which is the main problem of the entire world right at this time. In addition, forests play a great role in supporting life of population in rural areas, in providing a wide range of industrial wood products, in preserving biodiversity and in balancing the local climate [1]. The unlawful logging activities and conversion of habitats to croplands lead to the declining of expanse of forest areas across the globe [2].

In Ethiopia, clear cuts are also affecting the protected areas such as national parks. One of the Ethiopian national parks that has been suffering from such Unlawful deeds of humans is Gambella National Park (GNP). GNP is located in Gambella People's National Regional State of Ethiopia, 850 km west of Ethiopia's capital Addis Ababa. GNP has various tree species in addition to the other bio diversities it has. The different tree species in the park are suffering from Unlawful deeds of humans such as forest clearing for agricultural expansion and settlement needs, which are leading them to extinction. Research results showed that approximately 140,000 hectares of natural forests around GNP were cleared by the residents around the park for settlement purposes [3]. These profound impacts of humans on the earth's natural ecosystem have been unmonitored or roughly monitored for many years. Deforestation detection has become faster, more convenient and more accurate than before with advances in satellite imagery [4]. Remote sensing data or data from satellite sensors provide continuous datasets that can be used to detect and monitor different earth's phenomenon. Satellite sensors capture spectral bands reflected from the earth's surface and provide information for monitoring forest conditions on the ground [5].

The objective of this work is to design and develop deforestation detection: a remote sensing approach from satellite images in Gambella National Park (GNP), Ethiopia.

## 2. MATERIALS AND METHODS

The methods that we have employed in this work are Literature review, Data collection, Dataset creation, Data preprocessing, Designing and developing semantic segmentation models, evaluation of the developed models, and tree cutting detection.

- i) Literature Review: Available books, journals, case studies, and previous research works were surveyed in order to have clear understanding about the subject matter.



- ii) Data Collection: We have gathered multispectral satellite images of our study area (GNP) captured during leaf-off and leaf-on seasons by the Sentinel-2 satellites. The Sentinel-2 satellite images are freely available and we have downloaded Sentinel-2A and Sentinel-2B images from the USGS website.
- iii) Dataset Creation: Using the gathered satellite images, we have created a labelled sematic segmentation dataset which contains 128x128 pixels size image patches and their corresponding 128x128 pixels size masks. Our semantic segmentation dataset contains a total of 12,250 RGB images and their corresponding ground truth labels.
- iv) Data Preprocessing: data pre-processing operations such as image normalization, label encoding, feature extraction and feature selection were performed to make our data easily fit to the designed machine learning models.
- v) Designing and developing semantic segmentation model: machine learning classifiers such as deep learning model called U-Net and U-Net with modified encoders were designed and developed to perform semantic image segmentation.
- vi) Performance Evaluation: performance metrics such as confusion matrix, precision, recall, F-measure and accuracy were used to evaluate the developed semantic segmentation models.
- vii) Tree Cutting Detection: post classification comparison method was used to detect cuttings in our study area. Satellite images from two dates were taken and the developed semantic segmentation model was used to perform pixel-based land cover classification. The resulting segmented images were then compared to detect anti-Deforestation in our study area.

### 3. RESULTS AND DISCUSSION

#### 3.1 Performance Measures

The performance measures we have obtained during U-Net model evaluation using the testing set are given in Table 1. Here, we achieve performance of 86.69% average F1-Score. In addition, forest is the class that this model achieves highest accuracy at segmenting it. Conversely, this model is failed to segment the road class. The difficulty of segmenting the road class comes from the fact that the road class appears in very few images in our dataset and its spectral similarity with the bare ground class.

Table 1 Summary of Performance Measures for U-Net Model

Model	Performance-Measures	Land cover classes							
		Grass-land	Bare-ground	Water-bodies	Cutting-area	Cloud	Forest	Road	Average
U-Net	Precision	0.9111	0.7955	0.9164	0.8152	0.9215	0.8891	0.0000	0.8700
	Recall	0.6195	0.8034	0.6699	0.7431	0.8281	0.9762	0.0000	0.8739
	F1-Score	0.7375	0.7994	0.7740	0.7775	0.8723	0.9307	0.0000	0.8669
	Accuracy								0.8739

The performance of the UNet-Vgg16 model was also evaluated using the testing set and the obtained performance measures are given in Table 2. From the performance report, we can see that UNet-Vgg16 model achieves 88.08% average F1-Score. This shows an improvement in performance over the original U-Net model and we believe that this improvement comes from the modification of the encoder part of the original U-Net model. The table shows that the model achieves good results in segmenting most of the main land cover classes. Forest class is still the land cover class with highest F1\_Score, Precision and Recall. However, the road class appears as the difficult class to be segmented. This is due to the difficulty that the model faced to visually distinguish the road class from other classes and its less representation in pixel count in the training set. Similarly, this model performs less in segmenting water body’s class relative to the other main land cover classes. This can also be due to less visual distinction among the land cover classes and results spread among spectrally similar land cover classes.



Table 2 Summary of Performance Measures for UNet -Vgg16 Model

Model	Performance-Measures	Land cover classes							
		Grass-land	Bare-ground	Water-bodies	Cutting-area	Cloud	Forest	Road	Average
UNet-Vgg16	Precision	0.8248	0.7918	0.7350	0.7336	0.8793	0.9411	0.0778	0.8794
	Recall	0.8053	0.8115	0.5315	0.7738	0.7923	0.9549	0.0015	0.8833
	F1-Score	0.8149	0.8015	0.6169	0.7532	0.8335	0.9480	0.0030	0.8808
	Accuracy								0.8833

The testing set was used to evaluate the UNet-ResNet50 model and the performance report we have obtained is given in Table 3. This model achieves 91.28% average F1-Score that shows an improvement over the performance achieved by UNet-Vgg16 model by a margin of 3%. As we can see from the table, all land cover classes except the road class achieve >81% F1-Score. This shows that UNet-ResNet50 model comes with most improved performances for all land cover classes except the road class than the other models developed above. Moreover, the model scores >92% F1-Score, Precision and Recall values for the forest and cloud classes. The forest and cloud classes have visually distinct features so that the model can easily distinguish them from the other classes. But the road class is still left unrecognized by the model.

Table 3 Summary of Performance Measures for UNet -ResNet50 Model

Model	Performance-Measures	Land cover classes							
		Grass-land	Bare-ground	Water-bodies	Cutting-area	Cloud	Forest	Road	Average
UNet-ResNet50	Precision	0.8780	0.8406	0.8827	0.8354	0.9229	0.9498	0.6046	0.9121
	Recall	0.8775	0.8617	0.8577	0.7908	0.9364	0.9580	0.0253	0.9148
	F1-Score	0.8777	0.8510	0.8700	0.8125	0.9296	0.9539	0.0486	0.9128
	Accuracy								0.9148

### 3.2 Ensembled Model

Here, weighted averaging of the predictions from the models, U-Net, UNet-Vgg16 and UNet-ResNet50 was performed to build an ensembled model. The weight selection for the model outputs was done by try and error and it was set to be [0.4, 0.2, 0.4] for the models U-Net, UNet-Vgg16 and UNet-ResNet50 respectively. The final ensembled model was evaluated using the testing data and the obtained performance report is given in Table 4. The performance report shows that the ensembled model achieves best average F1-Score (0.92) than the individual models developed here. This indicates that the ensembled model is utilizing the combined performances of the individual models. The main land cover classes except the road class have achieved >83.64% F1-Score. And the forest and cloud classes are segmented at 95.81% and 93.3% F1-Scores respectively. But the road class is still not recognized by this model.

Table 4 Summary of Performance Measures for the Ensembled Model

Model	Performance-Measures	Land cover classes							
		Grass-land	Bare-ground	Water-bodies	Cutting-area	Cloud	Forest	Road	Average
Ensembled Model	Precision	0.9049	0.8434	0.9393	0.8723	0.9527	0.9463	0.9273	0.9192
	Recall	0.8679	0.8751	0.8224	0.8033	0.9141	0.9701	0.0019	0.9220
	F1-Score	0.8860	0.8589	0.8770	0.8364	0.9330	0.9581	0.0037	0.9212
	Accuracy								0.9220

The confusion matrix shows per-class pixel accuracies at its diagonal. The forest class achieves 97%-pixel accuracy which makes it the highly recognized class. But road is not recognized by the model. The road pixels from the testing set are mainly classified as bare ground and forest pixels. The road class remains as the difficult class to be segmented in all our experiments. We believe that this is due to two main reasons; the visual similarity of the road class with the other land cover classes such as bare ground and the less representation of the road class in our dataset. Generally, the strong predictions at the diagonal of the confusion matrix shows that the ensemble model performs well in segmenting all main land cover classes except the road class. The unlabeled pixels are still classified as bare ground and forest classes.

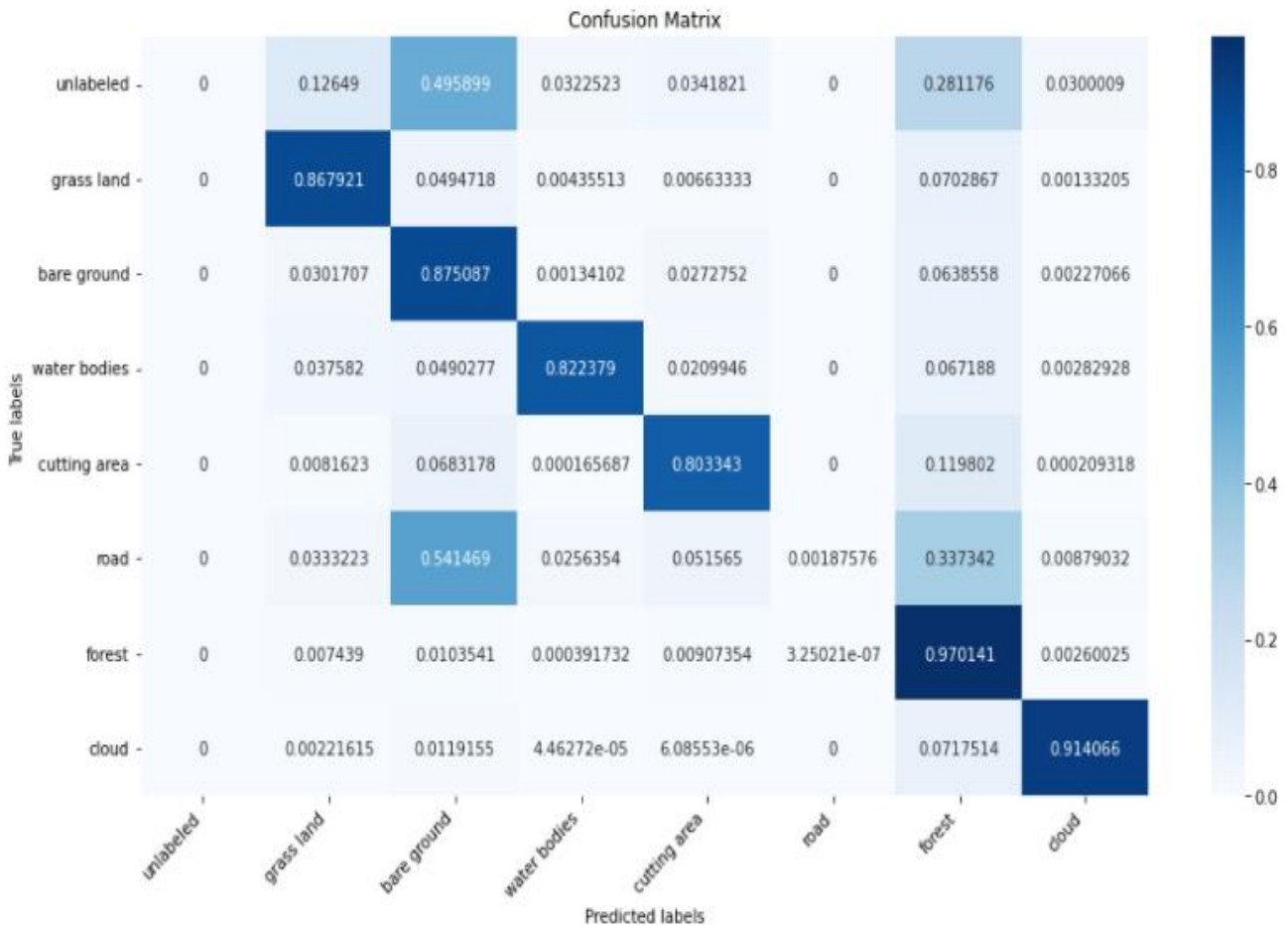


Figure 1: Confusion matrix for the Ensembled model

### 3.3 Model Selection

Model selection is the process of selecting the best model from the available set of models for a particular problem. In the model building section, a set of semantic segmentation models for land cover segmentation task were developed and evaluated using the novel dataset prepared in this work. And the developed segmentation models were compared to select the best model out of them. To compare the developed semantic segmentation models, we have preferred to use the Precision, Recall and F1-Score values that the models achieve during evaluation on the test data. These selected performance metrics are better to evaluate semantic segmentation models than the other metrics such as overall pixel accuracy. The following chart shows the comparison of the performances of the developed models using the depicted performance metrics.

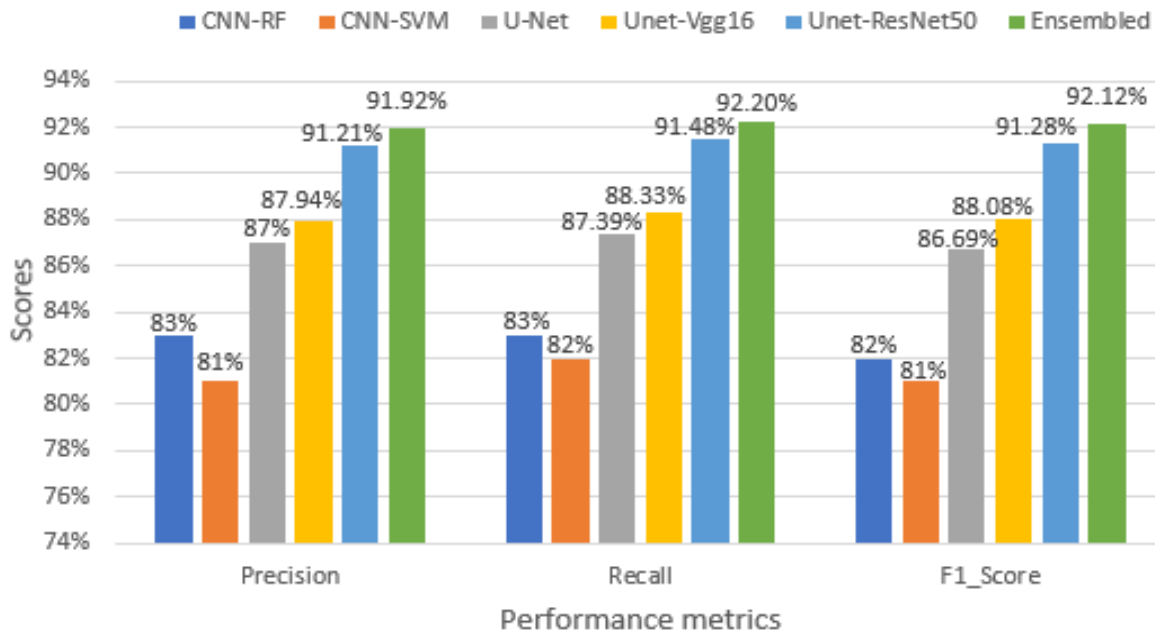


Figure 2: Chart for performance comparison

As we can see from the above figure, the Ensembled model outperforms the other models in terms of Precision, Recall and F1-Score. The Ensembled model achieves 91.92% Precision, 92.20% Recall and 92.12% F1-Score. Similarly, the Unet-ResNet50 model has almost comparable performance with the Ensembled model. It achieves 91.21% Precision, 91.48% Recall and 91.28% F1-Score. And the original U-Net and Unet-Vgg16 models have scored better performance. As a result, we have selected the Ensembled model as our semantic segmentation model to be used as a land cover classification scheme in our deforestation detection: a remote sensing approach using satellite imagery.

### 3.4 Deforestation Detection: A Remote Sensing Approach Using Satellite Imagery

Here, the downloaded and pre-processed Sentinel-2A images captured in 2021/11/30 (image at time T1) and 2021/12/10 (image at time T2) were used to detect cutting areas in our area of interest. The two images were first segmented into land cover classes using the selected model and the resulting segmentation maps are given in Figure 3.

The Figure 3 shows the input images from the two dates and their corresponding segmentation maps. The selected semantic segmentation model (the Ensembled model) was used to perform land cover classification at a pixel-level (at 10m resolution) on the input images. And the pixel values of the output segmentation map images represent the integer labels that correspond to the predicted classes at each pixel. The integer labels to represent our identified landcover classes in our study area are [1 to 7] that represent the classes [‘grass land’, ‘bare ground’, ‘water bodies’, ‘cutting area’, ‘road’, ‘forest’, ‘cloud’] respectively. After land cover classification is being done, the resulting segmentation maps were compared and “from-to” change matrix was computed to produce the change image map given in Figure 4.

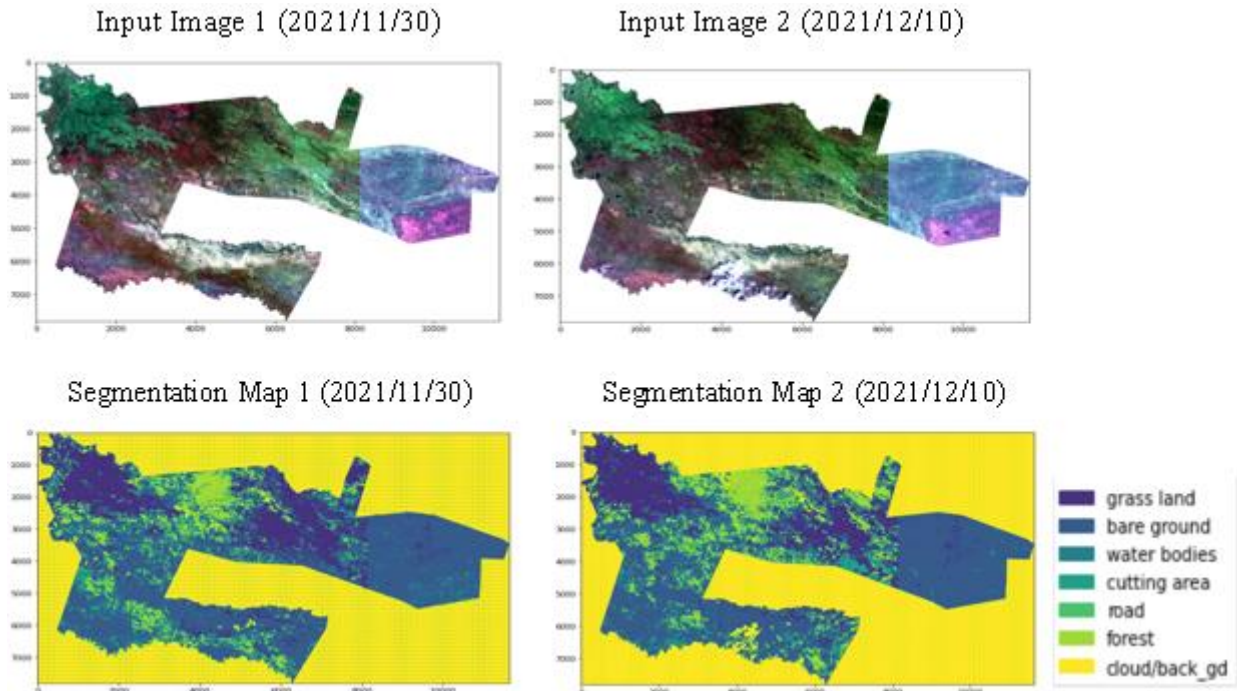


Figure 3: The two date images and corresponding segmentation maps

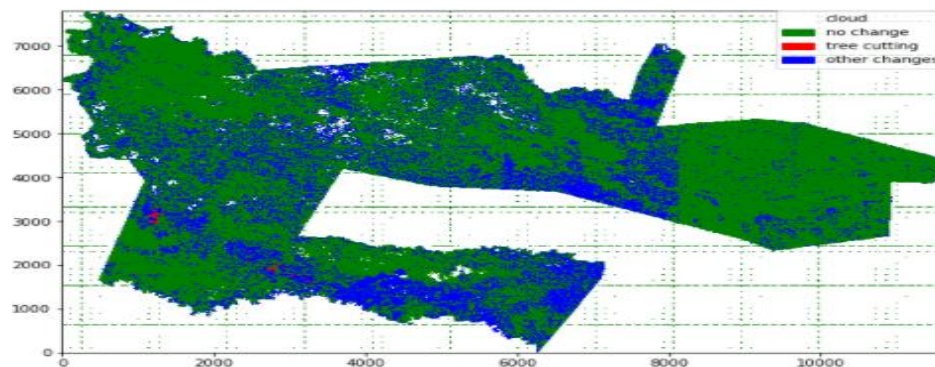


Figure 4: The change image map of the two date images

The change image map given above shows the anti-Deforestation (forest to cutting area changes) highlighted in red color, the no-change (labeled in green color), other changes (blue color) and cloud pixels (labeled in white color). The plot shows the changes tracked during comparison of the output segmentation maps of the two date images or the values of the computed "from-to" change matrix.

In this study, we have experimented to design appropriate land cover semantic segmentation model, which was our main research problem prior to cutting detection. The obtained results were not promising. And to further improve land cover segmentation performance, the CNN semantic segmentation model called U-Net was developed. The U-Net architecture was then modified to have new encoders for the sake of searching for a better model or seeking answer to our first research question. It was modified to have pre-trained VGG-16 network as its encoder part first and the obtained results were better than the results obtained by the original U-Net model. This shows that using state-of-the-art CNN architectures as encoder part of the U-Net model improves performance of the model to recognize land cover classes. The U-Net model was also modified to have pre-trained ResNet-50 as its encoder part which gives a huge improvement in performance over the original U-Net model. When we compare the results of the U-Net model with original encoder, VGG-16 encoder and ResNet-50 encoder, the U-Net with ResNet-50 encoder outperforms the rest by a margin of +3-4% accuracy. And in order to combine the capabilities of neural networks with different architectures in recognizing different image parts, we further ensembled the model outputs and attain a best landcover semantic segmentation result.



Anti-Deforestation were detected using the designed semantic segmentation model as a land cover classification scheme at a pixel-level prior to cutting detection. The detection is performed at a 10m spatial resolution which can be considered as it is enough to see the landcover changes that can happen in the area. And the obtained result shows our system is able to see small scale cuttings, it can be seen from the obtained change image map given in the above fig 4. This comes from our model design that we opted to use at pixel-level classification to see the small-scale cuttings and the deep learning approach to consider the contextual information existed around the pixels instead of merely depend on the spectral values of pixels to classify them into land cover classes.

#### 4. CONCLUSIONS AND RECOMMENDATION

The aim of this work was to develop deforestation detection: a remote sensing approach from satellite images. To achieve the outlined goal, experiments were done to build appropriate land cover semantic segmentation model to be used as a classifier for the post-classification comparison based cutting detection. The novel semantic segmentation dataset prepared in this work by using the freely available high-resolution Sentinel-2 satellite images of our study area was used to build the semantic segmentation models.

U-Net, U-Net with Vgg-16 encoder, U-Net with ResNet-50 encoder and Ensembled models were built and evaluated. The original U-Net model achieves 87.39% overall pixel accuracy. In addition, the U-Net model with modified encoders attain an improved accuracy of 88.33% and 91.48% for the U-Net with Vgg-16 encoder and U-Net with ResNet-50 encoder respectively. The proposed model designed by weighted averaging of the outputs of the U-Net, U-Net with Vgg-16 encoder and U-Net with ResNet-50 encoder models achieves 92.20% overall pixel accuracy which makes it the appropriate model for our tree cutting detection system. Moreover, tree cutting detection using post-classification comparison approach with the proposed model as a classifier was performed.

The proposed method in this work considers thick clouds as one land cover class and what is under it is left masked. Which means land cover changes cannot be monitored during cloud coverage. And this can be addressed by employing SAR imaging sensors that are able to record reflectance from the earth surface even in the presence of clouds. Image fusion of the Sentinel-1 SAR images and the Sentinel-2 optical images can be used to overcome this drawback.

During transfer learning, initial weights from network architectures pre-trained on the ImageNet dataset were used in our designed model training. Performance could be improved by applying transfer learning using network architectures pre-trained on satellite image datasets such as BigEarthNet since we are working with satellite data.

#### REFERENCES

- [1] H. Driss and B. M. El, "Deforestation Detection and Monitoring in Cedar Forests of the Moroccan Middle-Atlas Mountains," *IEEE*, 1-4244-1212, 2007.
- [2] "W. Ellen, "Participatory Forest Management in Ethiopia, Practices and Experiences," FAO Subregional Office for Eastern Africa, Addis Ababa, 2011".
- [3] B. A. Abreham, "Vegetation Composition and Deforestation Impact in Gambella National Park, Ethiopia," *Journal of Energy and Natural Resources*, vol. 5, pp. 30-36, 2016.
- [4] "R. Somnath , D. Soumyadeep and M. Dhiman, "Identifying Land Patterns from Satellite Imagery in Amazon Rainforest using Deep Learning," arXiv:1809.00340v1, Sep 2018".
- [5] "T. Taye, "Intelligent System Based Automatic Prediction of Drought Using Satellite Images," M.Sc. thesis, School of Graduate Studies, Addis Ababa university, Addis Ababa, 2011".



## Spatiotemporal Variations of Water Quality Parameters in Selected Semi-Arid Young Reservoirs in Tigray, Northern Ethiopia

Kalayu Mesfin Arefayne<sup>1,2,\*</sup>, Mekonen Teferi<sup>2,4</sup>, Tsehaye Asmelash<sup>3,4</sup>, Tsegazeabe Hadush Haileselesie<sup>2,4</sup>

<sup>1</sup>Department of Biology, Aksum University, Ethiopia

<sup>2</sup>Department of Biology, Mekelle University, Ethiopia

<sup>3</sup>Department of Medical Microbiology and Immunology, Mekelle University, Ethiopia

<sup>4</sup>Tigray Biological and Biodiversity Association (TB2A), Mekelle University, Ethiopia

\*Corresponding author, e-mail: [kalkx.123@gmail.com](mailto:kalkx.123@gmail.com)

### ABSTRACT

The health status of aquatic ecosystem is depended on the physicochemical and biological characteristics of water which provides significant information about the available resources for supporting life. This study aims to assess spatiotemporal variation of water quality parameters in selected young reservoirs in Tigray. Depth-integrated water samples (surface, middle, and just above bottom) were collected bimonthly (three times during the wet and dry seasons) at each sampling sites with a heart-valve sampler. Variation between the wet and dry seasons was examined using the independent t-test, and one-way ANOVA was used to analysis the differences among sites. We showed a significant ( $p < 0.05$ ) seasonal variation in temperature, pH and transparency in all the reservoirs investigated. Kalema reservoir was recorded with highest mean value of temperature, chlorophyll a and conductivity. Mean value of pH has a spatially significant difference ( $p < 0.05$ ) in all the study reservoirs except Kalema. None of the physicochemical water quality parameters in Kalema reservoir exhibited spatially significant ( $p > 0.05$ ) variations. Dissolved oxygen and pH showed spatially significant variation ( $p < 0.05$ ) in Mihtsab Azmati and Seisa reservoirs. A significant correlation ( $p < 0.01$ ) was recorded between temperature with turbidity, chlorophyll a, transparency and conductivity. The physicochemical parameters of the reservoirs showed distinct temporal and spatial variations. The result obtained in this study is very important as baseline information to know the ecology of reservoirs for future reservoir management. Further detailed studies that include total phosphorus, total nitrogen, etc., are needed to suggest the trophic conditions of the reservoirs.

**Keywords:** Chlorophyll a, Dissolved Oxygen, pH, Physicochemical, Temperature, Turbidity

### 1. INTRODUCTION

Water is vital to the existence of all living organisms, but this valued resource is increasingly being threatened as human populations grow and demand more water of high quality for domestic purposes and economic activities. Water quality assessment is the overall process of evaluating the physical, chemical and biological variables of water in relation to natural quality, human effects and intended uses of different substances, particularly uses that may affect human health and the health of aquatic species in general (Chapman, 1996). Water quality is affected by a wide range of natural and human influences. The quality of water may be described in terms of the concentration of the organic and inorganic material present in the water, together with certain physical characteristics of the water (Sheela, et al. 2012).

Limnology is the study of the structural and functional interrelationships of organisms of inland waters as their dynamic physical, chemical, and biotic environments affect them. It covers the attributes of all inland waters, both running as in rivers (lotic ecosystems) and standing as in lakes (lentic ecosystems) (Trenberth, et al. 2007). Generally, water quality is connected with physical, chemical and biological (including bacteriological) characteristics (Nancy, 2009) and these characteristics determine the healthy status of any aquatic ecosystem (Venkatesharaju, et al. 2010). Therefore, assessing the quality of water in any ecosystem provides significant information about the available resources for supporting life in that ecosystem.

Water is the major limiting factor for agriculture in Tigray, northern Ethiopia. To mitigate the water shortage and support subsistence agriculture of the dense population in north Ethiopia, several small reservoirs have been constructed in the past three decades for the purpose of irrigation and watering of cattle (Haregeweyn, et al., 2006;



Dejene, et al. 2008). This region is characterized by a tropical semi-arid climate with an extended dry period and a maximum effective rainy season of about two months, July-August (Nyssen, et al. 2005). To alleviate these water shortage related problems, the regional state of Tigray decided to construct a large number of small man-made reservoirs (Haregeweyn, et al. 2006).

Reservoirs are described as artificial lakes and separated from natural lakes with some of their characteristics, such as high water flow velocity, solid matter presence in influent suspend and short-term water exchange (Harper, et al. 1999). Reservoirs may exhibit particularly variable nutrient and light availability, both temporally and spatially. Nevertheless, a closer relationship between the catchment area and the aquatic system is a particular characteristic of reservoirs. Furthermore, these artificial ecosystems have a higher potential for eutrophication because of the release of nutrients from decomposing organic matter derived from flooded land (Kalff, 2002). Reservoirs are constructed for the main purpose of storing water and other uses, such as water supply for agriculture, urban activity, flood control, power generation, irrigation, recreational use and fish farming (Haregeweyn, et al. 2006).

Water must be tested for different physicochemical parameters. The selection of parameters for testing water depends upon the intended use. Physical parameters for which water samples are tested include temperature, pH, turbidity, water transparency (Secchi depth), total suspended solid (TSS), etc., while chemical tests are often performed for inorganic nutrients, dissolved oxygen, alkalinity, salinity (or conductivity), hardness and total dissolved Solids (TDS) (Patil, et al. 2012).

The water quality of freshwater habitats provides substantial information about existing resources, which depends on the influences of physicochemical parameters and biological features. Life in aquatic environments is largely governed by different physicochemical water quality characteristics and their stability. These characteristics have enabled biota to develop many adaptations that improve sustained productivity and regulate reservoir metabolism. The role of various factors, such as temperature, transparency, turbidity, water color, carbon dioxide, pH, alkalinity, hardness, ammonia, nitrite, nitrate, primary productivity, biochemical oxygen demand (BOD), plankton population, etc., cannot be overlooked for maintaining a healthy aquatic environment and for the production of sufficient fish food organisms in reservoirs for increasing fish production (Geneviève and James, 2008).

The quality of water resources is declining due to both natural (changes in precipitation; erosion) and anthropogenic (industrial and agricultural activities) factors (Sheela, et al. 2012). In addition, all reservoirs are subjected to periodic fluctuations in water levels due to rain, hydrological regimes that are influenced by irrigation of agricultural lands and temperature changes (Duncan and Kubečka, 1995). Moreover, the clearance of catchment land use and water extraction modifies the natural flow and associated water quality characteristics. The availability of water and its physical, chemical, and biological quality affect the ability of aquatic environments to sustain healthy ecosystems: as water quality and quantity are altered, organisms are often adversely affected and ecosystem services may be lost (Reynolds, 2006).

Previous studies were conducted on the ecology and related aspects of many manmade semiarid and arid reservoirs in Tigray (Asmelash, et al. 2007; Dejenie, et al. 2008; Teferi, et al. 2014; Zebib and Teame, 2017). However, there are no scientific data on spatiotemporal water quality parameters for the selected young reservoirs. Therefore, the present study aims to generate scientific data on spatiotemporal water quality parameters, which have never been studied. We hypothesized that during the dry season when the input of water is low, most physicochemical water quality parameters would have higher concentrations (as compared to the wet season) for different reasons, such as re-suspension, absence of dilution, and increased evaporation.

## 2. MATERIALS AND METHODS

### 2.1. Description of the Study Site

The study reservoirs are located in Tigray regional state of Ethiopia. Tigray is in northern Ethiopia with a rugged terrain ranging between 400 to almost 4000 m asl, covering a total area of 50,079 km<sup>2</sup> and it lies between latitudes 12°15' and 14°57'N and longitudes 36°27' to 39°59'E (CSA, 2006). It is bounded in the north by Eritrea, to the west by Sudan and to the east and south by the Afar and Amhara regions of Ethiopia, respectively

(Fig. 1). This study was conducted in four selected manmade young reservoirs: Seisa, Mihtsab Azmati, May Dimu and Kalema. Seisa reservoir is found in Debri Tabia of Adwa woreda in the Central Zone of Tigray. It was constructed in 2012 with a capacity of 12 Mm<sup>3</sup> and a canal length of 400 m. Mihtsab Azmati reservoir is found in Baekel Tabia (Tabia is the lowest administrative level in the Tigray Regional National State of Ethiopia), Mereb Leak woreda (district) in the Central Zone of Tigray. This reservoir was constructed in 2015 with 34000Mm<sup>3</sup> actual capacity and 2000 m canal length (Gebrehiwot, 2020). May Dimu reservoir is found in the May Dimu Tabia of Tahtay-Koraro woreda, northwestern Tigray, located 15 km west of Shire Endaselasie town. Kalema is found in Wolkait woreda, in the Western Zone of Tigray.

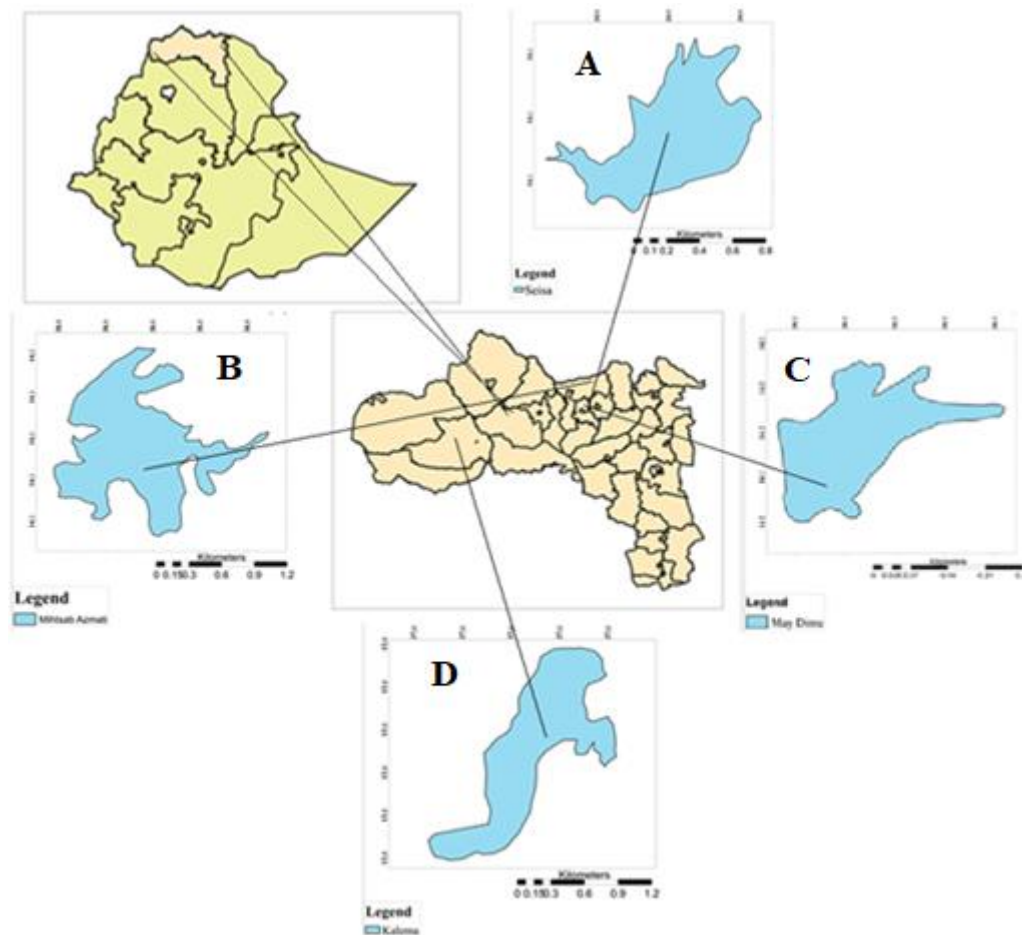


Figure 1. Location map of the study sites (A=Seisa, B= Mihtsab Azmati, C= May Dimu and D= Kalema reservoirs)

## 2.2 Sampling Design and Methodology

To select sampling sites characteristics of each reservoir were observed. Mihtsab Azmati and May Dimu reservoirs are relatively protected from direct human and animal contact. The waste from domestic animals and household disposals and other related agricultural byproducts may not easily reach the center of the reservoir, especially in the dry season when no flood carries waste matter from the watershed. Kalema reservoir is situated on the Kalema river (a tributary of the Tekeze river) having a continuous year round water flow but with low human and animal interference. Seisa reservoir was surrounded by agricultural land and human settlements. Hence, the site has a relatively high anthropogenic impact.

Water samples were collected bimonthly from November 2018 – September 2019 (three times in the dry season; Nov-2018, Jan-2019, Mar-2019 and three times in the wet season; May-2019, Jul-2019, Sep-2019). Taking the surface area of the study reservoirs into consideration, three littoral and two pelagic from Seisa, four littoral and two pelagic from Mihtsab Azmati, two littoral and two pelagic from May Dimu and two littoral and



two pelagic from Kalema reservoirs were selected. Spatial variables include geographical coordinates (altitude, latitude and longitude) and average depth was taken. A boat was used to take depth-integrated water samples (surface, middle, and just above bottom) at each site with a heart-valve sampler (volume: 3 L content). Temperature, dissolved oxygen, conductivity and pH of the water were measured in situ at three different depths (surface, middle, near-bottom) with a portable meter WTW Multi 340 I electrodes. We used calibrated fluorometer readings (Turner Aquafluor; an average of three measurements) on the pooled water sample to measure turbidity and chlorophyll-a concentration (as a proxy of phytoplankton biomass). Water transparency was measured using both a cylindrical Snell’s tube (length: 0.6 m; diameter: 60 mm; disc diameter: 55 mm) and a Secchi-disc (diameter: 30 cm). In shallow systems, the measurement of Snell’s depth is often the preferable method to quantify water transparency because it avoids missing data in cases when reservoir sediments are visible.

### 2.3 Data Analysis Method

Except pH, all variables were log or log(x + 1) transformed prior to statistical analysis. We studied patterns of association between the investigated variables with principal component analysis (PCA). Differences for each physicochemical water quality variable between the wet and dry seasons were examined using the independent t-test, and differences among sites were examined using one-way ANOVA, both at a significance level of  $p < 0.05$ . The degree of association between the water qualities parameters were analyzed using the Pearson correlation coefficient  $r$ . The significance of these coefficients was tested at different probability levels ( $p < 0.05^*$  and  $p < 0.05^{**}$ ) (Beguin, 1979). The reservoir physicochemical water quality variables were also subjected to multivariate statistical techniques using principal component analysis (PCA), which is one of the most commonly used multivariate statistical techniques (Quinn and Keough, 2002).

## 3. RESULTS

### 3.1 Physicochemical Characteristics

Average physicochemical water quality parameters is presented in (Table 1). The highest and lowest pH mean values were recorded in the Seisa and May Dimu reservoirs, respectively. The highest mean values of temperature ( $27.66 \pm 0.15$ ), chlorophyll a ( $108.81 \pm 6.55$ ) and conductivity ( $369.72 \pm 10.2$ ) were recorded in Kalema reservoir. However, lowest mean turbidity ( $4.07 \pm 0.28$ ) and Secchi disc transparency (cm) ( $193.55 \pm 3.53$ ) were recorded in Seisa and Mihtsab Azmati reservoirs during the study period. May Dimu and Kalema reservoirs had the highest and lowest mean dissolved oxygen contents ( $6.23 \pm 0.09$  mg/l and  $5.82 \pm 0.13$  mg/l), respectively.

Table 1. Annual average physicochemical water quality parameters (mean  $\pm$ SE) of the four study reservoirs

Reservoir	Altitude (masl)	Av/Depth (m)	pH	Dissolved Oxygen (mg/l)	Temperature (°C)	Chlorophyll a ( $\mu\text{g l}^{-1}$ )	Turbidity (NTU)	Secchi disc-transparency (cm)	Conductivity ( $\mu\text{S cm}^{-1}$ )
MA	1512	21.5	$8.22 \pm 0.02$	$6.19 \pm 1.10$	$24.78 \pm 0.15$	$38.88 \pm 1.17$	$2.43 \pm 0.19$	$193.55 \pm 3.53$	$182.73 \pm 5.64$
MD	1642	17	$7.97 \pm 0.03$	$6.23 \pm 0.09$	$22.77 \pm 0.17$	$50.85 \pm 1.77$	$3.10 \pm 0.80$	$113.87 \pm 2.55$	$67.95 \pm 2.38$
SE	1941	17	$8.23 \pm 0.04$	$6.10 \pm 1.10$	$22.29 \pm 1.14$	$67.16 \pm 2.16$	$4.07 \pm 0.28$	$93.06 \pm 2.74$	$159.96 \pm 4.88$
KA	827	10.5	$7.98 \pm 0.06$	$5.82 \pm 0.13$	$27.66 \pm 0.15$	$108.81 \pm 6.55$	$1.69 \pm 0.13$	$103.65 \pm 5.94$	$369.72 \pm 10.2$

Note: MA – Mihtsab Azmati, MD – May Dimu, SE – Seisa and KA – Kalema reservoirs

### 3.2 Spatial Variation in Physicochemical Water Quality Parameters

Spatial variations in physicochemical water quality parameters are presented in (Table 2). Overall littoral regions of the reservoirs showed statistically significant different values for pH, DO (mg/l) and Transparency (cm) (Table 2). However, the values for most of the other physicochemical parameters did not show significant



difference in spatial variation during the study period. The highest mean value of pH was recorded in the littoral site of Seisa and lowest mean values of pH was recorded from pelagic region of Kalema reservoir. The littoral and pelagic habitats of Mihtsab Azmati reservoir had the highest (6.53 mg/l) and lowest (5.52 mg/l) mean values of dissolved oxygen, respectively, compared with the other selected reservoirs during the study period (Table 2). The highest and the lowest water temperatures were recorded in the pelagic habitat of Kalema and Seisa reservoirs, respectively. Only the mean values of pH and dissolved oxygen (mg/l) were significantly different ( $p < 0.05$ ) in Mihtsab Azmati and Seisa reservoirs. Furthermore, the mean value of pH has a spatially significant difference ( $p < 0.05$ ) in May Dimu reservoir. None of the physicochemical water quality parameters in Kalema reservoir exhibited spatially significant ( $p > 0.05$ ) variations. Similarly, other physicochemical parameters such as temperature, chlorophyll a, turbidity, Secchi disc transparency and conductivity in all the four study reservoirs were also not significant ( $p > 0.05$ ) spatially.

Table 2. Spatial variation in physicochemical parameters with in the reservoirs (mean during the study period)

Physico-chemical parameters	Reservoirs											
	Mihtsab Azmati			May Dimu			Seisa			Kalema		
	Littoral	Pelagic	P value	Littoral	Pelagic	P value	Littoral	Pelagic	P value	Littoral	Pelagic	P value
pH	8.27	8.12	0.00	7.89	8.06	0.00	8.34	8.06	0.00	8.10	7.87	0.07
DO (mg/l)	6.53	5.52	0.00	6.37	6.22	0.44	6.36	5.70	0.00	5.72	5.93	0.45
Temp (°C)	25.01	24.49	0.13	22.72	22.82	0.79	22.46	22.02	0.13	27.48	27.85	0.22
Chl a ( $\mu\text{g l}^{-1}$ )	40.24	36.18	0.10	50.98	50.73	0.94	70.04	62.84	0.10	115.75	101.86	0.29
Turb (NTU)	2.54	2.88	0.65	3.61	2.59	0.53	3.84	4.41	0.32	1.53	1.85	0.22
Trans (cm)	193.45	193.75	0.97	112.08	115.66	0.48	87.88	100.83	0.02	101.40	105.90	0.70
Cond ( $\mu\text{Scm}^{-1}$ )	184.35	179.49	0.68	69.66	66.25	0.47	161.59	157.51	0.68	359.04	380.39	0.29

Note:  $p < 0.05$  (significant) and  $p > 0.05$  (not significant)

### 3.3 Seasonal Variation in Physicochemical Water Quality Parameters

Seasonal variation in physicochemical water quality parameters is described in (Table 3). In Mihtsab Azmati reservoir, pH mean value (8.34) and water temperature (25.83°C) measured for the wet season were higher than for the dry season. Both parameters were significantly different between the seasons ( $p < 0.05$ ; Table 3). However, mean values of secchi disc transparency (201.27 cm) and conductivity (232.79  $\mu\text{S/cm}$ ) measured for the dry season were higher than for the wet season, and both showed statistically significant difference ( $p < 0.05$ ). No significant differences between the two seasons were observed in the other water quality parameters measured in Mihtsab Azmati reservoir (Table 3). In May Dimu reservoir, all the sampled physicochemical water quality parameters except turbidity showed significant differences between the two seasons ( $p < 0.05$ ). The pH mean value (8.07) and water temperature (23.54 °C) measured for the wet season were higher than for the dry season. However, dissolved oxygen (6.79 mg/l), chlorophyll a (56.45  $\mu\text{g/l}$ ), Secchi disc transparency (126.91 cm) and conductivity (72.47  $\mu\text{S/cm}$ ) measured during the dry season were higher than during the wet season. In Seisa reservoir, pH mean value (8.34), water temperature (25.38°C), chlorophyll a (72.54  $\mu\text{g l}^{-1}$ ), and turbidity (4.72 NTU) measured for the wet season were higher than for the dry season, and these were statistically significantly different between the two seasons ( $p < 0.05$ ; Table 3). Nevertheless, mean value of Secchi disc transparency (111.26 cm) measured for the dry season was higher than for the wet season, and showed statistically significant difference ( $p < 0.05$ ).

In Kalema reservoir, pH mean value (8.19) and water temperature (28.19°C) measured for the wet season were higher than for the dry season. Both parameters were significantly different between the seasons ( $p < 0.05$ ; Table 3). However, chlorophyll a (120.00  $\mu\text{g/l}$ ) and secchi disc transparency (136.25 cm) measured for the dry seasons were higher than the wet season with statistically significant differences ( $p < 0.05$ ).



Table 3. Seasonal variation in physicochemical parameters within the four study reservoirs (mean value during the study period)

Physico-chemical parameters	Reservoirs											
	Mihtsab Azmati			May Dimu			Seisa			Kalema		
	Wet season	Dry season	P Value	Wet season	Dry season	P Value	Wet season	Dry season	P Value	Wet season	Dry season	P Value
pH	8.34	8.10	0.00	8.07	7.87	0.02	8.34	8.12	0.00	8.19	7.85	0.00
DO (mg/l)	6.37	6.02	0.08	5.80	6.79	0.00	6.11	6.09	0.93	5.56	6.00	0.10
Temp (°C)	25.83	23.84	0.00	23.54	21.70	0.00	23.38	21.19	0.00	28.19	27.31	0.00
Chl a (µg l <sup>-1</sup> )	40.88	36.89	0.09	45.26	56.45	0.00	72.54	61.78	0.01	92.02	120.00	0.05
Turb (NTU)	2.98	2.32	0.35	3.86	2.34	0.35	4.72	3.42	0.02	1.71	1.67	0.89
Trans (cm)	185.8	201.3	0.02	100.8	126.9	0.00	74.86	111.3	0.00	81.91	136.25	0.00
Cond (µScm <sup>-1</sup> )	132.7	232.8	0.00	63.44	72.47	0.05	159.2	160.8	0.87	366.17	372.08	0.77

Note:  $p < 0.05$  (significant difference) and  $p > 0.05$  (no significant difference)

### 3.4 Correlation Analysis between Physicochemical Water Quality Parameters

The degree of association between any two of the water quality parameters as measured by the simple correlation coefficient ( $r$ ) is presented in (Table 4). Accordingly, pH has a significant negative correlation with chlorophyll a ( $\mu\text{g/l}$ ) and conductivity ( $\mu\text{S/cm}$ ), with correlation values of  $r=-0.195$  and  $r=-0.100$ , respectively, with significance at  $p < 0.01$  and  $p < 0.05$ , respectively. However, a positive correlation was observed between pH and Secchi disc transparency (cm), pH and turbidity (NTU), pH and water temperature ( $^{\circ}\text{C}$ ) and pH and dissolved oxygen (mg/l), with correlation values of  $r=0.135$ ,  $r=0.007$ ,  $r=0.07$  and  $r=0.267$ , respectively, with significance at  $p < 0.05$ ,  $p < 0.05$ ,  $p > 0.05$  and  $p < 0.01$ , respectively. Dissolved oxygen (mg/l) was positively correlated with turbidity ( $r = 0.080$ ), but it was negatively correlated with Secchi disc transparency, water temperature ( $^{\circ}\text{C}$ ), chlorophyll a ( $\mu\text{g/l}$ ) and conductivity ( $\mu\text{S/cm}$ ), with correlation values of  $r = 0.049$ ,  $r = -0.095^*$ ,  $-0.088$  and  $-0.136^{**}$ , respectively. A highly significant negative correlation ( $r=-0.212$ ,  $p < 0.01$ ) was recorded between water temperature ( $^{\circ}\text{C}$ ) and turbidity (NTU), but a highly significant positive correlation ( $r=0.260$ ,  $p < 0.01$ ), ( $r=0.187$ ,  $p < 0.01$ ) ( $r=0.472$ ,  $p < 0.01$ ) was observed between water temperature ( $^{\circ}\text{C}$ ) and chlorophyll a ( $\mu\text{g/l}$ ), water temperature ( $^{\circ}\text{C}$ ) and Secchi disc transparency (cm) and water temperature ( $^{\circ}\text{C}$ ) and conductivity ( $\mu\text{S/cm}$ ). The value of chlorophyll a ( $\mu\text{g/l}$ ) was negatively correlated and highly significantly negatively correlated with turbidity (NTU) and Secchi disc transparency (cm) ( $r=-0.59$ ,  $p > 0.05$  and  $r=-0.300$ ,  $p < 0.01$ ) but highly positively correlated with conductivity ( $\mu\text{S/cm}$ ) ( $r=0.506$ ,  $p < 0.01$ ). Significant negative correlation analysis values ( $r = -0.143$   $p < 0.01$ ), ( $r=-0.123$ ,  $p < 0.05$ ) and ( $r=-0.006$ ,  $p < 0.05$ ) were recorded between turbidity (NTU) and Secchi disc transparency (cm), turbidity (NTU) and conductivity ( $\mu\text{S/cm}$ ) and between Secchi disc transparency (cm) and conductivity ( $\mu\text{S/cm}$ ), respectively.

Table 4. Correlation matrix between different physicochemical water quality parameters of the selected reservoirs. All parameters were analyzed using Pearson correlation

	pH	DO	Temp	Chl a	Turb	Transp	Condu
pH	1						
DO	0.267**	1					
Temp	0.007	-0.095*	1				
Chl a	-0.196**	-0.088	0.260**	1			
Turb	0.135*	0.080	-0.183**	-0.59	1		
Transp	0.007	-0.049	0.187**	-0.300**	-0.143**	1	
Condu	-0.100*	-0.136**	0.472**	0.506**	-0.123*	-0.006	1

\* Correlation is significant at  $p < 0.05$  level; \*\* Correlation is significant at  $p < 0.01$  level

### 3.5 Principal Component Analysis

More than 70% of the variation in environmental variables of the reservoirs is explained by two PCA axes, and axis 1 is highly loaded by conductivity, temperature and chlorophyll a. The Principal Component Analysis (PCA) showed that the second principal components (PCs) represented approximately 48.4% of the total variation in the entire data set (Fig. 2). The first PC axis accounted for 25.4% of the total variance. The principal components (PCs) helped to classify the water quality factor loadings as strong, moderate, or weak in correspondence with their absolute loading strengths of >0.75, 0.75-0.50, and 0.50-0.30, respectively.

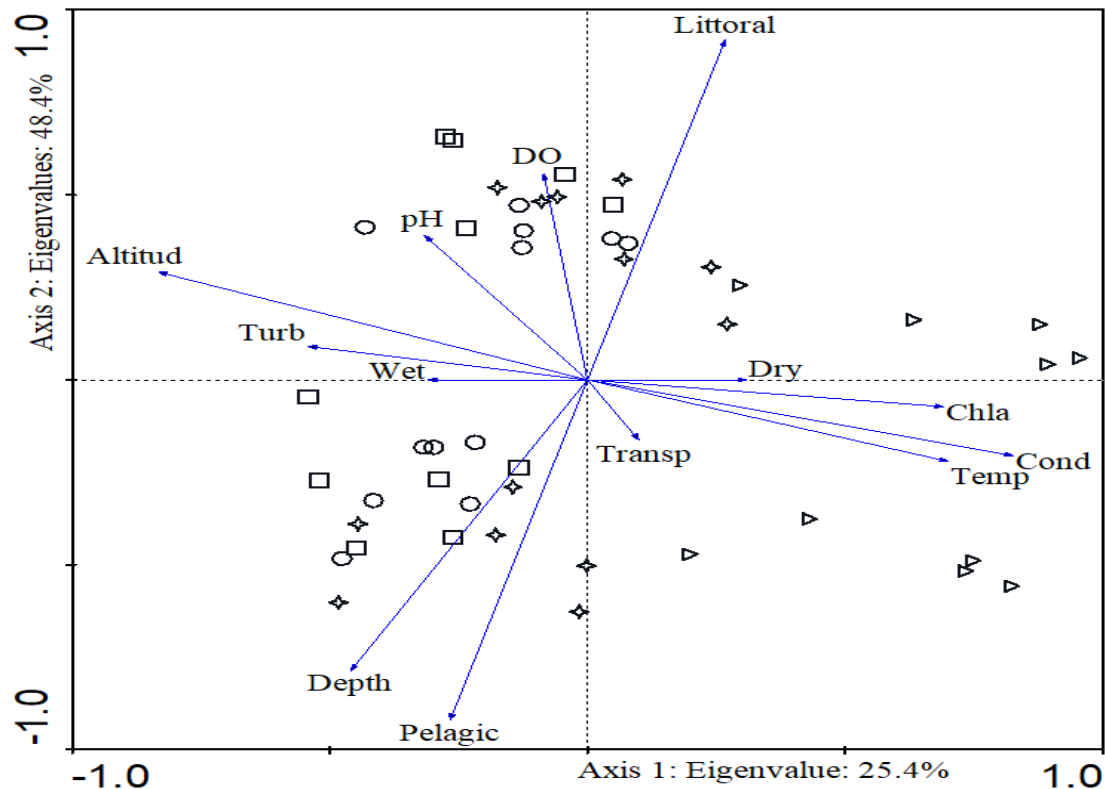


Figure 2. Biplot of standardized PCA results showing the association between environmental variables of the four study reservoirs (Mihtsab Azmati is indicated by empty stars, May Dimu is indicated by empty circles, Seisa is indicated by empty squares, and Kalema is indicated by empty right triangles). The abbreviations in the PCA: Altitud= altitude, Temp= temperature, cond= electrical conductivity, DO= dissolved oxygen, Chla= chlorophyll a, Transp= water transparency)

### 4. DISCUSSION

We have detected seasonal variation among the measured physicochemical parameters, with values for chlorophyll a, water transparency and electric conductivity being higher during the dry season while the values for pH, water temperature and turbidity was higher during the wet season.

During the study period a narrow spatial variation of mean pH value was recorded among the reservoirs, with minimum value (7.97) in May Dimu and maximum value (8.23) in Seisa. The mean pH values of young reservoirs studied here indicate that the reservoirs are relatively alkaline system. The pH range of these young reservoirs fall within the pH value accepted as good water quality (6.5 to 8.5) for drainage basins across the globe (Carr and Neary, 2008). The pH values reported here are similar to other young reservoirs previously reported by other researchers (Teferi, et al. 2013); Zebib and Teame, 2017; Tadesse, et al. 2015).

A previous study in Funil reservoir by Francisco, et al. (2011) reported higher mean values of pH during the wet season (8.6) and lower mean values during the dry season (7.2), with no significant seasonal differences, which disagrees with the current finding. Shallow tropical reservoirs critically exhibit longitudinal gradients in turbidity, nutrient concentration, mixing depth, euphotic depth, with sufficient light for photosynthesis, flushing



rates, chlorophyll concentration, plankton productivity, fish standing stocks, macrophytes abundance, benthic community structure and other limnological and biological variables. The highest pH was due to having much increased photosynthesis activity by phytoplanktons than the respiratory activity (Atobatele and Ugwumba, 2008; Meesukko, et al. 2007) and presence of high turbulence. However, low pH was recorded due to reduced photosynthetic activity (Rafique, et al. 2002); the absence of rain (Atobatele and Ugwumba, 2008) and the decomposition of organic matter by microbial activity which was enhanced by high temperature, causing excessive production of CO<sub>2</sub> and reduced pH (Moundiotiya, et al. 2004). According to Gupta and Gupta (2006), accumulation of free carbon dioxide due to little photosynthetic activities of phytoplankton (during rainy season) will lower the pH values of waterbody while intense photosynthesis by phytoplankton (during dry season) will increase pH values. pH is a very important factor of water body for the fish culture as it controls the amount of soluble ions in the water. An acidic pH of water reduces the growth rate, metabolic rate and other physiological activities of fishes (Mollah, et al. 2015), thus suggested that pH values varying from 6.5 to 9.0 as suitable for the normal growth of fishes.

Dissolved oxygen is one of the most important water quality parameters, and its correlation with water bodies provides direct and indirect information, e.g., bacterial activity, photosynthesis, availability of nutrients, and stratification (Premlata, 2009). A similar study by Thirupathaiiah, et al. (2012) and Hussain, et al. (2013) reported minimum and maximum values of dissolved oxygen (5.60 to 8.395 mg/l and 5.0 to 9.46 mg/l, respectively), which is a narrow range but higher value compared with the present finding. The variation in dissolved oxygen in different reservoirs may be due to the high metabolic rate of organisms and low atmospheric temperature. The mean dissolved oxygen in all reservoirs of the current finding was higher than previous finding (Zebib and Teame, 2017) with mean dissolved oxygen value (4.77 and 4.85 mg/l) but lower than Tadesse, et al. (2015) reported higher average dissolved oxygen value 7.03 mg/l from five tropical small dams (Korrir, Laelay Wukro, Mai Nigus, Mai Sessea and Mai Seye dams) and Berihun and Dejene (2012) reported 7.19 mg/l average dissolved oxygen value for Korrir and Laelay Wukro dams. Sources of dissolved oxygen in the aquatic environment include the atmosphere and photosynthesis. This depends on its solubility, while a loss of oxygen includes respiration, decay by aerobic bacteria and decomposition of dead decaying sediments (Gupta and Gupta, 2006).

In the present study, higher mean values of dissolved oxygen (6.37 mg/l and 6.11 mg/l) were recorded in Mihtsab Azmati and Seisa reservoirs in the wet season, which is in agreement with previous findings by Francisco, et al. (2011) in the Funil Reservoir. This may be due to the addition of varieties of biodegradable pollutants from domestic sewage, municipal wastes, run-off from agricultural land, etc., that stimulate the growth of microorganisms that consume dissolved oxygen for decomposition. Thus, the concentration gradually depletes during the dry season. Long days and intense sunlight seem to accelerate photosynthesis by phytoplankton, utilizing CO<sub>2</sub> and giving off oxygen, possibly for greater qualities of oxygen recorded during the dry season (Krishnamurthy, 1990). The dissolved oxygen concentration in the aquatic ecosystem is regulated by the process of diffusion of oxygen from the atmosphere, photosynthetic activity, respiration and decomposition of aquatic organisms (Mollah, et al. 2015).

The mean water temperature of the study sites has showed spatial variation with 20.90 to 27.90 °C in Mihtsab Azmati, 18.9 to 28.13 °C in May Dimu, 18.9 to 25.4 °C in Seisa and 24.6 to 30.9 °C in Kalema reservoirs, which is supported by Thirupathaiiah, et al. (2012). The water temperature of the lower manair reservoir of the Karimnagar district ranged from 24.75 °C to 28.5 °C in different seasons. The fluctuation in water temperature was high, which may be due to the low water level, high air temperature and clean atmosphere. The present finding was showed higher values compared to previous study by Zebib and Teame (2017) in Korrir (20.07 °C) and Laelay Wukro (21.98 °C) reservoirs. Berihun and Dejene (2012) also found an 18.88 °C average temperature value for Korrir and Laelay Wukro reservoirs for one year of data, which is lower than the present finding. The variation in water temperature among the reservoirs might depend on altitude because as altitude increases, water temperature decreases. Water temperature affects the activity, growth and reproduction of all organisms, including fish (Wetzel, 1983). In the present study, we found that there was a distinct seasonal pattern in water temperature, which was higher in the wet season in all the investigated reservoirs. The current finding was in line



with (Francisco, et al. 2011). Senthil and Prabakaran (2012) reported that higher average temperatures were recorded during the wet season. However, in contrast with the present finding, Woldeab, et al. (2018) reported higher water temperatures (22.49 to 25 °C) in the dry season from the Gilgel Gibe reservoir. Similar findings in the Eleyele reservoir (Olanrewaju, et al. 2017), Ado-Ekiti reservoir (Idowu, et al. 2013), Oyun reservoir (Mustapha, 2009) and Ero reservoir (Oso and Fagbuaro, 2008) also reported higher temperatures during the dry season. The low temperature observed during the rains could be due to high humidity and moderate or less sunlight in this period of the year.

Secchi disc depth is a good indicator of environmental health and ecological productivity. In the present study, spatiotemporal variation of secchi disc-water transparency was observed among reservoirs with higher mean value during the dry season. Zebib and Teame (2017) reported higher mean value of secchi disc-water transparency (29.55cm) in Laelay Wukro reservoir. Secchi disc-water transparency in Gereb Awso reservoir (0.15m), in Tsinkanet reservoir (0.7m) and in Mai Gassa I reservoir (0.3m) were also reported by Teferi, et al. (2013). In 32 reservoirs found in Tigray also reported a mean value of secchi disc-water transparency (0.46m) by Dejene, et al. (2008). However all these previous findings were lower than the current finding with 93.06 cm and 193.55 cm mean value of secchi disc-water transparency in Seisa and Mihtsab Azmati reservoirs, respectively. Therefore, these values reflect that the depth of light penetration is good in the present finding, which is worthy of a shallow reservoir as plankton grow, thus making food available to fish. The present finding agrees with similar previous findings of Syarifah, et al. (2018) in the Sembrong reservoir, Olanrewaju, et al. (2017) in the Eleyele reservoir, Francisco, et al. (2011) in the Funil reservoir and Thirupathaiyah, et al. (2012) in the lower Manair reservoir. This seasonal variation was due to erosion from the upper catchment that created a sediment load on reservoirs because most of the catchment of the reservoirs was not well protected. The main reason for lower Secchi disc-water transparency in the wet season may be due to high concentrations of dissolved and particulate substances (eroded soils and nutrients) that were transported from the surrounding catchment into the reservoir after rainfall reduced light transmission and water clarity. On the other hand, Khan and Chowdhury (1994) reported that higher water transparency occurred during the dry season, which may be due to the absence of rain, runoff and flood water as well as the gradual settling of suspended particles.

We found that there was a distinct seasonal pattern with a higher mean value of electrical conductivity in the dry season and littoral habitat in the studied reservoirs. This difference may be due to the difference in geological characteristics of these watersheds. Similar findings were also reported by Woldeab, et al. (2018) in the Gilgel Gibe reservoir, Fasil, et al. (2011) in Koka reservoir but highly lower than the previous finding of Tessema, et al. (2014) (569  $\mu\text{S}/\text{cm}$ ) in the Tendaho. During the dry season, the increased concentration of electrical conductivity may be associated with evaporation and the absence of a dilution effect, while the lower values during the wet season are hypothesized to be due to the effect of dilution arising from the tributaries. The higher conductivity values measured during the dry season in the sampling period, indicating the apparent correlation between conductivity and water level.

Turbidity is a measure of how particles suspended in water affect water clarity. Turbidity results in a decrease in the intensity of light that passes through cloudiness or turbidity water due to light, absorption, and reflection of light. It also increases sharply during and after rainfall, which causes sediment to be carried into the water body (Higham, et al, 2015). In the present finding, higher values of turbidity were recorded during the wet season and pelagic habitat in the studied reservoirs, and Seisa reservoir had the highest mean turbidity value of 4.72 NTU compared with the others. This finding is inline with previous research reports in Ajiwa reservoir Usman and Yerima (2017), Tono reservoir Akongyuure and Alhassan (2021), Gilgel Gibe reservoir Woldeab, et al. (2018). This might be because the watershed of the reservoirs is surrounded by agricultural farmlands and eroded silt particles by floods. Similar findings by Dagaonkar and Saksena (1992), Thirupathaiyah, et al. (2012) and Garg, et al. (2006b) have also reported that high turbidity during the rainy season may be due to higher incoming flows or run-offs which cause re-suspension of dissolved materials. During the rainy season, silt, clay and other suspended particles contribute to the turbidity values, while during the dry season, the settlement of silt and clay results in low turbidity. Turbidity is also able to increase the water temperature because the particles in the water to the



surface absorb more heat. These factors lead to the reduction of dissolved oxygen (Léziart et al., 2019). Turbidity measurement is an important test when trying to determine water quality.

Chlorophyll is a measure of the number of algae growing in a water body and is also used to classify the trophic condition of a water body. During the study period temporal variation in chlorophyll -a concentration was observed among the reservoirs with highest mean value (369.72 $\mu$ g/l) recorded in Kalema reservoir. Teferi, et al. (2013) also reported highest mean value of chlorophyll a (65.64  $\mu$ g/l) in Tsinkanet reservoir which is lower than the current finding. Highest mean value of chlorophyll-a was recorded in Kalema and May Dimu reservoirs during the dry season. Dejene, et al. (2008) also reported similar finding in the 32 reservoirs in Tigray. Largest concentrations of chlorophyll-a in the transition zone can be due to the theoretical relationship between light and phosphorous, with a higher concentration in this area, increasing the primary productivity. In this relationship, the possibility of resuspension of forms of phosphorus trapped in the sediment that, associated with light availability, may cause elevated concentrations of chlorophyll-a and phytoplankton in the shoreline of reservoirs.

Moreover, the present study also analyzed the correlation coefficient (r) between every physicochemical water quality parameter pair computed by taking the average values of the studied sites. Accordingly, pH with water temperature, turbidity, Secchi disc-water transparency and dissolved oxygen has been found to show positive correlations. The present finding disagrees with similar previous findings by Thirupathaiiah, et al. (2012); Usman and Kwang-Guk (2019) also reported a negative correlation between pH and dissolved oxygen, which is different from the present finding. However, a positive correlation of pH with electrical conductivity, pH with chlorophyll-a and dissolved oxygen with chlorophyll-a was also reported, which disagrees with the present finding. As indicated, the negative correlation of dissolved oxygen with numerous other water quality parameters (water temperature, electrical conductivity and chlorophyll a) in the present study revealed the persistence of organic pollution in reservoirs, which can be reflected as one of the main roots of chemical, ecological, and environmental degradation. The present finding reported a highly significant positive relationship between water temperature and Secchi disc-water transparency and was in line with previous findings from the Awab reservoir by Anago, et al. (2013). This could be possible because light heats the surface of the water before penetrating into other depths.

Negative correlation between turbidity and chlorophyll a was observed during the present finding. This is agreed with the finding of Bacroume, et al. (2015) studied in the Mansour Eddahbi reservoir, Morocco. This might be due to high water depth because in present finding the minimum average depth of the reservoirs is above ten meter. This means the fish species found in the reservoirs is less impact of increase turbidity by resuspended the bottom layer. The reservoirs were newly established and less effect of agricultural activity so they are not affected by algal bloome. Alternatively, the turbidity has a negative effect on algal photosynthesis. It influences the degree of light penetration in the water column; also the turbidity adsorbs phosphates (nutrient) by silt (Zhang, et al. 2010). This may explain the interaction of the turbidity and chlorophyll (a). However, Dejenie, et al. (2008) reported positive coorelation between chlorophyll a and turbidity which was conducted in 32 manmade tropical highland reservoirs. The maximum depths of the reservoirs were 11 meter which much shallow compared with the presently studied reservoirs. Often, water quality in such reservoirs is poor and is characterised by high nutrient levels, high turbidity and phytoplankton blooms. In addition the dominance Garra in the reservoirs can potentially have an impact on important ecosystem characteristics of the reservoirs (water transparency, nutrient availability, phytoplankton primary productivity).

## 5. CONCLUSIONS AND RECOMMENDATIONS

This study persuasively contributes to assessing spatiotemporal water quality dynamics to provide valuable insight into the general health status of the selected young reservoirs. The physicochemical parameters of Mihtsab Azmati, May Dimu, Seisa and Kalema reservoirs showed distinct temporal and spatial variations throughout the study period. Most physicochemical water quality variables (pH, dissolved oxygen, electrical conductivity and chlorophyll a) were also spatially higher in the littoral site. pH was significantly positively correlated with water transparency, turbidity and temperature. However, dissolved oxygen showed a negative correlation with transparency, turbidity, temperature, chlorophyll a and electrical conductivity. Turbidity also had a significantly negative correlation with water transparency and temperature. In this study, we tried to analyze some



physicochemical water quality variables, but further detailed studies that include total phosphorus, total nitrogen, etc., are needed to suggest the trophic conditions of the reservoirs.

## ACKNOWLEDGMENTS

This research was financially supported by the NORAD IV (MU-NMBU) project, Mekelle University and Aksum University. We also thank the aquatic ecology research team of the Biology Department of Mekelle University for logistical support and for their assistance in both field and laboratory work. Finally, we would like to thank all the individuals in all research sites for their valuable support during data collection.

## REFERENCES

- Akongyuure, D. N. and Alhassan, E. H. (2021): Variation of water quality parameters and correlation among them and fish catch per unit effort of the Tono Reservoir in Northern Ghana. *Journal of Freshwater Ecology*, 36(1): 253-269.
- Anago, I. J. Esenowo, I. K. and Ugwumba, A. A. (2013): The physico-chemistry and plankton diversity of Awba Reservoir University of Ibadan, Ibadan Nigeria. *Research Journal of Environmental and Earth Sciences*, 5(11): 638-644.
- Asmelash, T. Dejenie, T. Declerck, S. Nyssen, J. Van der Gucht, K. Risch, S. R. S. and Gebrekidan, A. (2007): Ecological atlas of reservoirs in Tigray, Northern Ethiopia. Tigray Livelihood Papers No. 4, VLIR-Mekelle University IUC Programme.
- Atobatele, O. E. and Ugwumba, O. A. (2008): Seasonal variation in the physicochemistry of a small tropical reservoir (Aiba Reservoir, Iwo, Osun, Nigeria). *African Journal of Biotechnology*, 7(12).
- Bacroume, S. Garras, S. Barcha, S. E. El Fehri, I. C. Bellaouchou, A. and Fekhaoui, M. (2015): Chlorophyll (a) and turbidity relationships with environmental variables in the Mansour Eddahbi lake reservoir (Ouarzazate, Morocco). *Journal of Material and Environmental Science*, 6(10): 2771-2777.
- Beguín, H. (1979): *Méthodes d'analyse géographique quantitative*. Librairies Techniques, Paris, p. 283.
- Berihun, A. and Dejenie, T. (2012): Population Dynamics and Condition Factor of *Oreochromis niloticus* L. in Two Tropical Small Dams, Tigray (Northern Ethiopia). *Journal of Agricultural Science and Technology*, 2(10B): 1062.
- Central Statistical Authority (CSA). (2006): Central Statistical Authority Annual report, Addis Ababa, Ethiopia.
- Chapman, D. V. (1996): *Water quality assessments: a guide to the use of biota, sediments and water in environmental monitoring*. 2nd ed. New York: UNESCO/ WHO/ UNEP.
- Dagaonkar, A. and Saksena, D. N. (1992): Physico-chemical and biological characterization of a temple tank Kailasagar, Gwalior, Madhya Pradesh. *Journal of Hydrobiology*, 8(1): 11-19.
- Dejenie, T. Asmelash, T. De Meester, L. Mulugeta, A. Gebrekidan, A. Risch, S. and Declerck, S. (2008): Limnological and ecological characteristics of tropical highland reservoirs in Tigray, Northern Ethiopia. *Hydrobiologia*, 610:193-209.
- Duncan, A. and Kubečka, J. (1995): Land/water ecotone effects in reservoirs on the fish fauna. *Hydrobiologia*, 303:11-30.
- Fasil, D. Kibru, T. Gashaw, T. Fikadu, T. and Aschalew, L. (2011): Some limnological aspects of Koka reservoir, a shallow tropical artificial lake, Ethiopia. *Journal of Recent Trends Bioscience*, 1: 94-100.
- Francisco, G. A. Marcia, C. C.A. and Maria, N. L. F. (2011): Seasonal changes and spatial variation in the water quality of a eutrophic tropical reservoir determined by the inflowing river. *Lake and Management*, 27:343–354.
- Garg, R. K. Saksena, D. N. and Rao, R. J. (2006b): Assessment of physico-chemical water quality of Harsi Reservoir, district Gwalior, Madhya Pradesh. *Journal of Ecophysiology and occupational Health*, 6(1): 33-40.
- Gebrehiwot, M. (2020): Analysis of seepage and slope stability in embankment dam case of mhatsab azmat earthen dam central Tigray, Ethiopia. A Thesis Submitted as a Palatial Fulfilment for the Degree of Master of Science in Civil Engineering (Specialization in Hydraulic and Water resource Engineering).
- Geneviève, M. James, C. and Neary, P. (2008): United Nations Environment Programme, Global Environment Monitoring System/Water Programme, 120 pp
- Gupta, S. K. and Gupta, P. C. (2006): *General and applied ichthyology : (fish and fisheries)*. S. Chand and Company Ltd., Ram Nagar, New Delhi, pp: 1130.
- Haregeweyn, N. Poesen, J. Nyssen, J. De Wit, J. Haile, M. Govers, G. and Deckers, S. (2006): Reservoirs in Tigray (Northern Ethiopia): characteristics and sediment deposition problems. *Land degradation & development*, 17(2): 211-230.
- Harper, D. M. (Ed.). (1999): *The ecological bases for lake and reservoir management* (Vol. 136). Springer Science & Business Media.
- Higham, T. E. Stewart, W. J. and Wainwright, P. C. (2015): Turbulence, temperature, and turbidity: the ecomechanics of predator–prey interactions in fishes. *Integrative and comparative biology*, 55(1): 6-20.



- Hussain, A. L. T. Sulehria, A. Q. K. Ejaz, M. U. H. A. and Maqbool, A. S. M. A. (2013): Monthly variations in physicochemical parameters of a flood plain reservoir on River Ravi near Balloki Headworks (Pakistan). *Biologia*, 59: 371-377.
- Idowu, E. O. Ugwumba, A. A. A. Edward, J. B. and Oso, J. A. (2013): Study of the seasonal variation in the physico-chemical parameters of a tropical reservoir. *Greener Journal of Physical Sciences*, 3(4): 142-148.
- Kalff, J. (2002): *Limnology: inland water ecosystems*. Prentice-Hall, Inc, NJ, pp. 1-592.
- Khan, M. A. G. and Chowdhury, S. H. (1994): Physical and chemical limnology of lake Kaptai, Bangladesh. *Tropical Ecology*, 35(1): 35-51.
- Krishnamurthy, R. (1990): Hydrobiological studies of Wohar reservoir Aurangabad (Maharashtra State) India. *Journal of Environmental Biology*, 11(3): 335-343.
- Léziart, T. Dutheil de la Rochere, P. M. Cheswick, R. Jarvis, P. and Nocker, A. (2019): Effect of turbidity on water disinfection by chlorination with the emphasis on humic acids and chalk. *Environmental technology*, 40(13): 1734-1743.
- Meesukko, C. Gajaseni, N. Peerapornpisa, Y. L. and Voinov, A. (2007): Relationships between seasonal variation and phytoplankton dynamics in Kaeng Krachan Reservoir, Phetchaburi Province, Thailand. *Tropical Natural History*, 7(2): 131-143.
- Mollah, M. F. A. Moniruzzaman, M. and Rahman, M. M. (2015): Effects of stocking densities on growth and survival of Thai Sharpunti (*Barbonymus gonionotus*) in earthen ponds. *Journal of the Bangladesh Agricultural University*, 9: 452-2016.
- Moundiotiya, K. Sisodia, R. Kulshreshtha, M. and Bhatia, A. L. (2004): A case study of the Jamwa Ramgarh wetland with special reference to physico-chemical properties of water and its environs. *Journal of Environmental Hydrology*, 12(24): 1-5.
- Mustapha, M. K. (2009): *Limnology and fish assemblages of Oyun reservoir, Offa, Nigeria* (Doctoral dissertation, University of Ilorin).
- Nancy, D. (2009): Florida Keys National Marine Sanctuary. *Water Quality: Frequently Asked Question*. pp. 1-2.
- Nyssen, J. Vandenreyken, H. Poesen, J. Moeyersons, J. Deckers, J. Haile, M. and Govers, G. (2005). Rainfall erosivity and variability in the Northern Ethiopian Highlands. *Journal of Hydrology*, 311(1-4): 172-187.
- Olanrewaju, A. N. Ajani, E. K. and Kareem, O. K. (2017): Physico-chemical status of Eleyele reservoir, Ibadan, Nigeria. *Journal of Aquaculture and Resource Development*, 8(9): 1-8.
- Oso, J. A. and Fagbuaro, O. (2008): An assessment of the physico-chemical properties of a tropical reservoir, Southwestern, Nigeria. *Journal of Fisheries International*, 3(2): 42-45.
- Patil, P. N. Sawant, D. V. and Deshmukh, R. N. (2012): Physico-chemical parameters for testing of water—A review. *International journal of environmental sciences*, 3(3): 1194-1207.
- Premlata, V. (2009): Multivariate analysis of drinking water quality parameters of lake Pichhola in Udaipur, India. In *Biological Forum* (Vol. 1, No. 2, pp. 86-91).
- Quinn, G. P. and Keough, M. J. (2002): *Experimental design and data analysis for biologists*. Cambridge university press.
- Rafique, R. M. Mahboob, S. H. A. Ahmad, M. S. S. and Saleem, S. A. M. (2002): Seasonal limnological variations in Mangla Reservoir at Sukhian, Mirpur (Azad Kashmir). *International Journal of Agricultural Biology*, 4(2): 223-226.
- Reynolds, C. S. (2006): *The ecology of phytoplankton*. Cambridge University Press.
- Senthil, M.A. and Prabaharan, C. (2012): Fish Diversity In Relation To Physico-Chemical Characteristics of Kamala Basin of Darbhanga District, Bihar, India. *International Journal of Pharmaceutical & Biological Archives*, 3(1): 211-217.
- Sheela, A. M. Letha, J. Joseph, S. Chacko, M. Sanal Kumar, S. P. and Thomas, J. (2012): Water quality assessment of a tropical coastal lake system using multivariate cluster, principal component and factor analysis. *Lakes & Reservoirs: Research & Management*, 17(2): 143-159.
- Syarifah, I. N. S. H. Siti, H. A. T. and Muhammad, S. A. (2018): Spatial and Temporal Variations of Water Quality and Trophic Status in Sembrong reservoir, Johor. *E3S Web of Conferences*, 34: 02015.
- Tadesse Dejenie, T. D. Atakilt Berihun, A. B. Solomon Kiros, S. K. Tsehaye Asmelash, T. A. Solomon Amare, S. A. and Solomon Tesfay, S. T. (2015): Yield and condition factor of *Oreochromis niloticus* L. in tropical small dams, Tigray, northern Ethiopia.
- Teferi, M. Declerck, S. A. De Bie, T. Gebrekidan, A. Asmelash, T. Dejenie, T. and De Meester, L. (2013): The ecology of the riverine Garra species (Teleostei, Cypriniformes) in reservoirs of the semi-arid highlands of northern Ethiopia: temporal dynamics of feeding activity. *Inland Waters*, 3(3): 331-340.



- Teferi, M. Declerck, S. A. De Bie, T. Lemmens, P. Gebrekidan, A. Asmelash, T. and De Meester, L. (2014): Strong effects of occasional drying on subsequent water clarity and cyanobacterial blooms in cool tropical reservoirs. *Freshwater Biology*, 59(4): 870-884
- Tessema, A. Mohammed, A. Birhanu, T. and Negu, T. (2014): Assessment of physico-chemical water quality of Bira dam, Bati Wereda, Amhara region, Ethiopia. *Journal of Aquaculture Research and Development*, 5(6).
- Thirupathaiah, M. Samatha, C. H. and Sammaiah, C. (2012): Analysis of water quality using physico-chemical parameters in lower manair reservoir of Karimnagar district, Andhra Pradesh. *International Journal of Environmental Sciences*, 3(1): 172-180.
- Usman, L. U. and Yerima, R. (2017): Effects of physico-chemical parameters on the composition and abundance of phytoplankton in Ajiwa reservoir Katsina state, north western Nigeria. *International Journal of Applied Biological Research*, 8(1): 50 – 69.
- Usman Atique and Kwang-Guk. (2019). Reservoir Water Quality Assessment Based on Chemical Parameters and the Chlorophyll Dynamics in Relation to Nutrient Regime. *Polish Journal of Environmental Studies*, 28(3): 1043-1061.
- Venkatesharaju, K. Somashekar, R. K. and Prakash, K. L. (2010): Study of seasonal and spatial variation in surface water quality of Cauvery river stretch in Karnataka. *Journal of ecology and the natural environment*, 2(1): 001-009.
- Wetzel, R.G. (1983): *Limnology*. 2nd Edition, Saunders College Publishing, New York, 767.
- Woldeab, B. Beyene, A. Ambelu, A. Buffam, I. and Mereta, S. T. (2018): Seasonal and spatial variation of reservoir water quality in the southwest of Ethiopia. *Environmental monitoring and assessment*, 190: 1-13.
- Zebib, H. and Teame, T. (2017): Assessment of monthly physico-chemical properties and fish yields of two micro dams of Tigray Region, Northern Ethiopia. *International Journal of Fisheries and Aquaculture*, 9(9): 92-97.
- Zhang, J. L. Zheng, B. H. Liu, L. S. Wang, L. P. Huang, M. S. and Wu, G. Y. (2010): Seasonal variation of phytoplankton in the DaNing River and its relationships with environmental factors after impounding of the Three Gorges Reservoir: a four-year study. *Procedia Environmental Sciences*, 2: 1479-1490



# Application of Artificial Neural Network to Streamflow and Hydrological Drought Forecasting for Sustainable Water Resource Development in Ethiopia

Kassa Abera Tareke\*

Department of Hydraulics and Water Resources Engineering, Kombolcha Institute of Technology, Wollo University, Dessie – Kombolcha, Ethiopia

\*Corresponding author, e-mail: [kassaabera21@gmail.com](mailto:kassaabera21@gmail.com)

## ABSTRACT

This research aims to examine the long-term forecasting of streamflow and hydrological drought in Ethiopia through the utilization of an artificial neural network (ANN) and the streamflow drought index (SDI). Observed streamflow and precipitation data from 1973 to 2014 were collected from 17 streamflow stations and 34 rainfall gauge stations to train and test the ANN model by 70 and 30% ratio, respectively. After training the model, future downscaled precipitation data from regional climate models (RCM) have been used as input data to forecast future streamflow. Three RCM models were used to downscale historical and future climate data from the RCP 4.5 scenario. RACMO is found a good RCM for all selected stations. The linear scaling bias correction technique results in less than 2% error compared to other alternative techniques. The result indicates that ANN is a robust tool to forecast streamflow in areas having a good correlation between precipitation and streamflow such as Abbay, Awash, Baro, Omo Gibe, and Tekeze river basins. But in arid areas for example Genale Dawa, Wabishebele, and Rift Valley basins, the model is not suitable because the input data (precipitation) have higher variation than the output variable (streamflow). In such areas, meteorological drought analysis and forecasting are better than hydrological drought analysis. Finally, future hydrological drought is analyzed using forecasted streamflow data as input to the streamflow drought index (SDI). The result indicates that 2028, 2036, 2042, 2044, 2062, and 2063 are the expected extreme drought years in most river basins of Ethiopia in the future. This shows that at least one extreme drought is expected in each decade in the future. Therefore, extensive research in drought analysis and forecasting is needed to develop an effective drought early warning system and water resource management policy.

**Keywords:** Artificial neural network (ANN), hydrological drought, linear scaling, regional climate model, streamflow forecasting

## 1. INTRODUCTION

Drought monitoring and streamflow forecasting play a great role in water resource management and early warning systems development for drought and flood hazard mitigation. Artificial Neural Networks are now widely applied in a broad range of fields (Modarres, 2007). Recently, ANN has been used in many aspects of hydrological and meteorological studies such as streamflow forecasting, groundwater analysis, precipitation forecasting, rainfall-runoff modeling, and water quality issues, flood and drought forecasting (Myronidis and Ioannou, 2018). Development in forecasting and early warning of drought phenomena is increasingly applied in many regions of the world. This is being done to mitigate the consequences of drought in vulnerable river basins and to save human life (Wambua, 2014).

Historically, time series-based streamflow and drought forecasting statistical models have been applied. Regression models and autoregressive moving average (ARMA) models are typically they are linear models used for statistical time series forecasting (Mishra and Desai, 2006). Therefore, the traditional statistical time series analysis in hydrology has several limitations related to non-linear variables. This problem is now overcome and improved by using robust time series predictive techniques like ANN (Zhao and Wang, 2022). Imprecise in nature, uncertainty, lack of data, and inconsistency, the physical characteristics of the region have a great influence on meteorological and hydrological variables in Ethiopia. In such circumstances, ANN techniques are renowned to be highly enhancing the modeling of such natural dynamics and variability (Khadr, 2016). So, due to their inherent nonlinear nature and modeling flexibility, artificial neural networks (ANNs) have recently demonstrated tremendous capacity in modeling and forecasting nonlinear and non-stationary time series in hydrology and water resource engineering (Mishra and Desai, 2006).

Since the objective of this study is focused on streamflow forecasting and hydrological drought monitoring related to climate change and SDI is selected for analysis. However, the future SDI value is directly dependent on future streamflow variation and it is important primarily to forecast streamflow to estimate SDI values. Therefore, observed precipitation data at various stations near to streamflow station was used as input and a single streamflow station data was used as output to train and test ANN model performance.

The major drawback of present studies in drought forecasting is using the same variable to forecast future drought conditions (Maca and Pech, 2016). A statistical error computation result from a similar variable will result in a good performance. However, it does not give good information about the nonlinear problems. Therefore, this study is aimed to forecast future hydrological drought by integrating two different variables (precipitation and streamflow data). The historical precipitation data were used as input and historical streamflow as output in the model training. After checking the performance of ANN model streamflow prediction, the future streamflow was forecasted using downscaled precipitation data. Then the hydrological drought condition from 2026 – 2100 is forecasted using future streamflow values.

Surface and sub-surface water resources are directly related to streamflow variability. So streamflow forecasting has a great role in reservoir optimization development to mitigate future drought impacts on society (Sherif et al., 2022). Besides this streamflow forecasting using ANN is very important in water resource planning and management under poor gauged river basins (Adnan and Yuan, 2018). In streamflow time series analysis both peak flow and low flow are important issues in hydrology to develop strategic water resources management during hydrological events such as floods and droughts. Therefore, in this study streamflow is forecasted to predict future drought conditions in Ethiopia.

## 2. MATERIALS AND METHODS

### 2.1. Description of the Study Area

Ethiopia is geographically located in East Africa at a latitude of 3° - 15°N and a longitude of 33° - 48° E. There are twelve major river basins of which four are now categorized under low flow to dry basins (Mereb, Denakil, Ayisha, and Ogaden). Therefore, this study was focused on eight river basins as shown in Figure 1.

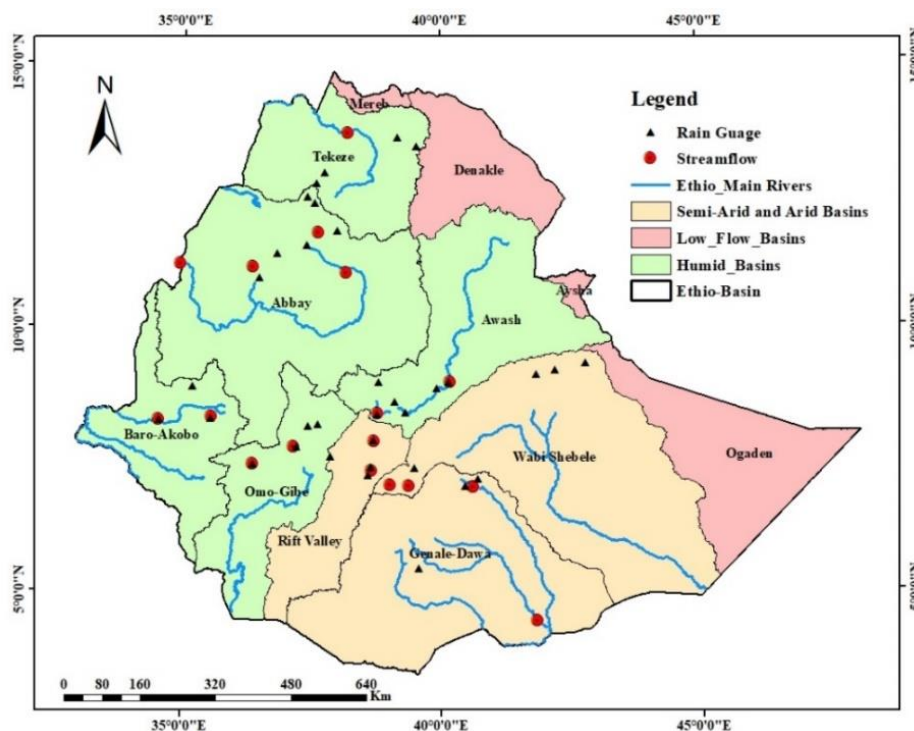


Figure 1 Major River basins in Ethiopia and spatial location of selected hydroclimatic stations



## 2.2 Data Collection and Preparation

Observed rainfall data were collected from 42 stations and streamflow was from 32 stations from 1973 to 2014. However, only 34 rainfall stations and 17 streamflow stations show a good correlation to forecast future streamflow. The observed streamflow and precipitation data were obtained from the Ministry of Water and Energy (MoWE) and the Ethiopian Meteorology Institute (EMI), respectively. The monthly rainfall was used as input and the mean monthly streamflow was used as an output for training and testing the artificial neural network (ANN) model using Python software. Downscaled precipitation data were also used for future forecasting of streamflow in all river basins from 2026 to 2099.

## 2.3 Downscaling Climatic Data and Bias Correction

For the last five and six decades, several researchers have conducted climate change investigations in different parts of the world. However, local climate changes force different sights of understanding the effect of natural disasters related to climate change. The successful understanding of local climate change impact has a great role in climate adaptation and early warning system development for drought and flood mitigation. Future and Historical daily precipitation data were projected from Global Climate Models (GCM) and Regional Climate Model (RCM) from the African domain using CORDEX projects. Since the GCM data spatially covers a large area and its resolution is coarser (Chokkavarapu and Ravibabu, 2019), the data for this study were generated from RCM for the Africa domain (AFR-44) using the RCP4.5 climate change scenario. MIROC5, KNMI, and SMHI were the driving GCM models, and RCA, RACMO, and RCA4 were the corresponding RCM models selected for this study. After bias correction using Climate Model data for the hydrological modeling (CMhyd) tool, the three models' data generation performance was checked by the coefficient of determination ( $R^2$ ), and mean absolute percentage error (MAPE).

## 2.4 Application of Artificial Neural Network (ANN) to forecasting streamflow

Recently there have been several physical-based hydrological models to predict streamflow. However, most of them require intensive input data and complex mathematical algorithms. Therefore, this complex and non-linear process is not easily described by a simple model. Nowadays, the application of Artificial intelligence and Machine learning is becoming a prominent tool for many aspects of water resource studies (Tealab, 2018; Wibawa et al., 2022).

In this study, ANN was applied to explore simulating the nonlinear hydrologic behavior of eight river basins to forecast future hydrological drought. In each river basin, the input data were selected by checking historically observed precipitation and streamflow correlation. Out of 42 rainfall stations and 32 streamflow stations, only 34 rainfall and 17 streamflow stations showed a good correlation. Therefore, two or more rainfall stations are used as input to forecast streamflow at a single station. 42 years of consecutive historical monthly precipitation and streamflow data were applied to train and test the ANN model. 70% of the data were used for model training while the remaining 30% were used for the evaluation of model performance. The architecture of the ANN structure contains three layers (input, hidden, and output), respectively (see Figure 2). The performance of the model was checked by coefficient determination ( $R^2$ ), root means square error (RMSE), and mean absolute error (MAE) with the observed data.

The main difficulty in the artificial neural network is deciding the number of hidden layers and the number of perceptrons in each hidden layer. Increasing the number of hidden layers makes the ANN architecture more complex and the performance of the overall system is reduced. Therefore, a single hidden layer is mostly recommended by scientists (Arifin et al., 2019).

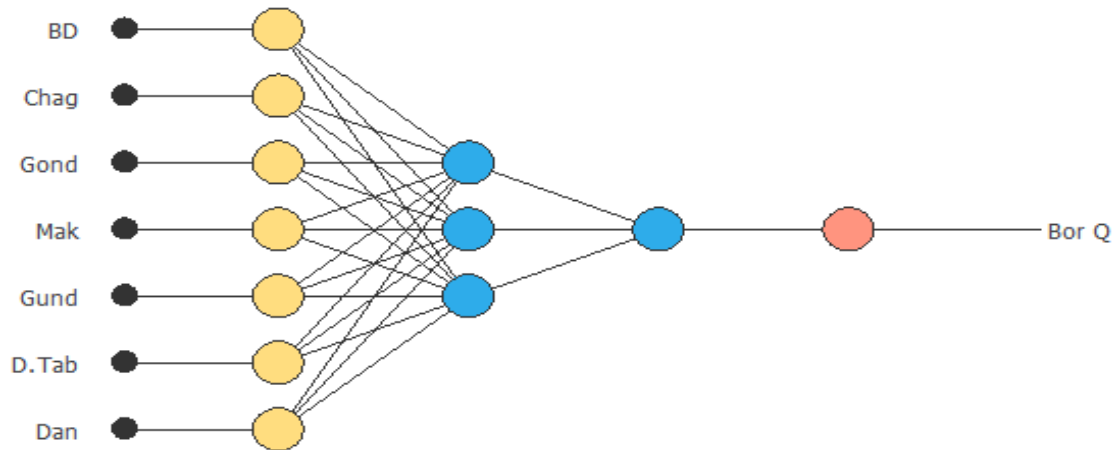


**Figure 2** A three-layer feedforward neural networks Architecture for streamflow forecasting

## 2.5 Future hydrological drought characterization

There are several hydrological drought indicators applied in many countries such as Palm Hydrological Drought Severity (PHDS), Surface Water Supply Index (SWSI) (Muli Wambua, 2018), and Streamflow Drought Index (SDI) (Wambua, 2020). However, the selection of these indicators depends on their input data requirement, simplicity, widely practiced, etc. Accordingly, the streamflow drought index (SDI) is selected for this study to characterize future hydrological drought trends in Ethiopia using forecasted streamflow data as an input. The analysis of SDI is given by Equation 1 below and Table 1 shows the hydrological drought severity criteria.

$$SDI = \frac{Q - Q_m}{\sigma} \quad 1$$

Where  $Q$  and  $Q_m$  are seasonal observed and mean streamflow, respectively and  $\sigma$  is the standard deviation of the observed streamflow.

**Table 1** SDI values for different drought severity levels

Drought Condition	Wet	Normal	Mild Drought	Moderate drought	Severe drought	Extreme drought
Criteria	$\geq 1.5$	-0.4 - 1.4	-0.5 - -0.99	-1 - -1.4	-1.5 - -1.99	$\leq -2$

## 3. RESULTS AND DISCUSSION

### 3.1 Climate Data Bias Correction

The downscaled precipitation data from RCM was extracted and bias-corrected using five techniques with the help of Climate Model data for the hydrologic modeling (CMhyd) tool. It is found that Linear Scaling (LS) has a minimum error and except the Omo Gibe River basin, all river basins satisfied that the RACMO model has a minimal error using the linear scaling bias correction technique whereas the Omo Gibe River basin has a minimum error using the RCA4 model, and the Linear Scaling bias correction technique also had a good performance. From Table 2, it is observed that RACMO has a minimum error of bias. Therefore, the linear scaling technique has good performance for bias correction of downscaled climate data by reducing the error below 2% and producing better climate-simulated outcomes in all river basins as shown in Table 2.

### 3.2 Streamflow Forecasting Using Artificial Neural Network (ANN)

In this study python software was applied to forecast future streamflow using generated monthly precipitation from the Regional Climate Model (RCM) as input for the ANN model Therefore, input – hidden – output layer architecture relation was developed by trial-and-error approach until the model performed to the acceptable range. The number of trials depends on the number of epochs, batch size per iteration, and the number of perceptions in a hidden layer. The epochs and batch size were tested from 50, 100, 1000 and 16, 32, 64, 128,



respectively. From many trials, 100 epochs and 64 batch sizes give a good performance. Then by fixing those values for all stations, the trail was repeated by changing the number of perceptron in the hidden layers.

Table 3 shows that relatively Abbay, Awash, Baro, Omo Gibe and Tekeze have good prediction performance whereas Genale Dawa, Wabishebele and Rift Valley have low performance. Even though the RMSE and MAPE values for Genale Dawa, Rift Valley, and Wabishebele are acceptable, the R<sup>2</sup> value is minimal. This indicates that ANN is suitable for humid and temperate climate zones to forecast streamflow from precipitation data.

**Table 2** Bias correction result of selected Regional Climate Models (RCM)

River Basin	Bias correction Technique	Model Error (%)		
		MIROC5	RACMO	RCA4
Abbay	Linear Scaling	2.43	1.67	1.89
Awash	Linear Scaling	3.57	1.44	1.96
Baro	Linear Scaling	2.14	1.12	1.22
Genale Dawa	Linear Scaling	4.00	1.54	2.63
Omo Gibe	Linear Scaling	2.55	2.43	2.01
Rift Valley	Linear Scaling	3.41	1.26	1.91
Tekeze	Linear Scaling	1.67	1.30	1.57
Wabishebele	Linear Scaling	5.88	2.37	3.98

**Table 3** Statistical performance of ANN model to forecast streamflow

River basin	Station	Modell Architecture	RMSE	MAPE	R <sup>2</sup>
Abbay	Gummera	3, 8, 1	1.9	1.1	0.9
	Gilgel Belles	3, 7, 1	0.83	0.47	0.83
	Kessie	3, 8, 1	3.6	2.3	0.81
	Border	4, 6, 1	11	8.32	0.84
Awash	Awash7	4, 6, 1	3.1	2.1	0.68
	Hombel	3, 16, 1	2.3	1.4	0.87
Baro	Gambela	2, 8, 1	16.1	11.6	0.77
	Sorie	3, 16, 1	2.03	1.4	0.83
Genale Dawa	Halewe	3, 8, 1	4.98	3.26	<b>0.59</b>
	Weib	2, 4, 1	12.45	9.4	<b>0.2</b>
Omo Gibe	Assendabo	3, 12, 1	6.5	4.7	0.77
	Gojeb	2, 4, 1	7.2	4.7	0.75
Rift Valley	Wosha	3, 8, 1	0.14	0.13	<b>0.24</b>
	Dedessa	3, 8, 1	1.31	0.89	<b>0.48</b>
Tekeze	Embamadre	4, 10, 1	12.5	8.8	0.7
Wabishebele	Wabishebele	2, 9, 1	5.66	4.22	<b>0.54</b>
	Leliso	3, 7, 1	1.82	1.29	<b>0.55</b>

3, 8, and 1 indicate number of input variables, Hidden perceptron, and output variable, respectively

Figure 3 (a, b, c, d) shows the observed versus forecasted streamflow time series graph for the Abbay, Awash, Baro, and Omo Gibe River basins, respectively, developed using Python software and the ANN model. The result revealed that the observed and simulated fitted with good performance. The analysis was computed using precipitation data as input and streamflow data as output in the ANN model setup. From this analysis, it is observed that streamflow forecasting from precipitation data has a significant relation. As shown in Figure 3, the loss decreases as the epoch increases in all selected streamflow stations. For a selected 100 epoch and 64 batch sizes, the train and test were best performed. The ultimate goal of forecasting streamflow in this study is to see the future hydrological drought trend in Ethiopia.

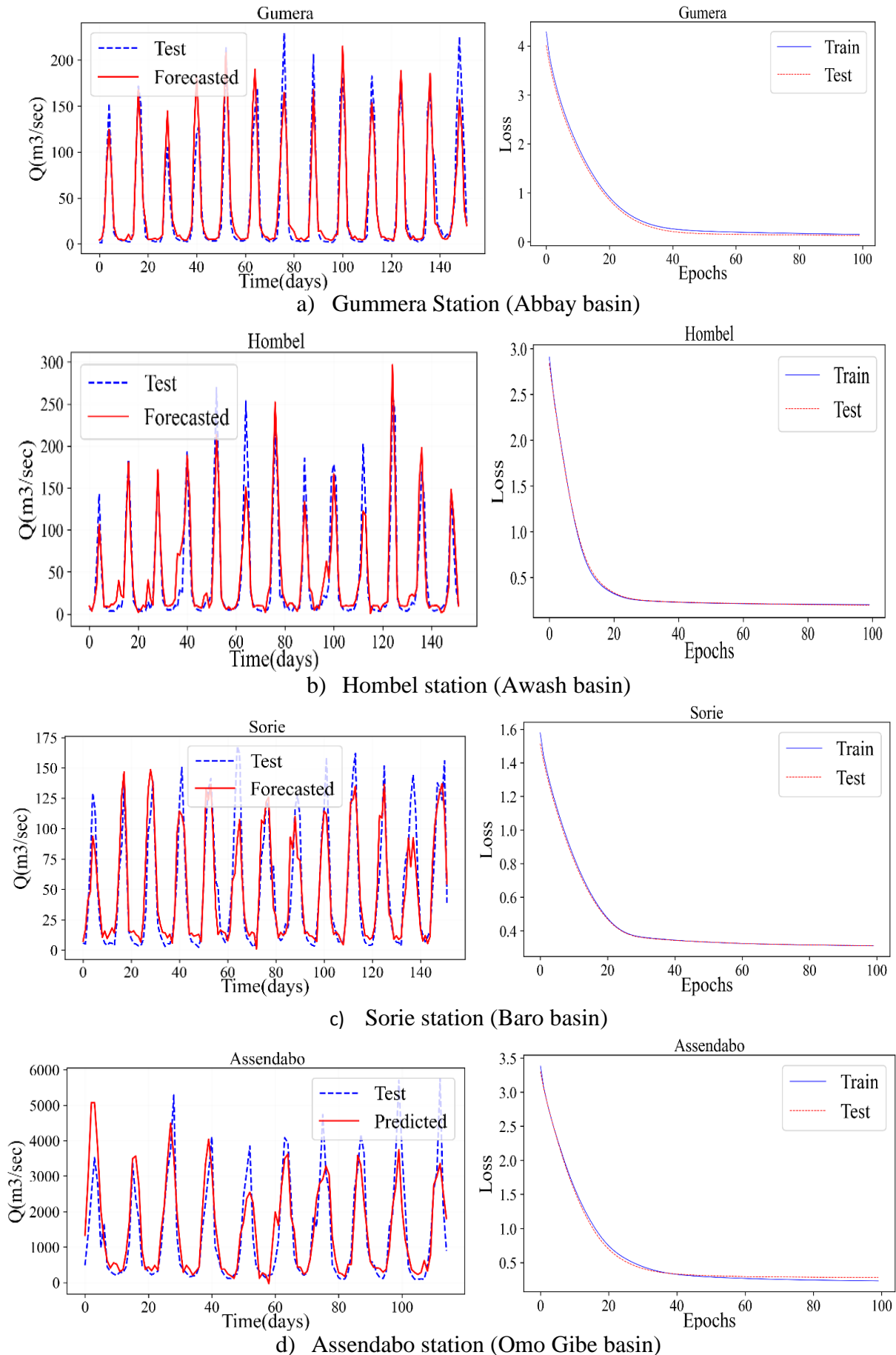


**Figure 3** Observed and forecasted streamflow time series plot using ANN in Python software



### 3.3 Future Hydrological Drought Analysis Using Streamflow Drought Index (SDI)

In all river basins except Genale Dawa and Rift Valley basins, the performance of streamflow forecasting using ANN indicated the possibility of using simulated streamflow time series to predict future hydrological drought conditions. Therefore, the forecasted streamflow was directly used to predict future hydrological drought conditions. However, in this study, Genale Dawa and Rift Valley basins were excluded due to the low performance of streamflow forecasting results. Therefore, the future hydrological drought analysis was conducted for six river basins as shown in Figures 4 - 9. The analysis was considered for four-time scales; monthly (SDI1), seasonal (SDI3), half-year (SDI6), and annual (SDI12) time scales. The result revealed that the frequency of drought occurrence is high for monthly (SDI1) and seasonal (SDI3) time scales compared to half-year and annual time scales (see Figure 8). However, the duration of severe and extreme drought is high for annual time-scale analysis. Therefore, for this study, the result and discussion part focused on the annual (SDI12) time scale.

In the Abbay River basin, four streamflow was considered for future drought analysis and the result indicated that the probability of severe and extreme drought occurrence from 2026 to 2041 was less in all stations. But in 2026, 2031, 2033, 2037, and 2040 moderate drought events are expected in some stations in the basin. However, Figure 4 shows that 2042 to 2045, 2049/2050, 2052 to 2054, 2062, 2065, 2072/2073, and 2097/2098 are the most expected moderate to extreme drought years in the Abbay River basin. The most severe magnitude and frequency were identified at the Gummera and Beles streamflow stations. The analysis indicated that the probability of severe drought occurrences in the future is higher in the Abbay River basin compared to other river basins.

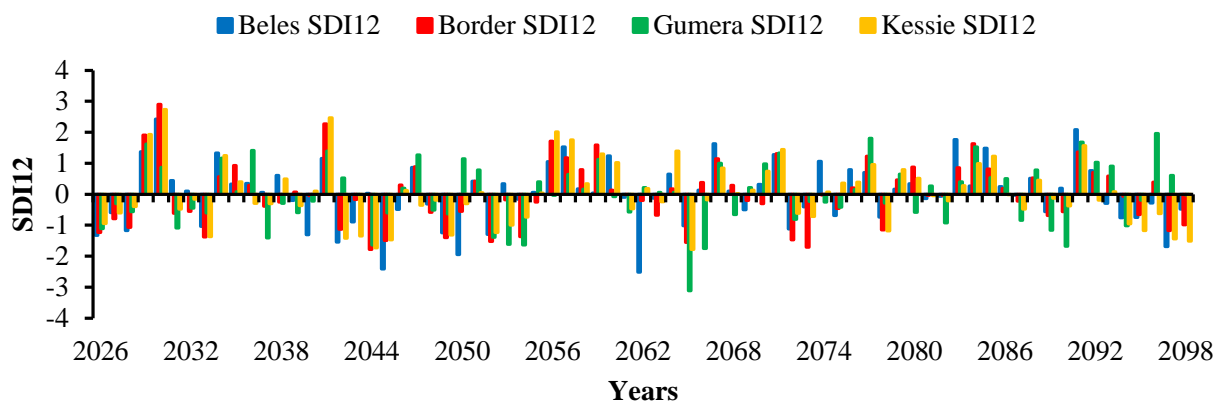


Figure 4 Future hydrological drought time series in the Abbay river basin

Figure 5 indicates that 2036, 2042, 2063, 2079, 2086, and 2097 are severe and extreme drought events in the future in the Awash River basin. This implies that a strong water resource management strategy, early drought warning system development, and good drought preparedness policies will be important in the future.

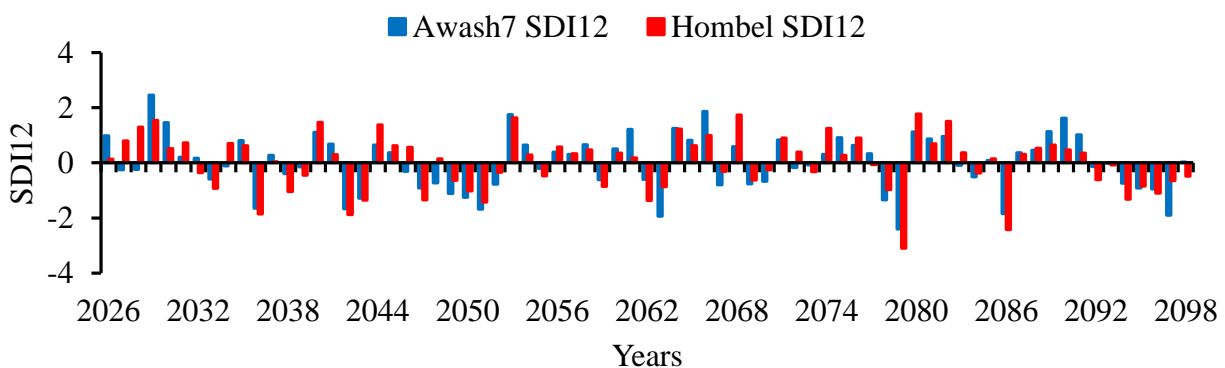
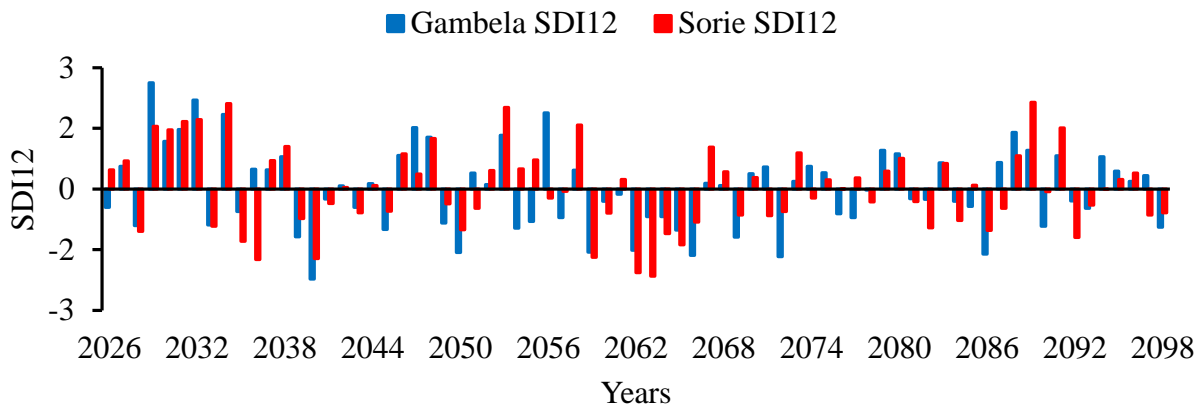


Figure 5 Future hydrological drought time series in the Awash River basin

Baro Akobo and Omo Gibe river basins receive rainfall twice a year and have good climate conditions compared to other river basins. Although they received good rainfall, hydroclimatic disasters such as floods and

droughts occurred in different parts of the basin (Stojanovic et al., 2022). However comprehensive drought studies were yet studied in both Baro Akobo and Omo Gibe River basins. Figures 6 and 7, respectively indicated that the frequency of severe and extreme drought occurrence is higher in the Baro river basin than in the Omo Gibe River basin. The future drought analysis implies that 2036, 2050, 2059, 2066, 2072, and 2086 are expected severe drought years and 2040, 2062, and 2063 are extreme drought years for the Baro river basin whereas 2036 and 2094 are severe and 2063 are extreme drought years for Omo Gibe basin, respectively.



**Figure 6** Future hydrological drought time series in the Baro Akobo river basin

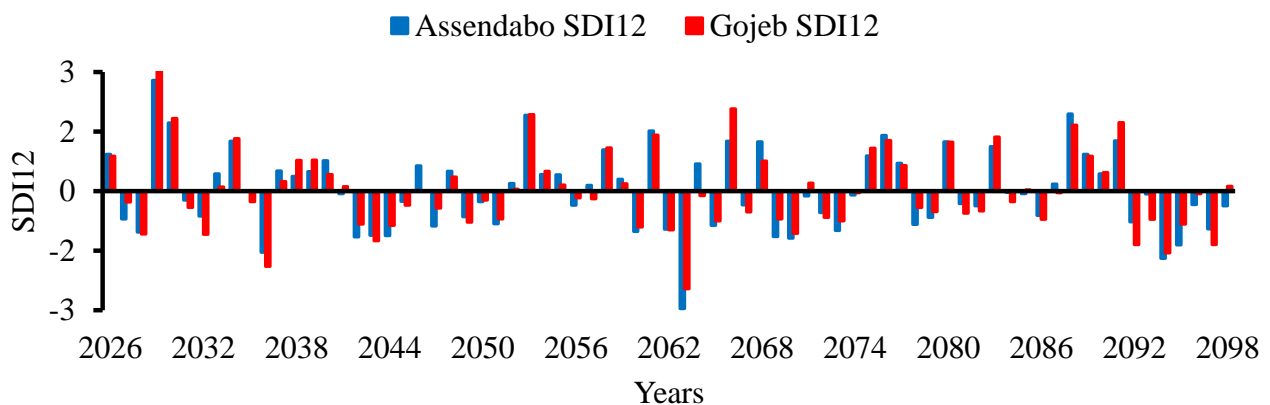


**Figure 7** Future hydrological drought time series in the Omo Gibe river basin

In the Tekeze river basin, a single station data at Embamadre station was used to estimate SDI values at different time scales as shown in Figure 8. Historically northeast part of Ethiopia is frequently affected by prolonged drought phenomena (Araya and Stroosnijder, 2011; Mohammed, 2018). The result of this study also revealed the previous studies. The annual time scale (SDI12) results, 2028, 2037, 2038, 2054, 2063, 2065, and 2082 are the expected severe drought events in the Tekeze river basin in the future.

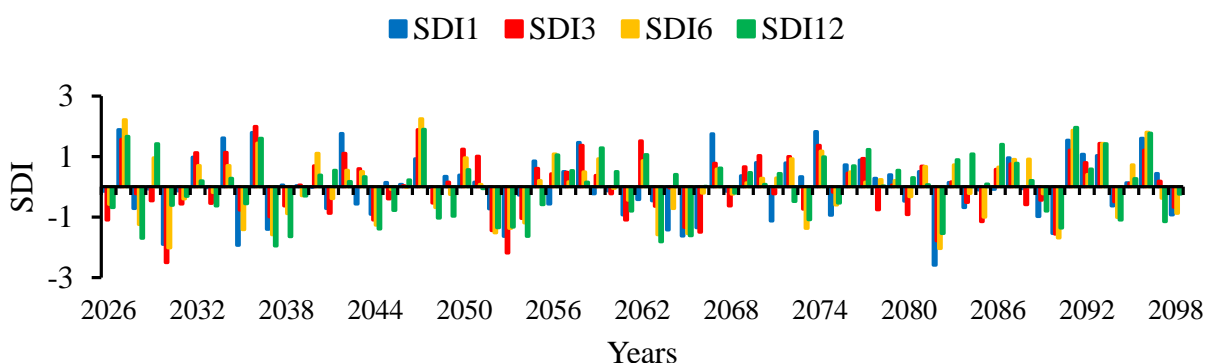


**Figure 8** Future hydrological drought time series in the Tekeze river basin

Wabishebele river basin is one of the arid climate zone basins in Ethiopia. Future hydrological drought analysis was explored in this basin at two stations as shown in Figure 9. It is found that 2036, 2037, 2063, 2065, and 2072 are severe drought years whereas 2028 and 2042 are the most extreme drought years in the future in Wabishebele Basin (see Figure 9).

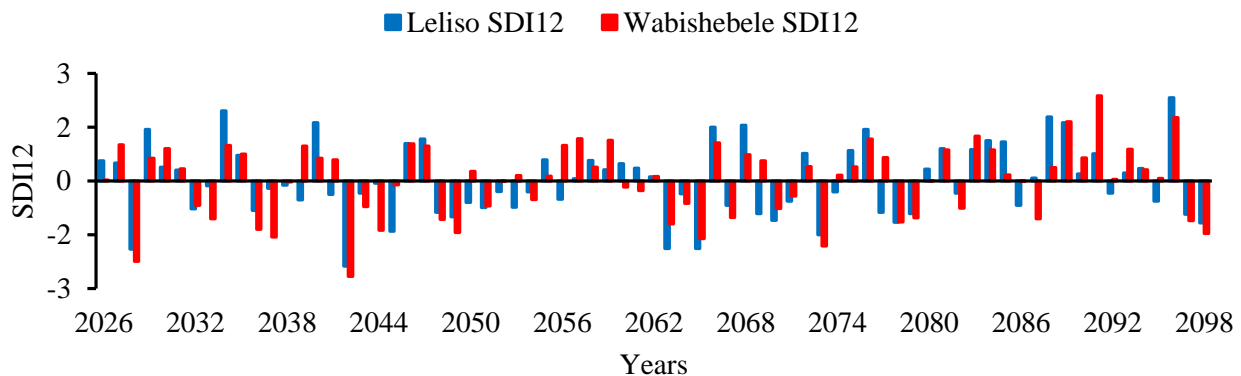


**Figure 9** Future hydrological drought time series in the Wabishebele river basin

#### 4. CONCLUSIONS AND RECOMMENDATION

The impact of climate change on streamflow and its consequences can be analyzed using projected climate data from GCM and RCM with observed hydroclimatic data. To minimize the effect of hydrological events on water resource projects, drought forecasting and monitoring system development are important for policymakers, drought preparedness, and water resource management sectors. This study intends to forecast long-term hydrological drought in Ethiopia using observed and projected climate data. A data-driven model such as ANN improves the problems related to non-linear and stationarity cases in water resource management analysis. The result of this study also indicated the possibility of forecasting long-time streamflow time series using precipitation data as an input for the ANN model. It is observed that humid and temperate climate zones can result in good streamflow forecasting performance compared to semi-arid and arid areas. In Ethiopia, the Abbay, Baro Akobo, and Omo Gibe River basins received mean annual precipitation of above 1200 mm, and the Awash and Tekeze river basins received mean annual precipitation between 700 to 1100 mm. Streamflow forecasting from those areas using the ANN model corresponding to areas having high precipitation results in acceptable  $R^2$  values. Genale Dawa, Rift Valley, and Wabishebele river basins are located in the lowland parts of Ethiopia and receive low annual precipitation. The source of streamflow for these basins is Bale Mountain and other highland areas of the country. As a result, the correlation between precipitation and streamflow data is very low. Therefore, the result revealed that forecasting streamflow directly using precipitation data will not give good performance in arid areas. The future hydrological drought analysis result indicates that there will be frequent moderate drought events in all river basins and the 2030s, 2040s, and 2060s were identified as the most expected severe and extreme drought event occurrence years. High population growth rates and dynamic climate change will increase water stress and water-sharing conflict in resource-limited areas in the future. In addition to this, drought has a worthwhile impact on the overall economic growth of the nation. Therefore, the government and policymakers should have to plan long-term drought preparedness and mitigation measures to minimize the risk associated with expected hideous drought events.

The government of Ethiopia is practically focused on drought crisis management rather than risk management. Drought crisis management is a short-term drought preparedness mechanism by supplies food and water to drought-prone areas. This kind of drought preparedness does not bring a sustainable solution. Therefore, in the future, the government should shift to a new paradigm by developing a national drought policy. Currently, a proactive approach is recommended as a short-term and long-term drought mitigation mechanism. A 2021 and 2022 Green Legacy in Ethiopia is a good initiative to prevent the climate change impact on water resources such



as rivers, lakes, and reservoirs as a long-term mitigation approach. So, Afforestation, and the development of alternative energy sources from solar and wind have to be strongly encouraged in the future.

## REFERENCES

- Adnan, R.M., Yuan, X. (2018) Stream flow forecasting of poorly gauged mountainous watershed by least square support vector machine , Fuzzy Genetic Algorithm and M5 Model Tree Using Climatic Data from Nearby Station. European Water Resources Association (EWRA), vol. 32(14), pages 4469-4486. <https://doi.org/10.1007/s11269-018-2033-2>
- Araya, A. & Stroosnijder, L. (2011) Agricultural and Forest Meteorology Assessing drought risk and irrigation need in northern Ethiopia. *Agric. For. Meteorol.* 151, 425–436. <https://doi.org/10.1016/j.agrformet.2010.11.014>
- Arifin, F., Robbani, H., Annisa, T., Ma'Arof, N. (2019) Variations in the Number of Layers and the Number of Neurons in Artificial Neural Networks: Case Study of Pattern Recognition. *J. Phys. Conf. Ser.* 1413. <https://doi.org/10.1088/1742-6596/1413/1/012016>
- Barua, S., Perera, B.J.C., Ng, A.W.M., Tran, D. (2010) Drought forecasting using an aggregated drought index and artificial neural network 193–206. <https://doi.org/10.2166/wcc.2010.000>
- Chokkavarapu, N., Ravibabu, V. (2019) Comparative study of GCMs , RCMs , downscaling and hydrological models : a review toward future climate change impact estimation. *SN Appl. Sci.* 1, 1–15.
- Khadr, M. (2016) Forecasting of meteorological drought using Hidden Markov Model ( case study : The upper Blue Nile river basin , Ethiopia ). *Ain Shams Eng. J.* 7, 47–56. <https://doi.org/10.1016/j.asej.2015.11.005>
- Khashei, M. & Bijari, M. (2010) An artificial neural network (p, d, q) model for timeseries forecasting. *Expert Syst. Appl.* 37, 479–489. <https://doi.org/10.1016/j.eswa.2009.05.044>
- Kolarik, T. & Rudorfer, G., (1994) Time series forecasting using neural networks. *Proc. Int. Conf. APL Lang. its Appl. APL* 1994 86–94. <https://doi.org/10.1145/190271.190290>
- Kwon, H. & Kim, S. (2006) Evaluation of Semi-Distributed Hydrological Drought using SWSI ( Surface Water Supply Index ). <https://doi.org/10.5389/KSAE.2006.48.2.037>
- M Wambua, R. (2014) Drought Forecasting Using Indices and Artificial Neural Networks for Upper Tana River Basin, Kenya-A Review Concept. *J. Civ. Environ. Eng.* 04. <https://doi.org/10.4172/2165-784x.1000152>
- Maca, P. & Pech, P. (2016) Forecasting SPEI and SPI drought indices using the integrated artificial neural networks. *Comput. Intell. Neurosci.* 2016. <https://doi.org/10.1155/2016/3868519>
- Mishra, A.K. & Desai, V.R. (2006) Drought forecasting using feed-forward recursive neural network 8, 127–138. <https://doi.org/10.1016/j.ecolmodel.2006.04.017>
- Modarres, R. (2007) Streamflow drought time series forecasting 223–233. <https://doi.org/10.1007/s00477-006-0058-1>
- Mohammed, Y. (2018) Meteorological drought assessment in north east highlands of Ethiopia. <https://doi.org/10.1108/IJCCSM-12-2016-0179>
- Muli Wambua, R. (2018) Analysis of Drought and Wet-Events Using SWSI-Based Severity-Duration-Frequency (SDF) Curves for the Upper Tana River Basin, Kenya. *Hydrology* 6, 43. <https://doi.org/10.11648/j.hyd.20180602.11>
- Myronidis, D. & Ioannou, K. (2018) Streamflow and Hydrological Drought Trend Analysis and Forecasting in Cyprus 100–110.
- Santos, C.A.G., Morals, B.S., Silva, G.B.L. (2009) Drought forecast using an artificial neural network for three hydrological zones in San Francisco River basin, Brazil. *IAHS-AISH Publ.* 333, 302–312.
- Sherif K. et lop. (2022) A review of the hybrid artificial intelligence and optimization modelling of hydrological streamflow forecasting. *Alexandria Eng. J.* 61, 279–303. <https://doi.org/10.1016/j.aej.2021.04.100>
- Stojanovic, M. et lop. (2022) Precipitation Moisture Sources of Ethiopian River Basins and Their Role During Drought Conditions 10, 1–17. <https://doi.org/10.3389/feart.2022.929497>
- Tealab, A. (2018) Time series forecasting using artificial neural networks methodologies: A systematic review. *Futur. Comput. Informatics J.* 3, 334–340. <https://doi.org/10.1016/j.fcij.2018.10.003>
- Wambua, R.M. (2020) Hydrological Drought Forecasting Using Modified Surface Water Supply Index ( SWSI ) and Streamflow Drought Index ( SDI ) in Conjunction with Artificial Neural Networks ( ANNs ). <https://doi.org/10.4018/IJSSMET.2019100103>
- Wibawa, A.P. et lop. (2022) Time-series analysis with smoothed Convolutional Neural Network. *J. Big Data* 9. <https://doi.org/10.1186/s40537-022-00599-y>
- Zhao, Y., & Wang, Z. (2022) Subset simulation with adaptable intermediate failure probability for robust reliability analysis: an unsupervised learning-based approach. *Struct. Multidiscip. Optim.* 65. <https://doi.org/10.1007/s00158-022-03260-7>



# Co-precipitation Technique Synthesis of Co, Ni co-doped WO<sub>3</sub> Nanoparticles: Structural, Optical and Electrical Properties

Wegene Lema Lachore<sup>4</sup>, Fekadu Gashaw Hone<sup>2,\*</sup>, Dinsefa Mensur Andoshe<sup>3</sup>, Mulualem Abebe

Mekonnen<sup>1</sup>

<sup>1</sup>Faculty of Materials Science and Engineering, Jimma Institute of Technology, Jimma University, P. O. Box: 1041, Jimma, Ethiopia.

<sup>2</sup>Department of Physics, Addis Ababa University, P.O. Box: 1176, Addis Ababa, Ethiopia

<sup>3</sup>Department of Materials Science and Engineering, Adama Science and Technology University, P. O. Box 1888, Adama, Ethiopia

<sup>4</sup>Department of Innovation and Technology Transfer and Grand Challenges Division, Armauer Hansen Research Institute, P.O. Box 1005, Addis Ababa, Ethiopian

\*Corresponding author, e-mail: [fekeye@gmail.com](mailto:fekeye@gmail.com)

## ABSTRACT

Pure WO<sub>3</sub>, singly-doped (Ni) and (Cu,Ni)-Co-doped WO<sub>3</sub> nanoparticles were made using co-precipitation synthesis methods with a fixed nickel content of 5% and various copper content of 2, 4, and 5%. Powder X-ray diffraction (XRD), UV-Vis diffraction reflectance spectroscopy (DRS) analysis, Photoluminescence (PL), Fourier transform infrared spectroscopy (FT-IR) and SEM analyses have all been used to characterize the sample. All doped/co-doped and un-doped samples have an orthorhombic structure, according to XRD analyses. The average crystalline size ranged from 43 to 12nm nm after the dopant concentration was increased, according to the XRD data. The optical characteristics of the produced nanomaterials were investigated using reflectance spectroscopy, which revealed that the optical band gap varied from 2.86 to 2.89 eV depending on dopant concentrations. The FTIR analyses described the many modes of band associated with functional groups contained in the materials, as well as the stretching mode of O-W-W found between 550 and 1050 cm<sup>-1</sup>. I-V tests revealed that the produced samples had good ohmic contact behavior and that the resistivity reduced as doping doses increased.

**Keywords:** Co- doping, WO<sub>3</sub>, Co- precipitation method, Electrical properties, Optical properties

## 1. INTRODUCTION

Metal oxide semiconductor nanoparticles have recently received a lot of consideration due to their unique potential for different applications. Tungsten trioxide has been highly studied because of its outstanding optical, structural and electrical properties [1]. It has reasonable amount of electrons in the valence band with band gap energy of 2.7 to 3.5 eV [2] and with significant absorption in the far-ultraviolet and visible regions. It has transition metal oxide semiconductor which is an excellent property for various applications, such as photovoltaic [3], electrochromic [4], photocatalyst [5], and photochromic [6], and gas sensor [7]. Various researchers have prepared tungsten trioxide nanostructures such as nanowires, nanotubes, nanoribbons, nanorods, and nanoplates which may influence their physical, optical and electrical properties [8-10]. Controlling the size, surface morphology, and dopant concentration of WO<sub>3</sub> are important to for different applications. Doping is one of the most essential mechanisms to increase material's optical and electrical properties. This means that increasing the materials' conductivity and the optical band gap of the host materials reduces or increases their energy. According to a recent study, substitutional doping of metal ions is a good way to adjust the electronic structure and electrical properties of WO<sub>3</sub> [11, 12]. So far, various researchers have been investigating transition metal ions as dopants to study the structural, electrical and band edge properties of WO<sub>3</sub>, including Mo [13], Co [14], Ni [15], Fe [16], Cu [17,18] Mn,[19] and Cd [20].

Moreover, various studies have been conducted co-doping transition metal ions to modify optoelectrical properties of WO<sub>3</sub> nanoparticles. For instant, S. Mohammadi et al. investigated the effects of pure, Zn, Cu, co-doping Zn and Cu in WO<sub>3</sub> nanoparticles prepared by using both precipitation and co-precipitation methods for the application of photocatalytic and antibacterial activity. They found that the co-doping WO<sub>3</sub> nanoparticles have



higher photocatalytic degradation of gentamicin than other sample [21]. Albalshi et al. investigated the electrochemical properties of Ti and Zn co-doped  $\text{WO}_3$  thin films synthesized by the sol-gel method [22]. Furthermore, compared to a single doped  $\text{WO}_3$  thin film, co-doped film has improved electrochemical and electrochromic properties as well as higher electrochemical stability [22]. N.Boonprakob et al. employed Ag and Cu co-doped  $\text{WO}_3$  nanoparticles synthesized by using a simple co-precipitation approach for photocatalytic removal of hexavalent chromium [23]. This co-doping effect has higher photocatalytic reduction under visible light irradiation than un-doped [23]. To synthesize  $\text{WO}_3$  nanostructures, researchers have used different synthesis methods, for example sol-gel [24], microwave irradiation [25], co-precipitation [26], spray pyrolysis [27], and hydrothermal [28]. Among them, the co-precipitation method is the simplest, cost-effective, the highest purity, and has good uniformity [reference]. To our knowledge, no studies have examined the optical and structural effects of Cu and Ni co doped on the pristine  $\text{WO}_3$  by using environmental friendly co-precipitation method. The objective of this work is to give an insight on how the mono doped and co-doped can affect the structure, electrical and optical properties of  $\text{WO}_3$  nanoparticles. The obtained results are suggested that the prepared materials are good candidates as charge transport layer for solar cell applications.

## 2. MATERIALS AND METHODS

### 2.1 Synthesis of Pure, Mono and Co- Doped (Cu, Ni) $\text{WO}_3$ Nanoparticles (NPs)

Pristine  $\text{WO}_3$ , 5wt%Ni:  $\text{WO}_3$  and (2wt. % Cu+5wt. %Ni): $\text{WO}_3$ , (4wt. % Cu+5wt. %Ni): $\text{WO}_3$  and 5wt.% (Cu:Ni) co-doped  $\text{WO}_3$  nanoparticle were synthesized by simple chemical co-precipitation method. The precursors used in the synthesis were sodium tungstates dehydrate, copper (ii) nitrate trihydrate, and nickel nitrate hexahdrate, using NaCl as a capping agent and HCl to control the pH of the solution. In a typical synthesis, a suitable amount of sodium tungstate dihydrate was dissolved in 100 mL of distilled water and agitated for 30 minutes. After the precursors had completely dissolved, a suitable amount of NaCl was added to the solution and agitated until a homogeneous solution was obtained. After that, a certain amount of HCl solution was added to these precursor solutions, drop by drop, to bring the pH to 1 and stirred for one hour on a hot plate. Afterwards, the solution aged for 24hrs and then centrifuged to acquire precipitates. The precipitates were washed several times with distilled water and ethanol then dried in an electric oven at 80°C overnight. Finally, the prepared samples were annealed at 500 °C for 3 hrs in a furnace in order to obtain  $\text{WO}_3$  nanoparticles. The 5% Ni:  $\text{WO}_3$  and (2% Cu+5% Ni): $\text{WO}_3$ , (4% Cu+5%Ni): $\text{WO}_3$  and 5% (Cu:Ni) co-doped  $\text{WO}_3$  nanoparticles have synthesized by chemical co- precipitation method with different molar ratio of 2 %, 4%, and 5% for Cu and fixed amount 5% for Ni using the same procedure explained above. By using the precursors copper (ii) nitrate trihydrate and nickel nitrate hexahdrate with sodium tungstate dehydrate as starting materials.

### 2.2 Characterization Techniques

The phase purity and structure of the pristine, mono and co-doped  $\text{WO}_3$  nanoparticles were analyzed by XRD-7000 X-ray diffractometer maxima with Cu  $K\alpha$  radiation ( $\lambda = 0.15406$  nm). The presence of different functional groups in the sample was confirmed by FTIR spectrophotometer. The surface morphology of the samples was analyzed by scanning electron microscopy. Optical measurements of the sample were carried out by using UV–Vis Spectroscopy (Model: UV-3600 Plus). Room temperature photoluminescence (PL) spectra were performed by a Fluoromax-4 Spectrofluorometer in the excitation wavelength of 350 nm using a 40 W Xenon arc lamp. The current-voltage characteristics of the junctions were measured using a Keithley source meter unit (model 2400) in the dark at room temperature.

## 3. RESULTS AND DISCUSSION

### 3.1 XRD Analysis

The prepared samples were analyzed by X-ray diffraction using the Cu $K\alpha$  wavelength of 0.15406 nm. Fig. 1a shows the XRD of pristine  $\text{WO}_3$ , 5% Ni:  $\text{WO}_3$  (2% Cu+5%Cu): $\text{WO}_3$ , (4% Cu+5%Ni): $\text{WO}_3$  and 5% (Cu:Ni) co-doped  $\text{WO}_3$  nanoparticles. The XRD result confirmed that the prepared samples had an orthorhombic crystal structure of with space group P and lattice parameter  $a = 7.3840$  Å,  $b = 7.5120$  Å, and  $c = 3.8460$  Å and  $\alpha = \beta = \gamma$

= 90 °C. The result agreed with the standard JCPDS card No. 020-1324. The incidence of sharp and number of diffraction peaks revealed the polycrystalline nature of the prepared nanomaterials. No impurity peaks of Ni and Cu were observed from the XRD diffraction pattern which implies a successfully incorporations of Ni<sup>2+</sup> and Cu<sup>2+</sup> ions into the WO<sub>3</sub> lattice. As demonstrated in Fig 1 the intensity of co-doped (Ni:Cu) WO<sub>3</sub> nanoparticles increased in the plane (001) when compared to 5% Ni:WO<sub>3</sub> and pure WO<sub>3</sub> nanoparticles. This is due to the fact that (Ni:Cu) co-doping improves the development rate of WO<sub>3</sub> nanoparticles and gives them a higher degree of crystallinity than 5% Ni:WO<sub>3</sub> and pure WO<sub>3</sub>, resulting in sharper diffraction peaks in XRD. The intensity of 5% Ni doped WO<sub>3</sub> nanoparticles is lower than that of pure WO<sub>3</sub> nanoparticles. As result, 5% Ni doping reduces the degree of crystallinity and the growth rate of WO<sub>3</sub> nanoparticle. The crystallite sizes for the prepared NPs were analyzed from the three most prominent diffraction peaks of (001), (020) and (200) planes using the Debye Scherer relation shown in equation 1.

$$D = \frac{K\lambda}{\beta \cos\theta} \dots\dots\dots (1)$$

Where, “D” is average crystallite size obtained from the three dominant peak, “K” is the shape factor taken as 0.9, “λ” is the wavelength of the incident beam, “β” is the full width at half maximum (radians) and “θ” is the Bragg angle.

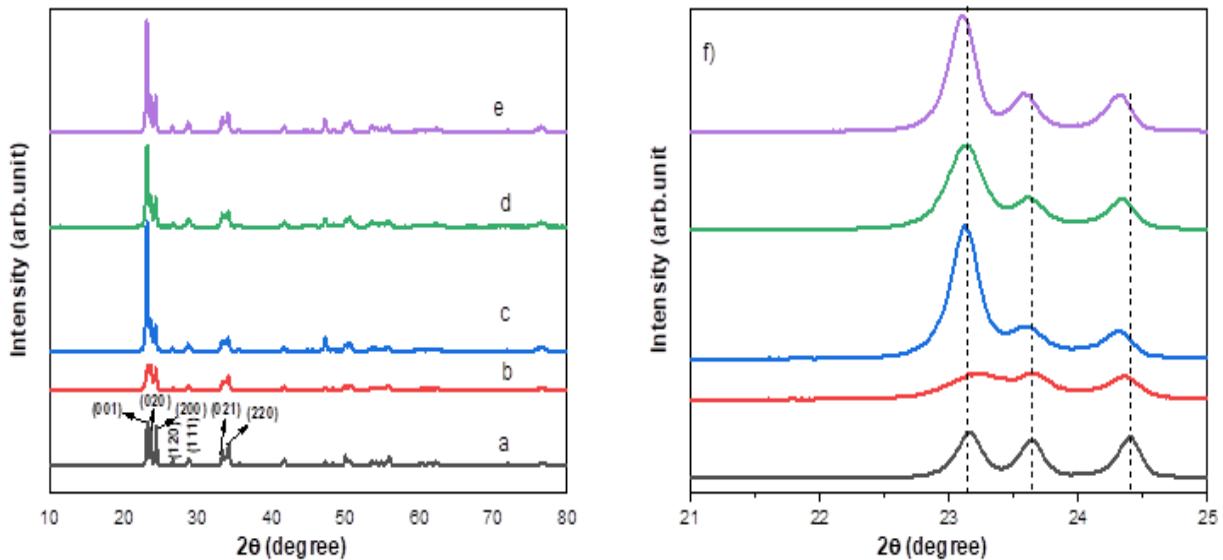


**Fig.1:** X-ray diffraction analysis of a) pure WO<sub>3</sub>, b) 5%Ni:WO<sub>3</sub>,c) (2% Cu+5%Ni):WO<sub>3</sub>, d) (4% Cu+5%Ni):WO<sub>3</sub>, e) 5%(Cu:Ni) co-doped WO<sub>3</sub> nanoparticles. f) Change in (001), (020) and (200) peaks positions with dopant concentrations

The average crystallite size of pure WO<sub>3</sub> was found to be 46 nm; 25 nm for 5% Ni:WO<sub>3</sub> furthermore, the crystalline size, it was decreased from 35 nm to 40 nm for various concentration of Cu at 2 wt.%, 4wt.%, 5 wt.% and fixed in Ni of 5wt. % doped WO<sub>3</sub> respectively. These results clearly indicate that Cu<sup>2+</sup> and Ni<sup>2+</sup> ions substituted in the WO<sub>3</sub> host lattice site and the growth rate was reduced by dopant concentration [29]. The expanded version of XRD (Fig. 1f) clearly shows the slight peak position shifts of (001), (020), (200) planes to the lower diffraction angles when compared to the pure WO<sub>3</sub> NPs. This peak shift to the lower angle for doped NPs indicates that the lattice parameters are slightly varied than the pure WO<sub>3</sub> and a successful substitution Ni<sup>2+</sup> and Cu<sup>2+</sup> ions onto the host lattice [30].

This can be associated to the smaller ionic radii difference between the host W (0.62 Å) and dopant 0.60 Å for Ni and 0.73 Å for Cu ions [31, 32].

As shown in Table 1, the unit cell volume of WO<sub>3</sub> NPs co-doped with fixed nickel and varying copper amounts decreased with dopant concentration, indicating quantitative substitution of Cu ion in the lattice size, as similar phenomena have been reported [44]. It is also observed that the value of the dislocation density of undoped WO<sub>3</sub>



NPs has the lowest value as compared to the doped sample, shown in Table 1. This indicates that Cu<sup>2+</sup> and Ni<sup>2+</sup> co-doping deteriorate the WO<sub>3</sub> crystal structure. Table 1 also reveals that the micro-strain and crystallite size have a strong relationship. The differing ionic radius of W<sup>6+</sup>, Cu<sup>2+</sup>, and Ni<sup>2+</sup> ions, which enhance the micro-strain during the substitution of W ions by both Cu and Ni ions, could explain these changes in micro-strain with crystal size. As a result, dopant concentrations diminish the development rate and crystallinity of WO<sub>3</sub> NPs, and crystal size increases produce a decrease in the strain [45, 46].

The from the XRD peaks the lattice parameters for the orthorhombic crystal structure was calculated by using equation (2):

$$\frac{1}{d^2} = \frac{h^2}{a^2} + \frac{k^2}{b^2} + \frac{l^2}{c^2} \dots\dots\dots (2)$$

Where “d” is the interplanar spacing; a, b, c are the lattice parameters and h, k, l are the Miller indices. Length of dislocation lines per unit volume of a crystal is dislocation density. The defect in the crystal structure of WO<sub>3</sub> nanoparticles is measured by the dislocation, and the presence of this strongly influences the properties of the sample. The dislocation density can also be calculated from the equation (3):

$$\delta = \frac{1}{D^2} \dots\dots\dots (3)$$

Where “δ” is dislocation density and “D” is the average crystallite size of the sample.

The micro-strian (ε) can be calculated using equation (4) [47].

$$\text{Micro-strain } (\epsilon) = \frac{\beta}{4 \tan\theta} \dots\dots\dots (4)$$

**Table 1:** XRD parameters of the prepared nanoparticles with fixed Ni and different Cu concentrations

Concentrations	Crystallite size (nm)	Dislocation density (x10 <sup>-3</sup> ) lines/m <sup>2</sup>	Strain (x10 <sup>-3</sup> ) lines <sup>-2</sup> m <sup>-4</sup>	Lattice parameters (Å)			Volume of unit cell a*b*c(Å) <sup>3</sup>
				a	b	c	
Pure WO <sub>3</sub>	46	0.4726	4.6025	7.3053	7.5375	3.8452	211.73
5% Ni:WO <sub>3</sub>	25	1.6	16.6950	7.3108	7.5789	3.8371	212.61
2% Cu+5% Ni:WO <sub>3</sub>	37	0.7305	6.3924	7.3134	7.5231	3.8375	211.13
4% Cu+5% Ni:WO <sub>3</sub>	35	0.8163	6.5447	7.3030	7.5168	3.8366	210.61
5% (Cu:Ni):WO <sub>3</sub>	40	0.625	5.2226	7.3076	7.5323	3.8408	211.41
JCPDS (020-1324).				7.3840	7.5120	3.8460	213.33

### 3.1.1 UV-Visible diffusion reflectance

The UV-Vis spectroscopy measurements were taken to assess the influence of 5% Ni:WO<sub>3</sub> 2% Cu +5% Ni :WO<sub>3</sub>, 4% Cu+ 5% Ni :WO<sub>3</sub> and 5% (Cu :Ni) co-doped on WO<sub>3</sub> NPs. Fig. 2 a-f shows the reflectance spectra and optical band gap of all WO<sub>3</sub> samples. Fig. 2 f shows all WO<sub>3</sub> samples have minimum reflectance in the UV region. In the entire sample in the visible region, the reflectance increases, but all the co-doped sample has higher reflectance than the 5% Ni:WO<sub>3</sub> and pure WO<sub>3</sub> nanoparticles. The optical band gap energy of WO<sub>3</sub> nanoparticles were analyzed using Kubelka–Munk function relation given by the following Equation 2 [33,34].

$$F(R) = \frac{(1-R)^2}{2R} \dots\dots\dots (5)$$

Where F(R) is known as kubelka–munk function and R is the reflection of the materials. The indirect band gap energy of the sample can be estimated using both along x –axis and y –axis intercept from a plot of (F(R)hν)<sup>1/2</sup> versus energy (hν) as shown in the Fig. 2 a-e. The Fig.2 a-e indicates that pure WO<sub>3</sub> nanoparticles has the optical band gap of about 2.80 eV which is decreased to 2.63eV for 5% Ni:WO<sub>3</sub> , 2.75eV for (2% Cu + 5%

Ni):WO<sub>3</sub>, 2.77 eV for (4% Cu + 5% Ni):WO<sub>3</sub> and 2.73 eV for 5% (Cu: Ni) co-doped WO<sub>3</sub> nanoparticles. The crystal size and dopant content increases the optical band gap energy decrease.

Therefore, the reduction in the optical band gap energy of WO<sub>3</sub> is due to the induced energy levels near to the conduction and valence band by Cu and Ni ions substitutions. While the electronic transition occurs from the filled valence band to the new energy levels, rather than the typical electronic transition from the filled valence band to the conduction band due to higher amount of defects state occurred [35]. This suggests that as (Ni, Cu) is co-doped into the WO<sub>3</sub> lattice, defect states are generated, resulting in a decrease in the band gap [51]. Also the reduction in the band gap energy with Cu and Ni doping may facilitate absorption of more light in the visible region and can help to improve the optoelectronic devices.

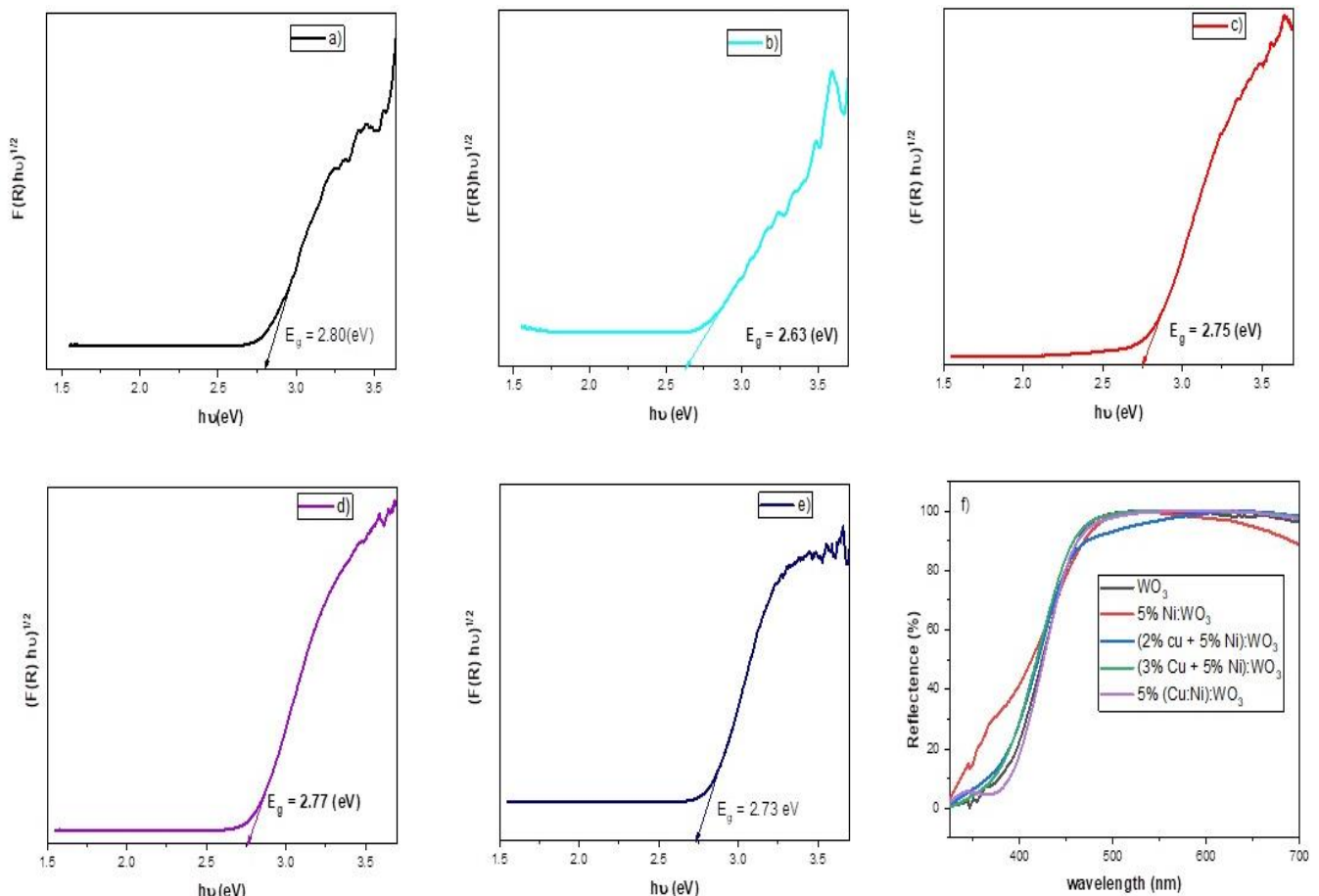


**Fig.2:** The optical band gap of a) pure WO<sub>3</sub>, b) 5% Ni:WO<sub>3</sub>, c) (2% Cu+5% Ni):WO<sub>3</sub>, d) (4% Cu+5% Ni):WO<sub>3</sub> e) 5% (Cu:Ni) co-doped WO<sub>3</sub> nanoparticles. f) UV-Vis Diffuse reflectance spectra of all sample

### 3.1.2 Photoluminescence (PL) studies

Fig. 3 shows the room-temperature PL emission spectra of the prepared samples at an excitation wavelength of 350 nm. The emission spectra of pure WO<sub>3</sub>, 5% Ni, WO<sub>3</sub>, (2% Cu+5% Ni): WO<sub>3</sub>, (4% Cu+5% Ni): WO<sub>3</sub> and 5% (Cu: Ni) co-doped WO<sub>3</sub> nanoparticles are all in the visible region. The greater emission spectrum in the (Ni,Cu) co-dopant has a higher percentage of surface oxygen vacancy. The emission spectra of pure WO<sub>3</sub>, 5%Ni:WO<sub>3</sub>,(2% Cu+5%Ni):WO<sub>3</sub>,(4% Cu+5% Ni):WO<sub>3</sub> and 5%( Cu:Ni) co-doped WO<sub>3</sub> nanoparticles were exhibited strong emission peaks centered at 431 nm related to violet emission, 440 and 445 related to blue emission, 494 nm, 500nm related to blue-green emission, 512,523, 524,531, 535, 536,542 and 546 nm related to green emission ,610 , 621 and 662 nm related to orange-red emission. The recombination of free excitons causes UV and blue emission, which is referred to as near band edge emission (NBE) [36]. This UV and blue emission corresponding to band gap energy of 2.82 eV, 2.87eV and 2.78 eV, which aligned with the band gap energy determined from UV absorption spectra. The blue emission peak about 440 and 445 nm can be attributed

to electron recombination in the conduction band with deep doubly ionized oxygen vacancies, as well as exciton recombination, as seen in Fig. 3. The transition from the conduction band to single ionized oxygen vacancies and defects, which were introduced by the presence of Ni and Cu in WO<sub>3</sub> samples, caused the blue-green and green emissions. The orange-red emission was caused by transitions associated with interstitial atomic defects found in the prepared samples [32,37]. These results are in good agreement with works reported in the literatures [52]. Pure WO<sub>3</sub> and 5% Ni:WO<sub>3</sub> nanoparticles exhibit lower intensity than (Ni: Cu) co-doped WO<sub>3</sub> samples due to a lack of crystallinity [38]. The lower the PL intensity; the lower the recombination rate of photo-induced electron-hole pairs [48]. The increased PL emission intensity was attributed to electron-hole recombination caused by surface imperfections or oxygen vacancies [49]. As a result of the higher growth and more intense PL emission peak observed in the Cu and Ni co-doped WO<sub>3</sub> samples. The PL emission peak of co-doped WO<sub>3</sub> samples shifts to the lower wavelength side and has a distinct intensity because of the substitution of W<sup>+6</sup> by Ni<sup>2+</sup> and Cu<sup>2+</sup> ions into the host WO<sub>3</sub> unit cell lattice site.

These defects form a number of trap states which are responsible for the various PL peaks in the visible region [50]. The generalized band gap structure and specific defect level emissions as shown in Fig. 4.

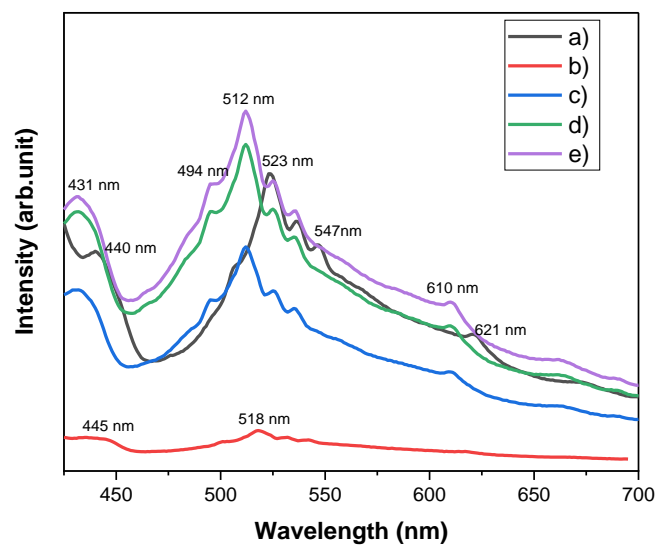


**Fig.3:** Photoluminescence spectra of a) pure WO<sub>3</sub>, b) 5% Ni:WO<sub>3</sub>, c) (2%Cu+5% Ni):WO<sub>3</sub>, d) (4% Cu+5% Ni):WO<sub>3</sub> and e) 5% (Cu:Ni) :WO<sub>3</sub> nanoparticles

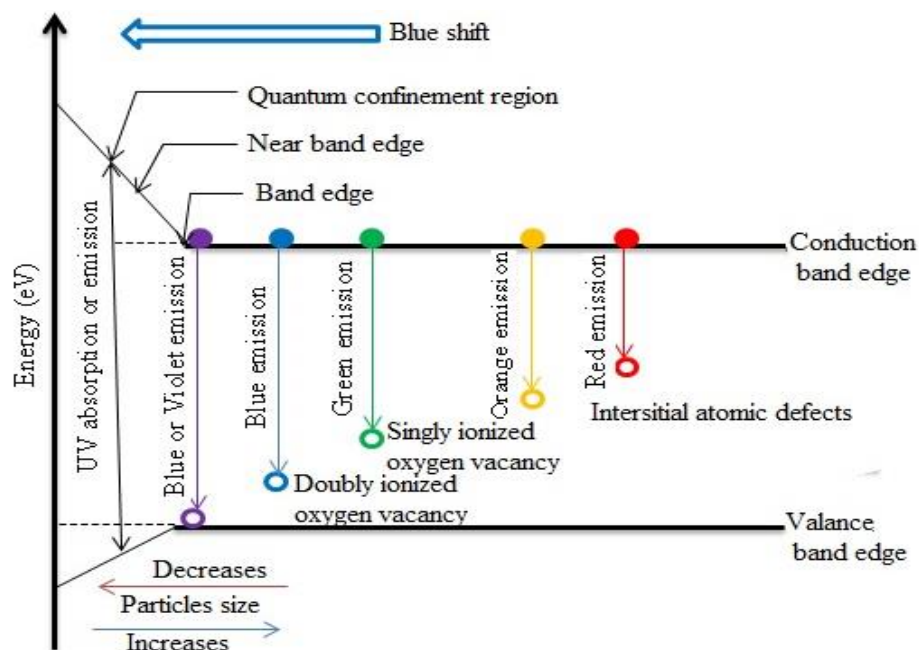


**Fig.4:** Generalized band gap structure, defect energy levels and different specific absorption/emission lines



### 3.1.3 Fourier transforms infra-red (FTIR) analysis

The FTIR spectroscopy was studied to the information about the surface chemistry and chemical quality of nanomaterial. Fig. 5 shows the FTIR spectra of pure  $\text{WO}_3$ , 5%  $\text{Ni}:\text{WO}_3$ , (2% $\text{Cu}+5\% \text{Ni}):\text{WO}_3$ , (4%  $\text{Cu}+5\% \text{Ni}):\text{WO}_3$  and 5%  $(\text{Cu}:\text{Ni}):\text{WO}_3\text{NPs}$ . The observed band located at  $1409 \text{ cm}^{-1}$  represented to bending modes of O-H groups and the band located at  $2955$  to  $3683 \text{ cm}^{-1}$  maybe represented to the stretching modes of O-H group in water or hydroxyls [32, 39]. Furthermore, the broad band observed at  $550$  to  $1050 \text{ cm}^{-1}$  is linked with the O-W-W stretching mode [32, 39]. The presence of  $\text{WO}_3$  stretching mode and absence of Ni and Cu oxide related mode further support that  $\text{Ni}^{2+}$  and  $\text{Cu}^{2+}$  ions are successfully doped  $\text{WO}_3$  crystal structure. These results are consistent with our XRD results.

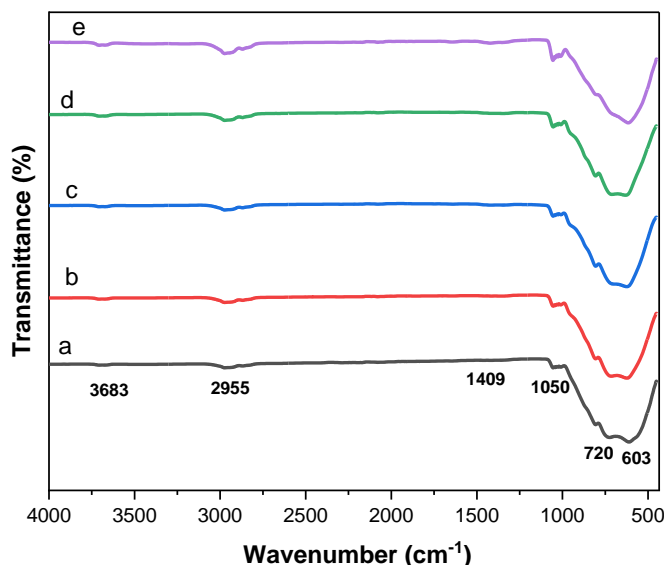


**Fig. 5:** FTIR spectra of a) pure  $\text{WO}_3$ , b) 5%  $\text{Ni}:\text{WO}_3$ , c) (2%  $\text{Cu}+5\% \text{Ni}):\text{WO}_3$ , d) (4%  $\text{Cu}+5\% \text{Ni}):\text{WO}_3$  and e) 5%  $(\text{Cu}:\text{Ni})$ co-doped  $\text{WO}_3$  nanoparticles

### 3.1.4 Surface morphology analysis

The surface morphology and histogram results of the synthesized pure  $\text{WO}_3$ , 5%  $\text{Ni}:\text{WO}_3$ , and 5%  $(\text{Ni}:\text{Cu})$  co-doped  $\text{WO}_3\text{NPs}$  are shown in Fig.6 a-f. It is clearly understood that the surface morphology of pure, mono, and co-doped  $\text{WO}_3$  nanoparticles is uniform and densely packed as shown in Fig. 6 a-c. The particles were clearly agglomerated in the SEM images. From the SEM images it is easily observed that doping with Ni and Cu plays a significant role on the morphological nature of the nanocrystalline of the prepared samples. The SEM micrographs also demonstrate that the surface morphology is dependent on the dopant element, indicating that  $\text{W}^{6+}$  replaced with transition metal in the  $\text{WO}_3$  unit cell. The average particle size distribution of  $\text{WO}_3$ , 5% Ni, and 5%  $(\text{Ni}:\text{Cu})$  co-doped  $\text{WO}_3$  was obtained by analyzing the SEM image using the software ImageJ as shown in Fig. 6d-f. The histograms represent  $\text{WO}_3$  nanoparticles with an average diameter of about 225 nm. However, the addition of  $\text{Ni}^{2+}$  influence the size morphology in which of average diameter of the nanoplates is decreased from 225 nm to 138 nm due to divalent nickel ions restrict the growth of  $\text{WO}_3$  and lead to growing in the nanoplate direction shown in Fig. 6b [32,40]. This decreased the average diameter which is a good agreement with average crystalline size calculated from the XRD.

When both  $\text{Ni}^{2+}$  and  $\text{Cu}^{2+}$  the dopant precursor concentration the morphology may be attributed to resulting in the change of surface feature from nanoplates shape to both nanorods and nanoplates shows in Fig. 6 c. The Ni and Cu co-doped  $\text{WO}_3$  nanoparticles increase the diameter from 225 to 252nm shown in Fig. 6f. These co-doping change both the shape and size of the  $\text{WO}_3$  nanoparticles.

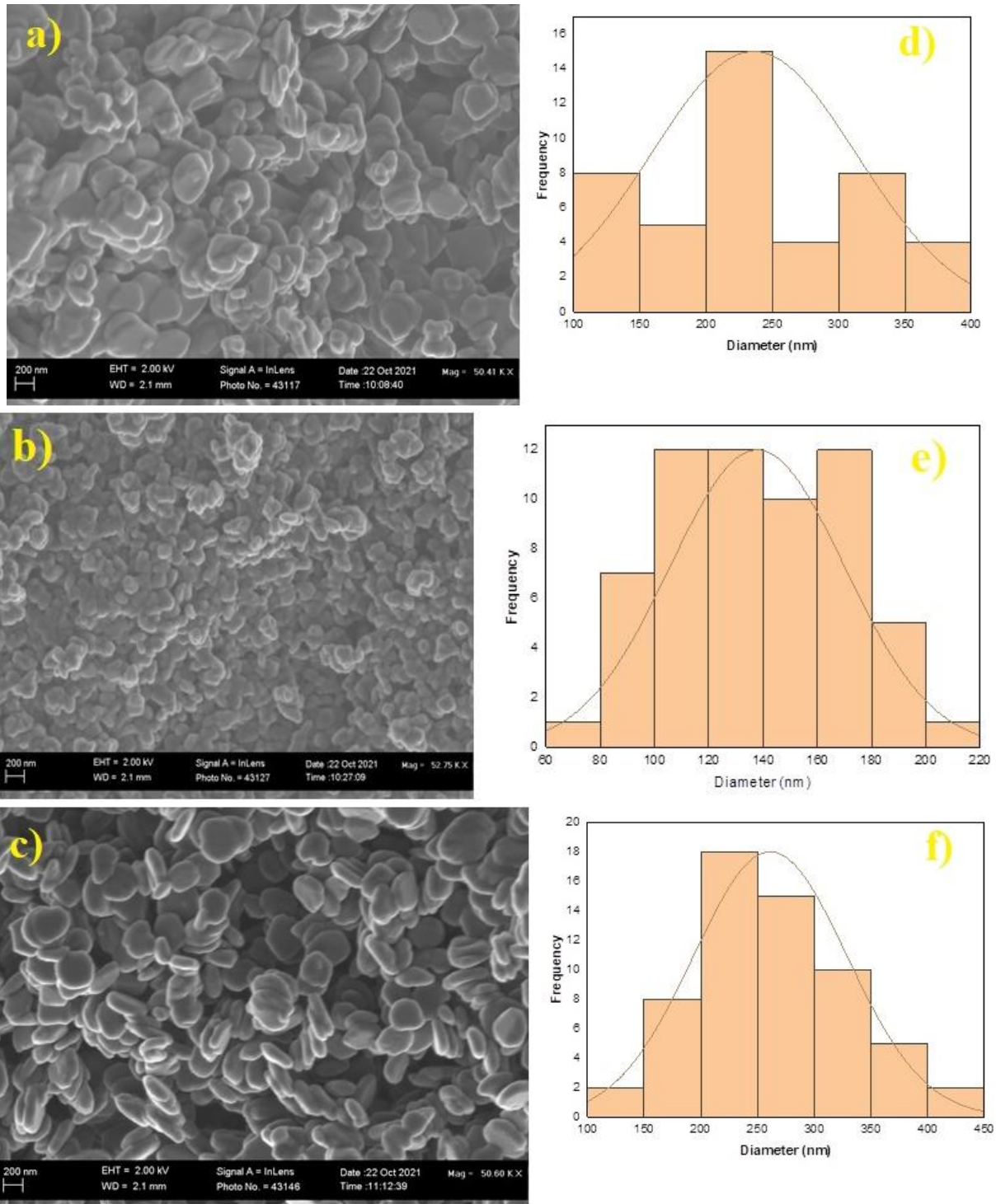


**Fig. 6:** SEM images of a) pure WO<sub>3</sub> b) 5% Ni: WO<sub>3</sub> and c) 5% (Cu:Ni):WO<sub>3</sub> NPs and the average grain size of d) pure WO<sub>3</sub>, e) 5% Ni:WO<sub>3</sub>, f) 5% (Cu:Ni):WO<sub>3</sub> NPs

### 3.1.5 I–V characteristic studies

The electrical properties measurement were carried out under dark condition at room temperature for pristine WO<sub>3</sub>, 5wt. % Ni: WO<sub>3</sub> and (2wt.% Cu+5% Ni):WO<sub>3</sub>, (4% Cu+5% Ni):WO<sub>3</sub> and 5% (Cu/Ni) co-doped WO<sub>3</sub> thin film. The prepared samples were used to deposit on glass substrate by simple spin coating method after dissolving in DFM. Then the spin coated film was dried at 100°C for 2 h in an oven, and the metal contact was made over the prepared film using silver past. The result of the I-V characteristics measured for the sample exhibits a good ohmic behavior as shown in Fig. 7. The resistivity was calculated from the slope of each curves and tabulated in Table 1.



**Table 2:** Resistivity of the prepared thin films with fixed Ni and different Cu concentrations

Samples	WO <sub>3</sub>	5% Ni:WO <sub>3</sub>	(2% Cu+5% Ni): WO <sub>3</sub>	(4% Cu+5% Ni): WO <sub>3</sub>	5%(Cu:Ni): WO <sub>3</sub>
Resistivity (Ω.cm)	6.3 x10 <sup>-3</sup>	0.63x10 <sup>-3</sup>	19.3 x10 <sup>-3</sup>	232.5 x10 <sup>-3</sup>	2.9 x10 <sup>-3</sup>

The resistivity of WO<sub>3</sub> film found to have between 0.63x10<sup>-3</sup>–2.33 x10<sup>-1</sup>Ω.cm with doping of Ni and Cu, as shown in Table 1. The resistivity of WO<sub>3</sub> decreases from 6.3 x10<sup>-3</sup>Ω.cm to 0.63 x10<sup>-3</sup>Ω.cm when 5% Ni doped and increases when Cu-Ni are co-doped in WO<sub>3</sub>.

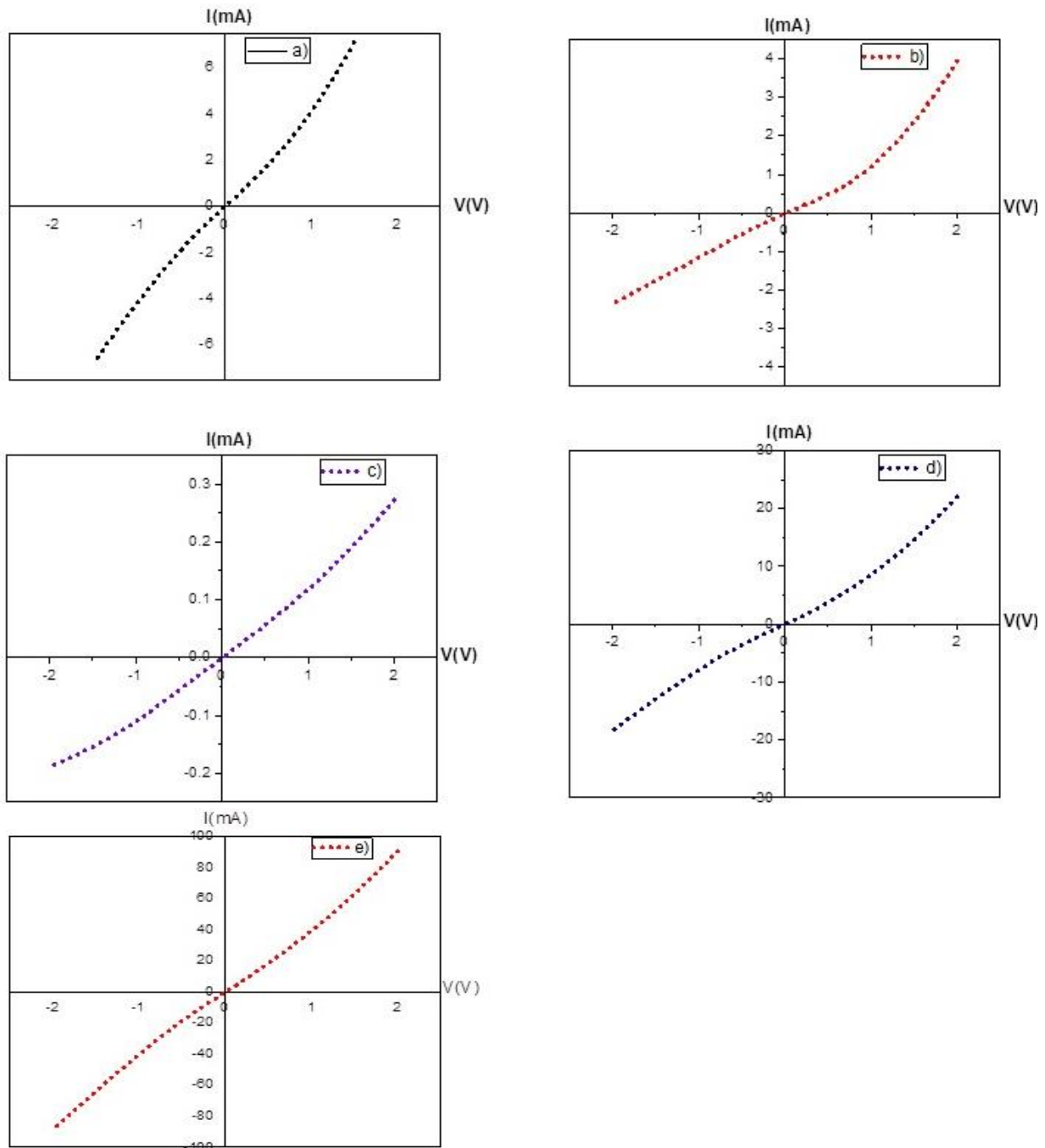


**Fig. 7:** I-V curves of a) pure WO<sub>3</sub>, b) (2% Cu + 5% Ni): WO<sub>3</sub>, c)(4% Cu + 5% Ni): WO<sub>3</sub>, d) 5% (Ni:Cu): WO<sub>3</sub> and e) 5% Ni:WO<sub>3</sub> NPs

When small amount of Cu is added in the Ni doped WO<sub>3</sub> the resistivity of the film increase from 0.63x10<sup>-3</sup> Ω.cm for 5% Ni-WO<sub>3</sub> thin film to 1.93 x10<sup>-2</sup>Ω.cm for (2% Cu,5% Ni)-WO<sub>3</sub> and to 2.33 x10<sup>-1</sup>Ω.cm for (4% Cu,



5% Ni)-WO<sub>3</sub>. However, the obtained resistivity of WO<sub>3</sub> films after doping of both Ni and Cu is slightly higher than the range of resistivity of semiconductors. Therefore, altering the dopant concentration in the unit cell lattice of WO<sub>3</sub> can cause crystalline defects, change the electronic structure and result in changes the electrical conductivity of WO<sub>3</sub> thin films [41-43]. Therefore, the prepared Ni-Cu doped WO<sub>3</sub> films shows good ohmic properties and is good candidates for solar cell window layer applications.

#### 4. CONCLUSIONS

Pristine WO<sub>3</sub>, 5%Cu:WO<sub>3</sub>, (2% Cu + 5% Ni): WO<sub>3</sub>, (4% Cu + 5% Ni): WO<sub>3</sub>, and 5% (Ni:Cu):WO<sub>3</sub> nanoparticles were successfully synthesized by co-precipitation methods. The structural, optical, and electrical properties of the prepared nanomaterials were investigated. The formation of the nanocrystalline orthorhombic structure of WO<sub>3</sub> was confirmed by XRD. Moreover, average crystalline size, microstrain, unit cell volume and lattice parameters were significantly influenced by the dopant concentrations. The UV-Vis analyses revealed that the band gaps of the prepared samples decreased as the dopant concentrations increased. Various PL emissions in visible region were observed due to defects from a number of trap states. The increased intensity of the PL emission peak at 431, 440, 512, and 523 nm of pristine WO<sub>3</sub> and (Ni: Cu) co-doped WO<sub>3</sub> samples was attributed to the high electron-hole recombination caused by nanoplates with little rod morphology. The SEM micrographs confirmed that the prepared samples have both nanoplate and nanorod shapes and are agglomerated irrespective of the dopants. The I-V curves revealed that all the films obey Ohms law and the resistivity decreased with doping. The obtained results revealed that the prepared materials are suitable for application in optoelectronic devices as the window layer.

#### REFERENCE

1. Fernández-Domene, R. M., Sánchez-Tovar, R., Lucas-Granados, B., Roselló-Márquez, G., & Garcia-Anton, J. (2017). A simple method to fabricate high-performance nanostructured WO<sub>3</sub> photocatalysts with adjusted morphology in the presence of complexing agents. *Materials & Design*, 116, 160-170.
2. Durrani, S. M. A., Khawaja, E. E., Salim, M. A., Al-Kuhaili, M. F., & Al-Shukri, A. M. (2002). Effect of preparation conditions on the optical and thermochromic properties of thin films of tungsten oxide. *Solar energy materials and solar cells*, 71(3), 313-325.
3. Feng, M., Pan, A. L., Zhang, H. R., Li, Z. A., Liu, F., Liu, H. W. & Gao, H. J. (2005). Strong photoluminescence of nanostructured crystalline tungsten oxide thin films. *Applied Physics Letters*, 86(14), 141901.
4. Granqvist, C. G. (2000). Electrochromic tungsten oxide films: review of progress 1993–1998. *Solar Energy Materials and Solar Cells*, 60(3), 201-262.
5. György, E., Socol, G., Mihailescu, I. N., Ducu, C., & Ciuca, S. (2005). Structural and optical characterization of WO<sub>3</sub> thin films for gas sensor applications. *Journal of applied physics*, 97(9), 093527.
6. Kim, K., Seo, C., Cheong, H., & Lee, S. H. (2006). Photochromic mechanism in a-WO<sub>3</sub> thin films based on Raman spectroscopic studies. *Journal of the Korean Physical Society*, 48(6), 1657-1660.
7. Avellaneda, C. O., & Bulhões, L. O. (2003). Intercalation in WO<sub>3</sub> and WO<sub>3</sub>: Li films. *Solid State Ionics*, 165(1-4), 59-64.
8. Granqvist, C. G. (Ed.). (1995). *Handbook of inorganic electrochromic materials*. Elsevier.
9. Kalantar-zadeh, K., Vijayaraghavan, A., Ham, M. H., Zheng, H., Breedon, M., & Strano, M. S. (2010). Synthesis of atomically thin WO<sub>3</sub> sheets from hydrated tungsten trioxide. *Chemistry of Materials*, 22(19), 5660-5666.
10. Su, J., Guo, L., Bao, N., & Grimes, C. A. (2011). Nanostructured WO<sub>3</sub>/BiVO<sub>4</sub> heterojunction films for efficient photoelectrochemical water splitting. *Nano letters*, 11(5), 1928-1933.
11. Upadhyay, S. B., Mishra, R. K., & Sahay, P. P. (2014). Structural and alcohol response characteristics of Sn-doped WO<sub>3</sub> nanosheets. *Sensors and Actuators B: Chemical*, 193, 19-27.
12. Kalanur, S. S., Yoo, I. H., Eom, K., & Seo, H. (2018). Enhancement of photoelectrochemical water splitting response of WO<sub>3</sub> by Means of Bi doping. *Journal of catalysis*, 357, 127-137.
13. Pooyodying, P., Ok, J. W., Son, Y. H., & Sung, Y. M. (2021). Electrical and optical properties of electrochromic device with WO<sub>3</sub>: Mo film prepared by RF magnetron Co-Sputtering. *Optical Materials*, 112, 110766.
14. Mehmood, F., Iqbal, J., Jan, T., Gul, A., Mansoor, Q., & Faryal, R. (2017). Structural, photoluminescence, electrical, anti-cancer and visible light driven photocatalytic characteristics of Co doped WO<sub>3</sub> nanoplates. *Vibrational Spectroscopy*, 93, 78-89.



15. Dakhel, A. A., & Ashoor, H. (2019). Synthesis of semiferromagnetic Ni-doped WO<sub>3</sub> nanoparticles by precipitation method: Evaluation of effect of treatment in hydrogen gas. *Materials Chemistry and Physics*, 230, 172-177.
16. Mehmood, F., Iqbal, J., Jan, T., & Mansoor, Q. (2017). Structural, Raman and photoluminescence properties of Fe doped WO<sub>3</sub> nanoplates with anti-cancer and visible light driven photocatalytic activities. *Journal of Alloys and Compounds*, 728, 1329-1337.
17. Mehmood, F., Iqbal, J., Gul, A., Ahmed, W., & Ismail, M. (2017). Facile synthesis of 2-D Cu doped WO<sub>3</sub> nanoplates with structural, optical and differential anti-cancer characteristics. *Physica E: Low-Dimensional Systems and Nanostructures*, 88, 188-193.
18. Tudorache, F. (2018). Investigations on microstructure, electrical and magnetic properties of copper spinel ferrite with WO<sub>3</sub> addition for applications in the humidity sensors. *Superlattices and Microstructures*, 116, 131-140.
19. Mohan, L., Avani, A. V., Kathirvel, P., Marnadu, R., Packiaraj, R., Joshua, J. R., ... & Saravanakumar, S. (2021). Investigation on structural, morphological and electrochemical properties of co-precipitation synthesis of Mn doped WO<sub>3</sub> nanoparticles for supercapacitor applications. *Journal of Alloys and Compounds*, 160670.
20. Kalaiarasi, S., Christy, H. K. S., & Muthuchudarkodi, R. R. (2020). Optical, structural and morphological characterization of cadmium ion doped WO<sub>3</sub> nanoparticles. *Journal of Advanced Scientific Research*, 11(4).
21. Mohammadi, S., Sohrabi, M., Golikand, A. N., & Fakhri, A. (2016). Preparation and characterization of zinc and copper co-doped WO<sub>3</sub> nanoparticles: application in photocatalysis and photobiology. *Journal of Photochemistry and Photobiology B: Biology*, 161, 217-221.
22. Albalshi, M. A. M. (2016). Electrochemical properties of Sol-gel WO<sub>3</sub> films Co-doped with Ti and Zn (Doctoral dissertation).
23. Boonprakob, N., Channei, D., & Zhao, C. (2021). Heterogeneous photocatalytic reduction of hexavalent chromium by modified Ag, Cu co-doped tungsten oxide nanoparticles. *Journal of the Australian Ceramic Society*, 1-12.
24. Saasa, V., Malwela, T., Lemmer, Y., Beukes, M., & Mwakikunga, B. (2020). The hierarchical nanostructured Co-doped WO<sub>3</sub>/carbon and their improved acetone sensing performance. *Materials Science in Semiconductor Processing*, 117, 105157.
25. Hariharan, V., Aroulmoji, V., Prabakaran, K., Gnanavel, B., Parthibavarman, M., Sathyapriya, R., & Kanagaraj, M. (2016). Magnetic and electrochemical behaviour of cobalt doped tungsten oxide (WO<sub>3</sub>) nanomaterials by microwave irradiation method. *Journal of Alloys and Compounds*, 689, 41-47.
26. Mehmood, F., Iqbal, J., Jan, T., Gul, A., Mansoor, Q., & Faryal, R. (2017). Structural, photoluminescence, electrical, anti-cancer and visible light driven photocatalytic characteristics of Co doped WO<sub>3</sub> nanoplates. *Vibrational Spectroscopy*, 93, 78-89.
27. Bertus, L. M., Faure, C., Danine, A., Labrugère, C., Campet, G., Rougier, A., & Duta, A. (2013). Synthesis and characterization of WO<sub>3</sub> thin films by surfactant assisted spray pyrolysis for electrochromic applications. *Materials chemistry and physics*, 140(1), 49-59.
28. Tehrani, F. S., Ahmadian, H., & Aliannezhadi, M. (2020). Hydrothermal synthesis and characterization of WO<sub>3</sub> nanostructures: effect of reaction time. *Materials Research Express*, 7(1), 015911.
29. Sivakarthish, P., Thangaraj, V., & Parthibavarman, M. (2017). A facile and one-pot synthesis of pure and transition metals (M= Co & Ni) doped WO<sub>3</sub> nanoparticles for enhanced photocatalytic performance. *Journal of Materials Science: Materials in Electronics*, 28(8), 5990-5996.
30. Wu, X., Wei, Z., Zhang, L., Zhang, C., Yang, H., & Jiang, J. (2014). Synthesis and characterization of Fe and Ni co-doped ZnO nanorods synthesized by a hydrothermal method. *Ceramics International*, 40(9), 14635-14640.
31. Mehmood, F., Iqbal, J., Ismail, M., & Mehmood, A. (2018). Ni doped WO<sub>3</sub> nanoplates: an excellent photocatalyst and novel nanomaterial for enhanced anticancer activities. *Journal of Alloys and Compounds*, 746, 729-738.
32. Deepa, B., & Rajendran, V. (2018). Pure and Cu metal doped WO<sub>3</sub> prepared via co-precipitation method and studies on their structural, morphological, electrochemical and optical properties. *Nano-structures & Nano-objects*, 16, 185-192.
33. Li, X., Mu, W., Xie, X., Liu, B., Tang, H., Zhou, G., & Luo, S. (2014). Strontium adsorption on tantalum-doped hexagonal tungsten oxide. *Journal of hazardous materials*, 264, 386-394.
34. Mehmood, F., Iqbal, J., Jan, T., Gul, A., Mansoor, Q., & Faryal, R. (2017). Structural, photoluminescence, electrical, anti-cancer and visible light driven photocatalytic characteristics of Co doped WO<sub>3</sub> nanoplates. *Vibrational Spectroscopy*, 93, 78-89.



35. Baraneedharan, P., Hussain, S. I., Dinesh, V. P., Siva, C., Biji, P., & Sivakumar, M. (2015). Lattice doped Zn–SnO<sub>2</sub> nanospheres: A systematic exploration of dopant ion effects on structural, optical, and enhanced gas sensing properties. *Applied Surface Science*, 357, 1511–1521.
36. Meenakshi, M., Gowthami, V., Perumal, P., & Sanjeeviraja, C. (2014). Effect of RF Power on the Structural and Optical characterization of (WO<sub>3</sub>)<sub>0.90</sub> (V<sub>2</sub>O<sub>5</sub>)<sub>0.10</sub> Thin Films. *Int. J. ChemTech. Res.* 6(13), 5412–5418
37. Mishra, S. K., Srivastava, R. K., Prakash, S. G., Yadav, R. S., & Panday, A. C. (2010). Photoluminescence and photoconductive characteristics of hydrothermally synthesized ZnO nanoparticles. *Opto-Electronics Review*, 18(4), 467–473.
38. Hirano, M., & Okamoto, T. (2018). Synthesis, morphology, and luminescence of ZnNb<sub>2</sub>O<sub>6</sub> nanocrystals by hydrothermal method. *Nano-Structures & Nano-Objects*, 13, 139–145.
39. Willis, H. A., Van der Maas, J. H., & Miller, R. G. (1987). *Laboratory methods in vibrational spectroscopy*.
40. F. Mehmood, J. Iqbal, T. Jan, Q. Mansoor, Structural, Raman and photoluminescence properties of Fe doped WO<sub>3</sub> nanoplates with anti-cancer and visible light driven photocatalytic activities, *J Alloys Compd.* 728 (2017) 1329–1337.
41. Serin, T., Serin, N., Karadeniz, S., Sari, H., Tuğluoğlu, N., & Pakma, O. (2006). Electrical, structural and optical properties of SnO<sub>2</sub> thin films prepared by spray pyrolysis. *Journal of Non-Crystalline Solids*, 352(3), 209–215..
42. Salah, N., Habib, S., & Azam, A. (2017). The influence of transition metal doping on the thermoelectric and magnetic properties of microwave synthesized SnO<sub>2</sub> nanoparticles. *Journal of Materials Science: Materials in Electronics*, 28(1), 435–445.
43. Soussi, L., Garmim, T., Karzazi, O., Rmili, A., El Bachiri, A., Louardi, A., & Erguig, H. (2020). Effect of (Co, Fe, Ni) doping on structural, optical and electrical properties of sprayed SnO<sub>2</sub> thin film. *Surfaces and Interfaces*, 19, 100467.
44. Phaomei, G., Rameshwar Singh, W., & Ningthoujam, R. S. (2011). Solvent effect in monoclinic to hexagonal phase transformation in LaPO<sub>4</sub>: RE (RE= Dy<sup>3+</sup>, Sm<sup>3+</sup>) nanoparticles: Photoluminescence study. *Journal of Luminescence*, 131.
45. Mishra, R. K., Kushwaha, A., & Sahay, P. P. (2014). Influence of Cu doping on the structural, photoluminescence and formaldehyde sensing properties of SnO<sub>2</sub> nanoparticles. *RSC Adv* 4: 3904–3912.
46. Mrabet, C., Boukhachem, A., Amlouk, M., & Manoubi, T. (2016). Improvement of the optoelectronic properties of tin oxide transparent conductive thin films through lanthanum doping. *Journal of Alloys and Compounds*, 666, 392–405.
47. Rajesh Kumar, B., & Hymavathi, B. (2017). X-ray peak profile analysis of solid-state sintered alumina doped zinc oxide ceramics by Williamson–Hall and size-strain plot methods. *Journal of Asian Ceramic Societies*, 5(2), 94–103.
48. Lubna Aamir, Novel p-type Ag-WO<sub>3</sub> nano-composite for low-cost electronics, photocatalysis, and sensing: Synthesis, characterization, and application, *Journal of Alloys and Compounds*, (2020).
49. Di Chen, Guozhen Shen, Kaibin Tang, Zhenhua Liang, Huagui Zheng, AOT microemulsions-based formation and evolution of PbWO<sub>4</sub> crystals, *J. Phys. Chem. B* 108 (2004) 11280–11284.
50. P.P. Sahay, R.K. Mishra, S.N. Pandey, S. Jha and M. Shamsuddin, Structural, dielectric and photoluminescence properties of co-precipitated Zn-doped SnO<sub>2</sub> nanoparticles, *Curr. Appl. Phys.*, 13 (2013), 479–486.
51. Ahmed, A., Ali, T., Naseem Siddique, M., Ahmad, A., & Tripathi, P. (2017). Enhanced room temperature ferromagnetism in Ni doped SnO<sub>2</sub> nanoparticles: A comprehensive study. *Journal of Applied Physics*, 122(8), 083906.
52. Mythili, N., & Arulmozhi, K. T. (2014). Characterization studies on the chemically synthesized  $\alpha$  and  $\beta$  phase PbO nanoparticles. *Int. J. Sci. Eng. Res.*, 5(1), 412–416.